

Microtechnology and MEMS

Valeriy Sharapov

# Piezoceramic Sensors

 Springer

# MICROTECHNOLOGY AND MEMS

---

# MICROTECHNOLOGY AND MEMS

---

*Series Editor:* H. Fujita D. Liepmann

The series Microtechnology and MEMS comprises text books, monographs, and state-of-the-art reports in the very active field of microsystems and microtechnology. Written by leading physicists and engineers, the books describe the basic science, device design, and applications. They will appeal to researchers, engineers, and advanced students.

Please view available titles in *Microtechnology and MEMS*  
on series homepage <http://www.springer.com/series/4526>

Valeriy Sharapov

# Piezoceramic Sensors

With 493 Figures

 Springer



Professor Valeriy Sharapov  
Cherkasy State Technological University  
Instrument-making  
Shevchenko blvd. 460  
18006 Cherkasy, Ukraine  
E-mail: v.sharapov@rambler.ru

*Series Editors:*

Professor Dr. Hiroyuki Fujita  
University of Tokyo, Institute of Industrial Science  
4-6-1 Komaba, Meguro-ku, Tokyo 153-8505, Japan

Professor Dr. Dorian Liepmann  
University of California, Department of Bioengineering  
6117 Echeverry Hall, Berkeley, CA 94720-1740, USA

Microtechnology and MEMS                      ISSN 1615-8326  
ISBN 978-3-642-15310-5                              e-ISBN 978-3-642-15311-2  
DOI 10.1007/978-3-642-15311-2  
Springer Heidelberg Dordrecht London New York

Library of Congress Control Number: 2011935342

© Springer-Verlag Berlin Heidelberg 2011

This work is subject to copyright. All rights are reserved, whether the whole or part of the material is concerned, specifically the rights of translation, reprinting, reuse of illustrations, recitation, broadcasting, reproduction on microfilm or in any other way, and storage in data banks. Duplication of this publication or parts thereof is permitted only under the provisions of the German Copyright Law of September 9, 1965, in its current version, and permission for use must always be obtained from Springer. Violations are liable to prosecution under the German Copyright Law.

The use of general descriptive names, registered names, trademarks, etc. in this publication does not imply, even in the absence of a specific statement, that such names are exempt from the relevant protective laws and regulations and therefore free for general use.

*Cover design:* eStudio Calamar S.L.

Printed on acid-free paper

Springer is part of Springer Science+Business Media ([www.springer.com](http://www.springer.com))

# Preface

This book is devoted to piezoceramic sensors, which are widely used in hydroacoustics, electroacoustics, medicine, measuring, test engineering and non-destructive control. The author and his co-workers' work results are described here for the first time.

This book gives complete update information on various types of piezosensors. Each sensor transforms a physical value into an electric signal. Piezoelectric transducers and sensors, based on piezoelectric effects, are universal tools, applied for measuring various processes. They are used in research and in different industries to control the quality of production processes.

There are individual requirements for parameters of transducers and sensors to be applied in each sphere. This book gives fundamental information on technical designs and practical application of transducers and sensors. Sensors with unique qualities can be designed, according to the new technologies described. New methods of measuring physical values and designing new sensors (including piezosensors) are discussed in this book.

This book is intended for graduate students and specialists in hydroacoustics, non-destructive control, measuring technology, and development of automatic control sensors.

Cherkasy, Ukraine  
March 2011

*Valeriy Sharapov*



# Contents

<b>1</b>	<b>General Information About Piezoelectric Sensors</b> .....	1
1.1	Short Historical Essay .....	1
1.2	Determination and Classification of Piezoelectric Sensors .....	2
1.3	Properties and Descriptions of Piezomaterials .....	5
1.4	Transducer Research Methods .....	7
1.5	Piezoceramic Material and Element Parameters .....	8
1.6	Determining Piezoceramic Element Parameters .....	9
1.6.1	Defining the Electromechanical Communication Coefficient .....	9
1.6.2	Phase Measurement of Resonant $f_r$ and Antiresonant $f_a$ Frequencies of Radial and Longitudinal Fluctuations .....	9
1.6.3	Measurement of Resonant Frequency $f_r$ .....	9
1.6.4	Measurement of Antiresonant Frequency $f_a$ .....	10
1.6.5	Best (Amplitude?) Method of Measuring Resonant $f_r$ and Antiresonant $f_a$ Frequencies .....	11
1.6.6	Measurement of Frequency in the First Overtone $f_{01}$ .....	11
1.6.7	Definition of Poisson's Coefficient $\sigma$ .....	12
1.6.8	Definition of the Least Positive Root of the Frequency Equation $\eta$ .....	12
1.6.9	Relative Dielectric Permeability (Constant, Permittivity?) $\varepsilon_{33}^T/\varepsilon_0$ .....	12
1.6.10	Specific Volume Electric Resistance $\rho_v$ .....	13
1.6.11	Defining Piezo-modules $d_{31}$ and $d_{33}$ in a Dynamic Mode .....	13
1.6.12	Piezo-module $d_{33}$ in a Static Mode .....	14
1.6.13	Young's Modulus $Y_{31}^Y$ .....	14
1.6.14	Speed of Sound $v_3^D$ .....	15

1.6.15	Good Mechanical Quality $Q_m$ .....	15
1.6.16	Definition of Curie Point Temperature $T_C$ .....	15
1.7	Piezoceramic Materials .....	16
1.8	Formulas for the Calculation of Piezoceramic Material Descriptions .....	18
1.8.1	Piezoceramic Disk (Fig. 1.5) .....	18
1.8.2	Piezoceramic Bar (Fig. 1.6) .....	19
1.8.3	Piezoceramic Rectangular Plate (Fig. 1.7) .....	19
1.9	Sensor [Physical Size] Descriptions .....	21
	References .....	22
<b>2</b>	<b>Monomorph Piezoceramic Elements</b> .....	<b>25</b>
2.1	Calculating Electric Piezoceramic .....	25
2.1.1	Resonator Parameters .....	25
2.2	Equivalent Schemes for Piezoresonators .....	28
2.3	Calculate Piezoresonator Electric Parameters .....	34
2.4	Fluctuations of Piezoceramic Rods .....	47
2.4.1	Longitudinal Fluctuations of a Rod in a Transverse Field .....	48
2.4.2	Longitudinal Fluctuations of a Rod in a Longitudinal Field .....	49
2.4.3	Fluctuations of a Piezoceramic Disk .....	50
2.5	Piezoceramic Transformers .....	51
2.5.1	Piezoelectric Transformer in the Form of Thin Disks and Rings .....	55
	References .....	68
<b>3</b>	<b>Spatial Energy–Force Structure of Piezoceramic Transducers</b> .....	<b>71</b>
3.1	Synthesis of Piezoelement Spatial Energy–Force Structure .....	71
3.2	Anisotropy of Piezoceramic Materials Characteristics .....	79
3.3	Transverse Piezoelectric Transducers .....	82
3.4	Piezotransformers .....	85
3.4.1	Disk Piezotransformers .....	93
	References .....	97
<b>4</b>	<b>Measuring Circuits of Piezoelectric Sensors</b> .....	<b>99</b>
4.1	Charge Amplifiers .....	99
4.2	Voltage Amplifiers .....	110
	References .....	111
<b>5</b>	<b>Feedback in Piezoceramic Sensors</b> .....	<b>113</b>
5.1	Feedback Effect on Sensor Characteristics .....	113
5.1.1	Influence of Frequency-Dependent Feedback .....	114
5.1.2	Influence of Frequency-Independent FB .....	116
5.1.3	Feedback Influence on Nonlinear and Frequency Distortions .....	117
5.1.4	Feedback Influence on Time Constant of Sensors .....	118

5.1.5	Feedback Influence on Input and Output Resistances ....	118
5.1.6	Feedback Influence on Static Systems Errors .....	119
5.2	Piezoceramic Sensors with Spatial Electromechanical NFB .....	120
5.3	Domain-Dissipative Piezoceramic Sensors with Spatial Electromechanical NFB .....	126
5.4	Piezoceramic Sensors with Piezoelement in FB Circuit of Charge Amplifier .....	130
5.5	Electric Feedback in Piezoceramic Sensors .....	139
5.6	Sensors with Combined Feedback .....	143
5.7	Electric Damping of Piezoceramic Sensors with Feedback .....	147
5.8	Sensors with Two Feedback Channels .....	151
5.8.1	Sensors with Output Charge Amplifier and Voltage Amplifier in Additional Feedback Channel .....	160
5.8.2	Sensors with Output Voltage Amplifier and Charge Amplifier in Additional FB Channel .....	165
5.8.3	Piezosensors with Two Charge Amplifiers with Piezoelements in FB Circuits of Amplifiers .....	170
5.9	Piezosensor with Charge Amplifier and FB Channel on Voltage Amplifier .....	174
	References .....	176
<b>6</b>	<b>Bimorph and Trimorph Piezoelements</b> .....	179
6.1	Symmetric Bimorph Piezoelements .....	179
6.2	Asymmetric Bimorph Piezoelements .....	184
6.3	Trimorph Piezoelements .....	196
6.3.1	Asymmetric Planar Trimorph Piezoelements .....	196
6.3.2	Asymmetric Coplanar Trimorph Piezotransducers .....	201
6.3.3	Symmetric Coplanar Trimorph Transducer .....	209
6.4	Vibrations of Asymmetric Coplanar Trimorph Piezotransducer with FB .....	216
6.5	Technology of Bimorph Piezoelement Production .....	224
	References .....	228
<b>7</b>	<b>Devices to Control and Diagnose Bimorph Piezoelements</b> .....	231
7.1	Defects of Bimorph Piezoelements .....	231
7.2	Defect Diagnostics by AFC .....	232
7.3	Diagnostics of Defects by Pulse Characteristic .....	237
7.4	Diagnostics of Defects by Transitive Characteristic .....	241
7.4.1	Device Based on Aperiodic Networks .....	245
7.5	Devices Based on Active Oscillator Circuit .....	247
	References .....	249

<b>8</b>	<b>Piezomagnetic Sensors</b> .....	253
8.1	Influence of Magnet Design Factors on Sensor Characteristics ....	253
8.1.1	Cylindrical Magnets .....	253
8.1.2	Rectangular Magnets .....	257
8.2	Piezomagnetic Sensors of Tachometers .....	261
8.2.1	Piezomagnetic Sensor Models .....	266
8.3	Improvement of Piezomagnetic Sensor Characteristics .....	273
8.3.1	Output Signal Enhancement .....	273
8.3.2	Accuracy Improvement Methods .....	276
8.3.3	Sensor Design Simplification .....	278
8.3.4	Suppression of Vibration Hindrances .....	280
8.4	Piezomagnetic Electro-acoustic Transducers .....	282
	References .....	284
<b>9</b>	<b>Hydroacoustic Transducers</b> .....	289
9.1	Classification and Characteristics .....	289
9.2	Ratios of Electromechanical Transformations .....	291
9.3	Cylindrical Piezoceramic Transducers .....	294
9.4	Lamellar and Spherical Piezoceramic Transducers .....	298
9.5	Basic Requirements for Projected Transducers .....	300
9.6	Selection of Energy Transformation Method and Mode Shape ....	301
9.7	Certain Transducer Designs .....	302
9.8	On One Method of Low-Frequency Acoustic Vibration Creation .....	309
	References .....	313
<b>10</b>	<b>Transducers with Non-destructive Control</b> .....	317
10.1	Designs and Specifications of Ultrasonic Monitor Piezotransducers .....	318
10.1.1	Coefficient of Electromechanical Transformation .....	320
10.1.2	Piezotransducer Amplitude–Frequency Response (AFR) .....	320
10.1.3	Form of Acoustic Field Created .....	321
10.2	Resonant Volume Piezotransducers .....	323
10.3	Non-resonant Excitation of Piezoelements .....	327
	References .....	331
<b>11</b>	<b>Sensors of Korotkoff Sounds</b> .....	333
11.1	General Information .....	333
11.2	Enhancement of KSS Sensitivity .....	337
11.3	On Optimum Load Resistance of KSS Piezoelements .....	344
11.4	Feedback in Korotkoff Sound Sensors .....	347
11.5	Hindrances at Arterial Pressure Measurement .....	350
11.6	Sensors of Pulse Waves .....	354
	References .....	355

- 12 Electro-acoustic Transducers** ..... 357
  - 12.1 General Information ..... 357
  - 12.2 Transfer Function Calculation of Electro-acoustic Transducers ... 361
  - 12.3 Chladni Figures and Transducer Directional Diagrams ..... 366
  - 12.4 Methods of Electro-acoustic Transducer Uprating ..... 367
  - 12.5 Electro-acoustic Transducers in Active Oscillator Schemes ..... 375
  - References ..... 379
  
- 13 Piezoceramic Accelerometers** ..... 381
  - 13.1 Monolithic Accelerometers ..... 382
  - 13.2 Multi-element Accelerometers ..... 386
  - 13.3 Accelerometer Designs ..... 390
  - 13.4 Three-Dimensional Accelerometers ..... 398
  - 13.5 Accelerometers Based on Bimorph and Piezoelectric Elements ... 400
  - 13.6 Domain-Dissipative Accelerometer  
and Accelerometers with Feedback ..... 404
  - References ..... 406
  
- 14 Resonant Piezoceramic Sensors** ..... 409
  - 14.1 Resonant Contact Sensors ..... 410
  - 14.2 Measurement of Contact Rigidity and Real Contact Area ..... 419
  - 14.3 Frequency-Modulated Oscillation Use  
for Resonant Piezosensor Excitation ..... 422
  - 14.4 Negative Feedback in Resonant Piezosensors ..... 425
  - 14.5 Piezosensors with Ultrasonic Concentrators ..... 428
  - 14.6 Constructive Control Methods of Force  
and Pressure Piezosensor Characteristics ..... 438
  - 14.7 Piezorezonant Accelerometer ..... 443
  - 14.8 Sensor on Acoustically Connected Resonators ..... 445
    - 14.8.1 For Gases ..... 446
  - References ..... 448
  
- 15 Sensors with Piezoelements in Scheme Electric Filters** ..... 453
  - 15.1 Schemes of Electric Filters ..... 453
    - 15.1.1 Low-Pass Filters ..... 456
    - 15.1.2 High-Pass Filters ..... 458
  - 15.2 Sensors with Piezoelements in Low-Pass Filter Schemes ..... 459
  - 15.3 Sensors with Piezoelements in High-Pass Filter Schemes ..... 460
  - 15.4 Sensors with Piezotransformers in Electric Filter Schemes ..... 461
  - References ..... 468
  
- 16 Piezoceramic Scanners for Probe Nanomicroscopes** ..... 471
  - 16.1 Nanotechnologies and Nanomicroscopes ..... 471
    - 16.1.1 Functional Mechanical Nodes ..... 472
  - 16.2 Methods of Scanning Probe Microscopy ..... 473
    - 16.2.1 Scanning Tunneling Microscopy ..... 473
    - 16.2.2 Atomic-Force Microscopy ..... 476



16.2.3	Electric Force Microscopy .....	478
16.2.4	Magnetic Force Microscopy .....	479
16.3	Scanners on Hollow Piezoceramic Cylinders .....	481
16.4	Scanners Based on Flat Bimorph Piezoelements .....	485
	References .....	488
<b>Index</b>	.....	491

# Chapter 1

## General Information About Piezoelectric Sensors

### 1.1 Short Historical Essay

The history of piezoelectricity development totals more than 120 years. In 1880, Pierre and Jacques Curie found that under pressure some materials develop surface electrical charges. Subsequently, this effect was named the “piezoeffect”; electricity caused by mechanical pressure was called “piezoelectricity”, and materials (quartz, turmalin, segnet salt, etc.) in which there is this phenomenon were called “piezoelectric” [1].

In 1881, G. Lippmann foretold that electric voltage enclosed in piezoelectric material would cause mechanical pressure and elastic deformations [2]. This was proven experimentally by P. Curie and J. Curie [3]. The phenomenon has been named the “return piezoeffect.” The word “piezo”, borrowed from Greek, means “I press.”

Practical application of the piezoelectric effect began in 1917 when a French mathematician and physicist, Paul Langevin, suggested using an ultrasonic echo ranging device for detection of underwater objects. In this device (a projector and receiver of ultrasonic signals), quartz plates were built between steel overlays, thus lowering the resonant frequency of the transducer [4]. Initially, an ultrasonic locator was used by Langevin in a quality echo sounder. Further improvement led to the creation of modern ultrasonic echo sounders and various underwater detection devices (including those attached to submarines).

Soon after Langevin’s invention, the first piezoelectric microphones, phones, sound pickups, devices for sound recordings, devices for vibration measurements, forces and accelerations, etc. were created.

Piezoelectric plates and pivots were to be used as the stabilizing elements; frequency of electronic high-frequency generators followed as an important stage in the application history of piezoelectricity. Applications were based on a strong frequency piezoelement dependence on electrical impedance near the mechanical resonance, as investigated by W. Cady in 1922 [5].

In 1925, G. Pierse used an acoustic interferometer for ultrasound speed measurement in gases [6]. It was the first piezoelectric plate application for measuring the acoustic properties of a substance.

This opened the possibility of detecting internal defects in solid materials by using ultrasonic waves; this was an important application of piezoelectricity for practical purposes. C. Sokolov received a USSR copyright for the invention of the first ultrasonic flaw detector (non-destructive testing) [7].

Development of measurement methods concerning speed and absorption of ultrasound, based on light diffraction effects on ultrasonic waves, followed. Piezoelectric transducers were used by P. Debye and F. Sears [8] in 1932, for hypersonic research of substances, as well as by R. Lucas and P. Biquard [9]. Work involving this method was used for speed measurement and measuring ultrasound absorption in liquids and solids, which began in 1936.

In 1944, at the USSR's Lebedev Physical Institute, B.M. Wool and I.P. Goldman first developed a method of synthesizing piezoceramic titanium barium ( $\text{BaTiO}_3$ ) [10, 11]. Titanium, a barium preliminary, was polarized in a strong electric field; soon, piezoceramic electroacoustic transducers were developed [12, 13].

The scope of piezoelectric transducers extended rapidly after 1945. A variety of new areas, such as ultrasonic delay lines, ultrasonic medical therapy and diagnostics, level gauges, devices for continuous industrial control of physical and chemical substance properties, and other devices with wide applications were found for piezoelectric transducers. At the same time, more effective electroacoustic transducers became available.

Development of the theory and practice of piezoelectric devices is connected also with: U. Mason [12, 14, 15], L. Bergman [16], W. Cady [5, 17], R. Thurston [18], G.V. Katts [19], M. Onoe [20], H. Tiersten [21], N.N. Andreev [22, 23], A.A. Harkevich [24], I.P. Goljamina [25], V. Domarkas and R. Kazys [26, 27], V.V. Malov [28], A.N. Kutsenko [29], L.J. Gutin [30], N.A. Shulga, A.M. Bolkisev [31], V.V. Lavrinenko [32], I.A. Glozman [33], S.I. Pugachev [34], O.P. Kramarov [35], A.F. Ulitko [36], I.G. Minaev [37], A.I. Trofimov [38], A.E. Kolesnikov [39], M.V. Korolev [35], I.N. Yermolov [40], R.G. Dzhagupov [41], V.M. Pluzhnikov [42], P.O. Gribovskiy [43], P.G. Pozdnyakov [44], V.M. Sharapov [45], and many others.

## 1.2 Determination and Classification of Piezoelectric Sensors

This book is devoted to piezoelectric transducers; therefore, it is necessary to agree on terminology. Transducers will transform one physical size or one type of information to another physical size or another type of information. Therefore, a sensor can be called a pressure transducer in an electrical signal, or a transducer of electric voltage from one level of voltage to another level (electric transformer).

In technical language there is also the concept "sensor", which is equivalent to the concept "primary transducer."

In this book, there will be information about piezoelectric sensors (transducers of physical sizes to an electric signal) and also about other piezoelectric transducers.

Piezoelectric transducers contain crystals or structures which electrosize under the influence of mechanical pressure (a “straight-line piezoeffect”) and deformed structures in an electric field called “return piezoeffect.”

A feature of the piezoeffect is sign sensitivity, when a charged sign changes or when compression is replaced; this sign stretching and changing produces a directional field change [46, 47].

Many crystal substances possess piezoelectric properties: quartz, turmalin, niobium, lithium, segnet salt, etc. Artificial polycrystalline materials are also produced which polarize in the electrical field (piezoelectric ceramics), e.g., titanium barium, titanium lead, zirconium lead, etc. [48].

Piezoelectric transducers are used for measuring mechanical parameters (effort, pressure, acceleration, weight, angular speed, moments, deformations, etc.), thermal sizes (temperature, expense, vacuum, electric parameters, etc.) and for structure control, gas concentration, humidity, and micro weights [28]. For accuracy, these devices in many cases surpass transducers based on other physical resolution principles.

Piezoelectric sensors can be divided into two large classes depending on their basic physical effects:

- Sensors in the first class use a straight-line piezoeffect. They are used for measuring linear and vibrating accelerations, dynamic and quasistatic pressure and efforts, as well as parameters of sound and ultrasonic fields, etc. [45].
- A second but no less extensive class of sensors concerns the so-called resonant piezotransducers [28, 38, 49], which use the return piezoeffect. They are resonant sensors from piezoelectric resonators, and they can also produce straight-line piezoeffects. (These are resonant piezoelectric transformer sensors.) In addition, other physical effects can be used, e.g., tensosensitivity, acoustosensitivity, thermosensitivity, etc., allow utilization for measurement of static and/or dynamic pressure and efforts, linear and vibrating accelerations, concentration of gas substances, viscosity, inclination corners, etc. [41, 45].

The largest class of piezoceramic sensors can be classified as follows:

1. Sensors on applied materials:
  - Monocrystal materials (quartz, niobium lithium, etc.)
  - Polycrystalline materials (piezoceramic)
2. By fluctuations:
  - On the linear size
  - On the radial
  - On curving
  - On torsion (rotation?)
  - On the shift (shear modes)
  - On surface acoustic waves
  - On a combined configuration

## 3. By the physical effects:

- Thermosensitivity
- Tensosensitivity
- Acoustosensitivity
- Gyrosensitivity
- Contact (using contact rigidity and the actual contact area, etc.)
- Domain dissipative, etc.

## 4. By the quantity of the piezoelements:

- Monoelement
- Bimorph (symmetric or asymmetric)
- Threemorph, etc.

## 5. By destination:

- For measurement of dynamic pressure and efforts
- For measurement of linear accelerations
- For measurement of vibration parameters
- For measurement of static pressure and efforts
- For measurement of blow parameters
- For measurement of sound pressure
- For humidity measurement
- For viscosity measurement
- For hydroacoustics
- For gyroscopes
- For gas analyzers
- For temperature measurement
- For contact rigidity measurement
- For measurement of the actual area of contact
- For magnetic size measurement
- For optics measurement
- For micromoving measurement
- For dust concentration measurement
- In ultrasonic technology
- In electroacoustics
- In automatics devices
- In communication
- In electronic techniques and radio engineering
- In medicine:
  - For ultrasonic tomographs
  - For pulse measurement
  - For tone measurement by Korotkov
  - For urology
  - For ophthalmology

And others.

### 1.3 Properties and Descriptions of Piezomaterials

The piezoeffect's physical nature can be shown with quartz, the most common piezoelectric crystal [46, 47]. Figure 1.1a shows the basic crystal quartz cell structure. The cell as a whole is electrically neutral; however, it is possible to allocate three directions which pass through the center and two different uniter ion polars. The polars are called electric axes or axes  $X$ , with polarization vectors  $P_1$ ,  $P_2$ , and  $P_3$ .

If force  $F_x$  in regular intervals is distributed on the side, a perpendicular axis  $X$  results; the broken electric neutrality of the elementary cell is enclosed in a quartz crystal along the axis. Shown in Fig. 1.1b, the unformed cell ( $P_2$  and  $P_3$  on axis  $X$  vector projections) decreases with compression or increases with vector  $P_1$  stretching. As a result, the polarization vector appears equally effective, and there are corresponding polarizing charges on the sides. Compression signs are shown in Fig. 1.1b. It is easy to see that cell deformation does not influence the electric condition along axis  $Y$ . Here the vector projection sum is equal to zero, for  $P_{2Y} = P_{3Y}$ .

Polarizing charge formation on the sides and perpendicular axes  $X$ , with force on axis  $X$ , is called the *longitudinal piezoeffect*.

Mechanical pressure enclosed along one of the  $Y$  axes is called *mechanical axes*. The geometrical sum of vectors  $P_2$  and  $P_3$  on a  $Y$  axis projection is equal to zero. When the  $Y$  axis piezoelement sides are perpendicular, charges are not

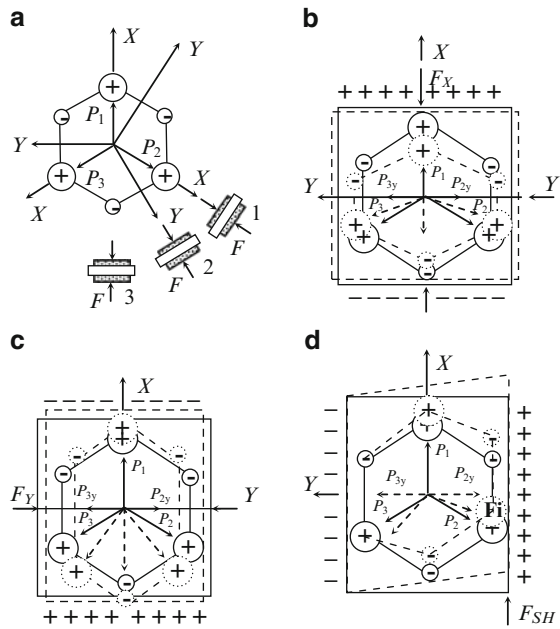


Fig. 1.1 Elementary quartz cell crystal structure

formed. However, vectors  $\mathbf{P}_2$  and  $\mathbf{P}_3$  on the  $X$  axis projection sum are not equal to vector  $\mathbf{P}_1$ . Hence, with piezoelement compression, as represented in Fig. 1.1c, the sum exceeds  $\mathbf{P}_1$ . As a result, the bottom side forms positive charges and the top side forms negative charges. The formation of side charges, perpendicular to the loaded sides, is called *transverse*.

When uniformly loaded from different directions, as for example in hydrostatic compression, the quartz crystal remains electrically neutral. When loading  $Z$  axis perpendicular to axes  $X$  and  $Y$  with a crystal optical axis, the quartz crystal remains electrically neutral. Mechanical pressure shift deformation is shown in Fig. 1.1d. When the geometrical sum of vectors  $\mathbf{P}_2$  and  $\mathbf{P}_3$  on  $X$  axis projections is equal to vector  $\mathbf{P}_1$  directed on  $X$  axes and on the sides of perpendicular  $X$  axes, the charge does not increase. However, when vectors  $\mathbf{P}_2$  and  $\mathbf{P}_3$  on the  $Y$  axis are not equal projections and the  $Y$  axis sides are perpendicular, there is a charge.

When considering the physical nature, the piezoeffect shows that intense quartz charges can rise between three side steams. The polarizing quartz charge is a vector that can be described by three components. The intense condition is characterized as a second-rank tensor with nine components.

A piezoelectric module defining charge dependences from an intense condition is a third-rank tensor; it is defined by 27 components.

However, tensor mechanical pressure contains only six independent components, which are designated as  $\sigma_{11} = \sigma_1$ ,  $\sigma_{22} = \sigma_2$ ,  $\sigma_{33} = \sigma_3$ ,  $\sigma_{23} = \sigma_4$ ,  $\sigma_{13} = \sigma_5$ , and  $\sigma_{12} = \sigma_6$ . It passes to a simplified piezo-module form presented in a table containing 18 components:

$$d_{ij} = \begin{bmatrix} d_{11}d_{12}d_{13}d_{14}d_{15}d_{16} \\ d_{21}d_{22}d_{23}d_{24}d_{25}d_{26} \\ d_{31}d_{32}d_{33}d_{34}d_{35}d_{36} \end{bmatrix}. \quad (1.1)$$

With the piezo-module table, it is possible to calculate charge density on all three sides after any pressure [46].

The basic advantages of quartz are great hardness, insolubility in water, stability when exposed to some acids, small thermal expansion, extremely good mechanical quality ( $10^5$ – $10^6$ ), and parameter stability ( $10^{-3}$ – $10^{-5}\%$ ).

However, the electromechanical communication coefficient of quartz is approximately ten times greater, and the piezo-modules are less than the corresponding piezoceramic parameters. In addition, quartz has low dielectric permeability and its own plate capacity; therefore, the shunting capacity of the cable and entrance chains in the measuring devices considerably reduces transducer sensitivity. The important constraining factor in pressure quartz transducer utilization is its high cost and production difficulties [50, 51].

The most utilized piezoelectric materials are piezoceramics, which appeared only in the early 1960s when industrial synthesized natural piezoelectric materials like quartz were mastered. With high-sensitivity segnet salt, turmalin and others, the mechanical durability was raised by temperature stability. Now in domestic and foreign literature, many publications speak about piezoceramic element applications, so they have been introduced to the industry [41].

Piezoceramics possess many advantages.

Piezoceramic elements are rather economical, and they possess high radiating firmness in various active environments. Only hydrofluoric acid is capable of having a destroying effect on piezoceramics; thus, piezoceramic devices can be utilized in many difficult chemical situations.

When compared with quartz, piezoceramic material has a low Curie  $T_K$  point value. For quartz this  $T_K$  value =  $570^\circ\text{C}$ , while for piezoceramics with titanium barium the  $T_K$  value is  $100\text{--}200^\circ\text{C}$ . There are high-temperature piezoceramic materials with Curie points within quartz matter. Hence, some piezoceramic-made elements of IITC (PZT) do not lose working capacity at temperatures of  $300\text{--}400^\circ\text{C}$ , e.g., IITC-21 has  $T_K = 400^\circ\text{C}$ . With cobalt, they are able to maintain a temperature of  $700^\circ\text{C}$  and more.

The wide temperature ranges allow piezoceramic sensor usage from  $400$  to  $270^\circ\text{C}$ . Moreover, special transducers can be used for pressure measurement in internal combustion engine cylinders, where temperatures fluctuate from normal to  $+1,600^\circ\text{C}$ .

Piezoceramic sensors with decimals increase the measurement range usage.

Piezoceramic sensors have high resolution; as an illustration, if a 100T locomotive is put on piezoelectric scales and the measurement range on the panel of the charging amplifier is switched, it is possible to measure the additional weight of a pencil put on the locomotive's footboard.

Piezoelectric transducers can maintain high pressures, measuring pressures to 10,000 bar. They have great rigidity; that is especially important when manufacturing measurement dynamometers in a wide range of frequencies.

## 1.4 Transducer Research Methods

The piezoelectric material “deformation” theory developed from a joint electro-dynamics and mechanics project; recently, this emerged as an independent field of study [31].

Anisotropy of piezoelectric material's physical and mathematical properties and electromagnetic field interrelations with mechanical movements complicate deformation and durability description processes. Considerable attention has been given to creating and developing quantitative analyses.

Basic linear theory electroelasticity parities [31] consisted of equations describing the mechanical piezoeffect. These equations follow preservation laws and necessary geometrical communications, and are fair for any linear environment. Maxwell equations describe the environmental electrical phenomena. Communication between two types of equation variables is defined by physical parities – the piezoeffect equations. Electric induction vectors, an intense electric field, and symmetric mechanical tensor pressure cause deformations. Linear communication factors are complex. Introduction of the complex factors makes it possible to consider dissipation in piezoelectric material cyclic deformation.



The piezoelectric body equation-defining system consists of 22 differential equations. Regional electroelasticity problems are possible only in rare instances for elementary areas. It is necessary to be satisfied with an approached decision [31].

Effective construction remedies of the approached decision vary. Different formulations make it necessary to find a corresponding variation principle with a stationary value.

To understand piezoelectric body proceeding processes, one-dimensional problems for bodies with a degenerative geometry, e.g., cores, thin disks and plates, rings, and infinite cylinders, have essential value. The fluctuations can be described by scalar equations when exact decisions are needed.

An alternative approach is piezoelectric material replacement by an equivalent electrical scheme, and then making subsequent calculations under the electric chains theory [19]. This approach is natural with coordination questions and with a general electric chain analysis, which is part of the piezoelectric material equivalent circuit. But questions of mechanical and electrical durability or optimum design remain in relation to electric chain frameworks.

One-dimensional problems have a special practical value. First, one-dimensional fluctuations are found in many concrete devices; second, complex physical parity factors are experimental on one-dimensional measurements.

Extensive problems exist with regard to axial symmetry piezoelectric body fluctuations. Mathematical axial symmetry fluctuations, spatial from a physical point, are usually described by two-dimensional equations [31].

Theoretical automatic control methods are also widely applied to transducer analysis [26, 27]. The most exact results can be derived by experimentation.

## 1.5 Piezoceramic Material and Element Parameters

Parameters of piezoceramic materials are normalized [52] and defined [53]. The basic characteristics in piezoceramic materials are:

1. Electromechanical communication ( $K_p$ )
2. Relative dielectric permeability (constant or permittivity) ( $\epsilon_{33}^T/\epsilon_0$ )
3. Specific volume electric resistance ( $\rho_V$ )
4. Density ( $\rho$ )
5. Water absorption ( $W$ )
6. Piezo-modules in a dynamic mode ( $d_{31}, d_{33}$ )
7. Piezo-modules in a static mode ( $d_{31}$ )
8. Young's modulus ( $Y_{31}^Y$ )
9. Speed of a sound ( $v_i^j$ )
10. Good mechanical quality ( $Q_M$ )
11. Relative frequency deviation in the range of working temperatures from the frequency measured at the adjustment temperature ( $\delta f_\Theta/f_i$ )

12. Corner of dielectric losses tangent in weak electric fields ( $\text{tg } \delta$ )
13. Electrical durability ( $E_{\text{np}}$ )
14. Temperature of Curie ( $T_C$ )
15. Mechanical durability limit with static compression ( $\sigma_{\text{compr}}$ )
16. Mechanical durability limit with static bend ( $\sigma_b$ )
17. Mechanical durability limit with static stretching ( $\sigma_{\text{str}}$ )

Additional characteristics:

18. Piezo-module in a dynamic mode
19. Piezo-module in quasistatic mode
20. Mechanical durability limit with static stretching

Additional characteristics would be defined when necessary by manufacturers.

## 1.6 Determining Piezoceramic Element Parameters

### 1.6.1 *Defining the Electromechanical Communication Coefficient*

The electromechanical communication  $K_p$  coefficient is calculated by the formula:

$$K_p = \sqrt{\frac{\eta^2 - \sigma^2}{2(1 + \sigma)} \left(1 - \frac{f_r^2}{f_a^2}\right)}, \quad (1.2)$$

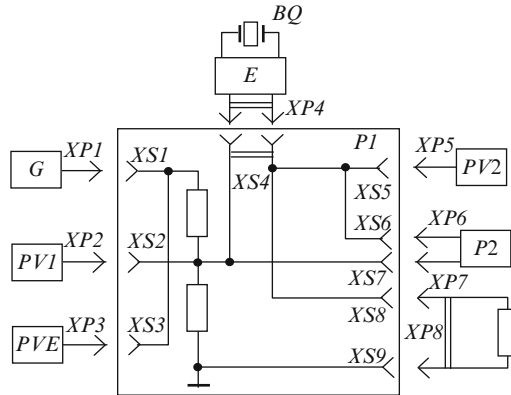
where  $\eta$ , the least positive root of the frequency equation;  $\sigma$ , Poisson's coefficient;  $f_r$ , resonant frequency, Hz;  $f_a$ , antiresonant frequency, Hz.

### 1.6.2 *Phase Measurement of Resonant $f_r$ and Antiresonant $f_a$ Frequencies of Radial and Longitudinal Fluctuations*

The installation diagram used for measurement is shown in Fig. 1.2.

### 1.6.3 *Measurement of Resonant Frequency $f_r$*

Established in nests  $XS4$  holder  $E$  with sample  $BQ$ . From generator  $G$  on a two-port network  $R1$  input (socket  $XS1$ ) gives a signal of such value that on an input of the sample (socket  $XS2$ ) the voltage was  $200 \pm 20$  mV. Voltage supervised with the help of millivoltmeter  $PV1$ . Socket  $XP8$  connects with loading resistor  $R3^*$  ( $R3^* =$



**Fig. 1.2** Installation for measuring  $f_r$  and  $f_a$ :  $G$ , generator of signals;  $PV1$ ,  $PV2$ , millivoltmeters;  $PF$ , electronic frequency meter;  $XP1$ - $XP8$ ,  $XS1$ - $XS9$ , sockets;  $BQ$ , test piece;  $E$ , test piece holder;  $P1$ , passive two-port network ( $R1 = 68 \text{ ohm}$ ,  $R2 = 7.6 \text{ ohm}$ )  $R1 = (8 - 10)R2$ ,  $R1 + R2 = R_{\text{out a gen}}$ ,  $R3^* = 1 \text{ ohm}/100 \text{ kohm}$ ; Connecting mark cables PK-75-4-11 – PK-75-4-16 no more than 0.5 m in length

2 kohm – for samples  $16 \times 3 \times 3 \text{ mm}$  and  $R3^* = 2 \text{ kohm}$  – for samples  $\varnothing 10 \times 1 \text{ mm}$ , resistance values are specified roughly). Smoothly changing generator  $G$  frequency achieves the maximum deviation of an arrow millivoltmeter  $PV2$ , thus voltage on the exit sample should be within 10–15 mV.

If voltage on millivoltmeter  $PV2$  is distinct from that specified above, it is necessary to pick up the resistance value of loading resistor  $R3^*$ . Then, changing the frequency of generator  $G$  achieves phase zero under the indication phase meter  $P2$ . If signal value for the phase meter is not enough, an amplifier with a minimum phase shift in a range of frequencies and its further account is supposed to be used. Thus, it is necessary to calibrate a new phase meter  $P2$ . In phase zero there is a corresponding resonant frequency  $f_r$  which measure by a frequency meter  $PF$ .

A tuning phase meter is not supposed to be for measuring resonant frequency  $f_r$ .

### 1.6.4 Measurement of Antiresonant Frequency $f_r$

To socket  $XP8$  connect loading resistor  $R3^*$  ( $R3^* = 50 \text{ kohm}$  – for samples  $16 \times 3 \times 3 \text{ mm}$  and  $R3^* = 50 \text{ ohm}$  – for samples  $\varnothing 10 \times 1 \text{ mm}$  of resistance value are specified roughly). Smoothly changing generator  $G$  frequency achieves the minimum deviation of an arrow millivoltmeter  $PV2$ , thus voltage should be within 1–3 mV.

If voltage on millivoltmeter  $PV2$  is different from that specified above, it is necessary to pick up the resistance value of the loading resistor  $R3^*$ . Then, change the generator  $G$  frequency achieves phase zero under the indication phase meter  $P2$ .

If a signal value for the phase meter is not enough, the amplifier takes into account the phase shift. Thus, it is necessary to calibrate a new phase meter  $P2$ .

When measuring antiresonant frequency, it is necessary to use the holder with a minimum electric capacity. If antiresonant frequency displacement, at the expense of the holder's electric capacity, is more than 5% from the static electric capacity, it can be defined by the formula:

$$\frac{\Delta f_a}{f_a} = \frac{f_a - f_r}{f_r - f_a} \frac{C_{\text{hol}} - 0.05C_0}{C_0 R_0^2}, \quad (1.3)$$

where  $f_a$ , antiresonant frequency, Hz;  $f_r$ , resonant frequency, Hz;  $C_{\text{hol}}$ , electric capacity of the holder, pF;  $C_0$ , electric static capacity, pF;  $R_0 = R_r/|X_{C_0}| = 2\pi f_r C_0 R_r$ , test piece resistance on the resonant to frequency of jet resistance of the test piece, ohm;  $|X_{C_0}|$ , jet resistance of electric static capacity;  $R_r$ , resistance of the sample on the resonant frequency, calculated with definition of good mechanical quality, ohm.

### 1.6.5 *Best (Amplitude?) Method of Measuring Resonant $f_r$ and Antiresonant $f_a$ Frequencies*

Measurements using Fig. 1.2 without a phase meter. The frequency  $f_r$  value corresponds to the maximum deviation millivoltmeter  $PV2$ ; and the minimum deviation millivoltmeter  $PV2$  corresponds to the frequency  $f_a$ . Frequency value is measured by a frequency meter  $PF$ .

### 1.6.6 *Measurement of Frequency in the First Overtone $f_{01}$*

Measurement of frequency in the first overtone  $f_{01}$  radial and longitudinal fluctuations on an earlier specified installation (Fig. 1.2) without applying a phase meter was performed in the following order: to socket  $XP8$ , connect loading resistor  $R3^*$  ( $R3^* = 2$  kohm, for samples  $16 \times 3 \times 3$  mm and  $R3^* = 1$  ohm for samples  $\varnothing 10 \times 1$  mm, values of resistance are specified roughly). Smoothly changing generator  $G$  frequency to increase from  $f_r$  will achieve the maximum deviation of an arrow on millivoltmeter  $PV2$ . Thus, voltage should be within 5–15 mV.

If voltage on millivoltmeter  $PV2$  is different from that specified above, it is necessary to pick up resistance values by loading resistor  $R3^*$ . The maximum deviation of the arrow millivoltmeter  $PV2$  corresponds to the frequency of the first overtone  $f_{01}$ , and is measured by a frequency meter  $PF$ .

### 1.6.7 Definition of Poisson's Coefficient $\sigma$

Poisson's coefficient  $\sigma$  depends on the value of factor  $\beta$  chosen from Table 1.1.

The coefficient is calculated by the formula:

$$\beta = \frac{f_{01}}{f_r}, \quad (1.4)$$

where  $f_{01}$ , frequency of the first overtone, Hz;  $f_r$ , the resonant frequency is defined by a peak method, Hz.

### 1.6.8 Definition of the Least Positive Root of the Frequency Equation $\eta$

The least positive root of the frequency equation  $\eta$  depends on the value of Poisson's coefficient  $\sigma$  chosen from Table 1.2.

### 1.6.9 Relative Dielectric Permeability (Constant, Permittivity?) $\epsilon_{33}^T/\epsilon_0$

Relative dielectric permeability of a material is calculated by the formula:

$$\epsilon_{33}^T/\epsilon_0 = \frac{11.3C_0b}{S_e}, \quad (1.5)$$

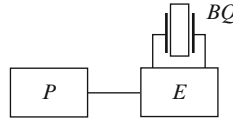
where  $C_0$ , static electrical capacity of the test piece, pF;  $b$ , thickness of the sample, cm;  $S_e$ , surface area of an electrode, cm<sup>2</sup>.

**Table 1.1**

$\beta$	2.6746	2.6670	2.6559	2.6529	2.6448	2.6375	2.6304	2.6237	2.6173
$\sigma$	0.24	0.25	0.26	0.27	0.28	0.29	0.30	0.31	0.32
$\beta$	2.6097	2.6040	2.5963	2.5897	2.5832	2.5775	2.5705	2.5642	
$\sigma$	0.33	0.34	0.35	0.36	0.37	0.38	0.39	0.40	

**Table 1.2**

$\sigma$	0.24	0.25	0.26	0.27	0.28	0.29	0.30	0.31	0.32
$\eta$	2.0112	2.0179	2.0238	2.0300	2.0362	2.0425	2.0488	2.0551	2.0612
$\sigma$	0.33	0.34	0.35	0.36	0.37	0.38	0.39	0.40	0.41
$\eta$	2.0673	2.0735	2.0795	2.0855	2.0915	2.0974	2.1041	2.1109	2.1150
$\sigma$	0.42	0.43	0.44	0.45	0.46	0.47	0.48	0.49	0.50
$\eta$	2.1208	2.1266	2.1323	2.1380	2.1436	2.1492	2.1548	2.1604	2.1659



**Fig. 1.3** Installation for measurement  $C_0.P$ , universal bridge;  $BQ$ , test piece;  $E$ , test piece holder

In the formula, actual linear size values for each sample should be substituted (Fig. 1.3).

### 1.6.10 Specific Volume Electric Resistance $\rho_v$

Specific volume electric resistance  $\rho_v$  (Gohm  $\cdot$  cm), the defined test sample, measuring resistance of its isolation with constant voltage no more than 100 V. Relative measurement error should remain under  $\pm 20\%$ . Resistance readout measured for 1 minute from giving the measured pressure.

Value of the specific volume electrical resistance  $\rho_v$  is calculated by the formula:

$$\rho_v = R \frac{S_e}{b}, \quad (1.6)$$

where  $R$ , resistance of isolation, Gohm;  $S_e$ , area of an electrode surface,  $\text{cm}^2$ ;  $b$ , thickness of the test piece, cm.

### 1.6.11 Defining Piezo-modules $d_{31}$ and $d_{33}$ in a Dynamic Mode

Piezo-module  $d_{31}$  (Kl/N) in a dynamic mode is calculated using the formula:

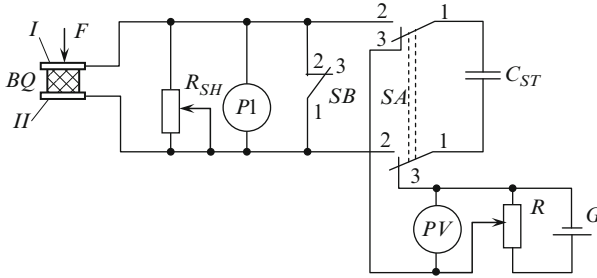
$$d_{31} = \frac{0.19 \times 10^{-5} K_p}{f_r} \frac{2}{D} \sqrt{\frac{\varepsilon_{33}^T}{\varepsilon_0} \frac{1}{\rho}}, \quad (1.7)$$

where  $K_p$ , electromechanical communication coefficient;  $D$ , disk diameter, cm;  $f_r$ , resonant frequency of the radial fluctuations, Hz;  $\varepsilon_{33}^T/\varepsilon_0$ , relative dielectric permeability;  $\rho$ , density,  $\text{cm}^3$ .

Piezo-module  $d_{33}$  (C/N) in a dynamic mode is defined by measuring resonant  $f_r$  and antiresonant  $f_a$  frequencies of longitudinal fluctuations using the formula:

$$d_{33} = \frac{0.24 \times 10^{-5} \pi}{f_r f_a l} \sqrt{\frac{(f_a^2 - f_r^2) \varepsilon_{33}^T}{2 \rho \varepsilon_0}}, \quad (1.8)$$

where  $f_r$ ,  $f_a$ , resonant and antiresonant frequencies, Hz;  $\varepsilon_{33}^T/\varepsilon_0$ , relative dielectric permeability;  $l$ , test piece length, cm;  $\rho$ , density,  $\text{g}/\text{cm}^3$ .



**Fig. 1.4** Installation for measurement  $d_{33}$ : 1, 2, 3 – switch and button positions;  $I$  – mobile electrode to which  $F$  is loaded;  $BQ$  – test piece;  $II$  – motionless electrode  $R_{SH}$  – shunting resistance for adjusting galvanometer sensitivity;  $P1$  – galvanometer ballistic mirror;  $SB$  – button closing galvanometer chain;  $SA$  – dual switch on two positions;  $C_{ST}$  – standard condenser (steals up experimentally, with approximate electric capacity 1,000–5,000 pF);  $PV$  – direct current voltmeter, a class 0.5 that limits measurements to 30 In;  $R$  – potentiometer, which helps establish necessary voltage on standard condenser;  $G$  – source of direct current voltage to 30 V

### 1.6.12 Piezo-module $d_{33}$ in a Static Mode

Piezo-module  $d_{33}$  in a static mode is defined by measuring the charge value on the electrodes of the test piece, when removing the loading enclosed on the polarization axis. The installation block diagram is shown in Fig. 1.4. Electrodes should be located perpendicularly to the loading direction.

Piezo-module  $d_{33}$  is calculated by the formula:

$$d_{33} = \frac{Q}{F} = K\alpha, \tag{1.9}$$

where  $Q$ , charge emergent on electrodes, C;  $F$ , force enclosed in the test piece, H;  $K$ , correction coefficient from  $F$ ;  $\alpha$ , mirror ballistic galvanometer light index deviation at measurement, mm.

The sample’s emergent charge under force is measured by a galvanometer.

Force exerted on the sample by a special adaptation gives a chance to sharply remove enclosed mechanical stress.

The wire capacitance, connecting the sample with the installation, should be no more than 10 pF from installation to the galvanometer, and no more than 110 pF. Relative error of the Piezo-module  $d_{33}$  should be no more than  $\pm 10\%$ .

### 1.6.13 Young’s Modulus $Y_{31}^Y$

Young’s modulus  $Y_{31}^Y$  (Pa), in a dynamic mode, is defined using the formula:

$$Y_{31}^Y = \frac{0.4\pi^2}{\eta^2} f_r^2 \frac{D^2}{4} \rho (1 - \sigma^2), \tag{1.10}$$

where  $f_r$ , resonant frequency of radial fluctuations, Hz;  $D$ , disk diameter, cm;  $\rho$ , density, g/cm<sup>3</sup>;  $\sigma$ , Poisson's coefficient;  $\eta$ , least positive root of frequency equation chosen from Table 1.2, depending on value  $\sigma$ .

### 1.6.14 Speed of Sound $v_3^D$

The speed of sound  $v_3^D$  (km/s) is calculated by the following formulas:

- for a bar-shaped test sample

$$v_3^D = 2 \times 10^{-2} f_a l, \quad (1.11)$$

where  $f_a$ , antiresonant frequency of longitudinal fluctuations, Hz;  $l$ , length of the test sample, m.

- for a disk-shaped test sample

$$v_1^E = \frac{f_r \pi D}{\eta} \sqrt{1 - \sigma^2}, \quad (1.12)$$

where  $f_r$ , resonant frequency of radial fluctuations, Hz;  $D$ , diameter of the test sample, m;  $\sigma$ , Poisson's coefficient was chosen from Table 1.2;  $\eta$ , least positive frequency equation root was chosen from Table 1.2 depending on value  $\sigma$ .

### 1.6.15 Good Mechanical Quality $Q_m$

Good mechanical quality  $Q_m$  was calculated by formulas

$$Q_m = \frac{f_a^2 \times 10^{12}}{2\pi R_r C_0 f_r (f_a^2 - f_r^2)}, \quad (1.13)$$

where  $R_r = R_1[(U_{in}/U_{out}) - 1]$ , resonator resistance on the resonant frequency calculated with a margin of error  $\pm 10\%$ , ohm;  $R_1 = R_3$ , loading resistance is included in the block diagram Fig. 1.1 at measurement  $f_r$ , ohm;  $U_{in}$ , device input voltage, measured millivoltmeter *PV1*, V;  $U_{out}$ , device exit voltage (resonant frequency) measured on millivoltmeter *PV2*, V;  $C_0$ , test piece static electric capacity measured on frequency of 1,000 Hz, pF.

### 1.6.16 Definition of Curie Point Temperature $T_C$

The Curie point temperature  $T_C$  in piezoceramic material is the temperature when the dielectric permeability's (constant, permittivity?) maximum size is observed, calculated on the sample's measured value of static capacity.



Temperatures of Curie point (C) samples are defined in a heat chamber. For a valid temperature value, ten samples were received for measurement and an average temperature value of the Curie point was accepted.

Measurement of static capacity begins at  $298 \pm 10 \text{ K}$  ( $25 \pm 10^\circ\text{C}$ ). Then static capacity, in the temperature ranges, is measured when temperatures rise. Heat the sample with a speed that is no more than  $5 \text{ K}$  ( $5^\circ\text{C}$ ) per minute, a  $30\text{--}50 \text{ K}$  ( $30\text{--}50^\circ\text{C}$ ) below Curie point temperature on the concrete mark. After that, temperatures increase at a speed less than  $2 \text{ K}$  ( $2^\circ\text{C}$ ) in a minute. During the process, it is necessary to measure the capacity of all tested samples; the heat chamber temperature should be supported with a margin error no more  $\pm 2 \text{ K}$  ( $\pm 2^\circ\text{C}$ ).

After establishing the set temperature of the static capacity  $C_0$ , directly control the chamber by means of a universal bridge or other device which will provide measurement on a frequency of  $1,000 \pm 200 \text{ Hz}$ , with a margin error of no more  $\pm 1\%$ .

## 1.7 Piezoceramic Materials

Piezoelectric ceramic materials (PCMs) present ferroelectric connections or firm solutions received by synthesizing various oxides and salts (Table 1.3) [43, 53, 54].

Modern PCM is made with solid solutions such as lead zirconate titanate (PZT, in Russian IITC), which has been modified by various components and additives. PCM based on titanate barium, titanate bismuth, titanate lead, and niobate lead is also produced. The basic properties in PCM, as revealed on standard ceramic test samples, are:

- High values of dielectric permeability (constant, permittivity?)
- Presence of spontaneous polarization in separate areas (domains)
- Presence of hysteresis loops in dependences, e.g., polarization-electric fields and deformation-electric fields
- Growth of dielectric permeability (constant, permittivity?) when temperatures rise
- Presence of Curie temperature point without curve dependence of dielectric permeability (constant, permittivity?) temperatures above ferroelectric properties
- Residual polarization occurrence and double cake-like electric layer on the surface after constant electric field influence, causing display possibilities by the piezoelectric effect body (transforming mechanical energy into electrical energy and/or vice versa)

Depending on their basic purpose, PCMs are subdivided as follows:

1. "Ferro-soft" PCM can be applied to high-sensitivity transducer manufacturing, working without rigid requirements on parameter stability to influence destabilizing factors (raised temperatures and electric or mechanical fields).

General purpose PCMs for materials IITC-19 (PZT-5A) and IITC-19 (IIT): IITC-19 (IIT) is the updated IITC-19 with raised values of piezoelectric modules ( $d_{ik}$ ). This increase is reached at the expense of replacement of raw

components zirconium oxide and titanium oxide on specially developed highly active raw materials – titanium zirconium.

PCM has a lowered dielectric permeability(constant, permittivity?) and high reception sensitivity ( $g_{ik}$ ). The material ИТС-36) is usually used in hot-extrusion blocks and is intended, mainly, for manufacturing transducers with ultrasonic delay lines.

PCM has raised values of dielectric permeability(constant, permittivity?) and piezo-module (ИТС-2). These materials are intended for use in telephone devices with hypersensibility.

2. “Ferro- hard” PCM is applied to transducers working in a reception environment and/or radiation where strong electric fields and/or mechanical pressure influence the conditions. They utilize ИТС-23, ИТССТ-3(ИТ), and ИТБС-7 materials. Materials ИТС-23 and ИТССТ-3(ИТ) are well proven in ignition and hydro-acoustic piezoelement systems. It is possible to recommend ИТССТ-3(ИТ) and ИТБС-7 for manufacturing piezotransformers and ultrasonic radiators (projectors?)of a raised capacity.
3. PCM, for frequency-selective devices, is applied to piezoelement manufacturing because it possesses characteristics that can cope with raised temperatures and time stability frequency. Frequency-selective devices are for volume and surface acoustic waves (SAW).

Materials for frequency-selective devices for volume waves of planar fluctuations are applied when creating filters on discrete piezoelements; the materials used include ИТС-38, ИТС-39, and ИТС-40.

Materials for frequency-selective devices with volume waves of a compression-stretching fluctuation (thickness) are in subgroups ИТС-35 and ИТС-35Y.

In hot compacting blocks, ИТС-35Y is issued.

Materials for frequency-selective devices with volume waves of a shift thickness fluctuation are represented by a subgroup material ИТС-35. Materials in subgroups 3.2 and 3.3 are used to create monolithic filters for frequency-modulated signals on frequencies to 10 MHz.

Materials for frequency-selective devices for superficial acoustic waves include ИТС-33, produced in hot compacting blocks. It is applied by setting filters to 40 MHz frequencies.

4. High-temperature PCM is used for piezoelement manufacturing in devices that work at temperatures at not less than 250°C, which includes the materials ИТС-21, ИТС-26, ТНБ-1, and ТНБ-1. For piezoelements with working temperatures of 250–750°C, the material ИТС-26 was developed. For increased temperature stability, piezo-module ( $d_{33}$ ), ТНБ-1, ИТС-26М, and ТНБ-1М have been developed.
5. Electro-optical materials are used for manufacturing active elements for light modulation, including protective devices and digital indicators. This group includes the materials ИТСЛ-А, ИТСЛ-Б, and ИТСЛ-В. Elements from a material ИТСЛ-А, with residual polarization, are used in the linear EO effect (Pockel’s effect). They are characterized also by record-breaking high

piezoelectric and pyroelectrical parameters. Elements from TSTSL-IN are used in light modulation; the devices work in a square law EO effect (the Kerr effect) with various temperature intervals.

Basic characteristics of some described piezoelectric ceramic materials are presented in Table 1.3. Additional information about piezoelectric materials can be found on Open Society “ELPA” (Zelenograd, Russia) at <http://www.aha.ru/~elpa/> and Open Society “Aurora” (Volgograd, Russia) at <http://www.avrora.vlink.ru>.

Transducer parameters are defined by problems which they solve.

## 1.8 Formulas for the Calculation of Piezoceramic Material Descriptions

### 1.8.1 Piezoceramic Disk (Fig. 1.5)

$$K_{31} = - \sqrt{\frac{\frac{\pi}{2} \frac{f_{a1}}{f_{r1}}}{\frac{\pi}{2} \frac{f_{a1}}{f_{r1}} - \operatorname{tg}\left(\frac{\pi}{2} \frac{f_{a1}}{f_{r1}}\right)}},$$

$$K_p = |K_{31}| \sqrt{\frac{2}{1-\sigma}} = \sqrt{\frac{2}{1-\sigma} \frac{\frac{\pi}{2} \frac{f_{a1}}{f_{r1}}}{\frac{\pi}{2} \frac{f_{a1}}{f_{r1}} - \operatorname{tg}\left(\frac{\pi}{2} \frac{f_{a1}}{f_{r1}}\right)}},$$

$$S_{11}^E = \frac{\chi^2}{\pi^2(1-\sigma^2)\rho} \frac{1}{(Df_{a1})^2}; \quad S_{12}^E = -S_{11}^E \sigma = -\frac{\sigma \chi^2}{\pi^2(1-\sigma^2)\rho} \frac{1}{(Df_{a1})^2};$$

$$\frac{\varepsilon_{33}^T}{\varepsilon_0} = \frac{11.3 \times 10^{10} h \times 4}{\pi D^2} C_0; \quad C_{01} = C_{ad1} \frac{f'_a - f_r}{f_{a1} - f'_{a1}}; \quad \frac{\varepsilon_{33}^S}{\varepsilon_0} = (1 - K_p^2) \frac{\varepsilon_{33}^T}{\varepsilon_0};$$

$$d_{31} = |K_{31}| \sqrt{S_{11}^E \varepsilon_{33}^T} = \frac{\chi}{\pi D f_{a1}} \sqrt{\frac{\frac{\pi}{2} \frac{f_{a1}}{f_{r1}}}{\frac{\pi}{2} \frac{f_{a1}}{f_{r1}} - \operatorname{tg}\left(\frac{\pi}{2} \frac{f_{a1}}{f_{r1}}\right)} \frac{\varepsilon_{33}^T}{(1-\sigma^2)\rho}};$$

$$g_{31} = \frac{d_{31}}{\varepsilon_{33}^T} = \frac{\chi}{\pi D f_{a1}} \sqrt{\frac{\frac{\pi}{2} \frac{f_{a1}}{f_{r1}}}{\frac{\pi}{2} \frac{f_{a1}}{f_{r1}} - \operatorname{tg}\left(\frac{\pi}{2} \frac{f_{a1}}{f_{r1}}\right)} \frac{1}{(1-\sigma^2)\rho \varepsilon_{33}^T}};$$

$$S_{11}^D = S_{11}^E - d_{31} g_{31} = \frac{\chi^2}{\pi^2 \rho (1-\sigma^2) (Df_{a1})^2} \left[ 1 - \frac{\frac{\pi}{2} \frac{f_{a1}}{f_{r1}}}{\frac{\pi}{2} \frac{f_{a1}}{f_{r1}} - \operatorname{tg}\left(\frac{\pi}{2} \frac{f_{a1}}{f_{r1}}\right)} \right].$$

Fig. 1.5 Piezoceramic disk

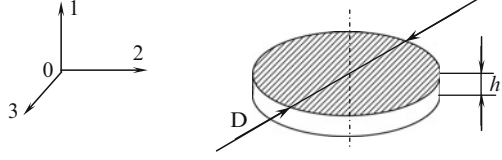
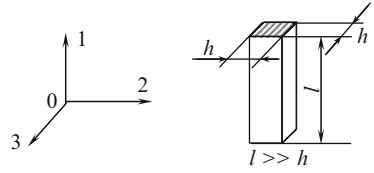


Fig. 1.6 Piezoceramic bar



### 1.8.2 Piezoceramic Bar (Fig. 1.6)

$$K_{33} = \sqrt{\frac{\pi}{2} \frac{f_{r2}}{f_{a2}} \operatorname{ctg} \left( \frac{\pi}{2} \frac{f_{r2}}{f_{a2}} \right)}; \quad S_{33}^E = \frac{1}{4l^2 \rho f_{a2}^2} \frac{1}{1 - \frac{\pi}{2} \frac{f_{r2}}{f_{a2}} \operatorname{ctg} \left( \frac{\pi}{2} \frac{f_{r2}}{f_{a2}} \right)};$$

$$S_{33}^D = S_{33}^E (1 - K_{33}^2) = \frac{1}{4l^2 \rho f_{a2}^2}; \quad \frac{\varepsilon_{33}^T}{\varepsilon_0} = \frac{11.3 \times 10^{10} l}{h^2} C_{02};$$

$$C_{02} = C_{ad2} \frac{f'_{a2} - f_{r2}}{f_{a2} - f'_{a2}}; \quad \frac{\varepsilon_{33}^S}{\varepsilon_0} = (1 - K_{33}^2) \frac{\varepsilon_{33}^T}{\varepsilon_0};$$

$$d_{33} = K_{33} \sqrt{S_{33}^E \varepsilon_{33}^T} = \frac{1}{2lf_{a2}} \sqrt{\frac{\varepsilon_{33}^T}{\rho} \frac{\frac{\pi}{2} \frac{f_{r2}}{f_{a2}} \operatorname{ctg} \left( \frac{\pi}{2} \frac{f_{r2}}{f_{a2}} \right)}{1 - \frac{\pi}{2} \frac{f_{r2}}{f_{a2}} \operatorname{ctg} \left( \frac{\pi}{2} \frac{f_{r2}}{f_{a2}} \right)}};$$

$$g_{33} = \frac{d_{33}}{\varepsilon_{33}^T} = \frac{1}{2lf_{a2}} \sqrt{\frac{1}{\varepsilon_{33}^T \rho} \frac{\frac{\pi}{2} \frac{f_{r2}}{f_{a2}} \operatorname{ctg} \left( \frac{\pi}{2} \frac{f_{r2}}{f_{a2}} \right)}{1 - \frac{\pi}{2} \frac{f_{r2}}{f_{a2}} \operatorname{ctg} \left( \frac{\pi}{2} \frac{f_{r2}}{f_{a2}} \right)}}.$$

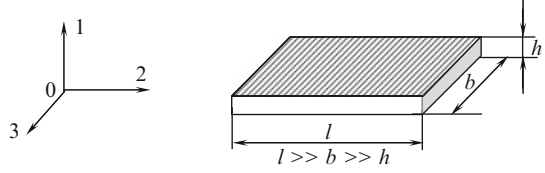
### 1.8.3 Piezoceramic Rectangular Plate (Fig. 1.7)

$$K_{15} = \sqrt{\frac{\pi}{2} \frac{f_{r3}}{f_{a3}} \operatorname{ctg} \left( \frac{\pi}{2} \frac{f_{r3}}{f_{a3}} \right)}; \quad C_{44}^D = 4\rho h^2 f_{a3}^2; \quad C_{55}^D = C_{44}^D = 4\rho h^2 f_{a3}^2;$$

$$S_{44}^D = \frac{1}{C_{44}^D} = \frac{1}{4\rho h^2 f_{a3}^2}; \quad S_{55}^D = S_{44}^D = \frac{1}{4\rho h^2 f_{a3}^2};$$

$$C_{44}^E = C_{44}^D (1 - K_{15}^2) = 4\rho h^2 f_{a3}^2 \left[ 1 - \frac{\pi}{2} \frac{f_{r3}}{f_{a3}} \operatorname{ctg} \left( \frac{\pi}{2} \frac{f_{r3}}{f_{a3}} \right) \right];$$

**Fig. 1.7** Piezoceramic rectangular plate



$$C_{55}^E = C_{44}^E = 4\rho h^2 f_{a3}^2 \left[ 1 - \frac{\pi}{2} \frac{f_{r3}}{f_{a3}} \operatorname{ctg} \left( \frac{\pi}{2} \frac{f_{r3}}{f_{a3}} \right) \right];$$

$$S_{44}^E = \frac{1}{C_{44}^E} = \frac{1}{4\rho h^2 f_{a3}^2 \left[ 1 - \frac{\pi}{2} \frac{f_{r3}}{f_{a3}} \operatorname{ctg} \left( \frac{\pi}{2} \frac{f_{r3}}{f_{a3}} \right) \right]};$$

$$S_{55}^E = S_{44}^E = \frac{1}{4\rho h^2 f_{a3}^2 \left[ 1 - \frac{\pi}{2} \frac{f_{r3}}{f_{a3}} \operatorname{ctg} \left( \frac{\pi}{2} \frac{f_{r3}}{f_{a3}} \right) \right]};$$

$$\frac{\varepsilon_{11}^T}{\varepsilon_0} = \frac{11.3 \times 10^{10} h}{lh} C_{03}; \quad C_{03} = C_{ad3} \frac{f'_{a3} - f_{r3}}{f_{a3} - f'_{a3}}; \quad \frac{\varepsilon_{11}^S}{\varepsilon_0} = (1 - K_{15}^2) \frac{\varepsilon_{11}^T}{\varepsilon_0};$$

$$d_{15} = K_{15} \sqrt{S_{44}^E \varepsilon_{11}^T} = \frac{1}{2hf_{a3}^2} \sqrt{\frac{\frac{\pi}{2} \frac{f_{r3}}{f_{a3}} \operatorname{ctg} \left( \frac{\pi}{2} \frac{f_{r3}}{f_{a3}} \right) \varepsilon_{11}^T}{\left[ 1 - \frac{\pi}{2} \frac{f_{r2}}{f_{a2}} \operatorname{ctg} \left( \frac{\pi}{2} \frac{f_{r2}}{f_{a2}} \right) \right] \rho}};$$

$$g_{15} = \frac{d_{15}}{\varepsilon_{11}^T} = \frac{1}{2hf_{a3}} \sqrt{\frac{\frac{\pi}{2} \frac{f_{r3}}{f_{a3}} \operatorname{ctg} \left( \frac{\pi}{2} \frac{f_{r3}}{f_{a3}} \right)}{\left[ 1 - \frac{\pi}{2} \frac{f_{r3}}{f_{a3}} \operatorname{ctg} \left( \frac{\pi}{2} \frac{f_{r3}}{f_{a3}} \right) \right] \varepsilon_{11}^T \rho}};$$

$$A = \frac{-2K_{33}K_p \pm \sqrt{4K_{33}^2K_p^2 - 4(K_{15}^2K_p^2 - K_{15}^2 - K_p^2)(K_{15}^2 - K_{15}^2K_p^2 - K_{33}^2)}}{2(K_{15}^2K_p^2 - K_{15}^2 - K_p^2)};$$

$$S_{13}^E = \frac{A}{\sqrt{2}} \sqrt{S_{33}^E(S_{11}^E + S_{12}^E)}; \quad S_{13}^D = S_{13}^E - d_{31}d_{33} \frac{1}{\varepsilon_{33}^T};$$

$$C_{11}^E = \frac{S_{11}^E S_{33}^E - (S_{13}^E)^2}{(S_{11}^E - S_{12}^E) [S_{33}^E(S_{11}^E + S_{12}^E) - 2(S_{13}^E)^2]};$$

$$C_{12}^E = \frac{-S_{12}^E S_{33}^E + (S_{13}^E)^2}{(S_{11}^E - S_{12}^E) [S_{33}^E(S_{11}^E + S_{12}^E) - 2(S_{13}^E)^2]};$$

$$C_{13}^E = \frac{-S_{13}^E}{S_{33}^E(S_{11}^E + S_{12}^E) - 2(S_{13}^E)^2}; \quad C_{33}^E = \frac{S_{11}^E + S_{12}^E}{S_{33}^E(S_{11}^E + S_{12}^E) - 2(S_{13}^E)^2};$$

$$\begin{aligned}
C_{11}^D &= \frac{S_{11}^D S_{33}^D - (S_{13}^D)^2}{(S_{11}^D - S_{12}^D) [S_{33}^D (S_{11}^D + S_{12}^D) - 2(S_{13}^D)^2]}; \\
C_{12}^D &= \frac{-S_{12}^D S_{33}^D + (S_{13}^D)^2}{(S_{11}^D - S_{12}^D) [S_{33}^D (S_{11}^D + S_{12}^D) - 2(S_{13}^D)^2]}; \\
C_{13}^D &= \frac{-S_{13}^D}{S_{33}^D (S_{11}^D + S_{12}^D) - 2(S_{13}^D)^2}; \quad C_{33}^D = \frac{S_{11}^D + S_{12}^D}{S_{33}^D (S_{11}^D + S_{12}^D) - 2(S_{13}^D)^2}; \\
h_{15} &= g_{15} C_{44}^D = \frac{d_{15}}{\varepsilon_{11}^T} C_{44}^D; \quad h_{31} = \frac{d_{31}(C_{11}^D + C_{12}^D) + d_{33} C_{13}^D}{\varepsilon_{33}^T}; \\
h_{33} &= \frac{2d_{31} C_{31}^D + d_{33} C_{33}^D}{\varepsilon_{33}^T}; \quad e_{15} = h_{15} \varepsilon_{11}^S = d_{15} C_{44}^E; \\
e_{31} &= h_{31} \varepsilon_{33}^S = d_{15}(C_{11}^E + C_{12}^E) + d_{33} C_{13}^E; \quad e_{33} = h_{33} \varepsilon_{33}^S = 2d_{31} C_{13}^E + d_{33} C_{33}^E; \\
C_{66}^D &= \frac{1}{2}(C_{11}^D + C_{12}^D); \quad C_{66}^E = C_{66}^D; \quad S_{66}^D = \frac{1}{C_{66}^D}; \quad S_{66}^E = S_{66}^D;
\end{aligned}$$

where  $h$ , thickness of the test piece, mm;  $D$ , diameter of the test piece, mm;  $l$ , length of the test piece, mm;  $C_{ad,1,2,3}$ , additional capacity  $F$  included in parallel to the sample for definition of dielectric permeability on antiresonant frequency;  $\rho$ , density, kg/sm<sup>2</sup>;  $\varepsilon_0$ , dielectric permeability is equal  $8.85 \times 10^{-12}$ ,  $\Phi/\text{M}$ ;  $f_{r1}$ ,  $f_{r2}$ ,  $f_{r3}$ , resonance frequency in the corresponding test piece, Hz;  $f_{a1}$ ,  $f_{a2}$ ,  $f_{a3}$ , antiresonance frequency of the corresponding test piece, Hz;  $f'_{a1}$ ,  $f'_{a2}$ ,  $f'_{a3}$ , antiresonance displacement frequency in additional capacity, Hz;  $g_{31}$ ,  $g_{33}$ ,  $g_{15}$ , piezoelectric constants, Vm/N;  $d_{31}$ ,  $d_{33}$ ,  $d_{15}$ , piezoelectric constants, Kl/N;  $h_{31}$ ,  $h_{33}$ ,  $h_{15}$ , piezoelectric deformation factors, V/m;  $e_{31}$ ,  $e_{33}$ ,  $e_{15}$ , piezoelectric constants;  $C_{11}$ ,  $C_{12}$ ,  $C_{13}$ ,  $C_{33}$ ,  $C_{44}$ ,  $C_{55}$ ,  $C_{66}$ , elastic constants with indexes  $E$  and  $D$ , H/M<sup>2</sup>;  $S_{11}$ ,  $S_{12}$ ,  $S_{13}$ ,  $S_{33}$ ,  $S_{44}$ ,  $S_{55}$ ,  $S_{66}$ , elastic constants with indexes  $E$  and  $D$ , m<sup>2</sup>/H;  $\chi$ , a constant equalling 2.069.

## 1.9 Sensor [Physical Size] Descriptions

Basic sensor characteristics are a range of measurements, sensitivity, a threshold of reaction (sensitivity), errors, time of indication establishment, and reliability [46, 55].

1. *Range of measurements* – measured size values in which we normalize supposed errors. This range is subject to measurement limits, greatest and least values of the measurement range.
2. *Sensitivity  $S$*  – change relationship between an output sensor  $\Delta Y$  signal to the change which caused it on the measured size  $\Delta X$ :  $S = \Delta Y / \Delta X$ .

3. *Errors* – with series graduation of the same sensors it appears that the characteristics differ from each other. In the measuring transducer passport, some average characteristics “nominal” are observed. Differences between the “nominal passport” and the real sensor characteristics are considered its “error.”
4. *Reliability* – transducer’s ability to keep characteristics in certain limits during the established time interval, under set operation conditions.

## References

1. J. Curie, P. Curie, Développement, par pression, de l'électricité polaire dans les cristaux hémihédres a faces inclinées. *Compt. Rend.* **91**, 294–295 (1880)
2. G. Lippmann, Principe de la conversation de l'électricité. *Ann. de Chim. et de Phys.* **24**, 145–178 (1881)
3. J. Curie, P. Curie, Contractions et dilatations produits par des tensions électriques dans les cristaux hémihédres a faces inclinées. *Compt. Rend.* **93**, 1137–1140 (1881)
4. P. Langevin, Précédé et appareil d'émission et de réception des ondes élastiques sous-marines a l'aide des propriétés piézoélectriques du quartz. *Fr. Pat.*, 1918, № 505703
5. W.G. Cady, Piezoelectric resonator. *Proc. Inst. Rad. Eng.* **10**, 83–114 (1922)
6. G.W. Pierce, Piezoelectric oscillators applied to the precision measurement of the velocity of sound in air and CO<sub>2</sub> at high frequencies. *Proc. Amer. Acad.* **60**, 271–302 (1925)
7. S.Ya. Sokolov, Way and the device for test of metals. The copyright certificate USSR, 1928, № 23246 (in Russian)
8. P. Debye, F.W. Sears, On the scattering of light by supersonic waves. *Proc. Nat. Acad. Sci.* **18**(6), 409–414 (1932)
9. R. Lucas, P. Biquard, Nouvelles propriétés optiques des liquides soumis à des ondes ultrasonores. *Compt. Rend.* **194**, 2132–2134 (1932)
10. B. Wool, I. Goldman, Dielectric permeability titanium barium depending on intensity in a variation field. *Rep. Acad. Sci. USSR* **49**(3), 179–182 (1945) (in Russian)
11. B. Wool, I. Goldman, Dielectric permeability titanium metals of 2nd group. *Rep. Acad. Sci. USSR* **46**(4), 154–157 (1945) (in Russian)
12. W.P. Mason, Barium-titanate ceramic as an electromechanical transducer. *Phys. Rev.* **74**(9), 1134 (1948); *Bell. Labor. Rec.* **27**, 285–289 (1949)
13. A. Ananyeva, V. Tsarev, Working out not directed sound detector for ultrasonic frequencies, The Report of Acoustic Laboratory of Physical Institute of Academy of Sciences, 1951 (in Russian)
14. W.P. Mason, *Electromechanical Transducers and Wave Filters*, 2nd edn. (Van Nostrand, Princeton, 1948)
15. W.P. Mason, *Piezoelectric Crystals and Their Applications to Ultrasonics* (Van Nostrand, New York, 1950)
16. L. Bergman, Zur Frage der Eigenschwingungen piezoelektrischer Quarzplatten bei Erregung in der Dickenschwingung. *Ann. d. Phys.* **21**, 553–563 (1935)
17. W. Cady, *Piezoelectricity. An Introduction to the Theory and Applications of Electromechanical Phenomena in Crystals* (Dover, New York, 1946)
18. R.N. Thurston, Effects of electrical and mechanical terminating resistances on loss and bandwidth according to the conventional equivalent circuit of a piezoelectric transducer. *IRE Trans. Ultrason. Eng.* **UE-7**(1), 16–25 (1960)
19. G. Katts (ed.), *Magnetic and Dielectric Devices*, Part 1 (Energiya, Moscow, 1964), p. 416 (in Russian)
20. M. Onoe, H.P. Tiersten, Resonant frequencies of finite piezoelectric ceramic vibrators with electromechanical coupling. *IEEE Trans. Son. Ultrason. Eng.* **10**(1), 32–39 (1963)

21. H.P. Tiersten, Thickness vibrations of piezoelectric plates. *J. Acoust. Soc. Am.* **35**, 53–58 (1963)
22. N. Andreev, Piezoelectric crystals and their application. *Electricity* **2**, 5–13 (1947) (in Russian)
23. N. Andreev, Calculation of the piezoelectric transmitter, *Works All-Union Correspondence Power Institute*, 1, pp. 5–12 (1951) (in Russian)
24. A.A. Harkevich, *The Theory of Transducers* (Gosenergoizdat, Moscow, 1948) (in Russian)
25. I. Golyamina, To a question about fluctuations by a thickness of the polarised titanium barium plates. *Acous. Mag.* **1**(1), 40–47 (1955)
26. V. Domarkas, R.-J. Kažys, *Piezoelectric Transducers for Measuring Devices* (Mintis, Vilnius, 1974), p. 258 (in Russian)
27. R.-J. Kažys, *Ultrasonic Information Measuring Systems* (Mokslas, Vilnius, 1986), p. 216 (in Russian) I ask to write name Kažys
28. V.V. Malov, *Piezoelectric Resonance Sensors* (Energoizdat, Moscow, 1989), p. 272 (in Russian)
29. A.N. Kutsenko, Matrix sensitivity acoustic strain-measuring device, *Works of Scientists OPI*. – 1995. – № 1. – C. 122–124 (in Russian)
30. L. Gutin, On the theory of piezoelectric effect. *Mag. Exp. Theor. Phys.* **15**(7), 367–379 (1945) (in Russian)
31. N.A. Shulga, A.M. Bolkisev, *Fluctuations of Piezoelectric Bodies. AS USSR. Mechanics Institute* (Naukova Dumka, Kyiv, 1990), p. 228 (in Russian)
32. V.V. Lavrinenko, *Piezoelectric Transformer* (Energiya, Moscow, 1975), p. 112 (in Russian)
33. I. Glozman, *Piezoceramics* (Energiya, Moscow, 1972), p. 288 (in Russian)
34. S.I. Pugachev (ed.), *Piezoelectric Ceramics Transducers: Reference Book* (Sudostroenie, Leningrad), p. 256 (in Russian)
35. M.V. Korolev, A.E. Karpelson, *Broadband Ultrasonic* (Mashinostroenie, Moscow, 1982), p. 157 (in Russian)
36. A.F. Ulitko, About definition of factor of electromechanical communication in problems of the established fluctuations in piezoelectric ceramics bodies, *Materials IX The All-Union Acoustic Conference, Moscow, Acoustic Institute of Academy of Sciences – C. 27–30* (1977) (in Russian)
37. I.G. Minaev, A.I. Trofimov, V.M. Sharapov, On a question about linearization target characteristics piezoelectric force measuring transducers, *Izv. vyzov USSR – “Priborostroenie”*, № 3 (1975) (in Russian)
38. A.I. Trofimov, *Piezoceramic Transducers Static Forces* (Mashinostroenie, Moscow, 1979), p. 95 (in Russian)
39. A.E. Kolesnikov, *Ultrasonic Measurements* (Izdatelstvo Standartov, Moscow, 1982), p. 248 (in Russian)
40. I.N. Ermolov, *The Theory and Practice of Ultrasonic Control* (Mashinostroenie, Moscow, 1981), p. 240 (in Russian)
41. P.G. Dzagupov, A.A. Erofeev, *Piezoelectronic Devices of Computer Facilities, Monitoring Systems and Control* (Politehnika, St. Petersburg, 1994), p. 608 (in Russian)
42. V.M. Pluzhnikov, V.S. Semenov, *Piezoceramic Firm Schemes* (Energiya, Moscow, 1971), p. 168 (in Russian)
43. P. Gribovskiy, *Ceramic Firm Schemes* (Energiya, Moscow, 1971), p. 448 (in Russian)
44. P.G. Pozdnyakov, I.M. Fedotov, V.I. Biryukov, *Quartz Resonators with Film Heaters. The Electronic Technics. Scientifically-techn. The Collection, A Series 9 – Radio Components, Release 4* (Energiya, Moscow, 1971), pp. 27–37 (in Russian)
45. V.M. Sharapov, M.P. Musienko, E.V. Sharapova, in *Piezoelectric Sensors*, ed. by V.M. Sharapov (Technosphaera, Moscow, 2006), p. 632 (in Russian)
46. E.S. Levshina, P.V. Novitskiy, *Electric Measurements of Physical Sizes: (Measuring Transducers). Studies. The Grant for High Schools* (Energoatomizdat, Leningrad, 1983), p. 320 (in Russian)
47. *Electric Measurements of Not Electric Sizes* (Energiya, Moscow, 1975), p. 576 (in Russian)
48. Yaffe B., U. Kuk, G. Yaffe. *Piezoelectric Ceramics* (Mir, Moscow, 1974), p. 288 (in Russian)



49. V. Sharapov et al., The copyright certificate SUN<sup>№</sup> 501306A. Piezoelectric static efforts sensor (in Russian)
50. Firm prospectuses “Bruel and Kjer”, Nerum, Denmark (1995)
51. Firm prospectuses “Kistler Instrumente AG”, Winterthur, Switzerland (1996)
52. Piezoceramic materials. Test methods. Standard of USSR 12370–80, Moscow (1980) (in Russian)
53. Piezoceramic materials. Types and marks. Technical requirements. Standard of USSR 13927–68, Moscow (1968) (in Russian)
54. ELPA, in *Products of Acoustoelectronics and Piezoceramics*, ed. by B.G.M. Parfenov (RIA Delovoy Mir, Zelenograd, 1992), p. 167 (in Russian)
55. V.I. Vinokurov (ed.), *Electric Radio Measurements. The Manual for High Schools* (Visshaya Shkola, Moscow, 1976) (in Russian)
56. O.P. Kramarov, et al., Piezotransducers from metaniobium of lead for ultrasonic resonant thickness gauge. Seminar materials “Radiators and receivers of ultrasonic fluctuations and methods of measurement of acoustic fields”, pp. 27–34 (1966) (in Russian)

# Chapter 2

## Monomorph Piezoceramic Elements

The industry makes a significant number of standard-sized piezoceramic elements from various materials [1, 2]. Some are shown in Fig. 2.1.

Monomorph piezoelements are as follows: elements of one piezoelement; on the surfaces electrodes appear, which can include piezoelements in an electrical circuit.

### 2.1 Calculating Electric Piezoceramic

#### 2.1.1 Resonator Parameters

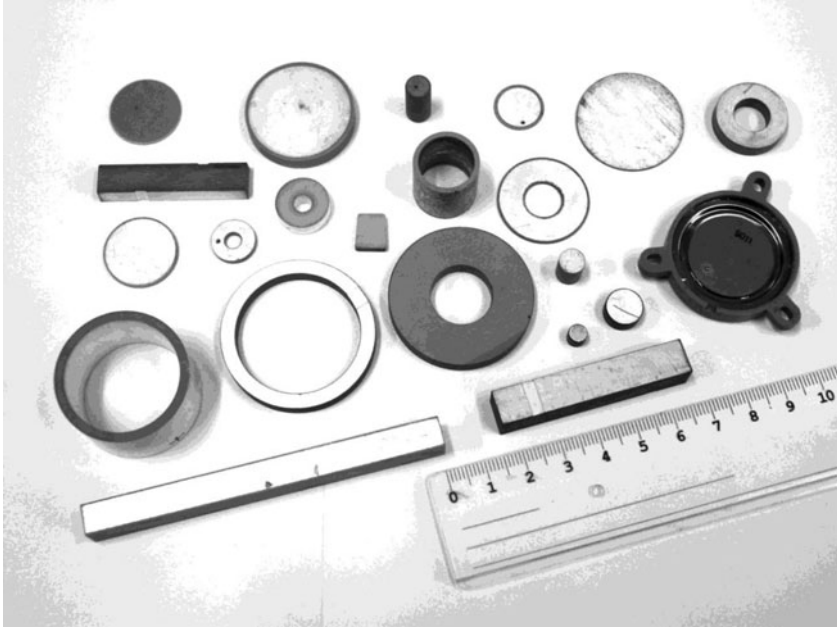
Piezoelements with two electrodes are named “resonators” [3] and for fluctuations the alternating voltage is brought to the resonator electrodes. When the frequency voltage is connected to the piezoelement fluctuation frequency, there is an electromechanical resonance phenomenon. Physically the resonance is characterized by a directional distribution of waves, where the integer of half waves lays within a piezoelement.

At the resonator simultaneously, there are various kinds of interconnected fluctuations that create hindrances to the fluctuations in the basic direction; therefore it is necessary to create conditions so that one kind of fluctuation prevails. Various fluctuation types can be raised in a piezoelement: longitudinal, fluctuations on thickness, radial, torsion, curving, and shift (shear mode?).

The most often met “resonance frequencies” are fluctuations represented by the following formulas:

*Longitudinal fluctuations:*

$$f_p = \frac{n}{2l} \sqrt{\frac{Y}{\rho}}; \tag{2.1}$$



**Fig. 2.1** Piezoceramic elements

*Shift fluctuations on a thickness:*

$$f_p = \frac{n}{2a} \sqrt{\frac{Y}{\rho} \frac{1 - \delta}{(1 + \delta)(1 - 2\delta)}}; \quad (2.2)$$

*Radial fluctuations:*

$$f_p = \frac{z_n}{2\pi r} \sqrt{\frac{Y}{\rho(1 - \delta)^2}}; \quad (2.3)$$

where  $Y$  – Young's modulus;  $\rho$  – density of piezoelement material;  $\delta$  – Poisson's coefficient;  $n$  – harmonic number;  $l$ ,  $a$ ,  $r$  – length, thickness, piezoelement radius;  $z_n$  – parameter defined through Bessel functions.

For longitudinal fluctuation resonant frequency definition, use the approximation formula:

$$f_p \approx \frac{c}{2l}; \quad (2.4)$$

where  $c$  – speed of a sound in the piezoelement material;  $l$  – resonant size.

Resonance frequency of a disk's radial fluctuations [4]

$$f_p \approx \frac{1.35c}{4r}. \quad (2.5)$$

The type of quartz resonator fluctuations depends on a cut; longitudinal fluctuation choose  $x$ -cuts and for cross-section-shift fluctuations use AT and VG cuts [5].

Piezoceramic resonators stimulation efficiency depends on a vector polarization direction. In rectangular piezoelements, with electrodes located on the sides perpendicular to the polarization direction, it is possible to stimulate longitudinal and cross-section fluctuations on corresponding geometrical sides. If the polarization vector is parallel to the electrode plane and the piezoelement is stimulated, shift fluctuations appear on certain frequencies. The raised resonator fluctuations depend also on the arrangement and sizes of electrodes [5,6]. If electrodes are placed along length surfaces of the piezoelement, the electric field creates mechanical pressure along the piezoelement length. It promotes basic fluctuations on the first harmonic and weaker fluctuations on the third, the fifth and higher harmonics. If electrodes are placed on the half surface length, this is a favorable condition for fluctuations on the second harmonic. In this case, mechanical pressure on the piezoelement's half length can create different signs. In the piezoceramic resonator, it is possible to stimulate fluctuations on the second harmonic; with continuous electrodes, this can polarize separate piezoelement sites in opposite directions [5,6].

With piezoelement stimulation on electrode resonant frequency, there are variable charges; the size and phase are defined by the amplitude. A phase of mechanical piezoelement fluctuations, external stimulating voltage, and a current are observed. There is a resonant dependence of piezoelement resistance with a frequently stimulating voltage. It means we must consider a piezoelement in resonant area as an electric chain (Fig. 2.2a) that consists of a static capacity  $C_0$ , dynamic inductance  $L$  and capacity  $C$ , and an active resistance of losses  $R$  [3,4].

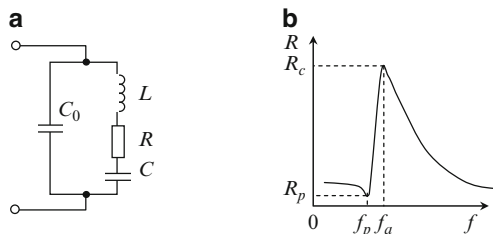
As a series-parallel, this contour has two resonant frequencies: a consecutive resonance  $f_p$  and a parallel resonance ( $f_a$ ) which is an anti-resonance. Piezoresonator resistance on a resonant frequency ( $R_p$ ) minimum, and on anti-resonant frequency ( $R_a$ ) maximum, also have active characteristics (Fig. 2.2b).

For a piezoelectric resonator with continuous resonant electrodes and anti-resonant frequencies, it is possible to express parameters of the equivalent scheme [4].

$$\left. \begin{aligned} f_p &= \frac{1}{2\pi\sqrt{LC}}, \\ f_a &= \frac{1}{2\pi\sqrt{\frac{LC C_0}{C+C_0}}}. \end{aligned} \right\} \quad (2.6)$$

A good quality piezoresonator is defined by the expression:

$$Q = \frac{2\pi f_p L}{R}. \quad (2.7)$$



**Fig. 2.2** (a) Equivalent electric scheme of the resonator. (b) Typical frequency characteristic

## 2.2 Equivalent Schemes for Piezoresonators

For piezoelectric resonator analysis use equivalent schemes [3, 7, 8].

Let us consider a piezoresonator with transverse polarization (Fig. 2.3).

In Fig. 2.3  $P$  – a polarization vector, the detailed piezoelement image is shown on Fig. 2.4, where for an axis  $X$  direction, the mechanical influence  $F$  direction is chosen.

For this purpose we will write the matrix form of the equation which is the most convenient approach for the problem: connecting mechanical pressure  $T$  and deformation  $S$  with electric field intensity  $E$  and electric displacement  $D$  [3]:

$$\begin{aligned} \|S\| &= \|s^E\| \|T\| + \|d\|_t \|E\|, \\ \|D\| &= \|d\| \|T\| + \|\varepsilon^T\| \|E\|. \end{aligned} \tag{2.8}$$

Here  $s^E$  is an elasticity constant,  $d$  is a piezoelectric constant,  $\varepsilon^T$  is a dielectric constant, and index  $t$  designates the transposed matrix.

The full system of the equations will register:

$$\begin{pmatrix} S_1 \\ S_2 \\ S_3 \\ S_4 \\ S_5 \\ S_6 \end{pmatrix} = \begin{pmatrix} s_{11} & s_{12} & s_{13} & 0 & 0 & 0 \\ s_{12} & s_{11} & s_{13} & 0 & 0 & 0 \\ s_{13} & s_{13} & s_{33} & 0 & 0 & 0 \\ 0 & 0 & 0 & s_{44} & 0 & 0 \\ 0 & 0 & 0 & 0 & s_{44} & 0 \\ 0 & 0 & 0 & 0 & 0 & s_{66} \end{pmatrix} \times \begin{pmatrix} T_1 \\ 0 \\ 0 \\ 0 \\ 0 \\ 0 \end{pmatrix} + \begin{pmatrix} 0 & 0 & d_{31} \\ 0 & 0 & d_{31} \\ 0 & 0 & d_{33} \\ 0 & d_{15} & 0 \\ d_{15} & 0 & 0 \\ 0 & 0 & 0 \end{pmatrix} \times \begin{pmatrix} 0 \\ 0 \\ E_3 \end{pmatrix}; \tag{2.9}$$

Fig. 2.3 Piezoelectric sensor with transverse polarization

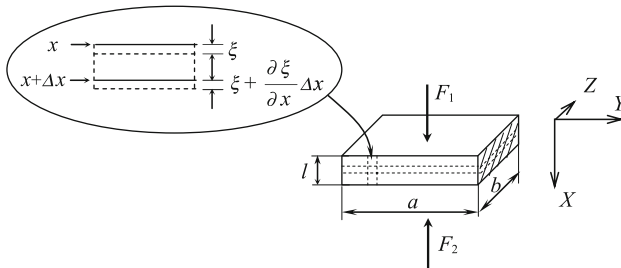
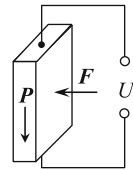


Fig. 2.4 Transducer piezoelement

$$\begin{pmatrix} D_1 \\ D_2 \\ D_3 \end{pmatrix} = \begin{pmatrix} 0 & 0 & 0 & 0 & d_{15} & 0 \\ 0 & 0 & 0 & d_{15} & 0 & 0 \\ d_{31} & d_{31} & d_{33} & 0 & 0 & 0 \end{pmatrix} \times \begin{pmatrix} T_1 \\ 0 \\ 0 \\ 0 \\ 0 \\ 0 \end{pmatrix} + \begin{pmatrix} \varepsilon_{11}^T & 0 & 0 \\ 0 & \varepsilon_{11}^T & 0 \\ 0 & 0 & \varepsilon_{33}^T \end{pmatrix} \times \begin{pmatrix} 0 \\ 0 \\ E_3 \end{pmatrix}. \quad (2.10)$$

It is possible to see that components  $S_4$ ,  $S_5$ ,  $S_6$ ,  $D_2$  and  $D_3$  are equal to zero. Fluctuations are defined only by members  $S_1$  and  $D$ , for which an equation in the algebraic form looks like this:

$$S_1 = s_{11}^E + d_{31} E_3; \quad (2.11)$$

$$D_3 = d_{31} T_1 + \varepsilon_{33}^T E_3. \quad (2.12)$$

The coefficient  $s_{11}^E$  for piezoelement in this case is the defining pressure size, except  $T_1$  is equal to zero. Usually it is considered a fundamental constant and size, returning to it; this Young's modulus  $Y_1^E$  is widely used.

Let us work out the equation of movement for the elementary volume. Under the influence of mechanical pressure  $T_1$  (Fig. 2.4) the left lateral surface was displaced on distance  $\xi$ , right – on distance  $\xi + (\partial\xi/\partial x)\Delta x$ , thus deformation is  $S_1 = \partial\xi/\partial x$ .

Similarly, if  $T_1$  – the pressure enclosed at the piezoelement top surface,  $T_1 + (\partial T_1/\partial x)\Delta x$  – pressure on the piezoelement bottom surface.

The general force operating on the elementary volume, is:

$$F = \frac{\partial T_1}{\partial x} \Delta x A,$$

where  $A$  is the transverse section bar area.

From Newton's law, it follows that:

$$\frac{\partial T_1}{\partial x} \Delta x A - \rho \Delta x A \frac{\partial^2 \xi}{\partial t^2} = 0,$$

where  $\rho$  is the substance density and thus,

$$\frac{\partial T_1}{\partial x} - \rho \frac{\partial^2 \xi}{\partial t^2} = 0. \quad (2.13)$$

There is a movement equation; using the (2.11):

$$\frac{\partial T_1}{\partial x} = \frac{1}{s_{11}^E} \frac{\partial S_1}{\partial x} = \frac{1}{s_{11}^E} \frac{\partial^2 \xi}{\partial x^2}. \quad (2.14)$$

From (2.13) and (2.14), with Young's modulus  $Y_1^E = 1/s_{11}^E$ .

Let us obtain the wave equation:

$$\frac{Y_1^E \partial^2 \xi}{\rho \partial x^2} = \frac{\partial^2 \xi}{\partial t^2}.$$

The decision of such an equation for harmonious fluctuations in time [3]:

$$\xi = (B_1 j \sin \gamma x + B_2 \cos \gamma x) e^{j\omega t}; \quad (2.15)$$

$$v = \frac{\partial \xi}{\partial t} = j\omega \xi,$$

$$S_1 = \frac{\partial \xi}{\partial x} = \beta (B_1 \cos \gamma x - B_2 j \sin \gamma x) e^{j\omega t}, \quad (2.16)$$

where  $\gamma$  is a constant of wave distribution, in the absence of attenuation

$$\gamma = \frac{j\omega}{\sqrt{\frac{Y_1^E}{\rho}}} = \frac{j\omega}{c} = j\beta, \quad (2.17)$$

here:

$$c = \sqrt{\frac{Y_1^E}{\rho}} \quad (2.18)$$

wave phase speed, using boundary conditions:

$$v_1 = j\omega \xi |_{x=0} = jB\omega_2, \quad v_2 = j\omega \xi |_{x=l}$$

we obtain:

$$B_1 = \frac{v_2 + v_1 \cos \gamma l}{\omega \sin \gamma l}; \quad B_2 = \frac{v_1}{j\omega}. \quad (2.19)$$

forces operating on the piezoelement ends are equal:

$$F_1 e^{j\omega t} = -abT_1 |_{x=0} = -abY_1^E (S_1 - d_{31} E_{03}) |_{x=0};$$

$$F_2 e^{j\omega t} = -abY_1^E (S_1 - d_{31} E_{03}) |_{x=l}.$$

Making substitution from parities (2.16) and (2.19), we obtain:

$$F_1 = abY_1^E \left[ d_{31} E_{03} e^{-j\omega t} - \frac{\beta}{\omega} \frac{v_2 + v_1 \cos \gamma l}{\sin \gamma l} \right]; \quad (2.20)$$

$$F_2 = abY_1^E \left[ d_{31} E_{03} e^{-j\omega t} - \frac{\beta}{\omega} \frac{v_1 + v_2 \cos \gamma l}{\sin \gamma l} \right]. \quad (2.21)$$

Based on initial assumptions:

$$E_{03} = U e^{j\omega t} / a, \quad (2.22)$$

and a current through the electrodes:

$$I e^{j\omega t} = \frac{d}{dt} \int_0^l b D_3 dx. \quad (2.23)$$

Expressions can be opened by (2.12), (2.11), (2.15) and (2.22):

$$\begin{aligned} I e^{j\omega t} &= j\omega b \int_0^l [d_{31} (Y_1^E S_1 - Y_1^E d_{31} E_{03}) + \varepsilon_{33}^T E_{03}] dx \\ &= j\omega b \left[ d_{31} Y_1^E \xi \Big|_{x=0}^l + \varepsilon_{33}^T \left( 1 - \frac{d_{31}^2 Y_1^E}{\varepsilon_{33}^T} \right) E_{03} l \right]; \\ I &= -bd_{31} Y_1^E (v_1 + v_2) + j\omega \frac{bl}{a} \varepsilon_{33}^T \left( 1 - \frac{d_{31}^2 Y_1^E}{\varepsilon_{33}^T} \right) U. \end{aligned} \quad (2.24)$$

Size is called ‘‘coefficient of electromechanical communication.’’

$$k_{31}^2 = \frac{d_{31}^2 Y_1^E}{\varepsilon_{33}^T}. \quad (2.25)$$

We will find a capacitor part of the entrance resistance:

$$Z_{\text{el.tr}} = \frac{U}{I} \Big|_{v_2=v_1=0} = \frac{1}{j\omega \frac{bl}{a} \varepsilon_{33}^T (1 - k_{31}^2)}. \quad (2.26)$$

Let us define wave resistance  $z_0$  as:

$$z_0 = abrc = ab \sqrt{\rho Y_1^E}. \quad (2.27)$$

Using these concepts and designations, we will transform (2.20), (2.21) and (2.24) to:

$$F_1 = \frac{z_0}{\text{tg} \gamma l} v_1 + \frac{z_0}{\text{sin} \gamma l} v_2 + bd_{31} Y_1^E U; \quad (2.28)$$

$$F_2 = \frac{z_0}{\text{sin} \gamma l} v_1 + \frac{z_0}{\text{tg} \gamma l} v_2 + bd_{31} Y_1^E U; \quad (2.29)$$

$$I = -bd_{31} Y_1^E (v_1 + v_2) + \frac{1}{Z_{\text{el.tr}}} U. \quad (2.30)$$



Let us substitute (2.30) in (2.28) and (2.29):

$$\begin{aligned} F_1 &= \left( \frac{z_0}{\operatorname{tg} \gamma l} + n_\varphi^2 Z_{\text{el.tr}} \right) v_1 + \left( \frac{z_0}{\sin \gamma l} + n_\varphi^2 Z_{\text{el.tr}} \right) v_2 + n_\varphi Z_{\text{el.tr}} I; \\ F_2 &= \left( \frac{z_0}{\sin \gamma l} + n_\varphi^2 Z_{\text{el.tr}} \right) v_1 + \left( \frac{z_0}{\operatorname{tg} \gamma l} + n_\varphi^2 Z_{\text{el.tr}} \right) v_2 + n_\varphi Z_{\text{el.tr}} I; \\ U &= n_\varphi Z_{\text{el.tr}} v_1 + n_\varphi Z_{\text{el.tr}} v_2 + Z_{\text{el.tr}} I, \end{aligned}$$

where  $n_\varphi = bY_1^E d_{31}$ .

The equivalent piezoelement scheme will be represented in Fig. 2.5.

Let us consider a further transducer variant with longitudinal polarization (Fig. 2.6).

Analyzing the scheme in Fig. 2.6, it is possible to imagine a similar scheme with transverse polarization. In this case it is distinct from zero, composed of mechanical pressure  $T_3$  [3]. We believe also, that transverse components  $D_1$  and  $D_2$  a vector of electric displacement are equal to zero, that is a regional effect is absent, and consequently,

$$\frac{\partial D_3}{\partial z} = 0. \quad (2.31)$$

The elementary system of the piezoelectric equations for this case is:

$$\begin{aligned} \|S\| &= \|s^D\| \|T\| + \|g\|_t \|D\|, \\ \|E\| &= -\|g\| \|T\| + \|\beta^T\|_t \|D\|. \end{aligned} \quad (2.32)$$

Here,  $s^D$  is an elasticity constant,  $g$  is a piezoelectric constant,  $\beta^T$  is the dielectric constant, and index  $t$  designates the transposed matrix.

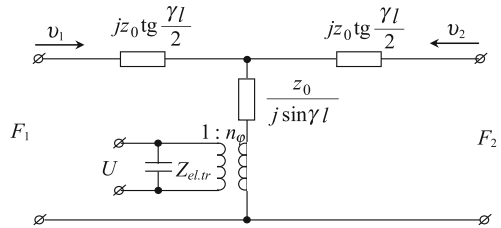


Fig. 2.5 Equivalent scheme

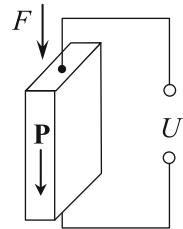


Fig. 2.6 Piezoelectric sensor with longitudinal polarization

Accepting assumptions, applying matrixes for a considered piezoelement, we see:

$$S_1 = S_2 = s_{13}^D + g_{31}D_3, \quad (2.33)$$

$$S_3 = s_{33}^D T_3 + g_{33}D_3, \quad (2.34)$$

$$S_4 = S_5 = S_6 = 0, \quad (2.35)$$

$$E_{01} = E_{02} = 0, \quad (2.36)$$

$$E_{03} = -g_{33}T_3 + \beta_{33}^T D_3, \quad (2.37)$$

where  $\beta_{33}^T = 1/\varepsilon_{33}^T$ .

The piezoelement movement equation looks like this:

$$\frac{\partial T_3}{\partial z} - \rho \frac{\partial^2 W}{\partial t^2} = 0. \quad (2.38)$$

Here  $W$  is mechanical movement

From (2.36), applying Young's modulus ( $Y_3^D = 1/s_{33}^D$ ) we see:

$$T_3 = Y_3^D S_3 - Y_3^D g_{33} D_3. \quad (2.39)$$

Now the movement equation can be written through mechanical displacement:

$$\rho \frac{\partial^2 W}{\partial t^2} = Y_3^D \left( \frac{\partial^2 W}{\partial z^2} - g_{33} \frac{\partial D_3}{\partial z} \right) = Y_3^D \frac{\partial^2 W}{\partial z^2}. \quad (2.40)$$

Lowering repetition gave the conclusion above; we will write the immediate values:

$$\begin{aligned} F_1 &= \frac{z_0}{j \operatorname{tg} \beta l} v_1 + \frac{z_0}{j \sin \beta l} v_2 + \frac{Y_3^D g_{33}}{j \omega} I, \\ F_2 &= \frac{z_0}{j \sin \beta l} v_1 + \frac{z_0}{j \operatorname{tg} \beta l} v_2 + \frac{Y_3^D g_{33}}{j \omega} I, \\ U &= \frac{Y_3^D g_{33}}{j \omega} v_1 + \frac{Y_3^D g_{33}}{j \omega} v_2 + Z_{\text{el.tr}} I, \end{aligned} \quad (2.41)$$

where:

$$\begin{aligned} Z_0 &= A \rho c = A \rho \sqrt{\frac{Y_3^D}{\rho}}, \\ \beta &= \frac{\omega}{c} = \omega \sqrt{\frac{\rho}{Y_3^D}}, \end{aligned}$$

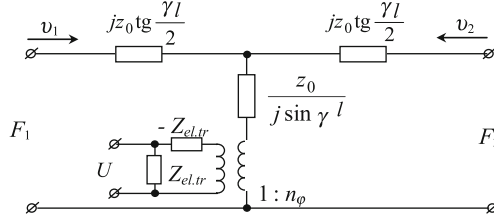


Fig. 2.7 Equivalent scheme of a piezoelement with longitudinal polarization

$$\frac{1}{Z_{el.tr}} = j\omega \varepsilon_{33}^T \left( 1 - \frac{Y_3^D g_{33}^2}{\varepsilon_{33}^T} \right) \frac{A}{l} = j\omega \varepsilon_{33}^T (1 - k_{33}^2) \frac{A}{l},$$

$$n_\varphi = \frac{AY_3^D g_{33}}{(\beta_{33}^T + Y_3^D g_{33}^2 l)} = \frac{A}{l} Y_3^D d_{33},$$

where  $k_3^2 = Y_3^D g_{31}^2 / \varepsilon_{33}^T$  is the electromechanical communication coefficient and  $A$  is the transverse section area.

The described piezoelement equivalent will become Fig. 2.7.

Thus, equivalent schemes, Figs. 2.5 and 2.7 describe piezoresonators, those with transverse polarization Fig. 2.3 and with longitudinal polarization Fig. 2.6.

### 2.3 Calculate Piezoresonator Electric Parameters

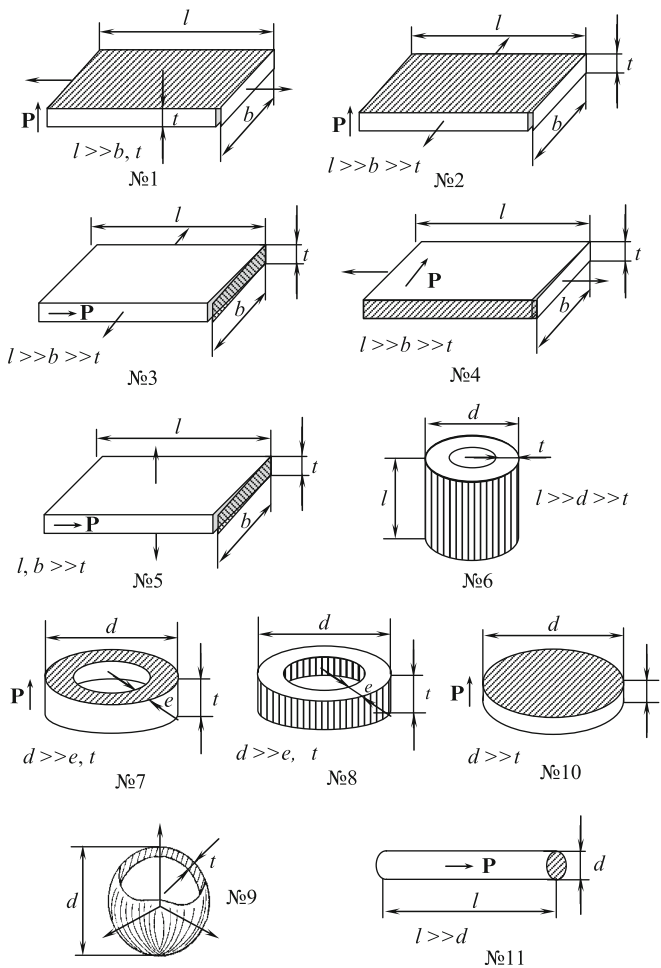
The basic piezoresonator electric parameters are frequencies of resonance  $f_r$  and anti-resonance  $f_a$ , an inter-resonant interval  $\Delta f$ , a full electric conductivity  $Y$  (or impedance  $Z$ ), and for scheme substitution a static capacitance  $C_0$ , the dynamic inductance  $L_1$  capacity  $C_1$  -or- for  $n$  harmonics  $L_n$  and  $C_n$  [9].

Parities between these piezoresonators parameters and the material's electrophysical constants piezomodul  $d_{ijk}$ , dielectric permeability  $\varepsilon_{ij}^T$  ( $\varepsilon_{ij}^S$ ), tightness  $\beta_{ij}^T$  ( $\beta_{ij}^S$ ), modules of elasticity  $c_{ijkl}^E$  ( $c_{ijkl}^D$ ),  $s_{ijkl}^E$  ( $s_{ijkl}^D$ ), etc. are diverse in different resonators. Different stimulating electrode configurations and fluctuations modes are utilized; the stimulation depends on the resonator design, as well as its form and size. Analysis of parities is [10] a joint decision about the wave equation of a purely elastic system, and the piezoelectric equations, electrical and mechanical boundary conditions must also be considered.

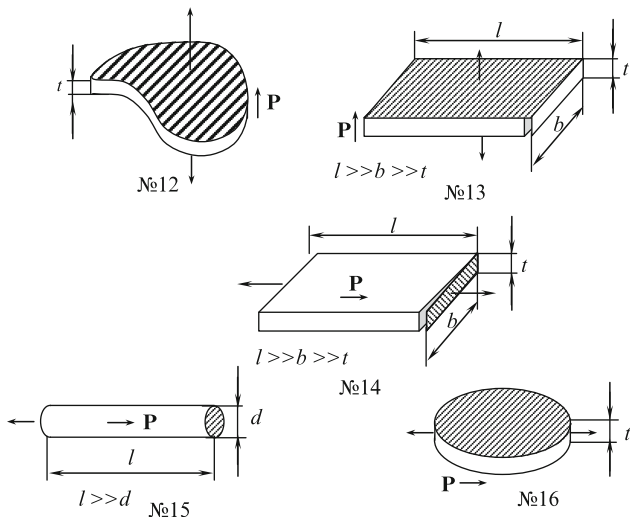
However, identification of boundary conditions and elastic fluctuations equations is done only for working size resonators which define a piezoelement resonant frequency. There are two design sizes that consider resonator wave movements as one-dimensional. In an ideal condition, this is done on infinitely long thin cores, bars and cylinders, and infinitely thin plates.

Some formulas are published; nevertheless they are not for all parameters in engineering practice and they are not systematized. Resonators with unusual sizes are not considered in published materials. Basically bars, cores and plates of a common size, and those which are most widely used, are considered. Often only approximations can be considered which satisfy conditions of the one-dimensional fluctuations.

Piezoresonator calculations use [11] a configuration factor based on the theory of the communication developed in work [12], referring to a frequency definition spectra for purely elastic bodies. The [9] formulas for calculations about piezoceramic resonators that industry has disclosed (Figs. 2.8 and 2.9) resulted in Tables 2.1–2.9,



**Fig. 2.8** Piezoelements in a non-rigid fluctuation mode (piezoelement design numbering corresponds to the numbering in Tables 2.1–2.9)



**Fig. 2.9** Piezoelements in a rigid fluctuation mode (piezoelement design numbering corresponds to the numbering in Tables 2.7–2.9)

where calculations of the capacitor relation  $r = C_0/C_1$  and the “operating” factor of electromechanical communication  $k$  are also given. Some of the formulas (Tables 2.1–2.9) concern resonators with elementary types of fluctuations (one-dimensional), which are borrowed from work by Mason and Cady [10, 13]. For simplification of some parities, factors  $A$  and  $B$ , and Poisson’s coefficient  $\sigma^E$  and  $\sigma^{E'}$  look like this:

$$A = \frac{\sqrt{2}s_{13}^E}{\sqrt{s_{33}^E(s_{11}^E - s_{12}^E)}}, \quad B = \frac{s_{13}^E}{\sqrt{s_{33}^E s_{11}^E}}, \quad \sigma^E = \frac{s_{12}^E}{s_{11}^E}, \quad \sigma^{E'} = \frac{\sigma + B^2}{1 - B^2}.$$

In Tables 2.1–2.9 designations are:  $k_t$  thickness and planar electromechanical communication factors,  $\rho$  – piezomaterial density,  $x$  – normalized frequency.

In Figs. 2.8 and 2.9, stimulating electrodes are shown (*shaded*), a *thick arrow* shows polarization direction, a *thin one* shows directional displacement of a material with piezoelement fluctuations. Piezoelement design numbering represented in Figs. 2.8 and 2.9 corresponds to the numbering in Tables 2.1–2.9.

In the drawing-up of tables as criteria of classification from the set listed above, the factors defining parameters of resonators, the type of excitation used which most essentially defines what is necessary for piezoelectric excitation and maintenance of a monofrequency spectrum of excitation resonator topology (its designer features) have been chosen.

Table 2.1

Mode oscillations	Numeration of piezoelements in Fig. 2.8				$k$	$f_p$	$f_a$
	$d_{ij}$	$\varepsilon_{nm}$	$s_{ij}(c_{ij})$	$k$			
Longitudinal on length	1	$d_{31} \varepsilon_{33}^T (1 - k_{31}^2)$	$s_{11}^E (c_{11}^E) k_{31} = d_{31} \sqrt{\frac{T^E}{\varepsilon_{33}^T s_{11}^E}}$	$k_{31} = \frac{k_{31}}{\sqrt{1 - k_{31}^2}}$	$\frac{1}{2l} \sqrt{\frac{T^E}{s_{11}^E \rho}}$	$\left(1 + \frac{4}{\pi^2} \frac{k_{31}^2}{1 - k_{31}^2}\right) f_p$	
Longitudinal on width	2	$d_{31} \varepsilon_{33}^T (1 - k_p^2)$	$s_{11}^E (c_{11}^E) k'_{31} = \frac{k_{31}}{\sqrt{1 - k_{31}^2}} \sqrt{\frac{1 + \sigma^E}{1 - \sigma^E}}$	$k'_{31} = \frac{k_{31}}{\sqrt{1 - k_{31}^2}}$	$\frac{1}{2b} \sqrt{\frac{1 - B^E}{s_{11}^E \rho}}$	$\left(1 + \frac{4}{\pi^2} \frac{k_{31}^2}{1 - k_{31}^2}\right) f_p$	
Longitudinal on width (face electrodes)	3	$\varepsilon_{33}^T (1 - k_{33}^2) \times$ $d_{31} \times (1 - k_{31}^2)$	$s_{11}^E (c_{11}^E) k''_{31} = \frac{k_{31} - B k_{33}}{\sqrt{1 - k_{33}^2}}$	$k''_{31} = \frac{k_{31} - B k_{33}}{\sqrt{1 - k_{33}^2}}$	$\frac{1}{2b} \sqrt{\frac{1 - \sigma^E}{s_{11}^E \rho}}$	$\left(1 + \frac{4}{\pi^2} \frac{k_{31}^2}{1 - k_{31}^2}\right) f_p$	
Longitudinal on length (face electrodes)	4	$d_{31} \varepsilon_{33}^T (1 - k_{33}^2) \times$ $d_{31} \times (1 - k_{31}^2)$	$s_{11}^E (c_{11}^E) k''_{31} = \frac{k_{31} - B k_{33}}{\sqrt{1 - k_{33}^2}}$	$k''_{31} = \frac{k_{31} - B k_{33}}{\sqrt{1 - k_{33}^2}}$	$\frac{1}{2l} \sqrt{\frac{(1 + \sigma^E)^2}{1 - B^2} - (1 - \sigma^E)^2} s_{11}^E \rho$	$\left(1 + \frac{4}{\pi^2} \frac{k_{31}^2}{1 - k_{31}^2}\right) f_p$	
Longitudinal on a thickness	5	$d_{31} \varepsilon_{33}^T (1 - k_{33}^2) \times$ $\times (1 - k_{31}^2) \times$ $\times (1 - k_{31}^2)$	$s_{11}^E (c_{11}^E) k''_{31} = \sqrt{\frac{(k_p - A k_{33})^2 - (k_{31} - B k_{33})^2}{1 - A^2} - (k_{31} - B k_{33})^2}$	$k''_{31} = \sqrt{\frac{(k_p - A k_{33})^2 - (k_{31} - B k_{33})^2}{1 - A^2} - (k_{31} - B k_{33})^2}$	$\frac{1}{2t} \sqrt{\frac{c_{11}^E}{\rho}} = \frac{1}{2t} \sqrt{\frac{1}{s_{11}^E \rho}}$	$\left(1 + \frac{4}{\pi^2} \frac{k_{31}^2}{1 - k_{31}^2}\right) f_p$	
Radial (polarisation on radius)	6	$d_{31} \varepsilon_{33}^T (1 - k_p^2)$	$s_{11}^E (c_{11}^E) k_p = k_{31} \sqrt{\frac{2}{1 - \sigma^E}}$	$k_p = k_{31} \sqrt{\frac{2}{1 - \sigma^E}}$	$\frac{1}{2\pi} \left(\frac{d-1}{2}\right) \sqrt{\frac{1}{s_{11}^E \rho}}$	$\left(1 + \frac{1}{2} \frac{k_p^2}{1 - k_p^2}\right) f_p$	

Table 2.2

Mode oscillations	Numeration of piezoelements in Fig. 2.8	$d_{ij}$	$\Delta f$	$C_0$	$C_1(C_n)$	$r = C_0/C_1$
Longitudinal on length	1	$d_{31}$	$\frac{4}{\pi^2} \frac{k_{31}^2}{1-k_{31}^2} f_p$	$\frac{lb\epsilon_{33}^T(1-k_{31}^2)}{t}$	$C_1 = \frac{8}{\pi^2} \frac{lb}{t} \frac{\epsilon_{33}^T k_{31}^2}{t} C_n = C_1/n^2$	$\frac{\pi^2}{8} \frac{1-k_{31}^2}{k_{31}^2}$
Longitudinal on width	2	$d_{31}$	$\frac{4}{\pi^2} \frac{k_{31}^2}{1-k_{31}^2} f_p$	$\frac{lb\epsilon_{33}^T(1-k_p^2)}{t}$	$C_1 = \frac{8}{\pi^2} \frac{lb}{t} \frac{1-k_p^2}{k_{31}^2} \epsilon_{33}^T k_{31}^2 C_n = C_1/n^2$	$\frac{\pi^2}{8} \frac{1-k_{31}^2}{k_{31}^2}$
Longitudinal on (width face electrodes)	3	$d_{31}$	$\frac{4}{\pi^2} \frac{k_{31}^2}{1-k_{31}^2} f_p$	$\frac{bt\epsilon_{33}^T(1-k_{33}^2)(1-k_{31}^2)}{l}$	$C_1 = \frac{8}{\pi^2} \frac{bt(1-k_{33}^2)}{l} \epsilon_{33}^T k_{31}^2 C_n = C_1/n^2$	$\frac{\pi^2}{8} \frac{1-k_{31}^2}{k_{31}^2}$
Longitudinal on length (face electrodes)	4	$d_{31}$	$\frac{4}{\pi^2} \frac{k_{31}^2}{1-k_{31}^2} f_p$	$\frac{lt\epsilon_{33}^T(1-k_{33}^2)(1-k_{31}^2)}{b}$	$C_1 = \frac{8}{\pi^2} \frac{lt}{b} \epsilon_{33}^T (1-k_{33}^2) k_{31}^2 C_n = C_1/n^2$	$\frac{\pi^2}{8} \frac{1-k_{31}^2}{k_{31}^2}$
Longitudinal on a thickness	5	$d_{31}$	$\frac{4}{\pi^2} \frac{k_{31}^2}{1-k_{31}^2} f_p$	$\frac{bt\epsilon_{33}^T(1-k_{33}^2)(1-k_{31}^2)}{l}$	$C_1 = \frac{8}{\pi^2} \frac{bt(1-k_{33}^2)(1-k_{31}^2)}{l} \epsilon_{33}^T k_{31}^2 C_n = C_1/n^2$	$\frac{\pi^2}{8} \frac{1-k_{31}^2}{k_{31}^2}$
Radial (polarisation on radius)	6	$d_{31}$	$\frac{1}{2} \frac{k_p^2}{1-k_p^2} f_p$	$\frac{2\pi \left(\frac{d_{31}}{2}\right) l \epsilon_{33}^T (1-k_p^2)}{t}$	$C_1 = \frac{2\pi \left(\frac{d_{31}}{2}\right) l \epsilon_{33}^T k_p^2 n}{t} = 1$	$1 - \frac{k_p^2}{k_{31}^2}$

Table 2.3

Numeration of piezoelements in Fig. 2.8		$d_{ij}$		$L_1(L_n)$	$Y_H(j2\pi f)$
Longitudinal on length	1	$d_{31}$	$L_1 = \frac{lt s_{11}^E \rho}{(8b \epsilon_{33}^T k_{31}^2)} L_n = L_1$	$j2\pi C_0 f$	$\left[ 1 + \frac{k_{31}^2}{1 - k_{31}^2} \left( 1 - \frac{f_p}{f - f_p} \right) \right] \times 0.405$
Longitudinal on width	2	$d_{31}$	$L_1 = \frac{bt(1 - k_{33}^2) s_{11}^E \rho}{8t(1 - k_{33}^2) \epsilon_{33}^T k_{31}^2 \left( 1 - \frac{1}{B^2} \right)} L_n = L_1$	$j2\pi C_0 f$	$\left[ 1 + \frac{k_{31}^2}{1 - k_{31}^2} \left( 1 - \frac{f_p}{f - f_p} \right) \right] \times 0.405$
Longitudinal on width (face electrodes)	3	$d_{31}$	$L_1 = \frac{lbs_{11}^E \rho}{8t(1 - k_{33}^2) \epsilon_{33}^T k_{31}^2 (1 - \sigma^E)} L_n = L_1$	$j2\pi C_0 f$	$\left[ 1 + \frac{k_{31}^2}{1 - k_{31}^2} \left( 1 - \frac{f_p}{f - f_p} \right) \right] \times 0.405$
Longitudinal on length (face electrodes)	4	$d_{31}$	$L_1 = \frac{lbs_{11}^E \rho}{8t(1 - k_{33}^2) \epsilon_{33}^T k_{31}^2 \left[ \frac{(1 + \sigma^E)^2}{1 - B^2} - (1 - \sigma^E)^2 \right]} L_n = L_1$	$j2\pi C_0 f$	$\left[ 1 + \frac{k_{31}^2}{1 - k_{31}^2} \left( 1 - \frac{f_p}{f - f_p} \right) \right] \times 0.405$
Longitudinal on a thickness	5	$d_{31}$	$L_1 = \frac{lt s_{11}^E \rho}{8b(1 - k_{33}^2) \epsilon_{33}^T k_{31}^2 (1 - k_{31}^2)} L_n = L_1$	$j2\pi C_0 f$	$\left[ 1 + \frac{k_{31}^2}{1 - k_{31}^2} \left( 1 - \frac{f_p}{f - f_p} \right) \right] \times 0.405$
Radial (polarisation on radius)	6	$d_{31}$	$L_1 = \frac{\left( \frac{d-1}{2} \right) t s_{11}^E \rho}{2\pi t \epsilon_{33}^T k_{31}^2} n = 1$	$j2\pi C_0 f$	$\left[ 1 + \frac{k_p^2}{1 - k_p^2} \left( 1 - \frac{2f_p}{f - f_p} \right) \right] \times 0.25$



Table 2.4

Numeration of piezoelements		Mode oscillations in Fig. 2.8				
	$d_{ij}$	$\epsilon_{nm}$	$s_{ij}(c_{ij})$	$k$	$f_p$	$f_a$
Radial	7	$d_{31} \epsilon_{33}^T (1 - k_{31}^2)$	$s_{11}^E (c_{11}^E)$	$k_{31} = \frac{d_{31}}{\sqrt{\epsilon_{33}^T s_{11}^E}}$	$\frac{1}{2\pi} \left(\frac{d-t}{2}\right) \sqrt{\frac{1}{\rho s_{11}^E}}$	$\left(1 + \frac{1}{2} \frac{1}{\sqrt{1 - k_{31}^2}}\right) f_p$
Radial (polarisation on radius)	8	$d_{31} \epsilon_{33}^T (1 - k_p^2)$	$s_{11}^E (c_{11}^E)$	$k_{31} = \frac{d_{31}}{\sqrt{\epsilon_{33}^T s_{11}^E}}$	$\frac{1}{2\pi} \left(\frac{d-t}{2}\right) \sqrt{\frac{1}{\rho s_{11}^E}}$	$\left(1 + \frac{1}{2} \frac{1}{\sqrt{1 - k_p^2}}\right) f_p$
Radial (the thin spherical cover)	9	$d_{31} \epsilon_{33}^T (1 - k_p^2)$	$s_C^E = \frac{1}{2} (s_{11}^E + s_{12}^E + s_{12}^E)$	$k_p = k_{31} \sqrt{\frac{2}{1 - \sigma^E}}$	$\frac{1}{\pi d} \sqrt{\frac{E}{\rho s_C^E}}$	$\left(1 + \frac{1}{2} \frac{1}{\sqrt{1 - k_p^2}}\right) f_p$
Radial	10	$d_{31} \epsilon_{33}^T (1 - k_p^2)$	$s_{11}^E (c_{11}^E)$	$k_p = k_{31} \sqrt{\frac{2}{1 - \sigma^E}}$	$\frac{2.03}{\pi d} \sqrt{\frac{1}{\rho s_{11}^E (1 - \sigma^E)}}$ $f_n = \frac{x_n}{\pi d} \sqrt{\frac{1}{\rho s_{11}^E (1 - \sigma^E)}}$	$\left(1 + \frac{1}{2} \frac{k_p^2}{1 - k_p^2}\right) f_p$
Radial	11	$d_{31} \epsilon_{33}^T (1 - k_{33}^2) \times \epsilon_{33}^T (1 - k_p^2)$	$s_{11}^E (c_{11}^E)$	$k_p' = \frac{k_p - A k_{33}}{\sqrt{1 - A^2} \sqrt{1 - k_{33}^2}}$	$\frac{2.19}{\pi d} \sqrt{\frac{1}{\rho s_{11}^E (1 - \sigma^E)}}$ $f_n = \frac{x_n}{\pi d} \sqrt{\frac{1}{\rho s_{11}^E (1 - \sigma^E)}}$	$\left(1 + \frac{1}{2} \frac{k_p'^2}{1 - k_p'^2}\right) f_p$

Table 2.5

Numeration of piezoelements in Fig. 2.8		Mode oscillations		$d_{ij}$	$\Delta f$	$C_0$	$C_1(C_n)$	$r = C_0/C_1$
Radial	7	$d_{31}$	$\frac{1}{2} \frac{k_{31}^2}{1 - k_{31}^2} f_p$	$C^T(1 - k_{31}^2)$	$C_1 = k_{31}^2 C_1$	$\frac{2\pi \left(\frac{d-c}{2}\right) e \varepsilon_{33}^T}{t}$	$\frac{2\pi \left(\frac{d-c}{2}\right) e \varepsilon_{33}^T}{t}$	$\frac{1 - k_{31}^2}{k_{31}^2}$
Radial (polarisation on radius)	8	$d_{31}$	$\frac{1}{2} \frac{k_{31}^2}{1 - k_{31}^2} f_p$	$\frac{2\pi \left(\frac{d-c}{2}\right) e \varepsilon_{33}^T (1 - k_{31}^2)}{t}$	$k_{31}^2 = \frac{\left(\frac{d-c}{2}\right) s_{11}^E}{2\pi e t} \times \left(\frac{2\pi e d_{31}}{s_{11}^E}\right)^2, n = 1$	$C_1 = k_{31}^2 C_1$	$\frac{2\pi \left(\frac{d-c}{2}\right) e \varepsilon_{33}^T}{t}$	$\frac{1 - k_{31}^2}{k_{31}^2}$
Radial (the thin cover)	9	$d_{31}$	$\frac{1}{2} \frac{k_{31}^2}{1 - k_{31}^2} f_p$	$\frac{2\pi d \varepsilon_{33}^T (1 - k_p^2)}{t}$	$C_1 = \frac{s^E}{4\pi t}, n = 1$	$C_1 = k_{31}^2 C_1$	$\frac{2\pi \left(\frac{d-c}{2}\right) e \varepsilon_{33}^T}{t}$	$\frac{1 - k_p^2}{k_p^2}$
Radial	10	$d_{31}$	$\frac{1}{2} \frac{k_p^2}{1 - k_p^2} f_p$	$\frac{\pi d^2 \varepsilon_{33}^T (1 - k_p^2)}{4 t}$	$C_1 = \frac{2(1 + \sigma^E)}{(2, 03)^2 - (1 - \sigma^E)^2} \frac{\pi d \varepsilon_{33}^T k_p^2}{4t}$	$C_n = \frac{2(1 + \sigma^E)}{x_n^2 - (1 - \sigma^E)^2} \frac{\pi d \varepsilon_{33}^T k_p^2}{4t}$	$\frac{2(1 + \sigma^E)}{(2, 03)^2 - (1 - \sigma^E)^2} \frac{\pi d \varepsilon_{33}^T k_p^2}{4t}$	$\frac{1 - k_p^2}{k_p^2}$
Radial	11	$d_{31}$	$\frac{1}{2} \frac{k_p^2}{1 - k_p^2} f_p$	$\frac{\pi d^2 \varepsilon_{33}^T (1 - k_p^2)(1 - k_{33}^2)}{4 t}$	$C_1 = \frac{2(1 + \sigma^E)}{(2, 19)^2 - (1 - \sigma^E)^2} \frac{\pi d^2 \varepsilon_{33}^T k_p^2 (1 - k_{33}^2)}{4l}$	$C_n = \frac{2(1 + \sigma^E)}{x_n^2 - (1 - \sigma^E)^2} \frac{\pi d^2 \varepsilon_{33}^T k_p^2 (1 - k_{33}^2)}{4l}$	$\frac{2(1 + \sigma^E)}{(2, 19)^2 - (1 - \sigma^E)^2} \frac{\pi d^2 \varepsilon_{33}^T k_p^2 (1 - k_{33}^2)}{4l}$	$\frac{1 - k_p^2}{k_p^2}$

Table 2.6

Mode oscillations	$d_{ij}$	Numeration of piezoelements in Fig. 2.8	$L_1(L_n)$	$Y_H(j2\pi f)$
Radial	$d_{31}$	7	$2\pi \left( \frac{d-e}{2} \right) \epsilon \rho \left( \frac{s_{11}^E}{2\pi e d_{31}} \right)^2$	$j2\pi C_0 f \left[ 1 + \frac{k_{31}^2}{1-k_{31}^2} \left( 1 - \frac{2f_p}{f-f_p} \right) \times 0.25 \right]$
Radial (polarisation on radius)	$d_{31}$	8	$2\pi \left( \frac{d-e}{2} \right) \epsilon \rho \left( \frac{s_{11}^E}{2\pi e d_{31}} \right)^2$	$j2\pi C_0 f \left[ 1 + \frac{k_{31}^2}{1-k_{31}^2} \left( 1 - \frac{2f_p}{f-f_p} \right) \times 0.25 \right]$
Radial (the thin spherical cover)	$d_{31}$	9	$\pi d^2 t \rho n = 1$	$j2\pi C_0 f \left[ 1 + \frac{k_p^2}{1-k_p^2} \left( 1 - \frac{2f_p}{f-f_p} \right) \times 0.25 \right]$
Radial	$d_{31}$	10	$L_1 = \frac{[(2.03)^2 - (1 - \sigma^E)^2] (1 - \sigma^E) s_{11}^E \rho}{2\pi (1 + \sigma^E) \epsilon_{33}^T k_p^2 (2.03)^2}$ $L_n = \frac{[x_n^2 - (1 - \sigma^E)^2] (1 - \sigma^E) s_{11}^E \rho}{2\pi (1 + \sigma^E) \epsilon_{33}^T k_p^2 x_n^2}$	$j2\pi C_0 f \left[ 1 + \frac{k_p^2}{1-k_p^2} \left( 1 - \frac{0.814f_p}{f-f_p} \right) \times 0.486 \right]$
Radial	$d_{31}$	11	$L_1 = \frac{[(2.19)^2 - (1 - \sigma^{E'})^2] (1 - \sigma^{E'}) s_{11}^E \rho}{2\pi (1 + \sigma^{E'}) \epsilon_{33}^T (1 - k_{33}^2) (2.19)^2 k_p^2}$ $L_n = \frac{[x_n^2 - (1 - \sigma^{E'})^2] (1 - \sigma^{E'}) s_{11}^E \rho}{2\pi (1 + \sigma^{E'}) \epsilon_{33}^T (1 - k_{33}^2) x_n^2 k_p^2}$	$j2\pi C_0 f \left[ 1 + \frac{k_p^2}{1-k_p^2} \left( 1 - \frac{0.823f_p}{f-f_p} \right) \times 0.459 \right]$

**Table 2.7**

Numeration of piezoelements in Fig. 2.8		$d_{ij}$	$\epsilon_{mn}$	$s_{ij}^D(c_{ij})$	$k$	$f_p$	$f_a$
Mode oscillations on a thickness	12	$d_{33}$	$\frac{1}{\beta_{33}^S}, (\epsilon_{33}^S)$	$s_{33}^D(c_{33})$	$k_t = k_{31} \sqrt{\frac{\epsilon_{33}^T}{D_{33}}}$	$\frac{1 - k_t^2}{1 - (1 - \frac{4}{\pi^2}) k_t^2}$	$\frac{1}{2l} \sqrt{\frac{c_{33}^D}{\rho}} = \frac{1}{2l} \sqrt{\frac{1}{\rho_s 33^D}}$
Longitudinal on width	13	$d_{33}$	$\frac{1 - k_{33}^{*2}}{\beta_{33}^S}$	$s_{33}^D(c_{33})$	$k_{33}^* = \frac{k_{33} - Bk_{31}}{\sqrt{1 - B^2} \sqrt{1 - k_{31}^2}}$	$\frac{1 - k_{33}^{*2}}{1 - (1 - \frac{4}{\pi^2}) k_t^2}$	$\frac{1}{2b} \sqrt{\frac{1 - B^2}{\rho_{s33}^E (1 - k_{33}^{*2})}}$
Longitudinal on length	14	$d_{33}$	$\epsilon_{33}^T (1 - k_{33}^2)$	$s_{33}^D(c_{33})$	$k_{33} = \frac{d_{33}}{\sqrt{\epsilon_{33}^T s_{33}^E}}$	$\frac{1 - k_{33}^2}{1 - (1 - \frac{4}{\pi^2}) k_{33}^2}$	$\frac{1}{2l} \sqrt{\frac{1}{\rho_{s33}^D}}$
Longitudinal on length	15	$d_{33}$	$\epsilon_{33}^T (1 - k_{33}^2)$	$s_{33}^D(c_{33})$	$k_{33} = \frac{d_{33}}{\sqrt{\epsilon_{33}^T s_{33}^E}}$	$\frac{1 - k_{33}^2}{1 - (1 - \frac{4}{\pi^2}) k_{33}^2}$	$\frac{1}{2l} \sqrt{\frac{1}{\rho_{s33}^D}}$
Shift on a thickness	16	$d_{15}$	$\frac{1}{\beta_{11}^S}, (\epsilon_{11}^S)$	$s_{44}^D(c_{44})$	$k_{15} = \frac{\sqrt{\epsilon_{11}^S}}{\sqrt{\epsilon_{11}^T s_{44}^E}} = h \sqrt{\frac{\epsilon_{11}^S}{D_{44}}}$	$\frac{1 - k_{15}^2}{1 - (1 - \frac{4}{\pi^2}) k_{15}^2}$	$\frac{1}{2l} \sqrt{\frac{c_{44}^D}{\rho}} = \frac{1}{2l} \sqrt{\frac{1}{\rho_s 44^D}}$

Table 2.8

Mode oscillations	Numeration of piezoelements in Fig. 2.8	$d_{ij}$	$\Delta f$	$C_0$	$C_1(C_n)$	$r = C_0/C_1$
Longitudinal on a thickness	12	$d_{33}$	$\frac{4}{\pi^2} \frac{k_t^2}{1 - k_t^2} f_p$	$\frac{lb}{\beta_{33}^S t}$	$C_1 = \frac{8}{\pi^2} \frac{lb}{\beta_{33}^S t} \frac{k_t^2}{1 - k_t^2} C_n = \frac{C_1}{n^2}$	$\frac{\pi^2}{8} \frac{1 - k_t^{*2}}{k_t^2}$
Longitudinal on width	13	$d_{33}$	$\frac{4}{\pi^2} \frac{k_{33}^{*2}}{1 - k_{33}^{*2}} f_p$	$\frac{lt}{b\beta_{33}^S} (1 - k_{33}^{*2})$	$C_1 = \frac{8}{\pi^2} \frac{lt}{b\beta_{33}^S} (k_{33}^{*2})^2$	$\frac{\pi^2}{8} \frac{1 - k_{33}^{*2}}{k_{33}^{*2}}$
Longitudinal on length	14	$d_{33}$	$\frac{4}{\pi^2} \frac{k_{33}^2}{1 - k_{33}^2} f_p$	$\frac{bt \epsilon_{33}^T (1 - k_{33}^2)}{l}$	$C_1 = \frac{8}{\pi^2} \frac{bt}{l} \epsilon_{33}^T k_{33}^2 C_n = \frac{C_1}{n^2}$	$\frac{\pi^2}{8} \frac{1 - k_{33}^2}{k_{33}^2}$
Longitudinal on length	15	$d_{33}$	$\frac{4}{\pi^2} \frac{k_{33}^2}{1 - k_{33}^2} f_p$	$\frac{\pi_d^2 \epsilon_{33}^T (1 - k_{33}^2)}{4l}$	$C_1 = \frac{8}{\pi^2} \frac{\pi_d^2}{4l} \epsilon_{33}^T k_{33}^2 C_n = \frac{C_1}{n^2}$	$\frac{\pi^2}{8} \frac{1 - k_{33}^2}{k_{33}^2}$
Shift on a thickness	16	$d_{15}$	$\frac{4}{\pi^2} \frac{k_{15}^2}{1 - k_{15}^2} f_p$	$\frac{lb}{\beta_{11}^S t}$	$C_1 = \frac{8}{\pi^2} \frac{lb}{\beta_{11}^S t} \frac{k_{15}^2}{1 - k_{15}^2} C_n = \frac{C_1}{n^2}$	$\frac{\pi^2}{8} \frac{1 - k_{15}^2}{k_{15}^2}$

**Table 2.9**

Mode oscillations	Numeration of piezoelement's in Fig. 2.9	$d_{ij}$	$L_1(L_n)$	$Y_{\ominus}(j2\pi f)$
Longitudinal on a thickness	12	$d_{33}$	$L_1 = \frac{t^3 \beta_{33}^S \left[ 1 - \left( 1 - \frac{4}{\pi^2} \right) k_t^2 \right] \delta_{33}^D \rho}{8bt_k^2 (1 - k_t^2)}$ $L_n = L_1$	$j2\pi C_0 f \frac{1}{1 - k_t^2 \left( 1 - \frac{f_a}{f-f_a} \right) \times 0.405}$
Longitudinal on width	13	$d_{33}$	$L_1 = \frac{b^3 \beta_{33}^S \delta_{33}^D \rho (1 - k_{33}^{*2})}{8htk_{33}^{*2}}$ $L_n = L_1$	$j2\pi C_0 f \frac{1}{1 - k_{33}^{*2} \left( 1 - \frac{f_a}{f-f_a} \right) \times 0.405}$
Longitudinal on length	14	$d_{33}$	$L_1 = \frac{t^3 \left[ 1 - \left( 1 - \frac{4}{\pi^2} \right) k_{33}^2 \right]^2 \delta_{33}^D \rho}{8bt k_{33}^2 (1 - k_{33}^2)^2 \epsilon_{33}}$ $L_n = L_1$	$j2\pi C_0 f \frac{1}{1 - k_{33}^2 \left( 1 - \frac{f_a}{f-f_a} \right) \times 0.405}$
Longitudinal on length	15	$d_{33}$	$L_1 = \frac{t^3 \left[ 1 - \left( 1 - \frac{4}{\pi^2} \right) k_{33}^2 \right]^2 \alpha_{33}^D \rho}{2\pi d^2 k_{33}^2 (1 - k_{33}^2)^2 \epsilon_{33}}$ $L_n = L_1$	$j2\pi C_0 f \frac{1}{1 - k_{33}^2 \times 0.19 \left( 1 - \frac{2.13f_a}{f-f_a} \right) \times 0.405}$
Shift on a thickness	16	$d_{15}$	$L_1 = \frac{t^3 \beta_{11}^S \left[ 1 - \left( 1 - \frac{4}{\pi^2} \right) k_{15}^2 \right]^2 \alpha_{44}^D \rho}{8lbt k_{15}^2 (1 - k_{15}^2)}$ $L_n = L_1$	$j2\pi C_0 f \frac{1}{1 - k_{15}^2 \left( 1 - \frac{f_a}{f-f_a} \right) \times 0.405}$

Thus, despite the great variety of various types of excitation, piezoceramic resonators of industrial design can be broken into two big groups: rigid and non-rigid types of piezoelectric excitation (Figs. 2.7 and 2.8; Tables 2.1–2.9).

On the basis of such a categorisation it is possible to establish [14]:

- Direction of the appendix of a vector of exciting electrical field and acoustic wave;
- Directions of a vector of polarization (see also chapter 3)

From Tables 2.3, 2.6 and 2.9 it is evident that expressions of full electric conductivity of nonrigid ( $Y_n$ ) and rigid ( $Y_r$ ) types of fluctuations for all types of resonators can be written down in the generalized form:

$$Y_n(j2\pi f) = j2\pi f C_0 \left\{ 1 + \frac{k^2}{1-k^2} \left[ -\frac{a}{\frac{x-x_p}{x_p}} + (1-b) \right] \right\}, \quad (2.42)$$

$$Y_r(j2\pi f) = \frac{j2\pi f C_0}{\left\{ 1 - k^2 \left[ -\frac{a}{\frac{x-x_a}{x_a}} + (b-a) \right] \right\}}, \quad (2.43)$$

where  $a$  and  $b$  – the coefficients which have for all types of rigid and the majority of non-rigid fluctuations the values 0.405 and 0.810 respectively;  $x$  – the normalized frequency:

$$x = \frac{\pi d}{V} = \begin{cases} \frac{\pi}{2} \frac{f}{f_a} & \text{for a rigid mode,} \\ \frac{\pi}{2} \frac{f}{f_p} & \text{for a nonrigid mode,} \end{cases}$$

$x_p, x_a$  – the normalized frequencies of a resonance and an anti-resonance;  $f, V$  – frequency and phase speed of an elastic wave;  $d$  – the size of the resonator defining frequency of its mechanical resonance.

More strictly, it is necessary to write

$$Y_n(j2\pi f) = j2\pi f C_0 \left[ 1 + \frac{k^2}{1-k^2} M(x) \right], \quad (2.44)$$

$$Y_r(j2\pi f) = \frac{j2\pi f C_0}{1 - k^2 M(x)}, \quad (2.45)$$

where  $M(x)$  – even function of the normalized frequency for all resonators with the rigid type and the majority with the non-rigid type of fluctuation  $M(x) = \text{tg } x/x$ .

In engineering practice, however, instead of the equations (2.44) and (2.45)  $M$  including transcendental dependence, it is more expedient to use expressions (2.42) and (2.43), development [9] of the equations (2.44) and (2.45) by means of  $M(x)$  decomposition alongside and near to the first pole  $x_1$ . Expressions (2.42) and (2.43), the decomposition received taking into account only two first members, provide an error no more than 1% in comparison with the equations (2.44) and (2.45) [9].

Let us notice, that a pole  $x_1$ , i.e., frequency of a mechanical resonance of the resonator, corresponds to the frequency of a consecutive resonance in the case of a non-rigid type and to the frequency of an antiresonance in the case of a rigid type of fluctuation, which along with distinction of expressions (2.42) and (2.43) is a consequence of the basic physical distinction between the rigid and non-rigid types of fluctuations. This distinction consists in that in the case of the rigid type, the excitation electrical field, being parallel to the direction of distribution of an elastic wave, influences the form of fluctuations through electrical boundary conditions (a piezoelectric feedback), while in the case of a non-rigid type this effect is absent.

An experimental check [9] which resulted in the formulas for piezoceramic system IITC materials given in Tables 2.1–2.9 has shown a deviation of the calculated and measured parameters of resonators of no more than on 1% for frequencies of a resonance and an antiresonance, and about 3% for  $\Delta f$ ,  $C_0$ ,  $C_1$ . This makes it possible to draw a conclusion of quite satisfactory accuracy of the given formulas from the point of view of engineering practice, and also regarding the possibility of their use for measurement of numerical values of the electrophysical constants of piezoceramic materials.

## 2.4 Fluctuations of Piezoceramic Rods

Because any piezoelectric element is a spatial body, on any mode of fluctuations it is necessary to analyze spatial distribution of fields of displacement and pressure. However in practice it is frequent because of geometrical features of transducers one-dimensional modes are realized. Considerable difference of one characteristic size allows to isolate this or that mode from others and to consider it as one-dimensional [2].

The advantage of the one-dimensional analysis consists in its being based on systems of the ordinary differential equations and equivalent circuits. Problems of the analysis of transducers on the basis of equivalent schemes are considered, for example, in work by Kats, Holland and EerNisse, and Domarkas and Kazys [3, 15, 16]. The deficiencies of one-dimensional models are obvious. But there is an area of extensions in which one-dimensional models retain their value and will in the future.

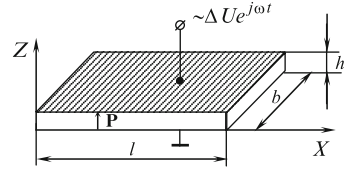
The theory of piezoelectric transducers in which the basis of scalar models lies was developed by L.J. Gutin [17–19], I.G. Rusakov [20, 21], A.A. Harkevich [22].

Methodological bases of rational designing of converters are stated in the work by Harkevich [22]. The author of this work enters a piezoelectric constant  $g$  and accurately formulates a distinction between elastic constants depending on electric conditions [23]. Thus, four equivalent forms of defining parities take a finished form. In the study by Gutin [17], the regular statement of settlement schemes of radiators and of receivers of sound working in water is given.

The analysis of fluctuations of cores is carried out by N.A. Shulga and A.M. Bolkisev [2].



Fig. 2.10 Piezoelectric rod



### 2.4.1 Longitudinal Fluctuations of a Rod in a Transverse Field

Let us consider the piezoelectric core polarized in a transverse direction (Fig. 2.10).

Electrodes on it are put on surfaces, perpendicular to a direction of a vector of polarization. We will arrange the system of the Cartesian coordinates so that axis  $X$  has been directed along a rod, and axis  $Z$  is parallel to a polarization vector. Longitudinal fluctuations are raised by electric field  $E_z$ . If the transverse sizes  $h$  and  $b$  of a core are much less than its length  $l$ , the equation of movement will become [6]:

$$d\sigma_{xx}/dx + \rho\omega^2 u_x = 0. \quad (2.46)$$

One of the most important characteristics of a piezoelectric material is the coefficient of electromechanical communication. A square of static coefficient of communication  $k_{31}^2$  we will define as the relation of the transformed electric (mechanical) energy to full energy, that is to the sum of provided mechanical (electric) and transformed electric (mechanical) energies:

$$k_{31}^2 = U_{el}/(U_{mech} + U_{el}). \quad (2.47)$$

dynamic coefficient of communication

$$k_d^2 = \frac{k_{31}^2(1 - k_{31}^2)\alpha^2}{k_{31}^2(1 - k_{31}^2)\alpha^2 + (1 - \alpha k_{31}^2)^2(1 + \text{tg}^2 \frac{\chi}{2})}, \quad (2.48)$$

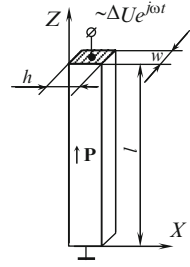
where

$$\alpha = \frac{\frac{2}{\chi} \text{tg} \frac{\chi}{2}}{k_{31}^2(1 - k_{31}^2)\alpha^2 + (1 - \alpha k_{31}^2)^2(1 - k_{31}^2 + k_{31}^2 \frac{2}{\chi} \text{tg} \frac{\chi}{2})}, \quad \chi = kl,$$

$$k = \omega \sqrt{\rho s_{11}^E}.$$

If we pass to static loading, having taken  $\chi = 0$  from (2.48) we will obtain  $k_d^2 = k_{31}^2$ .

Fig. 2.11 Piezoelectric rod



### 2.4.2 Longitudinal Fluctuations of a Rod in a Longitudinal Field

Let us consider further a piezoelectric rod, the length and which vectors of polarization coincide with axis  $Z$  (Fig. 2.11).

Electrodes are put on face surfaces  $z = 0, l$ . The length of a core is much more than its cross-section sizes. With such geometry, taking into account the fact that sides are free from normal and transverse-tangents mechanical pressure, not equal the zero still has only pressure  $\sigma_{zz}$ , and the equation of movement looks like [2]:

$$d\sigma_{zz}/dz + \rho\omega^2 u_z = 0. \tag{2.49}$$

Let us find the value of the static coefficient:

$$k_{33}^2 = \frac{W_{el}}{W_{mech} + W_{el}} = \frac{k_D^2}{1 + k_D^2}, \tag{2.50}$$

where  $k_D^2 = g_{33}^2 / (s_{33}^D \beta_{33}^T)$ .

For piezoelectric materials, except for crystals of classes of symmetry (1), (m), parities are fair  $g_{33}^2 = d_{33} \beta_{33}^T$ ,  $\epsilon_{33}^T = (\beta_{33}^T)^{-1}$ . Taking into consideration that  $s_{33}^D = s_{33}^E (1 - k_{33}^2)$ , from (2.50) we obtain [2]:

$$k_{33}^2 = d_{33}^2 / s_{33}^E \epsilon_{33}^T.$$

From the dynamic factor of communication of the given type

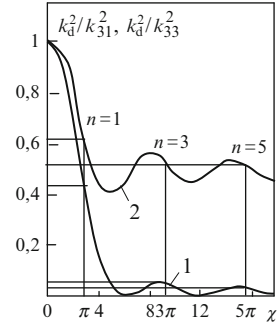
$$k_d^2 = \frac{U_{el}}{U_{mech} + U_{el}} = \frac{k_{33}^2}{1 + \text{tg} \frac{\chi}{2}} \frac{1}{l} \int_0^l f^2(z) dz. \tag{2.51}$$

if we pass to static loading, having put  $\chi = 0$  we will obtain  $k_d^2 = k_{33}^2$ .

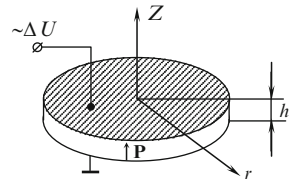
In Fig. 2.12, the dependence of dynamic factors of communication on frequency for cores with longitudinal and transverse polarization [2] is shown.

On an axis of ordinates relations  $k_d^2/k_{31}^2$  (1) and  $k_d^2/k_{33}^2$  (2) in which values  $K_d^2$  are calculated under the formula (2.48) are postponed. In calculation, tangents

**Fig. 2.12** Dependence on frequency of dynamic coefficients of communication



**Fig. 2.13** Piezoelectric disk



of corners of losses are accepted to be equal to 0.01. Relations of factors of communication in a core with longitudinal polarization near to the basic type  $\chi = \pi$  and its overtones  $\chi = 3\pi, 5\pi$  are more than in a core with transverse polarization. Dynamic coefficients for both types of fluctuations are 69% and 77% of the static coefficients on the basic type, 22% and 72% and 17% and 72% of the static coefficients on the first and second overtones respectively.

### 2.4.3 Fluctuations of a Piezoceramic Disk

Let us consider a piezoelectric disk, radius  $R$  which considerably surpasses its thickness (Fig. 2.13).

Radial fluctuations of a disk are described by the equation of movement [2]

$$\frac{d\sigma_{rr}}{dr} - \frac{1}{r}(\sigma_{rr} - \sigma_{\theta\theta}) + \rho\omega^2 u_r = 0. \tag{2.52}$$

For the planar coefficient of communication, we obtain

$$k_p^2 = \frac{W_{el}}{W_{mech} + W_{el}} = \frac{2}{1 - \nu} \frac{d_{31}^2}{s_{11}^E \epsilon_{33}^T}. \tag{2.53}$$

With radial polarization, the resolution of a problem on the compelled fluctuations of a ring is more difficult than with thickness polarization.

## 2.5 Piezoceramic Transformers

Piezoelectric transformers are piezoelements with two systems of electrodes – input and output.

The piezoelectric transformer is named a piezoelectric element with three and more electrodes connected to one or several sources of an electric signal and loadings [4, 24]. In the elementary case, the piezoelectric transformer represents a piezoelement with three electrodes, forming two systems of electrodes. The part of the piezoelectric transformer connected to a source of an electric signal is called the activator, and the part connected to loading is called the generator.

In the activator, the variable electric signal at the outflow of the return piezoeffect will be transformed to energy of acoustic waves which, arising on borders of electrodes, fill the whole volume of the transformer. On a frequency equal to one of resonant mechanical frequencies of the transformer, a standing wave with the maximum amplitude of fluctuations is formed. In the generator of the piezoelectric transformer, mechanical pressure at the expense of a direct piezoeffect will be transformed to an electric signal. On resonant frequencies, the transformation factor has the maximum value.

Piezoelectric transformers are voltage transformers. However, recently transformers with low coefficient of transformation on voltage, but working with the big currents reaching of several amperes [24], have been built. They have been referred to as piezoelectric transformers of a current.

In terms of transformation of energy in the activator and the generator, piezoelectric transformers can be classified as transverse–transverse, longitudinal–longitudinal, transverse–longitudinal, nad longitudinal–transverse.

In terms of fluctuations, piezoelectric transformers subdivide into those creating excitation of fluctuations longitudinally, radially, with a shift and with a bend.

The basic designs of piezoelectric transformers are shown in Fig. 2.14. Transformers with longitudinal polarization of the activator and the generator (Fig. 2.14) are referred to as transformers of ring type, and those with transverse–longitudinal

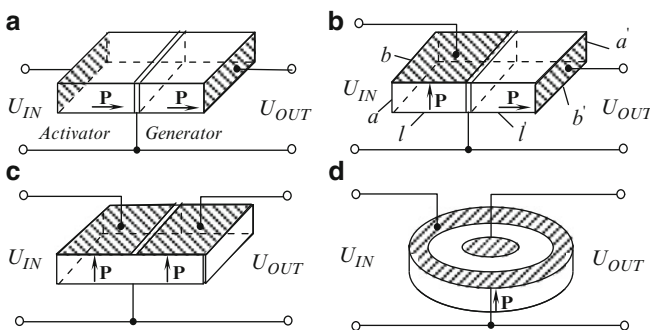


Fig. 2.14 Designs of piezoelectric transformers

and transverse polarization (Fig. 2.14) as transformers of transverse type. The disk transformer (Fig. 2.14) is also a transformer of transverse type, but has some features of work, therefore disk transformers are allocated to a separate group.

Longitudinal–longitudinal and transverse–transverse transformers are symmetric. Their factor of transformation does not depend on geometrical size and reaches several tens and even hundreds of units [4, 24].

The transverse–longitudinal transformer is asymmetrical, and its coefficient of transformation depends on a parity of the geometrical sizes. This design of the transformer represents the greatest practical interest. The coefficient of transformation of the transverse–longitudinal transformer can reach several thousand [4, 24].

The coefficient of transformation of the disk transformer is above rather than at the transverse. On excitation of a radial type of fluctuation, the energy stream through a cylindrical surface remains invariable for any radius, and, hence, in the disk centre there is a concentration of energy. If the generating section of the transformer is arranged in the disk centre, there is an additional increase of coefficient of transformation at the expense of concentration of energy.

Disk transformers usually apply as transducers of impedances. For effective excitation on frequency of the first overtone, the line of section of electrodes should pass on a circle of diameter equal to 0.45 diameters of a disk. Reduction of thickness of the transformer leads to an increase in the factor of transformation. Input and output impedances are defined mainly by capacities of systems of electrodes.

The analysis of work of piezoelectric transformers, as well as piezoelectric resonators, can be spent by means of equivalent schemes. The equivalent scheme of the piezoelectric transformer results from equivalent schemes of two piezoelectric resonators, one of which is the activator, the other the generator [3, 4, 24].

Thus, the equivalent scheme piezotransformer results from a cascade connection of the equivalent schemes of two piezorezonators, considered in Sect. 2.2. (Figs. 2.5 and 2.7), and looks like what is shown in Fig. 2.15.

After some transformations, the equivalent scheme will become shown in Fig. 2.16 [4].

Here, the equivalent scheme of the transverse–longitudinal transformer is shown. The equivalent scheme of the transverse–transverse transformer differs in terms of the absence of an element  $-jX_{eR}$  in a loading chain, and the longitudinal–longitudinal presence of a similar element in a generator chain. Parameters of the equivalent scheme are defined by expressions [4]:

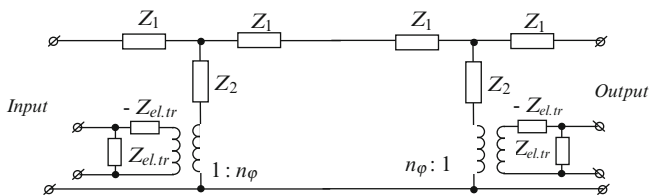


Fig. 2.15 Equivalent electric scheme piezoelectric transformer

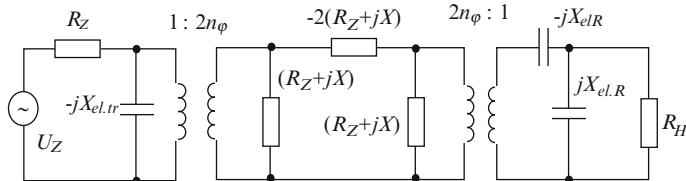


Fig. 2.16 Equivalent scheme transverse-longitudinal piezoelectric transformer

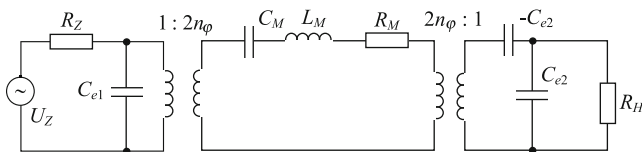


Fig. 2.17 Equivalent scheme piezoelectric transformer

$$\begin{aligned}
 X_{\text{etr}} &= \frac{1}{\omega \varepsilon_{33}^T (1 - k_{31}^2)} \frac{a}{bl}; \\
 X_{eR} &= \frac{1}{\omega \varepsilon_{33}^T (1 - k_{33}^2)} \frac{l'}{a'b'}; \\
 R &= \frac{\pi}{Q_M} ab \sqrt{\rho Y_1^E}; \\
 X &= 2\pi ab \sqrt{\rho Y_3^E} \frac{\omega - \omega_p}{\omega_p}; \\
 n_\phi &= bd_{31} Y_1^E; \quad n_\phi = \frac{k_{33}^2}{g_{33}} \frac{a'b'}{l'},
 \end{aligned} \tag{2.54}$$

where  $a$  and  $a'$ ,  $b'$ ,  $l'$  are the sizes obtained in Fig. 2.14б.

At excitation on resonant frequency of a mechanical part, it is possible to present the equivalent scheme in the form of a consecutive contour (Fig. 2.17) whose parameters are defined by equalities [24]:

$$\begin{aligned}
 C_{01} &= (X_{\text{etr}})^{-1}; \quad C_{02} = (X_{\text{el.R}})^{-1}; \\
 R_M &= R; \quad C_M = \frac{1}{\pi^2 ab Y^E}; \\
 L_M &= 4abl\rho = m_{\text{exc}},
 \end{aligned} \tag{2.55}$$

where  $C_{01}$  and  $C_{02}$  are static capacities of a piezoelectric transformer.

In Fig. 2.18, the simplified equivalent scheme of the disk piezoelectric transformer [25] is shown.

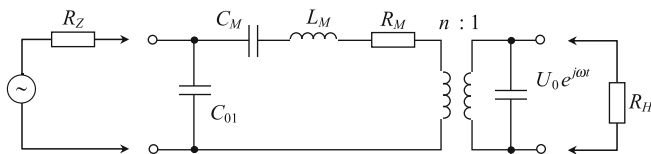


Fig. 2.18 Equivalent scheme disk piezoelectric transformer

Having replaced the mechanical scheme and an input electric chain for the equivalent generator, it is possible to obtain an expression for the transformation coefficient on the voltage of the transformer expressed through the following parameters:

For transverse–longitudinal

$$K_{u0} = \frac{4Q_M Y_{33}^E g_{33} d_{31} l}{\pi^2 (1 - k_{33}^2) a}; \quad (2.56)$$

for longitudinal–longitudinal

$$K_{u0} = \frac{4Q_M k_{33}^2}{\pi^2} = \frac{4Q_M g_{33} d_{33} Y_3}{\pi^2}; \quad (2.57)$$

for transverse–transverse

$$K_{u0} = \frac{4Q_M}{\pi^2} \frac{k_{31}^2}{1 - k_{31}^2} = \frac{4Q_M}{\pi^2} \frac{g_{31} d_{31} Y_3}{\pi^2}. \quad (2.58)$$

As was specified above, the transverse–longitudinal piezoelectric transformer has the maximum coefficient of transformation, if we assume the sizes  $l \rightarrow \infty$ ,  $a \rightarrow \infty$ ,  $K_{u0} \rightarrow \infty$ . However, the sizes are defined by admissible overall dimensions, complexity of technology of their performance, and losses. If we consider that the length  $l$  should not exceed 100 mm, and the thickness should not be less than 0.25 mm, geometry coefficient is  $N_G = l/a = 200$ . To this limit for the transformer from piezoceramic ИТС-23 (PZТ), there corresponds the coefficient of transformation equal to 7,000 [24]. In practice, this size is much less. In work by Lavrinenko [24], the influence on the coefficient of transformation of capacity of onductors was investigated. It is shown that connection to the piezoelectric transformer in the size  $100 \times 20 \times 0.5$  mm of a conductor in length of 50 mm reduces the transformation coefficient by 30%. In addition, case details in which the transformer is concluded also create losses in radiation at the expense of their higher dielectric permeability (in comparison with air). For example, approach besides to the transformer of a plate from plexiglass reduces the transformation coefficient by 5%. These losses are created at the expense of reduction of a surface of the generator. For this purpose, the generator section should be created in the form close to a square or a circle, and a multilayered activator applied.

### 2.5.1 Piezoelectric Transformer in the Form of Thin Disks and Rings

Free a axis symmetry radial fluctuations thin piezoceramic disks and the rings polarized on a thickness, are described [7, 26–29] by the movement equation [7, 26–29]:

$$\frac{E}{1-\sigma^2} \left( \frac{\partial^2 u}{\partial r^2} + \frac{1}{r} \frac{\partial u}{\partial r} - \frac{u}{r^2} \right) + \rho \omega^2 u = 0, \quad (2.59)$$

where  $u$ – radial displacement;  $r$  – current radius; boundary conditions: axis.

$$T_{rr} = 0 \quad \text{npu} \quad r = a, b \quad (2.60)$$

and the physical equations:

$$T_{rr} = \frac{E}{1-\sigma^2} (S_{rr} + \sigma S_{\Theta\Theta}) - \frac{Ed_{31}}{1-\sigma^2} E_z, \quad (2.61)$$

$$T_{\Theta\Theta} = \frac{E}{1-\sigma^2} (\sigma S_{rr} + S_{\Theta\Theta}) - \frac{Ed_{31}}{1-\sigma} E_z, \quad (2.62)$$

$$D_z = \frac{Ed_{31}}{1-\sigma} (S_{rr} + S_{\Theta\Theta}) + \varepsilon_{33}^* E_z, \quad (2.63)$$

where  $T_{rr}, T_{\Theta\Theta}$  – radial and angular component tensor pressure respectively;  $S_{rr}, S_{\Theta\Theta}$  – radial and angular components tensor deformations respectively;  $D_z$  – a component of a vector of electric displacement, perpendicular resonator planes;  $E_z$  – a component of a vector of electric field,

$$\varepsilon_{33}^* = \varepsilon_{33}^T \left[ 1 - \frac{2Ed_{31}^2}{(1-\sigma)\varepsilon_{33}^T} \right] = \varepsilon_{33}^T (1 - k^2), \quad (2.64)$$

where  $k = [2Ed_{31}^2 / (1-\sigma)\varepsilon_{33}^T]^{\frac{1}{2}}$  – coefficient of electromechanical communication;  $d_{31}, \varepsilon_{33}^T$  – piezoelectric and dielectric constants respectively.

Components tensor deformations  $S_{ij}$  are connected with displacement *and* parities

$$S_{rr} = \frac{\partial u}{\partial r}, \quad S_{\Theta\Theta} = \frac{u}{r}. \quad (2.65)$$

It is assumed that face surfaces of resonators are completely covered by electrodes, and field  $E_z$  is constant on a thickness. In these conditions, the common resolution of the equation (2.65) is represented as a linear combination of Bessel's functions of the first and second sort

$$u = AI_1 \left( \frac{\omega}{\vartheta} r \right) + BN_1 \left( \frac{\omega}{\vartheta} r \right), \quad (2.66)$$

where  $\vartheta = [E/\rho(1-\sigma^2)]^{\frac{1}{2}}$  – speed of a sound wave;  $A, B$ – unknown coefficient.



Substituting the equation (2.66) in expression (2.60), taking into account the equation (2.65), we obtain a system of two algebraic equations concerning unknown coefficients  $A$  and  $B$ :

$$\begin{aligned} A[XI_0(X) - (1 - \sigma)I_1(X)] + B[XN_0(X) - (1 - \sigma)N_1(X)] \\ = ad_{31}(1 + \sigma)E_z, \\ A[\varepsilon XI_0(\varepsilon X) - (1 - \sigma)I_1(\varepsilon X)] + B[\varepsilon XN_0(\varepsilon X) - (1 - \sigma)N_1(\varepsilon X)] \\ = bd_{31}(1 + \sigma)E_z, \end{aligned} \quad (2.67)$$

where  $x = \omega a / \vartheta$ ,  $\varepsilon = b/a$ .

The resolution of equation (2.67) gives

$$A = ad_{31}(1 + \sigma) \frac{\Delta_1}{\Delta} E_z, \quad B = ad_{31}(1 + \sigma) \frac{\Delta_2}{\Delta} E_z, \quad (2.68)$$

where

$$\Delta = \begin{vmatrix} XI_0(X) - (1 - \sigma)I_1(X) & XN_0(X) - (1 - \sigma)N_1(X) \\ XN_0(X) - (1 - \sigma)N_1(X) & \varepsilon XN_0(\varepsilon X) - (1 - \sigma)N_1(\varepsilon X) \end{vmatrix}, \quad (2.69)$$

$$\Delta_1 = \begin{vmatrix} 1 & XN_0(X) - (1 - \sigma)N_1(X) \\ \varepsilon & \varepsilon XN_0(\varepsilon X) - (1 - \sigma)N_1(\varepsilon X) \end{vmatrix}, \quad (2.70)$$

$$\Delta_2 = \begin{vmatrix} XI_0(X) - (1 - \sigma)I_1(X) & 1 \\ \varepsilon XN_0(\varepsilon X) - (1 - \sigma)N_1(\varepsilon X) & \varepsilon \end{vmatrix}. \quad (2.71)$$

In a stationary mode, the current  $I$  which is passing through the resonator, is equal to

$$I = j\omega Q = j\omega \int_s -D_z r dr d\theta, \quad (2.72)$$

where  $Q$  – integrated charge on face surfaces of the resonator;  $s$  – the area of electrodes.

Assuming  $E = (V_0/h)$ , where  $V_0$  – amplitude of the exciting electric voltage enclosed to electrodes;  $h$  – thickness of the resonator, we obtain with the account the equation (2.63) and (2.72)

$$I = YV_0,$$

where conductivity  $Y$  is equal to

$$\begin{aligned} Y = j\omega C_0 \left\{ 1 + \frac{k^2(1 + \sigma)}{(1 - k^2)(1 - \varepsilon^2)} \left[ \frac{\Delta_1}{\Delta} (I_1(X) - \varepsilon I_1(\varepsilon X)) \right. \right. \\ \left. \left. + \frac{\Delta_2}{\Delta} (N_1(X) - \varepsilon N_1(\varepsilon X)) \right] \right\}, \end{aligned} \quad (2.73)$$

$C_0 = \pi(a^2 - b^2)\varepsilon_{33}^*/h$  – static capacity of the resonator.

On resonant frequency conductivity  $Y = \infty$ , whence

$$\Delta = 0. \quad (2.74)$$

At  $\varepsilon \rightarrow 0$ , the equation (2.73) degenerates according to the known frequency equation of a continuous disk [10]

$$XI_0(X)/I_1(X) = 1 - \sigma. \quad (2.75)$$

on an antiresonance conductivity  $Y = 0$ , whence we receive the equation of antiresonant frequencies

$$1 + \frac{k^2(1 + \sigma)}{(1 - k^2)(1 - \varepsilon^2)} \left\{ \frac{\Delta_1}{\Delta} [I_1(X) - \varepsilon I_1(\varepsilon X)] + \frac{\Delta_2}{\Delta} [N_1(X) - \varepsilon N_1(\varepsilon X)] \right\} = 0. \quad (2.76)$$

At  $\varepsilon \rightarrow 0$ , the equation (2.76) degenerates according to the equation of antiresonant frequencies of a continuous disk

$$1 + \frac{k^2}{1 - k^2} \frac{(1 + \sigma)I_1(X)}{XI_0(X) - (1 - \sigma)I_1(X)} = 0. \quad (2.77)$$

Thus, the relative resonant interval  $\Delta f_{Rn}/f_{Rn}$  can be found from a parity

$$\frac{\Delta f_{Rn}}{f_{Rn}} = \frac{f_{An} - f_{Rn}}{f_{Rn}} = \frac{X_{An} - X_{Rn}}{X_{Rn}}, \quad (2.78)$$

where  $f_{An}$ ,  $f_{Rn}$  – respectively antiresonant and resonant frequencies  $n$ -й types of fluctuations;  $A_{Rn}$ ,  $A_{Rn}$  – accordingly roots of the equations (2.76) and (2.74), or (2.77) and (2.75).

For a continuous disk it is possible to write the approximated expression

$$\frac{\Delta f_{Rn}}{f_{Rn}} = \frac{k^2}{1 - k^2} = \frac{1 + \sigma}{X_{Rn}^2 - (1 - \sigma^2) + \frac{k^2(1 + \sigma)}{1 - k^2} \sigma}. \quad (2.79)$$

However, for the basic frequency the formula (2.79) gives a considerable error.

The coefficient of dynamic inductance  $K_{Ln}$  is calculated under the formula

$$K_{Ln} = \frac{\int_s u^{(n)^2} r dr d\theta}{\left[ \int_s -D_z^{(n)} r dr d\theta \right]^2}, \quad (2.80)$$

where  $n$  designates an order of a type of fluctuation, and displacement  $u^{(n)}$  on resonant frequency can be found within any constant from system (2.67) at the short-circuited electrodes, that is  $E_z = 0$ . As  $\Delta = 0$ , the homogeneous system (2.67) will have not trivial decisions and, hence, the relation of factors  $In^{(n)}/An d^{(n)}$  can be found.

From the second equation of homogeneous system (2.67) we will obtain

$$B^{(n)}/A^{(n)} = -\overline{A}_n = -\frac{\varepsilon X_{Rn} I_0(\varepsilon X_{Rn}) - (1 - \sigma) I_1(\varepsilon X_{Rn})}{\varepsilon X_{Rn} N_0(\varepsilon X_{Rn}) - (1 - \sigma) N_1(\varepsilon X_{Rn})}, \quad (2.81)$$

and displacement  $u^{(n)}$  on resonant frequency becomes

$$u^{(n)} = I_1\left(\frac{\omega_{Rn}}{\vartheta} r\right) - \overline{A}_n N_1\left(\frac{\omega_{Rn}}{\vartheta} r\right). \quad (2.82)$$

Substituting the equation (2.82) for (2.80), taking into account expressions (2.63) and (2.65), we obtain

$$K_{Ln} = \frac{\rho(1 - \sigma)^2 \left(1 - \frac{1 - \sigma^2}{X_{Rn}^2}\right) - \left(\varepsilon^2 - \frac{1 - \sigma^2}{X_{Rn}^2}\right) \left[\frac{I_1(\varepsilon X_{Rn}) - \overline{A}_n N_1(\varepsilon X_{Rn})}{I_1(X_{Rn}) - \overline{A}_n N_1(X_{Rn})}\right]^2}{4\pi d_{31}^2 E^2 \left[1 - \varepsilon \frac{I_1(\varepsilon X_{Rn}) - \overline{A}_n N_1(\varepsilon X_{Rn})}{I_1(X_{Rn}) - \overline{A}_n N_1(X_{Rn})}\right]^2}. \quad (2.83)$$

At  $\varepsilon \rightarrow 0$ , equation (2.83) turns into known expression  $K_{Ln}$  for a continuous disk [28]

$$K_{Ln} = \frac{\rho(1 - \sigma)^2}{4\pi d_{31}^2 E^2} \left(1 - \frac{1 - \sigma^2}{X_{Rn}^2}\right). \quad (2.84)$$

For disks with divided electrodes, the equations (2.77) and (2.84) will become

$$1 + \frac{k^2}{1 - k^2} \frac{(1 + \sigma^2) I_1(X)}{X I_0(X) - (1 - \sigma) I_1(X)} [1 - 2(p/a) I_1(Xp/a)/I_1(X)] = 0, \quad (2.85)$$

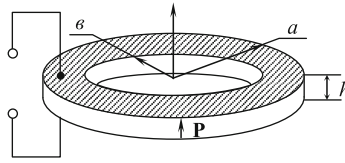
$$K_{Ln}^p = \frac{\rho(1 - \sigma)^2}{4\pi d_{31}^2 E^2} \frac{X_{Rn}^2 - (1 - \sigma^2)}{X_{Rn}^2 [1 - 2(p/a) I_1(X_{Rn}p/a)/I_1(X_{Rn})]^2}. \quad (2.86)$$

Optimum value of parameter  $p$  is defined from the equation

$$\frac{d}{dp} K_{Ln}^p = 0.$$

For small values of a difference ( $X_{An} - X_{Rn}$ ) the equation (2.85) can be changed into the following form

$$\frac{\Delta f_{Rn}}{f_{Rn}} \approx \frac{k^2}{1 - k^2} \frac{(1 + \sigma) [1 - 2(p/a) I_1(X_{Rn}p/a)/I_1(X_{Rn})]}{X_{Rn}^2 - (1 - \sigma^2) + \frac{k^2(1 + \sigma)}{1 - k^2} [\sigma - 2(p/a) I_1(X_{Rn}p/a)/I_1(X_{Rn})]}. \quad (2.87)$$



**Fig. 2.19** Piezoelement orientation:  $P$  – polarisation direction;  $a, b$  – external and internal radii accordingly;  $U_0$  – amplitude of the voltage enclosed to electrodes of a piezoelement, changing over time  $\sim e^{j\omega t}$ , where  $j = \sqrt{-1}$ ,  $t$  – time

Piezotransformers and resonators with the disk ceramic piezoelements making radial fluctuations are widely applied in measuring techniques. The requirement for expansion of a frequency range makes it necessary to use overtone fluctuations [30]. It is necessary to notice that the theory of flat pressure [26] is true only for thin disks and rings with a small enough parity of internal to external radius  $b/a$  (Fig. 2.19).

Therefore, this theory gives the chance to investigate basically only the qualitative character of fluctuations; that, however, makes it possible to draw conclusions useful in practice. In addition, because of the big influence of technology coefficients on parameters, piezoceramic transformers and resonators should not be expected steady exact quantitative (coincidence?) theoretical data with the experimental. However qualitative dimensionless character of theoretical conclusions, the general for all piezoceramic materials, well enough proves to be true experimental data [29].

Therefore this theory indicates as we already noted, in the linear theory of piezoelectricity, that the key resonator parameters are: resonant frequency  $f_{Rn}$  for a relative resonant interval  $\Delta f_{Rn}/f_{Rn}$ , and that the equivalent electric parameters are dynamic capacity  $C_n$  and inductance  $L_n$  connected among themselves by a parity

$$C_n \frac{1}{\omega_n^2 L_n}, \tag{2.88}$$

where  $\omega_n$  – resonant circular frequency.

However in practice, for the characteristics of electric parameters, a more convenient size coefficient of dynamic inductance,  $K_{Ln}$ , is used:

$$K_{Ln} = L_n/h, \tag{2.89}$$

where  $h$  is the thickness of the resonator.

It is assumed that face surfaces of disk and ring resonators are completely covered by electrodes. Under these conditions, fluctuation of disk resonators is most fully investigated by M. Onoe [28], the basic because the basic attention direct on resonator characteristics on the first overtone.

**Table 2.10**

$\sigma$	$X_{R1}$	$X_{R2}$	$X_{R3}$	$X_{A1}$	$X_{A2}$	$X_{A3}$	$\Delta f_{R1}/f_{R1}(\%)$	$\Delta f_{R2}/f_{R2}(\%)$	$\Delta f_{R3}/f_{R3}(\%)$	$K_{L1}$ (H/mm)	$K_{L2}$ (H/mm)	$K_{L3}$ (H/mm)
0.26	2.022	5.382	8.565	2.341	5.491	8.643	15.8	2.0	0.9	2.398	3.006	3.067
0.27	2.030	5.382	8.565	2.352	5.499	8.643	15.9	2.2	0.9	2.343	2.926	2.985
0.28	2.038	5.382	8.565	2.364	5.506	8.643	16.0	2.3	0.9	2.288	2.847	2.904
0.29	2.041	5.390	8.565	2.380	5.506	8.643	16.6	2.2	0.9	2.231	2.769	2.824
0.30	2.049	5.390	8.565	2.391	5.514	8.643	16.7	2.3	0.9	2.177	2.693	2.745
0.31	2.057	5.390	8.565	2.403	5.522	8.659	16.8	2.5	1.1	2.124	2.617	2.667
0.32	2.061	5.390	8.581	2.415	5.522	8.659	17.2	2.5	0.9	2.069	2.542	2.591
0.33	2.069	5.398	8.581	2.430	5.530	8.659	17.5	2.4	0.9	2.016	2.469	2.516
0.34	2.073	5.398	8.581	2.442	5.538	8.659	17.8	2.6	0.9	1.962	2.396	2.441
0.35	2.080	5.398	8.581	2.453	5.545	8.674	17.9	2.7	1.1	1.911	2.325	2.368
0.36	2.084	5.398	8.581	2.469	5.545	8.674	18.5	2.7	1.1	1.858	2.254	2.296

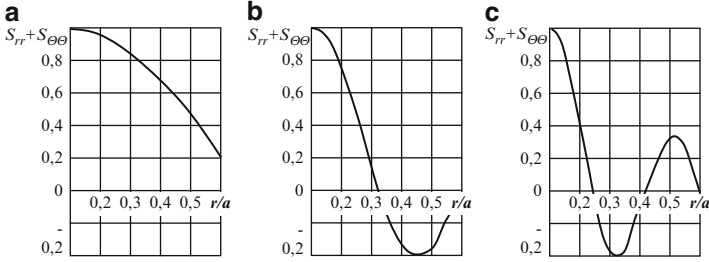
Resonant and antiresonant frequencies of disk and ring transformers and resonators are calculated under the formula

$$f = \frac{X}{\pi D} \left( \frac{E}{\rho(1 - \sigma^2)} \right)^{1/2}, \quad (2.90)$$

where  $E = 1/s_{11}^E$  – Young's modulus;  $\sigma = -s_{12}^E/s_{11}^E$  – Poisson's coefficient;  $\rho$  – material density;  $D$  – external diameter of the resonator;  $s_{ij}^E$  – flexibility constants;  $X$  – a root of the corresponding frequency or antiresonant equation.

In Table 2.10, depending on Poisson's coefficient  $\sigma$  values of roots  $X_{Rn}$  and  $X_{An}$  the equations of resonant and antiresonant frequencies, relative resonant intervals  $\Delta f_{Rn}/f_{Rn}$  H factors of inductance  $K_{Ln}$  of the first three types of fluctuation of a continuous disk are resolved accordingly. It is clearly visible that relative resonant interval overtone types of fluctuation of a disk sharply decrease with growth of an order of a type of fluctuation whereas factors of inductance of the same type differ slightly, and aspire to a constant with an increase in an order of a type of fluctuation. The basic type of fluctuations possesses the greatest relative resonant interval.

In Fig. 2.20, schedules of distribution of the deformations, characterizing distribution of a charge of the first three types of fluctuation of a continuous disk on radius from which it is well visible are resolved, that if the basic type of fluctuation possesses – sign-constant charge distribution, for overtone fashions of fluctuations there are areas of a different sign. Therefore at fluctuations piezoceramic a disk with continuous electrodes on (overtone modes) fashions of fluctuations there is indemnification of charges of different signs that leads to increase in factors of inductance  $K_{Ln}$  of corresponding fashions of fluctuations and to reduction of relative resonant intervals. This raises the question of how the relative resonant interval and factor of inductance  $K_{Ln}$  of a corresponding type of fluctuation will change if optimum conditions of excitation are to be created for this type?



**Fig. 2.20** Distribution of deformations, forming a piezoelectric charge: (a) on the basic fashion of fluctuations, (b) on the first overtone, (c) on the second overtone

Let us consider the first overtone, which is characterised by one change of a phase of a charge along the disk radius. We will divide continuous electrodes on both parts of a disk with concentric circles of variable radius  $p$  into the areas raised by fields of opposite polarity. The value of the optimum parameter  $p$  can be received from a condition of a minimality of factor of inductance  $K_{Rn}^p$  that leads to the equation

$$I_0(X_{Rn}p/a) = 0, \tag{2.91}$$

where  $I_0$  is Bessel’s function of the first sort, and  $a$  is disk radius. Roots of equation (2.91) make it possible to find optimum values  $p$  on a corresponding type of fluctuation. It is necessary to remember that the condition  $p/a < 1$  was always satisfied. From here it follows that for the basic type of fluctuation  $p = 0$ , otherwise

$$X_1/X_{R1} = p/a = 2.4048/2.049 > 1,$$

which contradicts physical sense. Here  $X_1 = 2.4048$  – the first root of the equation (2.91),  $X_{R1} = 2.049$  – the first root of the frequency equation (2.75) for the continuous disk, calculated at value of Poisson’s coefficient  $\sigma = 0.3$ .

For piezotransformers and resonators made from materials of type PZT-5 ( $\sigma = 0.35$ ) a relative resonant interval on the first overtone of a continuous disk with the divided electrodes will make  $\Delta f_{R2}/f_{R2} = 0.064$ , that is 2.37 times more than a relative resonant interval of the same type of fluctuation of a disk with continuous electrodes (Table 2.10), but almost 2.8 times less than a relative resonant interval on the basic type of fluctuation of a disk with continuous electrodes.

In Tables 2.11–2.16 depending on Poisson’s coefficient  $\sigma$  and parities of radiuses  $b/a$  are given respectively values of roots  $X_{Rn}$  and  $X_{An}$  the equations of resonant and antiresonant frequencies, relative resonant intervals and factors of inductance of the basic and the first overtone fashions of fluctuations of a ring. A prominent feature of the ring resonator is dependence of all its parameters on a parity of radiuses (Fig. 2.21).

**Table 2.11**

$\sigma$	$b/a$	$X_{R1}$	$X_{R2}$	$X_{A1}$	$X_{A2}$	$\frac{\Delta f_{R1}}{f_{R1}}(\%)$	$\frac{\Delta f_{R2}}{f_{R2}}(\%)$	$K_{L1}$ (H/mm)	$K_{L2}$ (H/mm)
0.260	0.050	2.006	5.281	2.313	5.405	15.303	2.355	2.486	2.803
	0.100	1.957	5.048	2.240	5.203	14.449	3.080	2.767	2.314
	0.150	1.883	4.853	2.131	5.056	13.158	4.164	3.273	1.816
	0.200	1.796	4.783	2.006	5.048	11.743	5.525	4.020	1.443
	0.250	1.704	4.838	1.883	5.157	10.491	6.588	5.007	1.182
	0.300	1.617	4.986	1.770	5.367	9.496	7.640	6.235	0.992
	0.350	1.535	5.227	1.671	5.662	8.861	8.329	7.702	0.847
	0.400	1.461	5.545	1.582	6.043	8.245	8.972	9.443	0.729
	0.450	1.395	5.965	1.504	6.525	7.800	9.383	11.470	0.630
	0.500	1.335	6.486	1.434	7.116	7.424	9.708	13.860	0.544
	0.550	1.281	7.147	1.374	7.862	7.284	10.007	16.716	0.467
	0.600	1.232	7.986	1.319	8.798	7.098	10.172	20.215	0.398
	0.650	1.187	9.078	1.271	10.027	7.038	10.446	24.599	0.335
	0.270	0.050	2.014	5.281	2.325	5.405	15.437	2.355	2.433
0.100		1.963	5.040	2.247	5.203	14.506	3.239	2.713	2.247
0.150		1.887	4.846	2.135	5.056	13.131	4.331	3.219	1.761
0.200		1.798	4.776	2.006	5.048	11.622	5.697	3.967	1.400
0.250		1.704	4.830	1.885	5.157	10.605	6.759	4.954	1.147
0.300		1.617	4.978	1.770	5.367	9.496	7.808	6.193	0.963
0.350		1.533	5.219	1.669	5.670	8.872	8.639	7.655	0.822
0.400		1.459	5.545	1.580	6.051	8.256	9.112	9.395	0.708
0.450		1.393	5.957	1.502	6.533	7.811	9.656	11.441	0.612
0.500		1.333	6.486	1.432	7.131	7.435	9.948	13.840	0.529
0.550		1.279	7.147	1.370	7.877	7.143	10.224	16.704	0.455
0.600		1.230	7.986	1.316	8.814	6.951	10.366	20.210	0.387
0.650		1.185	9.078	1.267	10.042	6.886	10.618	24.600	0.326

In Fig. 2.22, curves of roots  $X_{Rn}$  of the frequency equation (2.75) rings depending on a parity of radiuses are shown  $b/a$ .

At these curves, interesting features are observed:

1. They possess the minima specifying that the frequency factor overtone fluctuations decrease at a cutting of an aperture of a certain diameter in a continuous disk a little. In particular, for the first overtone the minimum of frequency coefficient is reached at  $b/a = 0.2$  (for all values of  $\sigma$ ), and the size of frequency factor goes down thus, for example, for  $\sigma = 0.28$  by 11.5%. Calculations show that with growth of an order of a type of fluctuation minima of frequency curves move towards parity reduction  $b/a$ .
2. There are parities of radiuses  $b/a$  at which the cutting of apertures in a disk does not change frequency coefficient overtone type of fluctuation of a disk.
3. With parity increase  $b/a$ , frequency coefficient overtone types of fluctuation sharply increase, which makes it possible to receive higher frequencies while preserving the external diameter of the resonator.

**Table 2.12**

$\sigma$	$b/a$	$X_{R1}$	$X_{R2}$	$X_{A1}$	$X_{A2}$	$\frac{\Delta f_{R1}}{f_{R1}}(\%)$	$\frac{\Delta f_{R2}}{f_{R2}}(\%)$	$K_{L1}$ (H/mm)	$K_{L2}$ (H/mm)
0.280	0.050	2.018	5.281	2.337	5.413	15.793	2.502	2.374	2.651
	0.100	1.967	5.032	2.259	5.203	14.872	3.398	2.655	2.181
	0.150	1.891	4.838	2.142	5.056	13.310	4.499	3.165	1.708
	0.200	1.799	4.768	2.010	5.048	11.718	5.869	3.915	1.357
	0.250	1.704	4.822	1.885	5.164	10.605	7.093	4.903	1.112
	0.300	1.615	4.970	1.770	5.374	9.627	8.133	6.139	0.934
	0.350	1.531	5.211	1.667	5.677	8.884	8.950	7.609	0.798
	0.400	1.457	5.538	1.578	6.058	8.267	9.405	9.359	0.688
	0.450	1.389	5.957	1.498	6.548	7.833	9.917	11.388	0.595
	0.500	1.329	6.478	1.428	7.147	7.457	10.320	13.792	0.514
	0.550	1.275	7.139	1.368	7.893	7.318	10.562	16.660	0.442
	0.600	1.226	7.986	1.312	8.845	6.974	10.756	20.170	0.377
	0.650	1.181	9.078	1.263	10.073	6.908	10.960	24.563	0.317
	0.290	0.050	2.026	5.281	2.348	5.413	15.924	2.502	2.321
0.100		1.972	5.032	2.267	5.203	14.927	3.398	2.601	2.116
0.150		1.893	4.822	2.146	5.056	13.399	4.837	3.108	1.655
0.200		1.799	4.760	2.014	5.048	11.934	6.042	3.857	1.315
0.250		1.704	4.815	1.885	5.164	10.605	7.266	4.853	1.078
0.300		1.615	4.962	1.768	5.382	9.507	8.459	6.100	0.906
0.350		1.529	5.211	1.665	5.685	8.895	9.100	7.565	0.775
0.400		1.455	5.538	1.574	6.074	8.145	9.686	9.325	0.668
0.450		1.387	5.950	1.496	6.556	7.844	10.191	11.364	0.578
0.500		1.327	6.478	1.426	7.162	7.468	10.560	13.777	0.499
0.550		1.273	7.139	1.364	7.908	7.176	10.780	16.654	0.429
0.600		1.222	7.978	1.310	8.861	7.155	11.058	20.132	0.366
0.650		1.180	9.078	1.259	10.089	6.755	11.131	24.571	0.308

4. That is especially important for monorating of resonators; spectral curves of radial fluctuations start to be moved apart with parity increase  $b/a$ . So, if for a continuous disk ( $\sigma = 0.28$ ) the relative distances from below and from above to the next frequencies in shares of the first overtone frequencies are respectively 0.622 and 0.592, for the ring resonator at  $b/a = 0.55$  the same distances are equal respectively to 0.822 and 0.965.

The most interesting characteristics of ring resonators are shown in Figs. 2.22 and 2.23, where curves of a relative resonant interval and coefficients of inductance of the basic and the first overtone type of fluctuation respectively depending on a parity  $b/a$  are represented. As the factor of inductance  $K_{Ln}$  serves as a measure of efficiency of excitation of fluctuations (the lower  $K_{Ln}$  is, the more intensive the fluctuations), from the schedules represented in Fig. 2.23 it is clearly visible that with parity increase  $b/a$  overtone the basic mode of fluctuation becomes more effective.



**Table 2.13**

$\sigma$	$b/a$	$X_{R1}$	$X_{R2}$	$X_{A1}$	$X_{A2}$	$\Delta f_{R1}/f_{R1}(\%)$	$\Delta f_{R2}/f_{R2}(\%)$	$K_{L1}$ (H/mm)	$K_{L2}$ (H/mm)	
0.300	0.050	1.030	5.281	2.360	5.413	16.276	2.502	2.263	2.503	
	0.100	1.976	5.024	2.275	5.195	15.094	3.404	2.545	2.052	
	0.150	1.897	4.815	2.154	5.048	13.576	4.844	3.055	1.603	
	0.200	1.801	4.745	2.018	5.048	12.029	6.390	3.807	1.273	
	0.250	1.704	4.807	1.887	5.164	10.719	7.439	4.804	1.045	
	0.300	1.613	4.962	1.768	5.382	9.639	8.459	6.049	0.880	
	0.350	1.527	5.203	1.663	5.693	8.906	9.412	7.524	0.752	
	0.400	1.452	5.530	1.572	6.082	8.300	9.981	9.271	0.649	
	0.450	1.384	5.950	1.492	6.571	7.866	10.453	11.315	0.561	
	0.500	1.323	6.470	1.422	7.178	7.489	10.933	13.734	0.485	
	0.550	1.269	7.139	1.360	7.932	7.198	11.107	16.616	0.417	
	0.600	1.220	7.978	1.306	8.876	7.007	11.253	20.138	0.356	
	0.650	1.176	9.078	1.255	10.120	6.777	11.474	24.540	0.300	
	0.310	0.050	2.038	5.281	1.372	5.421	16.405	2.650	2.211	2.431
		0.100	1.980	5.017	2.282	5.195	15.261	3.564	2.489	1.989
0.150		1.899	4.807	2.158	5.048	13.665	5.013	2.999	1.552	
0.200		1.803	4.737	2.018	5.048	11.908	6.564	3.758	1.233	
0.250		1.704	4.799	1.887	5.172	10.719	7.775	4.756	1.012	
0.300		1.611	4.955	1.766	5.390	9.651	8.786	5.999	0.852	
0.350		1.525	5.195	1.661	5.701	8.918	9.725	7.484	0.729	
0.400		1.450	5.222	1.570	6.089	8.311	10.276	9.242	0.629	
0.450		1.382	5.942	1.489	6.587	7.736	10.859	11.297	0.544	
0.500		1.319	6.470	1.419	7.193	7.512	11.173	13.694	0.471	
0.550		1.265	7.131	1.356	7.947	7.220	11.446	16.580	0.405	
0.600		1.216	7.978	1.302	8.907	7.029	11.643	20.106	0.346	
0.650		1.172	9.078	1.251	10.151	6.800	11.816	24.512	0.291	

From Fig. 2.22 and Tables 2.11–2.16, it follows that with parity increase  $b/a$  the relative resonant interval overtone type of fluctuation increases, whereas the relative resonant interval of the basic type of fluctuation falls. This phenomenon suggests the existence of an optimum for  $K_{Ln}$  parities  $b/a$ , which is observed in rectangular resonators working on planimetric fashions of fluctuations [31]. Unfortunately, with the theory used it was not possible to achieve a similar result. Initial data for calculation of relative resonant intervals and  $K_{Ln}$  are taken for a material PZT-5 [10].

For an experimental check of the existence of an optimum parity  $b/a$  on the first overtone, five rings from piezoceramic ИТС-22 (PZT) with internal diameter  $d = 8$  and external diameter  $D = 22.02$  mm were selected. Parity change  $b/a$  was made internal grinding external diameter.

**Table 2.14**

$\sigma$	$b/a$	$X_{R1}$	$X_{R2}$	$X_{A1}$	$X_{A2}$	$\frac{\Delta f_{R1}}{f_{R1}}(\%)$	$\frac{\Delta f_{R2}}{f_{R2}}(\%)$	$K_{L1}$ (H/mm)	$K_{L2}$ (H/mm)
0.320	0.050	2.041	5.281	2.383	5.421	16.755	2.650	2.155	2.360
	0.100	1.986	5.009	2.294	5.195	15.509	3.725	2.437	1.928
	0.150	1.901	4.799	2.162	5.048	13.753	5.183	2.944	1.502
	0.200	1.803	4.729	2.022	5.048	12.123	6.739	3.700	1.193
	0.250	1.704	4.791	1.187	5.172	10.719	7.950	4.710	0.980
	0.300	1.609	4.947	1.764	5.398	9.662	9.114	5.951	0.826
	0.350	1.524	5.188	1.660	5.709	8.929	10.039	7.446	0.707
	0.400	1.446	5.522	1.566	6.105	8.334	10.558	9.192	0.610
	0.450	1.378	5.942	1.487	6.595	7.899	10.980	11.254	0.529
	0.500	1.316	6.470	1.415	7.209	7.534	11.413	13.656	0.457
	0.550	1.261	7.131	1.352	7.971	7.242	11.773	16.548	0.393
0.330	0.600	1.213	7.978	1.298	8.923	7.052	11.838	20.078	0.336
	0.650	1.168	9.078	1.248	10.167	6.822	11.988	24.488	0.283
	0.050	2.049	5.281	2.395	5.429	16.881	2.797	2.104	2.290
	0.100	1.990	5.001	2.302	5.195	15.674	3.886	2.382	1.867
	0.150	1.904	4.791	2.170	5.048	13.929	5.354	2.894	1.453
	0.200	1.803	4.721	2.022	5.048	12.123	6.915	3.649	1.154
	0.250	1.702	4.783	1.887	5.180	10.845	8.288	4.655	0.949
	0.300	1.607	4.939	1.763	5.405	9.674	9.443	5.905	0.800
	0.350	1.522	5.188	1.656	5.716	8.813	10.189	7.411	0.685
	0.400	1.444	5.414	1.562	6.121	8.210	10.996	9.168	0.592
	0.450	1.374	5.934	1.483	6.610	7.921	11.397	11.213	0.512
0.500	1.312	6.463	1.411	7.224	7.556	11.788	13.622	0.443	
0.550	1.257	7.131	1.349	7.986	7.265	11.991	16.518	0.382	
0.600	1.209	7.971	1.294	8.914	7.074	12.337	20.054	0.326	
0.650	1.164	9.078	1.244	10.198	6.845	12.330	24.466	0.275	

In Table 2.17 average results of this measurement are shown [29].

From Table 2.17 the maximum  $\Delta f_{R2}/f_{R2}$  is clearly visible at  $b/a = 0.465$ . In the third column, the relative distance overtone frequencies to the basic, coinciding well with the calculated value shown in Fig. 2.22, is given. Thus, use of ring transformers and resonators with radial fluctuations on the first overtone gives the chance to expand considerably a range of frequencies, keeping thus key parameters ( $\Delta f/f$ ;  $K_L$ ) commensurate with parameters of disk transformers and resonators on the basic type of fluctuation.

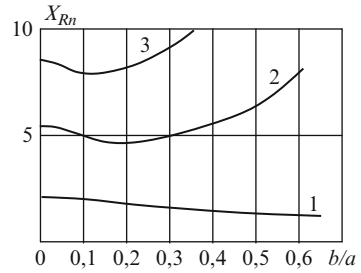
**Table 2.15**

$\sigma$	$b/a$	$X_{R1}$	$X_{R2}$	$X_{A1}$	$X_{A2}$	$\frac{\Delta f_{R1}}{f_{R1}}(\%)$	$\frac{\Delta f_{R2}}{f_{R2}}(\%)$	$K_{L1}$ (H/mm)	$K_{L2}$ (H/mm)	
0.340	0.050	2.053	5.273	2.407	5.429	17.227	2.948	2.048	2.219	
	0.100	1.994	5.001	2.310	5.195	15.839	3.886	2.328	1.808	
	0.150	1.906	4.783	2.174	5.048	14.017	5.525	2.840	1.405	
	0.200	1.803	4.714	2.026	5.056	12.339	7.256	3.595	1.116	
	0.250	1.702	4.768	1.885	5.188	10.731	8.804	4.612	0.917	
	0.300	1.605	4.931	1.761	5.413	9.686	9.774	5.861	0.774	
	0.350	1.518	5.180	1.654	5.732	8.963	10.655	7.359	0.664	
	0.400	1.440	5.514	1.558	6.128	8.233	11.137	9.123	0.574	
	0.450	1.370	5.934	1.479	6.626	7.944	11.659	11.175	0.497	
	0.500	1.308	6.463	1.407	7.248	7.578	12.149	13.590	0.430	
	0.550	1.253	7.123	1.345	8.006	7.287	12.386	16.492	0.370	
	0.600	1.205	7.971	1.288	8.985	6.936	12.727	20.032	0.316	
	0.650	1.160	9.063	1.240	10.229	6.868	12.866	24.449	0.266	
	0.350	0.050	2.057	5.273	2.418	5.436	17.573	3.096	1.994	2.151
		0.100	1.998	4.993	2.321	5.195	16.197	4.048	2.274	1.749
0.150		1.908	4.768	2.177	5.048	14.104	5.869	2.786	1.357	
0.200		1.805	4.706	2.026	5.056	12.218	7.434	3.551	1.079	
0.250		1.700	4.760	1.885	5.188	10.858	8.982	4.560	0.887	
0.300		1.603	4.923	1.759	5.421	9.697	10.105	5.819	0.749	
0.350		1.514	5.172	1.650	5.740	8.986	10.971	7.309	0.642	
0.400		1.436	5.506	1.557	6.144	8.390	11.576	9.081	0.555	
0.450		1.366	5.926	1.475	6.649	7.966	12.199	11.140	0.481	
0.500		1.304	6.455	1.403	7.263	7.601	12.525	13.561	0.416	
0.550		1.249	7.123	1.341	8.037	7.310	12.822	16.470	0.359	
0.600		1.201	7.971	1.284	9.001	6.958	12.922	20.015	0.306	
0.650		1.156	9.063	1.236	10.260	6.891	13.209	24.435	0.258	

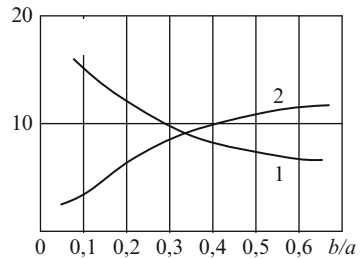
**Table 2.16**

$\sigma$	$b/a$	$X_{R1}$	$X_{R2}$	$X_{A1}$	$X_{A2}$	$\frac{\Delta f_{R1}}{f_{R1}}(\%)$	$\frac{\Delta f_{R2}}{f_{R2}}(\%)$	$K_{L1}$ (H/mm)	$K_{L2}$ (H/mm)
0.360	0.050	2.065	5.273	2.434	5.436	17.883	3.096	1.944	2.085
	0.100	2.003	4.986	2.329	5.195	16.303	4.210	2.223	1.691
	0.150	1.910	4.760	2.185	5.048	14.395	6.042	2.734	1.311
	0.200	1.805	4.690	2.030	5.056	12.433	7.790	3.500	1.041
	0.250	1.698	4.752	1.885	5.195	10.985	9.323	4.509	0.857
	0.300	1.599	4.916	1.757	5.429	9.843	10.437	5.763	0.724
	0.350	1.512	5.172	1.646	5.755	8.869	11.272	7.281	0.622
	0.400	1.432	5.499	1.553	6.159	8.413	12.016	9.041	0.538
	0.450	1.362	5.926	1.469	6.665	7.846	12.461	11.108	0.466
	0.500	1.300	6.455	1.399	7.287	7.624	12.886	13.536	0.404
	0.550	1.246	7.123	1.335	8.052	7.177	13.041	16.451	0.348
	0.600	1.195	7.963	1.281	9.032	7.155	13.423	19.958	0.297
	0.650	1.152	9.063	1.230	10.291	6.746	13.552	24.425	0.250

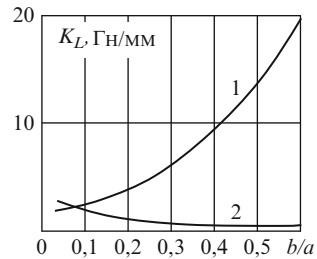
**Fig. 2.21** Dependence of roots of the frequency equations on a parity of radiuses  $b/a$  the basic and two overtone types of fluctuation: 1 – the basic type of fluctuation; 2, 3– the first and second overtones respectively



**Fig. 2.22** Dependence of the relative resonant interval the basic and the first overtone fashions of fluctuations from a parity of radiuses  $b/a$ : 1 – the basic type of fluctuation; 2 – the first overtone



**Fig. 2.23** Dependence of coefficient inductance  $K_L$  of a parity of radiuses  $b/a$ : 1 – the basic type of fluctuation; 2 – the first overtone



**Table 2.17**

$b/a$	$\Delta f_{R2}/f_{R2}(\%)$	$(\Delta f_{R2} - f_{R2})/f_{R2}(\%)$
0.364	6.95	0.724
0.418	7.03	0.753
0.465	8.05	0.783
0.491	7.38	0.800
0.541	6.33	0.828
0.600	5.76	0.858

## References

1. The Catalogue of Products of Open Society "Aurora". Volgograd, 1990 (in Russian)
2. N.A. Shulga, A.M. Bolkisev, *Fluctuations of Piezoelectric Bodies. AS USSR. Mechanics Institute* (Naukova dumka, Kiev, 1990), p. 228 (in Russian)
3. G. Katts (ed.), *Magnetic and Dielectric Devices* (Energiya, Moscow, 1964), p. 416 (in Russian)
4. A.I. Trofimov, *Piezoelectric Transducers Static Forces* (Mashinostroenie, Moscow, 1979), p. 95 (in Russian)
5. P.E. Kandiba, P.G. Pozdnyakov, *Quartz Resonators*, Moscow (in Russian)
6. V.M. Sharapov, M.P. Musienko, E.V. Sharapova, in *Piezoelectric Sensors*, ed. by V.M. Sharapov (Technosphaera, Moscow, 2006), p. 632 (in Russian)
7. Y. Mason, *Piezoelectric Crystals and Their Application in Ultraacoustics* (Publishing Foreign Literature Publishing House, Moscow, 1952), p. 423–431 (in Russian)
8. A.A. Harkevich, *The Theory of Transducers* (Gosenergoizdat, Moscow, 1948) (in Russian)
9. A.N. Alekseev, *Formulas of Communication of Electric Parametres Piezoceramic Resonators with Geometry of a Design and Electrophysical Properties. Electronic Technics. Radio Components. Series 10. Release 3* (The Central Research Institute "Electronics", Moscow, 1972), p. 119–132 (in Russian)
10. W. Mason, *Physical Acoustics. Methods and Devices of Ultrasonic Researches, Part A* (Mir, Moscow, 1966) (in Russian)
11. M. Onoe, H.F. Tiersten, Resonant frequencies of finite piezoelectric ceramic vibrators with high electromechanical coupling. *IEEE Trans. Ultrason. Eng.* **UE-10**(1), 32–39 (1963)
12. E. Giebe, E. Blechschmidt, Experimental and theoretical investigations of expanding and oscillating of the rods and tubes. *Ann. Phys.* **18**, 417–485 (1933)
13. Y. Cady, Piezoelectricity and its practical applications, 1949 (in Russian)
14. M. Onoe, Useful formularize for piezoelectric ceramic resonators. *J. Acoust. Soc. Am.* **41**(4), 974 (1967)
15. R. Holland, E.P. EerNisse, *Design of Resonant Piezoelectric Devices* (MIT Press, London, 1969), p. 857
16. V. Domarkas, R.J. Kazys, *Piezoelectric Transducers for Measuring Devices* (Mintis, Vilnus, 1974), p. 258 (in Russian)
17. L.Ya. Gutin, *The Selected Works* (Sudostroenie, Moscow, 1977), p. 559 (in Russian)
18. L.Ya. Gutin, On the theory of piezoelectric effect. *Mag. Exp. Theor. Phys.* **15**(7), 367–379 (1945) (in Russian)
19. L.Ya. Gutin, Piezoelectric radiators and receivers. *Mag. Exp. Theor. Phys.* **16**(1), 39–54 (1946) (in Russian)
20. I.G. Rusakov, Piezoelectric transducers low frequency. *Mag. Exp. Theor. Phys.* **13**(4-C), 473–482 (1943) (in Russian)
21. I.G. Rusakov, Piezoelectric transducers low frequency. *Mag. Exp. Theor. Phys.* **13**(4-P), 482–501 (1943) (in Russian)
22. A.A. Harkevich, *The Theory of Electroacoustic Transducers*, T.1, Wave Processes (Science, Moscow, 1973), 399c (in Russian)
23. A.A. Harkevich, About application ferroelectric salts in piezoelectric devices. *Mag. Exp. Theor. Phys.* **13**, 585–595 (1943)
24. V.V. Lavrinenko, *Piezoelectric Transformes* (Energiya, Moscow, 1975), p. 112 (in Russian)
25. O. Gribovskiy, *Ceramic Firm Schemes* (Energiya, Moscow, 1971), p. 448 (in Russian)
26. E.C. Munk, The equivalent electrical circuit for radial modes of a piezoelectric ceramic disc with concentric electrodes. *Philips Res. Repts* **20**, 170–189 (1965)
27. C.V. Stephenson, Radial vibrations in short, hollow cylinders of barium titanate. *J. Acoustic. Soc. Am.* **28**(1), 51–56 (1956)
28. M. Onoe, T. Kurati, Asymmetrical fluctuations concerning an axis in disk ceramic resonators. *Denki cusin gakkay dzassi* **49**(1), 104–110 (1966)

29. G.G. Chernih, L.C. Soboleva, V.V. Haritonov, *On a Question on Radial Fluctuations of Thin Piezoceramic Disks and Rings. Electronic Technics. Radio Components, Series 10. Release 1* (The Central Research Institute "Electronica", Moscow, 1972), p. 67–87 (in Russian)
30. E.G. Bronnikova, O.A. Genjentseva, Piezoceramic filters with the resonators working on the first overtone of radial fluctuations. Radio electronics questions, series III. Details and equipment components, 1965, release 2, p. 108–114 (in Russian)
31. G.G. Chernih, Ya.A. Gorbadey, On a question concerning planimetric fluctuations of quartz resonators. Electronic Techniques, Series IX, Radio Components, Release 1, 11–17 (1971) (in Russian)

# Chapter 3

## Spatial Energy–Force Structure of Piezoceramic Transducers

Those who have developed piezoelectric transducers or read the first two chapters of this book may have two stereotypes:

1. Any piezoelement is an electromechanical oscillatory system, and can be presented and described as a piezoelectric resonator or a piezoelectric transformer.
2. An electric charge, proportional to piezomodule  $d_{ij}$ , occurs on the piezoelement electrodes under the force action. The piezoelement still remains an electromechanical oscillatory system. The piezomodule is the transducer static sensitivity. The piezomodule depends on the method of force application to the piezoelement. Its values are shown in tables.

In fact, these stereotypes are true only for special cases. In other cases, the same piezoelement can have features of differentiating or integrating circuit. These properties vary, depending on the piezoelement connection circuit into an electric amplifier circuit.

### 3.1 Synthesis of Piezoelement Spatial Energy–Force Structure

Piezoceramic transducers are widely used in hydro- and electroacoustics, ultrasonic, medical, measuring engineering, and other areas of science and technology [1–6].

Piezoelectric transducers are based on the piezoeffect, discovered by P. and J. Curie in 1880. Practical application of the piezoelectric effect began in 1917 in a sonic depth finder (echo sounder), developed by Paul Langevin.

The piezoceramics synthesis (B. Wool, I. Goldman, 1944) stimulated the development of piezotechnology [7]. Piezoceramic piezoelements have a higher order of sensitivity than quartz, and can be made of practically any form.

When designing piezoceramic sensors, a piezoelement of a certain form, dimensions and material with certain electro-physical properties (specifications) is usually used. Traditionally the vector influencing force  $\mathbf{F}$  (pressure, etc.) piezoelement is parallel to the polarization  $\mathbf{P}$  vector, i.e., the force vector is perpendicular to the

surface with electrodes on it. This is evidently connected with the fact that these electrodes are used for piezoelement polarization in the process of production. They are also used for useful signal reading when physical values (forces, pressures, accelerations, etc.) are measured. In addition, they are used for voltage introduction when the piezoelement is used as a radiator.

Electric field vector  $E$  of the sensor output signal (voltage), supplied to the radiator, should be considered in the design of piezoceramic transducers, as suggested in [6, 8, 9].

The location of  $F$ ,  $P$  and  $E$  vectors in space characterizes the piezoelement spatial energy power structure.

A rectangular parallelepiped-shaped piezoelement is considered as an example (Fig. 3.1). Its electrodes are attached to the wide faces.

Polarization  $P$ , force  $F$  and electric field vectors of the output signal  $E$  are shown in this figure. This arrangement of vectors is the most widespread and traditional [1–6].

A piezoelement of other dimensions, shape and material was used in the past to change the characteristics of traditionally designed piezoceramic sensors.

Meanwhile, the sensor characteristics can be changed if polarization  $P$ , applied force  $F$  and electric field intensity vectors of output signal  $E$  are reciprocally rearranged.

This rectangular parallelepiped-shaped piezoelement is considered below (Fig. 3.2).

Let non-interconnected electrodes be attached to all parallelepiped faces, and the piezoelement be polarized between 1–1' faces. Let force  $F$  measured be applied parallel to polarization vector  $P$ , perpendicularly to face 1, while the output voltage is read from faces 1–1'. Thus, all three vectors are parallel to  $Z$ -axis in the case with the given transducer ( $F \downarrow P \downarrow E \downarrow$ ).

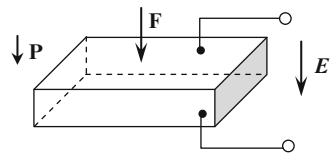


Fig. 3.1 Piezoelement with traditional arrangement of vectors  $F$ ,  $P$  and  $E$

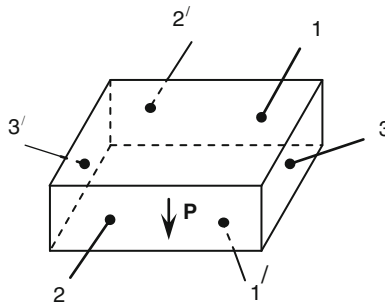


Fig. 3.2 Parallelepiped-shaped piezoelement



One hundred and eighty degree direction change of a vector leads only to the signal phase change.

The above-considered transducer with parallel arrangement of three vectors is the most widespread.

This expression is true for:

$$U_{\text{OUT}} = \frac{Q}{C_{1-1'}} = \frac{d_{31}F}{C_{1-1'}}, \quad (3.1)$$

where  $Q$  – the charge, generated by the piezoelement on faces 1–1';  $C_{1-1'}$  – capacitance between faces 1–1';  $d_{31}$  – piezomodule.

Let polarization vector  $\mathbf{P}$  not change its direction, and force  $\mathbf{F}$  can be applied to both face 1, and faces 2 and 3. Voltage can be read from faces 1–1', 2–2' or 3–3'. Thus, vectors  $\mathbf{F}$  and  $\mathbf{E}$  can be either parallel, or perpendicular to vector  $\mathbf{P}$  (Fig. 3.3).

The transducer is called transverse [1] in the case that the force measured is applied to the piezoelement for the angle between the direction of force  $\mathbf{F}$  and polarization vector  $\mathbf{P}$  to be  $90^\circ$  (transducers 2 and 5, in Fig. 3.3).

It appeared that sensitivity  $S$  for this transducer is written like this [10].

$$S = \frac{Q}{F} = d_{ij} \frac{h}{a}, \quad (3.2)$$

where  $Q$  – charge, generated on the corresponding face;  $h$  – piezoelement height;  $a$  – thickness.

Transverse piezoelements are used in sensors, made by Brüel and Kjer (Denmark), and Kistler Instrumente AG, for example [11, 12].

Transducers with an angle between the electric field vector of output signal  $\mathbf{E}$  and  $90^\circ$  polarization vector  $\mathbf{P}$  (transducers  $c$  and  $d$  in Fig. 3.3) are called domain-dissipative [1].

The physics of the processes occurring in these transducers has been insufficiently studied. It is assumed that the following factors influence the transducer characteristics:

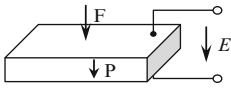
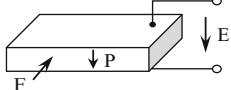
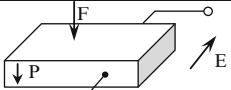
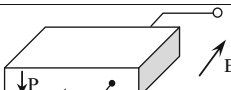

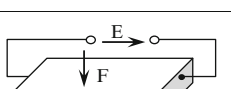
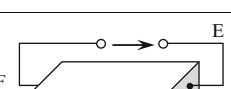
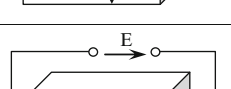
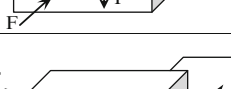
- Energy dissipation on domains [7, 13]
- Change of electric capacitance between electrodes
- Occurrence of other types of oscillations in the piezoelement

The possible influence of all the factors discussed should be studied.

The sensor with vectors  $\mathbf{F}$  and  $\mathbf{E}$  perpendicular to polarization vector  $\mathbf{P}$  (transducers  $d$  and  $g$  in Fig. 3.3) is of scientific interest. These transducers are called domain-dissipative.

When all vectors are perpendicular to each other, transducers are called volume transducers (transducers  $h$  and  $i$  in Fig. 3.3) [1].

The constructive circuits of the transducers shown in Fig. 3.3 are only several examples of their designs.

	Type transformers	The sensor scheme	Direction of vectors		
			F	P	E
a)	<i>The traditional</i>		↓	↓	↓
b)	Transverse		→	↓	↓
c)	Domain-dissipative		↓	↓	→
d)	Transverse domain-dissipative		→	↓	→
e)	Transverse		→	↓	↓
f)	Domain-dissipative		↓	↓	→
g)	Transverse domain-dissipative		→	↓	→
h)	The volume transverse domain-dissipative		↗	↓	→
i)	The volume transverse domain-dissipative		→	↓	↗

**Fig. 3.3** Classification of piezoceramic transducers, depending on directions of vectors  $F, P, E$

More transducer design variants are obtained if the polarization vector direction becomes perpendicular to parallelepiped faces 2–2', 9. By turning the polarization vector for it to be perpendicular to piezoelement faces 3–3', 9 more variants of transducer designs can be obtained. Twenty-seven transducer variants with various

characteristics can be obtained in total for a rectangular parallelepiped-shaped piezoelement.

Experimental dynamic characteristics of the transducers are shown in Fig. 3.3. Characteristics of the transducers in a dynamic mode are called dynamic, i.e., when the value reduced is the time function (process). These parameters characterise the internal (own) properties of transformers.

All real dynamic systems are theoretically nonlinear and nonstationary to some extent, and their parameters are distributed.

Practically all of them can be nominally considered linear stationary dynamic systems with concentrated parameters; those based on nonlinearity are not inclusive.

It is known that linear stationary dynamic systems with concentrated parameters is described by the differential equation with constant coefficients shown in [6]:

$$a_n \frac{d^n y}{dt^n} + \dots + a_1 \frac{dy}{dt} + a_0 y = b_m \frac{d^m x}{dt^m} + \dots + b_1 \frac{dx}{dt} + b_0 x, \quad (3.3)$$

which in the operational form looks like

$$(a_n p^n + \dots + a_1 p + a_0) y(t) = (b_m p^m + \dots + b_1 p + b_0) x(t) \quad (3.4)$$

or shorter

$$A_n(p)y(t) = B_m(p)x(t) \quad m \leq n, \quad (3.5)$$

whence

$$y(t) = \frac{B_m(p)}{A_n(p)} x(t) = Lx(t), \quad (3.6)$$

where  $p = d/dt$  – differentiation operator;  $L$  – linear operator of stationary dynamic system.

The differential equation is the exhaustive characteristic of the dynamic system. However, it is hard to calculate its coefficients experimentally.

Using Laplace transformation to the differential equation under initial zero conditions, the following transfer function is received:

$$W(S) = \frac{Y(s)}{X(s)} = \frac{b_m s^m + b_{m-1} s^{m-1} + \dots + b_1 s + b_0}{a_n s^n + a_{n-1} s^{n-1} + \dots + a_1 s + a_0}, \quad (3.7)$$

where  $s$  – Laplace operator;  $Y(s)$  – Laplace image of output and input values accordingly.

Complex frequency characteristic is received if Laplace operator is substituted by  $j\omega$  in the transfer function

$$K(j\omega) = \frac{b_m (j\omega)^m + b_{m-1} (j\omega)^{m-1} + \dots + b_1 (j\omega) b_0}{a_n (j\omega)^n + a_{n-1} (j\omega)^{n-1} + \dots + a_1 (j\omega) a_0} = P(\omega) + jQ(\omega), \quad (3.8)$$

where  $P(\omega)$  and  $jQ(\omega)$  – real and imaginary part of the complex frequency characteristic.

Whence the amplitude–frequency characteristic (AFC)

$$K(\omega) = |K(j\omega)| = \sqrt{P^2(\omega) + Q^2(\omega)} \quad (3.9)$$

and phase–frequency characteristic

$$\varphi(\omega) = \text{arctg} \frac{Q(\omega)}{P(\omega)}. \quad (3.10)$$

The pulse transitive characteristic is the dynamic system response to the so-called  $\delta$ -impulse

$$\delta(t) = \begin{cases} t & \\ 0, & \text{with } t \neq 0 \\ \infty, & \text{with } t = 0 \end{cases}$$

and

$$\int_{-\infty}^{\infty} \delta(t) dt = 1.$$

Transitive function is the response of the dynamic system to the input step action in the form of unit function  $1(t)$ , the derivative of which equals  $\delta$ -impulse.

$$\frac{d1(t)}{dt} = \delta(t).$$

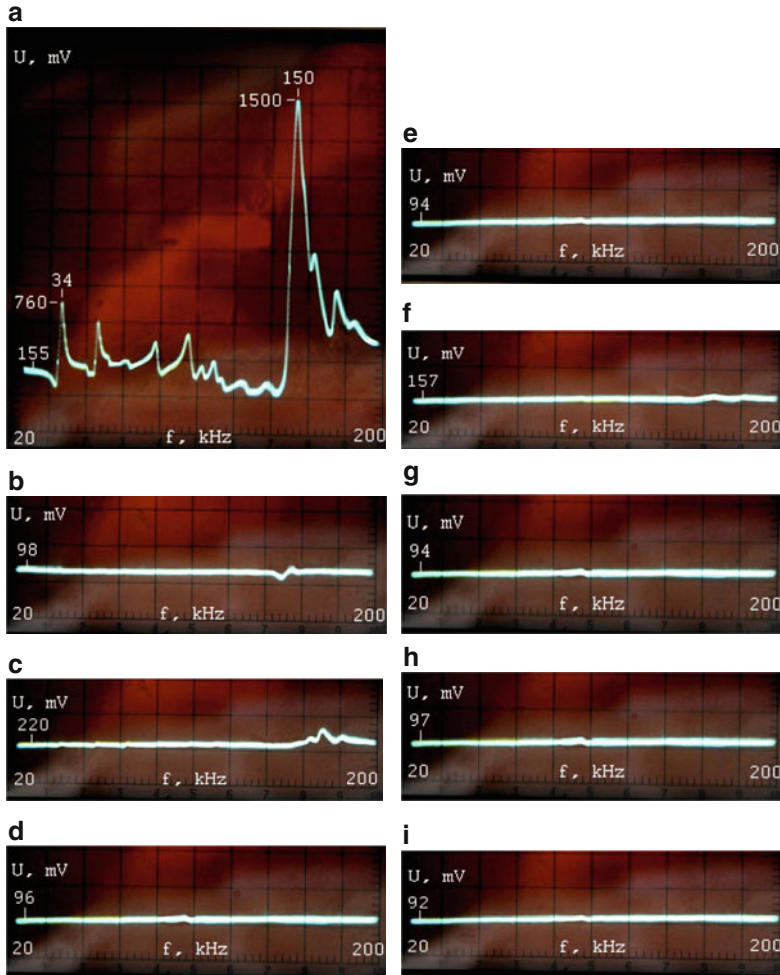
An experimental AFC of the transducers, shown in Fig. 3.3, is represented in in Fig. 3.4. These transducers are based on the piezoelement ( $9 \times 10 \times 90$  mm), made of IITC-19 (analogues to PZT-5A).

AFC was measured in piezotransformer mode by AFR X1-46 research device. The pictures were taken by the digital photo camera “Nikon-D90.”

As can be seen from Fig. 3.4, there are several peaks of amplitude–frequency characteristic for a traditional transducer (Fig. 3.4a). In transverse transducers, these resonances are partially suppressed (Fig. 3.4b). The AFC of domain-dissipative transducers is practically linear (Fig. 3.4c, f–i).

In this case, the transfer coefficient (sensitivity) is smaller in the low-frequency area for all transducer types than for traditional. However, a considerable increase of transfer coefficient is possible for domain-dissipative transducers in some cases [6].

The transient characteristics of the transducers represented in Fig. 3.3 are shown in Fig. 3.5. The measurements were made in piezotransformer mode under the action of meander-shaped voltage on the transducer ( $f = 500$  Hz,  $U = 3$  V). Pictures were taken using the digital photo camera “Nikon-D90.”



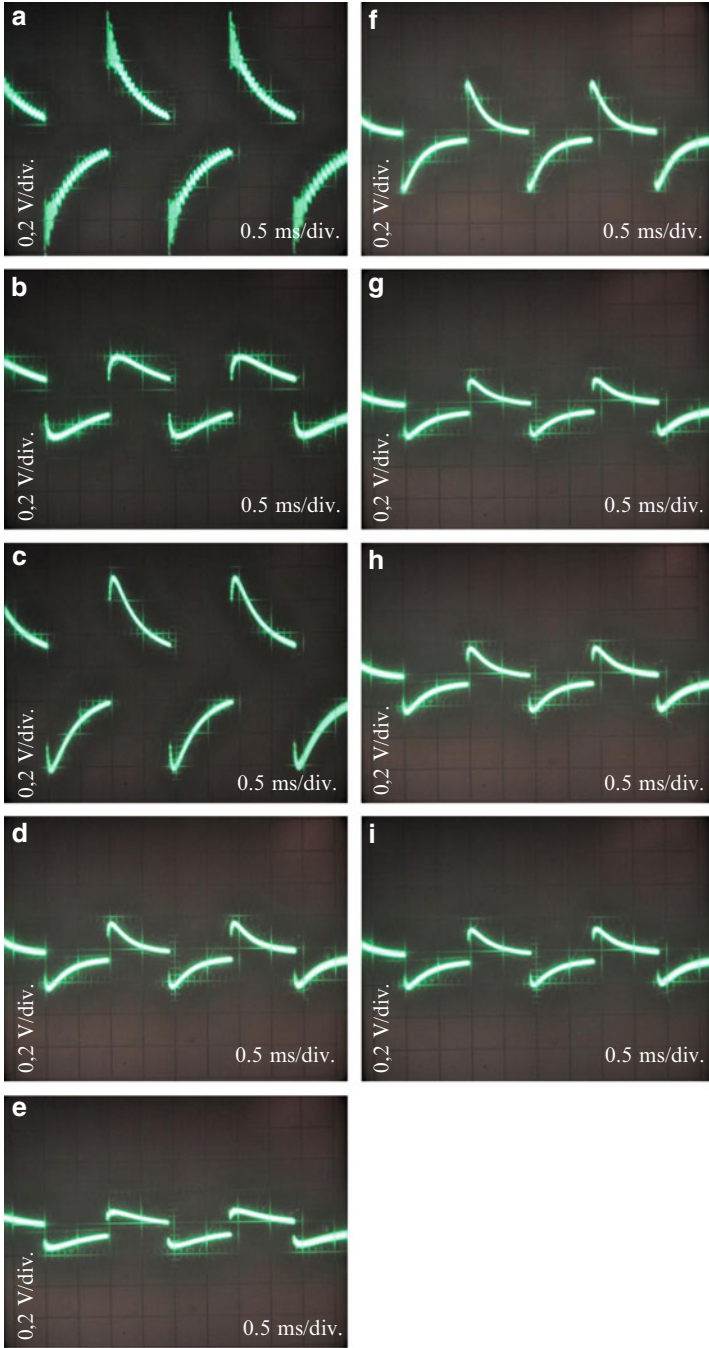
**Fig. 3.4** AFC of transducers from Fig. 3.3

As follows from Figs. 3.4 and 3.5, the change of vectors  $F$ ,  $P$ ,  $E$  position in space, i.e., change of the spatial energy power structure (SEPS), leads to essential changes to the transducer dynamic characteristics.

This SEPS change is assured by the corresponding arrangement of electrodes on the piezoelement surface and the choice of force application site.

As the experiments showed, the change of transducer characteristics occurs also if the angles between the vectors are less than  $90^\circ$ .

Many sensor designs can be created on the basis of the method offered [6, 14–24].



**Fig. 3.5** Transient characteristics of transducers from Fig. 3.3

### 3.2 Anisotropy of Piezoceramic Materials Characteristics

Many properties of crystal substances are vector or tensor. They vary in different crystallographic directions. Among them are the following: coefficient of linear thermal dilatation, diffusion, heat conductivity, elasticity module, specific electric resistance, refractive index or dielectric permeability values. The anisotropic character of these properties is connected with the symmetry of crystal lattice [7, 13].

Polycrystalline ceramics, consisting of numerous randomly oriented small crystal grains, should be isotropic. Textured ceramics can have anisotropy of properties in which crystal phase grains are preferably oriented. Ferroelectric ceramics of barium titanate, zirconate lead titanate PZT and other similar substances, preliminarily polarized by heating in electric field, is also anisotropic [6].

Barium titanate, a common piezoceramic material, is considered as an example.

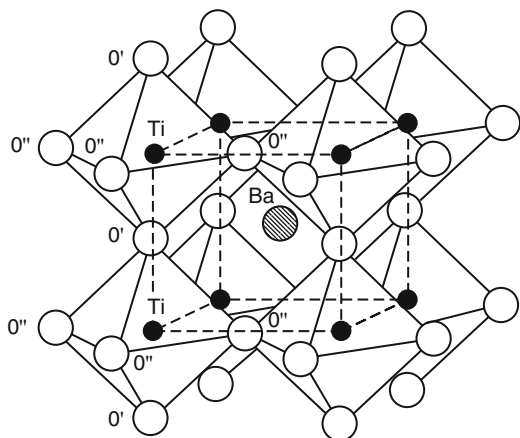
Perovskite structure, shown in Fig. 3.6, is a crystal structure of barium titanate. The structure is cubic, with ions of  $Ba^{++}$  in the cube angles, ions of  $O^{2-}$  in the faces centers of sides and an ion of  $Ti^{++++}$  in the cube centre. The fact that the titan ion is surrounded by six ions of oxygen, forming an octahedron, is of a great importance [5, 7, 13].

Octahedron  $TiO_6$  has the symmetry centre above Curie temperature; as a result, dipole moment equals zero. The octahedron will have its dipole moment only when the positive ion of titan displaces relative to a negative oxygen ion.

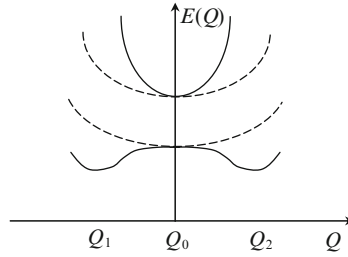
Existence of ferroelectricity in  $BaTiO_3$  is a consequence of polarization “accident.” Then the electric field, created in polarization, increases faster, than elastic restoring forces between ions.

Cluster compounds, including the central atom of metal and ligands (metal or covalent connected groups of atoms) are always characterized by degeneration of the basic electronic condition or close excited states.

The problem of nuclei movement if electronic degeneration is available is solved by the Jahn–Teller theorem [5, 7, 13]. The Jahn–Teller pseudo-effect is more often



**Fig. 3.6** Barium titanate structure



**Fig. 3.7** Adiabatic potentials near pseudo-crossing point (*dashed line*) in Jahn–Teller pseudo-effect:  $Q$  – normal co-ordinate for vibronic-active oscillation;  $Q_0$  – equilibrium cluster geometry;  $Q_1$  and  $Q_2$  – equilibrium position displacement of symmetric structure

realized in low-symmetry ceramics. A complicated system of vibronic equations should be solved in this case. This demands information on adiabatic potentials.

There are many Jahn–Teller centers, i.e., clusters of transition metals (Ti, Zr, etc.), in ferroelectric materials with perovskite structure. The following is important for our purposes. These centers are in electron-degenerate (more precisely, pseudo-expressed) state, i.e., they have adiabatic potentials, as shown in Fig. 3.7.

These ferroelectric materials have a highly symmetrical crystal lattice. These symmetric structures have no dipole moments. However, dipoles appear in the process of ferroelectric phase transition. Then the whole crystal or its separate domains (ceramics) is strongly electrically polarized.

The nature of this polarization is explained by the Jahn–Teller effect in vibronic theories of ferroelectricity [5]. The gist of the effect is shown in Fig. 3.7.

For example, for octahedral cluster  $\text{TiO}_6^{8-}$ , electronic wave function of the ground state “mixes” with wave functions of excited states at nuclear displacement  $t_{1u}$  like this [13]. These nuclei oscillations decrease the cluster symmetry and displace the central atom, for the system inversion center to disappear and dipole moment to arise. The ground state becomes unstable, relative to atoms displacement. Then two new structural minima appear on adiabatic potential. Dipole instability start condition in compounds like  $\text{BaTiO}_3$  is determined from the Jahn–Teller pseudo-effect criterion:

$$E_{1,2} < \frac{4F_{1,2}}{K}, \quad (3.11)$$

$$F_{1,2} = \left\langle \psi_1 \left| \frac{\partial V}{\partial Q} \right| \psi_2 \right\rangle, \quad (3.12)$$

where  $F_{1,2}$  – vibronic interactions parameter of two quasi-degenerate conditions  $\psi_1$  and  $\psi_2$ ; energies of these unperturbed states are shown in Fig. 3.7 by *dashed lines*;  $\Delta E_{1,2}$  – difference of energies  $E_1$  and  $E_2$ ;  $K$  – force coefficient for  $Q$  oscillations (vibronic corrections not inclusive)  $K = (\partial^2 V / \partial^2 Q)_0$  considered identical in both states for simplicity.



Minima on the lower of two new potential curves (*heavy lines* in Fig. 3.7) are received from the condition

$$Q_1 = -Q_2 = \sqrt{\frac{F_{1,2}^2}{K^2} - \frac{\Delta E_{1,2}^2}{F^2}}. \quad (3.13)$$

The Jahn–Teller pseudo-effect is connected with occurrence of additional chemical bonds when the system is distorted. More accurately, chemical bonding increases. It is not of simple covalent character. It is of a delocalization nature, characteristic of semi-valent and metal compounds.

We should note that a strong Jahn–Teller effect with dipole instability (Fig. 3.7) can also occur if  $\Delta E_{1,2}$  value is big, with  $K$  small or  $F_{1,2}$  big. The instability criterion (3.11) can be rather “soft” either for  $\Delta E$ ,  $F$  or  $K$ .

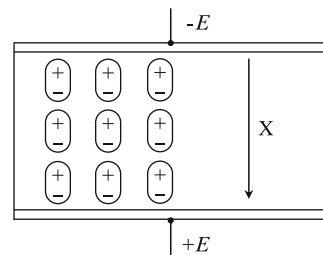
As the clusters of titan coordinated atoms are strongly interconnected by general atoms of oxygen in ferroelectric crystal with perovskite structure, the Jahn–Teller cooperative pseudo-effect can be considered. By introducing an additional vibronic connection inter-cluster parameter at the expense of phonons, structural phase transition in crystal macro-polarized state can be explained. This can be reached if a certain temperature (ferroelectricity) is selected, necessary phonons are activated, or if external electric field (ceramics polarization) is applied. The group of Jahn–Teller clusters, interconnected by vibronic connection, forms a domain. Alignment of polarized domains gives the effect known.

Knowledge of polarization nature in the domain allows understanding of sharply anisotropic conductance mechanism in ceramics.

Domains are polarized and aligned by voltage, as shown in Fig. 3.8.

The inter-domain medium is a crystal solid solution. Its atoms are of the photon-connected type, different from the domain type. There is no vibronic correlation of Jahn–Teller centers in this medium. However, this medium can be also conductive if there is an electric field of polarized domains.

Electrons are injected into the substrate electrode medium and are transferred from one cluster to the other, similar to semi-conductor conductivity, amplified by the domains field. The transfer of electrons along the atom train of crystal lattice to domain clusters is easy. But their further advancement in the domain should be slowed down because of polarization in the domain. However, the problem is



**Fig. 3.8** Domain structure of piezoceramic

solved, as soon as the character of chemical and physical interactions, which lead to ferroelectricity creation in the domain, is considered. Displacement of atoms, which causes dipole instability, is connected with vibronic mixing of ground and excited states inside the clusters. It is physically equivalent to mixing valence and conductivity zones inside the whole domain.

The delocalized character of chemical bonds in each cluster and no characteristic oscillations in chemical bonds, vibronic activity of the “smeared” oscillations in and between clusters in the domain, assure free migration of an electron inside the cluster.

Thus, electron transport along axis  $X$ , marked by an arrow in Fig. 3.8, should be much easier than in the perpendicular direction when voltage is applied to lateral ( $a$ ) faces of the crystal.

The final anisotropic reason for ceramic material conductivity is the strict directivity of atom nuclear displacement in each cluster along coordinate  $Q$  (Fig. 3.7), caused by vibronic activity of these phonons [25].

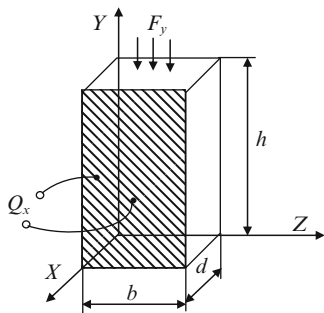
### 3.3 Transverse Piezoelectric Transducers

Sensors with longitudinal piezoelements are more frequently used for measurement of big forces ( $10^3$  N and higher); a considerably high output charge  $Q$  ( $10^{-9}$ – $10^{-8}$  C) occurs quite often. The longitudinal piezoelement sensitivity:

$$d_{11} = \frac{Q_x}{F_x}, \quad (3.14)$$

where  $F_x$  – force applied along axis  $x$ ;  $Q_x$  – charge arising, usually does not exceed this value  $d_{11} = 2.31 \times 10^{-12}$  C/N [10, 26].

More sensitive transverse piezoelements are used for measurement of small forces. The general view of a plate-shaped transverse piezoelement is shown in Fig. 3.9.



**Fig. 3.9** Transverse piezoelement

This piezoelement sensitivity is expressed as:

$$S = \frac{Q_x}{F_y} = -d_{11} \frac{h}{a}, \quad (3.15)$$

where  $Q_x$  – charge, generated on the corresponding face;  $h$  – piezoelement height;  $a$  – thickness.

Comparing expressions (3.14) and (3.15), we can see that the transverse piezoelement sensitivity is in  $h/a$  time higher than the longitudinal; it can change, depending on  $h/a$  correlation. However,  $h/a$  correlation cannot be indefinitely increased.

When designing real sensors, durability and stability conditions of the design and the piezoelement should be considered. The durability condition can be written like this [10, 26]:

$$F_y \leq \sigma_{\max} S_y = \sigma_{\max} ab, \quad (3.16)$$

where  $\sigma_{\max} = 5 \times 10^7 \text{ H/m}^2$  – permissible pressure of quartz compression;  $S_y$  – load-bearing face area.

Stability condition of the plate, evenly loaded by force  $F_y$  from two parts and freely supported along the edges, is determined by the expression:

$$\sigma_{\text{crit}} = \left(\frac{b}{h}\right)^2 \pi \frac{D}{b^2 a}, \quad (3.17)$$

where  $D = E_{\text{elast}} a^3 / 12(1 - \mu)^2$  – cylindrical rigidity [ $E_{\text{elast}} = 80 \times 10^9 \text{ N/m}^2$  – elasticity module of quartz;  $\mu$  – Poisson coefficient (for quartz  $\mu^2 \approx 0.1$ )].

Assuming, that the piezoelement works on maximum permissible values of the force applied, and solving the variation problem for the system of equations (3.15)–(3.17), one obtains:

$$\left(\frac{Q_x}{F_y}\right)_{\max} = -\frac{\pi d_{11}}{2} \sqrt{\frac{E_{\text{elast}}}{3(1 - \mu^2)\sigma_{\max}}}. \quad (3.18)$$

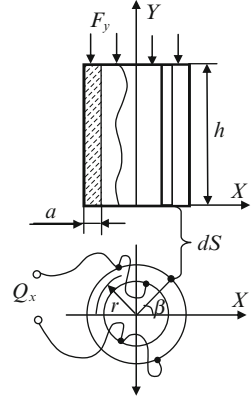
The following can be concluded from this expression [26]. The piezoelement, working on a transverse piezoeffect, has the maximum possible ultimate sensitivity, independent from geometry, and determined only by material properties. Substituting the quartz parameter values in expression (3.18), the ultimate sensitivity of the transverse piezoelement is calculated as follows:

$$(Q_x / F_{\text{elast}})_{\max} = -8.833 \times 10^{-11} \text{ Kl/N}. \quad (3.19)$$

It is almost 40 times higher than the sensitivity of a piezoelement on longitudinal piezoeffect.

However, a rectangular plate-shaped piezoelement has a considerable disadvantage: complexity of fastening and centering in the sensor. It becomes especially noticeable when big forces and pressures are measured.

**Fig. 3.10** Quartz transverse cylinder-shaped piezoelement



It is known that revolution bodies have maximum stability. One of these thin-walled cylinder piezoelements is shown in Fig. 3.10 [26].

The cylinder is cut from mono-crystal quartz for the cylinder axis to coincide with crystallographic axis  $y$ . The cylinder basis is in the plane of  $x$  and  $z$  axes.

This piezoelement sensitivity [26]:

$$S = \frac{Q_x}{F_{\text{elast}}} = -\frac{4}{3\pi} d_{11} \frac{h}{a}. \quad (3.20)$$

Expressions for maximum permissible sensitivity and mechanical durability are written like this:

$$F_{\text{elast}} \leq \sigma_{\text{max}} 2\pi r a; \quad (3.21)$$

$$\sigma_{\text{max}} \leq \frac{\pi^2 E_{\text{elast}} a^2}{12(1 - \mu^2) h^2}. \quad (3.22)$$

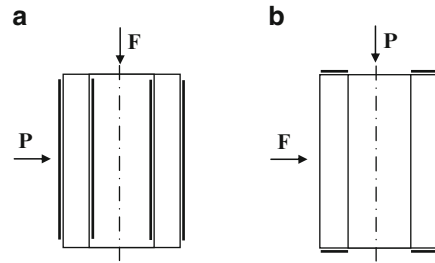
The parameters of optimum cylindrical piezoelement are received from the solution of the variation problem for equations system (3.20)–(3.22), which gives [26]:

$$r = \frac{F_{\text{elast}} 12(1 - \mu^2) h^2}{2\pi^3 a^3 E_{\text{elast}}}; \quad \frac{h}{a} = \frac{\pi}{2} \sqrt{\frac{E_{\text{elast}}}{3(1 - \mu^2) \sigma_{\text{max}}}}; \quad (3.23)$$

$$\left( \frac{Q_x}{F_y} \right)_{\text{max}} = \frac{2}{3} d_{11} \sqrt{\frac{E_{\text{elast}}}{3(1 - \mu^2) \sigma_{\text{max}}}}.$$

Substituting the quartz parameters values in (3.23), the ultimate sensitivity of the cylindrical piezoelement is obtained:

**Fig. 3.11** Transverse cylinder-shaped element: (a) radially polarized, (b) axially polarized



$$\left( \frac{Q_x}{F_{\text{elast}}} \right)_{\text{max}} = 3.75 \times 10^{-11} \text{ KI/N.}$$

The found value is 2.35 times smaller than the sensitivity of the plate, calculated under this formula (3.11). Nevertheless, use of cylinder-shaped piezoelements is preferable for the measurement of big forces while the element remains small. This is proved by a number of calculations.

A cylinder-shaped transverse ceramic piezoelement has a simpler design (Fig. 3.11).

In the first case (Fig. 3.11a) the piezoelement is radially polarized. Force  $F$  is applied along the cylinder axis. In the second case (Fig. 3.11b) the cylinder is axially polarized, and force (pressure)  $F$  is applied perpendicularly.

### 3.4 Piezotransformers

The effect of a change in piezoelement characteristics, where the spatial energy power structure is changed too, can be used in two types of transducers:

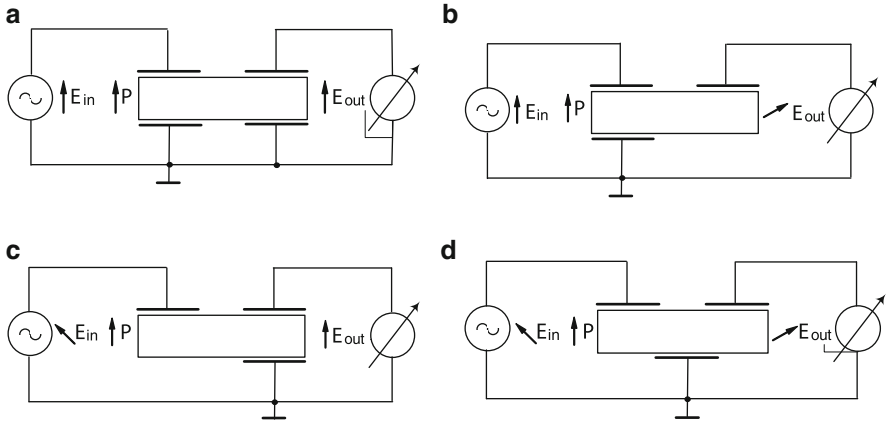
- In transducers, transforming voltage of one level into another – piezotransformers
- In mechanical value sensors, based on direct piezoeffect

Piezotransformers are of scientific interest. A piezotransformer circuit is very convenient for determination of the internal (i.e., peculiar only to the given object) system of piezoelement properties (characteristics).

Mechanical value sensors can be constructed on the basis of piezotransformers.

In addition to that, piezotransformer can be used for creation of adders (summers, summators), amplitude modulators and acoustic transducers with lowered work frequency.

Idle mode is usually used for determination of piezotransformer characteristics. A test-generator signal with small output resistance is supplied to the piezotransformer input. The piezotransformer output signal is registered by the indicator with the big input resistance.



**Fig. 3.12** Circuits of piezotransformers: (a) Tr–Tr, (b) Tr–DD, (c) DD–Tr, (d) DD–DD

These characteristics used to be considered unique (see Chap. 2). It was believed that they characterize piezotransformer (piezoelement, sensor) unequivocally.

Meanwhile, as it will be shown later, the characteristics defined strongly depend on the spatial energy–power structure of the piezoelement, i.e., reciprocal positioning of polarization vectors, force and electric field of input and output signals.

The analysis of piezotransformer circuits shows that all of them can be reduced to four basic types (Fig. 3.12).

1. Traditional (known) circuit. In this case, the angle  $\alpha$  between polarization vector  $\mathbf{P}$  and the electric field vector, activating voltage  $\mathbf{E}_{in}$  (generator voltage), equals zero. Angle  $\beta$  between polarization vector  $\mathbf{P}$  and the electric field vector of output voltage  $\mathbf{E}_{out}$  also equals zero.
2. Circuit Tr–D with traditional input section circuit ( $\alpha = 0$ ), and for the output angle  $\beta \leq 90^\circ$  (domain-dissipative circuit).
3. Circuit Dd–Tr, in which the input section is based on domain-dissipative circuit ( $0 < \alpha \leq 90^\circ$ ), and the output on traditional circuit  $\beta = 0$ .
4. Circuit DD–DD. In this case,  $0 < \alpha \leq 90^\circ$  and  $0 < \beta \leq 90^\circ$ .

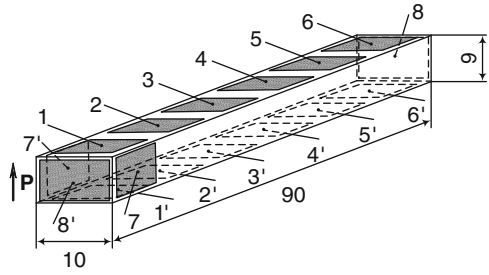
Characteristics of these piezotransformers were studied experimentally.

A IITC-19 piezoceramic rectangular parallelepiped-shaped piezotransformer ( $9 \times 10 \times 90$  mm) was made for the experiments (Fig. 3.13).

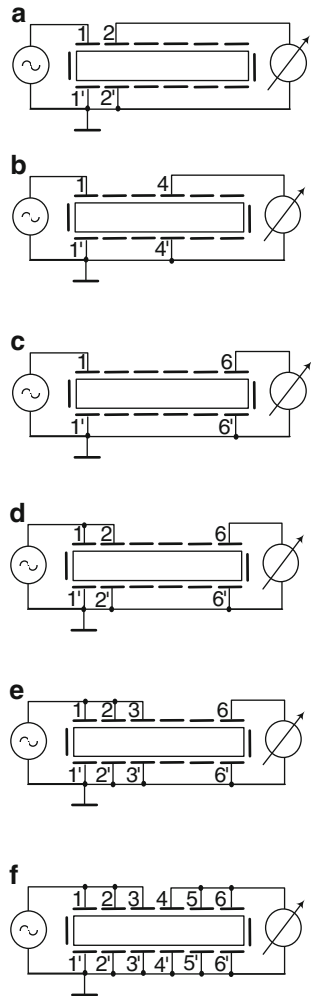
Electrodes are attached to the piezoelement faces, sized  $10 \times 90$  mm and are paired (sections 1–1', 2–2', . . . , 6–6'). In addition to that, the electrodes are located on the end surfaces (8–8') and lateral faces (7–7').

The electrode dimensions on the faces  $10 \times 90$  mm (1–1', . . . , 6–6')— $10 \times 15$  mm, on lateral faces (7–7') —  $8 \times 15$  mm, on the ends (8–8') —  $8 \times 9$  mm.

**Fig. 3.13** Piezoceramic transformer

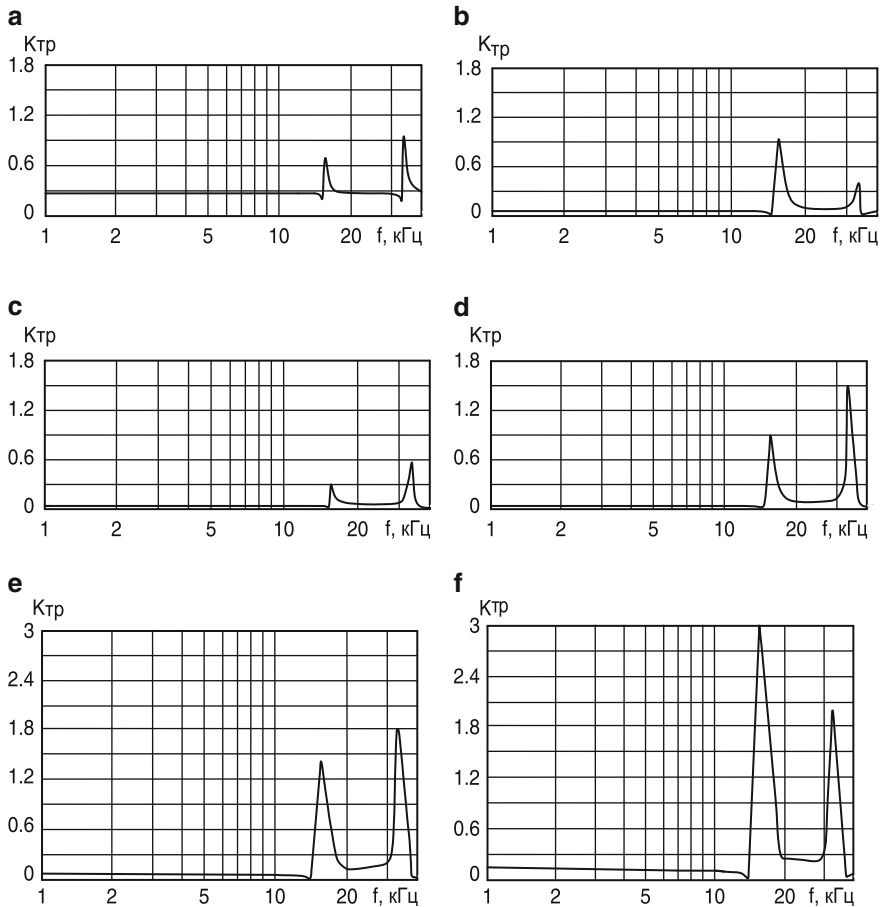


**Fig. 3.14** Circuits of traditional piezotransformers



**Table 3.1**

Electrodes	1–1'	2–2'	3–3'	4–4'	5–5'	6–6'	7–7'	8–8'	1–1' + 2–2'	1–1' + 2–2' + 3–3'	4–4' + 5–5' + 6–6'
C (pF)	253	253	253	254	252	250	61	29	506	759	756



**Fig. 3.15** AFC of traditional piezotransformers: (a) Fig. 3.14a, (b) Fig. 3.14b, (c) Fig. 3.14c, (d) Fig. 3.14d, (e) Fig. 3.14e, (f) Fig. 3.14f

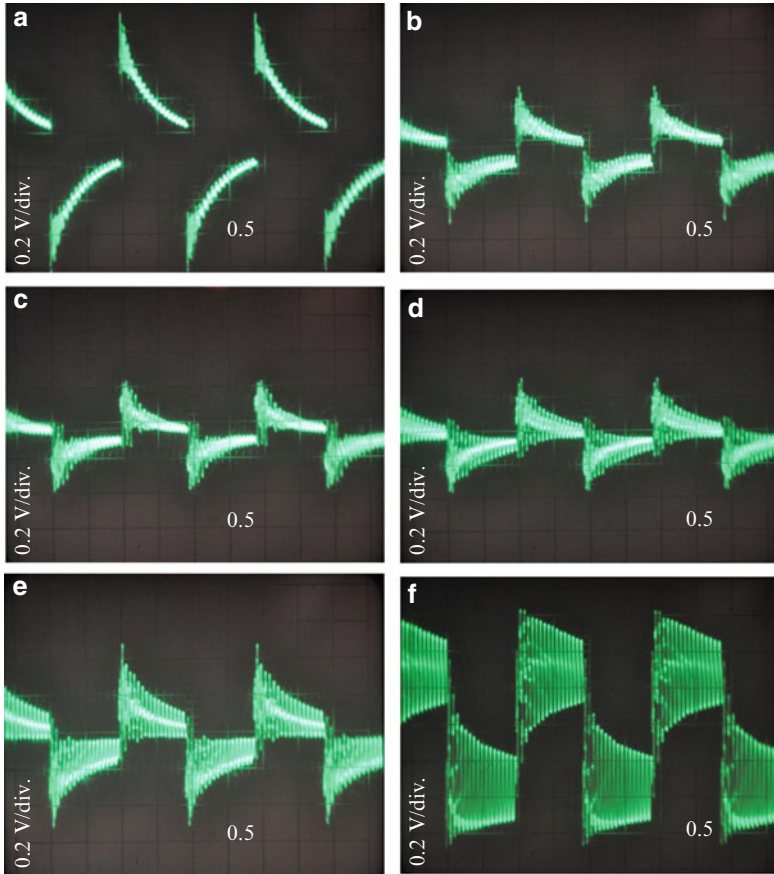
**1. Traditional Circuit (Tr–Tr)**

The circuits of piezotransformers studied are shown in Fig. 3.14.

The capacitance between the electrodes of these piezotransformers was measured by digital multi-meter ДТ9207А. The measurement results are given in Table 3.1.

Amplitude–frequency and transient characteristics of these piezotransformers are shown in Figs. 3.15 and 3.16.





**Fig. 3.16** Transient characteristics of traditional piezotransformers: (a) Fig. 3.14a, (b) Fig. 3.14b, (c) Fig. 3.14c, (d) Fig. 3.14d, (e) Fig. 3.14e, (f) Fig. 3.14f

As follows from Figs. 3.15 and 3.16, in the given case piezotransformers are an oscillatory system with several resonant frequencies, independent from the distance between input and output electrodes and electrode dimensions (polarization vector  $\mathbf{P}$  is parallel to vectors  $\mathbf{E}_{\text{in}}$  and  $\mathbf{E}_{\text{out}}$ ).

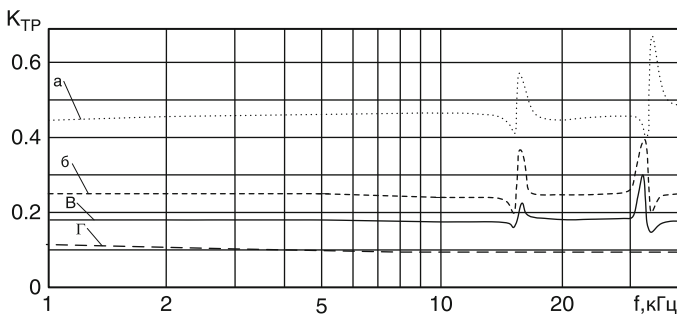
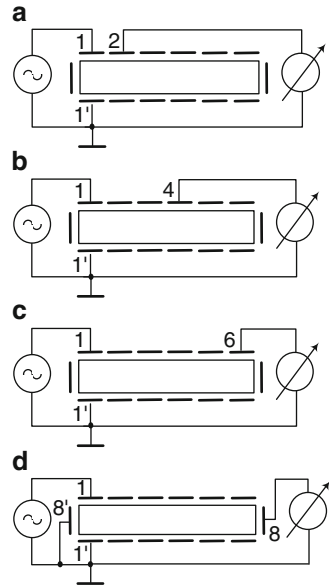
## 2. Circuit Tr-DD

In this case, the generator was connected to electrodes 1–1', and the output voltage was measured on electrodes 2–1', 4–1', 6–1', 8–1' (Fig. 3.17).

Measurement results of amplitude–frequency and transient characteristics are shown in Figs. 3.18 and 3.19.

The capacitance between electrodes and also angle  $\beta$  between the centers of the corresponding electrodes are changed for this case (Table 3.2).

**Fig. 3.17** Circuits of piezotransformers



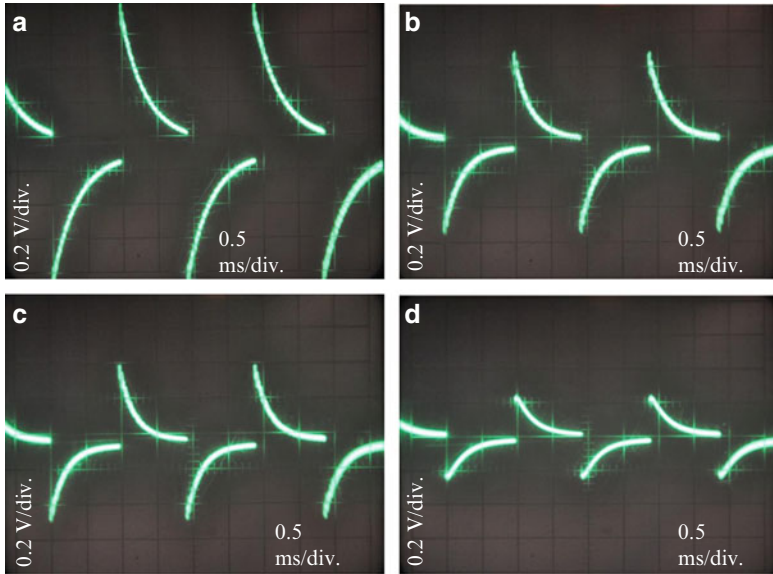
**Fig. 3.18** AFC of piezotransformers, shown in Fig. 3.17: (a) Fig. 3.16a, (b) Fig. 3.16b, (c) Fig. 3.16c, (d) Fig. 3.16d

As follows from Figs. 3.18 and 3.19, in this case the bigger angle  $\beta$  is, and the smaller the capacitance between the output electrodes, the smaller is the transformation coefficient in pre-resonant area, and at resonant frequency ( $\sim 17$  and  $34 \text{ kHz}$ ). AFC for the circuit in Fig. 3.17d) ( $\beta \approx 90^\circ$ ,  $S_{8-1'} = 37 \text{ pF}$ ) becomes linear.

### 3. Circuit DD–Tr

In this case, the generator and the measuring device were connected according to the circuits, shown in Fig. 3.19.

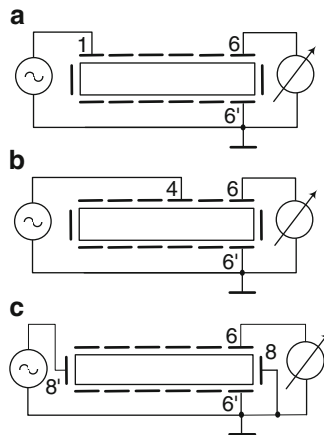
The results of amplitude–frequency and transient characteristics are shown in Figs. 3.21 and 3.22 and in Table 3.3 (Fig. 3.20).



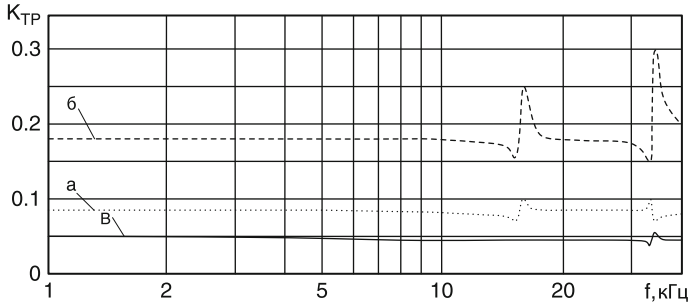
**Fig. 3.19** Transient characteristics of piezotransformers: (a) Fig. 3.17a, (b) Fig. 3.17b, (c) Fig. 3.17c, (d) Fig. 3.17d

**Table 3.2**

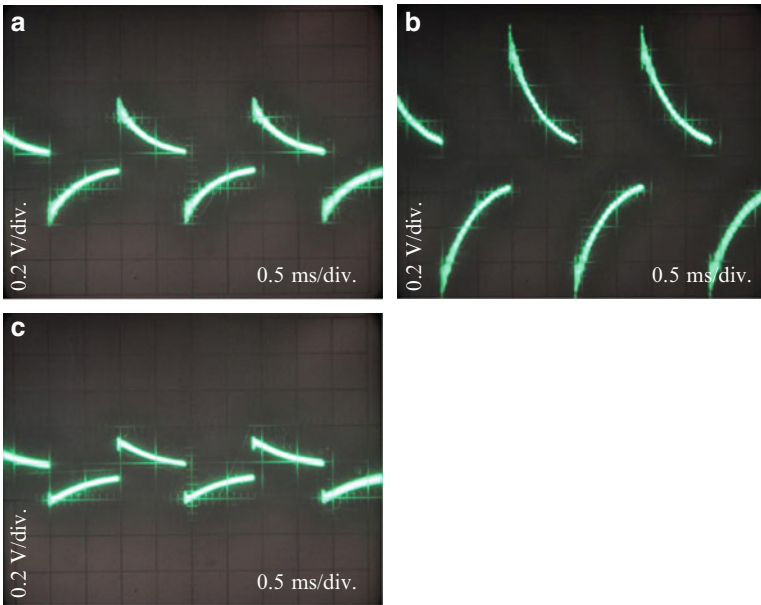
Electrodes	2-1'	3-1'	4-1'	5-1'	6-1'	8-1'
Capacitance (pF)	167	94	73	57	49	37
Angle $\beta$	$56^\circ$	$72^\circ$	$78^\circ$	$80^\circ$	$82^\circ$	$87^\circ$



**Fig. 3.20** Circuits of piezotransformers



**Fig. 3.21** AFC of piezotransformers, shown in Fig. 3.20: (a) Fig. 3.20a, (b) Fig. 3.20b, (c) Fig. 3.20c



**Fig. 3.22** Transient characteristics of piezotransformers, shown in Fig. 3.20: (a) Fig. 3.20a, (b) Fig. 3.20b, (c) Fig. 3.20c

It follows from Figs. 3.21 and 3.22 and Table 3.3 that the bigger angle  $\alpha$  (the smaller the capacitance between the activating electrodes) is, the smaller the output voltage level, while the resonances are suppressed.

**4. Circuit DD–DD**

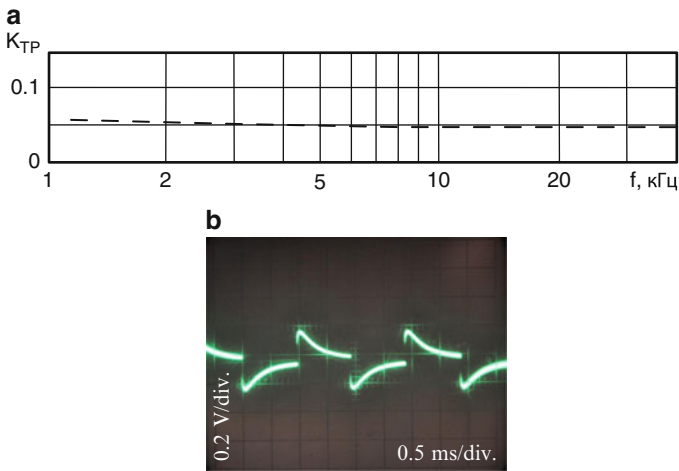
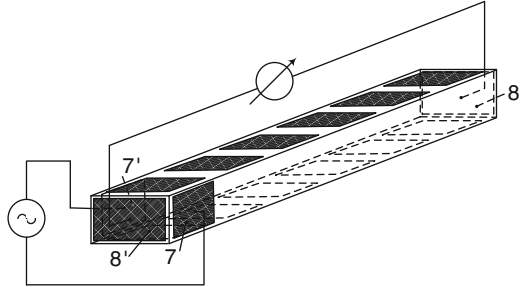
A variant of this piezotransformer is shown in Fig. 3.23, with AFC and transient characteristics in Fig. 3.24.

Capacitance between the electrodes:  $C_{7-7'} = 61$  pF,  $C_{8-8'} = 29$  pF, and angle  $\alpha = \beta \approx 90^\circ$ .

**Table 3.3**

Electrodes	1–6'	4–6'	8'–6'
Capacitance (pF)	48	92	32
Angle $\alpha$	82°	72°	87°

**Fig. 3.23** Piezotransformer circuit



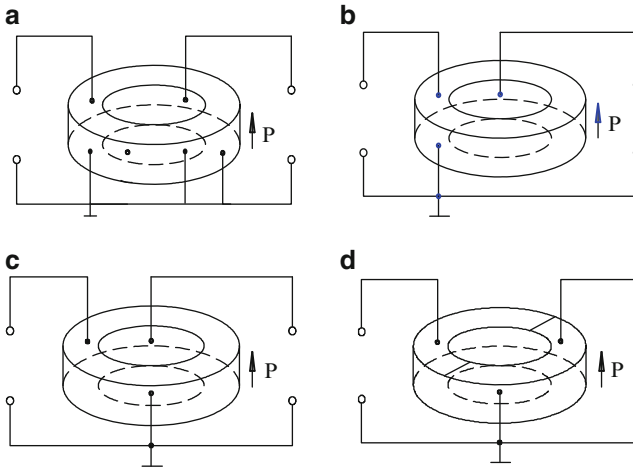
**Fig. 3.24** Amplitude–frequency (a) and transient characteristics (b) of piezotransformer, shown in Fig. 3.23

As can be seen from Fig. 3.23, AFC for the piezotransformer, design by DD–DD circuit, is linear in the range of 1–40 kHz.

### 3.4.1 Disk Piezotransformers

The analysis of a significant amount of possible disk piezotransformer connection circuits shows that they also can be reduced to four basic types (Fig. 3.25).

A piezoceramic ИТС-19 piezotransformer 30 mm in diameter and 0.8 mm thick was made for the experiments. There are piezotransformer electrodes located on the



**Fig. 3.25** Circuits of disk piezotransformers: (a) Tr–Tr, (b) Tr–DD, (c) DD–Tr, (d) DD–DD

end surfaces. The upper electrodes are projected on the lower. A glass-cloth laminate plate 36 mm in diameter and 0.5 mm thick is glued to the piezoelement.

Measurement results of AFC for this piezotransformer are shown in Fig. 3.26.

It is seen from Fig. 3.26 that AFC of DD piezotransformers became linear, and the transformation coefficient considerably increased.

A piezotransformer circuit with oscillatory, differentiating and integrating properties simultaneously is also offered.

The schematic design of the piezotransformer offered is shown in Fig. 3.27. The disk-shaped piezotransformer ( $\text{Ø}30 \times 0.8$ ) is made of piezoceramic IITC-19. The end electrodes are divided into equal five parts, and are connected as it is shown in Fig. 3.27.

Electrodes 1–1' and 5–5' form a traditional transformer (output 1). Electrodes 3–5' and 4–5' are connected according to circuit DD–DD (output 2). Finally, output signal 3 is received if electrode 4 is connected with electrode 2 via the resistor.

The transient characteristic measurement results are shown in Fig. 3.28 [45].

The piezotransformer variant described, assuring the input signal processing, is certainly not the only one. As a result of a change in electrode dimensions and their reciprocal positioning, the output signal parameters can be influenced. This also opens up various opportunities in piezotransformer designing [14, 15, 27–30].

Sound pressure sensors can be created on the basis of bimorph domain-dissipative piezotransformers.

A possible variant of a sensor design is shown in Fig. 3.29 [31].

The sensor consists of a piezoelement 30 mm in diameter and 0.8 mm thick. The piezoelement is fastened to a metal (brass) plate 0.3 mm thick. The piezoelement has three systems of electrodes – 1–1', 2–2' and 3–3'.

Electrodes 1' and 2' are interconnected via the metal plate.

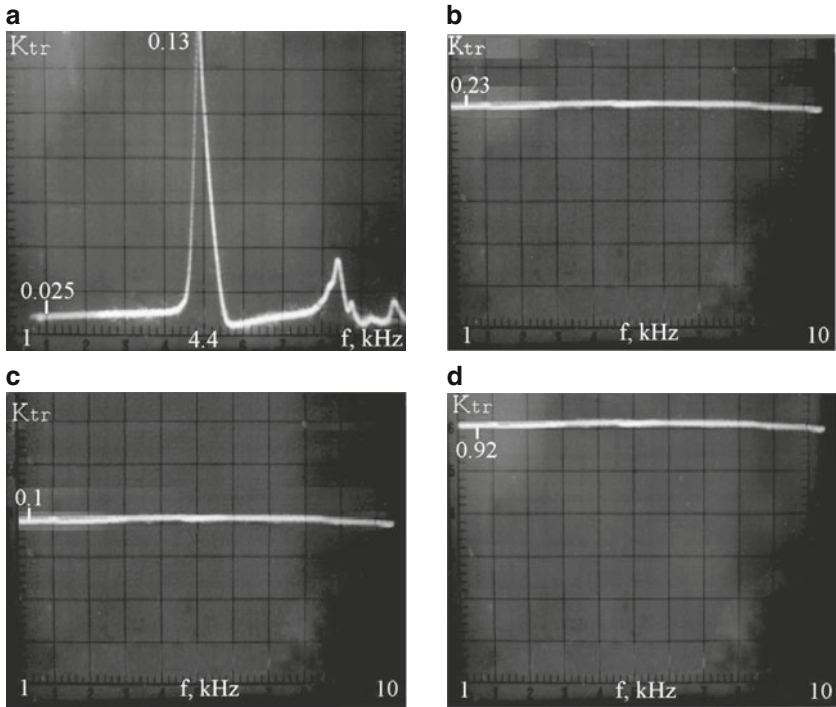


Fig. 3.26 AFC: (a) Tr-Tr, (b) Tr-DD, (c) DD-Tr, (d) DD-DD

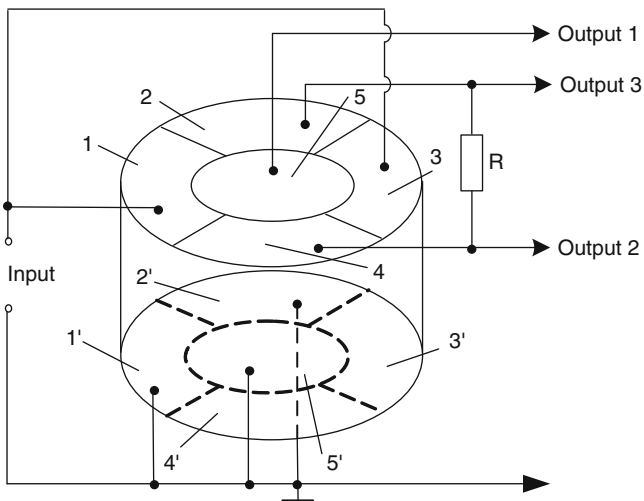
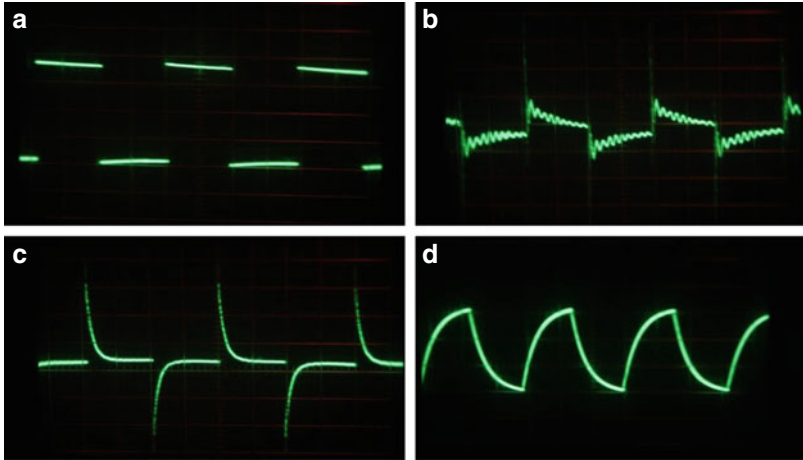
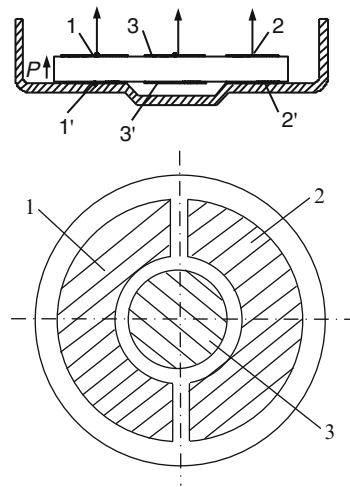


Fig. 3.27 Piezotransformer circuit



**Fig. 3.28** Oscillograms of piezotransformer signals: (a) input signal (meander), (b) output 1, (c) output 2, (d) output 3

**Fig. 3.29** Sensor design



**Table 3.4**

Electrodes	1–1'	3–1'	2–2'	3–3'	1–3'	2–3'
Voltage sensitivity (mV/Pa)	2.6	2.7	1.4	1.3	4.0	4.2
Capacitance between electrodes (nF)	4.08	3.93	1.36	0.34	0.31	0.32

The sensor is put in an acoustic chamber. It is influenced by sound pressure 10 Pa (114 dB) at the frequency of 200 Hz.

Measurement results of the output voltage are given in Table 3.4.

As it is seen from Table 3.4, the sensor sensitivity can change practically three times, depending on electrode connection to the measuring device. In cases when the



angle between the electric field vector of the output signal and polarization vector is almost  $90^\circ$ , the sensitivity increases. At the same time, the capacitance between these electrodes decreases.

## References

1. V. Domarkas, R.J. Kazys, *Piezoelectric Transducers for Measuring Devices* (Mintis, Vilnius, 1974), p. 258 (in Russian)
2. I.N. Ermolov, *Theory and Practice of Ultrasonic Control* (Mashinostroenie, Moscow, 1981), p. 240 (in Russian)
3. R.J. Kazys, *Ultrasonic Information Measuring Systems* (Mokslas, Vilnius, 1986), p. 216 (in Russian)
4. M.V. Korolev, A.E. Karpelson, *Broadband Ultrasonic* (Mashinostroenie, Moscow, 1982), p. 157 (in Russian)
5. G.V. Kats (ed.) *Magnetic and Dielectric Devices* (Energiya, Moscow, 1964), p. 416 (in Russian)
6. V.M. Sharapov, M.P. Musienko, E.V. Sharapova, in *Piezoelectric Sensors*, ed. by V.M. Sharapov (Technosphaera, Moscow, 2006), p. 632 (in Russian)
7. I.V. Bersuker, *Jahn-Teller Effect and Vibronic Interactions in Modern Chemistry* (Nauka, Moscow, 1987), p. 344
8. V.M. Sharapov et al., On a piezoceramic transducers classification. *Bull. Cherkasy State Technol. Univ.* **3**, 116–120 (2003)
9. V.M. Sharapov et al., On AFC linearization method of piezoceramic transducers. *Bull. Cherkasy State Technol. Univ.* **1**, 14–18 (2003)
10. E.A. Kudryashov, B.E. Mager, Methods of piezoquartz sensors sensitivity increase. “Devices and Control Systems” **4**, 20–22 (1982) (in Russian)
11. Company prospectuses “Brüel and Kjer”, Nerum, Denmark
12. Company prospectuses “Kistler Instrumente AG”, Winterthur, Switzerland
13. I.V. Bersuker, B.G. Vekhter, *Ferroelectrics* **19**(3/4), 137–150 (1978)
14. V.M. Sharapov et al., Patent of Ukraine #62726. Method of physical value measuring by piezoelectric elements. Publication 15 Dec 2003 (2003) (in Ukrainian)
15. V.M. Sharapov et al., Patent of Ukraine #62730. Piezoelectric transducer of mechanical values. Publication 15 Dec 2003 (2003) (in Ukrainian)
16. V.M. Sharapov et al., Patent of Ukraine #64316. Piezoelectric transducer of mechanical values. Publication 16 Feb 2004 (2004) (in Ukrainian)
17. V.M. Sharapov et al., Patent of Ukraine #65037. Piezoelectric transducer of mechanical values. Publication 15 Mar 2004 (2004) (in Ukrainian)
18. V.M. Sharapov et al., Patent of Ukraine #65324. Piezoelectric transducer of mechanical values. Publication 15 Mar 2004 (2004) (in Ukrainian)
19. V.M. Sharapov et al., Patent of Ukraine #65325. Piezoelectric transducer of mechanical values. Publication 15 Mar 2004 (2004) (in Ukrainian)
20. V.M. Sharapov et al., Patent of Ukraine 69875. Piezoelectric transducer of forces. Publication 15 Sept 2004 (2004) (in Ukrainian)
21. V.M. Sharapov et al., Patent of Ukraine 69876. Piezoelectric transducer of forces. Publication 15 Sept 2004 (2004) (in Ukrainian)
22. V.M. Sharapov et al., Patent of Ukraine 69877. Piezoelectric transducer of pressure. Publication 15 Sept 2004 (2004) (in Ukrainian)
23. V.M. Sharapov et al., Patent of Ukraine 69884. Piezoelectric transducer of efforts. Publication 15 Sept 2004 (2004) (in Ukrainian)
24. V.M. Sharapov et al., Patent of Ukraine 69885. Piezoelectric transducer of pressure. Publication 15 Sept 2004 (2004) (in Ukrainian)

25. V.M. Sharapov, B.F. Minaev, M.P. Musienko et al., Study of domain-dissipative piezoceramic transducers. Bull. Cherkasy State Technol. Univ. **2**, 17–22 (2003)
26. E.A. Kudryashov, B.E. Mager, S.h.M. Rafikov, Transverse piezoelements for force and pressure sensors. “Devices and Control Systems” **9**, 9–10 (1989)
27. V.M. Sharapov et al., Patent of Ukraine #61808. Piezoelectric transformer. Publication 17 Nov 03 (2003) (in Ukrainian)
28. V.M. Sharapov et al., Patent of Ukraine #61809. Piezoelectric transformer. Publication 17 Nov 03 (2003) (in Ukrainian)
29. V.M. Sharapov et al., Patent of Ukraine #62728. Piezoelectric transformer. Publication 15 Dec 2003 (2003) (in Ukrainian)
30. V.M. Sharapov et al., Patent of Ukraine #62729A. Piezoelectric transformer. Publication 15 Dec 2003 (2003) (in Ukrainian)
31. V.M. Sharapov, I.G. Minaev, J.V. Sotula, K.V. Basilo, L.G. Kunitskaya, *Piezoceramic Transformers and Sensors* (Vertical, Cherkasy, 2010), p. 278 (in Russian)
32. V.M. Sharapov et al., Patent of Ukraine #61807. Piezoelectric transformer. Publication 17 Nov 2003 (2003) (in Ukrainian)
33. V.M. Sharapov et al., Patent of Ukraine #62727. Piezoelectric transformer. Publication 15 Dec 2003 (2003) (in Ukrainian)

# Chapter 4

## Measuring Circuits of Piezoelectric Sensors

Preamplifiers are the basic element of piezoelectric sensor metering circuits. The main task of the preamplifiers is transformation of the high input impedance of these sensors into lower impedance. This gives the sensors direct connection with relatively low impedance for measuring, analyzing or recording systems.

These are the other tasks of preamplifiers [1]:

- Matching of parameters, displaying the mechanical values studied, with the signalsparameters (sensitivity, in particular) of the equipment used
- Signal multiplication
- Integration of accelerometer signals, proportional to acceleration and, consequently, reception of signals, proportional to velocity and vibration displacement
- Input and output overload warning
- Filtration of signals processed, and therefore, elimination of unnecessary or undesirable constituents of these signals

Simultaneously with obligatory transformation of impedance, certain preamplifiers perform all or several of the functions listed above.

Preamplifiers, forming two groups, are used together with transducers:

- Charge amplifiers: their output pressure is proportional to the signal arriving at their input. These amplifiers do not reinforce the electric charge
- Voltage amplifiers: their output voltage is proportional to the voltage arriving at their input

### 4.1 Charge Amplifiers

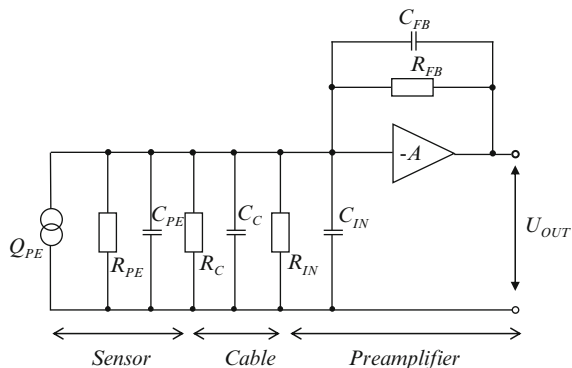
Charge amplifiers are used by preference in the majority of modern vibration meter systems [2, 3]. This is to be seen, for example, in the range produced by the firm of Brüel and Kjer, which makes preamplifiers for vibration transducers with practically no voltage amplifiers (excluding preamplifier 2650, containing both

charge and voltage amplifiers). The basic advantage of charge amplifiers is the fact that they exclude the effect of the length of connecting cables on the general sensitivity. Therefore, connecting cables of practically any length can be used. The amplification coefficient of the equipment used has to be adjusted and the system has to be calibrated again if the length of the connecting cable is changed in a system with voltage amplifiers.

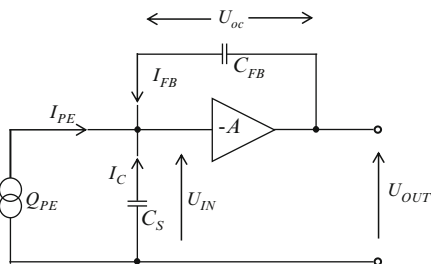
The input cascade of charge amplifiers consists of an operational amplifier with capacitive feedback. The operational amplifier with the condenser in the feedback circuit is an electronic integrator, integrating electric current arriving at its input [1, 4–9].

The equivalent electric circuit of the charge amplifier, connected to the piezoelectric sensor, is shown in Fig. 4.1.

Resistances of the preamplifier piezoelement, input circuit and feedback circuit usually have high values. Therefore, the equivalent electric circuit, shown in Fig. 4.1, can be simplified (Fig. 4.2).



**Fig. 4.1** Equivalent electric circuit of charge amplifier, connected to piezoelectric sensor.  $Q_{PE}$  – electric charge, given away by the accelerometer piezoelement and proportional to vibrations acceleration;  $C_{PE}$  – piezoelement capacitance;  $R_{PE}$  – piezoelement resistance;  $C_C$  – connecting cable capacitance;  $R_C$  – connecting cable resistance;  $C_{IN}$  – capacitance of the preamplifier input circuit;  $R_{IN}$  – resistance of the preamplifier input circuit;  $C_{FB}$  – feedback circuit capacitance;  $R_{FB}$  – resistance of feedback circuit;  $A$  – amplification coefficient of operational amplifier;  $U_{OUT}$  – amplifier output voltage



**Fig. 4.2** Simplified equivalent electric circuit of charge amplifier, cable-connected with piezoelement

In Fig. 4.2:

$$C_S = C_{PE} + C_S + C_{IN},$$

where  $I_{PE}$  – general current, caused by the charge, given away by the piezoelement;  $I_C$  – current from  $C_C$ ;  $I_{FB}$  – current in feedback of the operational amplifier.

Preamplifier input and output voltages ( $U_{IN}$  and  $U_{OUT}$ ) are interconnected by this expression:

$$U_{OUT} = -AU_{IN}.$$

This expression can be written for voltage  $U_{FB}$  as follows:

$$U_{FB} = U_{OUT} - U_{IN} = \left(1 + \frac{1}{A}\right) U_{OUT}.$$

The input current of the ideal operational amplifier equals zero. The currents shown in Fig. 4.2 are connected (Kirchhoff's law) by the equation:

$$I_{PE} + I_S + I_{FB} = 0.$$

Considering the other parameters of the equivalent circuit, shown in Fig. 4.2, the following expressions can be written for currents  $I_{PE}$ ,  $I_C$  and  $I_{FB}$ .

$$\begin{aligned} I_{PE} &= \frac{dQ_{PE}}{dt}; \\ I_{FB} &= C_{FB} \frac{dU_{FB}}{dt} = \left(1 + \frac{1}{A}\right) C_{FB} \frac{dU_{OUT}}{dt}; \\ I_C &= -C_S \frac{dU_{IN}}{dt} = \frac{1}{A} C_S \frac{dU_{OUT}}{dt}. \end{aligned}$$

This expression is obtained after substitution of these expressions into Kirchhoff's equation:

$$\frac{dQ_{PE}}{dt} = -\left(1 + \frac{1}{A}\right) C_{FB} \frac{dU_{OUT}}{dt} - \frac{1}{A} C_S \frac{dU_{OUT}}{dt}. \quad (4.1)$$

This differential equation can be solved by integration. It is assumed that constants corresponding to initial pressure of direct current on the operational amplifier output equal zero. This is quite possible, as any displacement voltage quickly decreases to zero if the operational amplifier is active. Therefore, this equation can be solved like this:

$$U_{OUT} = -\frac{Q_{PE}}{\left(1 + \frac{1}{A}\right) C_{FB} + \frac{1}{A} C_S}. \quad (4.2)$$

Considering the high value of the gain coefficient peculiar to modern operational amplifiers ( $A \approx 10^5$ ), expression (4.2) becomes simpler. The solution of the differential equation looks like this:

$$U_{OUT} \approx \frac{Q_{PE}}{C_{FB}}. \quad (4.3)$$

It follows from expression (4.3) that output voltage of the preamplifier is proportional to the input charge, and is inversely proportional to the feedback capacitance.

Equivalent capacitance on the preamplifier input does not affect the signal voltage on its output, as in the ideal case  $A \rightarrow \infty$  and input voltage equals zero.

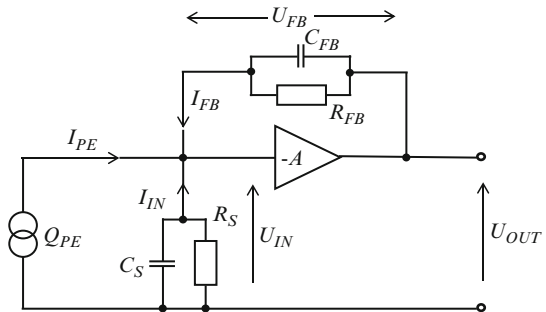
Therefore, equivalent input resistance does not affect voltage of the preamplifier output signal. This means that there are only currents from the transducer and from the condenser in the feedback circuit of the operational amplifier. These currents have identical amplitude, but opposite signs. Hence, all the piezotransducer electric charge is supplied to the condenser in the operational amplifier feedback circuit.

A more complicated model of the preamplifier, considering resistances  $R_{PE}$ ,  $R_C$ ,  $R_{IN}$  and real measurements condition, should be analyzed (Fig. 4.3).

All voltages and currents corresponding to the sensor and the preamplifier are also shown in Fig. 4.3. The following expressions can be written for Fig. 4.3 [1]:

$$\begin{aligned} \frac{1}{R_S} &= \frac{1}{R_{PE}} + \frac{1}{R_S} + \frac{1}{R_{BX}}; \\ U_{OUT} &= -AU_{IN}; \\ U_{FB} &= \left(1 + \frac{1}{A}\right) U_{OUT}; \\ I_{FB} &= C_{FB} \frac{dU_{FB}}{dt} + \frac{U_{FB}}{R_{FB}} = \left(1 + \frac{1}{A}\right) \left[ C_{FB} \frac{dU_{OUT}}{dt} + \frac{U_{OUT}}{R_{FB}} \right]; \\ I_{IN} &= -C_S \frac{dU_{IN}}{dt} - \frac{U_{IN}}{R_S} = \frac{1}{A} \left[ C_S \frac{dU_{OUT}}{dt} + \frac{U_{OUT}}{R_S} \right]; \\ \frac{dQ_{PE}}{dt} &= -\left(1 + \frac{1}{A}\right) \left[ C_{FB} \frac{dU_{OUT}}{dt} + \frac{U_{OUT}}{R_{FB}} \right] - \frac{1}{A} \left[ C_S \frac{dU_{OUT}}{dt} + \frac{U_{OUT}}{R_S} \right]. \end{aligned} \quad (4.4)$$

Differential equation (4.4) can be solved like this [1]:



**Fig. 4.3** Equivalent electric circuit of charge amplifier, cable-connected with transducer piezoelement

$$j\omega Q_{PE} = -\left(1 + \frac{1}{A}\right) \left[ j\omega U_{OUT} C_{FB} + \frac{U_{OUT}}{R_{FB}} \right] - \frac{1}{A} \left[ j\omega U_{OUT} C_S + \frac{U_{OUT}}{R_S} \right]. \quad (4.5)$$

An expression for the preamplifier output voltage can be obtained by this simple transformation:

$$U_{OUT} = -\frac{Q_{PE}}{\left(1 + \frac{1}{A}\right) \left(C_{FB} + \frac{1}{j\omega R_{FB}}\right) + \frac{1}{A} \left(C_S + \frac{1}{j\omega R_S}\right)}. \quad (4.6)$$

Believing that  $A \rightarrow \infty$  and  $R_S \rightarrow \infty$ , one obtains:

$$U_{OUT} \approx \frac{Q_{PE}}{C_{FB}}. \quad (4.7)$$

Considering the finite value  $R_{FB}$

$$U_{OUT} = -\frac{Q_{PE}}{C_{FB} \left(1 + \frac{1}{j\omega R_{FB} C_{FB}}\right)}. \quad (4.8)$$

The general sensitivity of the sensor and the preamplifier can be controlled by feedback capacitance change ( $C_{FB}$ ), as electric charge  $Q_{PE}$  is proportional to force (or to acceleration). In addition to that, the preamplifier AFC can be controlled (at low frequencies) by the time constant adjustment of feedback [1].

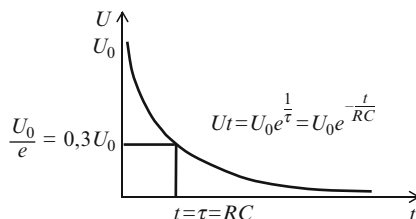
The AFC of the charge amplifier is determined by the time constant of the feedback circuit at low frequencies. It does not depend on load on the preamplifier input. The lower frequency limit (cutoff frequency) of the charge amplifier is regulated by the resistance adjustment of the feedback circuit.

It is known that a condenser is an element able to accumulate electric charges. The condenser capacitance is determined by the electric charge quantity. The charge is accumulated per voltage unit attached to this condenser. We should note that the transducer piezoelement is an almost ideal condenser, therefore [5]:

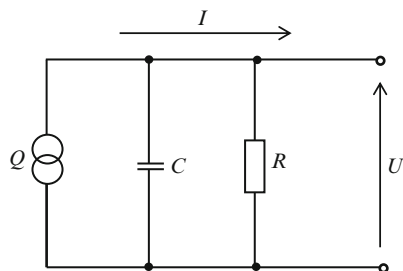
$$I = C \frac{dU}{dt}.$$

The ideal unloaded condenser, charged by a certain voltage application, keeps the electric charge after elimination of the charge voltage. Therefore, the voltage of the ideal condenser does not change, as this condenser has infinite leakage resistance. However, leakage resistance always has a finite value for a real condenser. Consequently, the leak current causes gradual reduction of the charge accumulated, and exponential voltage recession of the real condenser. The speed of this process is determined by time constant  $\tau$ , which is the product of capacitance  $C$  and resistance  $R$  (Fig. 4.4) [8]:

**Fig. 4.4** Exponential voltage recession on condenser



**Fig. 4.5** Equivalent electric circuit of piezoelectric accelerometer, loaded by equivalent capacitance and resistance of connecting cable and preamplifier



Time constant  $\tau$  plays an important role in the processing of sinusoidal form signals. It considerably affects AFC in the low-frequency range. A charge source (sensor piezoelement), connected to several capacitance–resistance networks, is considered below (Fig. 4.5). Here, the resistor and condenser combinations are presented as a resistor and a condenser respectively.

Considering the expressions discussed above, the following can be written for the scheme, shown in Fig. 4.5:

$$I = \frac{dQ}{dt} = \frac{U}{R} + C \frac{dU}{dt}. \quad (4.9)$$

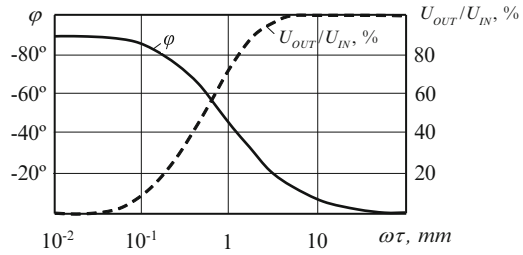
The solution of this differential equation (4.9) [1] can be found for harmonious currents and voltage:

$$U = \frac{Q}{\left(1 + \frac{1}{j\omega RC}\right) C} = \frac{Q}{\left(1 + \frac{1}{j\omega\tau}\right) C} = \frac{Q (1 + j\frac{1}{\omega\tau})}{\left(1 + \frac{1}{\omega^2\tau^2}\right) C}. \quad (4.10)$$

To simplify this solution, reference quantities and constants are believed to equal zero. As output voltage  $U$  is a complex value, it can also be expressed by module  $|U|$  and phase angle  $\varphi$ .



**Fig. 4.6** Amplitude and phase characteristics of accelerometer



$$\operatorname{tg} \varphi = \frac{1}{\omega\tau};$$

$$|U| = \frac{Q \sqrt{1 + \left(\frac{1}{\omega\tau}\right)^2}}{\left[1 + \left(\frac{1}{\omega\tau}\right)^2\right] C}.$$

At  $\omega\tau = 1$ ,  $\operatorname{tg} \varphi = 1$ ,  $\varphi = 45^\circ$  and  $U = Q/\sqrt{2}C$ .

Amplitude and phase correlations between input and output voltages, depending on  $\omega\tau$ , are shown in Fig. 4.6. The frequency when  $\omega\tau = 1$  ( $2\pi fRC = 1$ ) is determined by the expression:  $f_c = 1/2\pi RC = 1/2\pi\tau$ .

This frequency is called low-frequency limit (or cutoff frequency). It corresponds to AFC recession and, consequently, to a 3 dB reduction of the output signal level and a  $-45^\circ$  change of the phase angle value.

Thus, the lower frequency limit of the charge amplifier is determined by the time constant of the operational amplifier feedback circuit, i.e.,  $\tau_{OC} = R_{OC} C_{OC}$ . The phase difference of input and output signals is usually  $-180^\circ$  (the preamplifier functions as a phase inverter). There is an additional  $-45^\circ$  phase shift on the lower frequency limit. As also follows from expression (4.6), resistive load on the charge amplifier input does not affect the value of the lower frequency limit until the load resistance has a value commensurate with  $R_{OC}/A$ . Therefore, if  $C_{OC} \approx C_C$ , the load resistance influence is  $A$  times smaller than its influence on the resistance-capacitance network when the charge amplifier is applied.

For example, to assure this low-frequency limit 1 Hz ( $A = 10^5$ ,  $C_{FB} = 1$  nF), the following is received:

$$R_{FB} = \frac{1}{2\pi C_{FB}} = 1.6 \text{ kOhm}.$$

This example shows that the lower frequency limit of the charge amplifier does not depend much on its input load. General resistance of the electric sensor, connectors, cable, and preamplifier input circuit is practically reduced to the level discussed above.

The lower frequency limit of charge amplifiers has values of several hertz fractions. The preamplifier feature to process low-frequency component signals is important for long-pulse and quasi-static vibrations study.

The gain coefficient of the charge amplifier almost does not change when the capacitance of the connecting cable changes. The application of long connecting cables establishes a minor AFC recession in the high-frequency range.

It was shown earlier that the signal voltage on the charge amplifier output is determined by  $C_{FB}$  capacitance of the amplifier feedback circuit and electric charge  $Q_{PE}$  of the piezoelement. The feedback circuit capacitance of the operational charge amplifiers is in the 100 pF to 10 nF range [1]. One nanofarad can be considered a nominal value, i.e., the value corresponding to the gain coefficient, equal to 1 mV/pC. This value hardly changes until capacitance  $C_S$  takes the value, commensurate with  $AC_{FB}$  product. Minor dependence of the charge amplifier operating characteristic on the connecting cable capacitance is illustrated by the example, given below [1].

The maximum length of connecting cable is determined. As a result of its application, the general charge sensitivity of accelerometer and charge amplifier kit will change less than 1%.

$$C_S = 0.01 (A + 1) C_{FB} = 0.01 (10^5 + 1) 1 \text{ nF} = 10^3 \text{ nF} = 1 \text{ mkF}.$$

This follows from the expression given before for  $U_{OUT}$  if  $C_{FB} = C_{PE} = 1 \text{ nF}$  and  $A = 10^5$ .

The calculated value corresponds to the general connecting cable capacitance. It is 10,000 m long. Its capacitance is 100 pF/m.

A high capacitive load on the preamplifier input can affect its AFC, a high-frequency site, in particular. This influence is possible because of the gain coefficient reduction in the high-frequency range, characteristic of operational amplifiers. Output signal voltage of the charge amplifier decreases in the high frequency range. Expression (4.6) should be considered, determining it, i.e.,

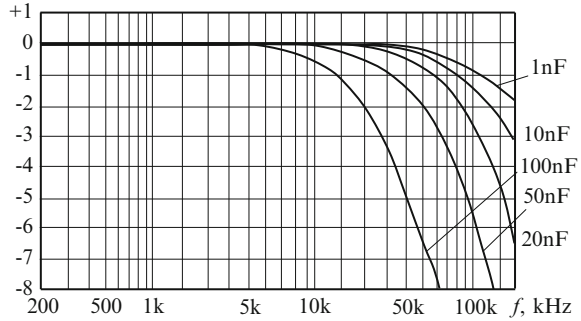
$$U_{OUT} = - \frac{Q_{PE}}{\left(1 + \frac{1}{A}\right) \left(C_{FB} + \frac{1}{j\omega R_{FB}}\right) + \frac{1}{A} \left(C_S + \frac{1}{j\omega R_S}\right)}.$$

We assume that the gain coefficient  $A$  of the operational amplifier in the high-frequency range decreases up to  $10^3$ , and that its feedback circuit  $C_{FB}$  capacitance equals 1 nF. A 2 hundred meter long connecting cable, with 100 pF/m capacitance, is connected to the preamplifier input. The capacitive load (20 nF) of this cable determines 5% preamplifier AFC recession in the high-frequency range. Therefore, this influence can be considered imperceptible in the practical operation of the preamplifier.

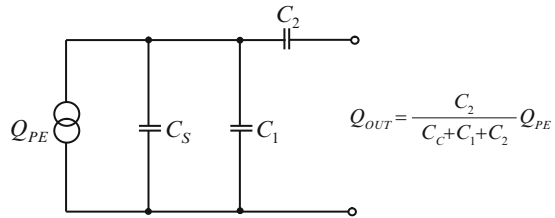
The curves in Fig. 4.7 show the influence of input capacitive load on the AFC site of the charge amplifier.

Relative amplitude, dB

**Fig. 4.7** Influence of input capacitive load on charge amplifier AFC



**Fig. 4.8** Equivalent electric circuit of accelerometer, connected with charge capacitance divider (attenuator)



Though the parallel capacitance increase almost does not affect charge sensitivity of the accelerometer, the addition of a tandem condenser leads to a reduction in the input electric charge. Charge reduction on the preamplifier input can be reasonable when looking at high-amplitude vibrations, in particular when a high-sensitivity accelerometer is used. Thus, the input overload of the charge amplifier can be prevented. Consequently, the electric charge on the preamplifier input can be weakened if carefully selected condensers with precisely determined capacitances are tandem and parallel-connected to the accelerometer input. The equivalent electric circuit of the accelerometer, connected with the capacitor attenuator described, is shown in Fig. 4.8.

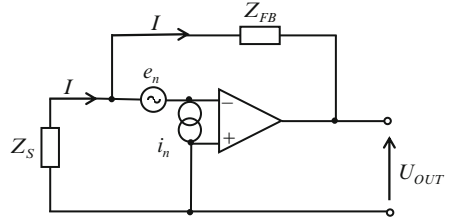
It is necessary to note that Brüel and Kjer, for example, produces capacitance attenuators WB0726\* (with 12 dB attenuation) and WB0778\* (with 20 dB attenuation) [1].

Application of long connecting cables and small values of the charge amplifier gain coefficient are accompanied by intrinsic noise increase and, consequently, reduction of general signal–noise correlation. The intrinsic preamplifier noise increases if the load capacitance on the amplifier input is essentially decreased.

The equivalent electric circuit of the piezoelectric sensor and charge amplifier with intrinsic noise sources kit is shown in Fig. 4.9. We should stress that external noise sources are not considered in this scheme, i.e., triboelectric noise sources. This is the noise caused by ground and electromagnetic noise loops, perceived by the connecting cable.

The following notations are used in Fig. 4.9:  $Z_S$  – equivalent impedance of the electric sensor and the connecting cable;  $Z_{FB}$  – equivalent impedance of the

**Fig. 4.9** Equivalent electric circuit of piezoelectric accelerometer and charge amplifier



operational amplifier feedback circuit;  $e_n$  – noise voltage;  $i_n$  – noise current;  $U_{OUT}$  – voltage of the preamplifier output signal.

Current noise can be neglected in the system, containing a high-impedance piezoelectric sensor and a charge amplifier with an operational amplifier with capacitance feedback. It is known that the inverting input of the operational amplifier has a zero potential (“virtual land”) and that current does not go through the corresponding input contour. Therefore,

$$I = \frac{-e_n}{Z_S} = \frac{e_n - U_{OUT}}{Z_{FB}};$$

$$U_{OUT} = e_n \left( 1 + \frac{Z_{FB}}{Z_S} \right).$$

To obtain the expression for the input signal, the result obtained should be divided into the gain coefficient, i.e.,  $Z_{OC}/Z_C$ . Thus [1]:

$$e_s = -U_{OUT} \frac{Z_S}{Z_{FB}} = -e_n \left( 1 + \frac{Z_S}{Z_{FB}} \right).$$

In the medium-frequency range, impedances  $Z_{OC}$  and  $Z_C$  are of a capacitance–resistance character. Consequently,

$$\frac{Z_S}{Z_{FB}} = \frac{C_{FB}}{C_S},$$

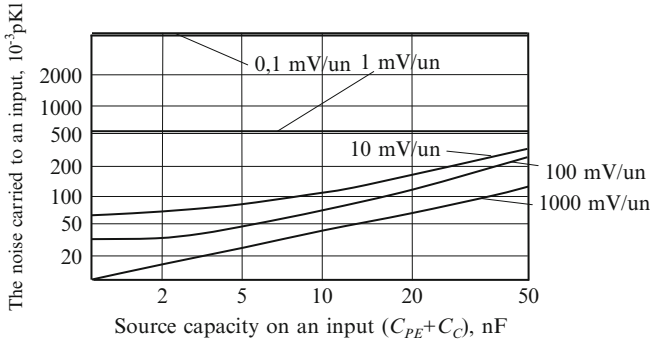
where

$$C_S = C_{PE} + C_{IN} + C_C;$$

$$e_s = -e_n \left( 1 + \frac{C_{FB}}{C_S} \right).$$

The equivalent noise charge  $q_C$  can be defined by multiplication of the above-described expression and capacity  $C_S$ , i.e.,

$$q_s = e_s C_S = -e_n (C_S + C_{FB}).$$



**Fig. 4.10** Dependence of charge amplifier intrinsic noise, referred to input, on capacitive load on its input

It follows from this expression that  $C_{FB}$  and  $C_S$  capacitance increase is accompanied by intrinsic noise increase, despite the almost imperceptible influence of the input load on gain coefficient and on the charge amplifier lower frequency limit. Consequently, application of long connecting cables always affects signal–noise ratio. The curves in Fig. 4.10 show the dependence of intrinsic noise, referred to the input, on capacitance load on its input.

As capacitance  $C_{FB}$  determines the preamplifier gain coefficient, its intrinsic noise increases with the gain coefficient reduction, i.e., with capacitance value increase of feedback circuit in the preamplifier of the operational amplifier. Therefore, application of highly sensitive piezotransducers and/or big values of preamplifier gain coefficient helps increase signal–noise ratio.

One should stress that connecting cables, subject to vibrations, generate electric noise. Low-noise cable application is especially important in the systems used for small-amplitude vibration research. The connecting cables used should be securely fastened.

The charge amplifier intrinsic noise is usually inversely proportional to its frequency in the low-frequency range ( $<100$  Hz). Its amplitudes increase with the frequency decrease. The intrinsic noise increase at low frequencies is an unwanted property of operational amplifiers. Use of additional upper frequencies filters is effective for this noise reduction.

It is known that almost all Brüel and Kjer preamplifiers have the filters discussed [1–3].

Essential reduction of load resistance on the preamplifier input (smaller than approximately 10 Mohm) is also accompanied by intrinsic noise increase. Increase of the preamplifier intrinsic noise is more noticeable in the low-frequency range. However, it is hard to determine the reasons for this, as detailed information on separate circuit members' parameters and their connections in the preamplifier input cascade is necessary. The curves shown in Fig. 4.11 are received experimentally. They show the dependence of narrow-band intrinsic noise of the charge amplifier

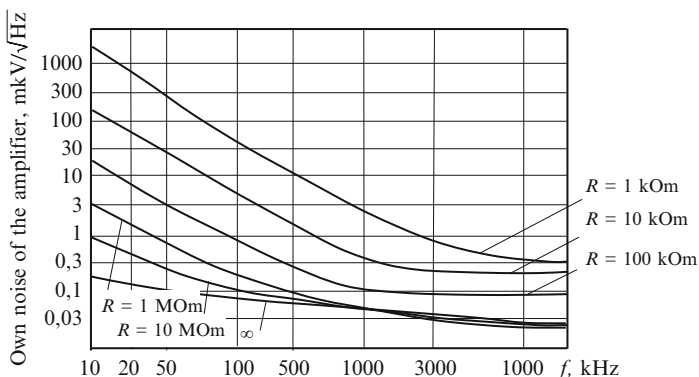


Fig. 4.11 Dependence of charge amplifier narrow-band intrinsic noise on resistance on its input

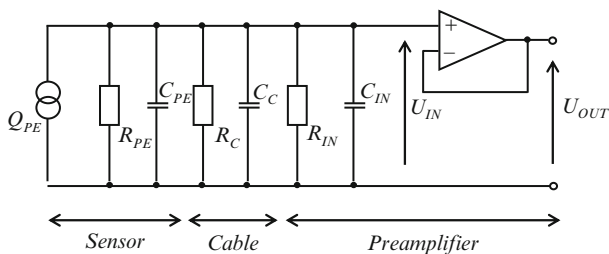


Fig. 4.12 Equivalent electric circuit of voltage amplifier, cable-connected with piezoelectric sensor

on the load resistance on its input [1]. Intrinsic noise values are expressed in voltage units, referred to the square root of the frequency bandwidth, i.e.,  $\text{mkV}/\sqrt{\text{Hz}}$ .

## 4.2 Voltage Amplifiers

Voltage amplifiers (VA) have a simple design. Their operational characteristics are lower than charge amplifier characteristics. Therefore, Brüel and Kjer, for example, produces only one preamplifier with VA [1,2].

An equivalent electric circuit of the sensor and VA is shown in Fig.4.12 [1,4–9]. This scheme and the charge amplifier circuit are almost identical. The only difference is in the connection circuit of the operational amplifier. The operational amplifier uses functions as a buffer amplifier with  $A = 1$ .

The input resistance of the voltage amplifier is formed by parallel connection of resistance  $R_{IN}$  and capacitance  $C_{IN}$ .

The output voltage of the piezoelectric sensor  $U_{PE}$

$$U_{PE} = \frac{Q_{PE}}{C_{PE}}. \quad (4.11)$$

As the parallel  $R_{PE}$  is of a high value, it can be neglected. The voltage on the operational amplifier input is expressed as follows:

$$S_U = \frac{S_q}{C_{PE} + C_C + C_{IN}} = S_{IN} \frac{C_{PE}}{C_{PE} + C_C + C_{IN}}. \quad (4.12)$$

Charge and voltage sensitivities ( $S_q$  and  $S_U$  respectively) can be introduced into this expression, where  $S_{PE}$  is the voltage sensitivity of a non-loaded piezoelectric sensor.

As can be seen from the expressions discussed, the sensitivity of a piezoelectric sensor–cable–voltage amplifier system depends on the cable length. This requires additional calibration if the cable is replaced.

The lower frequency limit for the given case is (the point of 3 dB).

$$f_H = \frac{1}{2\pi R_{SUM} C_{SUM}},$$

where  $C_{SUM} = C_{PE} + C_C + C_{IN}$ ,  $1/R_{SUM} = 1/R_{PE} + 1/R_C + 1/R_{IN}$ .

There are two possibilities for ensuring small values of flow frequency:

- General capacitance increase of the piezoelectric sensor–voltage amplifier kit. If the cable is increased, this can be achieved for the concrete sensor with a fixed value  $C_{PE}$ . However, this is practically impossible, as it is accompanied by voltage sensitivity reduction.
- Use of an amplifier with high input resistance. This method is used for voltage amplifiers. However, the input resistance decrease under any circumstances (for example, moisture penetrations) is accompanied by an increase in the lower frequency limit.

Intrinsic noise of the voltage amplifier does not depend on capacitive load on the input. However, the increase of this capacitance is accompanied by voltage sensitivity reduction and, consequently, by deterioration of signal–noise ratio.

## References

1. Piezoelectric accelerometers and preamplifiers/directory: theory and operation, Denmark (in Russian)
2. Firm prospectuses of Brüel and Kjer, Nerum, Denmark
3. Firm prospectuses of Kistler Instrumente AG, Winterthur, Switzerland
4. V.S. Gutnikov, *Integrated Electronics in Measuring Devices* (Energatomizdat, Leningrad, 1988), p. 304 (in Russian)
5. E.S. Levshina, P.V. Novitskiy, *Electric Measurements of Physical Values (Measuring Transducers). Manual for Higher Educational Establishments* (Energatomizdat, Leningrad, 1983), p. 320 (in Russian)

6. G.S. Ostapenko, *Amplifying Devices: Manual for Higher Educational Establishment* (Radio and Communication, Moscow, 1989), p. 286 (in Russian)
7. A.D. Peiton, V. Walsh, *Analogue Electronics on Operational Amplifiers* (Binom, Moscow, 1994), p. 124 (in Russian)
8. U. Titse, K. Shenk, *Semi-conductor Circuitry. Reference Guide* (Mir, Moscow, 1983), p. 512 (in Russian)
9. P. Horovits, U. Hill, *Circuitry Art. In Three Volumes* (Mir, Moscow, 1993) (in Russian)



# Chapter 5

## Feedback in Piezoceramic Sensors

### 5.1 Feedback Effect on Sensor Characteristics

Parameters of automatic control systems (for example, time constants, input and output resistances, frequency and transitive characteristics, etc.) can be widely changed as a result of feedback (FB) introduction [12].

Application of FB in equipment gives excellent results [5, 12, 13, 16, 38, 39]. FB is also widely used and in measuring devices [1, 13, 14, 16, 32]. For example, resonant vibrations are activated in piezoelectric sensors under the effect of positive feedback. Sensors of various physical values [5] can be built on this basis. Negative feedback in resonant piezoceramic sensors gives a chance to linearize their graduation characteristics [13].

Feedback has unique properties, due to which parameters of measuring devices can be essentially improved.

FB in measuring devices is usually introduced along the input action. The general view of the transducer with FB can be represented by the simplified block diagram (Fig. 5.1), where  $W(p)$  – direct transform circuit,  $\beta(p)$  – FB circuit.

Using methods of automatic control theory [12], the operational form of the expression for the transducer with FB sensitivity can be written:

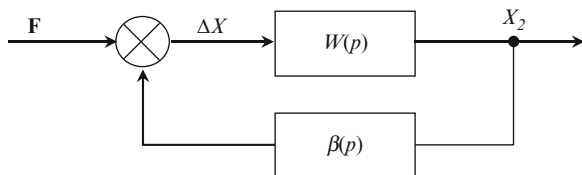
$$W_{\text{FB}}(p) = \frac{X_2}{X_1} = \frac{W(p)}{1 \pm W(p)\beta(p)}, \quad (5.1)$$

where  $X_1$  and  $X_2$  – input and output values.

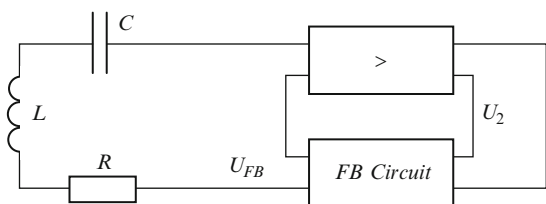
Complex FB is the most common case of FB. Then operator  $p$  can be substituted for  $j\omega$  in the equation (5.1):

$$W_{\text{FB}}(j\omega) = \frac{X_2}{X_1} = \frac{W(j\omega)}{1 \pm W(j\omega)\beta(j\omega)}. \quad (5.2)$$

**Fig. 5.1** Block diagram of piezotransducer with feedback



**Fig. 5.2** Equivalent circuit of piezoelectric sensor with feedback



Expressing sensitivity of direct transform and FB circuits in the algebraic form, the module sensitivity  $W_{FB}(\omega)$  and phase displacement  $\varphi_{FB}$  after transformations will look like this:

$$W(\omega) = \frac{W}{\sqrt{1 \pm 2W\beta \cos(\varphi_C + \varphi_\beta) + W^2\beta^2}}, \quad (5.3)$$

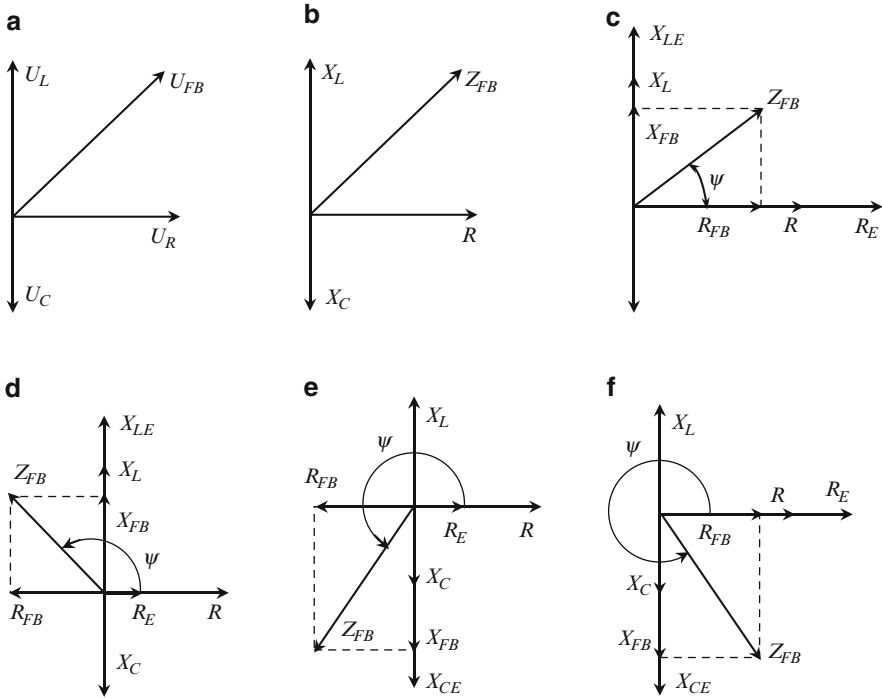
$$\varphi_{FB}(\omega) = \text{arctg} \frac{\text{tg}\varphi_C + W\beta \frac{\sin\varphi_\beta}{\cos\varphi_C}}{1 \pm W\beta \frac{\sin\varphi_\beta}{\cos\varphi_C}}. \quad (5.4)$$

The expressions obtained show that both sensitivity module and phase displacement angle depend not only on modules  $W$  and  $\beta$ , but also on values and signs of phase displacement angles in direct  $\varphi_C$  and inverse  $\varphi_\beta$  transforms.

### 5.1.1 Influence of Frequency-Dependent Feedback

Working at a close to resonant frequency area, FB is frequency-dependent. A piezoelectric sensor can be represented as a series oscillatory element (Fig. 5.2). As can be seen from Fig. 5.2, the oscillatory contour is connected to the amplifier, for the amplifier output to be reconnected with it via a phase-shift device [16].

If all voltages, operating in the contour are divided into the current in the contour, the voltage diagram (Fig. 5.3a) will change into the resistance diagram (Fig. 5.3b). Feedback introduction can be formally considered as introduction of certain complex resistance into the contour. This can essentially alter both frequency and transitive contour characteristics, or any other system covered by feedback, as the equivalent parameters of this system are changed.



**Fig. 5.3** Voltage and resistance diagrams in piezosensor with feedback

Several possible cases are considered below.

1. Angle  $\psi$ , formed by FB resistance  $Z_{FB}$ , and active resistance  $R$ , is within the limits  $0^\circ < \psi < 90^\circ$ , as shown in Fig. 5.3c.

Resolving  $Z_{FB}$  into active and reactive components, one can see that the reactive component of FB resistance directionally coincides with  $X_L$ . As a result, equivalent inductive resistance of contour  $X_{LE}$  increases. This is equal to the equivalent inductance increase. Equivalent active resistance  $R_E$  also increases in this case.

This implies that FB introduction leads to a resultant reduction of the own frequency of an electric contour or mechanical system. In this case, its attenuation increases while  $Q$  factor decreases.

2. Angle  $\psi$  satisfies inequalities  $90^\circ < \psi < 180^\circ$ . Now, as can be seen from Fig. 5.3d, equivalent inductive resistance  $X_{LE}$ , and, consequently, equivalent inductance increases. However, active component  $R_{FB}$  has a negative value. This leads to a decrease in the equivalent contour active resistance. This resistance may equal zero if equality  $R_{FB} = R$  exists.

Thus, the resultant own frequency of the electric contour or mechanical system decreases in the case considered, while  $Q$  factor increases. It can become infinitely big. As a result, continuous oscillations appear in the contour under the action of any charge fluctuation.

3. The following case is possible if angle  $\psi$  equals  $180^\circ < \psi < 270^\circ$ . As follows from Fig. 5.3e, this FB increases contour or system equivalent capacitive resistance. It means that equivalent capacitance is reduced. In this case, resultant active resistance decreases simultaneously. Resultant own frequency or  $Q$  factor increases if contour or mechanical system equivalent parameters decrease.
4. And finally, inequality  $270^\circ < \psi < 360^\circ$  is true when vector  $Z_{FB}$  is in the fourth quadrant, as is shown in Fig. 5.3f. Equivalent capacitive resistance is increased by feedback in this case. The contour equivalent capacity is decreased, while active resistance increases under its action.

Thus, the resultant own frequency of the contour or corresponding mechanical system is increased by FB, while its  $Q$  factor is decreased.

The analysis shows that FB can essentially alter the system properties, its frequency and transitive characteristics. Then own frequencies, attenuation values, etc., can be either increased, or decreased.

### 5.1.2 Influence of Frequency-Independent FB

Frequency-independent FB is used more often. It can be in the narrow range of below resonance area, where FB can be considered frequency-independent with constant phase displacement ( $\varphi_\beta \approx 180^\circ$  or  $\varphi_\beta = 0^\circ$ ). Two cases are possible in a direct transform circuit (with matching amplifier as the basic element): with or without inverting of the signal phase ( $\varphi_K = 180^\circ$  or  $\varphi_\beta = 0^\circ$ ). Thus, if  $\varphi_K = 0$  or  $\varphi_\beta = 0$  (either  $\varphi_K = 180^\circ$  or  $\varphi_\beta = 180^\circ$ ) FB is positive, then:

$$W_{FB} = \frac{W}{1 - W\beta}. \quad (5.5)$$

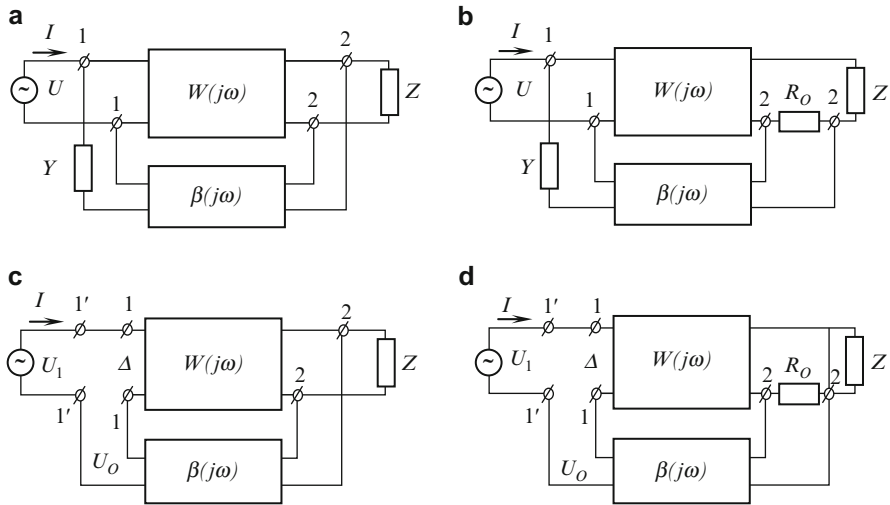
If  $\varphi_C = 0^\circ$  or  $\varphi_\beta = 180^\circ$  (or  $\varphi_K = 180^\circ$ , and  $\varphi_\beta = 0^\circ$ ) FB is negative, then:

$$W_{FB} = \frac{W}{1 + W\beta}. \quad (5.6)$$

As follows from (5.5), positive FB increases the sensitivity of the transducer with FB if  $W\beta < 1$  (indefinitely if  $W\beta = 1$ ).  $W_{FB}$  is always lower than the direct transform sensitivity for negative FB.

There are several variants of FB introduction and relief circuits. FB voltage can be proportional to either output voltage or output current, depending on the circuit. Voltage feedback is obtained in the first case, and current feedback in the second. Depending on FB voltage supply method, series and parallel FBs are distinguished.

The listed variants of FB circuits are shown in Fig. 5.4. Each FB circuit influences the system individually. Series voltage feedback circuit is the most widely used among all circuits of negative feedback (NFB). It is explained by the most successful



**Fig. 5.4** Basic feedback circuits: (a) voltage parallel, (b) current parallel, (c) voltage series, (d) current series

combination of positive properties of NFB in it. Parallel voltage feedback also gives scientifically interesting results.

Basic properties of this FB are considered. Special attention is devoted to NFB influence on nonlinear and frequency distortions, input and output resistances, time constant, frequencies pass-band and the whole circuit relative error.

### 5.1.3 Feedback Influence on Nonlinear and Frequency Distortions

FB essentially affects nonlinear distortions. Thus, it can be shown that

$$U'_{2k} = \frac{U_{2k}}{1 + W\beta}, \tag{5.7}$$

where  $U'_{2k}$  – voltage of the corresponding harmonic on the transducer output;  $U_{2k}$  – voltage of the corresponding harmonic on the transducer output with NFB. Value  $1 + W\beta$  is called the NFB depth.

Thus, by reducing voltage of harmonics on the closed system output, NFB linearizes the system, reducing nonlinear distortions. The deeper FB is, the easier is harmonics suppression. Harmonics occur as a nonlinearity result.

For positive feedback, the denominator sign in expression (5.7) must be changed for the opposite. Consequently, positive feedback leads to nonlinear distortions increase.

NFB decreases while positive FB increases frequency distortions [14].

### 5.1.4 Feedback Influence on Time Constant of Sensors

It can also be simply shown [16] that introduction of FB changes sensor time constant  $\tau$  in  $(1 \pm W\beta)$  times. It has only one constant, i.e., for aperiodic element with NFB:

$$\tau_E = \frac{\tau}{1 + W\beta}, \quad (5.8)$$

for positive FB:

$$\tau_E = \frac{\tau}{1 - W\beta}, \quad (5.9)$$

where  $\tau_E$  – equivalent constant of time for a transducer with FB.

However, change of time constant (increase or decrease) depends not only on FB type (positive or negative), but also on the transducer type and the method of FB introduction.

Time constant change is closely connected with the change of all attenuation characteristics. Thus, FB introduction into an oscillatory system (a piezoceramic sensor) can either increase, or decrease its  $Q$  factor, equivalent capacitive or inductive resistance. In addition to that, amplifier pass-band can be widened by NFB introduction. NFB use is of a great scientific interest for damping of piezoceramic sensors [40].

Thus, sensors can acquire absolutely new and unexpected properties under the influence of FB.

### 5.1.5 Feedback Influence on Input and Output Resistances

Considering FB influence on the sensor input resistance, one should stress that the input resistance change depends only on the method of FB introduction, but not on its relief form from the system output [14, 16].

The sensor equivalent input resistance increases by  $(1 + W\beta)$  times if NFB is in series. This can be physically explained by minor  $\Delta U$  difference, but not voltage  $U_1$  influence on the closed system input. As a result, input current  $I_1$  in NFB circuit drops sharply, while the input resistance appears to be high.

Parallel NFB reduces the sensor equivalent input resistance, as  $W\beta Y_\beta$  conductivity is added to FB circuit conductivity. This is equivalent to parallel joining of resistance  $Z_{FB}$ , with  $Z_{FB} = 1/W\beta Y_\beta$ .

Everything is opposite with positive FB.

Considering FB influence on the transducer output resistance, one should mention the fact that the output resistance change, caused by FB, does not depend

on the method of FB voltage introduction (i.e., either series, or parallel), but depends on its relief method.

The analysis shows that voltage NFB reduces equivalent output resistance by  $(1 + W\beta)$  times. Current NFB increases equivalent output resistance by the same number of times. Positive FB acts in the opposite way.

### 5.1.6 Feedback Influence on Static Systems Errors

Relative error of the sensor with NFB is analyzed. Its circuit is shown in Fig. 5.1.

The formula for relative error of this sensor with FB looks like this [14, 16]

$$\gamma_{\text{FB}} = \frac{dW_{\text{FB}}}{W_{\text{FB}}} = \frac{dW}{W} \frac{1}{1 + W\beta} - \frac{d\beta}{\beta} \frac{W\beta}{1 + W\beta}. \quad (5.10)$$

Expressions  $dW/W$  and  $d\beta/\beta$  are relative errors of direct and inverse transforms circuit in this equation. They are caused by inconstancy of their sensitivity, i.e.,  $\gamma_k = dW/W$  and  $\gamma_\beta = d\beta/\beta$ . Coefficient  $\delta = 1/(1 + W\beta)$  is called relative quasi-error or relative undercompensation [14, 16].

Therefore

$$\gamma_{\text{FB}} = \gamma_C \delta - \gamma_\beta (1 - \delta). \quad (5.11)$$

A transducer in an FB circuit is usually rather simple. The stability of its parameters is considerably higher than the parameters of direct transform circuit stability. It usually consists of several transducers. Thus, if we consider that  $\gamma_C \gg \gamma_\beta$ , value  $\delta$  should decrease. This can be done either by FB action increase, or by increase of the amplifier gain coefficient. The latter cannot be increased infinitely without loss of system stability.

Consequently, to decrease the error this condition  $W\beta \rightarrow \infty$  should be reached. Here,  $W$  is a transfer coefficient of direct transform circuit, influenced by the FB,  $\beta$  is an FB circuit transfer coefficient. In this case  $\delta \approx 0$ , and expression (5.11) is transformed to this

$$|\gamma_{\text{FB}}| \approx |\gamma_\beta|, \quad (5.12)$$

i.e., the error of the transducer with NFB when  $W\beta \rightarrow \infty$  will be determined by the FB circuit error.

Thus, NFB introduction can sharply decrease the resultant error of the whole closed system only if the error in the FB circuit is quite small.

Thus, the main conclusion is that the error of automatic control static systems is minimum if the NFB level when  $W\beta \rightarrow \infty$  is reached.

## 5.2 Piezoceramic Sensors with Spatial Electromechanical NFB

NFB in measuring devices is usually introduced by input action, as shown in Sect. 5.1. The error is reduced when the condition  $W\beta \rightarrow \infty$  is fulfilled, where  $W$  – transfer coefficient of direct transform circuit with FB, and  $\beta$  – transfer coefficient of FB circuit. Then the FB circuit error must be smaller than in a direct transform circuit.

Power compensators in FB circuit should be made to introduce NFB in pressure sensors. Therefore, to reduce the FB error and, consequently, the sensor error, these compensators should be rather complicated and accurate. This reduces the advantages of FB introduction.

As output characteristics of piezoelectric transducers are functions of two or more parameters, NFB, enveloping the auxiliary channel, can be introduced [13, 14]. As the output value of the sensors (charge or voltage) depends not only on mechanical action (force, pressure, accelerations), but also on voltage, it is proposed to introduce NFB along the auxiliary channel. This is created by an additional system of electrodes or an additional piezoelement, positioned planar or coplanar, relative to the main piezoelement [1, 14].

No power compensators are used if the method proposed is used. As a result, the design of piezoceramic sensors with NFB becomes simpler. In this case, the piezoelement is also a power compensator. In addition to that, as the summation of direct transform and FB signals is made in the piezoelement volume, this type of FB has been called spatial electromechanical [1, 14].

A circuit of a piezoceramic sensor with FB, based on the method discussed, is shown in Fig. 5.5 [17].

The sensor represented in Fig. 5.5 is a closed static follow-up system [16]. It consists of piezoelement  $PE$  and matching voltage preamplifier  $A$ . Three electrodes  $1$ ,  $2$  and  $3$  are attached to the piezoelement. Electrode  $1$  is connected to the preamplifier input, electrode  $2$  to the common wire of the circuit, and electrode  $3$  – an additional piezoelement electrode – to the preamplifier output.

The block diagram of this sensor is shown in Fig. 5.6.

Transformation of force  $F$ , influencing piezoelement  $PE$ , into stress  $\sigma_1$  corresponds to an element with transfer coefficient  $W_1$ . Stress  $\sigma$  is numerically equal to

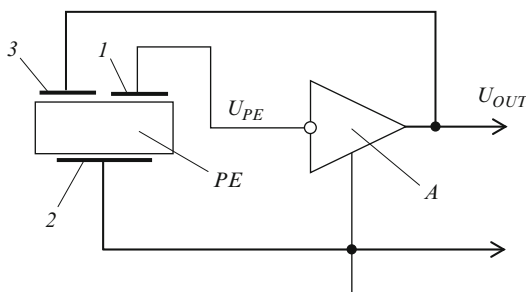
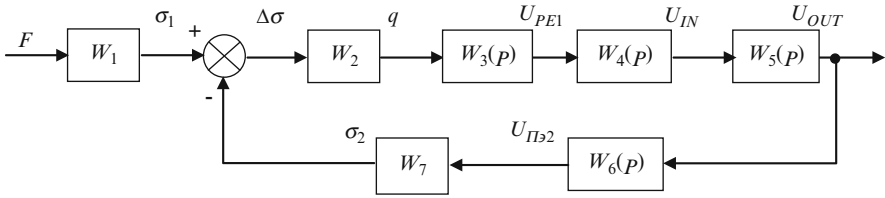


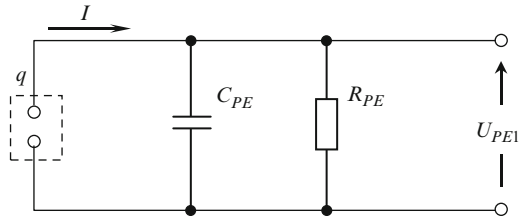
Fig. 5.5 Piezoceramic sensor with FB





**Fig. 5.6** Block diagram of piezoceramic sensor with electromechanical FB

**Fig. 5.7** Equivalent circuit of element  $W_3$  transformation



the force of body sectional area, i.e.,  $\sigma = \Delta F / \Delta S$ . If the stress is constant along the whole sectional area, then  $\sigma = F / S$ . Thus, in this case  $\sigma_1 = F / S$ . Thus, the following is obtained:

$$W_1 = \frac{\sigma_1}{F} = \frac{1}{S}. \tag{5.13}$$

Element  $W_2$  corresponds to  $\Delta \sigma$  transformation into charge  $q$  on the piezoelement electrodes. As  $q = d_{31} \Delta \sigma S$ , then

$$W_2 = \frac{q}{\Delta \sigma} = d_{31} S, \tag{5.14}$$

where  $d_{31}$  – piezomodule.

Element  $W_3$  corresponds to  $q$  charge transformation into voltage on piezoelement electrodes  $U_{PE1}$ . This transformation is displayed by the equivalent circuit, shown in Fig. 5.7.

The equivalent circuit, represented in Fig. 5.7, corresponds to the piezoelement, working in below resonance mode.

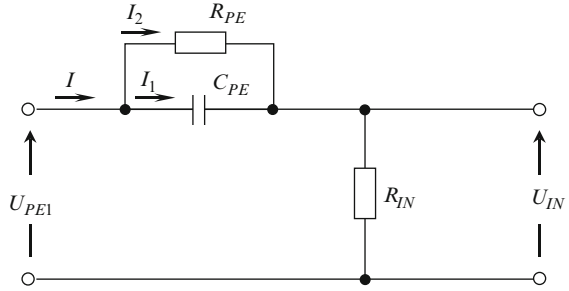
The following can be written for current  $I$ :

$$I = \frac{dq}{dt} = \frac{U_{PE1}}{R_{PE}} + C_{PE} \frac{dU_{PE1}}{dt}. \tag{5.15}$$

If initial conditions equal zero, the differential equation (5.15) is solved like this:

$$U_{PE1} = \frac{q}{\left(1 + \frac{1}{j\omega R_{PE} C_{PE}}\right) C_{PE}}. \tag{5.16}$$

**Fig. 5.8** Modified differentiating circuit (Element  $W_4(p)$ )



Hence transfer function is:

$$W_3(p) = \frac{U_{PE1}}{q} = \frac{1}{\left(1 + \frac{1}{j\omega R_{PE} C_{PE}}\right) C_{PE}}. \quad (5.17)$$

Considering high value of piezoelement resistance  $R_{PE}$ :

$$W_3 = \frac{1}{C_{PE}}. \quad (5.18)$$

Element  $W_4(p)$  describes the process which occurs when the load is connected to the piezoelement (transfer of voltage  $U_{PE1}$  into circuit –  $U_{IN}$ ).

The transfer function of this element corresponds to the transfer function of the modified differentiating element. Its circuit is presented in Fig. 5.8.

Here  $R_{IN}$  is the input resistance of the voltage amplifier. Considering the high value of piezoelement resistance and a certain degree of circuit simplification, the input part of the amplifier (as well as the output part further) is represented only by resistance  $R_{IN}$ .

The following can be written for this circuit:

$$U_{IN} = (I_1 + I_2) R_{IN},$$

where

$$I_1 = C_{PE} \frac{dU_{C_{PE}}}{dt}, \quad I_2 = \frac{U_{C_{PE}}}{R_{PE}}.$$

The following is obtained after the substitution:

$$U_{IN} = \left( C_{PE} \frac{dU_{C_{PE}}}{dt} + \frac{U_{C_{PE}}}{R_{PE}} \right) R_{IN}.$$

This can be written according to Kirchhoff's law:

$$U_{C_{PE}} = I_2 R_{PE} = U_{PE1} - U_{IN}.$$

Then the following is obtained:

$$U_{IN} = C_{PE} R_{IN} \frac{d(U_{PE1} - U_{IN})}{dt} + \frac{R_{IN}}{R_{PE}} (U_{PE1} - U_{IN}). \quad (5.19)$$

This coefficient is introduced for further calculations:

$$\varepsilon_R = \frac{R_{PE} + R_{IN}}{R_{IN}}.$$

Having divided (5.17) by coefficient  $\varepsilon_R$ , and having grouped the equation terms, the following is obtained:

$$U_{IN} + C_{PE} R_{PE} \frac{1}{\varepsilon_R} \frac{dU_{IN}}{dt} = \frac{1}{\varepsilon_R} \left( U_{PE1} + C_{PE} R_{PE} \frac{dU_{PE1}}{dt} \right). \quad (5.20)$$

The time constant is denoted like this:

$$\tau = R_{PE} C_{PE}.$$

Having substituted the time constant in (5.20), and having introduced the Laplace operator, this equality is obtained:

$$\left( 1 + \frac{\tau}{\varepsilon_R} p \right) U_{IN} = \frac{1}{\varepsilon_R} (1 + \tau p) U_{PE1}.$$

Then the transitive function of the circuit will be equaled:

$$W_4(p) = \frac{U_{IN}}{U_{PE1}} = \frac{1}{\varepsilon_R} \frac{1 + \tau p}{1 + \frac{\tau}{\varepsilon_R} p}. \quad (5.21)$$

Element  $W_5$  corresponds to the transfer characteristic of the voltage amplifier. This characteristic works as an inertial element of the first order. Its transfer function will look like this [4]:

$$W_5(p) = \frac{K_{SL}}{1 + p\tau_{OA}}, \quad (5.22)$$

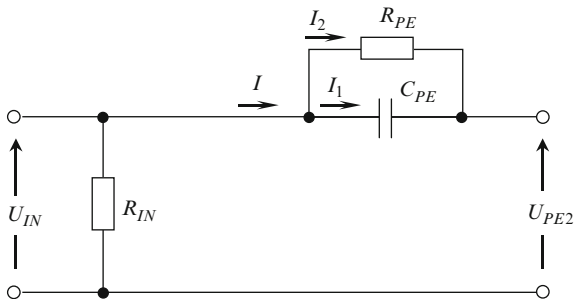
where  $K_{SL}$  – gain coefficient of an operational amplifier on low frequencies (Hertz units);  $p$  – Laplace operator;  $\tau_{OA} = K_{SL}/2\pi f_1$  – time constant;  $f_1$  – unity gain frequency.

Considering that the transducer works in a rather narrow frequency range (with linear dependence between input and output), the transfer characteristic can be considered linear and equal to the gain coefficient of the voltage amplifier [12, 13, 16]:

$$W_5 = K_{SL}. \quad (5.23)$$

Element  $W_6(p)$  describes the process, opposite to element  $W_4(p)$ . It occurs when the voltage is supplied from the amplifier to the piezoelement complementary electrode.

**Fig. 5.9** Modified differentiating circuit (Element  $W_6(p)$ )



Voltage  $U_{IN}$  is transferred to voltage between piezoelement electrodes  $U_{PE2}$ . The equivalent circuit of this process also corresponds to the modified differentiating element. It is presented in Fig. 5.9.

Here  $R_{IN}$  is the output resistance of the voltage amplifier.

Solving this problem similarly to element  $W_4(p)$  solution, the following is obtained:

$$W_6(p) = \frac{U_{PE2}}{U_{IN}} = \frac{\gamma_R \left(1 + \frac{\tau}{\gamma_R} p\right)}{1 + \tau p}, \quad (5.24)$$

where  $\gamma_R = (R_{PE} + R_{IN})/R_{IN}$ ,  $\tau = R_{PE}C_{PE}$ .

Element  $W_7$  corresponds to transformation of voltage  $U_{PE2}$  into stress  $\sigma_2$ . As  $\sigma_2 = E_{EL}d_{31}U_{PE2}/l$ , then

$$W_7 = \frac{\sigma_2}{U_{PE2}} = \frac{E_{EL}d_{31}}{l}, \quad (5.25)$$

where  $E_{EL}$  – Young's modulus,  $l$  – distance between electrodes.

The general transfer function will look like:

$$W_{FB}(p) = \frac{W_1 W_2 W_3(p) W_4(p) W_5(p)}{1 + W_2 W_3(p) W_4(p) W_5(p) W_6(p) W_7} = W_1 \frac{W(p)}{1 + W(p)\beta(p)}, \quad (5.26)$$

where  $W(p) = W_2 W_3(p) W_4(p) W_5(p)$  – transfer coefficient of direct transform circuit with NFB;  $\beta(p) = W_6(p) W_7$  – transfer coefficient with NFB circuit.

The errors of piezoceramic sensors are mainly determined by instability of piezomodules or electromechanical coupling coefficient under the influence of destabilizing factors.

The expression of piezosensor with NFB relative error, introduced along the auxiliary channel, is found by known methods of automatic control theory [12, 13, 16].

General transfer function of a piezoceramic sensor with NFB:

$$W_{FB}(p) = W_1 W_{CHFB}(p), \quad (5.27)$$

where  $W_{FBC}(p)$  – transfer function of the subcircuit with FB.

Total increment of transfer function with simultaneous change of direct transform subcircuit transfer functions with NFB, element  $W_1$  and NFB should be determined to calculate the total relative sensitivity of a piezosensor with FB.

$$dW_{\text{FB}}(p) = \frac{\partial W_{\text{FB}}(p)}{\partial W_1} dW_1 + \frac{\partial W_{\text{FB}}(p)}{\partial W(p)} dW(p) + \frac{\partial W_{\text{FB}}(p)}{\partial \beta(p)} d\beta(p).$$

The result after differentiation:

$$\begin{aligned} dW_{\text{FB}}(p) &= \frac{W(p)}{1 + W(p)\beta(p)} dW_1 + \frac{W_1}{(1 + W(p)\beta(p))^2} dW(p) \\ &+ \frac{W_1 W^2(p)}{(1 + W(p)\beta(p))^2} d\beta(p). \end{aligned}$$

Relative error is found after the division of this equality right and left parts by  $W_{\text{FB}}(p)$

$$\gamma_{\text{FB}} = \frac{dW_{\text{OC}}(p)}{W_{\text{OC}}(p)} = \frac{dW_1}{W_1} + \frac{dW(p)}{W(p)} \frac{1}{1 + W(p)\beta(p)} - \frac{d\beta(p)}{\beta(p)} \frac{W(p)\beta(p)}{1 + W(p)\beta(p)}.$$

The equality obtained can be rewritten like this:

$$\gamma_{\text{FB}} = \gamma_{W_1} + \gamma_W \frac{1}{1 + W(p)\beta(p)} - \gamma_{\beta} \left( 1 - \frac{1}{1 + W(p)\beta(p)} \right), \quad (5.28)$$

where  $\gamma_W = dW(p)/W(p)$  – relative error of direct transfer subcircuit with NFB;  $\gamma_{\beta} = d\beta/\beta$  – relative error of FB circuit;  $\gamma_{W_1} = dW_1/W_1$  – relative error of element  $W_1$ .

The condition when the accuracy of a piezosensor with FB essentially increases is determined. Certain preliminary remarks are needed.

Practically  $\gamma_{W_1} \ll \gamma_{W_2}$ . In addition to that, one can assume that errors  $\gamma_{W_2}$  and  $\gamma_{\beta}$  of direct and inverse piezoeffects, determined by the piezomodule instability under the influence of destabilizing factors, are equal, i.e.,  $|\gamma_{W_2}| = |\gamma_{W_7}|$ .

In addition, it is hard to practically assure the condition when relative error, determined by instability of the amplifier gain coefficient  $\gamma_{W_5}$ , will be considerably smaller than  $\gamma_{W_2}$ , i.e.,  $\gamma_{W_5} \ll \gamma_{W_2}$ . One can also assume that  $\gamma_{W_4} \ll \gamma_{W_2}$  and  $\gamma_{W_6} \ll \gamma_{W_7}$ .

Considering these conditions, the following expression is obtained from (5.28):

$$\gamma_{\text{FB}} = \gamma_{W_2} \frac{1}{1 + W(p)\beta(p)} - \gamma_{W_2} \left( 1 - \frac{1}{1 + W(p)\beta(p)} \right). \quad (5.29)$$

The condition under which the error of a piezosensor with NFB will equal zero can easily be seen from this equation, i.e.,  $\gamma_{\text{FB}} = 0$ :

$$W(p)\beta(p) = 1. \quad (5.30)$$

Thus, as it follows from (5.30), the error minimum is reached under the condition when the product of direct transform with feedback  $W(p)$  circuit coefficient and FB circuit transfer coefficient  $\beta(p)$  equals 1 [1, 40].

This is the main difference between the device proposed and known astatic and static control systems. These conditions tend to fulfillment in them:  $W(p)\beta(p) \rightarrow \infty$  [4, 12].

However, the product  $W(p)\beta(p)$  can be practically different from 1, as these coefficients depend also on form, dimensions and spatial arrangement of electrodes. They also depend on electric and mechanical fields, stresses and voltages (which were not considered in the given example), created in channels of piezoelement direct and inverse transforms.

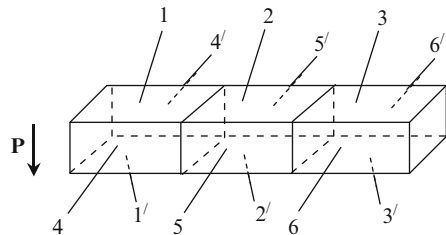
### 5.3 Domain-Dissipative Piezoceramic Sensors with Spatial Electromechanical NFB

The mechanism of electromechanical FB influence on domain-dissipative piezoceramic sensors characteristics is of scientific interest [14, 40, 43, 44, 46, 47, 55, 56].

A slug-shaped piezoceramic IITC-19 piezoelement ( $50 \times 10 \times 10$  mm), shown in Fig. 5.10, was used in the research [40].

The piezoelement is polarized as shown in Fig. 5.10. The electrodes on corresponding faces are divided into three parts, forming six pairs of electrodes. Polarization vector  $\mathbf{P}$  is perpendicular to these three pairs of electrodes (1–1', 2–2', 3–3'). This corresponds to the traditional transducer design with resonant oscillatory system properties if force vector  $\mathbf{F}$  (or electric field, activating voltage  $\mathbf{E}_{\text{GEN}}$ ) and also electric field vectors of output signal  $\mathbf{E}_{\text{OUT}}$  and feedback  $\mathbf{E}_{\text{FB}}$  are in the same direction.

Several transducer circuits with various combinations of vectors  $\mathbf{E}_{\text{GEN}}$ ,  $\mathbf{E}_{\text{OUT}}$ ,  $\mathbf{E}_{\text{FB}}$  and  $\mathbf{P}$  reciprocal positioning [14] are considered below. Vectors  $\mathbf{E}_{\text{GEN}}$ ,  $\mathbf{E}_{\text{OUT}}$  and  $\mathbf{E}_{\text{FB}}$  are denoted by vertical arrows if their directions coincide with the direction of polarization vector  $\mathbf{P}$ . In this case, the generator, the amplifier input, and the FB circuit are connected to electrodes 1–1', 3–3' and 2–2' respectively.



**Fig. 5.10** Piezoceramic element: 1–1', 2–2', 3–3' – main electrodes; 4–4', 5–5', 6–6' – complementary electrodes

If vectors  $E_{\text{GEN}}$ ,  $E_{\text{OUT}}$  and  $E_{\text{FB}}$  are denoted by horizontal lines, this means that the generator, the amplifier input, and the FB circuit are connected to electrodes 4–4', 6–6' and 5–5' respectively.

The amplifier is based on field transistor KP303E. Its input resistance is 4.4 Mohm, gain coefficient – 6.5. Meter X1–46, millivoltmeter B7–38 and frequency meter Ч3–57 were used to measure AFC. Pulse generator Г5–67 and oscillograph C1–55 were used to measure pulse and transitive characteristics.

Voltage test generators simulated mechanical action on the piezoelement. The traditional transducer circuit without FB is shown in Fig. 5.11a. Its AFC, pulse, and transitive characteristics are represented in Fig. 5.11b–d respectively. It may be seen that the transducer is an oscillatory system with a rather high  $Q$  factor.

The same transducer with negative electromechanical FB is shown in Fig. 5.11e–h. As can be seen from the figure, the transducer  $Q$  factor decreases with FB introduction.

A transducer with FB, supplied to electrodes 5–5', i.e., vector  $E_{\text{FB}}$  is perpendicular to vector  $P$ , is shown in Fig. 5.12. Vectors  $E_{\text{GEN}}$  and  $E_{\text{OUT}}$  are parallel to vector  $P$ .

As can be seen from Fig. 5.12, the sensor remains an oscillatory system. However, the signal level at resonant frequencies changes even in the case when an FB circuit is not connected: only electrode 5 is connected to the circuit common wire. This is evidently connected with the control of volume charge distribution on the piezoelement surface. Below resonance sensitivity increases in this case.

The sensor whose output voltage is read from electrodes 6–6' (vector  $E_{\text{OUT}}$  is perpendicular to vector  $P$ , and vectors  $E_{\text{GEN}}$  and  $E_{\text{FB}}$  are parallel to vector  $P$ ), is shown in Fig. 5.13. The transducer oscillatory properties are partially suppressed without FB (Fig. 5.13b–d). The transducer AFC becomes linear; its sensitivity decreases with FB introduction.

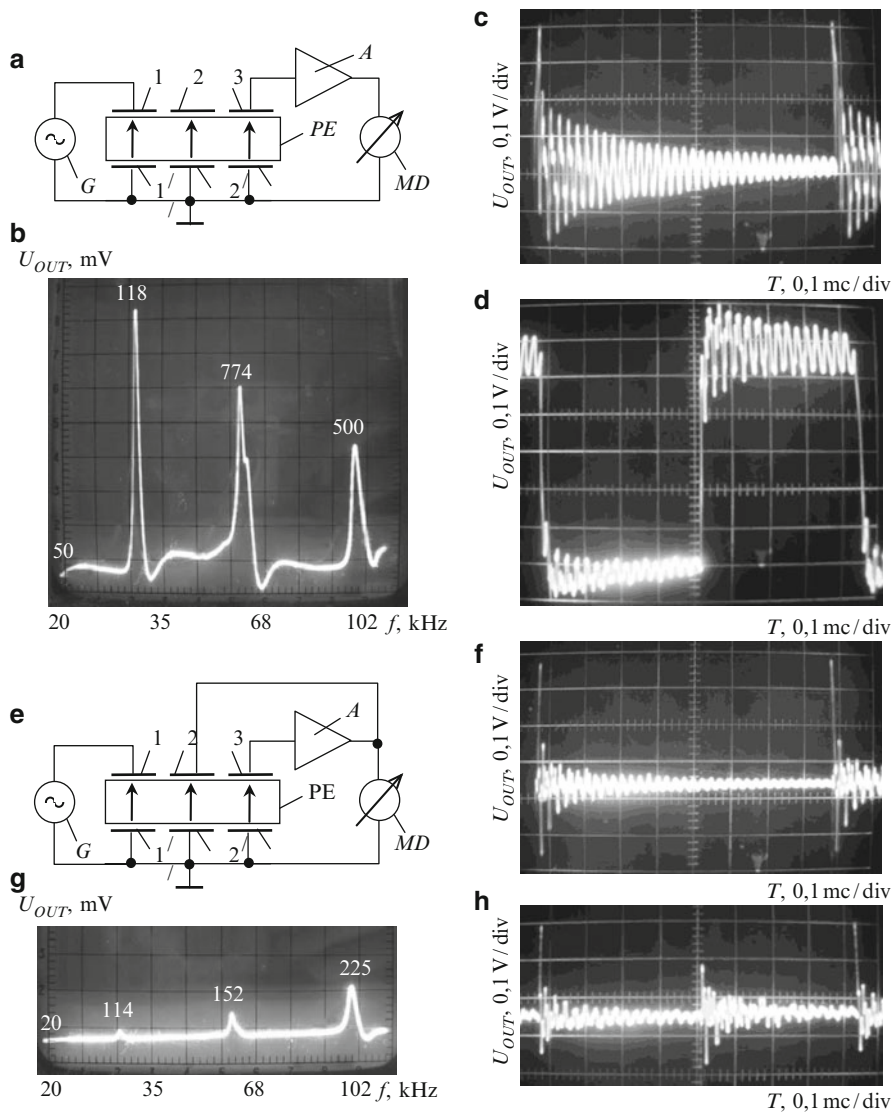
A sensor with vector  $E_{\text{GEN}}$  parallel to vector  $P$ , and vector  $E_{\text{OUT}}$  perpendicular to  $E_{\text{FB}}$  is shown in Fig. 5.14.

As can be seen from Figs. 5.13a and 5.14a, sensitivity is increased and resonance is suppressed (35 kHz) only if electrode 5' is connected to the common wire of the circuit. Sensitivity decreases if FB circuit is connected to electrode 5.

The sensor with all three vectors  $E_{\text{GEN}}$ ,  $E_{\text{OUT}}$  and  $E_{\text{FB}}$  perpendicular to vector  $P$  is shown in Fig. 5.15. AFC of this sensor is linear. The transducer has ideal amplifying circuit properties.

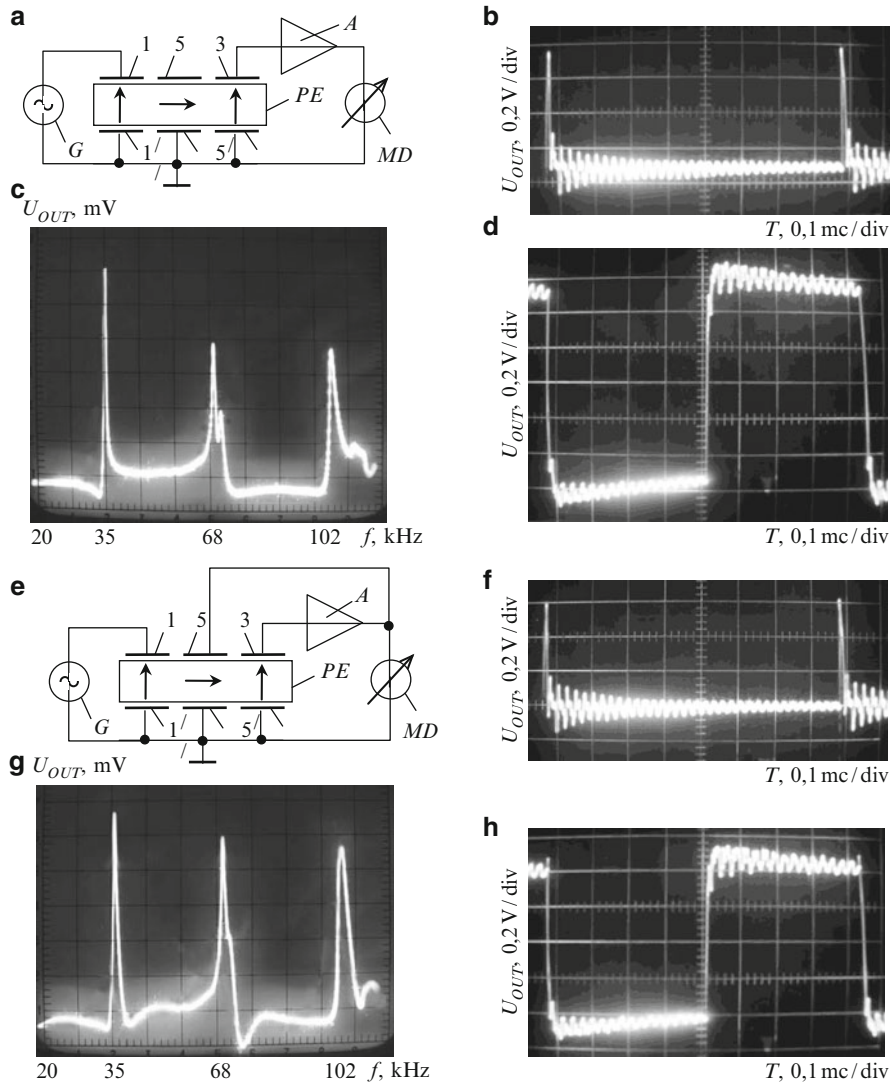
Thus, the following is discovered after the study of piezoceramic sensors with FB [32, 40, 48, 52]:

- FB introduction changes sensitivity and time constant of the transient process. It transforms the piezoelement in differentiating relaxation, differentiating ideal and ideal amplifying circuits.
- Only connection of electrodes positioned parallel to polarization vector  $P$ , to the circuit common wire, leads to sensitivity increase and main resonance suppression (35 kHz).

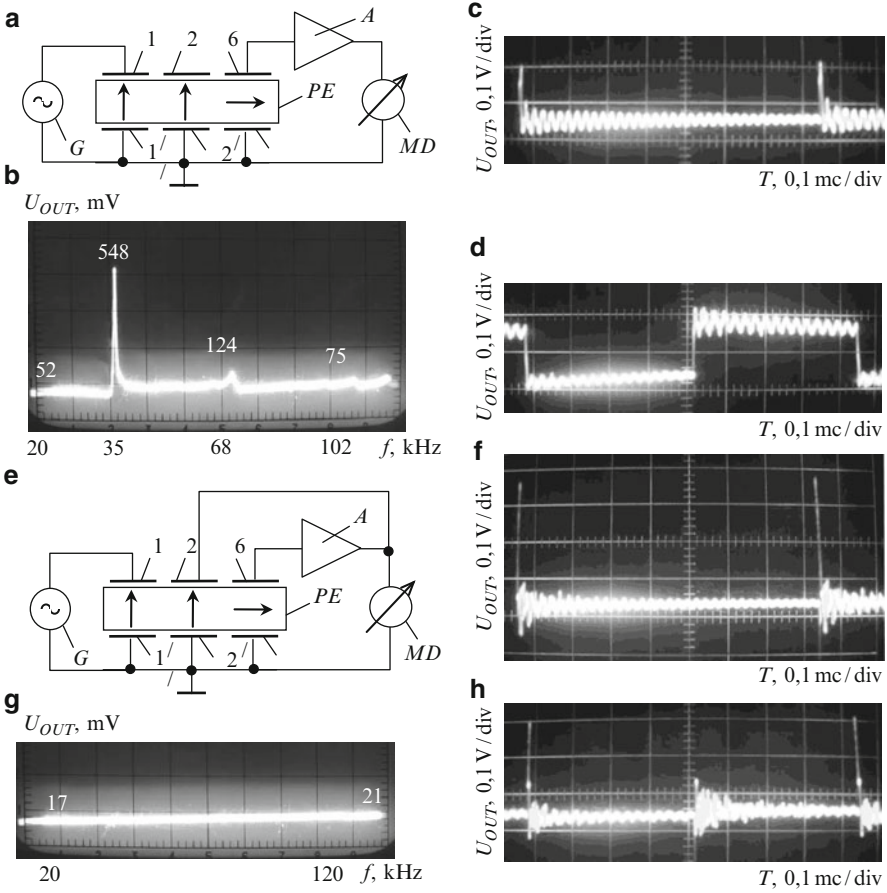


**Fig. 5.11** Traditional piezoceramic sensor:  $G$  – generator,  $PE$  – piezoelement,  $A$  – amplifier,  $MD$  – measuring device; (a, b, c, d) – without FB, (e, g, f, h) – with FB, (a, e) – circuit, (b, g) – AFC, (c, f) – pulse, (d, h) – transitive characteristics





**Fig. 5.12** Piezoceramic sensor:  $G$  – generator,  $PE$  – piezoelement,  $A$  – amplifier,  $MD$  – measuring device; **(a, b, c, d)** – without FB, **(e, g, f, h)** – with FB, **(a, e)** – circuit, **(b, g)** – AFC, **(c, f)** – pulse, **(d, h)** – transitive characteristics

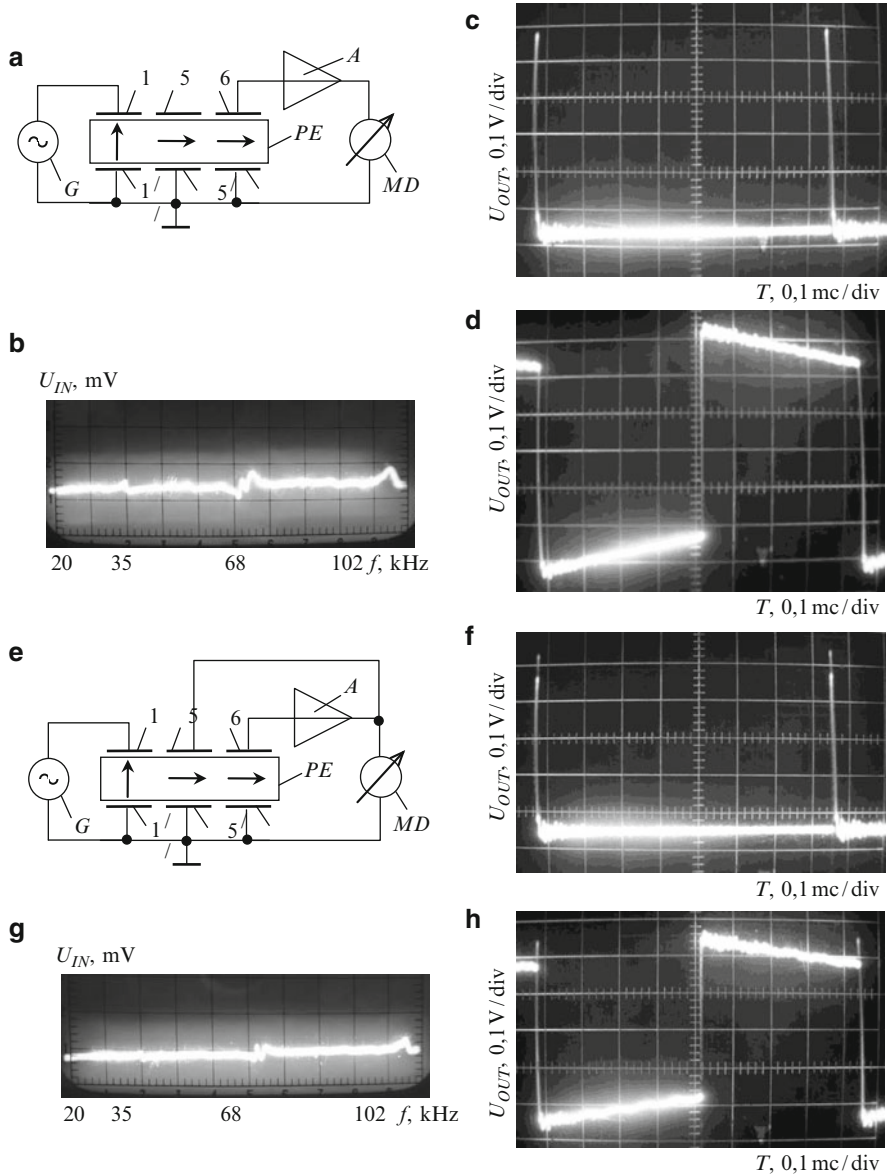


**Fig. 5.13** Piezoceramic sensor:  $G$  – generator,  $PE$  – piezoelement,  $A$  – amplifier,  $MD$  – measuring device; (a, b, c, d) – without FB, (e, g, f, h) – with FB, (a, e) – circuit, (b, g) – AFC, (c, f) – pulse, (d, h) – transitive characteristics

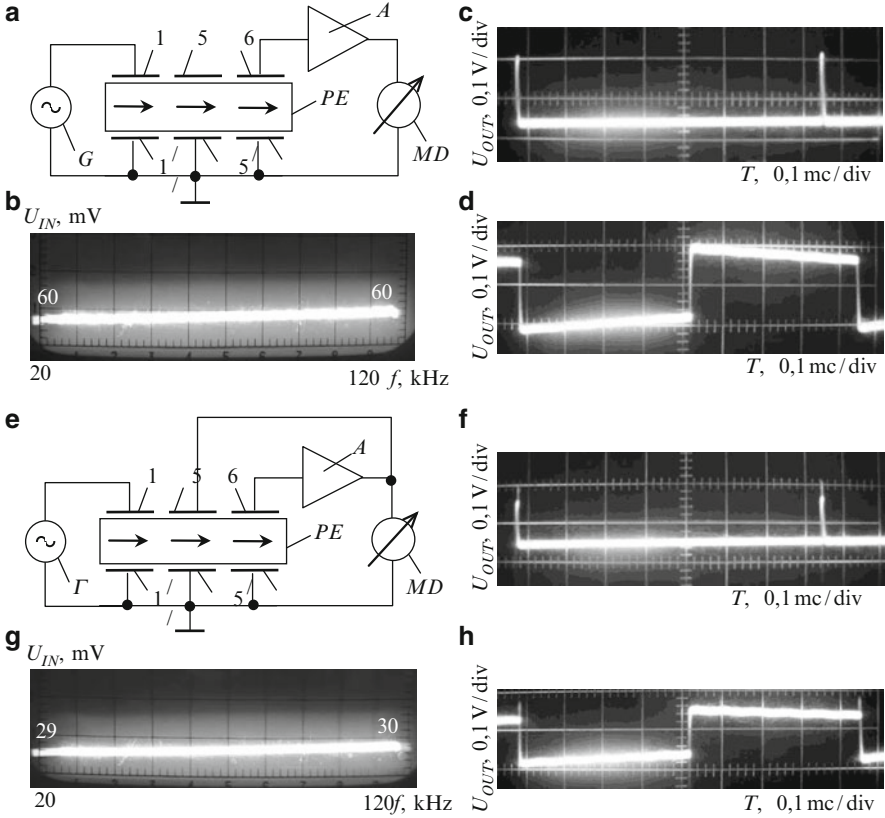
– The sensor with all three vectors  $E_{GEN}$ ,  $E_{OUT}$  and  $E_{FB}$  perpendicular to polarization vector  $P$  has the biggest AFC linearity. This transducer has the properties of an ideal amplifying circuit.

### 5.4 Piezoceramic Sensors with Piezoelement in FB Circuit of Charge Amplifier

The circuit of this sensor is represented in Fig. 5.16 [14, 18, 40].



**Fig. 5.14** Piezoceramic sensor:  $G$  – generator,  $PE$  – piezoelement,  $A$  – amplifier,  $MD$  – measuring device; (a, b, c, d) – without FB, (e, g, f, h) – with FB, (a, e) – circuit, (b, g) – AFC, (c, f) – pulse, (d, h) – transitive characteristics



**Fig. 5.15** Piezoceramic sensor: *G* – generator, *PE* – piezoelement, *A* – amplifier, *MD* – measuring device; (**a**, **b**, **c**, **d**) – without FB, (**e**, **g**, **f**, **h**) – with FB, (**a**, **e**) – circuit, (**b**, **g**) – AFC, (**c**, **f**) – pulse, (**d**, **h**) – transitive characteristics

The block diagram of the transducer, shown in Fig. 5.16, is represented in Fig. 5.17.

The following can be written for this circuit [40]:

$$K_{FB} = K_{PE} \frac{K_A}{1 + K_A \beta}. \tag{5.31}$$

At  $K_A \beta \gg 1$

$$K_{FB} \approx \frac{K_{PE} K_A}{K_A \beta} \approx \frac{K_A}{\beta}. \tag{5.32}$$

As was already mentioned, a charge amplifier is an operational amplifier with capacitive FB. An operational amplifier with a condenser in FB circuit is an electronic integrator, integrating the current supplied to its input. In this case, the

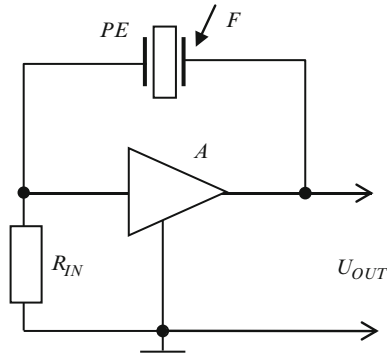


Fig. 5.16 Piezoelectric sensor with piezoelement in FB circuit

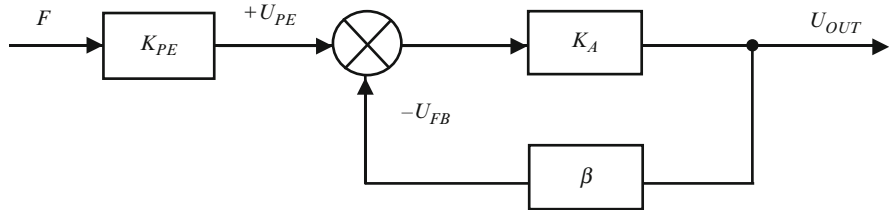


Fig. 5.17 Block diagram of piezoelectric transducer

current is created by a charge which arises on the piezoelement-sensor under the action of mechanical force, pressure, acceleration, etc.

The equivalent electric circuit of the piezoelectric transducer is shown in Fig. 5.18.

As piezoelement  $R_{PE}$  resistance and operational amplifier  $R_{IN}$  input resistance are big values, this circuit can be simplified and reduced to the view shown in Fig. 5.19.

The following can be written for this circuit:

$$i_Q = \frac{dQ}{dt};$$

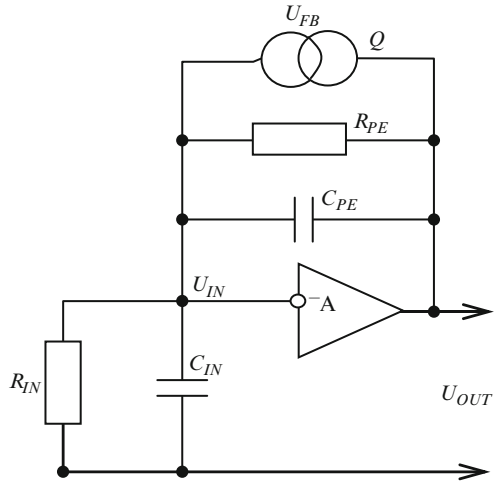
$$i_C = -C_{IN} \frac{dU_{IN}}{dt} = \frac{1}{A} C_{IN} \frac{dU_{OUT}}{dt};$$

$$i_{FB} = C_{PE} \frac{dU_{FB}}{dt} = C_{PE} \left( 1 + \frac{1}{A} \right) \frac{dU_{OUT}}{dt};$$

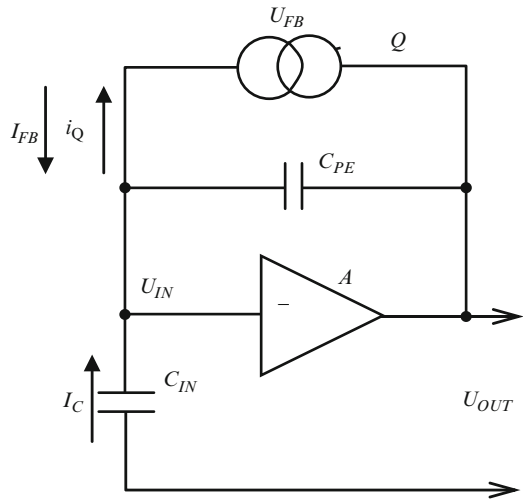
$$U_{OUT} = -U_{IN} A; \quad U_{IN} = -\frac{1}{A} U_{OUT};$$

$$U_{FB} = U_{OUT} - U_{IN} = U_{OUT} \left( 1 + \frac{1}{A} \right).$$

**Fig. 5.18** Equivalent circuit of charge amplifier with piezoelement in FB circuit:  $Q$  – charge, generated by the piezoelement;  $A$  – operational amplifier with gain coefficient  $A = 10^4-10^5$ ;  $R_{PE}$ ,  $C_{PE}$  – insulation resistance and piezoelement capacitance;  $R_{IN}$ ,  $C_{IN}$  – input resistance and capacitance of the operational amplifier



**Fig. 5.19** Simplified equivalent circuit of transducer with charge amplifier



According to Kirchoff's law

$$i_Q - i_{OC} + i_C = 0$$

or

$$i_Q = i_{FB} - i_C.$$

Substituting the current values, this differential equation is obtained:

$$\frac{dQ}{dt} = C_{PE} \left( 1 + \frac{1}{A} \right) \frac{dU_{OUT}}{dt} - \frac{1}{A} C_{IN} \frac{dU_{OUT}}{dt}. \tag{5.33}$$

The following is obtained after the integration:

$$Q = U_{OUT}C_{PE} \left( 1 + \frac{1}{A} \right) - \frac{1}{A}C_{IN}U_{OUT}. \tag{5.34}$$

Whence:

$$U_{OUT} = \frac{Q}{C_{PE} \left( 1 + \frac{1}{A} \right) - \frac{1}{A}C_{IN}}. \tag{5.35}$$

At  $A \gg 1$

$$U_{OUT} \approx \frac{Q}{C_{PE}}, \tag{5.36}$$

i.e., the transducer output voltage with a charge amplifier and a piezoelement in FB circuit is equal to output voltage of the piezoelement in general, without any amplifier, i.e., direct piezoeffect voltage. Therefore, measurement error depends only on piezoelement characteristics.

A slug-shaped ПТС-19 piezoceramic piezoelement of these dimensions  $50 \times 10 \times 10$  mm was used in the research (Fig. 5.20).

An electric signal, simulating mechanical action on the piezoelement, can be connected to electrodes 1-1' or 3-3', while the amplifier input and output should be connected to electrodes 2-2' or 4-4'.

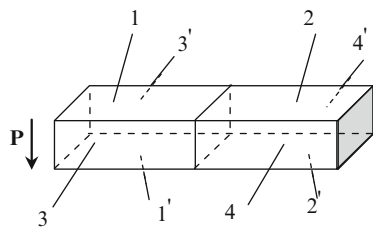
The amplifier is based on microcircuit К140УД8. Input resistance is 4.4 Mohm, gain coefficient – 6.5. Meter АЧХ X1-46, millivoltmeter B7-38 and frequency meter Ч3-57, were used for AFC measurement; pulse generator Г5-67 and oscillograph C1-55 were used to measure pulse and transitive characteristics.

Characteristics of a piezoelement without amplifier are shown in Fig. 5.21.

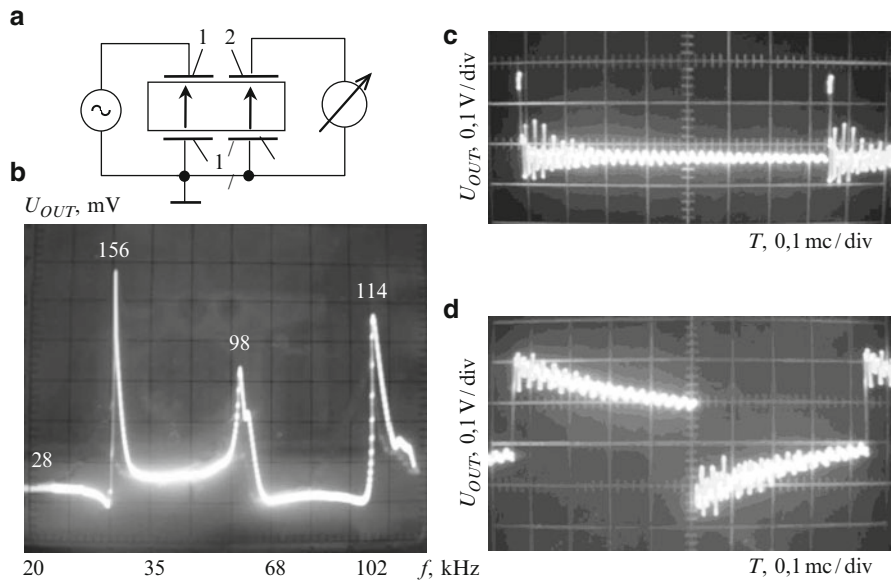
The same piezoelement with the amplifier; its characteristics are shown is shown Fig. 5.22. As can be seen from Figs. 5.21 and 5.22, the transducer is an oscillatory element. Connection of the amplifier only increases the output signal level.

Characteristics of sensors, depending on generator and amplifier connection circuit to the piezoelement (parallel or perpendicularly to the polarization vector), are shown in Figs. 5.23–5.26.

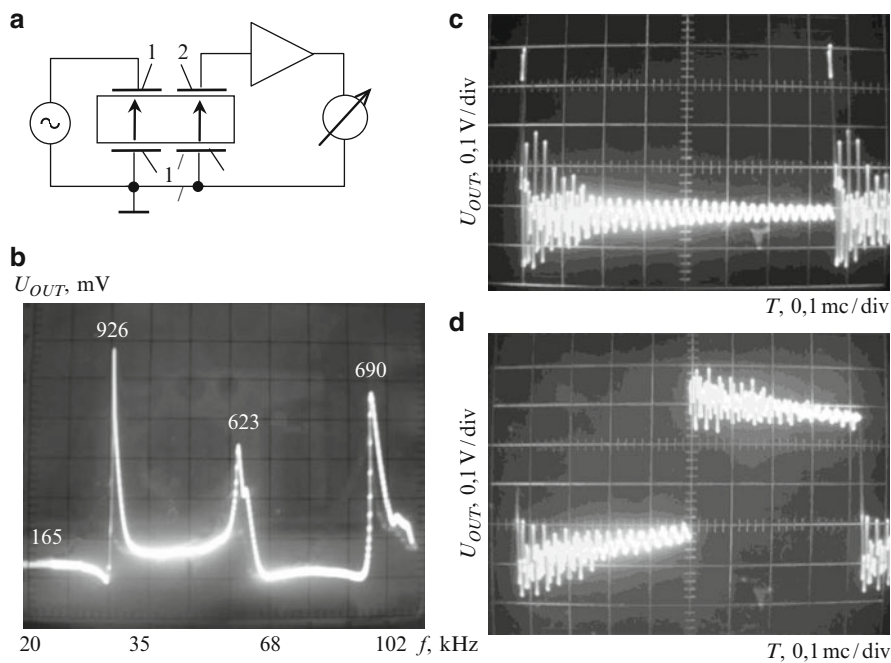
In that case (Fig. 5.23a) the direction vector of electric field  $E_{GEN}$  intensity, created by the generator and also the intensity vector of FB electric field  $E_{FB}$ , are parallel with polarization vector  $P$ . This is assured by generator and amplifier



**Fig. 5.20** Piezoceramic element: 1-1', 2-2' – main electrodes; 3-3', 4-4' – complementary electrodes

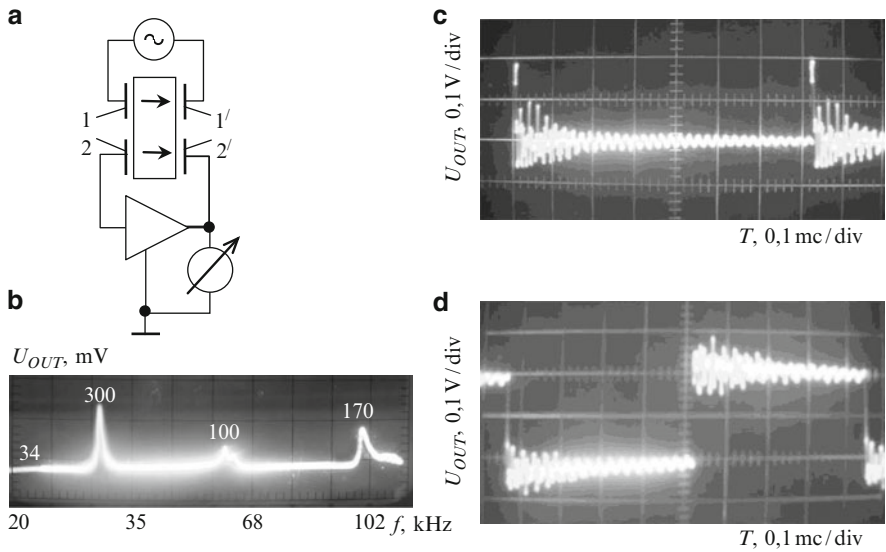


**Fig. 5.21** Circuit and characteristics of piezoelement: (a) circuit, (b) AFC, (c) pulse, (d) transitive characteristics

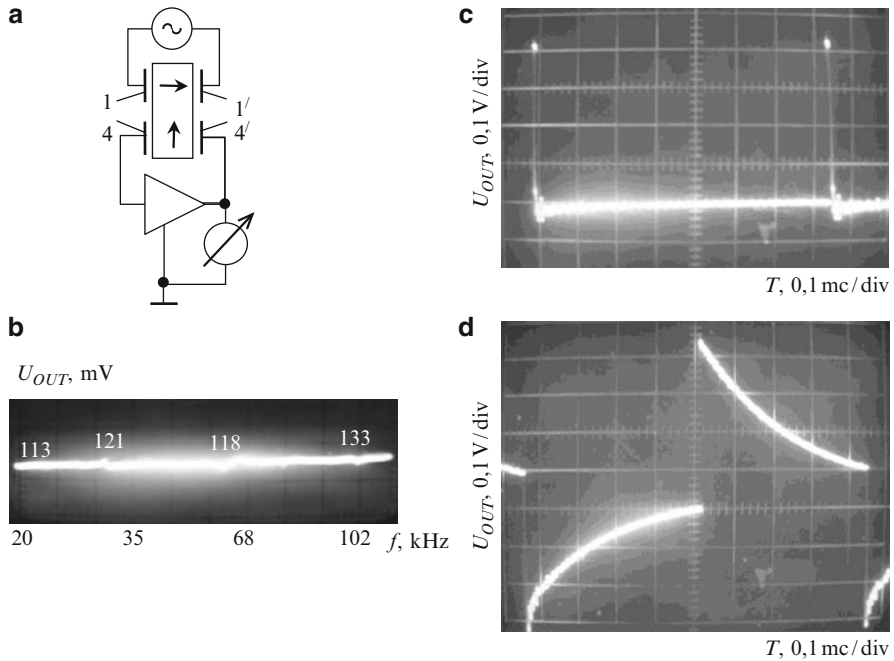


**Fig. 5.22** Circuit and characteristics of piezoelement with amplifier: (a) circuit, (b) AFC, (c) pulse, (d) transitive characteristics

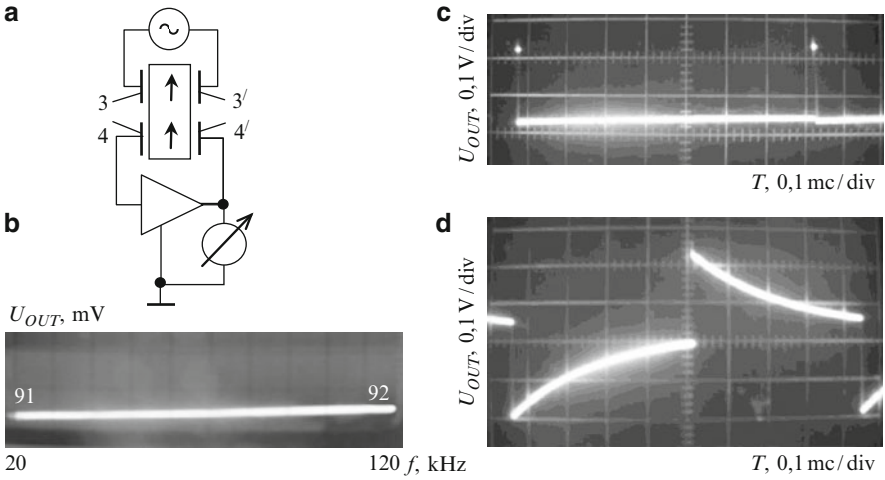




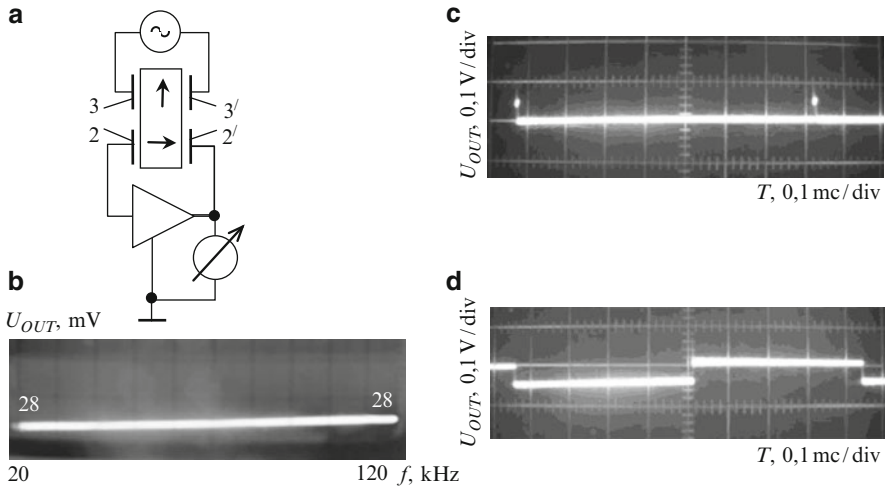
**Fig. 5.23** Piezosensor circuit and characteristics: (a) circuit, (b) AFC, (c) pulse, (d) transitive characteristics



**Fig. 5.24** Piezosensor circuit and characteristics: (a) circuit, (b) AFC, (c) pulse, (d) transitive characteristics



**Fig. 5.25** Piezosensor circuit and characteristics: (a) circuit, (b) AFC, (c) pulse, (d) transitive characteristics



**Fig. 5.26** Piezosensor circuit and characteristics: (a) circuit, (b) AFC, (c) pulse, (d) transitive characteristics

connection to the corresponding electrodes of the piezoelement. The sensor is also an oscillatory element. However, the sensor AFC was changed.

A sensor for which vector  $E_{GEN}$  is parallel to vector  $P$ , and  $E_{FB}$  is perpendicular, is shown in Fig. 5.24. In this case, the sensor AFC is practically linear. The sensor is a differentiating element with inertial properties.

A sensor with vectors  $E_{GEN}$  and  $E_{FB}$  perpendicular to vector  $P$  is shown in Fig. 5.25. The transducer is a differentiating inertial element with linear AFC.

And finally, a sensor with vector  $E_{GEN}$  perpendicular to vector  $P$  and vector  $E_{FB}$  parallel to it is shown in Fig. 5.26. In this case, the sensor is an ideal amplifying circuit.

Thus, a sensor with a piezoelement in the amplifier FB circuit, depending on the connection circuit, can be an oscillatory element (Fig. 5.30), a differentiating element with inertia properties (Figs. 5.24 and 5.25), and an ideal amplifying circuit (Fig. 5.26).

The case in which the piezoelement in the charge amplifier FB circuit is connected according to the domain-dissipative transducer circuit – the vector of electric field feedback  $E_{FB}$  intensity is perpendicular to polarization vector  $P$  (Figs. 5.24 and 5.25) – can be of scientific interest. In this case, the linear AFC is obtained. As a result, the sensor work frequency range is widened by several times.

Several variants of piezosensors with a piezoelement in the charge amplifier FB circuit are described in [27–29].

### 5.5 Electric Feedback in Piezoceramic Sensors

Many sensors of dynamic force, pressure, accelerometers, etc. with a monomorph piezoelement are used and produced [31, 34]. Separation of electrodes in the piezoelement of this sensor, or introduction of a complementary piezoelement in its design, causes certain difficulties. Development of an FB introduction method in sensors with a monomorph piezoelement when the piezoelement signals and FB are summarized on the amplifier input is of scientific interest. These sensors have been called sensors with electric FB [14, 32].

A simplified block diagram of a piezoceramic sensor with FB is considered for this case (Fig. 5.27).

The following can be written for this diagram:

$$K_{FB}(p) = K_1(p) \frac{K_A}{1 + K_A \beta(p)}, \tag{5.37}$$

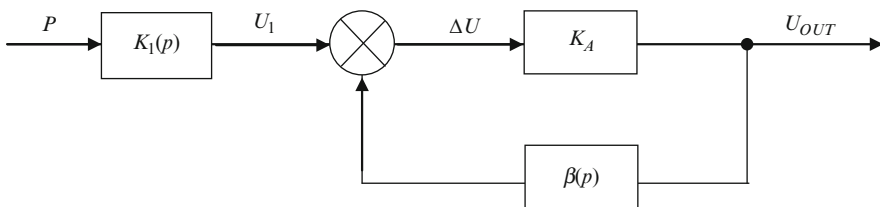


Fig. 5.27 Block diagram of piezoelectric sensor with electric FB

where  $K_{FB}(p)$  – transfer coefficient of the transducer with negative FB;  $K_1(p)$  – transformation coefficient of the sensor piezoelement;  $K_A$  – gain coefficient of the amplifier;  $\beta(p)$  – transfer coefficient of FB element.

AFC linearization condition looks like this [14, 32]:

$$K_{FB}(p) = \text{const.} \quad (5.38)$$

This condition is easily realized with:

$$\frac{K_1(p)}{\beta(p)} = \text{const.} \quad (5.39)$$

AFC and phase characteristic of elements  $K_1(p)$  and  $\beta(p)$  should change identically, as follows from expression (5.39). In the specific case

$$\frac{K_1(p)}{\beta(p)} = 1, \text{ i.e., } K_1(p) = \beta(p). \quad (5.40)$$

The relative error  $\gamma_{FB}$  of the device, represented in Fig. 5.27, can easily be determined from expression (5.37):

$$\gamma_{FB} = \delta_{K_1(p)} + \delta_{K_{FB}} \frac{1}{1 + K_{FB}\beta(p)} - \delta_{\beta} \frac{K_{FB}\beta(p)}{1 + K_{FB}\beta(p)}, \quad (5.41)$$

where  $\delta_{K_1}$ ,  $\delta_{K_{FB}}$ ,  $\delta_{\beta}$  are relative errors, created by elements  $K_1(p)$ ,  $K_{FB}$ ,  $\beta(p)$  respectively.

These conditions can be easily assured in practice:

$$\begin{aligned} \delta_{K_{FB}} &<< \delta_{K_1(p)}, \\ \delta_{K_{FB}} &<< \beta(p). \end{aligned} \quad (5.42)$$

Special cases are discussed below.

Let  $K_{FB}\beta(p) = 1$ .

Then, considering (5.40) and (5.42):

$$K_{FB} = \frac{1}{\beta(p)}, \quad \gamma_{FB} \approx \frac{1}{2}\delta_{K_1}.$$

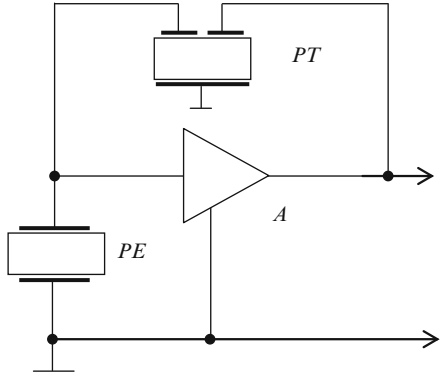
Thus, with  $K_{FB}\beta(p) = 1$ , the transducer AFC is linear with the double reduction of sensitivity and relative error.

It is assumed that  $K_A\beta(p) \gg 1$ .

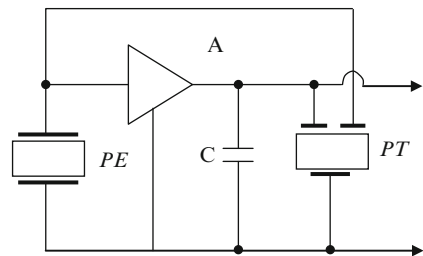
Then, considering (5.40) and (5.42):

$$K_{FB} \approx 1, \quad \gamma_{FB} \rightarrow 0.$$

**Fig. 5.28** Sensor with piezotransformer in FB circuit: *PE* – piezoelement-sensor control; *PT* – piezotransformer; *A* – amplifier



**Fig. 5.29** Sensor with piezotransformer and correcting capacitance in FB circuit: *PE* – piezoelement-sensor; *PT* – piezotransformer; *A* – amplifier



Therefore, with  $K\beta(p) \gg 1$  the transducer AFC is linear if  $K_{FB} = 1$ , while the relative error tends to zero.

A piezotransformer can be introduced in FB circuit to realize this condition (5.40) (Fig. 5.28) [14, 21].

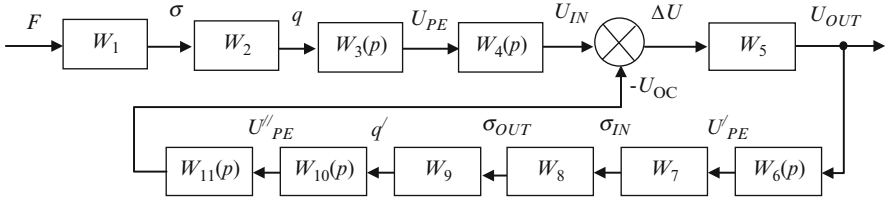
Piezoelement resonant frequency (sensor and piezoelement in FB circuit) depends on form, dimensions and piezoelement material/electrode arrangement. If forms, dimensions and materials of the piezoelements are identical, the characteristics spread is in  $\pm 2\%$  limits. This requires their individual selection.

In this case, creating a piezotransformer, its input static capacitance is smaller than the static capacitance of the piezoelement sensor. This leads to resonant frequency change.

Correcting capacitance  $C$  can be switched on the piezotransformer input to select a resonant frequency (Fig. 5.29) [14, 22].

A block diagram of the transducer (Fig. 5.30) is created to study the sensors accuracy with a piezotransformer in electric FB circuit (Fig. 5.28).

Here  $W_i$  – elements transfer functions, describing the following processes:  $W_1$  – transformation of  $F$  force, influencing the piezoelement, into stress  $\sigma$ ;  $W_2$  and  $W_9$  – transformation of stresses into charges on the piezoelement electrodes;  $W_3(p)$  and  $W_{10}(p)$  – transformation of charges into voltage on the piezoelement electrodes;  $W_4(p)$  and  $W_{11}(p)$  – transformation of voltage on piezoelement electrodes into voltage on the amplifier input;  $W_5$  – gain of the voltage amplifier;  $W_6(p)$  – transformation of the amplifier output voltage into voltage between the



**Fig. 5.30** Transducer block diagram with piezotransformer in FB circuit

piezotransformer electrodes;  $W_7$  – transformation of voltage on electrodes into stress on the piezotransformer input;  $W_8$  – transformation of piezotransformer input–output stresses.

The general transfer function will look like this [12, 14, 45]:

$$W_{\text{FB}}(p) = \frac{W_1 W_2 W_3(p) W_4(p) W_5}{1 + W_5 W_6(p) W_7 W_8 W_9 W_{10}(p) W_{11}(p)}. \quad (5.43)$$

Equation (5.43) can be rewritten like this after the elementary transformations:

$$K_{\text{FB}} = \frac{K_1(p) K_2}{1 + K_2 K_3(p) K_4(p)}. \quad (5.44)$$

$K_1(p) = W_1 W_2 W_3(p) W_4(p)$  – transformation coefficient of force  $F$ , influencing the piezoelement, into voltage on the amplifier input  $U_{\text{IN}}$ ;  $K_2 = W_5$  – gain coefficient of voltage amplifier;  $K_3(p) = W_6(p) W_7$  – coefficient of the amplifier output voltage transformation into stress on the piezotransformer input;  $K_4(p) = W_8 W_9 W_{10}(p) W_{11}(p)$  – coefficient of stress transformation on the piezotransformer input into voltage on its output (FB voltage  $U_{\text{FB}}$ ).

To find the relative error of the transducer sensitivity total increment (transfer function  $K_{\text{FB}}$ ) with simultaneous sensitivities change of direct transform,  $K_1(p)$ ,  $K_2$  and FB  $K_3(p)$  and  $K_4(p)$  circuits should be determined [12, 14]:

$$dK_{\text{FB}} = \frac{\partial K_{\text{FB}}}{\partial K_1} dK_1 + \frac{\partial K_{\text{FB}}}{\partial K_2} dK_2 + \frac{\partial K_{\text{FB}}}{\partial K_3} dK_3 + \frac{\partial K_{\text{FB}}}{\partial K_4} dK_4. \quad (5.45)$$

The following is obtained after differentiation:

$$\begin{aligned} dK_{\text{FB}} &= \frac{K_2}{1 + K_2 K_3 K_4} dK_1 + \frac{K_1}{(1 + K_2 K_3 K_4)^2} dK_2 \\ &\quad - \frac{K_1 K_2^2 K_4}{(1 + K_2 K_3 K_4)^2} dK_3 - \frac{K_1 K_2^2 K_3}{(1 + K_2 K_3 K_4)^2} dK_4. \end{aligned} \quad (5.46)$$

The relative error is found by division of the right and left parts of this equality by  $K_{\text{FB}}$ :

$$\frac{dK_{FB}}{K_{FB}} = \frac{dK_1}{K_1} + \frac{1}{1 + K_2K_3K_4} \frac{dK_2}{K_2} - \frac{K_2K_3K_4}{1 + K_2K_3K_4} \frac{dK_3}{K_3} - \frac{K_2K_3K_4}{1 + K_2K_3K_4} \frac{dK_4}{K_4}. \quad (5.47)$$

The obtained equality can be rewritten like this:

$$\gamma_{oc} = \gamma_{K_1} + \gamma_{K_2} \frac{1}{1 + K_2K_3K_4} - \gamma_{K_3} \frac{K_2K_3K_4}{1 + K_2K_3K_4} - \gamma_{K_4} \frac{K_2K_3K_4}{1 + K_2K_3K_4}, \quad (5.48)$$

where  $\gamma_{K_i} = dK_i/K_i$  – relative error of the subcircuit with transfer function  $K_i$ .

Practically,  $\gamma_{k1} \ll \gamma_{k2}$ . In addition to that, one can assume that errors  $\gamma_{k1}$  and  $\gamma_{k3}$ ,  $\gamma_{k4}$  of direct and inverse piezoeffects, determined by piezomodule instability under destabilizing factors action, are equal, i.e.,  $|\gamma_{k1}| = |\gamma_{k3}| = |\gamma_{k4}|$ .

Considering these conditions, the following expression is:

$$\gamma_{FB} = \gamma_{k1} - \gamma_{k1} \frac{K_2K_3K_4}{1 + K_2K_3K_4} - \gamma_{k1} \frac{K_2K_3K_4}{1 + K_2K_3K_4} = \gamma_{k1} \left( \frac{1 - K_2K_3K_4}{1 + K_2K_3K_4} \right). \quad (5.49)$$

The condition under which the sensor error equals zero can be easily seen from this equation, i.e.,  $\gamma_{FB} = 0$ :

$$K_2K_3K_4 = 1. \quad (5.50)$$

Thus, the error minimum is reached under the condition when the product of direct transform with FB transfer coefficient ( $K_2$ ), and FB circuit transfer coefficient ( $K_3K_4$ ) equals 1. This condition coincides with the condition of minimum error achievement for transducers with FB [32, 40].

In this case, the transducer sensitivity is determined. Substituting (5.50) in (5.44) we receive:

$$K_{FB} = \frac{K_1K_2}{1 + K_2K_3K_4} = \frac{K_1K_2}{2}. \quad (5.51)$$

Thus, the sensitivity of the transducer with FB decreases two-fold.

## 5.6 Sensors with Combined Feedback

Piezosensors with advantages of charge amplifiers and spatial electromechanical NFB are of scientific interest. They are called piezosensors with combined FB [14, 54].

A rectangular parallelepiped-shaped piezoelement is used in the research. As usual, directions of polarization vectors  $\mathbf{P}$ , force applied  $\mathbf{F}$ , and also arrangement of electrodes, connected to the input and output of the matching charge amplifier (on faces, parallel or perpendicular to the polarization vector), are considered.

Possible variants of transducers are given in Table 5.1.

**Table 5.1** Piezosensors with combined FB

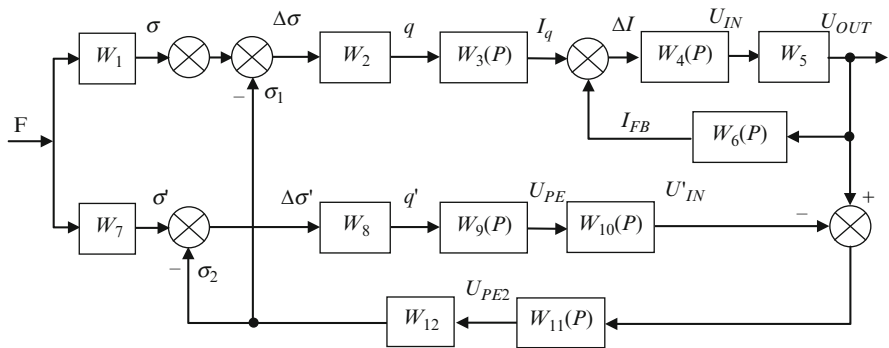
No. of variant	Electrode numbers		Transducer diagram
	Input	Output	
1	1-1'	2-2'	
2	3-3'	2-2'	
3	1-1'	4-4'	
4	3-3'	4-4'	
5	1-1'	2-2'	
6	3-3'	2-2'	
7	1-1'	4-4'	
8	3-3'	4-4'	

(continued)



**Table 5.1** (continued)

No. of variant	Electrode numbers		Transducer diagram
	Input	Output	
9	1-3	2-3	
10	1-3	2-3	



**Fig. 5.31** Block diagram of piezosensor with combined FB

Here, in transducer variants No. 1–4, the vector of force  $F$  is parallel to polarization vector  $P$ ; in the other cases (variants No. 5–8), the vector of force  $F$  is perpendicular to polarization vector  $P$ . Use of combined FB in asymmetric bimorph piezosensors is shown in designs of variants No. 9 and 10.

The block diagram for the sensors is shown in Fig. 5.31.

Two FB circuits are used. The first is current FB. It characterizes the work of the charge amplifier. The second is stress FB. It characterizes spatial electromechanical FB. These transducers are called transducers with combined FB [14, 54].

In Fig. 5.31,  $W_1$  and  $W_7$  – element transfer coefficients, corresponding to transformation of force  $F$ , influencing the piezoelement, into stress  $\sigma$ ;  $W_2$  and  $W_8$  – determine  $\sigma$  and  $\sigma'$  transformation into charges  $q$  and  $q'$  on piezoelement electrodes;  $W_3(p)$  – charge  $q$  transformation into current  $I_q$ , created by the piezoelement;  $W_4(p)$  – determines total current transformation into input voltage on amplifier  $U_{IN}$  input;  $W_5$  – gain of the charge amplifier;  $W_6(p)$  – determines transformation of amplifier output voltage  $U_{OUT}$  into FB current  $I_{FB}$  in FB condenser of the operational amplifier;  $W_9(p)$  – determines  $q'$  transformation into voltage on the

piezoelement electrode  $U_{PE}$ ;  $W_{10}(p)$  – determines  $U_{PE}$  transformation into voltage, transferred to the circuit (when the electrode from the amplifier output is connected);  $W_{11}(p)$  – characterizes the total output voltage  $\Delta U$  transfer into voltage between piezoelement electrodes  $U'_{PE}$ ;  $W_{12}$  – determines  $U'_{PE}$  transformation into stress  $\sigma'$ .

$$W_{FB}(p) = W_2 W_3(p) W_4(p) W_5 \frac{W_1 - W_8 W_9(p) W_{10}(p) W_{11}(p) W_{12} [W_1 - W_7]}{\left[ \begin{array}{c} 1 + W_4(p) W_5 [W_6(p) + W_2 W_3(p) W_{11}(p) W_{12}] \\ - W_8 W_9(p) W_{10}(p) W_{11}(p) W_{12} [1 + W_4(p) W_5 W_6(p)] \end{array} \right]}. \quad (5.52)$$

In this case, the expression of relative error looks like this after transformations [14]:

$$\begin{aligned} \gamma_{FB} = & \frac{dW_1}{W_1} + \frac{dW_2}{W_2} \frac{1}{1 - W_2 W_4 \beta + W_2 W_3 \beta} + \frac{dW_3}{W_3} \frac{1 - W_2 W_4 \beta}{1 - W_2 W_4 \beta + W_2 W_3 \beta} \\ & + \frac{dW_4}{W_4} \frac{W_2 W_4 \beta}{1 - W_2 W_4 \beta + W_2 W_3 \beta} - \frac{d\beta}{\beta} \frac{W_2 W_3 \beta}{1 - W_2 W_4 \beta + W_2 W_3 \beta}. \end{aligned} \quad (5.53)$$

The obtained equality can be rewritten like this:

$$\begin{aligned} \gamma_{FB} = & \gamma_{W1} + \gamma_{W2} \frac{1}{1 - W_2 W_4 \beta + W_2 W_3 \beta} + \gamma_{W3} \frac{1 - W_2 W_4 \beta}{1 - W_2 W_4 \beta + W_2 W_3 \beta} \\ & + \gamma_{W4} \frac{W_2 W_4 \beta}{1 - W_2 W_4 \beta + W_2 W_3 \beta} - \gamma_{\beta} \frac{W_2 W_3 \beta}{1 - W_2 W_4 \beta + W_2 W_3 \beta}, \end{aligned} \quad (5.54)$$

where  $\gamma_{W_i} = dW_i / W_i$  – relative error of direct transform subcircuits;  $\gamma_{\beta} = d\beta / \beta$  – relative error of FB circuit.

Practically,  $\gamma_{k1} \ll \gamma_{k2}$ . In addition to that, one can assume that errors  $\gamma_{k2}$  and  $\gamma_{k10}$  of direct and inverse piezoeffects, determined by the piezomodule instability under destabilizing factors action, are equal, i.e.,  $|\gamma_{k2}| = |\gamma_{k10}|$ . The condition under which the relative error, determined by instability of the amplifier gain coefficient  $\gamma_{k5}$  will be considerably smaller  $\gamma_{k2}$ , i.e.,  $\gamma_{k5} \ll \gamma_{k2}$ . It is also assumed that  $\gamma_{k3}, \gamma_{k7} \ll \gamma_{k2}$ ;  $\gamma_{k4} \approx \gamma_{k6} \ll \gamma_{k2}$ ,  $\gamma_{k8} \approx \gamma_{k9} \ll \gamma_{k2}$ .

For this case:  $\gamma_{W1} \ll \gamma_{k2}$ ,  $\gamma_{W2} \approx \gamma_{k2}$ ,  $\gamma_{W3} \ll \gamma_{k2}$ ,  $\gamma_{W4} \ll \gamma_{k2}$ ,  $\gamma_{\beta} \approx \gamma_{k10} = \gamma_{k2}$ .

Considering the conditions discussed, the following expression is obtained from (5.54):

$$\gamma_{FB} = \gamma_{k2} \frac{1 - W_2 W_3 \beta}{1 - W_2 W_4 \beta + W_2 W_3 \beta}. \quad (5.55)$$

The condition under which the piezosensor error tends to zero, i.e.,  $\gamma_{oc} \rightarrow 0$ , can easily be seen from this expression:

$$W_2 W_3 \beta = 1. \quad (5.56)$$

In this case, the sensor sensitivity is expressed as follows:

$$W_{\text{FB}} = \frac{W_1 W_2 W_3}{1 - W_2 W_4 \beta_1 + W_2 W_3 \beta} = \frac{W_1 W_2 W_3}{2 - W_2 W_4 \beta_1} = \frac{W_{\text{WITHOUTFB}}}{2 - W_2 W_4 \beta_1}. \quad (5.57)$$

As can be seen from expression (5.57), sensitivity of the sensor with combined FB is smaller than sensitivity of the sensor without FB by  $(2 - W_2 W_4 \beta)$  times.

Thus, sensitivity of transducers with combined FB is higher than the sensitivity of transducers with single-loop FB.

## 5.7 Electric Damping of Piezoceramic Sensors with Feedback

A possibility of piezoceramic transducer linearization by electric damping with additional resistors, included in feedback circuit in series with the piezoelement, is considered in this section.

It was shown in Chap. 2 that piezoelectric transducers can be analyzed by various methods [32]. A transducer can be considered a vibratory system. Its motion can be described by the differential equation of the second order [35].

$$m \frac{d^2 x}{dt^2} + R \frac{dx}{dt} + kx = F \sin \omega t, \quad (5.58)$$

where  $m$ ,  $k$  – equivalent mass and elasticity (rigidity) of the piezoelement;  $R = R_0$  – losses in the piezoelement (internal friction);  $F \sin \omega t$  – sinusoidally changing activating force, equivalent to voltage.

Switching of additional electric resistance in series with the piezoelement corresponds to mechanical resistance increase.

The attenuation indicator of this system equals  $\delta = R/2m$ . Thus, the mechanical resistance increase leads to  $Q$  factor reduction and to AFC linearization respectively.

Consideration of the transducer electric equivalent circuit is the most demonstrable and effective. As a result, well-developed methods of circuit theory and be applied. The relevant experiments can be carried out.

It is known [6, 9, 11, 14] that a piezosensor can be represented as an equivalent series oscillatory contour. For this  $LCR$ -contour under the influence of emf, changing sinusoidally,  $e = E_m \sin(\omega t)$ , the following can be written [7]:

$$e = U_L + U_R + U_C \quad (5.59)$$

or after the substitution

$$L \frac{di}{dt} + Ri + \frac{1}{c} \int i dt = E_m \sin(\omega t). \quad (5.60)$$

Having expressed current by charge, we obtain:

$$L \frac{d^2q}{dt^2} + R \frac{dq}{dt} + \frac{q}{C} = E_m \sin(\omega t) \quad (5.61)$$

or after the transformation

$$LC \frac{d^2q}{dt^2} + RC \frac{dq}{dt} + q = q_m \sin(\omega t), \quad (5.62)$$

where  $q_m = CE_m$ .

Complex sensitivity (output–input–value ratio) for this circuit:

$$S(j\omega) = \frac{1}{1 - \frac{\omega^2}{\omega_0^2} + jd \frac{\omega}{\omega_0}}, \quad (5.63)$$

where  $d = 2\delta/\omega_0$  – contour attenuation;  $\delta = R/2L$  – indicator attenuation;  $\omega_0$  – resonant frequency. Denoting frequency  $\omega$  of driving voltage-to-own (resonant)  $\omega_0$  frequency ratio by  $\eta = \omega/\omega_0$ , the expression for a complex sensitivity module will look like this:

$$S(\eta) = |S(j\eta)| = \frac{1}{\sqrt{(1 - \eta^2)^2 + (d\eta)^2}}. \quad (5.64)$$

After  $d$  attenuation replacement by attenuation degree  $\beta = (1/2)d = \delta/\omega_0$  the expression (5.64) will look like this:

$$S(\eta) = \frac{1}{\sqrt{(1 - \eta^2)^2 + (2\beta\eta)^2}}. \quad (5.65)$$

This known expression describes AFC of oscillatory contour.

Its phase–frequency characteristic will look like this:

$$\varphi(\eta) = \text{arctg} \frac{d\eta}{1 - \eta^2} = \text{arctg} \frac{2\beta\eta}{1 - \eta^2}. \quad (5.66)$$

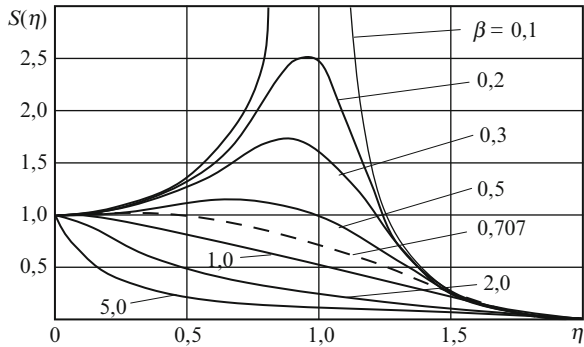
The family of AFC, based on equation (5.65), is presented in Fig. 5.32.

It follows from equation (5.65), that AFC is linear under this condition:

$$\eta = \frac{\omega}{\omega_0} \rightarrow 0. \quad (5.67)$$

If  $\omega \neq 0$ , then  $\omega_0 \rightarrow \infty$ . This system can be considered a low-frequency filter. Phase characteristic would be ideal under the conditions described (5.66). This condition is practically impossible, as equality  $\omega_0 = \infty$ . It shows that the sensor should have properties of a perfectly rigid body [14, 16].

**Fig. 5.32** AFC of piezoceramic sensor, represented as series contour



If this condition  $\omega \ll \omega_0$  is observed, real correlation between  $\omega$  and  $\omega_0$ , determining  $S(\eta)$  deviation from 1, depends on the value of attenuation degree  $\beta$ .

Equality  $S(\eta) \approx 1$  can be observed in a narrow range of frequency ratio change with certain values of attenuation degree, as follows from Fig. 5.32.

There are several variants to determine the degree of approximation to the ideal of the amplitude characteristic:

- Approximate choice of the curve, maximum approaching the horizontal
- Determination of absolute error by equating  $\Delta S(\omega) = S(\omega) - S(0)$ . Minimum  $\Delta S(\omega)$  can be found from it, differentiating expression by parameter  $\beta$
- Use of a relatively simple and universal method of frequency characteristics analysis [2]

The last method consists in the fact that analytical expression of frequency characteristic is resolved into a Taylor series near frequency value  $\omega$ , corresponding to constant value of sensitivity  $S(\omega) = \text{const}$ . If  $S(\omega)$  is represented as frequency ratio function, i.e., as  $S(\eta)$ , expansion into a series should be started next to point  $\eta_0$ , close to zero, as  $S(0) \approx S(\eta_0) \approx 1$ .

As a result of  $S(\eta)$  Taylor expansion, the following is obtained:

$$S(\eta) = S(\eta_0) + S(\eta_0) \cdot \frac{\eta - \eta_0}{1!} + \ddot{S}(\eta_0) \times \frac{\eta - \eta_0}{2!} + \dots + R_n. \tag{5.68}$$

It follows from (5.68) that if all frequency derivatives equaled zero sensitivity  $S(\eta)$  would have been a constant value, equal  $S(\eta_0)$ .

Thus, the more terms of series with frequency derivatives vanish, the closer function  $S(\eta)$  to a constant value. This is well-explained by geometrical interpretations of derivatives. There is no slant if the first derivative equals zero, no curvature if the second derivative equals zero, etc.

We will find the value of  $\beta$  when a possible number of derivatives, starting with the first, vanishes. The AFC expression is rewritten for this purpose:

$$S(\eta) = \frac{1}{\sqrt{(1 - \eta^2)^2 + (2\beta\eta)^2}}. \tag{5.69}$$

As when  $\eta_0 \rightarrow 0$  sensitivity  $S(\eta_0) = 1$ , there should be the first derivative, equal zero, at this point, i.e.,

$$S(\eta_0) = \left. \frac{dS(\eta)}{d\eta} \right|_{\eta \rightarrow 0} = 0. \quad (5.70)$$

Using the expression of squared sensitivity for simplification, the second derivative is determined. As a result, equating the second derivative to zero, we will have:

$$\ddot{S}(\eta_0) = \left. \frac{d^2S(\eta)}{d\eta^2} \right|_{\eta \rightarrow 0} = 4\eta^2(1 - 2\beta^2) = 0. \quad (5.71)$$

Trivial  $\eta = 0$  and the wanted solutions are obtained from here:

$$1 - 2\beta^2 = 0 \quad (5.72)$$

or

$$\beta = \sqrt{\frac{1}{2}} = 0.707. \quad (5.73)$$

Value  $\beta$  is known in radio engineering as characterizing transition of an oscillatory contour into an aperiodic circuit. The curve corresponding to this optimal value of attenuation degree is indicated by a *dashed line* in Fig. 5.32.

The family of phase characteristics for the system studied is shown in Fig. 5.33.

$Q$  factor of contour  $Q_0$  is expressed by value  $\beta$

$$Q_0 = \frac{1}{2\beta} = \frac{\omega_0 L_0}{R_0}. \quad (5.74)$$

The value of the multiplier, series-connected with the contour, to receive  $Q$  factor, equal to 0.707, is determined as follows:

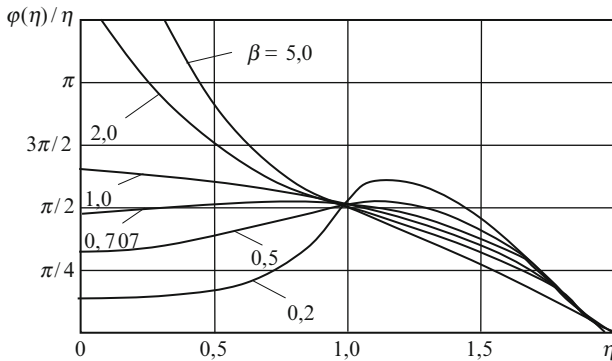


Fig. 5.33 Phase characteristics

$$Q_{\text{COR}} = \frac{\omega_0 L_0}{R_0 + R_{\text{QUAL}}} = 0.707. \quad (5.75)$$

Dividing  $Q_{\text{COR}}$  by  $Q_0$ , the following is obtained:

$$\frac{Q_{\text{COR}}}{Q_0} = \frac{\frac{\omega_0 L_0}{R_0 + R_{\text{QUAL}}}}{\frac{\omega_0 L_0}{R_0}} = \frac{0.707}{Q_0}. \quad (5.76)$$

The following is obtained after the elementary transformations:

$$R_{\text{QUAL}} = R_0 \left( \frac{Q_0}{0.707} - 1 \right) \quad (5.77)$$

Piezoelements are high- $Q$  oscillatory systems, i.e.,  $Q_0 \gg 1$ . Then

$$R_{\text{QUAL}} \approx 1.41 R_0 Q_0 \quad (5.78)$$

However, one should note that the models discussed above are not quite adequate for the piezoelectric sensor. In particular, overtone frequencies are not considered. This leads to a rise in AFC, with  $\eta > 0.5$ .

Thus, connecting additional resistance in series to the oscillatory contour and, consequently, obtaining reduction of oscillatory contour  $Q$  factor when attenuation degree  $\beta = 0.707$ , linear AFC up to value  $\eta = 0.5$ – $0.6$  is obtained.

An asymmetric bimorph sensor with a series-connected active resistance was produced for the research. The sensor consists of a metal plate (steel 40×; 0.15 mm thick, 32 mm in diameter) and IITC-19 piezoceramic piezoelement (0.2 thick and 24 mm in diameter). Active resistance is at resonant frequency of 3.2 kohm.

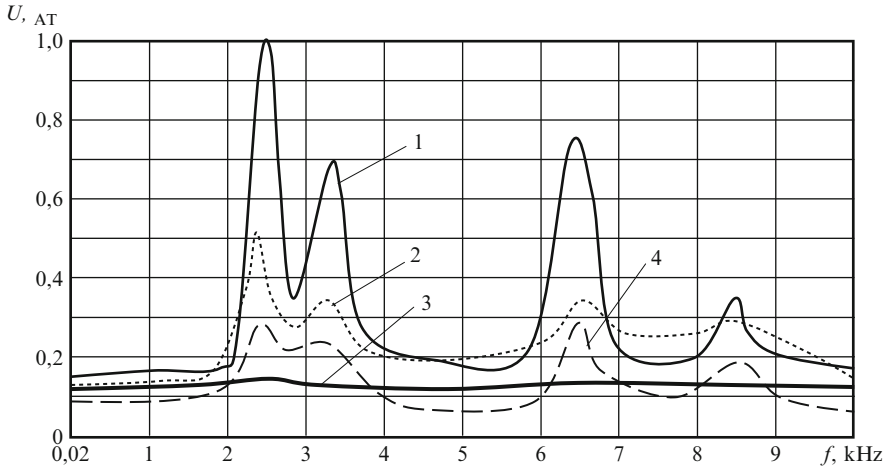
The sensor was in an acoustic chamber. It was influenced by sound pressure 10 Pa (114 dB) in this frequency range 20 Hz–10 kHz. The AFCs are shown in Fig. 5.34.

Here the measured maximal voltage ratio ( $U_R$ ) at the first resonant frequency is vertically shown.

As can be seen from Fig. 5.34, the maximum of AFC linearization is reached if an additional resistor is connected. The latter is calculated by this expression:  $R_{\text{QFactor}} = 36$  kohm.

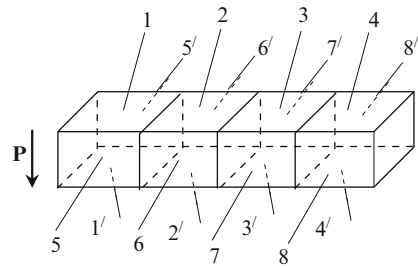
## 5.8 Sensors with Two Feedback Channels

Electric signals are introduced and read from the piezoelement by metal electrodes located on the piezoelement surface. However, as electrode dimensions are limited, the feedback electric signal cannot influence the whole piezoelement. This reduces the effect of feedback introduction, and in some cases does not make it possible to achieve the results demanded.



**Fig. 5.34** AFC of asymmetric bimorph transducer with: 1 –  $R_{QFactor} = 0$ ; 2 –  $R_{QFactor} = 8.2 \text{ kohm}$ ; 3 –  $R_{QFactor} = 36 \text{ kohm}$ ; 4 –  $R_{QFactor} = 100 \text{ kohm}$

**Fig. 5.35** Piezoceramic element: 1–1', 2–2', 3–3'/4–4' – main electrodes; 5–5', 6–6', 7–7', 8–8' – complementary electrodes



Introduction of an additional channel of spatial electromechanical NFB [7, 9, 14, 18] is proposed to eliminate the drawback discussed.

Both charge and voltage amplifiers can be used as matching amplifiers in piezosensors. Useful signal is read from their outputs. Both charge and voltage amplifiers can be used in an additional FB channel.

Three variants are possible here.

1. Voltage amplifiers are switched in basic (output) and additional channels.
2. A charge amplifier, switched into spatial electromechanical FB circuit, is used in the output channel. The voltage amplifier is switched in the additional channel.
3. The voltage amplifier is switched in the output channel, while the charge amplifier is switched in the additional channel.

Piezosensors with double-loop FB are considered below. Voltage amplifiers are used in their FB channels.

A rectangular parallelepiped-shaped piezoelement is used to study the influence of matching amplifier inputs and output connection methods (Fig. 5.35).



The piezoelement is polarized as it is shown in Fig. 5.35. The electrodes on the corresponding faces are divided into four parts, creating eight electrode pairs. Polarization vector  $\mathbf{P}$  is directed perpendicularly to these electrode pairs (1–1', 2–2', 3–3', 4–4'). Connection to such electrodes is denoted by a vertical arrow ( $\downarrow$ ) on sensor circuits.

Polarization vector  $\mathbf{P}$  is parallel to these electrode pairs (5–5', 6–6', 7–7', 8–8'). Connection to these electrodes is denoted by a horizontal arrow ( $\rightarrow$ ) on the sensor diagrams.

Possible variants of piezosensors are shown in Table 5.2 [14, 18]. The force  $\mathbf{F}$  vector is parallel to polarization vector  $\mathbf{P}$  in these sensors (variants nos. 1–16). In the other variants (nos. 17–32), the force  $\mathbf{F}$  vector is perpendicular to polarization vector  $\mathbf{P}$ .

Here elements with transfer coefficients  $W_1$  and  $W_8$  correspond to transformation of force  $F$ , influencing the piezoelement, into stress  $\sigma$ ,  $\sigma = F/S$ , where  $S$  is area:

$$W_1 = s/F = 1/S. \quad (5.79)$$

Elements  $W_2$  and  $W_9$  correspond to stress  $\sigma$  transformation into charge  $q$  on the piezoelement electrodes. As  $q = d_{ij}\Delta\sigma S$ , then

$$W_2 = q/Ds = d_{ij}S, \quad (5.80)$$

where  $d_{ij}$  is piezomodule.

Elements  $W_3(p)$  and  $W_3(p)$  correspond to charge  $q$  transformation into voltage on electrodes of piezoelement  $U_{PE1}$ . Transfer function of these elements looks like this:

$$W_3(p) = \frac{U_{PE1}}{q} = \frac{L_D C_D p^2 + R_{PE} C_D p + 1}{L_D C_D C_{PE} p^2 + R_{PE} C_D C_{PE} p + C_D + C_{PE}}, \quad (5.81)$$

where  $R_{PE}$  – resistance,  $C_{PE}$  – piezoelement capacitance,  $C_D$ ,  $L_D$  – dynamic capacitance and piezoelement inductance,  $p = j\omega$ .

Elements  $W_4(p)$  and  $W_{11}(p)$  correspond to the process occurring when load is connected to the piezoelement (transfer of voltage  $U_{PE1}$  into circuit –  $U_{IN}$ ) $t$ . Its transfer function corresponds to the transfer function of the modified differentiating element [8, 14]:

$$W_4(p) = \frac{U_{IN}}{U_{PE1}} = \frac{\alpha L_R p^3 + \alpha R_{PE} p^2 + R_{IN} p (C_{PE} + C_D)}{\alpha L_R p^3 + (C_D L_D + \alpha R_{PE}) p^2 + \beta p + 1}, \quad (5.82)$$

where  $\beta = R_{PE} C_D + R_{IN} C_{PE} + C_D R_{IN}$ ,  $\alpha = C_{PE} C_D R_{IN}$ , ( $R_{IN}$  is input resistance of the amplifier).

Elements  $W_5$  and  $W_{12}$  corresponds to processes in voltage amplifiers. They are relaxation circuits of the first order. However, considering that sensors work in

**Table 5.2** Sensor block diagram is shown in Fig. 5.36 [7, 40]

No. of variant	Numbers of electrodes				Sensor circuit
	Main channel		Additional channel		
	Input	Output	Input	Output	
1	1-1'	2-2'	3-3'	4-4'	
2	1-1'	2-2'	3-3'	8-8'	
3	1-1'	2-2'	7-7'	4-4'	
4	1-1'	2-2'	7-7'	8-8'	
5	1-1'	6-6'	3-3'	4-4'	
6	1-1'	6-6'	3-3'	8-8'	
7	1-1'	6-6'	7-7'	4-4'	
8	1-1'	6-6'	7-7'	8-8'	
9	5-5'	2-2'	3-3'	4-4'	

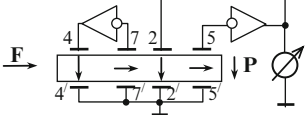
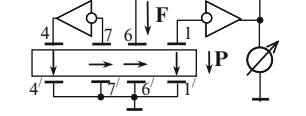
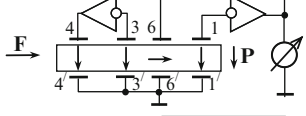
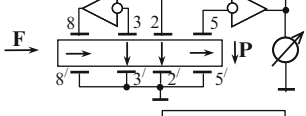
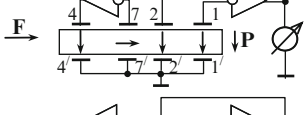
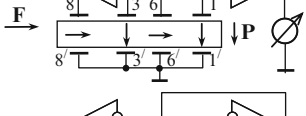
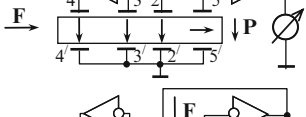
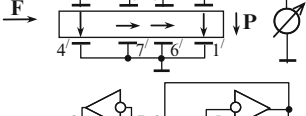
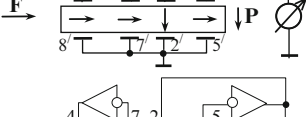
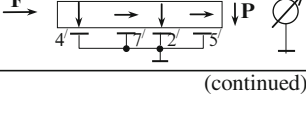
(continued)

**Table 5.2** (continued)

No. of variant	Numbers of electrodes				Sensor circuit
	Main channel		Additional channel		
	Input	Output	Input	Output	
10	5-5'	2-2'	3-3'	8-8'	
11	5-5'	2-2'	7-7'	4-4'	
12	5-5'	2-2'	7-7'	8-8'	
13	5-5'	6-6'	3-3'	4-4'	
14	5-5'	6-6'	3-3'	8-8'	
15	5-5'	6-6'	7-7'	4-4'	
16	5-5'	6-6'	7-7'	8-8'	
17	1-1'	2-2'	3-3'	4-4'	
18	1-1'	2-2'	3-3'	8-8'	

(continued)

**Table 5.2** (continued)

No. of variant	Numbers of electrodes				Sensor circuit
	Main channel		Additional channel		
	Input	Output	Input	Output	
19	1-1'	2-2'	7-7'	4-4'	
20	1-1'	2-2'	7-7'	8-8'	
21	1-1'	6-6'	3-3'	4-4'	
22	1-1'	6-6'	3-3'	8-8'	
23	1-1'	6-6'	7-7'	4-4'	
24	1-1'	6-6'	7-7'	8-8'	
25	5-5'	2-2'	3-3'	4-4'	
26	5-5'	2-2'	3-3'	8-8'	
27	5-5'	2-2'	7-7'	4-4'	
28	5-5'	2-2'	7-7'	8-8'	

(continued)

**Table 5.2** (continued)

No. of variant	Numbers of electrodes				Sensor circuit
	Main channel		Additional channel		
	Input	Output	Input	Output	
29	5-5'	6-6'	3-3'	4-4'	
30	5-5'	6-6'	3-3'	8-8'	
31	5-5'	6-6'	7-7'	4-4'	
32	5-5'	6-6'	7-7'	8-8'	

a quite narrow frequency range, the transfer function can be considered linear. It equals the gain coefficient of the voltage amplifier.

Processes in elements  $W_8(p)$  and  $W_{13}(p)$  are opposite to the processes to which elements  $W_4(p)$  and  $W_{11}(p)$  correspond. They occur with voltage introduction from the voltage amplifier to an additional electrode of the piezoelement. Transfer of voltage  $U_{IN}$  into voltage between the electrodes of piezoelement  $U_{PE}$  [8, 14]:

$$W_8(p) = \frac{U_{PE2}}{U_{IN}} = \frac{\alpha L_R p^3 + (C_D L_D + \alpha R_{PE}) p^2 + \beta p + 1}{\alpha L_R p^3 + \alpha R_{PE} p^2 + R_{OUT} p (C_{PE} + C_D)}, \quad (5.83)$$

where  $\beta = R_{PE} C_D + R_{IN} C_{PE} + C_D R_{OUT}$ ,  $\alpha = C_{PE} C_D R_{OUT}$ , ( $R_{OUT}$  is output resistance of the voltage amplifier).

Elements  $W_7$  and  $W_{14}$  characterize transformation of voltages  $U_{PE2}$  и  $U'_{PE2}$  into stress  $\sigma_1$  and  $\sigma_2$ . As  $\sigma = E d_{ij} U_{PE2} / l$ , then

$$W_7 = s / U_{PE2} = E d_{ij} / l, \quad (5.84)$$

where  $E$  – Young’s modulus,  $l$  – distance between electrodes.

As a result, the transfer function looks like this [14]:

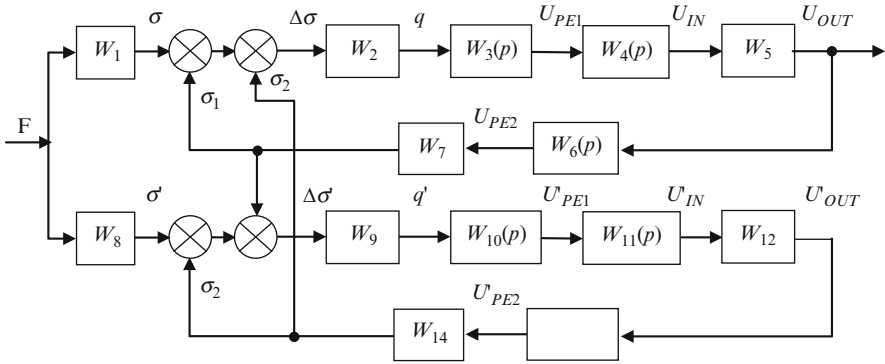


Fig. 5.36 Block diagram of sensors with double-loop FB

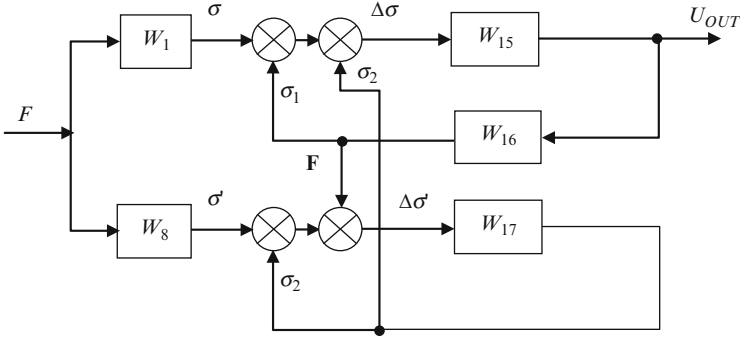


Fig. 5.37 Block diagram of piezosensor with double-loop FB

$$W_{FB}(p) = W_2 W_3(p) W_4(p) W_5 \times \frac{W_1 + W_9 W_{10}(p) W_{11}(p) W_{12} W_{13}(p) W_{14} (W_1 - W_8)}{1 + W_9 W_{10}(p) W_{11}(p) W_{12} W_{13}(p) W_{14} + W_2 W_3(p) W_4(p) W_5 W_6(p) W_7} \quad (5.85)$$

Relative error of piezotransducers with double-loop FB and voltage amplifiers [14, 17] is determined.

For this purpose, the block diagram of sensors, shown in Fig. 6.2, is transformed into the diagram represented in Fig. 5.37.

In this case,  $W_{15} = W_2 W_3 W_4 W_5$ ;  $W_{16} = W_6 W_7$ ;  $W_{17} = W_9 W_{10} W_{12} W_{13} W_{14}$ .

Then the formula (5.85) will look like this:

$$W_{FB} = \frac{W_1 W_{15} + W_1 W_{15} W_{17} - W_8 W_{15} W_{17}}{1 + W_{17} + W_{15} W_{16}} \quad (5.86)$$

Total increment of sensitivity (transfer function  $W_{FB}$ ) with simultaneous change of direct transform circuit sensitivities  $W_1$ ,  $W_8$ ,  $W_{15}$  and feedback  $W_{16}$  and  $W_{17}$  [10, 14]:

$$dW_{FB} = \frac{\partial W_{FB}}{\partial W_1} dW_1 + \frac{\partial W_{FB}}{\partial W_8} dW_8 + \frac{\partial W_{FB}}{\partial W_{15}} dW_{15} + \frac{\partial W_{FB}}{\partial W_{16}} dW_{16} + \frac{\partial W_{FB}}{\partial W_{17}} dW_{17}. \quad (5.87)$$

The expression for the relative error of the sensor with double-loop FB will look like this after elementary transformations:

$$\begin{aligned} \gamma_{FB} = & \frac{W_1 W_{15} (1 + W_{17})}{W_1 W_{15} (1 + W_{17}) - W_8 W_{15} W_{17}} \gamma_{W_1} - \frac{W_8 W_{15} W_{17}}{W_1 W_{15} (1 + W_{17}) - W_8 W_{15} W_{17}} \gamma_{W_8} \\ & + \frac{W_{15} [W_1 + W_{17} (2W_1 - W_8) + W_{17}^2 (W_1 - W_8)]}{(W_1 W_{15} (1 + W_{17}) - W_8 W_{15} W_{17}) (1 + W_{17} + W_{15} W_{16})} \gamma_{W_{15}} \\ & - \frac{W_{15} W_{16}}{1 + W_{17} + W_{15} W_{16}} \gamma_{W_{16}} \\ & + \frac{W_{17} [W_{15}^2 W_{16} (W_1 - W_8) - W_8 W_{15}]}{(W_1 W_{15} (1 + W_{17}) - W_8 W_{15} W_{17}) (1 + W_{17} + W_{15} W_{16})} \gamma_{W_{17}}, \end{aligned} \quad (5.88)$$

where  $\gamma_{W_i} = dW_i/W_i$  is relative error of subcircuit  $W_i$

After substitution of values  $W_{15}$ ,  $W_{16}$ ,  $W_{17}$  and simplifications, we obtain [14]:

$$\begin{aligned} \gamma_{FB} = & \frac{dW_1}{W_1} + \frac{dW_2}{W_2} \frac{1}{1 + W_2 \beta_1 + W_2 W_3 \beta_2} + \frac{dW_3}{W_3} \frac{1 + W_2 \beta_1}{1 + W_2 \beta_1 + W_2 W_3 \beta_2} \\ & - \frac{d\beta_1}{\beta_1} \frac{W_2 \beta_1}{1 + W_2 \beta_1 + W_2 W_3 \beta_2} - \frac{d\beta_2}{\beta_2} \frac{W_2 W_3 \beta_2}{1 + W_2 \beta_1 + W_2 W_3 \beta_2}. \end{aligned} \quad (5.89)$$

The equality obtained can be rewritten like this:

$$\begin{aligned} \gamma_{FB} = & \gamma_{W_1} + \gamma_{W_2} \frac{1}{1 + W_2 \beta_1 + W_2 W_3 \beta_2} + \gamma_{W_3} \frac{1 + W_2 \beta_1}{1 + W_2 \beta_1 + W_2 W_3 \beta_2} \\ & - \gamma_{\beta_1} \frac{W_2 \beta_1}{1 + W_2 \beta_1 + W_2 W_3 \beta_2} - \gamma_{\beta_2} \frac{W_2 W_3 \beta_2}{1 + W_2 \beta_1 + W_2 W_3 \beta_2}, \end{aligned} \quad (5.90)$$

where  $\gamma_{W_i} = dW_i/W_i$  – relative error of direct transform subcircuit;  $\gamma_{\beta_i} = d\beta_i/\beta_i$  – relative error of FB circuits.

After simplifications and transformations, the following is obtained [14]:

$$\gamma_{FB} = \gamma_{k2} \frac{1 - W_2 \beta_1 - W_2 W_3 \beta_2}{1 + W_2 \beta_1 + W_2 W_3 \beta_2}.$$

The condition under which the piezosensor error will tend to zero (i.e.,  $\gamma_{\text{FB}} \rightarrow 0$ ) is easily noticeable from this expression:

$$W_2\beta_1 + W_2W_3\beta_2 = 1.$$

In this case the sensor sensitivity is expressed as:

$$W_{\text{FB}} = \frac{W_1W_2W_3}{1 + W_2\beta_1 + W_2W_3\beta_2} = \frac{W_1W_2W_3}{2}.$$

Thus, the sensor sensitivity decreases two-fold.

As the experiments showed [14], use of double-loop FB makes it possible to increase temporary stability of piezoceramic sensors by approximately 1.2–1.5 times in comparison with single-loop FB and by 5–11 times in comparison with sensors without FB.

### 5.8.1 Sensors with Output Charge Amplifier and Voltage Amplifier in Additional Feedback Channel

Piezosensors with two FB circuits are considered in this section. A charge amplifier is used as the output amplifier in them. A voltage amplifier is used for this purpose in additional FB channel.

The piezoelement shown in Fig. 5.35 is used for this purpose. Directions of polarization vectors  $\mathbf{P}$  and force  $\mathbf{F}$  applied are considered, as in the case with two FB channels and voltage amplifiers. Arrangement of electrodes connected to the input and output of matching amplifiers, parallel or perpendicularly to the polarization vector, is also considered.

Possible variants of piezosensors are shown in Table 5.3. The vector of force  $\mathbf{F}$  applied is parallel to polarization vector  $\mathbf{P}$  in the transducers variants nos. 1–16. Force  $\mathbf{F}$  vector is perpendicular to polarization vector  $\mathbf{P}$  in the other variants (nos. 17–32).

The sensor block diagram is shown in Fig. 5.38.

Here,  $W_1$  and  $W_9$  – coefficients of elements transfer, corresponding to transformation of force  $F$ , influencing the piezoelement, into stress  $\sigma$ ,  $W_2$  and  $W_{10}$  – determine  $\sigma$  transformation into charge  $q$  on the piezoelement electrodes;  $W_3(p)$  – transformation of charge  $q$  into current  $I_q$ , created by the piezoelement;  $W_4(p)$  – transformation of total current into input voltage, arriving at the input of charge amplifier of  $U_{\text{IN}}$ ;  $W_5$  – gain of the charge amplifier;  $W_6(p)$  – determines transformation of the amplifier output voltage  $U_{\text{OUT}}$  into FB current  $I_{\text{FB}}$  in FB condenser of the operational amplifier;  $W_7(p)$  and  $W_{14}(p)$  – determine the output voltage transfer of amplifier  $U_{\text{OUT}}$  into voltage between the piezoelement electrodes  $U_{\text{PE}}$ ;  $W_8$  and  $W_{15}$  – determine  $U_{\text{PE}}$  transformation into stress  $\sigma$ ,  $W_{11}(p)$  – determines  $q'$  transformation into voltage on the piezoelement



**Table 5.3** Piezosensor with output charge amplifier and voltage amplifier in additional FB channel

No. of variant	Electrodes				Sensor diagram
	Basic channel		Additional channel		
	Input	Output	Input	Output	
1	1	1'	3-3'	4-4'	
2	1	1'	3-3'	8-8'	
3	1	1'	7-7'	4-4'	
4	1	1'	7-7'	8-8'	
5	5	5'	3-3'	4-4'	
6	5	5'	3-3'	8-8'	
7	5	5'	7-7'	4-4'	
8	5	5'	7-7'	8-8'	
9	1	2	3-3'	4-4'	
10	1	2	3-3'	8-8'	

(continued)

**Table 5.3** (continued)

No. of variant	Electrodes				Sensor diagram
	Basic channel		Additional channel		
	Input	Output	Input	Output	
11	1	2	7-7'	4-4'	
12	1	2	7-7'	8-8'	
13	5	6	3-3'	4-4'	
14	5	6	3-3'	8-8'	
15	5	6	7-7'	4-4'	
16	5	6	7-7'	8-8'	
17	1	1'	3-3'	4-4'	
18	1	1'	3-3'	8-8'	
19	1	1'	7-7'	4-4'	
20	1	1'	7-7'	8-8'	

(continued)

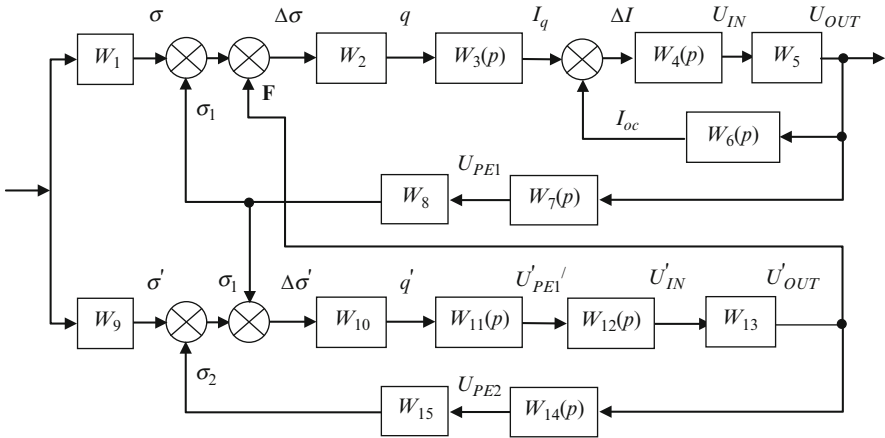
**Table 5.3** (continued)

No. of variant	Electrodes				Sensor diagram
	Basic channel		Additional channel		
	Input	Output	Input	Output	
21	5	5'	3-3'	4-4'	
22	5	5'	3-3'	8-8'	
23	5	5'	7-7'	4-4'	
24	5	5'	7-7'	8-8'	
25	1	2	3-3'	4-4'	
26	1	2	3-3'	8-8'	
27	1	2	7-7'	4-4'	
28	1	2	7-7'	8-8'	
29	5	6	3-3'	4-4'	
30	5	6	3-3'	8-8'	

(continued)

**Table 5.3** (continued)

No. of variant	Electrodes				Sensor diagram
	Basic channel		Additional channel		
	Input	Output	Input	Output	
31	5	6	7-7'	4-4'	
32	5	6	7-7'	8-8'	



**Fig. 5.38** Block diagram of piezosensor with double-loop FB, with output charge amplifier and voltage amplifier in additional FB channel

electrodes  $U'_{PE1}$ ;  $W_{12}(p)$  – determines  $U'_{PE1}$  transformation into the voltage on the voltage amplifier input;  $W_{13}$  – determines the gain of the voltage amplifier.

The transfer function looks like this in this case:

$$\begin{aligned}
 W_{FB}(p) &= W_2 W_3(p) W_4(p) W_5 \\
 &\times \frac{W_1 + [W_1 + W_{10} W_{11}(p) W_{12}(p) W_{13} W_{14}(p) W_{15} (W_1 - W_9)]}{[1 + W_{10} W_{11}(p) W_{12}(p) W_{13} W_{14}(p) W_{15} [1 + W_4(p) W_5 W_6(p)] + W_4(p) W_5 [W_6(p) + W_2 W_3 W_7(p) W_8]} \quad (5.91)
 \end{aligned}$$

After transformations and simplifications we obtain [10, 14]:

$$W_{FB} = \frac{W_1 W_2 W_3}{1 + W_2 W_3 \beta_1 + W_2 \beta_2} \quad (5.92)$$

In this case, the expression to determine the relative error looks like this [14]:

$$\gamma_{\text{FB}} = \gamma_{k2} \frac{1 - W_2 W_3 \beta_1 - W_2 \beta_2}{1 + W_2 W_3 \beta_1 + W_2 \beta_2}. \quad (5.93)$$

The condition under which the piezosensor error tends to zero, i.e.,  $\gamma_{\text{FB}} \rightarrow 0$ , can easily be seen from this expression:

$$W_2 W_3 \beta_1 + W_2 \beta_2 = 1. \quad (5.94)$$

The sensor sensitivity is expressed as:

$$W_{\text{FB}} = \frac{W_1 W_2 W_3}{1 + W_2 W_3 \beta_1 + W_2 \beta_2} = \frac{W_1 W_2 W_3}{2} = \frac{W_{\text{WITHOUTFB}}}{2}. \quad (5.95)$$

Thus, the sensitivity of the sensor with FB decreases two-fold.

### 5.8.2 Sensors with Output Voltage Amplifier and Charge Amplifier in Additional FB Channel

The piezoelement shown in Fig. 6.1 is used. Directions of polarization vectors  $\mathbf{P}$  and force applied  $\mathbf{F}$  are also considered, as in the previous cases. Arrangement of electrodes, connected to the input and output of the matching amplifiers (located on faces parallel or perpendicularly to the polarization vector), is also considered.

Possible variants of piezosensors are shown in Table 5.4. In these variants of sensors (nos. 1–16), the vector of applied force  $\mathbf{F}$  is parallel to polarization vector  $\mathbf{P}$ . In the other variants (nos. 17–32), the vector of force  $\mathbf{F}$  is perpendicular to polarization vector  $\mathbf{P}$ .

The block diagram of sensors is shown in Fig. 5.39.

Here,  $W_1$  and  $W_8$  – coefficients of elements transfer, corresponding to transformation of force  $F$ , influencing the piezoelement, in stress  $\sigma$ ;  $W_2$  and  $W_9$  – determine  $\sigma$  transformation into charge  $q$  on the piezoelement electrodes;  $W_3(p)$  – determines  $q$  transformation into voltage on piezoelement electrodes  $U_{\text{PE}}$ ;  $W_4(p)$  – determines  $U_{\text{PE}}$  transformation into voltage on the amplifier inputs;  $W_5$  and  $W_{12}$  – determine the gain of voltage amplifiers;  $W_6(p)$  and  $W_{14}(p)$  – transfer of amplifier output voltage  $U_{\text{OUT}}$  into voltage between the piezoelement electrodes  $U_{\text{PE2}}$ ;  $W_7$  and  $W_{15}$  – determine  $U_{\text{PE2}}$  transformations into stress  $\sigma_1$  and  $\sigma_2$ ;  $W_{10}(p)$  – determines  $q$  transformation into current  $I_q$ , arriving at the charge amplifier input;  $W_{11}(p)$  – determines transformation of input current  $I_q$  of the charge amplifier into its input voltage;  $W_{13}(p)$  – determines the output voltage transformation into current  $I_{\text{FB}}$  of the operational amplifier FB. The current goes through the FB condenser.

**Table 5.4** Piezosensors with output voltage and charge amplifiers in additional FB channel

No. of variant	Electrodes				Sensor diagram
	Voltage amplifier		Charge amplifier		
	Input	Output	Input	Output	
1	1-1'	2-2'	4	4'	
2	1-1'	2-2'	8	8'	
3	1-1'	6-6'	4	4'	
4	1-1'	6-6'	8	8'	
5	5-5'	2-2'	4	4'	
6	5-5'	2-2'	8	8'	
7	5-5'	6-6'	4	4'	
8	5-5'	6-6'	8	8'	
9	1-1'	2-2'	3	4	

(continued)

**Table 5.4** (continued)

No. of variant	Electrodes				Sensor diagram
	Voltage amplifier		Charge amplifier		
	Input	Output	Input	Output	
10	1-1'	2-2'	7	8	
11	1-1'	6-6'	3	4	
12	1-1'	6-6'	7	8	
13	5-5'	2-2'	3	4	
14	5-5'	2-2'	7	8	
15	5-5'	6-6'	3	4	
16	5-5'	6-6'	7	8	
17	1-1'	2-2'	4	4'	
18	1-1'	2-2'	8	8'	

(continued)

**Table 5.4** (continued)

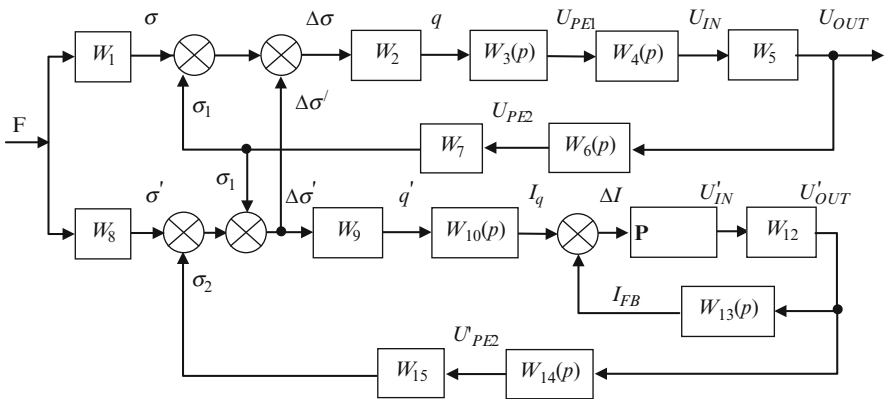
No. of variant	Electrodes				Sensor diagram
	Voltage amplifier		Charge amplifier		
	Input	Output	Input	Output	
19	1-1'	6-6'	4	4'	
20	1-1'	6-6'	8	8'	
21	5-5'	2-2'	4	4'	
22	5-5'	2-2'	8	8'	
23	5-5'	6-6'	4	4'	
24	5-5'	6-6'	8	8'	
25	1-1'	2-2'	3	4	
26	1-1'	2-2'	7	8	
27	1-1'	6-6'	3	4	
28	1-1'	6-6'	7	8	

(continued)



**Table 5.4** (continued)

No. of variant	Electrodes				Sensor diagram
	Voltage amplifier		Charge amplifier		
	Input	Output	Input	Output	
29	5-5'	2-2'	3	4	
30	5-5'	2-2'	7	8	
31	5-5'	6-6'	3	4	
32	5-5'	6-6'	7	8	



**Fig. 5.39** Block diagram of piezosensors with double-loop FB, with output voltage and charge amplifiers in additional FB channel

In this case, the transfer function looks like this:

$$\begin{aligned}
 W_{FB}(p) &= W_2 W_3(p) W_4(p) W_5 \\
 &\times \frac{W_1 - W_8 + W_{11}(p) W_{12} [W_1 (W_{13}(p) + W_9 W_{10}(p) W_{13}(p) W_{14}(p) W_{15})]}{1 + W_{11}(p) W_{12} W_{15} [1 + W_9 W_{10}(p) W_{14}(p) (1 + W_2 W_3(p) W_4(p) W_5 W_6(p) W_7)]} \\
 &- \frac{W_2 W_3(p) W_4(p) W_5 W_8 W_{11}(p) W_{12} W_{13}(p)}{1 + W_{11}(p) W_{12} W_{15} [1 + W_9 W_{10}(p) W_{14}(p) (1 + W_2 W_3(p) W_4(p) W_5 W_6(p) W_7)]}.
 \end{aligned}
 \tag{5.96}$$

The expression to determine the relative error [14] is:

$$\gamma_{\text{FB}} = \frac{W_1 W_{18}(2 + W_{18} - W_{16} W_{17} W_{18})}{(1 + W_{18} + W_{16} W_{17} W_{18})(W_1 + W_1 W_{18} - W_8)} \gamma_{k2}. \quad (5.97)$$

The condition under which the piezosensor error tends to zero, i.e.,  $\gamma_{\text{FB}} \rightarrow 0$ , can easily be seen from this expression:

$$2 + W_{18} - W_{16} W_{17} W_{18} = 0. \quad (5.98)$$

Whence, after simple transformations [14]:

$$W_3(W_2 \beta_1 - 1) = 2, \quad (5.99)$$

where  $W_2$  and  $W_3$  – transfer coefficient of direct transform ( $W_2 = W_{16}$ ,  $W_3 = W_{18}$ ) circuits, and  $\beta_1$  – FB circuit ( $\beta_1 = W_{17}$ ).

### 5.8.3 Piezosensors with Two Charge Amplifiers with Piezoelements in FB Circuits of Amplifiers

Possible piezosensor variants are shown in Table 5.5. In these variants (nos. 1–10) of transducers, the vector of applied force  $F$  is parallel to polarization vector  $P$ . In the other variants (nos. 11–20), the vector of force  $F$  is perpendicular to polarization vector  $P$ .

The block diagram of the sensors is shown in Fig. 5.40.

Here,  $W_1$  and  $W_9$  – coefficient of elements transfer, corresponding to transformation of force  $F$ , influencing the piezoelement, in stress  $\sigma$ ;  $W_2$  and  $W_{10}$  – determine  $\sigma$  transformation into charge  $q$  on the piezoelement electrodes;  $W_3(p)$  and  $W_{11}(p)$  – determine charge  $q$  transformation into current  $I_q$ , created by the piezoelement;  $W_4(p)$  and  $W_{12}(p)$  – determine transformation of total current into input voltage on the amplifier  $U_{\text{IN}}$  input;  $W_5$  and  $W_{13}$  – determine the gain of the charge amplifier;  $W_6(p)$  and  $W_{14}(p)$  – determine transformation of the amplifier output voltage  $U_{\text{OUT}}$  into FB current  $I_{\text{FB}}$  in FB condenser of the operational amplifier;  $W_7(p)$  and  $W_{15}(p)$  – determine transformation of the amplifier output voltage  $U_{\text{OUT}}$  into voltage between the piezoelement electrodes  $U_{\text{PE}}$ ;  $W_8$  and  $W_{16}$  – determine  $U_{\text{PE}}$  transformation into stress  $\sigma$ .

Piezosensors with two charge amplifiers are shown in Table 5.5.

In this case the transfer function will look like this:

**Table 5.5** Piezosensors with two charge amplifiers

No. of variant	Electrodes				Sensor circuit
	Main charge amplifier		Additional charge amplifier		
	Input	Output	Input	Output	
1	1	1'	4	4'	
2	1	1'	8	8'	
3	5	5'	4	4'	
4	5	5'	8	8'	
5	3	4	4	4'	
6	7	8	4	4'	
7	3	4	8	8'	
8	7	8	8	8'	
9	4	1	4'	1'	

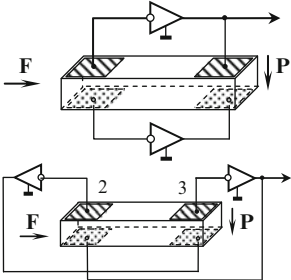
(continued)

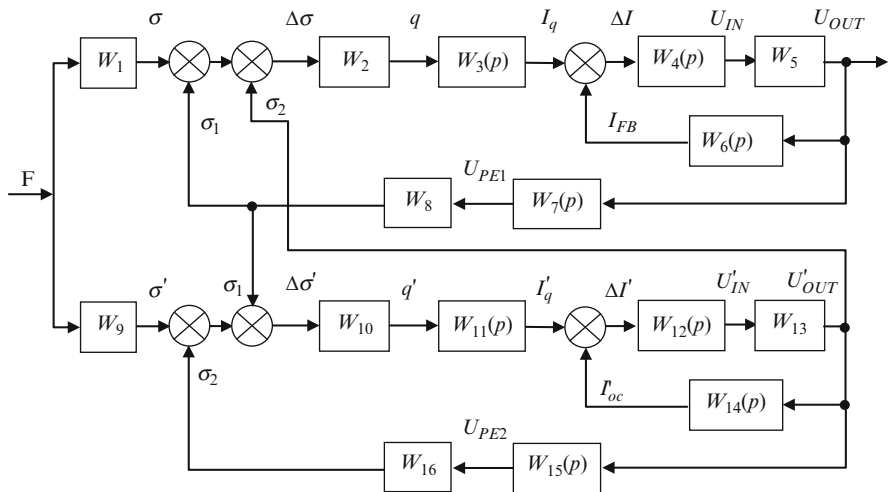
**Table 5.5** (continued)

No. of variant	Electrodes				Sensor circuit
	Main charge amplifier		Additional charge amplifier		
	Input	Output	Input	Output	
10	1	4'	4	1'	
11	1	1'	4	4'	
12	1	1'	8	8'	
13	5	5'	4	4'	
14	5	5'	8	8'	
15	3	4	4	4'	
16	7	8	4	4'	
17	3	4	8	8'	
18	7	8	8	8'	

(continued)

**Table 5.5** (continued)

No. of variant	Electrodes				Sensor circuit
	Main charge amplifier		Additional charge amplifier		
	Input	Output	Input	Output	
19	4	1	4'	1'	
20	1	4'	4	1'	



**Fig. 5.40** Block diagram of piezosensors with charge amplifiers

$$W_{FB}(p) = W_2 W_3(p) W_4(p) W_5 \times$$

$$\frac{W_1 + [W_1 + W_{12}(p) W_{13} (W_1 W_{14}(p) + W_{10}(p) W_{11}(p) \{W_{15}(p) W_{16} - W_{11}\})]}{1 + W_4(p) W_5 W_6(p) [1 + W_{12}(p) W_{13} (W_{14}(p) + W_{10}(p) W_{11}(p) \{W_{15} W_{16}(p) + W_7(p) W_8\})] + W_2 W_3(p) W_4(p) W_5 W_7(p) W_8 [1 + W_{12}(p) W_{13} \{W_4(p) + W_{10}(p) W_{11}(p) W_{15} W_{16}(p)\}] + W_{12}(p) W_{13} [W_{14}(p) + W_{10}(p) W_{11}(p) \{W_{15} W_{16}(p) - W_7(p) W_8\}]}$$

(5.100)

After transformations and simplification the following is obtained [14]:

$$W_{\text{FB}} = \frac{W_1 W_2 W_3}{1 + W_2 W_3 \beta_1 + W_2 \beta_2}. \quad (5.101)$$

In this case, the expression to determine the relative error is [14]:

$$\gamma_{\text{FB}} = \gamma_{k2} \frac{1 - W_2 W_3 \beta_1 - W_2 \beta_2}{1 + W_2 W_3 \beta_1 + W_2 \beta_2}. \quad (5.102)$$

The condition under which the piezosensor error tends to zero, i.e.,  $\gamma_{\text{FB}} \rightarrow 0$ , can easily be seen from this expression [14]:

$$W_2 W_3 \beta_1 + W_2 \beta_2 = 1. \quad (5.103)$$

The sensor sensitivity in this case:

$$W_{\text{FB}} = \frac{W_1 W_2 W_3}{1 + W_2 W_3 \beta_1 + W_2 \beta_2} = \frac{W_1 W_2 W_3}{2}. \quad (5.104)$$

Thus, the sensitivity of this sensor is decreased two-fold [11, 17, 40].

## 5.9 Piezosensor with Charge Amplifier and FB Channel on Voltage Amplifier

In this case the piezoelement, traditionally connected to the charge amplifier, is used. In addition to that, an additional voltage amplifier, connected to complementary piezoelement electrodes, is switched into the sensor circuit.

Some variants of sensor circuits for a piezoelement shown in Fig. 5.35 are represented in Table 5.6.

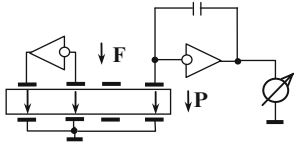
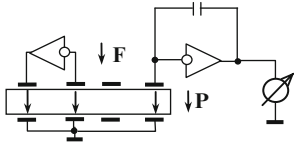
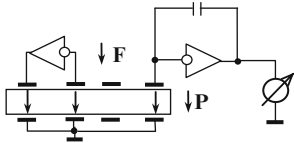
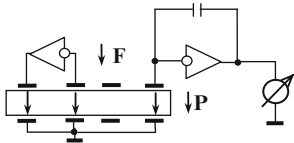
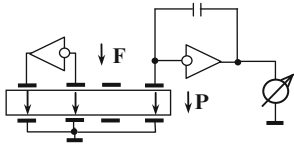
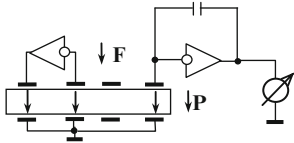
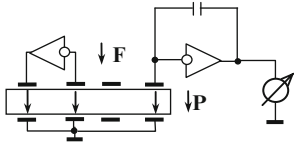
It is also shown in this case [14] that the sensor error minimum can be reached if this condition is observed

$$w\beta = 1, \quad (5.105)$$

where  $W$  is the transfer coefficient of direct transform circuit for the channel on the voltage amplifier;  $\beta$  – transfer coefficient of FB circuit.

In this case, the sensitivity of the whole sensor is decreased two-fold.

**Table 5.6** Piezosensors with output charge and voltage amplifiers in additional FB channel

No. of variant	Electrodes				Sensor circuit
	Main charge amplifier		Additional charge amplifier		
	Input	Output	Input	Output	
1	1		3-3'	4-4'	
2	1		3-3'	8-8'	
3	1		7-7'	4-4'	
4	1		7-7'	8-8'	
5	1		3-3'	4-4'	
6	1		3-3'	8-8'	
7	1		7-7'	4-4'	

## References

1. V. Sharapov et al., *The Electromechanical Feed-back in Piezoceramic Sensors and Transducers*. IEEE International Ultrasonics Symposium, Sendai, Japan (1998)
2. G.V. Braude, On correction of frequency and phase characteristics of intensifying devices. *J. Theor. Phys.* **T.4** (1934)
3. V.N. Bruyanov, M.G. Kosov, S.P. Protopopov et al., *Theory of Automatic Control*, ed. by J.M. Solomentseva (Vyssh. Shk., Moscow, 2000), p. 268 (in Russian)
4. V.S. Gutnikov, *Integrated Electronics in Measuring Devices* (Energoatomizdat, Leningrad, 1988), p. 304 (in Russian)
5. P.G. Dzagupov, A.A. Erofeev, *Piezoceramic Elements in Instrument Making and Automatics* (Mashinostroenie, Leningrad, 1986), p. 256 (in Russian)
6. V. Domarkas, R.J. Kazys, *Piezoelectric Transducers for Measuring Devices* (Mintis, Vilnus, 1974), p. 258 (in Russian)
7. V.A. Kotelnikov, *Basics of Radio Engineering* (Gostehizdat, Moscow, 1950) (in Russian)
8. E.A. Kudrayshov, V.E. Mager, Methods of sensitivity increase in piezoelectric quartz crystal sensors. *Devices and control systems* **4**, 20–22 (1982) (in Russian)
9. E.S. Levshina, P.V. Novitskiy, *Electric Measurements of Physical Values: (Measuring Transducers). Studies. Manual for High Educational Establishments* (Energoatomizdat, Leningrad, 1983), p. 320 (in Russian)
10. B. Ya. Lurie, P.Dg. Enrait, *Classical Methods of Automatic Control*, ed. by A.A. Lanne (St. Petersburg, 2004), p. 640 (in Russian)
11. G.V. Katz (ed.), *Magnetic and Dielectric Devices* (Energiya, Moscow, 1964), p. 416 (in Russian)
12. I.M. Makarov, B.M. Menskiy, *Linear Automatic Systems (Theory Elements, Calculation Methods, Reference Material). Manual for Higher Educational Establishments* (Mashinostroenie, Moscow, 1977), p. 464 (in Russian)
13. I.G. Minaev, A.I. Trofimov, V.M. Sharapov, On output characteristics linearization of piezoelectric force-measuring transducers. *News of USSR Higher Learning Institutions, Priborostroenie*, No. 3 (1975) (in Russian)
14. V.M. Sharapov, M.P. Musienko, E.V. Sharapova, *Piezoelectric Sensors*, ed. by V.M. Sharapov (Technosphaera, Moscow, 2006), p. 632 (in Russian)
15. V.M. Sharapov et al., Electromechanical feedback in piezoelectric transducers. *Visnyk ChITI.2000*, No. 1, p. 63–69 (in Russian)
16. L.A. Ostrovskiy, *Theoretical Basics of Electric Measuring Instruments* (Energiya, Leningrad, 1971), p. 544 (in Russian)
17. V.M. Sharapov et al., Patent of Ukraine #34318. Piezoelectric transducer of mechanical values. Publication 15 Feb 2001 (in Ukrainian)
18. V.M. Sharapov et al., Patent of Ukraine #34319. Piezoelectric transducer of mechanical values. Publication 15 Feb 2001 (in Ukrainian)
19. V.M. Sharapov et al., Patent of Ukraine #40815. Piezoelectric transducer of mechanical values. Publication 15 Aug 2001 (in Ukrainian)
20. V.M. Sharapov et al., Patent of Ukraine #43964. Piezoelectric transducer of mechanical values. Publication 15 Jan 2002 (in Ukrainian)
21. V.M. Sharapov et al., Patent of Ukraine #55803. G01P1/09. Piezoelectric transducer of mechanical values. Publication 15 Apr 2003 (in Ukrainian)
22. V.M. Sharapov et al., Patent of Ukraine #55806. G01P1/09. Piezoelectric transducer of mechanical values. Publication 15 Apr 2003 (in Ukrainian)
23. V.M. Sharapov et al., Patent of Ukraine #61267. G01L1/16, G01P15/09. Piezoelectric transducer of mechanical values. Publication 17 Nov 2003 (in Ukrainian)
24. V.M. Sharapov et al., Patent of Ukraine #61268. Piezoelectric transducer of mechanical values. Publication 17 Nov 2003 (in Ukrainian)



25. V.M. Sharapov et al., Patent of Ukraine #61270. Piezoelectric transducer of mechanical values. Publication 17 Nov 2003 (in Ukrainian)
26. V.M. Sharapov et al., Patent of Ukraine #61272. Piezoelectric transducer of mechanical values. Publication 17 Nov 2003 (in Ukrainian)
27. V.M. Sharapov et al., Patent of Ukraine #65324. Piezoelectric transducer of mechanical values. Publication 15 Mar 2004 (in Ukrainian)
28. V.M. Sharapov et al., Patent of Ukraine 65325. Piezoelectric transducer of mechanical values. Publication 15 Mar 2004 (in Ukrainian)
29. V.M. Sharapov et al., Patent of Ukraine 66014. Piezoelectric transducer of mechanical values. Publication 15 Apr 2004 (in Ukrainian)
30. M.G. Popovich, O.V. Kovalchuk, *Theory of Automatic Control* (Lybid, Kiev, 1997), p. 544 (in Ukrainian)
31. Bruel and Kjer, *Piezoelectric Accelerometers and Preamplifiers* (Larsen and Son, Glostrup, 1987), p. 186
32. V.M. Sharapov, M.P. Musienko et al., *Piezoelectric Transducer (Handbook)*, ed. by V.M. Sharapov (Cherkasy State Technological University, Cherkasy, 2004), p. 435 (in Russian)
33. V.M. Sharapov, M.P. Musienko, Detection of conditions to increase the accuracy of piezotransducers with two feedback circuits. *Bull. Cherkasy State Technol. Univ.* **1** (2005) (in Russian)
34. A.P. Evtyukov, A.E. Kolesnikov, E.A. Korepin et al., *Directory on Hydroacoustics* (Sudostroenie, Leningrad, 1988), p. 552 (in Russian)
35. S.P. Strelkov, *Introduction to Vibration Theory* (Nauka, Moscow, 1964), p. 436 (in Russian)
36. N.A. Babakov, A.A. Voronov, A.A. Voronova et al., *Theory of Automatic Control: Textbook on Speciality "Automatics and Telemechanics". Theory of Linear Automatic Control Systems*, ed. by A.A. Voronov (Vyssh. Shk., Moscow, 1986), p. 367 (in Russian)
37. P. Hemmong, *Feedback Theory and Its Application* (Svyaz, Moscow, 1940) (in Russian)
38. G.S. Tsykin, *Negative Feedback and Its Applications* (Svayz, Moscow, 1940), p. 348 (in Russian)
39. V.M. Sharapov et al., Amplitude–frequency characteristics linearization of piezoelectric transducers with monomorph or bimorph sensitive element. *Bull. Cherkasy State Technol. Univ.* **1**, 41–45 (2002) (in Russian)
40. V.M. Sharapov et al., Expansion of frequency range in piezoceramic transducers with feedback. *Bull. Cherkasy State Technol. Univ.* **2**, 80–83 (2002) (in Russian)
41. V.M. Sharapov et al., Electromechanical feedback in piezoelectric transducers. *Visnik ChITI*, No. 1, 63–69 (2000) (in Russian)
42. V.M. Sharapov et al., Domain-dissipative piezoceramic transducers. Materials of XII international Scientific and Technical Conference "Priborostroenie-2003", Vinnitsa-Koreiz, p. 5–8 (2003) (in Russian)
43. V.M. Sharapov et al., Study of domain-dissipative piezoceramic transducers. *Bull. Cherkasy State Technol. Univ.* **2**, 17–22 (2003)
44. V.M. Sharapov et al., *Theory of Automatic Control* (Cherkasy State Technological University, Cherkasy, 2005), p. 200 (in Russian)
45. V.M. Sharapov et al., Domain-dissipative piezoceramic transducers. Materials of XII International Scientific and Technical Conference "Sensors-2004", Moscow, p. 37–38 (2004) (in Russian)
46. V.M. Sharapov et al., Piezoceramic transducers with two circuits of spatial electromechanical negative feedback. *Bull. Cherkasy State Technol. Univ.* **1** (2005) (in Russian)
47. V.M. Sharapov et al., Domain-dissipative piezoceramic transducers with feedback. *Bull. Cherkasy State Technol. Univ.* **1**, 74–79 (2004) (in Russian)
48. V.M. Sharapov et al., Study of symmetric coplanar trimorph piezoceramic transducers with feedback. *Bull. Cherkasy State Technol. Univ.* **2**, 33–38 (2001) (in Russian)
49. V.M. Sharapov et al., Feedback in piezoelectric transducers of mechanical values. *Research and Computer Facilities in Technological Processes*, No. 2, p. 64–67 (1999) (in Russian)
50. V.M. Sharapov et al., Piezoelectric transducers with a piezoelement in feedback circuit of voltage amplifier. *Bull. Cherkasy State Technol. Univ.* **2**, 132–136 (2004) (in Russian)

51. V.M. Sharapov et al., Study of domain-dissipative piezoceramic transducers with feedback. Vesnik ONPU, Odessa (2004) (in Russian)
52. V.M. Sharapov et al., Accuracy increase of piezosensors with two circuits of spatial electromechanical negative feedback. Bull. Cherkasy State Technol. Univ. **2** (2005) (in Russian)
53. V.M. Sharapov et al., Piezoelectric transducers with combined feedback. Bull. Cherkasy State Technol. Univ. **2** (2005) (in Russian)

# Chapter 6

## Bimorph and Trimorph Piezoelements

Bimorph piezoelements consist of two parts – two interconnected piezoelements or a piezoelement and a metal plate, soldered or glued to each other by epoxy compound [39, 43].

Bimorph elements consisting of two piezoelements are named symmetric [43]. Bimorph elements consisting of a piezoelement and a metal plate are named asymmetric [22].

Elements consisting of two piezoelements and a metal plate are called trimorph [44].

It is necessary to note that joining of two piezoelements or a piezoelement and a metal plate in one design leads to essential change of sensor characteristics. For example, the minimal resonant frequency of a IITC-19 piezoceramic piezoelement (30 mm in diameter and 0.3 mm thick) is  $\sim 70$  kHz (radial vibrations). Its sensitivity to the sound field at the frequency of 100 Hz is  $\sim 1$  mV/Pa, for example. Joining of these two piezoelements in a symmetric bimorph leads to the occurrence of resonant frequencies  $\sim 2.5$  and 3.5 kHz (flexural vibrations). Its sensitivity increases to 20–30 mV/Pa under the same conditions. Thus, it increases not two, but 20–30 times.

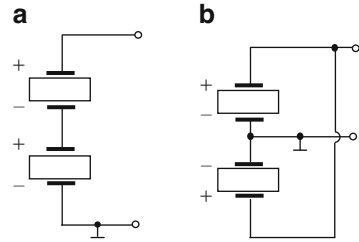
At the same time, joining of piezoceramic and metal (amorphous) plates in an asymmetric bimorph increases sensitivity by 10–20 times.

### 6.1 Symmetric Bimorph Piezoelements

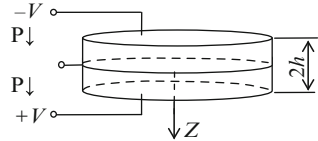
Two schemes of piezoelements communication are known: series and parallel (Fig. 6.1a, b, respectively) [24].

Traditionally, these transducers are made of identical-dimensioned plates. Their thickness is also identical. This is very important (Fig. 6.2). This assures maximal sensitivity. However, it is necessary to note whether dimensions of piezoelements are identical: the sensitivity of the voltage sensor in a parallel circuit and its own resistance is four times smaller than the corresponding characteristics of the sensor in a series communication circuit [39, 40].

**Fig. 6.1** Communication diagrams of piezoelements in symmetric bimorph transducers: (a) series, (b) parallel



**Fig. 6.2** Symmetric bimorph transducer with identically thick piezoelements



Electric transformation of energy, occurring when piezoceramic elements are deformed, substantially depends on coordination between the deformation type and the direction of initial polarization vector (see Chap. 3).

Static electromechanical coupling coefficients (EMCC) are a quantitative effectiveness measure of the homogeneous deformation coordination mentioned above. Homogeneous planar deformation occurs in the electric field of the single-layered plate, polarized along its thickness. Static EMCC  $C_P$  for this deformation type is a table value. It has different values for various compositions of piezoceramics (see Chap. 1).

Dynamic (effective) EMCC is introduced to consider the efficiency of electromechanical energy transformation under oscillatory deformations. It is calculated by simple formulas [18] for homogeneous deformation. For inhomogeneous deformation, the effective EMCC is found by the solution of the electroelasticity boundary-value problem, and with the help of “energetic theory” [27].

The bimorph plate deformation is generally flexural. However, it is synthesized from two opposed planar (homogeneous) rigidly connected single-layer (monomorph) plates. It is proposed in [21] that the effective EMCC value of round bimorph flexural vibrations  $K_D$  should be evaluated. The bimorph consists of identically thick plates in comparison with the static EMCC value of each plate planar deformation  $C_P$ . This should also be compared with the effective EMCC theoretical value of the bimorph element. This value is found in accordance with “energetic theory” [18].

The analysis of vibrations and effective EMCC expression for a symmetric bimorph piezoelement are shown in [21, 39, 45].

The flexural vibration problem of a round bimorph plate with radius  $r = a$  under the action of mechanical force, changing according to harmonious law, is considered. Voltages  $U_1$  and  $U_2$  of the same frequency occurred on the piezoelement electrodes.

The flexural vibration equation of the piezoceramic plate, relative to inflection function of middle surface, looks like this [47]:

$$\nabla^2 \nabla^2 W + \frac{\rho h}{\tilde{D}} \frac{\partial^2 W}{\partial t^2} = \frac{q}{\tilde{D}}, \quad (6.1)$$

where  $\tilde{D} = h^3/12S_{11}^E(1 - \tilde{\nu}^2) \left[ 1 + (1 + \nu/8) \left( K_p^2/1 - K_p^2 \right) \right]$  – rigidity under cylindrical bending of piezoceramic plate;  $\tilde{\nu} = \left\{ \nu + [(1 + \nu)/8] \left[ K_p^2 / (1 - K_p^2) \right] \right\} / \left\{ 1 + [(1 + \nu)/8] \left[ K_p^2 / (1 - K_p^2) \right] \right\}$  – reduced Poisson coefficient;  $K_p^2 = [2/(1 - \nu)] (d_{31}^2/S_{11}^E \varepsilon_{33}^T)$  – static planar EMCC;  $q$  – lateral distributed load;  $W(x, y, z)$  – inflection function;  $h$  – thickness of the plates;  $\rho$  – density of plates material.

The solution of this equation for a bimorph round plate looks like this [26]: with open electrodes:

$$A_{\text{OPEN}} = \frac{1}{2} \pi \beta^2 \tilde{D} \left( (\beta a)^2 \left\{ [AJ_1(\beta a) - BI_1(\beta a)]^2 + [AJ_1(\beta a) - BI_1(\beta a)]^2 \right\} \right), \quad (6.2)$$

with short-circuited electrodes:

$$A_{\text{SH-CIR}} = \frac{1}{2} \pi \beta^2 \tilde{D} \left( (\beta a)^2 \left\{ [AJ_0(\beta a) - BI_0(\beta a)]^2 + [AJ_1(\beta a) - BI_1(\beta a)]^2 \right\} \right). \quad (6.3)$$

Then the effective EMCC expression  $C_D$  will look like this:

where  $U_{\text{OPEN}}$  – the energy reserved in a plate at bends in case of opened electrodes;

$$K_D^2 = \frac{12 \frac{\tilde{\nu} - \nu}{1 - \tilde{\nu}} [AJ_1(\beta a) - BI_1(\beta a)]^2}{(\beta a)^2 \left\{ [AJ_0(\beta a) - BI_0(\beta a)]^2 + [AJ_1(\beta a) - BI_1(\beta a)]^2 \right\} - 2(1 - \tilde{\nu}) [AJ_1(\beta a) - BI_1(\beta a)]^2 + 12 \frac{\tilde{\nu} - \nu}{1 - \tilde{\nu}} [AJ_1(\beta a) - BI_1(\beta a)]^2}, \quad (6.4)$$

where  $U_{\text{OPEN}}$  – plate energy while bending when the electrodes are open;  $\beta = \sqrt[4]{\rho \omega^2 h / \tilde{D}}$  – coefficient, introduced to simplify the calculations;  $a = r$  – radius of the bimorph plates;

$$A = -\frac{h^2}{4} \frac{d_{31} a}{S_{11}^E (1 - \nu)} \frac{1}{\beta \tilde{D}} \left( \frac{V_0}{h} \right) \frac{I_1(\beta a)}{\Delta} \quad \text{and} \quad B = -A \frac{J_1(\beta a)}{I_1(\beta a)} \quad \text{– constants, with}$$

$J_1(z) = -(dJ_0/dz)$ ;  $I_1(z) = dI_0/dz$ ;  $J_0(\beta r)$  constants, with  $I_0(\beta r)$  – Bessel functions.

These are the values for piezoceramics IITC-19 composition:  $\nu = 0.33$ ;  $K_p^2 = (0.58)^2 = 0.34$ .

To compare the effective EMCC value for flexural (inhomogeneous) deformations with the value of static planar EMCC  $C_p^2$  one should proceed from vibrations to static deformations, i.e., consider  $C_D^2$  when vibrations frequency tends to zero. Then

$$\lim_{\beta a \rightarrow 0} K_D^2 = 0,252 \approx \frac{3}{4} K_p^2. \tag{6.5}$$

This result conforms to the EMCC theoretical value for inhomogeneous deformation of the bimorph element shown in [18]:

$$K^2 = \frac{A_{OPEN} - A_{SH-CIR}}{A_{OPEN}} = \frac{3}{4} K_p^2 = 0.255. \tag{6.6}$$

The constant values for IITC-19 piezoceramics are:

$$S_{11}^E = 12.3 \times 10^{-12} \text{ m}^2/\text{N}, \quad \varepsilon_{33}^T = 1,300 \times 8.85 \times 10^{-12} \text{ F/m},$$

$$d_{31} = -5.2 \text{ Kl/m}^2 \text{ respectively.}$$

Then after numerical search [21] of the first three  $\omega_a$  and  $\omega_r$  values, corresponding to roots of antiresonance and resonance equations (first three main vibration modes), when  $\beta a$  changes with a 0.1 step over a 0–10 interval, the corresponding values are found by Mason formula  $K_D^2$ :  $K_{D1}^2 = 0.23$ ,  $K_{D2}^2 = 0.12$ ,  $K_{D3}^2 = 0.06$ .

Accuracy increases and AFC linearization of symmetric bimorph transducers can be reached by introduction of negative electromechanical feedback.

In this case, FB is introduced by a bimorph piezoelement or by an additional electrode on a piezoelement.

Some variants of FB introduction circuits in symmetric bimorph are shown in Fig. 6.3. Their block diagram is presented in Fig. 6.4.

Here, transformation of force  $F$ , influencing the piezoelement, into stress  $\sigma_1$  and  $\sigma_2$  corresponds to elements with transfer coefficient  $W_1(p)$  and  $W_5(p)$ ;

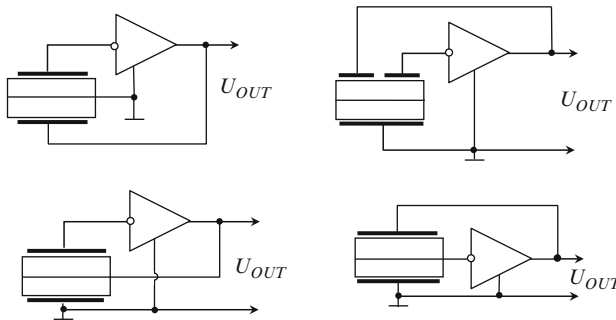
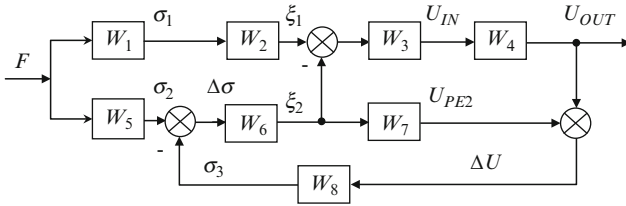
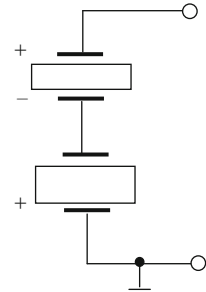


Fig. 6.3 Bimorph piezotransducers with FB



**Fig. 6.4** Block diagram of bimorph piezotransducers with FB

**Fig. 6.5** Electrical circuit of symmetric bimorph sensor



transformation of stresses into  $\xi_1$  and  $\xi_2$  deformations to elements  $W_2(p)$  and  $W_6(p)$ ; deformation transformation into pressure  $U_{PE1}$  and  $U_{PE2}$  on electrodes of piezoelements  $PE1$  and  $PE2$  to elements  $W_3(p)$  and  $W_7(p)$  [ $W_4(p)$  is transformation of pressure  $U_{PE1}$  into voltage  $U_{OUT}$  on the voltage amplifier output]. An FB element is characterized by transfer coefficient  $\beta(p)$  of amplifier output voltage  $U_{OUT}$  into stress  $\sigma_3$ . Amplifier phase displacement and polarization direction of piezoelements are selected for the stress sign created by voltage, to be opposite to the stress sign created by force  $F$ .

The sensor transfer characteristic looks like this [39, 45]:

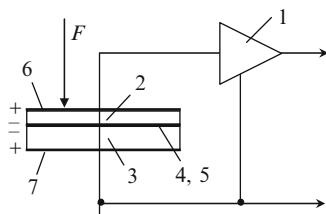
$$\begin{aligned}
 W_{FB}(p) = & \frac{W_1(p)W_2(p)W_3(p)W_4(p) - W_3(p)W_4(p)W_5(p)W_6(p)}{1 - W_3(p)W_4(p)W_6(p)W_8(p) - W_6(p)W_7(p)W_8(p)} \\
 & - \frac{W_1(p)W_2(p)W_3(p)W_4(p)W_6(p)W_7(p)W_8(p)}{1 - W_3(p)W_4(p)W_6(p)W_8(p) - W_6(p)W_7(p)W_8(p)}.
 \end{aligned}
 \tag{6.7}$$

There is another method of reaching AFC linearization [33, 40].

It is proposed that a bimorph with piezoelements of different thickness should be used for this purpose (Fig. 6.5).

Total (general) sensitivity of a bimorph transducer equals zero for series circuit and opposite communication if sensitivities of separate elements are equal. If piezoelements have different thicknesses and sensitivities, then the bimorph transducer sensitivity will be equal to the difference of separate element = sensitivities. Then the AFC of this transducer can become linear [33, 40].

**Fig. 6.6** Electrical circuit of sensor: 1 – preamplifier; 2, 3 – piezoelements; 4, 6 – electrodes of piezoelement 2; 5, 7 – electrodes of piezoelement 3



A symmetric bimorph sensor was experimentally studied. It consists of two ПТC-19 piezoceramic piezoelements 30 mm in diameter, 0.3 mm and 0.8 mm thick respectively. A voltage amplifier, assembled using microcircuit К140У Д8, was used. The sensor circuit is represented in Fig. 6.6.

Piezoelements were interconnected mechanically by epoxy glue and electrical homopolar electrodes (Fig. 6.6).

The sensor was put in an acoustic chamber with sound pressure 10 Pa in the frequency range 20–5,000 Hz.

Mechanical action  $F$  created voltage on piezoelements which was amplified. As the piezoelement thicknesses were different, the voltage on them was also different. The thinner the piezoelement is, the higher the voltage. As a result, difference voltage arrived to the amplifier input. This difference in voltage under  $F$  fixed action appeared to be practically constant at any frequency. Thus, the transducer AFC became linear.

As the experiments showed [33], this effect is observed if piezoelement thicknesses are selected from this correlation:

$$0.4 < \delta_1/\delta_2 < 0.8. \quad (6.8)$$

AFC measurement results of this sensor are shown in Fig. 6.7. As can be seen from Fig. 6.7, the linearity of the proposed bimorph sensor AFC increased.

Piezoelements of different piezomaterials can be used for AFC linearization of a symmetric bimorph with opposite-connected identically thick piezoelements of identical diameter. For example, one can be of ПТC-19 piezoceramic (with piezomodule  $d_{31} = 120$  pC/N), and the other of ПТБC-1 ( $d_{31} = 220$  pC/N).

The AFC of this sensor became more linear too [39].

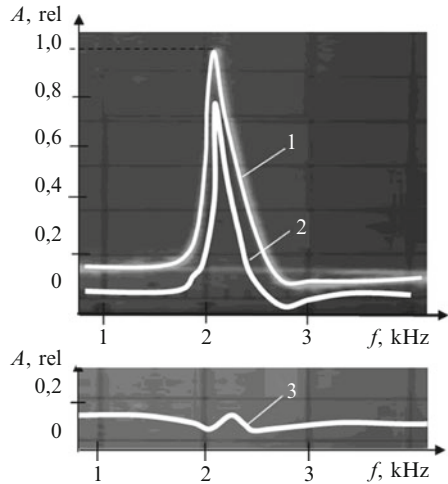
## 6.2 Asymmetric Bimorph Piezoelements

Asymmetric bimorph piezoelements are more mechanically durable. They consist of a metal plate and a flat piezoelement, polarized along its thickness.

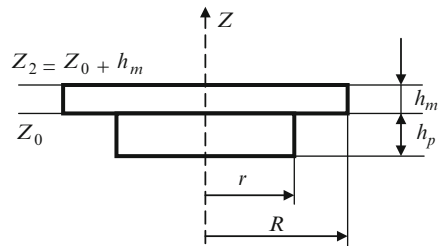
Idle sensitivity is an important characteristic of sensors working in reception/radiation mode [22, 37, 39]. A mathematical model of this transducer type



**Fig. 6.7** AFC of symmetric bimorph sensor: 1 – piezoelement 0.3 mm thick; 2 – piezoelement 0.8 mm thick; 3 – bimorph sensor



**Fig. 6.8** Asymmetric bimorph piezosensor



should be constructed to estimate the sensitivity and other dynamic characteristics of bimorph pressure sensors.

A sensor, consisting of round metal plates glued to each other and thickness-polarized piezoceramic plates with radius  $R$  and  $r$  respectively, is considered (Fig. 6.8). Their thicknesses are denoted as  $h_m$  and  $h_p$  respectively. A cylindrical system of coordinates  $r, \theta$  and  $z$  is used. Its axis  $OZ$  coincides with a two-layer disk axis.  $z = 0$  relative to the reduction surface. Its position is determined lower. Coordinates of interface (separation surface), piezoelement lower surface and metal plate top surface are denoted as  $z_0, z_1 = z_0 - h_p$ , and  $z_2 = z_0 + h_m$  respectively.

Potential difference  $U_x e^{j\omega t}$  is generated on open piezoelement electrodes under the harmonious load (sound pressure) influence  $pe^{j\omega t}$  ( $p = \text{const}$ ), normally applied to the flat surface of the metal plate. The thickness of electrodes covering flat surfaces of the piezoceramic disk and glued joint between the plates is neglected. The mathematical model of this transducer was constructed by A.N. Shulga and other scientists [39, 40, 46]. Kinematic hypotheses are used to construct a mathematical axially symmetric model of asymmetric bimorph vibrations.

$$u_r(r, z) = u(r) + z\psi(r); \quad u_z(r, z) = \varpi(r). \tag{6.9}$$

Here,  $u$  and  $\varpi$  are the tangential and normal displacement of initial surface respectively, and  $\psi$  is the rotation angle of the normal; time factor (multiplier)  $e^{i\omega t}$  is always omitted. These are the expressions for deformation tensor components:

$$e_{rr} = \varepsilon_r + z\chi_r; \quad e_{\theta\theta} = \varepsilon_\theta + z\chi_\theta; \quad e_{rz} = \varepsilon_{rz}; \quad e_{zz} = 0, \quad (6.10)$$

in which:

$$\varepsilon_r = \frac{du}{dr}; \quad \varepsilon_\theta = \frac{u}{r}; \quad \chi_r = \frac{d\psi}{dr}; \quad \chi_\theta = \frac{\psi}{r}; \quad 2\varepsilon_{rz} = \frac{d\varpi}{dr} + \psi. \quad (6.11)$$

Hypotheses (6.9) mastering the law of movement variation along the two-layer plate thickness are expanded by the hypothesis of electric potential change along the piezoceramic disk thickness. Quadratic approximation is used as this hypothesis. It was used in the theory of homogeneous cover piezoceramic [36] with electrodes on lateral surfaces

$$\varphi(r, \bar{z}) = \frac{U_x}{h_p} \bar{z} + \frac{3}{2} \left( 1 - \frac{4\bar{z}^2}{h_p^2} \right) \Phi(r). \quad (6.12)$$

Here  $U_x$  is the amplitude of an unknown potential difference on the open electrodes. In expression (6.12),  $\bar{z}$  is the co-ordinate, calculated from the middle surface of the piezoceramic disk. The distance between this surface and the initial bimorph surface is denoted as  $b = z_0 - (h_p/2)$ . Formula (6.12) is rewritten in the system of coordinates. The latter is normally connected with the initial surface:

$$\varphi(r, \bar{z}) = \frac{U_x}{h_p} (z - b) + \frac{3}{2} \left( 1 - \frac{4(z - b)^2}{h_p^2} \right) \Phi(r). \quad (6.13)$$

So these are the expressions for components of the electric field intensity vector in the piezoceramic disk:

$$E_r(r, z) = f(z)E_r^{(0)}(r); \quad E_z(r, z) = E_z^{(0)}(r) + (z - b)E_z^{(1)}(r);$$

$$f(z) = \frac{3}{2} \left[ 1 - \frac{4(z - b)^2}{h_p^2} \right], \quad (6.14)$$

in which:

$$E_r^{(0)} = -\frac{d\Phi}{dr}; \quad E_z^{(0)} = -\frac{V_x}{h_p}; \quad E_z^{(1)} = -\frac{12}{h_p^2}\Phi. \quad (6.15)$$

The generalized Hamilton principle is applied for derivation of vibrations, electrostatics and natural boundary conditions equations [48]. With regard to axially symmetric bimorph stationary vibrations, we will start with the functional stationarity condition

$$\delta_{u_p u_z \phi} \left\{ \int_0^R \int_{z_1}^{z_2} (\sigma_{rr} e_{rr} + \sigma_{\theta\theta} e_{\theta\theta} + \sigma_{zz} e_{zz} + 2\sigma_{rz} e_{rz}) r dr dz - \int_0^R \int_{z_1}^{z_0} (D_r E_r + D_z E_z) r dr dz - \frac{\omega^2}{2} \int_0^R \int_{z_1}^{z_2} \rho(z) \{u_r^2 + u_z^2\} r dr dz - \int_0^R p u_z r dr \right\} = 0. \quad (6.16)$$

Here  $\rho(z)$  is the piecewise constant function of density. The densities of ceramic and metal plates are denoted as  $\rho_p$  and  $\rho_m$  respectively.

After consideration of intense condition integrated characteristics of the two-layer plate:

$$N_r(\theta) = \int_{z_1}^{z_2} \sigma_{rr}(\theta) dz; \quad M_r(\theta) = \int_{z_1}^{z_2} \sigma_{rr}(\theta) z dz; \quad Q_r = \int_{z_1}^{z_2} \sigma_{rz} dz, \quad (6.17)$$

and electric condition of the piezoceramic plate:

$$\hat{D}_r = \int_{z_1}^{z_0} D_r f(z) dz; \quad \hat{D}_z^{(0)} = \int_{z_1}^{z_0} D_z dz; \quad \hat{D}_z^{(1)} = \frac{12}{h_p^2} \int_{z_1}^{z_0} D_r (z - b) dz, \quad (6.18)$$

with regard to dependences (6.10) and (6.11), variation equation (6.16) can be rearranged like this:

$$\int_0^R \left\{ N_r \delta \varepsilon_r + N_\theta \delta \varepsilon_\theta + M_r \delta \chi_r + M_\theta \delta \chi_\theta + 2Q_r \delta \varepsilon_{rz} - \hat{D}_r \delta E_r^{(0)} - \hat{D}_z^{(0)} \delta E_z^{(0)} - \frac{h_p^2}{12} \hat{D}_z^{(1)} \delta E_z^{(1)} - \omega^2 [\rho_1 (u \delta u + \varpi \delta \varpi) + \bar{\rho} (u \delta \psi + \psi \delta u) + \rho_2 \psi \delta \psi] - p \delta \varpi \right\} r dr = 0, \quad (6.19)$$

where  $\rho_1 = \rho_p h_p + \rho_m h_m$ ;  $\rho_2 = \rho_p \frac{z_0^3 - z_1^3}{2} + \rho_m \frac{z_2^3 - z_0^3}{2}$ ;  $\bar{\rho} = \rho_p \frac{z_0^2 - z_1^2}{2} + \rho_m \frac{z_2^2 - z_0^2}{2}$ .

Vibration equations follow from variation equation (6.19) where independent variations  $\delta u$ ,  $\delta \varpi$ ,  $\delta \psi$ ,  $\delta \Phi$  and  $\delta U_x$  are considered:

$$\begin{aligned} \frac{dN_r}{dr} + \frac{1}{r} (N_r - N_\theta) + \rho_1 \omega^2 u + \bar{\rho} \omega^2 \psi &= 0; & \frac{dQ_r}{dr} + \frac{1}{r} Q_r + \rho_1 \omega^2 \varpi + p &= 0; \\ \frac{dM_r}{dr} + \frac{1}{r} (M_r - M_\theta) - Q_r + \rho_2 \omega^2 \psi + \bar{\rho} \omega^2 u &= 0, \end{aligned} \quad (6.20)$$

electrostatics equation:

$$\frac{d}{dr} \left( r \hat{D}_r \right) - r \hat{D}_z^{(1)} = 0, \quad (6.21)$$

integral relation:

$$\int_0^R \hat{D}_z^{(0)} r \, dr = 0. \quad (6.22)$$

The fact that displacement current equals zero is the physical sense of condition (6.22). It is accurate within multiplier  $2\pi i\omega$  through the middle piezoelement surface. This integral relation is an additional requirement for unambiguous determination of potential difference on equipotential surfaces of the piezoceramic disk.

Natural boundary conditions follow from the equality:

$$\left[ N_r \delta u + M_r \delta \psi + Q_r \delta w + \hat{D} \delta \Phi \right]_{r=0}^{r=R} = 0,$$

which follows from (6.19).

Electroelasticity ratios of an asymmetric bimorph are obtained by integration, using formulas (6.17) and (6.18) of three-dimensional state equations, simplified according to assumptions of the thin plate theory. Forces and moments are written in the following way:

$$\begin{aligned} N_r &= C_1 \varepsilon_r + C_2 \varepsilon_\theta + B_1 \chi_r + B_2 \chi_\theta - N_{EL}; \\ N_\theta &= C_2 \varepsilon_r + C_1 \varepsilon_\theta + B_2 \chi_r + B_1 \chi_\theta - N_{EL}; \\ M_r &= B_1 \varepsilon_r + B_2 \varepsilon_\theta + D_1 \chi_r + D_2 \chi_\theta - M_{EL}; \\ M_\theta &= B_2 \varepsilon_r + B_1 \varepsilon_\theta + D_2 \chi_r + D_1 \chi_\theta - M_{EL}. \end{aligned} \quad (6.23)$$

Rigid characteristics and the electric components  $N_{EL}$  and  $M_{EL}$  from correlations (6.23) are determined by the equalities:

$$N_{EL} = \frac{d_{31}}{S_{11}^p (1 - \nu_p)} \int_{z_1}^{z_0} E_z \, dz; \quad M_{EL} = \frac{d_{31}}{S_{11}^p (1 - \nu_p)} \int_{z_1}^{z_0} E_z z \, dz; \quad (6.24)$$

$$\begin{aligned} C_1 &= h_p c_{11}^p + h_m c_{11}^m; \quad C_2 = h_p \nu_p c_{11}^p + h_m \nu_m c_{11}^m; \\ B_1 &= \frac{z_0^2 - z_1^2}{2} c_{11}^p + \frac{z_2^2 - z_0^2}{2} c_{11}^m; \quad B_2 = \frac{z_0^2 - z_1^2}{2} c_{11}^p \nu_p + \frac{z_2^2 - z_0^2}{2} \nu_m c_{11}^m; \\ D_1 &= \frac{z_0^3 - z_1^3}{3} c_{11}^p + \frac{z_2^3 - z_0^3}{3} c_{11}^m; \quad D_2 = \frac{z_0^3 - z_1^3}{3} \nu_p c_{11}^p + \frac{z_2^3 - z_0^3}{3} \nu_m c_{11}^m. \end{aligned} \quad (6.25)$$

In equalities (6.24)  $d_{31}$  is a piezomodule;  $s_{11}^p$  and  $\nu_p$  are the compliance and Poisson coefficients of the piezoceramic disk. These are the notations, introduced

to equalities (6.25):

$$c_{11}^p = \frac{1}{s_{11}^p (1 - \nu_p^2)} \quad \text{and} \quad c_{11}^m = \frac{1}{s_{11}^m (1 - \nu_m^2)}.$$

In the theory of homogeneous elastic (electroelastic) plates and covers, the simplest connection of forces and moments with middle surface deformations is established by selection of the middle surface, used as the reduction surface. The forces depend only on tangential, and the moments only on flexural deformations [27]. Correlations (6.23) give a more complicated connection between the specified characteristics of the stressed and deformed states. This additional connection (coupling) from the homogeneous plates view point is fulfilled by rigid characteristics  $B_1$  and  $B_2$ . The expression analysis for these characteristics shows that if Poisson coefficients of both plates are considered equal, conditions  $B_1 = B_2 = 0$  are met by the corresponding choice of the initial surface. Then dependences (6.23) will be as simple as for the homogeneous problem. This simplification is reached only if Poisson coefficients of layer material are equal [16].

The position of reduction surface is determined from conditions  $B_1 = B_2 = 0$  (with  $\nu_p = \nu_m$ ) by the dependences:

$$z_0 = h_p \gamma_0; \quad z_1 = h_p (\gamma_0 - 1); \quad z_2 = h_p (\gamma_0 + \beta); \quad \gamma_0 = \frac{1}{2} \frac{\alpha - \beta^2}{\alpha + \beta}, \quad (6.26)$$

in which  $\alpha = s_{11}^m / s_{11}^p$  and  $\beta = h_m / h_p$ .

Special case  $\beta = 0$  ( $h_p \neq 0$ ) corresponds to the single-layer piezoceramic plate with middle initial surface. In the case  $\alpha = 1$  ( $\beta \neq 0$ ), the initial surface coincides with the middle surface of the two-layer package.

Thus, under condition  $\nu_m = \nu_p = \nu$ , material correlations for bimorph can be written like this:

$$\begin{aligned} N_r &= C_{11} (\varepsilon_r + \nu \varepsilon_\theta) - e_{31} h_p E_z^{(0)}; \quad N_\theta = C_{11} (\nu \varepsilon_r + \varepsilon_\theta) - e_{31} h_p E_z^{(0)}, \\ M_r &= D_{11} (\chi_r + \nu \chi_\theta) - e_{31} h_p^2 \left[ E_z^{(0)} \left( \gamma_0 - \frac{1}{2} \right) + \frac{h_p}{12} E_z^{(1)} \right]; \\ M_\theta &= D_{11} (\nu \chi_r + \chi_\theta) - e_{31} h_p^2 \left[ E_z^{(0)} \left( \gamma_0 - \frac{1}{2} \right) + \frac{h_p}{12} E_z^{(1)} \right]; \\ Q_r &= C_{44} 2 \varepsilon_{rz} - e_{15} h_p E_r^{(0)}; \quad \hat{D}_r = \varepsilon_{11} h_p E_r^{(0)} - e_{15} h_p 2 \varepsilon_{rz}; \\ \hat{D}_z^{(0)} &= \varepsilon_{33} h_p E_z^{(0)} + e_{31} h_p (\varepsilon_r + \varepsilon_\theta) + e_{31} h_p^2 \left( \gamma_0 - \frac{1}{2} \right) (\chi_r + \chi_\theta); \\ \hat{D}_z^{(1)} &= \varepsilon_{33} h_p E_z^{(1)} + e_{31} h_p (\chi_r + \chi_\theta). \end{aligned} \quad (6.27)$$

These notations are proposed:

$$\begin{aligned}
 C_{11} &= \frac{h_p}{s_{11}^p(1-\nu^2)} \left(1 + \frac{\beta}{\alpha}\right); & C_{44} &= \frac{h_p}{s_{44}^p} \left(1 + \frac{\beta}{\alpha}\right); & e_{31} &= \frac{d_{31}}{s_{11}^p(1-\nu)}; \\
 e_{15} &= \frac{d_{15}}{s_{44}^p}; & D_{11} &= \frac{h_p^3}{s_{11}^p(1-\nu^2)} \left(\gamma_0^3 - \gamma_1^3 + \frac{\gamma_2^3 - \gamma_1^3}{\alpha}\right); \\
 \varepsilon_{33} &= \varepsilon_{33}^T (1 - K_p^2); & \varepsilon_{11} &= \varepsilon_{11}^T (1 - K_{15}^2),
 \end{aligned} \tag{6.28}$$

in which:  $s_{11}^p$ ,  $s_{44}^p$  – compliances if electric field is constant;  $d_{31}$ ,  $d_{15}$  – piezomodules;  $\varepsilon_{11}^T$ ,  $\varepsilon_{33}^T$  – dielectric permeability under constant voltage;  $K_p$ ,  $K_{15}$  – planar and shear factors of electromechanical coupling.

Vibration (6.20) and electrostatics (6.27) equations, dependences (6.11), (6.14), material correlations (6.27) and integral condition (6.22) are a closed equation system of axially symmetric bimorph transducer vibrations. The transducer type is metal – piezoceramics with decreased shear rigidity of layers.

The simplified variant of the equations represented above should be used to evaluate dynamic characteristics of a thin bimorph with a high shear rigidity of layers.

The Kirchhoff–Love model is considered below. It is assumed that lateral shear deformation equals zero ( $\varepsilon_{rz} = 0$ ) and shear rigidity is infinite ( $C_{44} = \infty$ ). Overcut force, reaching its final value in the limit, can be determined from the third equation of the system (6.20). Inertial members are not considered. The rotation angle of the normal is dependent. It is connected with the inflection by equality  $\psi = -d\varpi/dr$ .

The equation is further simplified, assuming that:

$$\hat{D}_z^{(1)} = 0. \tag{6.29}$$

From the obvious equality:

$$D_z(r, z) = \frac{1}{h_p} \hat{D}_z^{(0)}(r) + \frac{z-b}{h_p} \hat{D}_z^{(1)}(r)$$

It is clear that acceptance of additional restriction (6.29) indicates the transition to a more rigid hypothesis [14]. It is about normal component constancy of electric induction vector along the piezoelement thickness. Using equality (6.29) in (6.27), linear correction of electric field  $E_z^{(1)}$  intensity can be carried out by curvature change parameters of the initial surface:

$$E_z^{(1)} = -\frac{1}{2d_{31}} \frac{K_p^2}{1 - K_p^2} (\chi_r + \chi_\theta),$$

and to exclude it from equations in this way (6.27). The electrostatics equation (6.21), considering (6.29), becomes simpler ( $\bar{D}_r = \text{const}/r$ ) and, obviously, is satisfied if there are no charges on the cylindrical surface of the piezoceramic disk.

Simplifications connected with transition to more rigid mechanical and electric hypotheses lead to a simpler electromechanical model and a smaller number of the unknown. The rotation angle and function  $F$  are now functions of the initial surface inflection.

Material correlations (6.27), simplified according to the discussed above ideas and by use of these correlations (6.10) and (6.15), can be written in the form of equalities:

$$\begin{aligned} N_r &= C_{11} \left( \frac{du}{dr} + \nu \frac{u}{r} \right) + e_{31} U_x; & N_\theta &= C_{11} \left( \nu \frac{du}{dr} + \frac{u}{r} \right) + e_{31} U_x; \\ M_r &= -\bar{D}_{11} \left( \frac{d^2 \varpi}{dr^2} + \bar{\nu} \frac{1}{r} \frac{d\varpi}{dr} \right) + e_{31} h_p \left( \gamma_0 - \frac{1}{2} \right) U_x, \\ M_\theta &= -\bar{D}_{11} \left( \bar{\nu} \frac{d^2 \varpi}{dr^2} + \frac{1}{r} \frac{d\varpi}{dr} \right) + e_{31} h_p \left( \gamma_0 - \frac{1}{2} \right) U_x; \\ \hat{D}_z^{(0)} &= -\varepsilon_{33} U_x + e_{31} h_p \left[ \left( \frac{du}{dr} + \frac{u}{r} \right) - h_p \left( \gamma_0 - \frac{1}{2} \right) \left( \frac{d^2 \varpi}{dr^2} + \frac{1}{r} \frac{d\varpi}{dr} \right) \right]. \end{aligned} \quad (6.30)$$

There are reduced flexural rigidity and Poisson coefficient in the ratios for the moments

$$\bar{D}_{11} = \frac{h_p^3}{S_{11}^p (1 - \nu^2)} d; \quad \bar{\nu} = \frac{8g\nu + K}{8g + K},$$

where

$$d = \frac{8g + K}{24}; \quad K = \frac{(1 + \nu)K_p^2}{1 - K_p^2}; \quad g = \gamma_0^3 - \gamma_1^3 + \frac{\gamma_2^3 - \gamma_1^3}{\alpha}.$$

The expression for unknown potential difference can be found from this integral condition (6.30), in which (6.37) is substituted. The result after integration is

$$U_x = \frac{1}{d_{31}} \frac{K_p^2}{1 - K_p^2} \frac{h_p}{R} \left[ u(R) - h_p \left( \gamma_0 - \frac{1}{2} \right) \varpi'(R) \right]. \quad (6.32)$$

Thus, the output potential difference is expressed by tangential displacement values of the initial surface and the rotation angle on the plate edge ( $r = R$ ). Evidently, if the edge is built in (rigidly fastened) there is no potential difference.

Substituting correlations (6.30) in system (6.20), the vibration equations in movements are obtained. Small inertial members of squared/cubed bimorph thickness are not considered.

$$\Delta u + \left( \lambda^2 - \frac{1}{x^2} \right) u = 0, \quad (6.33)$$

$$\Delta \Delta \varpi - \mu^4 \varpi = q. \quad (6.34)$$

The following notations are introduced:

$$\text{Operator } \Delta = \frac{d^2}{dx^2} + \frac{1}{x} \frac{d}{dx};$$

$x = r/R$  – dimensionless coordinate;  $u$  and  $\varpi$  – dimensionless movements, divided by radius; and dimensionless values:

$$\lambda^2 = \alpha_1 \Omega^2; \quad \mu^4 = \alpha_2 \Omega^2; \quad q = \frac{pR^3}{D_{11}}; \quad \Omega^2 = \omega^2 R^2 \rho_p s_{11}^p (1 - \nu^2)$$

$$\alpha_1 = \alpha \frac{1 + \rho\beta}{\alpha + \beta}; \quad \alpha_2 = \frac{1 + \rho\beta}{\varepsilon^2 d}; \quad \rho = \frac{\rho_m}{\rho_p}; \quad \varepsilon = \frac{h_p}{R}.$$

Planar and flexural equations of bimorph vibrations (6.33) and (6.34) look similar to analogous equations for a homogeneous isotropic plate. These equations can be solved by functions  $J_n$  and modified Bessel functions  $I_n$ . Radial displacement, equal zero, and finiteness of the inflection in the plate center are considered:

$$u = A_1 J_1(\lambda x); \quad \varpi = A_2 J_0(\mu x) + A_3 I_0(\mu x) - \frac{q}{\mu^4}. \quad (6.35)$$

Using (6.35), equality (6.32) is written like this:

$$U = \frac{K^2}{1 + \nu} \varepsilon \left[ A_1 J_1(\lambda) + \varepsilon \left( \gamma_0 - \frac{1}{2} \right) \{ A_2 J_0(\lambda) + A_3 I_0(\lambda) \} \right], \quad (6.36)$$

where:  $U = U_x(d_{31}/R)$  – dimensionless potential. To determine unknown  $U$  and integration constants,  $A_1$ ,  $A_2$  and  $A_3$  equality (6.36) is complemented by boundary conditions.

An algebraic system to determine unknown constants is obtained from boundary conditions:

$$u(1) = 0; \quad \varpi(1) = 0; \quad M_x(1) = 0 \quad (6.37)$$

and equalities (6.36) if the edge is hinged merely supported.

Obviously,  $A_1 = 0$  and the following expression [46] is obtained for output voltage if bimorph vibrates (flexural vibrations):

$$U_{\text{OUT}} = \frac{qK\varepsilon^2 \left( \gamma_0 - \frac{1}{2} \right)}{(1 + \nu) \mu} \times \frac{I_0(\mu) J_1(\mu) - J_0(\mu) I_1(\mu)}{\left[ -2\mu^2 J_0(\mu) I_0(\mu) + \mu \left( 1 - \bar{\nu} - \frac{K(\gamma_0 - \frac{1}{2})^2}{d} \right) [I_0(\mu) J_1(\mu) - J_0(\mu) I_1(\mu)] \right]}. \quad (6.38)$$



If the case is that the edge is reely supported:

$$N_x(1) = 0; \quad \varpi(1) = 0; \quad M_x(1) = 0, \quad (6.39)$$

Constants  $A_1$  and  $A_2$ ,  $A_3$  cannot be determined independently, as there are also planar vibrations, and (6.36) is dependent. A system of algebraic equations is obtained from boundary conditions (6.39), using (6.36). Its determinant equals zero. It is an equation of own (resonant) frequencies.

$$\begin{aligned} & [\lambda J_0(\lambda) + (v_1 - 1) J_1(\lambda)] [-2\mu^2 I_0(\mu) J_0(\mu) + \mu(1 - v_2) \{I_0(\mu) J_1(\mu) \\ & + I_1(\mu) J_0(\mu)\}] - \bar{K} J_1(\lambda) \mu [J_1(\mu) I_0(\mu) + I_1(\mu) J_0(\mu)] = 0. \end{aligned} \quad (6.40)$$

where  $v_1 = v + (K\alpha/\beta + \alpha)$ ;  $v_2 = \bar{v} + \left\{ K [\gamma_0 - (1/2)]^2 / d \right\}$ ;  
 $\bar{K} = K^2 \alpha [\gamma_0 - (1/2)] / [(\beta + \alpha) d]$ .

In the specific case  $\beta = 0$  ( $\gamma_0 = 1/2$ ), the equation (6.40) is disintegrated into independent frequency equations of piezoceramic disk radial vibrations. Its electrodes are open:

$$\lambda J_0(\lambda) + (v - 1 + K) J_1(\lambda) = 0, \quad (6.41)$$

and own frequency equations of flexural vibrations:

$$-2\mu^2 J_0(\mu) I_0(\mu) + \mu(1 - \bar{v}) [J_1(\mu) I_0(\mu) + I_1(\mu) J_0(\mu)] = 0. \quad (6.42)$$

Generally,  $\beta \neq 0$  planar and flexural vibrations are related. Vibration connectedness is shown as a result of inverse piezoeffect only if the electrodes are open. In the equations, this relatedness is realized by dependence (6.36) if boundary conditions are met (6.39).

Correlation (6.36) is not considered in the case that potential difference on the piezoelement electrodes is given. As a result, planar and flexural vibrations will not be connected.

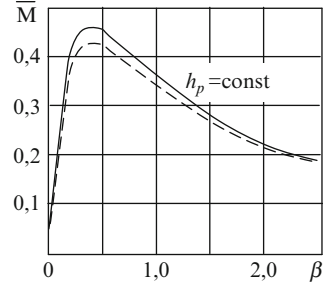
The dependence of dimensionless sensitivity is shown in Fig. 6.9:

$$\bar{M} = \frac{U_x}{p} \frac{d_{31}}{R s_{11}^p (1 - v^2)} \quad (6.43)$$

It depends on the ratio of metal and piezoceramic disk thicknesses  $\beta$  for (*hinged*) merely supported (*a continuous line*) and freely supported (*a dashed line*) bimorph.

The calculations are made in below resonance range at a dimensionless frequency of  $\Omega = 0.0179$  for following physical–mechanical and geometrical parameters of the transducer:

**Fig. 6.9** Dependence of dimensionless sensitivity  $\bar{M}$  on  $\beta = h_m/h_p$  ratio



$$s_{11}^p = 15.2 \times 10^{-12} \text{ m}^2/\text{N}; \quad s_{12}^p = -5.8 \times 10^{-12} \text{ m}^2/\text{N}; \quad s_{11}^m = 9.9 \times 10^{-12} \text{ m}^2/\text{N};$$

$$\varepsilon_{33}^T = 1,540\varepsilon_0 \quad (\varepsilon_0 = 8.854 \times 10^{-12} \text{ F/m}); \quad d_{31} = -100 \times 10^{-12} \text{ Kl/N};$$

$$\rho_p = 7.74 \times 10^3 \text{ kg/m}^3; \quad \rho_m = 8.3 \times 10^3 \text{ kg/m}^3; \quad R = 9 \times 10^3 \text{ m}.$$

The sensitivity dependence on dimensionless parameter  $\beta$  is constructed for the fixed thickness of the piezoceramic element  $h_p = 3 \times 10^{-4} \text{ m}$  (Fig. 6.9). As can be seen from the diagram, there are values  $\beta^*$  with which the sensitivity maximum is reached ( $\beta^* \approx 0.4$ ). Consequently, the thickness of the metal plate should be selected from the ( $h_m \approx 0.4h_p$ ) condition to assure the highest sensitivity of the transducer.

However, this dependence does not give any information on deformation and electric potential distribution along the bimorph piezoelement radius. Therefore, this information was obtained experimentally.

A bimorph piezoelement with  $40\times$  steel plate was used in the experiments. It is 0.15 mm thick and 32 mm in diameter. It was rigidly fastened along the generating line. A IITC-19 piezoceramic piezoelement element 0.2 mm thick and 24 mm in diameter was attached to the plate in alignment. The external piezoelement electrode was divided into squares,  $4 \times 4 \text{ mm}$  each (Fig. 6.10a).

The piezoelement was put in an acoustic chamber. A sound pressure of 10 Pa (114 dB) at a frequency of 100 Hz was created there.

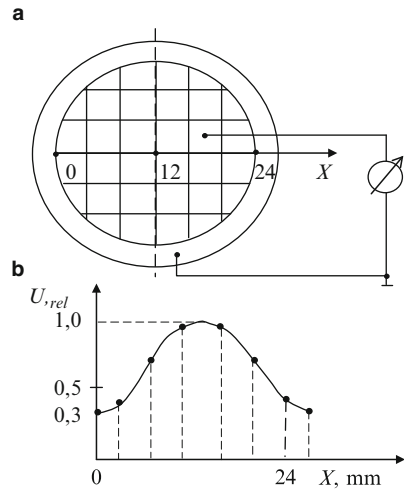
The voltage on each electrode square, located along the OX axis, was measured by millivoltmeter B3–38.

The measurement results are given in Fig. 6.10b. As can be seen from this figure, higher voltage is generated in the central part of the transducer.

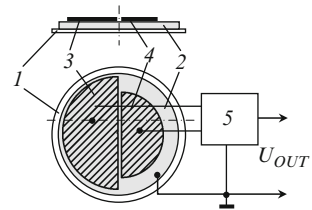
This can be used in sensor design. For example, if an electrode is in the piezoelement centre, while the second electrode on its periphery and the difference signal or correlation signal is obtained, AFC linearity of this sensor can be increased [32, 34, 35, 38, 39].

For example, a piezoelement with semi-disk shaped electrodes 3 and 4, connected to differential amplifier 5 [34], is shown in Fig. 6.11. The AFC of the known piezoelement has a resonance at the frequency of  $\sim 2.5 \text{ kHz}$ . Electrodes 3 and 4 are

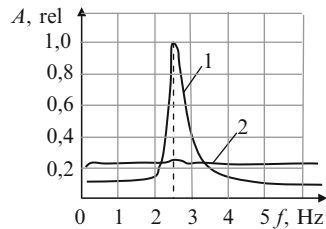
**Fig. 6.10** Potential distribution along piezoelement diameter: (a) transducer design, (b) distribution of potential  $U$  along piezoelement diameter



**Fig. 6.11** Piezoelectric sensor: 1 – metal plate; 2 – piezoelement; 3, 4 – piezoelement semi-disk-shaped electrodes; 5 – amplifier



**Fig. 6.12** AFC of known sensor (curve 1) and sensor, shown in Fig. 6.11 (curve 2)

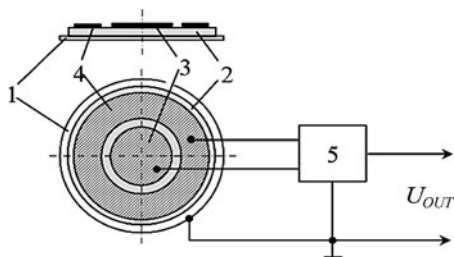


interconnected and switched to the matching amplifier input. The AFC of the sensor, shown in Fig. 6.11, is practically linear (Fig. 6.12).

One more variant of a bimorph sensor is shown in Fig. 6.13 [35, 41].

In this case, electrodes 3 and 4 are disk- and ring-shaped respectively. The signals from electrodes arrive at the voltage divider. As the experiments showed [35], the frequency characteristic of this sensor tends to linear.

**Fig. 6.13** Piezoelectric asymmetric bimorph sensor:  
 1 – metal plate; 2 – piezoelement; 3 – disk-shaped piezoelement electrode; 4 – ring-shaped piezoelement electrode; 5 – voltage divider



### 6.3 Trimorph Piezoelements

As was already mentioned, trimorph elements consist of three parts – a metal plate and two piezoelements.

Depending on reciprocal positioning of piezoelements and the metal plate, there are planar and coplanar trimorph elements. In planar elements, piezoelements are positioned in one plane from one side of the metal plate. Coplanar piezoelements are positioned from one side of the metal plate in asymmetric coplanar trimorph elements. Piezoelements are positioned from both sides of the metal plate in symmetric coplanar trimorph elements.

Adding one more piezoelement to the asymmetric bimorph element increases the rigidity of the vibratory system and its resonant frequency, while its sensitivity decreases. Simultaneous connection of the second piezoelement leads to an increase in charge sensitivity (parallel communication) and voltage sensitivity (series communication). These two processes should lead to the appearance of maximum on sensitivity – areas (diameters) ratio of additional and basic piezoelements. These dependences are represented in the work by Sharapov [42].

Introduction of the second piezoelement in the asymmetric bimorph element opens additional possibilities for piezoelectric sensor design. Electro-mechanical FB can be introduced into the transducer because of this piezoelement. The transducer characteristics can be controlled by it.

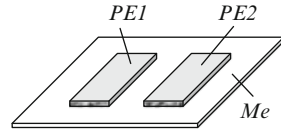
#### 6.3.1 Asymmetric Planar Trimorph Piezoelements

A variant of this transducer design is shown in Fig. 6.14.

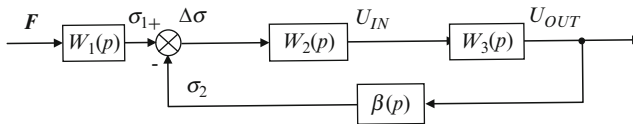
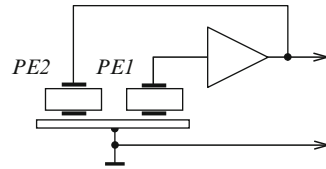
To here Piezoelements of this transducer are attached to the metal plate by homopolar electrodes (negative, in particular). It is necessary to note that piezoelements can be also attached by heteropolar electrodes. As a result, transducers characteristics can be essentially changed in some cases [39, 45].

A variant of the transducer joining to the amplifier and to the common wire of the circuit is shown in Fig. 6.15. Free electrodes are connected to the amplifier

**Fig. 6.14** Trimorph planar asymmetric element (transducer): *PE1*, *PE2* – piezoelements; *Me* – metal plate



**Fig. 6.15** Communication circuit of transducer



**Fig. 6.16** Transducer block diagram

input and output, while the metal plate and, connected to it, second electrodes of the piezoelements are attached to the common wire of the circuit.

The block diagram of this transducer is shown in Fig. 6.16.

Here, the element with transfer coefficient  $W_1(p)$  corresponds to transformation of mechanical action  $F$  into stress  $\sigma_1$  in piezoelements *PE1* and *PE2* and the metal plate. In piezoelement *PE1*, mechanical pressure  $\sigma_1$  is transformed into voltage  $U_{IN}(W_2(p))$ , arriving at the amplifier input with transfer coefficient  $W_3(p)$ .

The device is impacted by NFB circuit with transfer coefficient  $\beta(p)$ . Output voltage  $U_{OUT}$  is transformed into stress  $\sigma_2$  in piezoelement *PE2* [the element with transfer coefficient  $\beta(p)$ ]. The stress is transferred to piezoelement *PE1*. It is summed with stress  $\sigma_1$ , and is transformed into voltage on the amplifier input.

The transfer coefficient of the whole system is

$$W_{FB}(p) = W_1(p) \frac{W(p)}{1 + W(p)\beta(p)}, \tag{6.44}$$

where  $W(p) = W_2(p)W_3(p)$ .

If this condition  $W(p)\beta(p) = 1$  is observed, the minimal relative error is reached in the given case. Then, the transducer sensitivity decreases twofold [49].

There are six variants of amplifier connection to the transducer and the common wire of the circuit [43].

A sample based on electro-acoustic transducer (piezoelectric bell)ЗП-19, produced by the joint-stock company “Aurora” (Volgograd), was made for experimental research of these variants.

### 6.3.1.1 Variant 1

The piezoelement of this transducer is divided into two semi-rings and a disk (Fig. 6.17). A signal electrode of oscillation (sinusoidal, rectangular or meander) generator, simulating mechanical action on the transducer was constantly connected to a semi-ring. The common wire of the circuit was connected to the metal plate. The amplifier input or output was connected to the piezoelements (Fig. 6.17).

The transducer AFC and then AFC of the transducer with the amplifier were measured. And finally, AFC of a trimorph transducer with NFB was measured. The measurement results are given in Fig. 6.18a–c. Introduction of NFB smoothes the resonant peak, as can be seen from the figures.

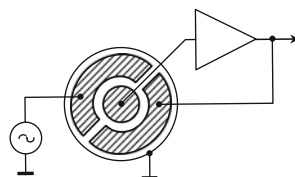
As the form of the piezoelement AFC is completely identical with the AFC of the piezoelement with the amplifier, the former is not shown in Fig. 6.18.

Circuits (a, b, c) and measurement results of pulse (d, e, f) and transitive (g, h, i) characteristics of the considered transducer are shown in Fig. 6.19: of the transducer only (a, d, g), the transducer with the amplifier (b, e, h), and the transducer with the amplifier and NFB (c, f, i).

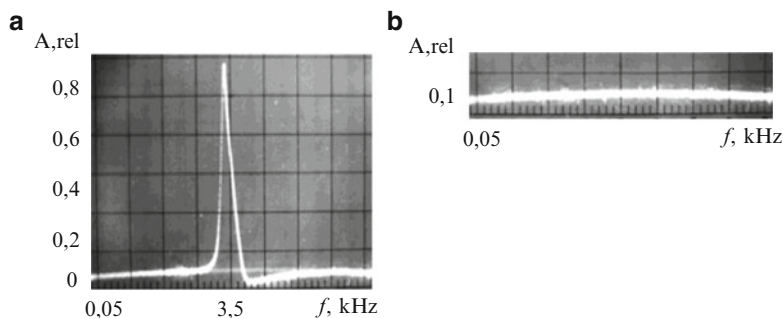
As can be seen from Figs. 6.18 and 6.19, the transducer studied is a vibratory system. Transfer function [28, 39]:

$$W = \frac{k}{T^2s^2 + 2\xi Ts + 1}, \quad (6.45)$$

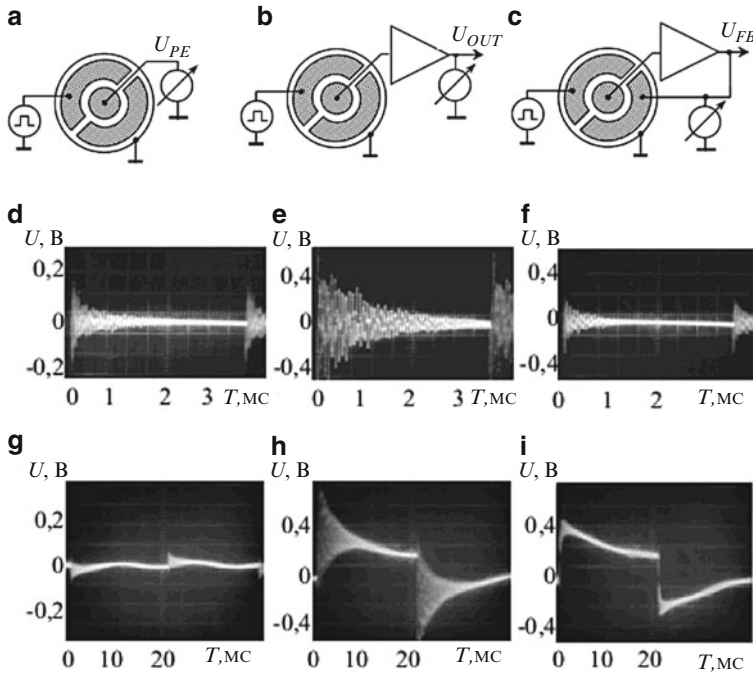
where  $s$  – complex value;  $T$  – time constant;  $\xi$  – damping coefficient.



**Fig. 6.17** Variant 1 of asymmetric trimorph planar transducer



**Fig. 6.18** AFC asymmetric trimorph planar transducer (variant 1): (a) without FB; (b) with FB



**Fig. 6.19** Measurement circuits (a, b, c) and results obtained for pulse (d, e, f) and transitive (g, h, i) characteristics, variant 1

NFB introduction increases the vibratory system attenuation. It also leads to the transition into a differentiating relaxation circuit with the parameters [28, 39]:

Transfer function

$$W = \frac{ks}{Ts + 1}. \tag{6.46}$$

Transitive characteristic

$$h(t) = \frac{k}{T} e^{-\frac{t}{T}}; \tag{6.47}$$

Pulse characteristic

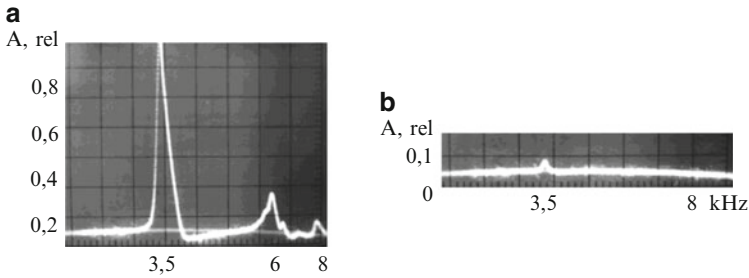
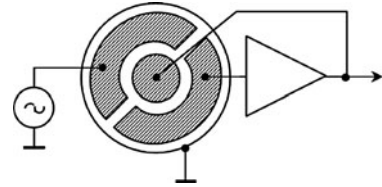
$$\delta(t) = \frac{k}{T^2} e^{-\frac{t}{T}}, \tag{6.48}$$

where  $k$  is the element transfer coefficient (ratio of stationary output and input values).

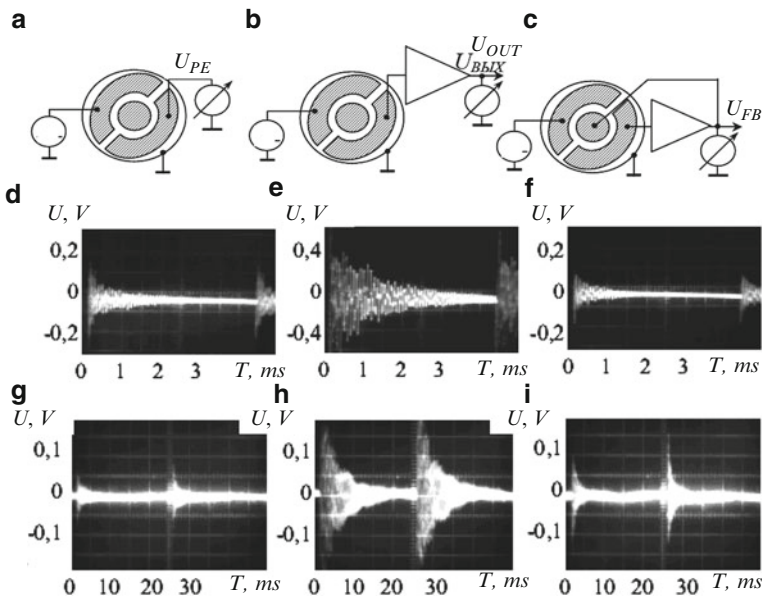
### 6.3.1.2 Variant 2

A metal plate, the amplifier input (to the semi-ring), and the amplifier output (to the disk) are connected to the system common wire in this case (Fig. 6.20).

**Fig. 6.20** Variant 2 of asymmetric trimorph planar transducer



**Fig. 6.21** AFC of trimorph transducer variant 2: (a) without FB, (b) from FB



**Fig. 6.22** Measurement circuits (a, b, c), pulse (d, e, f) and transitive (g, h, i) characteristics, variant 2

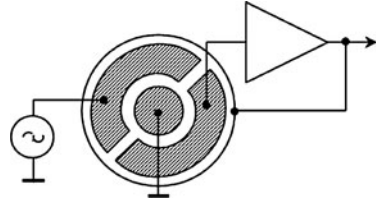
Measurement results of AFC, pulse, and transitive characteristics, and also variants of measurement circuits are represented in Figs. 6.21 and 6.22.

As in the previous case, the given transducer is an oscillatory system.

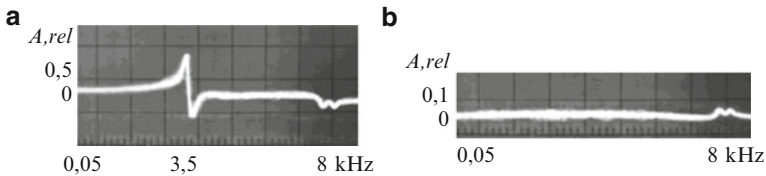
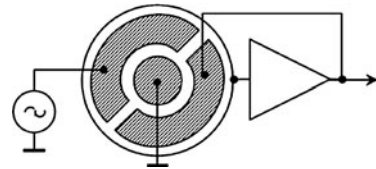
NFB introduction increases attenuation, and transforms the oscillatory circuit into differentiating relaxation.



**Fig. 6.23** Variant 3 of asymmetric trimorph planar transducer



**Fig. 6.24** Variant 4 of asymmetric trimorph planar transducer



**Fig. 6.25** AFC of trimorph transducer, variant 3: (a) without FB, (b) from FB

### 6.3.1.3 Variants 3 and 4

The transducer with a grounded disk electrode (Figs. 6.23 and 6.24) is studied in the same way. The results are given in Figs. 6.25, 6.26, 6.27, and 6.28. These transducers are a differentiating relaxation circuit with weakly expressed oscillatory properties. NFB introduction suppresses oscillatory and strengthens differentiating properties.

### 6.3.1.4 Variants 5 and 6

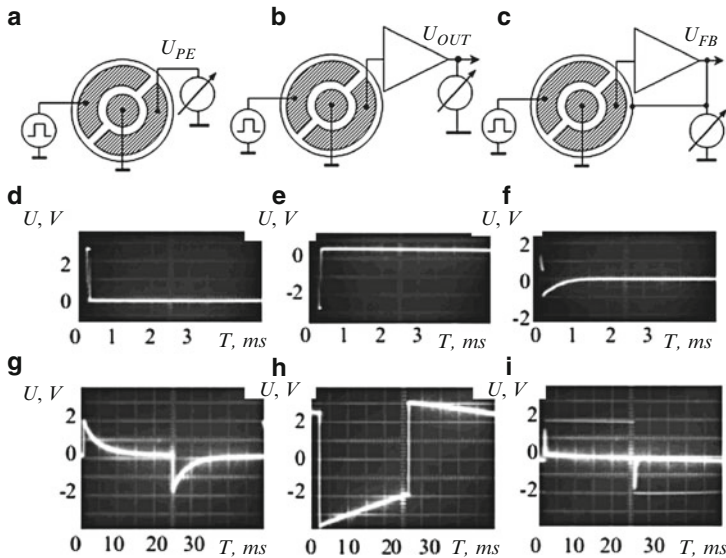
And finally, a transducer with grounded semi-ring-shaped electrode is shown in Figs. 6.29 and 6.30. The results of this study of transducers are shown in Figs. 6.31, 6.32, 6.33, and 6.34.

The given transducer is a differentiating relaxation circuit. NFB introduction linearizes the AFC and also amplifies the differentiating properties.

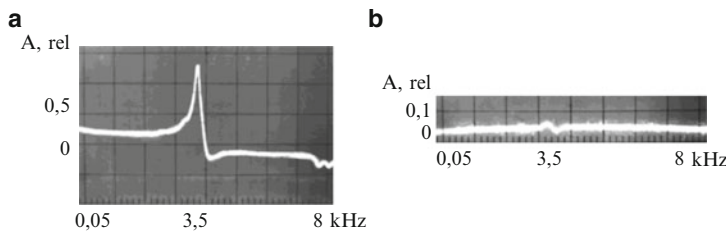
## 6.3.2 Asymmetric Coplanar Trimorph Piezotransducers

A design of an asymmetric coplanar trimorph piezoelement is shown in Fig. 6.35.

Selection of piezoelements and metal plate diameters ratios to achieve the sensitivity maximum are considered in work by Sharapov [42].



**Fig. 6.26** Measurement circuits (a, b, c), pulse (d, e, f) and transitive (g, h, i) characteristics, variant 3



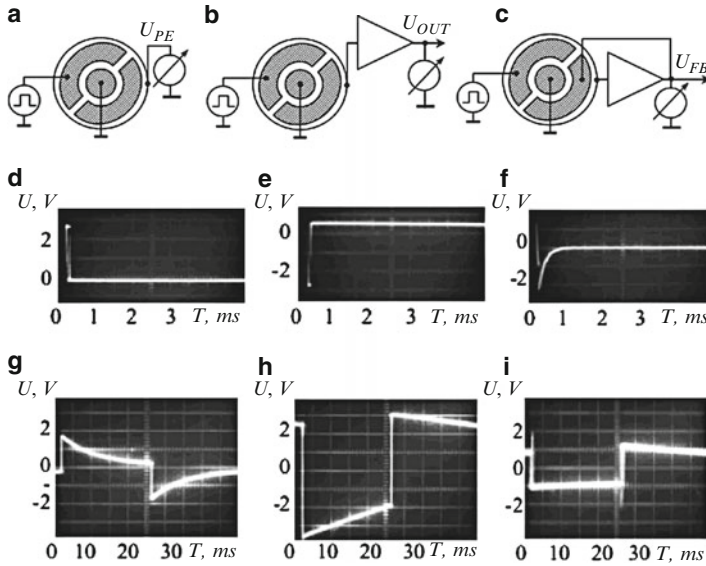
**Fig. 6.27** AFC of trimorph transducer variant 4:(a) without FB, (b) from FB

The difference between a coplanar and planar trimorph piezotransducers is in the fact that piezoelements are positioned not in one, but in parallel planes from one side of the metal plate. The first piezoelement (also called internal piezoelement) is attached to the metal plate by a negative polarity electrode. The second (also called head piezoelement) of the same polarity is fastened to the first electrode.

There are six connection variants of asymmetric coplanar trimorph transducer to the amplifier and to the common wire of the circuit.

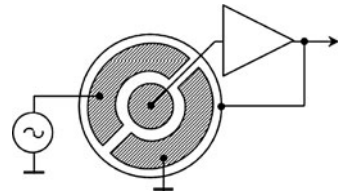
### 6.3.2.1 Variant 1

The electrode of the head piezoelement is connected to the input, and the electrode of the internal piezoelement to the amplifier output. The metal plate and the

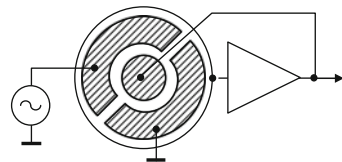


**Fig. 6.28** Measurement circuits (a, b, c), pulse (d, e, f) and transitive (g, h, i) characteristics, variant 4

**Fig. 6.29** Variant 5 of asymmetric trimorph planar transducer



**Fig. 6.30** Variant 6 of asymmetric trimorph planar transducer



electrode of the internal piezoelement connected to it) are attached to the common wire of the circuit (Fig. 6.36).

The block diagram of this transducer is shown in Fig. 6.37.

Here, the element with transfer coefficient  $W_1(p)$  corresponds to transformation of mechanical action  $F$  into stress  $\sigma_1$  in piezoelements  $PE1$  and  $PE2$  and the metal plate. Stress  $\sigma_1$  is transformed in piezoelement  $PE1$  into voltage  $U_{IN}(W_2(p))$ , arriving at the amplifier input with transfer coefficient  $W_3(p)$ .

The amplifier is impacted by the voltage NFB circuit with transfer coefficient  $\beta_1(p)$ . The latter is a transformation coefficient of trimorph piezotransformer. At the

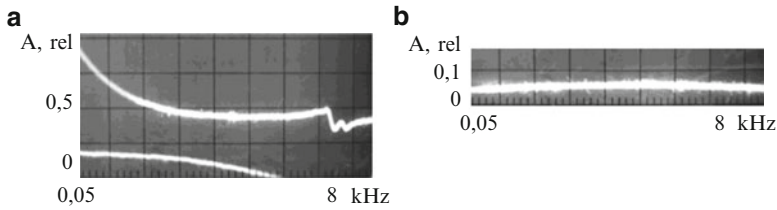


Fig. 6.31 AFC of trimorph transducer variant 5: (a) without FB, (b) from FB

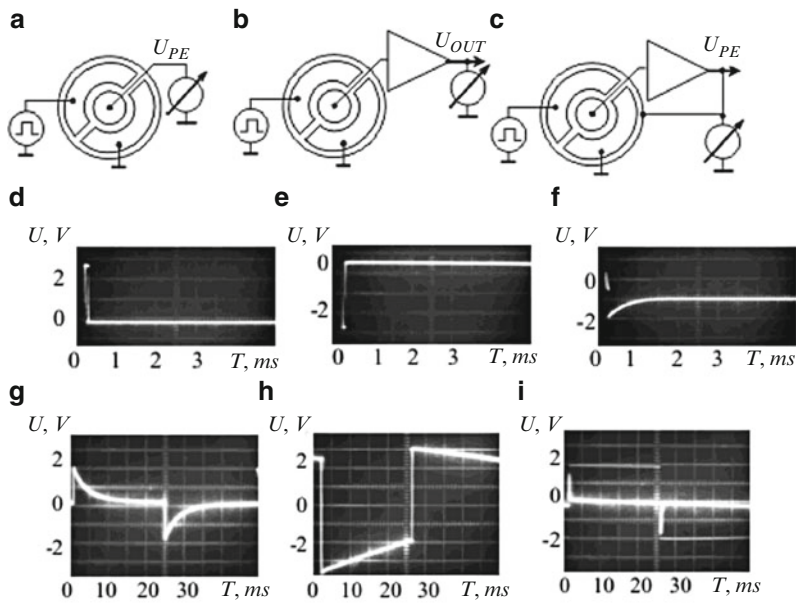


Fig. 6.32 Measurement circuits (a, b, c), Pulse (d, e, f) and transitive (g, h, i) characteristics, variant 5

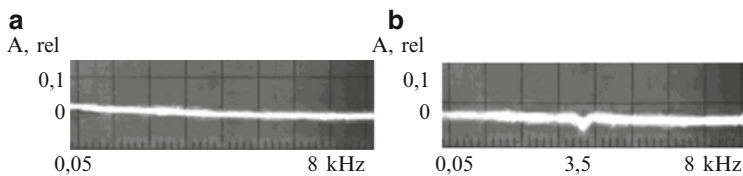
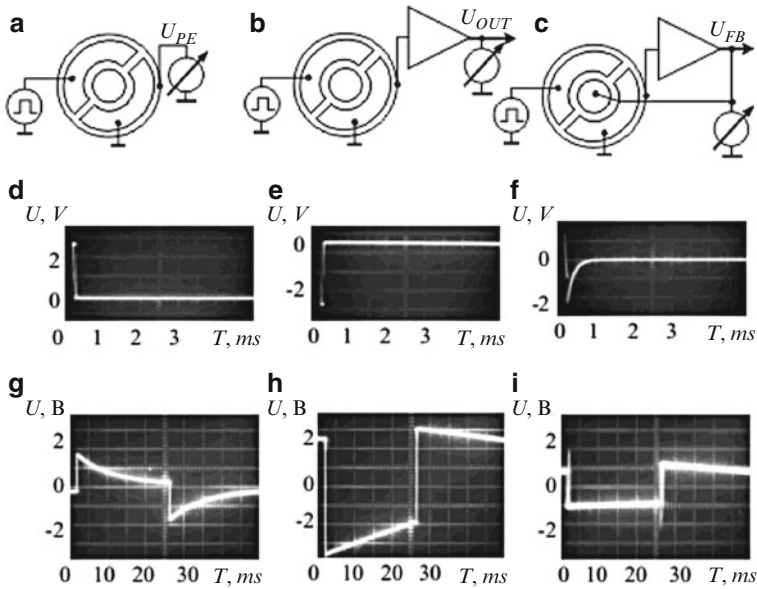


Fig. 6.33 AFC of trimorph transducer variant 6:(a) without FB, (b) from FB

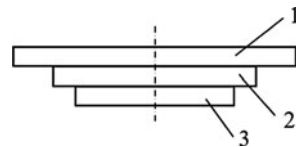
same time, output voltage  $U_{OUT}$  is transformed into stress  $\sigma_2$  in piezoelement  $PE2$  [the element with transfer coefficient  $\beta_2(p)$ ] which is transferred to piezoelement  $PE1$ .

The transfer coefficient of the whole system is

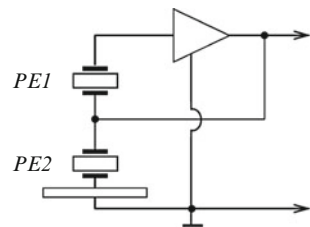


**Fig. 6.34** Measurement circuits (a, b, c), pulse (d, e, f) and transitive (g, h, i) characteristics, variant 6

**Fig. 6.35** Asymmetric trimorph piezoelement: 1 – metal membrane; 2, 3 – piezoelements



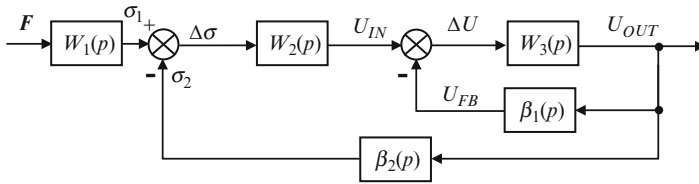
**Fig. 6.36** Communication circuit of transducer



$$W_{FB}(p) = W_1(p) \frac{W(p)}{1 + W(p)\beta_2(p)}, \tag{6.49}$$

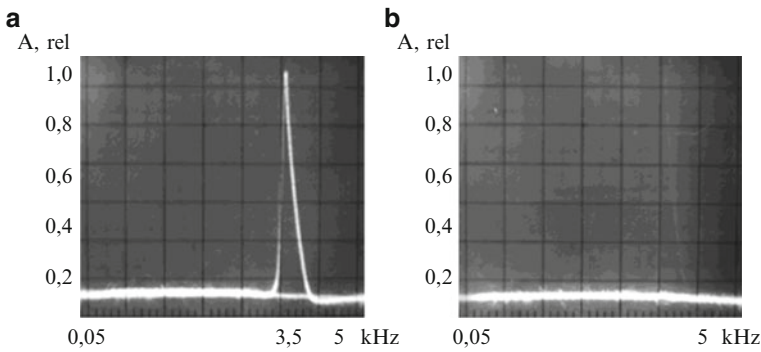
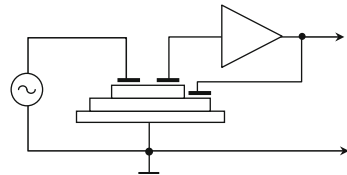
where  $W(p) = W_2(p)W_3'(p)$ ;  $W_3'(p) = \frac{W_3(p)}{1 + W_3(p)\beta_1(p)}$ .

Similarly to the minimum relative error is reached in this case if the condition of  $W(p)\beta_2(p) = 1$  is observed. Then the transducer sensitivity decreases twofold.



**Fig. 6.37** Transducer block diagram

**Fig. 6.38** Variant 1 of asymmetric trimorph coplanar transducer

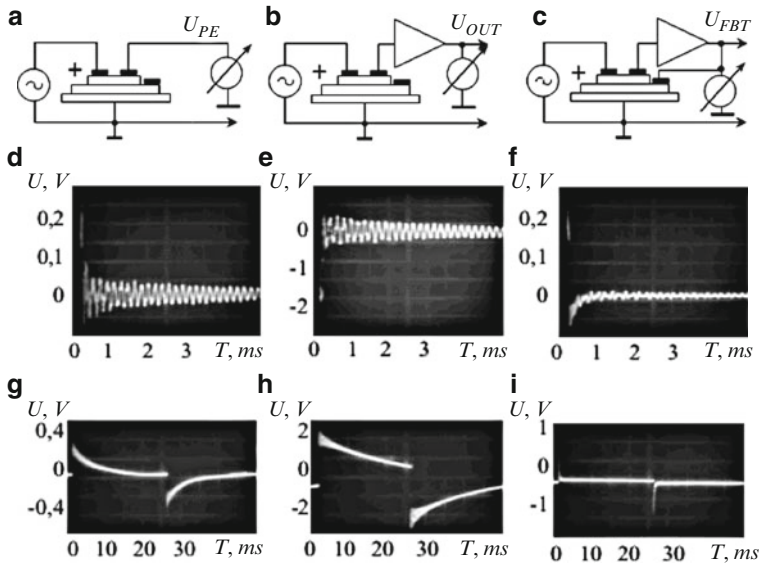


**Fig. 6.39** AFC of trimorph transducer variant 1: (a) without FB, (b) from FB

A sample based on a bimorph element of the electro-acoustic transducer (piezo-electric bell) 3Π-19, produced by the joint-stock company “Aurora” (Volgograd) was made for the experimental research. Another piezoelement was glued to the bimorph piezoelement by a negative polarity electrode. The other electrode of this piezoelement was divided into two parts (Fig. 6.38).

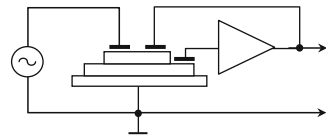
A signal electrode of an oscillation (sinusoidal, rectangular or meander) generator was constantly connected to a part of the divided electrode. The generator simulated mechanical influence on the transducer. The common wire of the circuit was connected to the metal plate. The amplifier input and output were connected to the electrode of the head and internal piezoelements respectively (Fig. 6.38).

The transducer AFC and then the AFC of the transducer and the amplifier were measured. And finally, AFC of a trimorph transducer with NFB was measured. The measurement results are given in Fig. 6.39. As can be seen from the figure, NFB introduction reduces the  $Q$  factor of the vibratory system.



**Fig. 6.40** Measurement diagrams (a, b, c), pulse (d, e, f) and transitive (g, h, i) characteristics, variant 1

**Fig. 6.41** Variant 2 of asymmetric trimorph coplanar transducer



AFC can be formed, selecting amplification coefficient  $K_{SiV}$  of the voltage amplifier. AFC is linear in the wide frequency range. The transducer AFC is not shown in Fig. 6.39, as it is identical to the AFC of the transducer with the amplifier.

Diagrams (a, b, c) and measurement results of pulse (d, e, f) and transitive (g, h, i) characteristics of the transducer considered are shown in Fig. 6.40: of the transducer only (a, d, g), of the transducer with the amplifier (b, e, h), and of the transducer with the amplifier and NFB (c, f, i).

As can be seen from Figs. 6.39 and 6.40, the transducer studied has both oscillatory and differentiating properties. NFB increases differentiating and reduces oscillatory properties.

### 6.3.2.2 Variant 2

In this case, a metal plate is connected to the common wire of the circuit, the amplifier input to the internal piezoelement electrode, and the amplifier output to the head piezoelement electrode (Fig. 6.41).

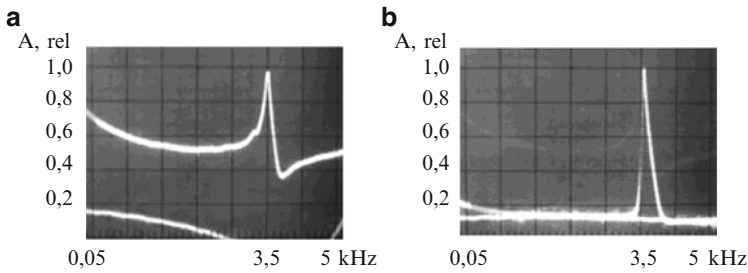


Fig. 6.42 AFC of trimorph transducer variant 2: (a) without FB, (b) from FB

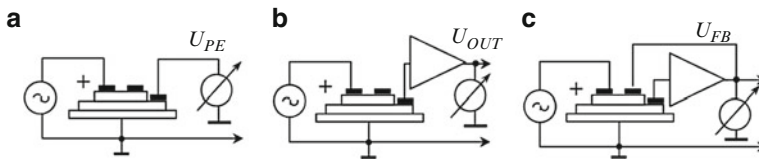


Fig. 6.43 Measurement circuits of asymmetric trimorph coplanar transducer variant 2

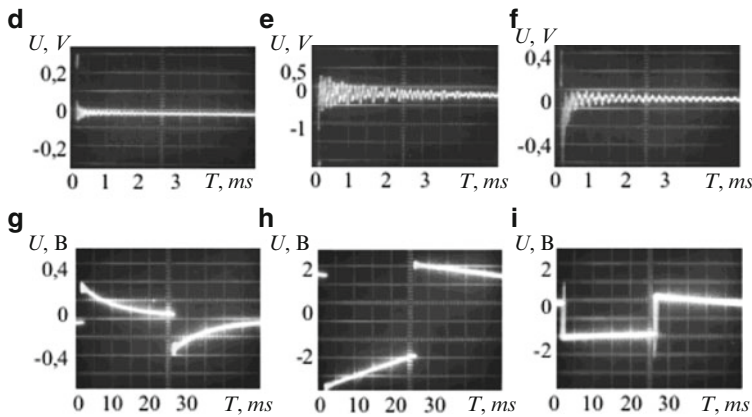


Fig. 6.44 Pulse (d, e, f) and transitive (g, h, i) characteristics for circuits in Fig. 6.43, variant 2

The AFC of this transducer are represented in Fig. 6.42. Possible communication circuits and the characteristics measurement results are given in Figs. 6.43 and 6.44, respectively.

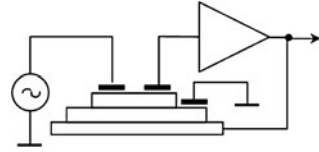
In this case introduction of NFB also increases attenuation and transforms an oscillatory element into a differentiating inertial one.

### 6.3.2.3 Variants 3 and 4

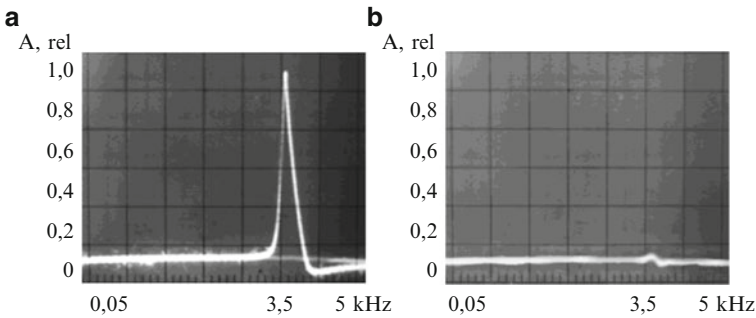
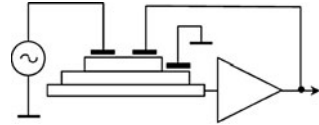
A transducer with a grounded electrode of the internal piezoelement (Figs. 6.45 and 6.46) is studied in the same way. The results are given in Figs. 6.47–6.50.



**Fig. 6.45** Variant 3 of asymmetric trimorph coplanar transducer



**Fig. 6.46** Variant 4 of asymmetric trimorph coplanar transducer



**Fig. 6.47** AFC of trimorph transducer variant 3: (a) without FB, (b) from FB

These transducers are also systems of both oscillatory and differentiating properties. NFB introduction increases attenuation in this case.

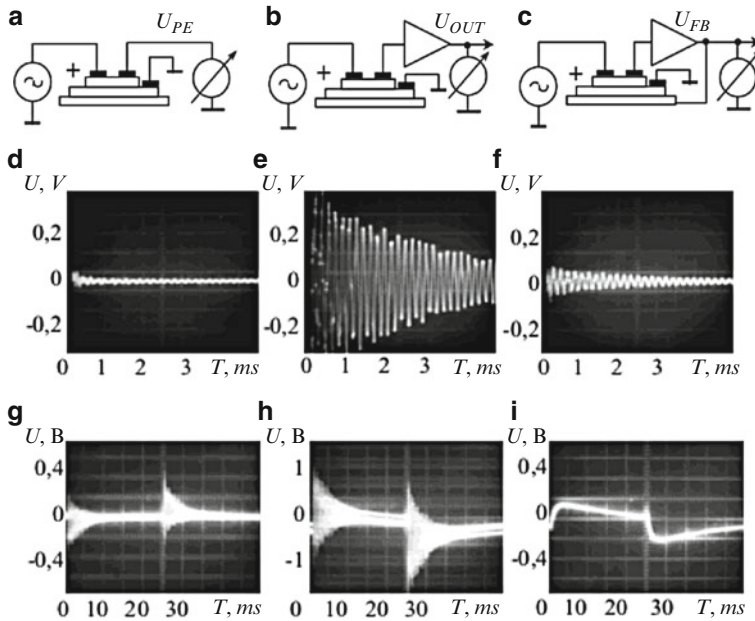
### 6.3.2.4 Variants 5 and 6

And finally, a transducer with the grounded electrode of the head piezoelement is shown in Figs. 6.51 and 6.52. The measurement results are shown in Figs. 6.53–6.56.

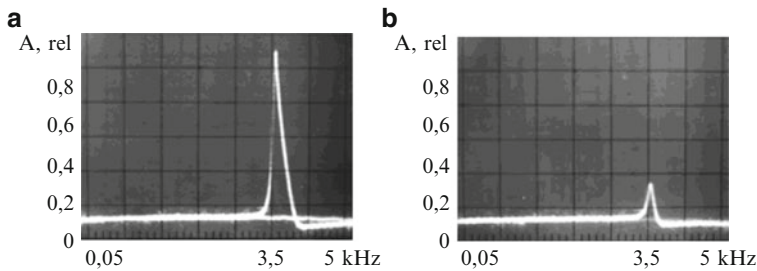
The given transducer is a differentiating relaxation circuit. NFB introduction linearizes AFC and amplifies differentiating properties.

### 6.3.3 Symmetric Coplanar Trimorph Transducer

The position of the neutral plane is important for bimorph and trimorph elements. Rigidity increase of the oscillatory system, sensitivity decrease, connected with it, and sensitivity increase when the second piezoelement is connected are also important.



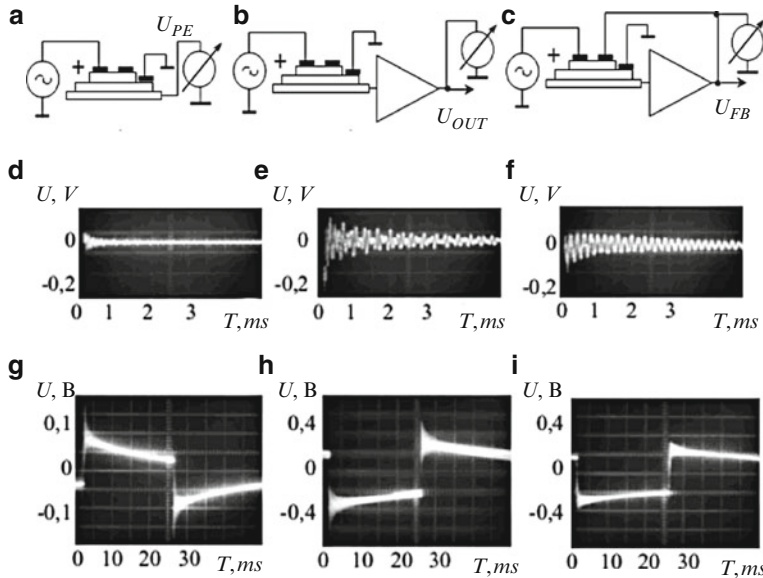
**Fig. 6.48** Measurement diagrams (a, b, c), of pulse (d, e, f) and transitive (g, h, i) characteristics, variant 3



**Fig. 6.49** AFC of trimorph transducer variant 4: (a) without FB, (b) from FB

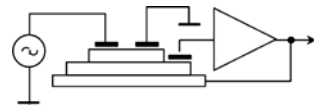
This can lead to partial- or even full-charge compensation on a piezoelement, and consequently to essential sensitivity loss. The ideal position for this plane is between the main and additional piezoelements. It is hard to reach it in cases with an asymmetric trimorph element. The design of a symmetric (relative to the neutral plane) trimorph piezoelement meets these requirements (Fig. 6.57) [42]. The diagram of the piezoelectric transducer with FB, based on a symmetric coplanar trimorph piezoelement, is shown in Fig. 6.58 [12, 19].

The transducer consists of voltage amplifier  $AV$ , piezoelements  $PE1$  and  $PE2$ , metal plate  $Me$ , and electrodes 1, 2 and 3, 4 on piezoelements  $PE1$  and  $PE2$  respectively. Metal plate  $Me$  is fastened between piezoelements  $PE1$  and  $PE2$  and

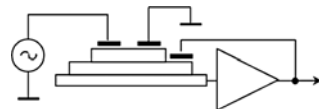


**Fig. 6.50** Measurement diagrams (a, b, c), of pulse (d, e, f) and transitive (g, h, i) characteristics, variant 4

**Fig. 6.51** Variant 5 of asymmetric trimorph coplanar transducer



**Fig. 6.52** Variant 5 of asymmetric trimorph coplanar transducer



connected to the voltage amplifier input *AV* and electrodes 2 and 4 of piezoelements *PE1* and *PE2*. Electrode 1 on piezoelement *PE1* is connected to the output amplifier *AV*, and electrode 3 on piezoelement *PE2* with the common wire of the circuit.

The product transformation coefficient of direct transform circuit, influenced by *FB* and transformation coefficient in *FB* circuit, equals 1.

Six variants of piezoelement connection to the voltage amplifier and to the common wire of the circuit are shown in Fig. 6.59.

Piezoelements are attached to the metal plate from two sides by homopolar or heteropolar electrodes. The change of piezoelement polarization direction essentially influences transducer characteristics.

The transducer block diagram for all six transducer variants is shown in Fig. 6.60 [39].

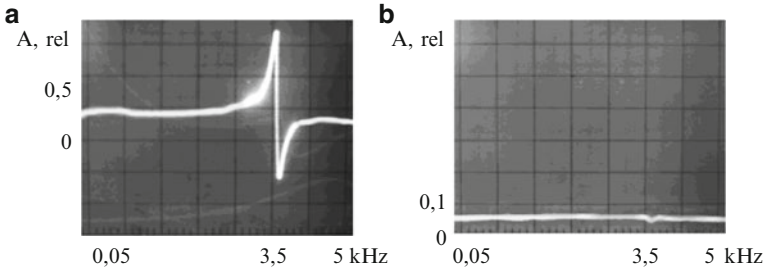


Fig. 6.53 AFC of trimorph transducer variant 4: (a) without FB, (b) from FB

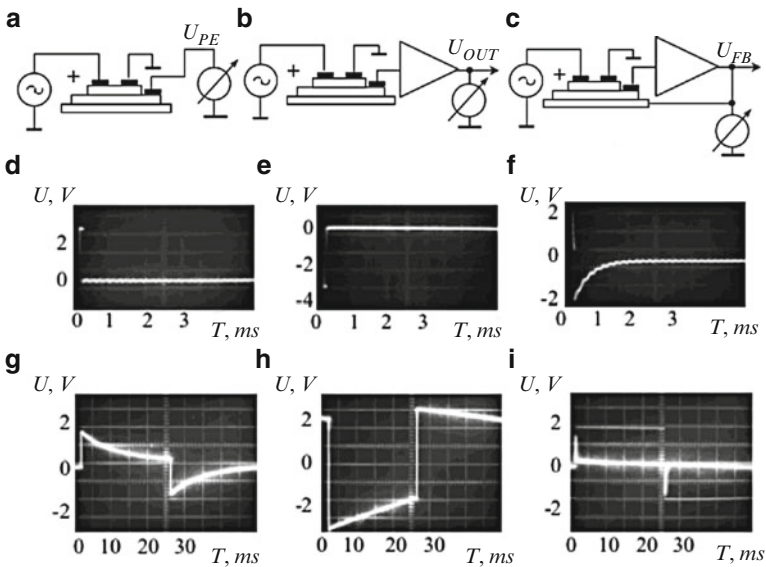


Fig. 6.54 Measurement diagrams (a, b, c), of pulse (d, e, f) and transitive (g, h, i) characteristics, variant 5

Here the element with transfer coefficient  $W_1$  corresponds to transformation of amplifier  $F$  into stress  $\sigma_1$  in piezoelements PE1 and PE2 and the metal plate. Stress  $\sigma_1$  is transformed in piezoelement PE1 into voltage  $U_{IN}$  ( $W_2$ ), arriving at the amplifier input with transfer coefficient  $W_3$ .

The amplifier is impacted by voltage NFB circuit with transfer coefficient  $\beta_1$ . It is the transformation coefficient of a trimorph piezotransformer. At the same time, output voltage  $U_{OUT}$  is transformed into stress  $\sigma_2$  in piezoelement PE2 (the element with transfer coefficient  $\beta_2$ ), transferred to piezoelement PE1.

The transfer coefficient of the whole system is

$$W_{FB} = W_1 \frac{W}{1 + W\beta_2}, \tag{6.50}$$

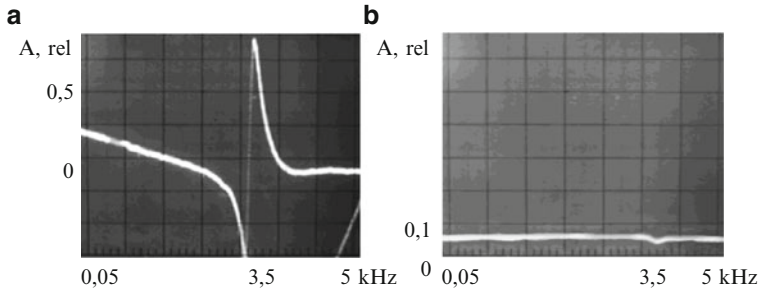


Fig. 6.55 AFC of trimorph transducer variant 4: (a) without FB, (b) from FB

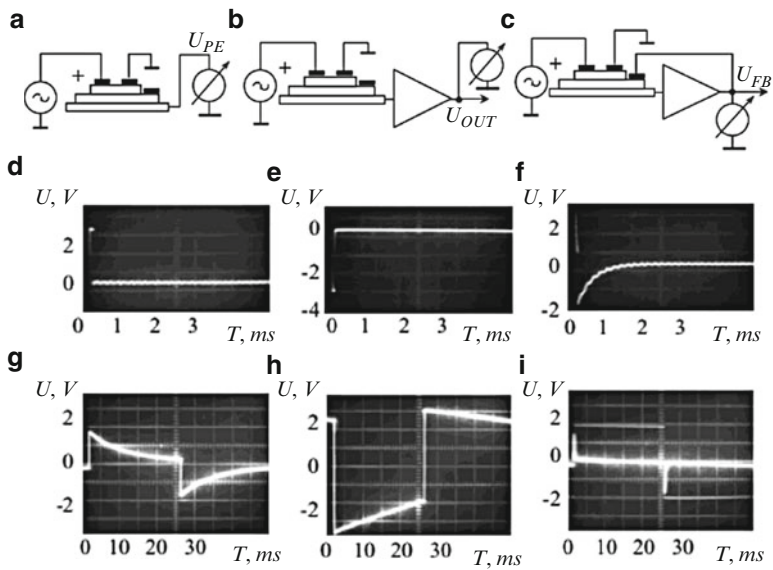
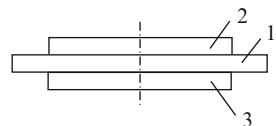


Fig. 6.56 Measurement diagrams (a, b, c), of pulse (d, e, f) and transitive (g, h, i) characteristics, variant 6

Fig. 6.57 Symmetric trimorph piezoelement: 1 – metal plate; 2, 3 – piezoelements

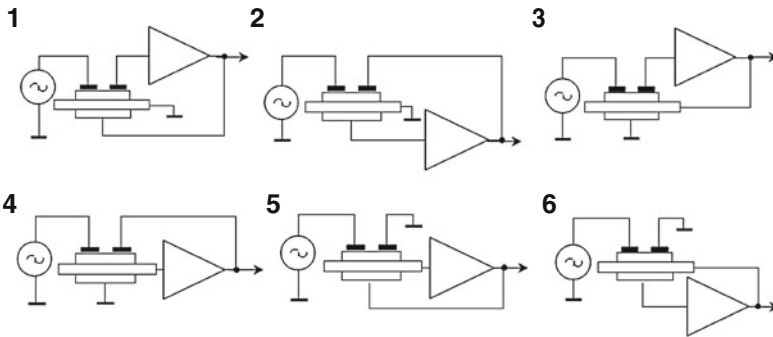
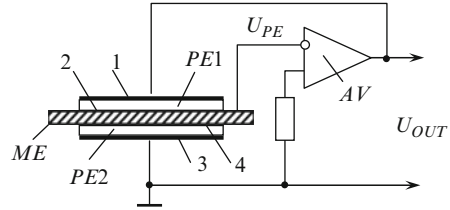


where  $W = W_2 W'_3$ ;  $W'_3 = W_3 / (1 + W_3 \beta_1)$ .

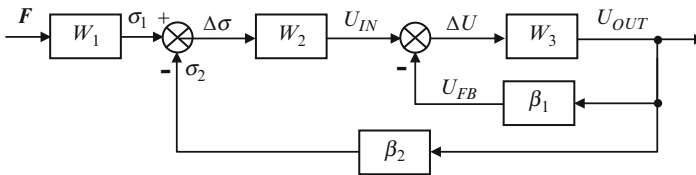
The minimum value of the relative error is reached if the condition  $W\beta_2 = 1$  is observed [28, 29, 39, 49].

The research is conducted on the basis of a serially produced bimorph electroacoustic transducer (3П-19). The second piezoelement, identical to the first, is

**Fig. 6.58** Diagram of trimorph symmetric transducer with FB



**Fig. 6.59** Diagrams of trimorph symmetric transducer



**Fig. 6.60** Block diagram of symmetric trimorph transducer

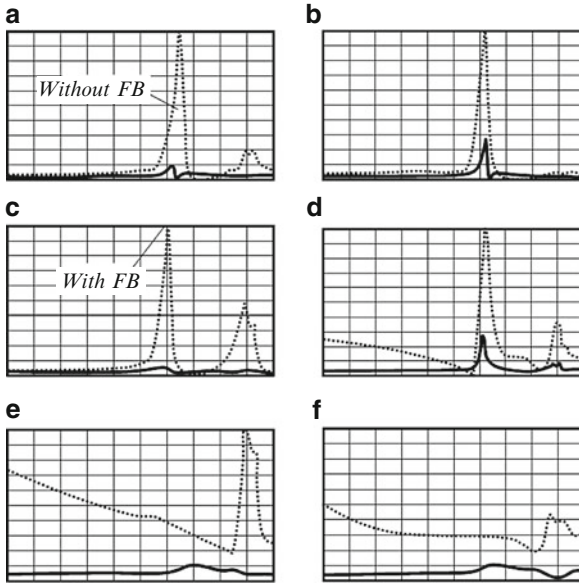
glued to the metal plate by epoxy adhesive. The electrode of this piezoelement was divided into two parts. The signal electrode of sinusoidal, rectangular or meander oscillations generator was constantly connected to one of them. The generator simulated mechanical action on the transducer.

The research results are given in Figs. 6.61–6.66.

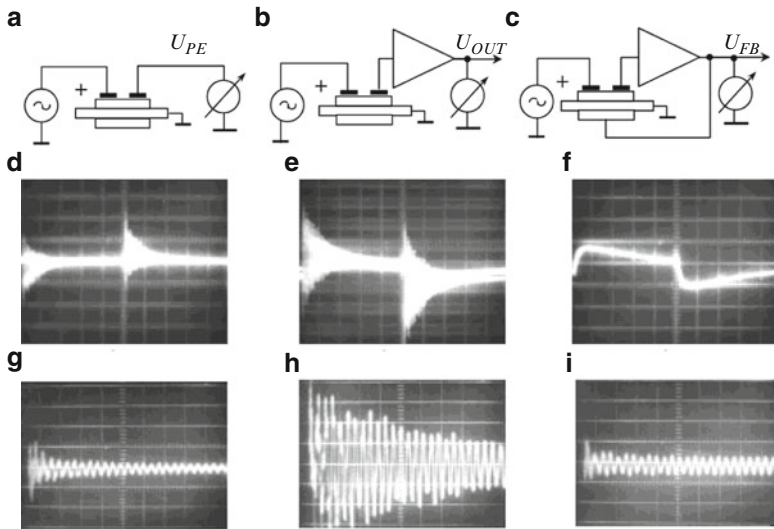
AFC are shown in Fig. 6.61. Pulse and transitive characteristics are given in Figs. 6.62–6.66.

In addition to that, as can be seen from the figures, the transducers studied have both oscillatory and differentiating properties. NFB increases differentiating and reduces oscillatory properties.

NFB introduction leads to attenuation increase in the transducer and transforms an oscillatory circuit into differentiating relaxation.



**Fig. 6.61** AFC of symmetric trimorph transducer: (a) variant no. 1, (b) variant no. 2, (c) variant no. 3, (d) variant no. 4, (e) variant no. 5, (f) variant no. 6



**Fig. 6.62** Measurement diagrams (a, b, c), of pulse (d, e, f) and transitive (g, h, i) characteristics, variant 1

It can be seen from the figures that NFB introduction leads to the characteristic linearization. It results in expansion of the transducer work frequency band. AFC,

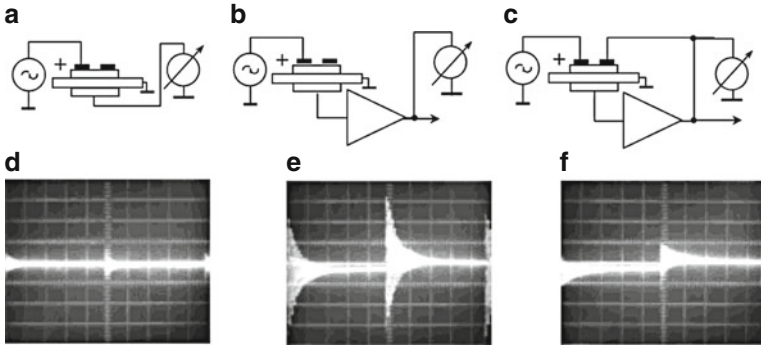


Fig. 6.63 Measurement diagrams (a, b, c), of transitive (d, e, f) characteristics, variant 2

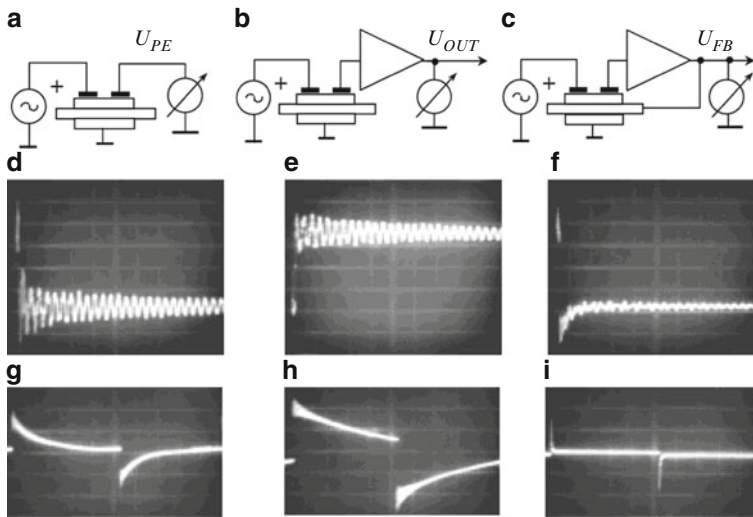


Fig. 6.64 Measurement diagrams (a, b, c), of pulse (d, e, f) and transitive (g, h, i) characteristics, variant 3

linear in the wide frequency range, can be formed by amplification coefficient selection of the voltage amplifier.

#### 6.4 Vibrations of Asymmetric Coplanar Trimorph Piezotransducer with FB

The design diagram of this transducer is shown in Fig. 6.67.

A trimorph piezoceramic transducer with FB, designed by the circuit shown in Fig. 6.68, is considered.



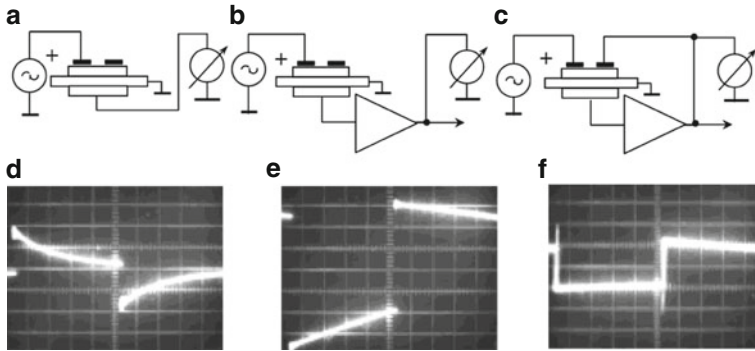


Fig. 6.65 Measurement diagrams (a, b, c), of transitive (d, e, f) characteristics, variant 4

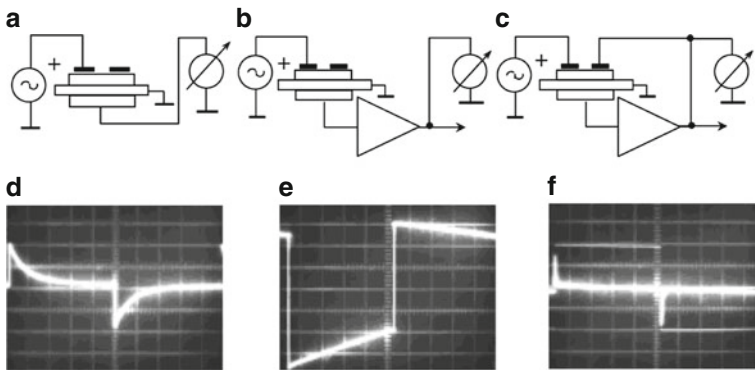
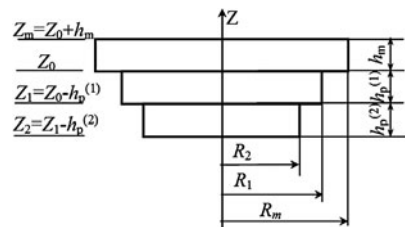


Fig. 6.66 Measurement diagrams (a, b, c) of transitive (d, e, f) characteristics, variant 5

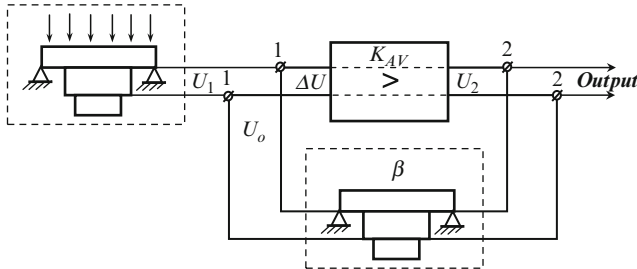
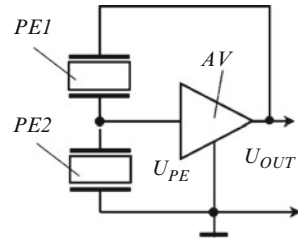
Fig. 6.67 Trimorph piezoelement



The electromechanical transducer considered is represented similarly to electric systems with FB [23]. It is connected in accordance with the circuit (Fig. 6.68) of direct and return circuits (Fig. 6.69).

As can be seen, in this case FB is voltage communication, according to the method of its reading, and is parallel, referring to the method of its introduction. The transfer coefficient of voltage amplifier  $k_{AV}$  is considered frequency-independent, while the amplifier is ideal, i.e., with high input and small output resistances. Value

**Fig. 6.68** Diagram of trimorph piezoceramic transducer with FB



**Fig. 6.69** Piezoceramic transducer with FB

$\Delta U$  is supplied to the amplifier input. This value is the sum of voltage  $U_1$  and FB voltage  $\Delta U_{FB}$ . Voltage is  $U_2 = k_{AV} \Delta U$  the output value. If the FB circuit sensitivity is denoted by  $\beta$ , i.e., the piezotransformer transfer coefficient, it is found that:

$$U_{FB} = \beta U_2 = \beta k_{AV} \Delta U. \tag{6.51}$$

With regard to equality  $\Delta U = U_1 + U_{AV}$ , it is obtained as follows:

$$\Delta U = \frac{U_1}{1 - \beta k_{AV}}. \tag{6.52}$$

If the sensitivity of the direct transform circuit is denoted by  $S$  (terminals 1–1 are open), the following is obtained:

$$S_{TR} = \frac{U_2}{p} = \frac{k_{AV} U_1}{p}, \tag{6.53}$$

and the sensitivity ( $S$ ) of the transducer with FB is determined like this:

$$S_{FB} = \frac{k_{AV} \Delta U}{p} = \frac{S_{TR}}{1 - \beta k_{AV}}. \tag{6.54}$$

Thus, two independent problems have to be solved to determine sensitivity of a trimorph piezoceramic transducer with FB:

1. Electro-acoustic sensitivity of the transducer without FB  $S_1 = U_1/p$ , ( $S_{TR} = k_{AV}S_1$ ), where:  $U_1$  – potential difference, occurring at the expense of direct piezoeffect on the main electrode;  $p$  – amplitude of the external mechanical activating load. Then the additional piezoelement is not used.
2. Determination of FB circuit sensitivity (or transfer coefficient of the piezotransformer  $\beta$ ).

These problems are studied separately. Planar vibrations of the plate are not considered at their solutions. It is believed that electric fields in piezoceramic layers are distributed as in the flat condenser. The thicknesses of electrodes covering flat surfaces of piezoceramic disks, and glued joints are neglected. It is considered that the piezoelements are made of the same material and are polarized along their thicknesses.

**Solution of Problem 1.** Cylindrical system of coordinates  $r, \theta, z$ , where  $z$  is normal coordinate, is introduced.

Kirchhoff–Love kinematic hypotheses are used to construct a mathematical model of transducer vibrations. They can be written like this if the planar component of movements is not considered:

$$U_r^{(i)}(r, z) = -z \frac{dW_i}{dr}, \quad (6.55)$$

Where:  $W_i$  – normal displacement of reduction surface in  $i$ -area of the plate ( $i = 1$  – corresponds to the single-layered,  $i = 2$  – two-layer,  $i = 3$  – three-layer sites).

The equation of stationary vibrations looks like this:

$$\frac{d^2 M_r^{(i)}}{dr^2} + \frac{1}{r} \frac{d}{dr} \left( 2M_r^{(i)} - M_\theta^{(i)} \right) + \rho_i \omega^2 W_i + p = 0. \quad (6.56)$$

Here,  $\rho_1 = \rho_m h_m$ ;  $\rho_2 = \rho_m h_m + \rho_p h_p^{(1)}$ ;  $\rho_3 = \rho_2 + \rho_p h_p^{(2)}$ ; where  $\rho_2 = \rho_m$  and  $\rho_p$  – density of metal and piezoceramics respectively. Deducing vibration equations (6.56) for multilayered areas ( $i = 2, 3$ ), small inertial members are neglected.

The moments on site  $i$  ( $i = \overline{1, 3}$ ) are calculated by corresponding voltage like this:

$$\left( M_{r(\theta)}^{(1)}; M_{r(\theta)}^{(2)}; M_{r(\theta)}^{(3)} \right) = \left( \int_{Z_0}^{Z_m} \sigma_{rr(\theta\theta)}^{(1)} z dz; \int_{Z_0}^{Z_m} \sigma_{rr(\theta\theta)}^{(2)} z dz; \int_{Z_0}^{Z_m} \sigma_{rr(\theta\theta)}^{(3)} z dz \right); \quad (6.57)$$

where  $Z_m = h_m/2$ ;  $Z_0 = -h_m/2$ ;  $Z_1 = Z_0 - h_p^{(1)}$ ;  $Z_2 = Z_1 - h_p^{(2)}$ .

With regard to physical correlations, Cauchy equations, connecting deformations with movements and simplifying hypotheses (6.55), expressions for moments (6.57) can be written like this:

$$\begin{aligned}
M_r^{(1)} &= -D_1 \left( W_1'' + \frac{\nu}{r} W_1' \right), \\
M_\theta^{(1)} &= -D_1 \left( \nu W_1' + \frac{1}{r} W_1 \right)_1, \\
M_r^{(2)} &= -D_2 \left( W_2'' + \frac{\nu}{r} W_2' \right)_2 - e_{31} E_Z^{(1)} (Z_0^2 - Z_1^2) / 2, \\
M_\theta^{(2)} &= -D_2 \left( \nu W_2' + \frac{1}{r} W_2 \right) - e_{31} E_Z^{(1)} (Z_0^2 - Z_1^2) / 2, \\
M_r^{(3)} &= -D_3 \left( W_3'' + \frac{\nu}{r} W_3' \right) - \frac{e_{31}}{2} \left[ (Z_0^2 - Z_1^2) E_Z^{(1)} + (-1)^n (Z_0^2 - Z_1^2) E_Z^{(2)} \right], \\
M_\theta^{(3)} &= -D_3 \left( \nu W_3' + \frac{1}{r} W_3 \right) - \frac{e_{31}}{2} \left[ (Z_0^2 - Z_1^2) E_Z^{(1)} + (-1)^n (Z_0^2 - Z_1^2) E_Z^{(2)} \right],
\end{aligned} \tag{6.58}$$

where these notations are introduced:

$$\begin{aligned}
D_1 &= \frac{h_m^3 C_{11}^{(m)}}{12}; \quad D_2 = \frac{C_{11}^{(m)}}{3} (Z_m^2 - Z_0^2) + \frac{C_{11}^p}{3} (Z_1^2 - Z_0^2); \\
D_3 &= \frac{C_{11}^{(m)}}{3} (Z_m^3 - Z_0^3) + \frac{C_{11}^p}{3} (Z_1^3 - Z_0^3).
\end{aligned}$$

$E_Z^{(1)}$  and  $E_Z^{(2)}$  – normal components of electric field intensity in the first and second piezoelements respectively;  $n = 1$  – corresponds to the case when both piezoelements have opposite directions of preliminary polarization vectors, and  $n = 2$  – parallel. Substituting expressions (6.58) in the corresponding equations (6.56), we obtain the vibration equations in movements:

$$\Delta W_i - \mu_i^4 W_i = \frac{p}{D_i} \quad (i = 1, 2, 3), \tag{6.59}$$

where  $D = (d^2/dr^2) + (1/r)(d/dr)$ ;  $\mu_i^4 = \rho_i \omega^2 / D_i$ .

The general solution (6.59) is known [26], and looks like this:

$$W_i(r) = A_1^{(i)} J_0(\mu_{ir}) + A_2^{(i)} I_0(\mu_{ir}) + A_3^i Y_0(\mu_{ir}) + A_4^{(i)} K_0(\mu_{ir}) - \frac{p}{\mu_i^4 D_i}, \tag{6.60}$$

where  $J_0$ ,  $I_0$ ,  $Y_0$ ,  $K_0$  are Bessel functions of zero order, and  $A_k^{(i)}$ , ( $k = 1, 4$ ) is an arbitrary constant to determine. It follows from problem symmetry conditions and inflection boundedness condition in the plate centre ( $r = 0$ ) that:

$$A_3^{(3)} = A_4^{(3)} = 0.$$

Another ten arbitrary constants are found from the linear system solution of algebraic equations. The system is obtained after substitution of general solutions into kinematic

$$W_i = W_{i+1}; \quad \frac{dW_i}{dr} = \frac{dW_{i+1}}{dr} \quad (6.61)$$

and static correlation conditions on area interface

$$\begin{aligned} r &= R_1 \text{ and } r = R_2 \\ M_r^{(i)} &= M_r^{(i+1)}; \quad Q_r^{(i)} = Q_r^{(i+1)} \end{aligned} \quad (6.62)$$

where  $Q_r^{(i)} = \left( dM_r^{(i)}/dr \right) + (1/r) \left( M_r^{(i)} - M_\theta^{(i)} \right)$ , and also extreme conditions on the metal substrate contour. If  $r = R_m$  boundary condition for rigid fastening is written like this:

$$W_1 = 0; \quad \frac{dW_i}{dr} = 0, \quad (6.63)$$

$$W_1 = 0; \quad M_r^{(i)} = 0 \quad (6.64)$$

Condition of currents  $I_1$  and  $I_2$  equal zero is used to determine intensities of electric fields  $E_Z^{(1)}$  and  $E_Z^{(2)}$ . The currents go through the first and second piezoelements respectively.

$$I_1 = \int_0^{R_1} \int_0^{2\pi} \int_{Z_1}^{Z_0} \frac{1}{h_p^{(1)}} D_Z^{(1)} dz d\theta dr = 0, \quad I_{21} = \int_0^{R_1} \int_0^{2\pi} \int_{Z_1}^{Z_0} \frac{1}{h_p^{(2)}} D_Z^{(2)} dz d\theta dr = 0, \quad (6.65)$$

where  $D_Z^{(i)}$  – normal components of electric induction vectors are determined like this:

$$D_Z^{(1)} = \varepsilon_{33}^S E_Z^{(1)} + e_{31}(e_{rr} + e_{\theta\theta}), \quad D_Z^{(2)} = \varepsilon_{33}^S E_Z^{(2)} + (-1)^n \times e_{31}(e_{rr} + e_{\theta\theta}), \quad (6.66)$$

where  $e_{rr} = -Z(d^2W/dr^2)$ ;  $e_{\theta\theta} = -Z(1/r)(dW/dr)$ .

Considering that electric potential of the surface  $z = z_0 = -h_m/2$  equals zero, and that the field in piezoelements is distributed as in the flat condenser, it is possible to write this:

$$E_Z^{(1)} = -\frac{V_1}{h_p^{(1)}}; \quad E_Z^{(2)} = -\frac{V_2 - V_1}{h_p^{(2)}} \quad (6.67)$$

where  $V_1$  and  $V_2$  are potentials to determine on surfaces of the first and second piezoelements.

Thus, the total system of equations is obtained. Electro-acoustic sensitivity  $S_1$  can be determined. It equals the ratio of potential difference  $V_1$  to the amplitude of driving automatic force  $p$ .

**Solution of Problem 2 (Transformer Problem).** The solution of this problem is similar to the previous in many respects. The difference is in the fact that in this case mechanical pressure influences the transducer while voltage (denoted by  $V_2$ ) is supplied to the electrodes of the main  $z = z_0$  and auxiliary  $z = z_2$  piezoelements. The transformation coefficient should be defined  $\beta = V_1/V_2$ , where  $V_1$  is an unknown potential difference, occurring on the first piezoelement. FB voltage  $U_{FB}$  corresponds to potential differences  $V_1$ , and  $V_2 - U_2$  in Fig. 6.61. The condition of current equality is used to determine potential  $V_1$ :

$$I_1 = I_2 \quad (6.68)$$

It is necessary to note that the physical sense of conditions (6.65) and (6.68) is Kirchhoff's condition for currents. These conditions can be obtained also by variation method. The condition when variation of the functional electric part equals zero is considered. The latter follows from the general principle of Hamilton:

$$\delta I_{EL} = \frac{1}{2} \int \int \int_V D_Z \delta E_Z dV = 0. \quad (6.69)$$

Deducting the design geometry and expressions (6.57), the variation equation (6.69) is represented like this:

$$\int_0^{R_1} \int_0^{2\pi} \int_{Z_1}^{Z_0} \frac{D_Z^{(1)}}{h_p^{(1)}} \delta V r dr d\theta dz + \int_0^{R_1} \int_0^{2\pi} \int_{Z_1}^{Z_0} \frac{D_Z^{(2)}}{h_p^{(2)}} \delta (V_2 - V_1) r dr d\theta dz = 0$$

or considering notations (6.65) in a more compact form:

$$(I_1 - I_2) \delta V_1 + I_2 \delta V_2 = 0. \quad (6.70)$$

Potentials  $V_1$  and  $V_2$  are unknown in problem 1. Therefore, corresponding variations  $\delta V_1$  and  $\delta V_2$  are independent. Considering the multipliers of independent variations equal zero, two conditions are obtained from (6.70):

$$I_1 - I_2 = 0; \quad I_2 = 0,$$

or, the same

$$I_1 = 0; \quad I_2 = 0.$$

Potential  $V_2$  is preselected in problem 2. Therefore, only the multiplier of equation (6.70) equals zero if  $\delta V_1$ . As a result, single equation for currents (6.68) follows from it.

Sensitivity of trimorph transducer with FB determination is considered at the end of this section. The transducer works in a quasistatic mode. The radiuses of the first and second piezoelements equal the radius of the metal substrate  $R_m = 1$ . Hinge

support conditions (6.64) are considered satisfied in the piezoelement ends. In this case, the equation solution (6.59) looks like this:

$$W_{3(r)} = A_1^{(3)} + A_2^{(3)}r^2 + \frac{P}{64D_3}r^4, \quad (6.71)$$

(index 3 of variable and arbitrary constants will be omitted further). Substituting (6.71) into the boundary condition (6.64) and considering correlations (6.58), the expression for the constant is obtained:

$$A_2 = -\frac{E + (\nu + 3)/16}{2D_3(1 + \nu)}, \quad (6.72)$$

where  $E = e_{31} \frac{(Z_0^2 - Z_1^2)E_Z^{(1)}}{2} + (-1)^n \frac{(Z_0^2 - Z_1^2)E_Z^{(2)}}{2}$ .

The expression for currents (6.65) looks like this:

$$\begin{aligned} I_1 &= \pi \varepsilon_{33}^S \left( E_Z^{(1)} + \frac{e_{31}}{\varepsilon_{33}^S} \frac{Z_0^2 - Z_1^2}{h_p^1} \gamma(1) \right), \\ I_2 &= \pi \varepsilon_{33}^S \left( E_Z^{(2)} + (-1) \frac{e_{31}}{\varepsilon_{33}^S} \frac{Z_0^2 - Z_1^2}{h_p^1} \gamma(1) \right), \end{aligned} \quad (6.73)$$

where  $\gamma(r) = -dW/dr$  is a rotation angle of the normal.

Considering expressions (6.71) and (6.72), the following is obtained

$$g(1) = \frac{E + \frac{P}{S}}{D_3(1 + \nu)}. \quad (6.74)$$

Solving problem 1, (6.73) is inserted in (6.65), and in (6.68), solving problem 2. Considering correlations (6.67), (6.69), the expressions for direct transform  $S$  sensitivity circuit and transformation coefficient  $\beta$  (sensitivity of inverse transform circuit) are obtained:

$$\begin{aligned} S &= \frac{k_{AV} \frac{e_{31}(Z_0^2 - Z_1^2)}{4}}{2D_3(1 + \nu)\varepsilon_{33}^S + e_{31}^2 \left[ \frac{(Z_0^2 - Z_1^2)^2}{h_p^{(1)}} + \frac{(Z_0^2 - Z_1^2)^2}{h_p^{(2)}} \right]}, \\ \beta &= \frac{1}{1 + \frac{h_p^{(2)}}{h_p^{(1)}} \frac{1 - b \frac{e_{31}(Z_0^2 - Z_1^2)^2}{2}}{1 + (-1)^n b \frac{e_{31}(Z_0^2 - Z_1^2)^2}{2}}}, \end{aligned} \quad (6.75)$$

where  $b = \frac{\left[ (-1)^n e_{31} \frac{(Z_0^2 - Z_1^2)}{h_p^{(2)}} - e_{31} \frac{(Z_0^2 - Z_1^2)}{h_p^{(2)}} \right]}{D_3(1 + \nu)\varepsilon_{33}^S}$ .

As can be seen from the given correlations (6.75), sensitivity of direct transform circuit does not depend on the direction of an additional piezoelement preliminary polarization vector. As for transformation (transition) coefficient of coplanar piezotransducer  $\beta$ , as follows from (6.75), when  $n = 2$  (i.e., in the case that the polarization direction vectors of the first and the second piezoelements are parallel),  $\beta$  is bigger than when  $n = 1$  (opposite polarization). Thus, in the field of transducer from FB stability, determined by the inequality:

$$1 - k_{AV} > 0,$$

the polarization vector direction of the second piezoelement in the FB circuit should be the same as for the first piezoelement.

## 6.5 Technology of Bimorph Piezoelement Production

Joint parameters of piezoelements and a piezoelement and a metal plate in a bimorph element essentially influence characteristics of the bimorph element. Certain technological features of bimorph element production are considered.

Electrodes on piezoelements are usually made of silver or nickel. Sheets and strips of firm and semi-firm brass, bronze (tin, fluoric or beryllium) and steel are used as a plate.

Quick and soft solders and epoxy glues are usually used to join piezoelements and a metal plate.

Diffusion welding is recommended in certain cases instead of soldering and gluing. Methods of piezoceramics diffusion welding are described in [4, 5, 8, 12].

As is known, solder is an alloy of metals, intended for soldering. It should have a good yield in the molten state. Surfaces of the materials connected should also be moistened, and the required characteristics should be in a dependable state (mechanical durability, exposure resistance, shrinkage stress, coefficients of thermal expansion, etc.).

Melting (fusion) temperature is very important in bimorph piezoelement production. In most cases, it should be at least two to three times lower than the piezoelement Curie temperature.

Information on composition and melting (fusion) temperature of certain soft solders is given in Table 6.1 [1, 2, 6, 7, 9, 10, 17].

Fluxes are used to protect the soldered surfaces from oxidation and to improve their wettability by molten solder. Fluxes also help reduce fat and oxide films on the surface connected. Some information about fluxes, used in quick and soft soldering of silver, brass, bronze, nickel, aluminium and stainless steel are given in Table 6.2.

Soldering can be performed in ovens to avoid superheat and depolarization of the piezoelement. The temperature in them should be 10–15 °C higher than the soldering molten temperature. The connected piezoelements are compressed to reduce the thickness of the solder layer. The pressure of 1–2 N/cm<sup>2</sup> is created.



**Table 6.1** Characteristics of soft solders

Solder	Tin	Bismuth	Composition (%)			Fusion (melting) temperature (°C)
			Lead	Cadmium	Other	
Guthrie's alloy	21	50	20	14	–	45
Wood's alloy	12.5	50	25	12.5	–	68
Lipowitz's alloy	12.9	49.4	27.7	10	–	70
Bismuth alloy	9.6	45.3	45.1	–	–	79
Rose's alloy	25	50	25	–	–	93.7
Newton's alloy	18.75	50	31.25	–	–	96
ПОС 32–15–53	32	53	15	–	–	96
–*	50	–	–	–	Indium 50	117
ПОС 33	33.4	33.3	33.3	–	–	130
ПОС 60	59–61	–	rest	–	Antimony 0–0.8	185
Avia 1**	55	–	rest	20	Zinc 25	200

\*Used for glass and ceramics soldering.

\*\*Used for aluminium soldering.

**Table 6.2** Flux characteristics

Flux name or brand	Composition, % weight	Materials connected
1	2	3
Activated Flux-paste	Rosin – 40; salicylic acid – 3; triethanolamine – 2; ethanol – 55	Brass, bronze, silver
	Olive oil – 50, rosin – 34; zinc chloride – 16	Aluminium and its alloys
ВТС	Vaseline – 63; triethanolamine – 6.3; acid salicylic – 6.3; ethanol- 24.4	Copper, brass, bronze, silver, platinum and their alloys
Прима – 1	Zinc chloride – 1.4; glycerol – 3; ethanol- 40; water – 55.6	Nickel, platinum
–	Zinc chloride – 14; hydrochloric acid – 40; water – 46	Stainless steels
–	Glycerol – 95; muriatic diethanolamine – 5	Copper and its alloys, nickel, silver, etc.
–	Vaseline – 68; glycerol sodium fluoride – 5; zinc chloride – 5; ethanol – 18	Beryllium bronze
ЛТИ – 120	Ethanol – 63–74; rosin – 20–25; triethanolamine – 1–2; muriatic diethanolamine – 3–5	Almost all metals and alloys
–	Zinc chloride – 90; sodium fluoride – 0.2; ammonium chloride – 8; potassium fluoride – 1.2; lithium fluoride – 0.6	Aluminium and its alloys

Epoxy glues, based on resins ЭД-20 (ЭД-20 – 90 weight parts, polyethylene polyamine – 10 weight parts) and СЭДМ-2 (СЭДМ-2 – 100 weight parts; pitch ЛИ-20 – 50 weight parts) [13, 15, 25] are mainly used in series manufacture. In this case, galvanic electric coupling between the piezoelement and the metal plate is assured at the expense of mechanical compression when they are glued together (1–2 N/cm). Polymerization is conducted at temperature 50–60 °C over a period of 1–2 h.

However, electric contact in the bimorph can be lost because of stresses occurring at polymerization. This effect is shown especially often when small piezoelements are glued together.

There is no electric contact if epoxy glues are used after their pot lives were determined.

Conductive adhesives are used to reduce the problems discussed [19, 20].

Conduction of adhesives depends on current-conducting filler, its concentration, availability of oxide and other films on the particles surface, method and degree of filler dispersion in the polymer, temperature, and some other factors. In some researchers' opinion, charge transfer is made along the chains, consisting of the filler particles. There is direct contact among them. Other scientists consider that conduction is mainly realized by emission of electrons through the gaps between particles (tunnel effect) [20].

At present, the majority of authors consider the tunnel effect to be the most probable mechanism of charge transfer in electroconductive compositions [15].

Metal fillers are widely used to obtain conductive polymeric coverings and glues.

It is mentioned in literature [15, 19, 20] that not only silver, but also gold, copper, bronze, aluminium, tin, nickel, and mixes of these powders in various proportions are used in current-conducting compositions.

The majority of glues are based on epoxy resins, assuring a relatively durable gluing [19, 20].

Amines, such as polyethylene polyamine, diethylenetriamine, triethylenetetraamine, hexamethylenediamine, polyamides, etc., are mainly used as curing agents (hardeners).

Mechanical and especially electric properties of glued joints substantially depend on glue technology and its induration. The filler, usually sinking during glue storage, should be evenly distributed in the whole volume. The glue and the filler should be stirred together for at least 5 minutes. The hardening process affects electrical conduction even more. Electric conduction of glue is in all respects higher if after gluing and surface-joining, the products glued are soaked at high temperature [20].

Formulations of conducting compositions are described in literature, for example the glue described in patent [30]. It contains 27% of silver with scaly shaped particles, 46% of colloid silver, 24.5% of epoxy resin with 2.5% of curing agent (hardener). The glue is cured at 145 °C within 1.5 h.

The other glue contains 69% of silver, 26.5% of epoxy resin, 1.5% of dimethylaminepropylamine and 3% of triglycedyl ether.

After induration at 100 °C over a period of 4 h, transitive resistance of glued joints brass–brass is  $(5-12) \times 10 \text{ ohm} \times \text{m}^2$ . The increase of hardener content from 5 to 10 mass parts leads to a four-fold transitive resistance reduction of glued joints.

Formulation of the single-component adhesive, containing 25–35% of novolak epoxy resin, 0.5–1.4% of 2.4-ethyl methyl nidazolium and 65–75% of silver, is given in the patent [31]. Solvent is used to improve the mixing of components. It is later removed under the action of vacuum. Current-conducting glue, based on alkylcyanoacrylate, is developed [3]. It can cure at room temperature in less than in 1 h. The powder is completely pre-damped by freon to prevent instant

polymerization of the glue when silver powder is introduced. The mixture obtained is left in the air till 50–70% of freon evaporates. Then alkyl- $\alpha$ -cyanoacrylate is added to the powder, for example, an ethyl ether of cyanoacrylate acid, and mix 2–3 min. The glue time is 1–1.5 h. It hardens in 10–15 min.

Ukrainian current-conducting glues are mainly based on epoxy and acryl oligomers.

Current-conducting glues contain from 60 to 400% to epoxy resin weight of metal filler. Metal content decrease reduces electrical conduction, i.e., resistances are big for compositions with pre-critical concentration of metal filler.

Concentration of conductive powder when continuous conductive circuits appear is called first critical. Concentration when resistance stops if the concentration of conductive powder increases is called second critical. [20].

Concentration when polymeric composition becomes conductive is called critical. Resistance is very high if concentration is lower than critical. This can be called “pre-critical.” This is a dielectric ( $10^{11}$ – $10^{16}$  ohm) resistance. Concentration higher than critical can be called “supercritical.”

However, glues with high viscosity cannot be used in gluing bimorphs.

This problem can be solved in two ways.

In the first case, it is proposed that acetone is added (2 to 20% of the composition mass) to increase conduction of pre-critical epoxy compositions [11].

In the second case, it is proposed that metal powders are used to glue flat piezoelements. The particles in these powders are sized as microroughnesses of glued surfaces.

It is not clear why conduction of epoxy glues with pre-critical concentration of metal filler is increased when acetone is added. It may be connected with these effects:

- (a) Acetone influence on the element form and dimensions of composition crystal structure
- (b) Reduction of composition viscosity, and maybe surface tension of the polymeric cover, enveloping the particles of the conductive powder
- (c) Increase of internal pressures, occurring at polymerization [19]
- (d) More even distribution of conductive powder particles
- (e) Quantum-mechanical effects [20]

There are no convincing data to prove any of these effects now. In this case, conduction increase can result from unknown effects. Meanwhile, it has been experimentally discovered that conduction of pre-critical composition increases by  $10^8$ – $10^{10}$  and more times if acetone is added to the mixture of epoxy resin and conductive powder. As is known from literature, resistance of conductive compositions increases if solvents are added into them [19].

Methods of gluing quality control are considered in Chap. 7.

## References

1. L.Z. Shenfil et al., Patent of USSR #228147. Method of electric contact manufacturing, No. 31 (1968) (in Russian)
2. A.M. Bruk et al., Patent of USSR #355668. Method of conductive mass manufacturing, No. 31 (1972) (in Russian)
3. N.I. Bavykin et al., Patent of USSR #430141. Conductive composition, No. 20 (1974) (in Russian)
4. D.I. Kotelnikov et al., Patent of USSR #893424. Soldering or welding method, No. 48 (1981) (in Russian)
5. D.I. Kotelnikov et al., Patent of USSR #935221. Creation method of permanent connection. No. 22 (1982) (in Russian)
6. L.V. Dibikovskaya et al., Patent of USSR #1227642. Glue. Discovery. Inventions, No. 16 (1986) (in Russian)
7. N.S. Enikonolov et al., Patent of USSR #1240761. Current-conducting material and its production, No. 24 (1986) (in Russian)
8. D.I. Kotelnikov et al., Patent of USSR #1308597. Production of piezoceramics, No. 17 (1987) (in Russian)
9. V.M. Sharapov, E.A. Vasil'tsov et al., Patent of USSR #1405813. Bimorph element control of Korotkoff sound sensor, No. 24 (1988)
10. V.M. Sharapov, R.Yu. Kazhys et al., Patent of USSR #1571795. Device to control piezotransducers, No. 22 (1990) (in Russian)
11. V.M. Sharapov, V.I. Bykov, E.A. Vasil'tsov et al., Patent of USSR #1582612. Production of conductive composition (in Russian)
12. D.I. Kotelnikov et al., Patent of USSR #1602302. Creation of acoustic contact, No. 44 (1989) (in Russian)
13. V.M. Bazhenov et al., *Study and Development of Piezoquartz Sensors to Determine Vapor Concentration of Alcohols and Aromatic Hydrocarbons in Gases/Automation of Chemical Manufacturing* (Techno-Economic Research in Chemical Industry, Moscow, 1983), p. 37–41 (in Russian)
14. V.A. Boriseyko, V.T. Grinchenko, A.F. Ulitko, Electroelasticity correlations for piezoceramic rotation covers. *Appl. Mech.* **T.12**(2), 26–33 (1976) (in Russian)
15. B.S. Galperin, *Non-wire Resistors* (Energiya, Moscow, 1968) (in Russian)
16. E.I. Grigoluk, On initial surface selection in theory of heterogeneous covers (theory of nonuniform shells). *News ASC of USSR. Branch of Engineering Science* **8**, 120–121 (1956) (in Russian)
17. M.S. Grizno, E.V. Moskalev, *Glue and Gluing* (Chemistry, Leningrad, 1980) (in Russian)
18. V.T. Grinchenko, A.F. Ulitko, N.A. Shulga, *Mechanics of the Connected Fields in Design Elements* (Naukova dumka, Kiev, 1989), Electroelasticity **T.5**, 36–38, 102–116 (in Russian)
19. V.E. Gul, L.N. Tsarskiy et al., *Current-Conducting Polymeric Materials* (Chemistry, Moscow, 1968)
20. V.E. Gul, L.Z. Shenfil, *Current-Conducting Compositions* (Chemistry, Moscow, 1984) (in Russian)
21. Yu.M. Difuchin, Electromechanical oscillations of bimorph round plates. *Bull. Cherkasy State Technol. Instit.* **1**, 39–45 (1998) (in Ukrainian)
22. V. Domarkas, R.J. Kazys, *Control Piezoelectric Transducers* (Mintis, Vilnius, 1975), p. 255 (in Russian)
23. V. Domarkas, A. Petrauskas, Vibrations of asymmetric bimorph piezoradiators. *Ultrasound* **8**, 57–64 (1976) (in Russian)
24. Yu.I. Iorish, *Vibrometry* (Mashgiz, Moscow, 1963), p. 771 (in Russian)
25. D.A. Kardahsov, *Epoxy Glues* (Chemistry, Moscow, 1973)
26. V.A. Kotelnikov, *Bases of Radio Engineering* (Gostehizdat, Moscow, 1950)
27. A. Love, *Mathematical Theory of Elasticity* (ONTI, Moscow, 1935)

28. I.M. Makarov, B.M. Menskiy, *Linear Automatic Systems* (Mashinostroenie, Moscow, 1977), p. 464 (in Russian)
29. L.A. Ostrovskiy, *Theoretical Bases of Electric Devices* (Energiya, Leningrad, 1971), p. 544 (in Russian)
30. Patent of USA No. 2774747 (1956)
31. Patent of USA No. 3677974 (1965)
32. V.M. Sharapov et al., Patent of Ukraine 40816. G01L1/16. Piezoelectric transducer of mechanical values. Publication 15 Aug 2001 (2001) (in Ukrainian)
33. V.M. Sharapov et al., Patent of Ukraine 61323. G01L1/16. Piezoelectric transducer of mechanical values. Publication 17 Nov 2003 (2003) (in Ukrainian)
34. V.M. Sharapov et al., Patent of Ukraine 61500. G01L1/16. Piezoelectric transducer of mechanical values. Publication 17 Nov 2003 (2003) (in Ukrainian)
35. V.M. Sharapov et al., Patent of Ukraine 61501. G01L1/16. Piezoelectric transducer of mechanical values. Publication 17 Nov 2003 (2003) (in Ukrainian)
36. S.I. Rudnitskiy, A.M. Bolkisev, N.A. Shulga, On applied vibration theories of piezoceramic covers. *Appl. Mech.* **T.22**(9), 117–120 (1986) (in Russian)
37. I.P. Golyamina (ed.), *Ultrasound. Small Encyclopedia* (The Soviet Encyclopedia, Moscow, 1979), p. 400 (in Russian)
38. I.N. Ermolov (ed.), *Ultrasonic Piezotransducers for Non-destructive Control* (Mashinostroenie, Moscow, 1986), p. 280 (in Russian)
39. V.M. Sharapov, M.P. Musienko, E.V. Sharapova, in *Piezoelectric Sensors*, ed. by V.M. Sharapov (Technosphaera, Moscow, 2006), p. 632 (in Russian)
40. V.M. Sharapov et al., Symmetric bimorph piezoceramic transducer with linear amplitude–frequency characteristic. *Bull. Cherkasy State Technol. Univ.* **3**, 43–46 (2002) (in Russian)
41. V.M. Sharapov et al., Study of asymmetric planar trimorph piezoelectric transducers with feedback. *Bull. Cherkasy State Technol. Univ.* **4**, 29–38 (2000) (in Russian)
42. V.M. Sharapov et al., Trimorph piezoelements for sensors of mechanical values. *Papers of Bauman MSTU Branch, Kaluga*, p. 262–265 (1999)
43. V.M. Sharapov et al., Calculation of asymmetric bimorph piezoelements. *Bull. Cherkasy State Technol. Instit.* **3**, 3–7 (1998) (in Russian)
44. V.M. Sharapov et al., Coplanar trimorph piezoelements with feedback. *Works 4 Conference “Automatics-97”, Volume 4, Cherkassy, 1997*, 73–75 (in Russian)
45. V.M. Sharapov, M.P. Musienko et al., *Piezoelectric Transducer (Handbook)*, ed. by V.M. Sharapov (ChSTU, Cherkasy, 2004), p. 435 (in Russian)
46. N.A. Shulga, V.M. Sharapov, S.I. Rudnitskiy, Vibrations of disk bimorph transducer of metal–piezoceramic type. *Appl. Mech.* **26**(10), 64–72 (1990) (in Russian)
47. M. Redwood, Piezoelectric generation of an electrical impulse. *JASA* **33**(10), 1386–1390 (1961)
48. R.D. Mindlin, High frequency vibrations of piezoelectric crystals. *Int. J. Solids Struct.* **8**(7) (1972) (in Russian)
49. V. Sharapov et al., The electromechanical feedback in piezoceramic sensors and transducers. *IEEE International Ultrasonics Symposium, Sendai, Japan, 1998* (in Russian)

# Chapter 7

## Devices to Control and Diagnose Bimorph Piezoelements

### 7.1 Defects of Bimorph Piezoelements

First of all certain terms should be specified in this chapter.

**Control** as a noun is translated from French as “supervision,” “observation to check”; “check of anything”. At the same time, in technical literature, written in English, “control” as a noun is used with the following meanings: control, check, management, regulation and measurement [1].

Determination and study of signs showing defects in machines, devices, their nodes, elements etc.; development of methods and sensors for localization of defects is called **diagnostics** (technological) [1].

**Defect** (from Latin) – defect, drawback, malfunction [1].

Thus, parameters and characteristics of bimorph piezoelements can be controlled to detect defects, if any.

Results of bimorph piezoelement (BPE) serial production show that the following manufacturing defects are possible [2]:

1. No electric contact between the metal plate and the piezoelement electrode, or in the circuit going from the piezoelement to the amplifier.
2. Short circuit between piezoelement electrodes. This occurs at the expense of various metal conductors on the piezoelement external surface, and if the piezoelement is broken down when polarized.
3. No piezoeffect in the piezoelement material.
4. Insufficient mechanical durability of piezoelement and metal membrane glued connection.

Defects 1–3 reduce the transducer sensitivity practically to zero. However, “zero” sensitivity also occurs if the preamplifier is not functioning or if there are errors in its assembly: short circuit between the signal wire and the screen of the sensor cable, false connection of the piezoelement to the general wire of the amplifier.

It is proposed that a change of bimorph piezoelement dynamic characteristics (AFC, pulse and transitive characteristics) may be used to detect defects.

In addition to that, connection of the monomorph piezoelement with the metal plate or other piezoelement causes flexural vibrations. Therefore, the level of these vibrations can point out a defect if any.

The devices used in bimorph piezoelements diagnostics and control are considered below. They are grouped by types of controlled dynamic characteristic.

## 7.2 Defect Diagnostics by AFC

It has been proposed that flexural vibrations should be activated in bimorph piezoelements to control them. In this case, the amplitude of these vibrations at resonant frequency (if other conditions are equal) is proportional to the durability of the piezoelement and the metal membrane (or two piezoelements) connection in the bimorph element [3, 4].

The reservation of “if other conditions are equal” narrows the application sphere of this method to some extent. In fact, the amplitude of these vibrations should depend on a number of piezoelement and metal plate characteristics [2, 5]. Therefore, these characteristics should be known to receive quantitative information on the durability of the glued connection. It is hard and time-consuming to get these data.

However, “yes/no” or “meets/doesn’t meet the requirements” information is often enough for serial production.

Evaluation criteria can be developed if “improper” connection or any other BPE defect is clearly simulated on a quite demonstrative statistical material.

As is known [6], gluing quality and its efficiency can be determined by both destructive and non-destructive methods of control.

Depending on the deformation type, there are several destructive method modifications to determine durability:

- At displacement
- At separation
- At torsion
- At compression
- At inflexion

However, all these methods are not only considerably complicated and insufficiently exact, but also destructive, as their name suggests.

Acoustic, radiating, optical, and electromagnetic methods can be named among non-destructive methods of control. The device tested is exposed to electro-magnetic (sound) vibrations. Radiation intensities on proper and improper device sites are compared.

Acoustic (ultrasonic) methods are the most widespread [7–9]. These methods for layer-built constructions can be divided into two groups:

- Special low-frequency acoustic methods, realized by dry dot contact between the transducer of the device finding head and the product
- Ultrasonic methods, usually realized by contact liquid to create acoustic contact between the device head and the product

These methods belong to the **first group**: impedance, velocimetric (unilateral and bilateral variants of the phase method, using a pulse meaning; time and phase ways with use of pulse value), free vibrations (spectral method) and vibration-tomographic methods.

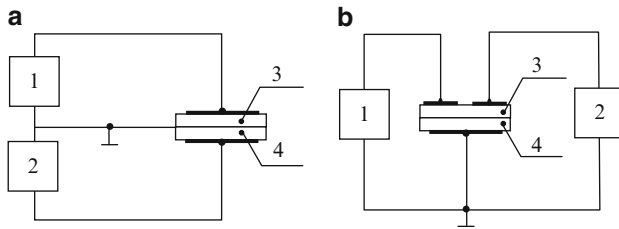
Shadow (amplitude and time) and resonant methods belong to the **second group**.

Application of these methods is comparatively complicated. In addition to that, the transducer has to contact with a glued sample to activate vibrations. As a result, pre-pressure force, elastic characteristics of transducer and sample contact, ultrasonic losses in contact, etc., affect the characteristic measurement. These factors decrease the accuracy of the results received.

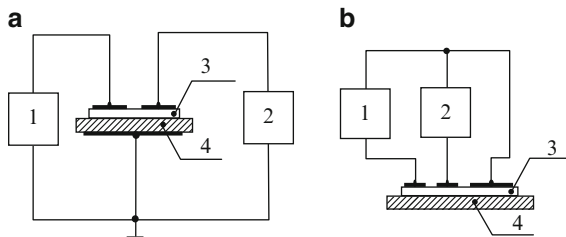
The characteristics measured are determined by bimorph piezoelement properties in the ultrasonic method proposed [1]. These characteristics are connected with durability of the glued joint [2–4].

The method is based on the idea that there are no flexural vibrations if the piezoelement and the metal plate are not mechanically connected. The amplitude of these vibrations depends on the connection durability.

The variants of this method realization are shown in Figs. 7.1–7.3.

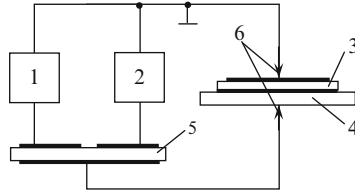


**Fig. 7.1** Monitoring circuit of symmetric bimorph piezoelements: (a) with middle output, (b) with additional electrodes: 1 – generator, 2 – millivoltmeter, 3,4 – piezoelements

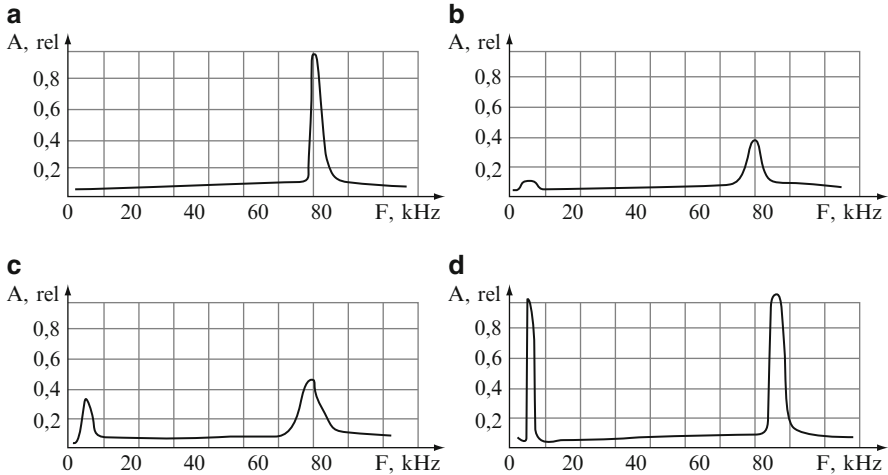


**Fig. 7.2** Monitoring circuit of asymmetric bimorph piezoelements: (a) with one additional electrode, (b) with two additional electrodes: 1 – generator, 2 – millivoltmeter, 3 – piezoelement, 4 – metal plate





**Fig. 7.3** Device Monitoring of Bimorph Piezoelements: 1 - generator; 2 - millivoltmeter; 3 - piezoelement; 4 - metal plate; 5 - piezoelement with three electrodes; 6 - contact device



**Fig. 7.4** AFC of symmetric bimorph: (a) “dry” contact, (b) glue 88H, (c) not hardened epoxy compound, (d) Rose’s alloy

Monitoring circuits of symmetric and asymmetric bimorph elements are shown in Figs. 7.1–7.3.

Generator 1 is connected to a symmetric bimorph piezoelement, and millivoltmeter 2 to the other, in the variant shown in Fig. 7.1. Bimorph AFC is measured.

Bimorph AFC is shown in Fig. 7.4.

This experiment is demonstrative for this system. Firstly, bimorph piezoelements contact with each other. Electric contact occurs as a result of the light pressure (0.2–0.5 N) (“dry” contact). AFC is measured (Fig. 7.4a).

Then bimorph piezoelements are glued by 88H (Russian name). It is a glue based on dissolved rubber, assuring electric contact between the piezoelements. Then AFC of this system is measured (Fig. 7.4b).

After that, the glue is removed by an organic solvent (nonane or xylene, for example). Then piezoelements are glued by incompletely hardening epoxy compound, for example, 100 weight parts of ЭД-20 resin and five weight parts of polyethylenepolyamine. AFC is measured (Fig. 7.4c). After that, epoxy compound

is removed by the solvent again. Piezoelements are connected by Rose's alloy (Fig. 7.4d).

The analysis of characteristics shows that the higher the piezoelement connection durability in bimorph, the higher the amplitude of resonant vibrations.

In the variant shown in Fig. 7.1, a piezoelement electrode is split into two parts. Generator 1 is connected to one of them, while millivoltmeter 2 is connected to the other. Flexural vibrations are also activated in this case. Their amplitude is proportional to the piezoelement durability in the bimorph if other conditions are equal.

Midpoint extraction (junction points of piezoelements, shown in Fig. 7.1a) or division of electrodes (Fig. 7.1b) are considered the disadvantages of these variants. This is hardly acceptable in serial production.

Electrodes should be also divided in asymmetric bimorph variants (Fig. 7.2).

The device shown in Fig. 7.3 does not have the drawbacks mentioned [4]. An additional piezoelement (piezotransformer) 5 is used to activate flexural vibrations in it.

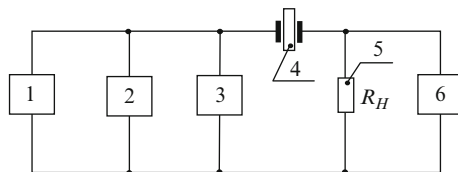
Flexural vibrations cannot be recorded if AFC is measured according to the known resonator circuit known (Fig. 7.5).

Durability of glued connection, and the characteristics mentioned below, can be determined by this device:

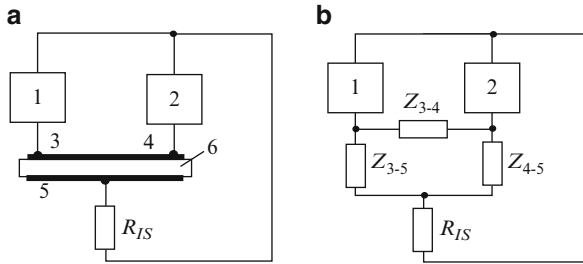
- (a) No electric contact between the piezoelement and the metal plate (or between two piezoelements)
- (b) Short circuit of the piezoelement electrodes
- (c) No piezoeffect

In the first case, the piezotransformer is loaded for high resistance – insulation resistance (Fig. 7.6a). Then the generator voltage will be distributed between the piezodielectric resistance and electrodes 3–5, 3–4, 4–5 and  $R_{INS}$ , i.e.,  $Z_{3-5}$ ,  $Z_{3-4}$ ,  $Z_{4-5}$ ,  $R_{IS}$  (Fig. 7.6a). As  $(Z_{3-5} + R_{IS}) \gg Z_{3-4}$ , then almost all the voltage will be applied to the millivoltmeter and will practically not depend on frequency.

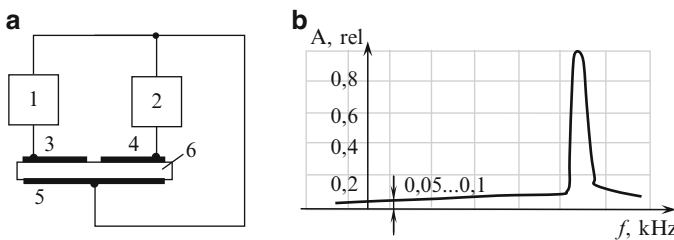
The device is simply a piezotransformer, working in the below resonance area (Fig. 7.7a), if the piezoelement circuit is short. The transformation factor approximately equals 0.05–0.1 (Fig. 7.7b) in this area. Therefore, the millivoltmeter



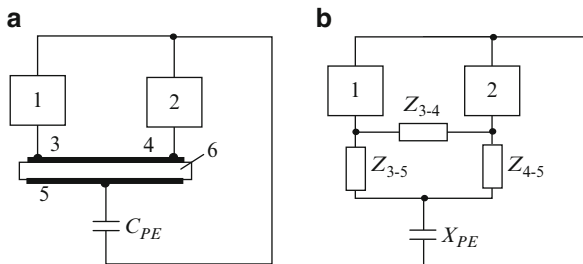
**Fig. 7.5** Resonators AFC measuring circuit: 1 – generator; 2 – frequency meter, 3 – millivoltmeter; 4 – resonator; 5 – load resistance; 6 – millivoltmeter



**Fig. 7.6** Equivalent circuits of device (Fig. 7.3) if there is no contact between piezoelement and metal plate



**Fig. 7.7** Equivalent circuit (a) and AFC (b) of device in Fig. 7.3 if circuit of bimorph piezoelement electrodes is short

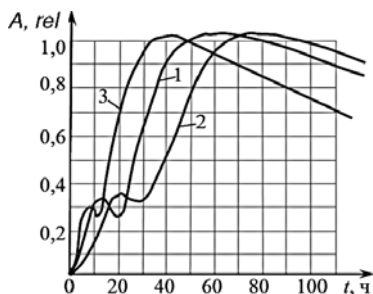


**Fig. 7.8** Equivalent diagrams of device (Fig. 7.3) if there is no piezoeffect

will show voltage equal to  $(0.05-0.1) U_{GEN}$ . This voltage hardly depends on frequency in the given frequency area.

And finally, there is no piezoeffect if flexural vibrations are not activated. The piezoelement is a condenser (Fig. 7.8.). The millivoltmeter voltage will be determined by the correlation of  $Z_{3-5}$ ,  $Z_{3-4}$ ,  $Z_{4-5}$  resistances and the bimorph piezoelement capacitive resistance at the given  $Z_P$  frequency (Fig. 7.8). Depending on the piezotransformer and the bimorph piezoelement dimensions (and their capacitances), this voltage can be  $(0.3-0.6)$  from  $U_{GEN}$ . and also practically hardly depend on frequency.

Thus, there is at least one of the defects mentioned if there are no resonant vibrations. The voltage value, measured by a millivoltmeter, can help determine the defect in each case.



**Fig. 7.9** Dependence of bimorph piezoelement flexural vibration amplitude on epoxy compound polymerization time (ten weight parts of ЭД-20 resin and two ПЭПА weight parts): 1 – compound without filler,  $t = 60^\circ\text{C}$ ; 2 – filler (20%),  $t = 60^\circ\text{C}$ ; 3 – compound without filler,  $t = 80^\circ\text{C}$

This method is useful to study glue polymerization (i.e., hardening) dynamics, depending on concentration of components, fillers, temperatures, etc.

Dependences of flexural vibration amplitude when epoxy compounds are polymerized are shown as an example in Fig. 7.9: without any filler at  $60^\circ\text{C}$  (curve 1), with 20% aluminum oxide at  $60^\circ\text{C}$  (curve 2) and without any filler at higher temperature (curve 3).

These results are easily interpreted when compared with the data obtained by other methods [10]. So the “hump” (plateau) at the characteristic beginning is explained by the change of epoxy compound structure, while the amplitude (durability) reduction at the end of the characteristic is explained by its thermal destruction.

Compounds with fillers are polymerized slowly (curve 2).

### 7.3 Diagnostics of Defects by Pulse Characteristic

Pulse characteristic is the system response on  $\delta$  – impulse action (see Chap. 3).

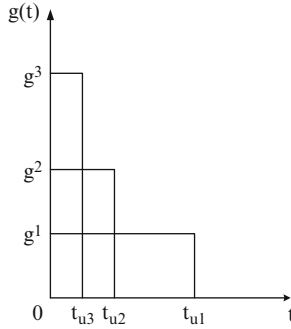
For research normalization, pulse action can be considered a unit, i.e., the product of the pulse duration and its dimension equals 1. Graphs of unit pulses are shown in Fig. 7.10

$$g_1 t_{u1} = g_2 t_{u2} = n_3 t_{u3} = 1,$$

where  $t_{u1}$  – sufficiently small.

Unit pulse function is the limit to which the unit pulse tends when its duration tends to zero

$$\delta(t) = \begin{cases} 0 & \text{при } t \neq 0, \\ \infty & \text{при } t = 0, \end{cases} \quad \text{и} \quad \int_{-\infty}^{\infty} \delta(t) dt = 1. \quad (7.1)$$



**Fig. 7.10** Graphs of unit pulses

Unit pulse function belongs to the class of generalized functions, and is a derivative of unit step function

$$\delta(t) = \frac{d1(t)}{dt}. \quad (7.2)$$

Element or system reaction on unit pulse function is called pulse characteristic (weight function)  $\omega = \omega(t)$ . It is known that the image of element or system pulse characteristic equals transfer function of the element or system. Pulse characteristic (weight function) equals derivative of transitive characteristic:

$$\omega = \frac{dh}{dt}. \quad (7.3)$$

Piezoelement behavior at pulse excitation is studied.

This problem can be also solved by Duhamel and Fourier integrals, operational method or, finally, classical method by voltage differential equation.

A transitive characteristic, i.e., the response to unit function-shaped action, is found.

In this case, the voltage equation looks like this

$$LC \frac{d^2U}{dt^2} + RC \frac{dU}{dt} + U = e. \quad (7.4)$$

Dividing by  $LC$  and using usual notations, the following is obtained:

$$\frac{d^2U}{dt^2} + 2a \frac{dU}{dt} + \omega_0^2 U = \omega_0^2 e. \quad (7.5)$$

Equation (7.5) is rewritten in operational form

$$(p^2 + 2\alpha p + \omega_0^2)U = \omega_0^2 e. \quad (7.6)$$

Hence

$$K(p) = \frac{\bar{U}}{\bar{e}} = \frac{\omega_0^2}{p^2 + 2\alpha p + \omega_0^2}. \quad (7.7)$$

Transitive function is found as the original for this image, considering that

$$e(t) = \sigma(t), \text{ a } U(t) = h(t).$$

Firstly, the characteristic equation is

$$H_2(p) = p^2 + 2\alpha p + \omega_0^2 = 0.$$

The roots of this equation are

$$p_1 = -\alpha + i\omega_1, \quad p_2 = -\alpha - i\omega_1,$$

where

$$\omega = \sqrt{\omega_0^2 - \alpha^2} = \omega_0 \sqrt{1 - \frac{1}{4}d^2}.$$

As can be seen, so-called own frequency is obviously lower than the resonant frequency.

We have

$$\begin{aligned} H_1(p) &= \omega_0^2, & H_2'(p) &= 2(p + \alpha), \\ H_2'(p_1) &= 2i\omega_1, & H_2'(p_2) &= -2i\omega_1, \\ H_2(0) &= \omega_0^2. \end{aligned}$$

Substituting all this in the Heaviside formula, we obtain

$$L(t) = 1 + \frac{\omega_0^2 e^{(-\alpha+i\omega_1)t}}{2(-\alpha+i\omega_1)i\omega_1} - \frac{\omega_0^2 e^{(-\alpha-i\omega_1)t}}{2(-\alpha-i\omega_1)i\omega_1}.$$

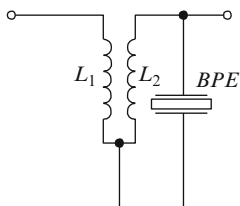
Removing common factors, reducing to the common denominator and using Euler's formula, we finally have

$$h(t) = 1 - e^{-\alpha t} \left[ \frac{\alpha}{\omega_1} \sin \omega_1 t + \cos \omega_1 t \right] \quad (t > 0). \quad (7.8)$$

At small attenuation  $\alpha/\omega \ll 1$ , the first member in brackets can be neglected, and then

$$h(t) = 1 - e^{-\alpha t} \cos \omega_1 t \quad (t > 0).$$

Pulse characteristic can be found by differentiation (7.8)



**Fig. 7.11** Device to diagnose defects of bimorph piezoelement based on transformer

$$g(t) = \frac{\omega_0^2}{\omega_1} e^{-\alpha t} \sin \omega_1 t \quad (7.9)$$

or approximately at small attenuation

$$g(t) = \omega_0 e^{-\alpha t} \sin \omega_0 t. \quad (7.10)$$

A device to diagnose bimorph piezoelectric element defects, based on transformer circuit, is developed. A controlled bimorph piezoelectric element is parallel-connected to it (Fig. 7.11). The device is activated by rectangular-shaped pulses of small duration [2].

A bimorph element of electro-acoustic transducer 3Π-13 was used in experiments.

Rectangular impulses (amplitude – 1 V, duration – 1 ms, repetition frequency – 1 kHz) were supplied to the device input (Fig. 7.11) from pulse generator Γ5–72.

Pulse characteristics are shown in Fig. 7.12. The images from the screen of oscillograph C1–55 were taken by a Canon Power Shot G2 camera.

As can be seen from Fig. 7.12, the defect of a bimorph piezoelement (BPE) can be determined by the pulse characteristic view.

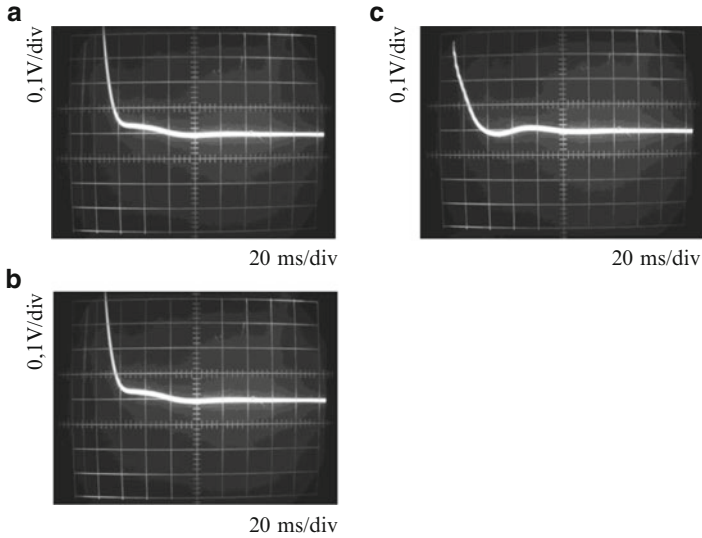
A device based on oscillatory contour circuit with transformer coupling (Fig. 7.13) [11] is proposed. The device is a series oscillatory circuit. The bimorph piezoelement diagnosed is connected to its output (Fig. 7.14).

In this case, the bimorph piezoelement defect can also be detected by the pulse characteristics view. One more device, based on a series oscillatory circuit with transformer coupling, is represented in Fig. 7.15 [12]. In this case, the piezoelement is connected to the general point of the contour (Fig. 7.16).

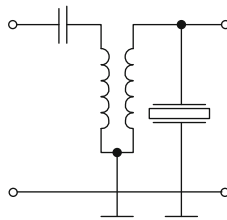
The device, based on a series oscillatory circuit with autotransformer coupling, is shown in Fig. 7.17 [13].

The piezoelement control is connected to the device output.

The bimorph piezoelement defects can be detected by the pulse characteristics view, as it is seen from Fig. 7.18.



**Fig. 7.12** Pulse characteristics for device shown in Fig. 7.11, if: (a) BPE is qualitative, (b) no polarization in piezoelement, (c) no electric contact in piezoelement circuit



**Fig. 7.13** Device based on oscillatory contour with transformer coupling, to detect BPE defects

### 7.4 Diagnostics of Defects by Transitive Characteristic

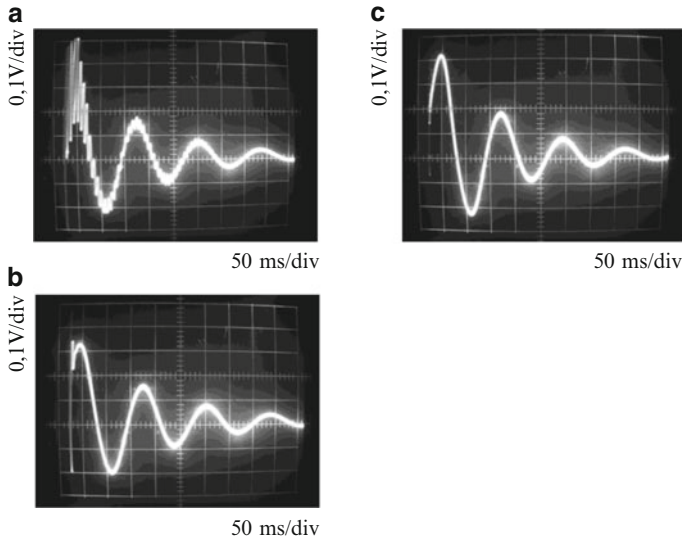
A bimorph piezoelement defect can be also detected if a step function-shaped signal is supplied to it.

Depending on the reference point choice, the function can be odd (for the signal in Fig. 7.19a) or even (for the signal in Fig. 7.19b). Fourier series for the odd function signal (Fig. 7.19, a) looks like this:

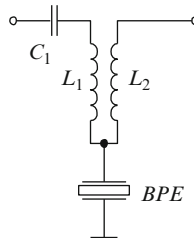
$$s(t) = \dots c_{-1}e^{-i\omega_1 t} + c_0 + c_1e^{i\omega_1 t} + c_2e^{-i\omega_2 t} + \dots = \sum_{n=-\infty}^{\infty} c_n e^{in\omega_1 t}. \quad (7.11)$$

where  $c_n = c_{nc} - ic_{ns}$ ,  $c_{nc} = 0$ ,





**Fig. 7.14** Pulse characteristics for device shown in Fig. 7.13, if: (a) BPE is qualitative, (b) no polarization in piezoelement, (c) no electric contact in piezoelement circuit

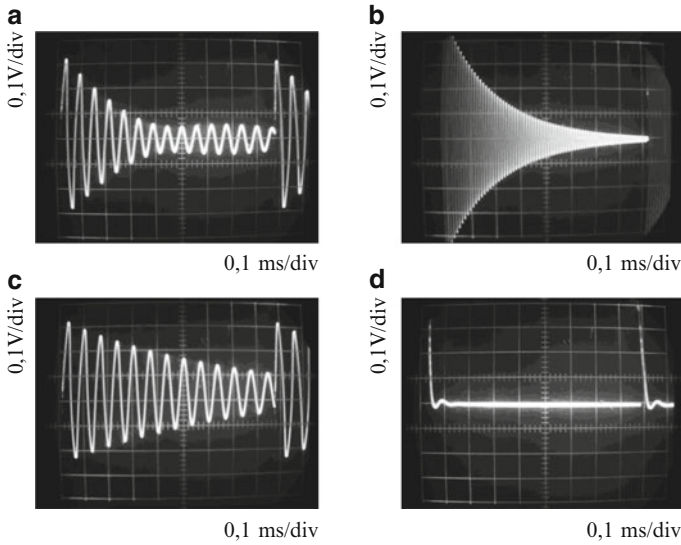


**Fig. 7.15** Device based on oscillatory contour with transformer coupling, to detect BPE defects

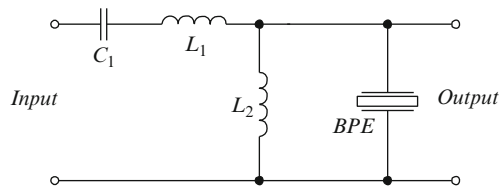
$$c_{ns} = \frac{2S}{Tn\omega_1} [1 - \cos(n\omega_1 T/2)].$$

Considering  $T\omega_1 = 2\pi$ :

$$\begin{aligned}
 s(t) &= \sum_{n=1,3,5,\dots}^{\infty} 2 |c_{ns}| \cos(n\omega_1 t - \pi/2) \\
 &= \frac{4S}{\pi} \left( \sin \omega_1 t + \frac{1}{3} \sin 3\omega_1 t + \frac{1}{5} \sin 5\omega_1 t + \dots \right). \tag{7.12}
 \end{aligned}$$



**Fig. 7.16** Pulse characteristics for device shown in Fig. 7.15, if: (a) BPE is qualitative, (b) no polarization in piezoelement, (c) no electric contact in piezoelement circuit



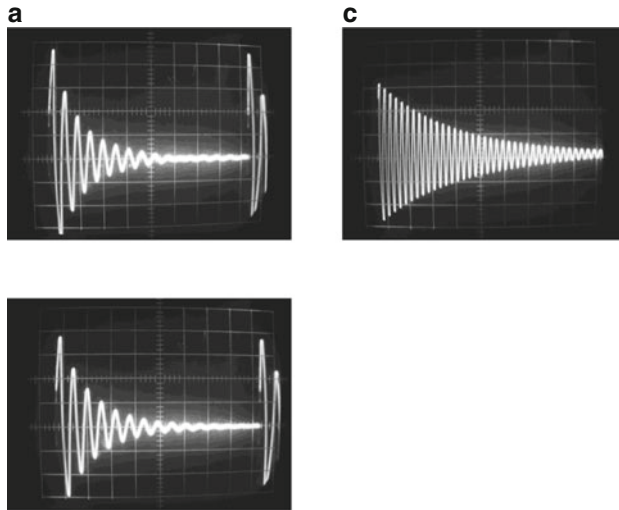
**Fig. 7.17** Device based on oscillatory contour with autotransformer coupling, to detect BPE defects

For the signal of the even function:

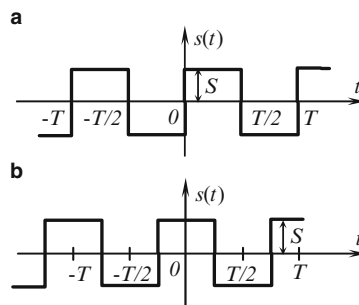
$$s(t) = \frac{4S}{\pi} \left( \cos \omega_1 t - \frac{1}{3} \cos 3\omega_1 t + \frac{1}{5} \cos 5\omega_1 t - \dots \right). \quad (7.13)$$

The spectral density of a rectangular impulse (Fig. 7.20a), corresponding to the single impulse of the even function of a meander-shaped signal (Fig. 7.20), is determined by the expression:

$$\begin{aligned} S_1(\omega) &= A \int_{-\tau_i/2}^{\tau_i/2} e^{-i\omega t} dt = \frac{A}{-i\omega} \left( e^{-\frac{i\omega\tau_i}{2}} - e^{\frac{i\omega\tau_i}{2}} \right) = \frac{2A}{\omega} \sin \frac{\omega\tau_i}{2} \\ &= A\tau_i \left[ \frac{\sin(\omega\tau_i/2)}{\omega\tau_i/2} \right]. \end{aligned} \quad (7.14)$$



**Fig. 7.18** Pulse characteristics for device shown in Fig. 7.17, if: (a) BPE is qualitative, (b) no polarization in piezoelement, (c) no electric contact in piezoelement circuit



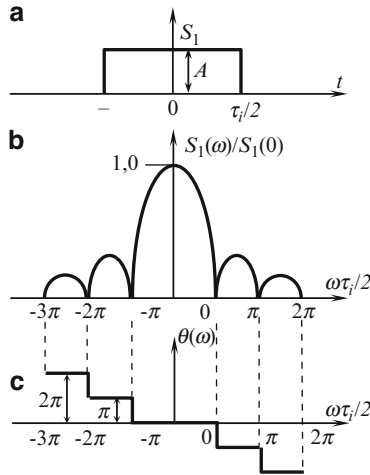
**Fig. 7.19** Meander-shaped oscillation

The wider (narrower) the pulse is, the smaller (larger) the distance between function  $S_1(\omega)$  zeros. This is similar to spectrum narrowing (spreading). Then the value  $S_1(0)$  increases (decreases). Thus, if the cycle of the meander-shaped signal, influencing the piezotransformer, is changed, the influencing signal spectrum is also changed. This results in the change of the output signal type.

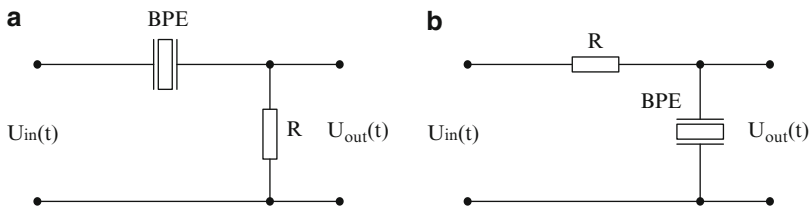
Pulse time ( $\tau_i/2$ ) shift towards delay should be considered, reading time from the pulse middle. This corresponds to the odd function of the meander-shaped signal.

Activation of piezoelements by meander-shaped electric signal is proposed as a method of their control [14].

This method, unlike the method of piezotransformer activation by a short pulse, controls both traditional (oscillatory systems) and domain-dissipative piezoelements (differentiating elements).



**Fig. 7.20** Rectangular pulse: (a) shape, (b) spectral density module, (c) spectral density argument (phase-frequency characteristic)



**Fig. 7.21** Devices for BPE control based on: (a) differentiating circuit, (b) integrating circuit

### 7.4.1 Device Based on Aperiodic Networks

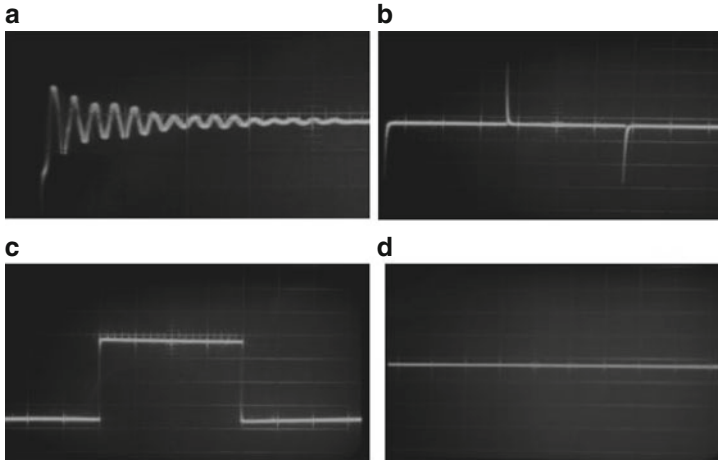
The operating principle of the device proposed consists in the following: the BPE controlled is switched to differentiating or integrating circuit instead of its condenser. Meander-shaped voltage is supplied to this circuit input. BPE defects can be diagnosed by the network response form (transitive characteristic): chains can be judged defects [15].

Elementary devices for BPE control are shown in Fig. 7.21.

The voltage on the differentiating circuit output is

$$U_{OUT}(t) \approx \tau_0 \frac{dU_{inBx}(t)}{dt}, \tag{7.15}$$

And similarly for the integrating circuit



**Fig. 7.22** Transitive characteristic of control unit based on differentiating circuit (Fig. 7.21a): (a) qualitative BPE, (b) no polarization in BPE, (c) short circuit in BPE circuit, (d) BPE open-circuit fault (failure)

$$U_{\text{OUT}}(t) \approx \frac{1}{\tau_0} \int U_{\text{IN}}(t) dt, \quad (7.16)$$

where  $\tau_0 = RC_{\text{PE}}$

$C_{\text{PE}}$  is piezoelement capacity.

The signal shape on the signal output depends on BPE state if meander influences the circuits to which BPE is connected (Fig. 7.21).

Differentiation (or integration) of meander occurs, studying useable BPE (an oscillatory system with 10–100 order  $Q$  factor). Damped oscillations occur at the same time in BPE (Figs. 7.22a and 7.23a).

It is experimentally found that this process occurs if the following condition is observed:

$$\frac{T}{2} \gg \tau_0, \quad (7.17)$$

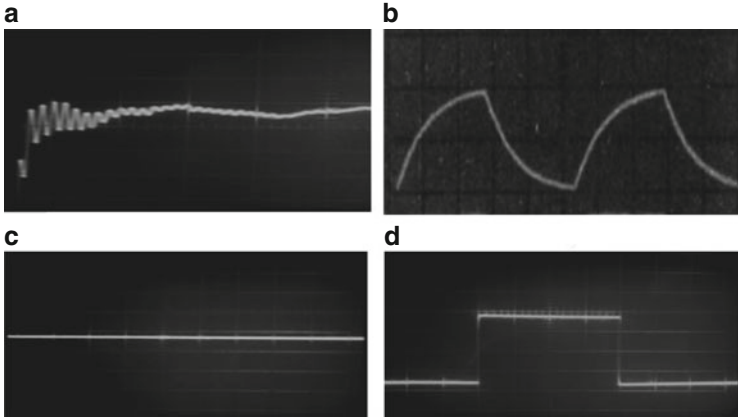
where  $\tau_0 = RC_{\text{PE}}$ ;

$T$  is meander oscillation cycle.

The measurement results are given in Figs. 7.22 and 7.23. BPE of 3II-19 type, generator GZ-106, and oscillograph C1-55 (with resistor resistance equal  $R = 100$  ohm) were used for measurements.

The piezoelement functions as a usual condenser, and devices (Fig. 7.21) as differentiating or integrating circuits (Figs. 7.22b and 7.23b) if the piezoelement material is not polarized.

Voltage is meander-shaped, and the voltage on the integrating circuit output equals zero (Figs. 7.22c and 7.23c) if the piezoelement circuit on the differentiating circuit output is short.



**Fig. 7.23** Transitive characteristic of control unit based on differentiating circuit (Fig. 7.21b): (a) qualitative BPE, (b) no polarization in BPE, (c) short circuit in BPE circuit, (d) BPE open-circuit fault (failure)

And finally, voltage equals zero (or meander) if the piezoelement open-circuit fails on the differential (or integrating) circuit output.

So, the transitive characteristic view gives an possibility to disclose of the BPE defect, as can be seen from Figs. 7.22 and 7.23 as by the form.

## 7.5 Devices Based on Active Oscillator Circuit

In this case it is proposed that a BPE be connected to an active oscillator positive FB to diagnose defects [16].

Active oscillator oscillations occur if the BPE is “qualitative” and “useable.” Oscillations do not occur if there are some defects in the active oscillator [16].

It is a well-known fact that an active oscillator is an amplifier-type device. A frequency-driving element is connected to its positive FB circuit [11]. The BPE is the element discussed in this case. BPE is activated on the fundamental frequency of flexural vibrations.

The circuit of an active oscillator with a BPE in FB circuit is shown in Fig. 7.24.

The expression for operating resistance  $R_O$  and self-oscillation frequency can be written for this circuit [16]:

$$R_O = \cos \varphi_{SC} R_{eq} \frac{K_0}{1 + K_0} \frac{A_1 + B_1 \alpha + D_1 \alpha^2}{A_2 + B_2 \alpha + D_2 \alpha^2}; \quad (7.18)$$

$$\lambda = \frac{A + B \alpha + D \alpha^2}{A_1 + B_1 \alpha + D_1 \alpha^2}, \quad (7.19)$$

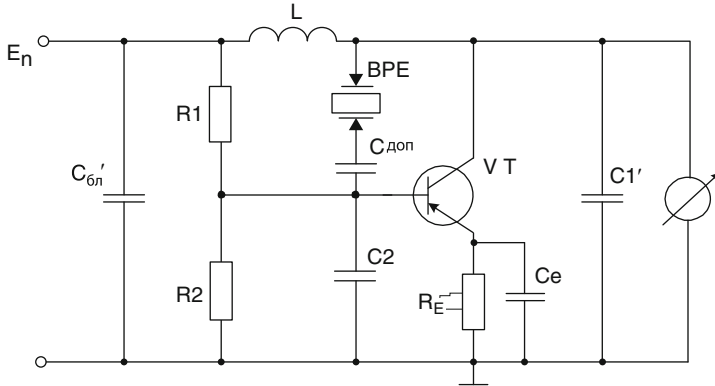


Fig. 7.24 Circuit of active oscillator with BPE in FB circuit

where:  $\varphi_s$  is the first harmonic slope phase of the collector current;  $c = R_5/r_k$ ;  $R_{eq} = 1/\{\omega_k [C_1 C_2 / (C_1 + C_2)]\}^2 r$  is the contour equivalent resistance, considering the losses introduced by the load;

$$r = \frac{1}{(\omega_k C_1)^2 R_2} + \frac{1}{\omega_k \frac{C_1 C_2}{C_1 + C_2} Q_{xx}};$$

$$R_2 = \frac{R_{ne} R_{out}}{R_{ne} + R_{out}},$$

where:  $Q_{xx}$  – contour  $Q$  factor shunting by resistances  $Z_{ne}, Z_4, Z_5$  is not considered;

$$K_0 = C_1/C_2; C_1 = C'_1 + C_{out}; C_2 = C'_2 + C_{in};$$

$$A = \delta_0 - \tau_5 - \tau_5(1 + \delta_0)^2 b \frac{K_0^2}{(1 + K_0)} + \left[ 1 + c + \delta_0(\tau_5 + \delta_0 c) + (1 + \delta_0^2) b \frac{K_0^2}{(1 + K_0)} \right] \text{tg} \varphi_s;$$

$$B = -1 + 2\delta_0 \tau_5 b \frac{K_0^2}{(1 + K_0)^2} - \left[ \tau_5 + \delta_0 c + 2\delta_0 b \frac{K_0^2}{(1 + K_0)^2} \right] \text{tg} \varphi_s;$$

$$D = \delta_0 - \tau_5 \delta_0^2 b \frac{K_0^2}{(1 + K_0)^2} + \tau_5 \delta_0^3 \left[ c + b \frac{K_0^2}{(1 + K_0)^2} \right] \text{tg} \varphi_s;$$

$$A_1 = 1 + c + \tau_5 \delta_0 + \tau_5 (1 + \delta_0^2) \frac{b}{Q} \frac{K_0}{1 + K_0} - \left[ \delta_0 - \tau_5 + (1 + \delta_0^2) \frac{b}{Q} \frac{K_0}{1 + K_0} \right] \text{tg} \varphi_s;$$

$$B_1 = - \left[ \tau_5 + 2\delta_0 \left( c + \tau_5 \frac{b}{Q} \frac{K_0}{1 + K_0} \right) \right] - \delta_0 \left( 1 + \delta_0 \frac{b}{Q} \frac{K_0}{1 + K_0} \right) \operatorname{tg} \varphi_s;$$

$$D_1 = \tau_5 \delta_0 + \delta_0^2 \left( c + \tau_5 \frac{b}{Q} \frac{K_0}{1 + K_0} \right) - \delta_0 \left( 1 + \delta_0 \frac{b}{Q} \frac{K_0}{1 + K_0} \right) \operatorname{tg} \varphi_s;$$

$$A_2 = (1 + c)^2 + (\tau_5 + \delta_0 c)^2 + [c \tau_5 (1 + \delta_0^2) + \delta_0 (1 + \tau_5^2)] \frac{b}{Q} \frac{K_0}{1 + K_0} \\ + [1 + c (1 + \delta_0^2) + \tau_5^2] b \frac{K_0}{(1 + K_0)};$$

$$B_2 = -2c(\tau_5 + \delta_0 c) - (1 + \tau_5^2 + 2\delta_0 \tau_5 c) \frac{b}{Q} \frac{K_0}{1 + K_0} - 2\delta_0^2 c b \frac{K_0^2}{(1 + K_0)^2};$$

$$D_2 = 1 + (\tau_5 + \delta_0 c)^2 + \delta_0^2 c b \frac{K_0^2}{(1 + K_0)^2} + [\delta_0 (1 + \tau_5^2) + \delta_0^2 \tau_5 c] \frac{b}{Q} \frac{K_0}{1 + K_0};$$

$$b = R_{\text{eq}}/r; \quad Q = 1/\omega_k \frac{C_1 C_2}{C_1 + C_2} r; \quad \tau_5 = \omega_k C_{\text{in}} R_5; \quad R_5 = \frac{R_5' R_{\text{in}}}{R_5' + R_{\text{in}}};$$

$$\delta_0 = \omega_k C_0 r_K.$$

As the experiments showed, oscillations are activated in the generator at the basic flexural oscillation frequency ( $\sim 2.5$  kHz for BPE of 3П-19 type) if there are no BPE defects.

There are no oscillations if one of the BPE electrodes is broken. If the circuit between BPE electrodes is short oscillations is activated at the following frequency

$$f_{\text{shc}} = \frac{1}{2\pi \sqrt{LC_{\text{ad}}}}.$$

If the BPE piezoelement is not polarized, oscillations are activated at the following frequency

$$f_{\text{ap}} = \frac{1}{2\pi \sqrt{LC_{\text{eq}}}},$$

Where  $C_{\text{eq}} = C_{\text{pe}} C_{\text{ad}} / (C_{\text{pe}} + C_{\text{ad}})$ ,  $C_{\text{pe}}$  – interelectrode capacity of BPE piezoelement [17–40].

## References

1. *New Dictionary of Foreign Words* (Sovremenny Literator, 2005), p. 1088
2. V.M. Sharapov, M.P. Musienko, E.V. Sharapova, in *Piezoelectric Sensors*, ed. by V.M. Sharapov (Technosphere, Moscow, 2006), p. 632 (in Russian)



3. V.M. Sharapov, E.A. Vasil'tsov et al., Patent of USSR No 1405813. Control of bimorph piezoelement used in Korotkoff sound sensor, No 24 (1988) (in Russian)
4. V.M. Sharapov, R.J. Kazys et al., Patent of USSR No 1571795. Devices for piezosensors control, No 22 (1990) (in Russian)
5. V.M. Sharapov, N.V. Raevskiy, Zh.V. Sotula, V.M. Nikolaenko, Control of bimorph piezoelements. Bull. Cherkasy State Technol. Univ. **1**, 95–97 (2006) (in Russian)
6. M.S. Grizno, E.V. Moskalev, *Glue and Gluing* (Chemistry, Leningrad, 1980) (in Russian)
7. I.N. Ermolov, *Theory and Practice of Ultrasonic Control* (Mashinostroenie, Moscow, 1981), p. 240 (in Russian)
8. I.N. Ermolov (ed.), *Ultrasonic Transducers for Non-destructive Control* (Mashinostroenie, Moscow, 1986), p. 280 (in Russian)
9. R. Sharp (ed.), *Methods of Non-destructive Testing* (Mir, Moscow, 1972), p. 494 (in Russian)
10. D.A. Kardahsov, *Epoxy Glues* (Chemistry, Moscow, 1973) (in Russian)
11. V.P. Popov, *Basics of Circuit Theory* (Vyssh shk., Moscow, 1985), p. 496 (in Russian)
12. V.M. Sharapov, N.V. Raevskiy, Patent of Ukraine 20940. Device for bimorph piezoelements control (in Ukrainian)
13. V.M. Sharapov, N.V. Raevskiy, Bimorph piezoelement control by bimorph piezotransformers. Bull. Cherkasy State Technol. Univ. **2**, 95–97 (2006) (in Russian)
14. V.M. Sharapov, A.N. Gurziy, M.P. Musienko, Zh.V. Sotula, Patent of Ukraine No 22603. H04R31/00. Way of the control bimorph piezoelements. Publication 25 Apr 2007 (2007) (in Ukrainian)
15. V.M. Sharapov et al., Patent of Ukraine No 17437. Device for bimorph piezoelement control. Publication No 9 (2006) (in Ukrainian)
16. V.M. Sharapov et al., Patent of Ukraine No 26614. Method of bimorph piezoelement control. Publication No 15 (2007) (in Ukrainian)
17. V.M. Sharapov, N.V. Raevskiy, I.G. Minaev, Patent of Ukraine 17422. Device for bimorph piezoelement control (in Ukrainian)
18. V.M. Sharapov, N.V. Raevskiy, Zh.V. Sotula, Patent of Ukraine 20941. Device for bimorph piezoelement control (in Ukrainian)
19. V.M. Sharapov, N.V. Raevskiy, Patent of Ukraine 20942. Device for bimorph piezoelement control (in Ukrainian)
20. V.M. Sharapov, N.V. Raevskiy, Zh.V. Sotula, Patent of Ukraine 20943. Device for bimorph piezoelement control (in Ukrainian)
21. V.M. Sharapov, N.V. Raevskiy, Patent of Ukraine 20944. Device for bimorph piezoelement control (in Ukrainian)
22. V.M. Sharapov, A.N. Gurziy, Zh.V. Sotula, Device for bimorph piezoelement control, based on aperiodic circuits. Meas. Comput. Fac. Technol. Process. **2**, 182–185 (2006) (in Russian)
23. V.M. Sharapov, V.Ya. Korr, T.G. Tymchik, Zh.V. Sotula, Device for diagnostics of bimorph piezoelement defects, based on active oscillator. Bull. Cherkasy State Technol. Univ., Special release, 270–273 (2007) (in Russian)
24. V.M. Sharapov, N.V. Raevskiy, Zh.V. Sotula, Patent of Ukraine No 28332. H04R31/00. Device for control bimorph piezoelements (2007) (in Ukrainian)
25. V.M. Sharapov, A.N. Gurziy, Zh.V. Sotula, Patent of Ukraine No 24437. H04R31/00. Device for bimorph piezoelements control. Publication 25 Jun 2007 (2007) (in Ukrainian)
26. V.M. Sharapov, A.N. Gurziy, Zh.V. Sotula, Patent of Ukraine No 24441. H04R31/00. Device for bimorph piezoelements control. Publication 25 Jun 2007 (2007) (in Ukrainian)
27. V.M. Sharapov, A.N. Gurziy, Zh.V. Sotula, Patent of Ukraine No 24797. H04R31/00. Device for bimorph piezoelements control. Publication 10 Jul 2007 (2007) (in Ukrainian)
28. V.M. Sharapov, A.N. Gurziy, Zh.V. Sotula, Patent of Ukraine No 24806. H04R31/00. Device for bimorph piezoelements control. Publication 10 Jul 2007 (2007) (in Ukrainian)
29. V.M. Sharapov, E.V. Malahov, Zh.V. Sotula, Patent of Ukraine No 26431. H04R31/00. Device for bimorph piezoelements control. Publication 25 Sept 2007 (2007) (in Ukrainian)
30. V.M. Sharapov, Zh.V. Sotula, Patent of Ukraine No 26614. H04R31/00. Way of the control bimorph piezoelements. Publication 25 Sept 2007 (2007) (in Ukrainian)

31. V.M. Sharapov, A.N. Gurziy, Zh.V. Sotula, Patent of Ukraine No 26434. H04R31/00. Device for bimorph piezoelements control. Publication 25 Sept 2007 (2007) (in Ukrainian)
32. V. Sharapov, M. Musiyenko, Zh.V. Sotula, L. Kunickaya, About the effect of expansion of reproduced frequency band by electroacoustic transducer. *Ultragarsas (Ultrasound)* **64**(3) (2009), ISSN 1392-2114
33. M. Kaufman, A.G. Cidman, *Practical Guidance by Schemes Calculations in Electronics. Directory (2 volumes)* (Energoatomizdat, Moscow, 1993), p. 288 (in Russian)
34. C.I. Baskakov, *Radio Engineering Circuits and Signals* (Vyssh shk., Moscow, 1988), p. 488 (in Russian)
35. T.A. Tatur, *Basics of Electric Circuits Theory. Manual* (Vyssh shk., Moscow, 1980), p. 271 (in Russian)
36. V.P. Sigorskiy, A.I. Petrenko, *Analysis Algorithms of Electronic Circuits* (Soviet Radio, Moscow, 1976) (in Russian)
37. V.M. Sharapov et al., Patent of Ukraine No 22603. Method of bimorph piezoelement control. Publication No 5 (2007) (in Ukrainian)
38. V.M. Sharapov, N.V. Rayevskiy, Application of LC-contours for bimorph piezoelectric element control. *Bull. Cherkasy State Technol. Univ., Special Release*, 268–270 (2006) (in Russian)
39. V.M. Sharapov, N.V. Rayevskiy, T.Ju. Kisil, Ju.Ju. Bondarenko, E.V. Malahov, Control of bimorph piezoelectric elements by bimorph piezoelectric transformers. *Bull. Cherkasy State Technol. Univ., Special Release*, 271–273 (2006) (in Russian)
40. V.M. Sharapov, N.V. Raevskiy, Zh.V. Sotula, Patent of Ukraine 17437. Device for bimorph piezoelement control (in Ukrainian)

# Chapter 8

## Piezomagnetic Sensors

Devices using piezoelectric or magnetic properties are widely used in instrument making, measuring, computer facilities, automatic control, etc. [1–3].

The idea of simultaneous use of these properties is rather perspective, and can be realized in two ways. In the first case, the elements with piezoelectric or magnetic properties have various volumes. In the second, ceramics with both piezoelectric and magnetic properties are used.

### 8.1 Influence of Magnet Design Factors on Sensor Characteristics

Cylinder- and rectangular parallelepiped-shaped magnets are widely used in practice. We will consider the influence of the design factors of these magnets on piezomagnetic transducer characteristics [4–6].

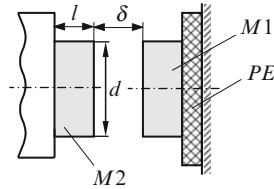
#### 8.1.1 Cylindrical Magnets

The scheme of piezomagnetic transducer with cylindrical magnets is shown in Fig. 8.1.

Output voltage of the piezomagnetic transducer, caused by constant magnet attraction force, is determined by using the formula [4, 7, 8]:

$$U_{\text{OUT}} = \frac{d_{ij} F}{C}, \quad (8.1)$$

where:  $d_{ij}$  – piezomodule,  $\text{Kl/N}$ ;  $F$  – magnet attraction force,  $\text{N}$ ;  $C$  – piezoelement capacity,  $\text{F}$ .



**Fig. 8.1** Scheme of piezomagnetic cylindrical transducer  $M1$ ,  $M2$  – constant magnets;  $\delta$  – gap (distance) between magnets;  $PE$  – piezoelement;  $l$  – magnet length;  $d$  – magnet diameter

Attraction force  $F$  developed on the magnet surface equals [9]:

$$F = \frac{B^2 S}{2\mu_0}, \quad (8.2)$$

where:  $B$  – magnetic induction, T;  $\mu_0$  – magnetic constant,  $\mu_0 = 4\pi \times 10^{-7}$ , H;  $S$  – magnet pole surface area,  $m^2$ .

Thus, the dependence of cylindrical magnet magnetic induction  $B$  on its geometry is calculated by using the formula [10]:

$$B = \frac{\mu_0 M}{2} \left[ \frac{l - 2u}{\sqrt{d^2 + (l - 2u)^2}} + \frac{l + 2u}{\sqrt{d^2 + (l + 2u)^2}} \right], \quad (8.3)$$

where:  $M$  – magnet magnetization, A/m;  $l$ ,  $d$  – magnet length and diameter, m;  $u = l/2 + \delta$  ( $\delta$  – distance between magnets, m).

It is possible to obtain dependence of the sensor output voltage  $U_{OUT}$  on cylindrical magnet geometry, using (8.1)–(8.3):

$$U_{OUT} = \frac{\mu_0 M^2 d_{ij} S}{8C} \left[ \frac{l - 2a}{\sqrt{d^2 + (l - 2a)^2}} + \frac{l + 2a}{\sqrt{d^2 + (l + 2a)^2}} \right]^2. \quad (8.4)$$

Using the correlation (8.4), we can show the dependence of sensor output voltage on ЮНДК15 (Alnico 15) cylinder magnets diameter  $d$ , length  $l$  and correlation change  $d/l$ .

In Fig. 8.2 the dependence of sensor output voltage on the gap  $\delta$  is shown with various  $d/l$  correlations and constant volume  $V$  of magnets ( $V = 0.63 \text{ cm}^3$ ).

The dependences shown in Fig. 8.5 can be approximated by power function  $y = 1/(\delta^b + 1/b)$ , where the value of constant  $b$  corresponds to correlation change  $d/l$ . Constant  $b$  decreases if the  $d/l$  correlation increases.

Figure 8.2 shows that gap  $\delta$  increase is followed by the sensor output voltage decrease. The smaller  $d/l$  correlation is, the faster the output voltage decreases with the gap increase between magnets.

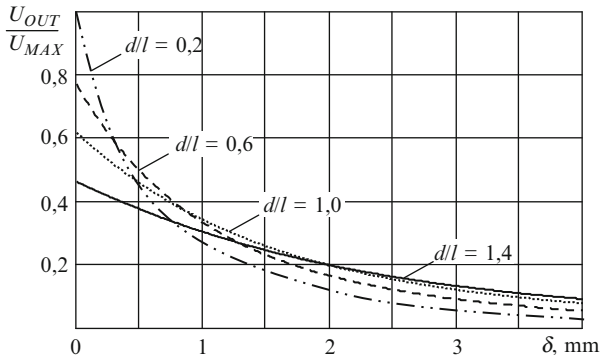


Fig. 8.2 Sensor output voltage dependence on gap  $\delta$  with various magnet  $d/l$  correlations

Table 8.1 Output voltage  $U_{OUT}/U_{MAX}$  at  $V = \text{const}$

$d/l$	$\delta(\text{mm})$			
	0.2	0.5	1.25	2.75
0.2	<b>0.7</b>	0.45	0.21	0.06
0.6	0.65	<b>0.5</b>	0.27	0.12
1.0	0.55	0.45	<b>0.30</b>	0.15
1.4	0.43	0.35	0.27	<b>0.16</b>

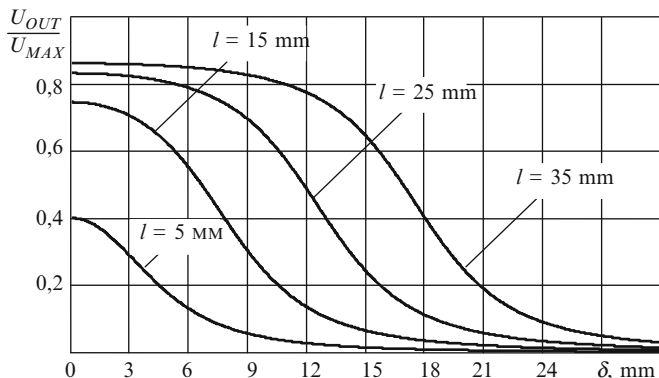


Fig. 8.3 Sensor output voltage dependence on gap  $\delta$  if magnet length  $l$  varies

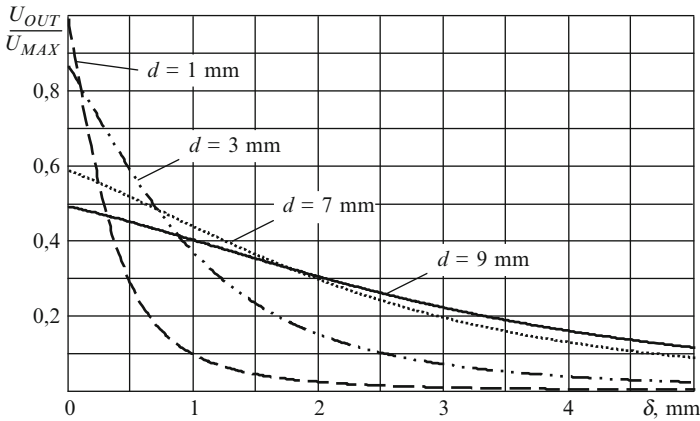
This  $d/l$  correlation, where the maximum level of output voltage is observed, corresponds to each gap  $\delta$  value. The more the gap  $\delta$  is, the bigger the correlation value  $d/l$  is (Table 8.1).

The sensor output voltage dependence on the gap  $\delta$  with various length  $l$  and  $d = 5$  mm values is shown in Fig. 8.3.

The pre-flex point dependences (gap value  $\delta$  when level 0.707 of the maximum output voltage is reached), shown in Fig. 8.3, are of a linear character. They take a form of exponential dependence  $y = 1/e^\delta$  after the flex point.

**Table 8.2** Output voltage  $U_{OUT}/U_{MAX}$  at  $d = \text{const}$

$l(\text{mm})$	$\delta(\text{mm})$			
	3	6	9	12
5	0.3	0.12	0.06	0.03
15	0.7	0.55	0.3	0.12
25	0.82	0.79	0.7	0.49
35	<b>0.86</b>	<b>0.85</b>	<b>0.83</b>	<b>0.78</b>



**Fig. 8.4** Sensor output voltage dependence on gap  $\delta$  (distance) if magnet diameters  $d$  vary

As is shown in Fig. 8.3, the sensor output voltage increases dramatically with the gap  $\delta$  decrease to the flex point. Further gap  $\delta$  decrease does not result in considerable output voltage increase.

A sensor with a greater magnet length  $l$  (Table 8.2) has a higher level of output voltage with the same  $\delta$  value.

The dependence of sensor output voltage on the gap  $\delta$  with different magnet diameters  $d$  and length  $l = 3 \text{ mm}$  values is represented in Fig. 8.5.

The dependences shown in Fig. 8.4 can be approximated by power function  $y = 1/(\delta^b + 1/b)$ , where the value of constant  $b$  corresponds to changes in diameter  $d$ . Constant  $b$  decreases with diameter  $d$  increase.

As is shown in Fig. 8.4, the sensor output voltage increases with gap  $\delta$  decrease. The smaller the diameter  $d$ , the faster the output voltage with gap  $\delta$  increase between magnets drops.

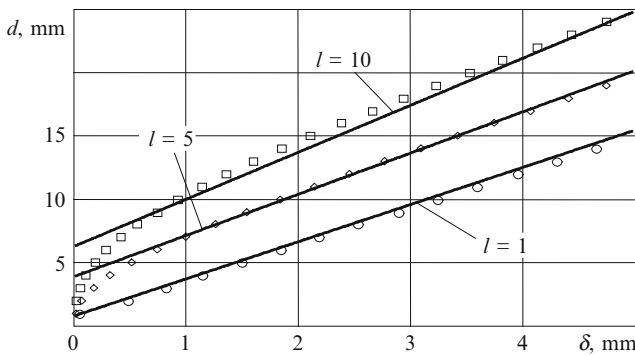
The diameter  $d$  with the maximum level of output voltage corresponds to each gap  $\delta$  value. The bigger the gap  $\delta$  is, the bigger the diameter  $d$  (Table 8.3).

The dependences of magnet diameter–gap  $\delta$  diagrams and their approximating curves for certain length  $l$  values are shown in Fig. 8.5.

They are of a linear character, and are shown by the equation:  $y = kx + b$ . Having this, we can calculate the necessary diameter  $d$  value for any gap  $\delta$  value.

**Table 8.3** Output voltage  $U_{OUT}/U_{MAX}$  at  $l = \text{const}$

$d(\text{mm})$	$\delta(\text{mm})$			
	0.1	0.5	1.0	2.5
1	<b>0.9</b>	0.29	0.1	0.02
3	0.84	<b>0.59</b>	0.38	0.11
7	0.58	0.52	<b>0.45</b>	0.25
9	0.49	0.45	0.4	<b>0.27</b>



**Fig. 8.5** Diagrams of magnet diameter–gap  $\delta$  dependences and their approximating curves

**Table 8.4** Factor values of approximating curves

$l$ (mm)	1	2	3	4	5	6	7	8	9	10
$k$	2.844	2.894	2.946	3.043	3.137	3.222	3.289	3.45	3.541	3.706
$b$	0.769	1.706	2.581	3.213	3.894	4.377	5.283	5.378	6.01	6.272

$k$  and  $b$  values of approximating curve equations for magnets with various length  $l$  are shown in Table 8.4.

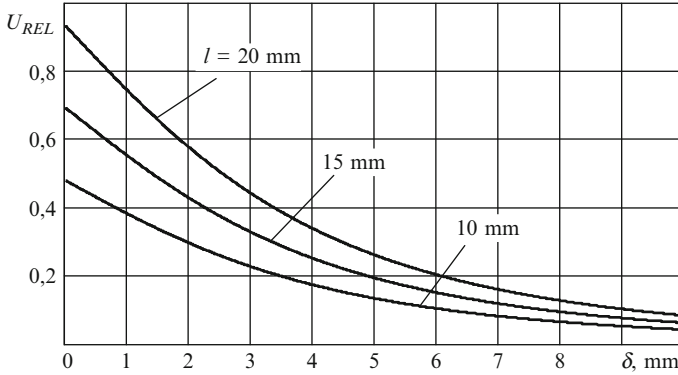
### 8.1.2 Rectangular Magnets

The dependence of rectangular magnet magnetic induction  $B$  on its geometry is determined by using the formula [10]:

$$B = \frac{\mu_0 M V}{4\pi} \left( \frac{l}{a^2 + u^2} + \frac{l}{b^2 + u^2} \right), \tag{8.5}$$

where:  $M$  – magnet magnetization, A/m;  $V$  – magnet volume,  $\text{m}^3$ ;  $l$  – magnet length, m;  $u = l/2 + \delta$  ( $\delta$  – gap between magnets, m).

We investigate dependences of piezomagnetic transducer output voltage on magnet width  $a$ , length  $l$  and also correlation changes  $a/b$ .



**Fig. 8.6** Sensor output voltage–gap  $\delta$  dependence if magnet length  $l$  varies

**Table 8.5** Output voltage  $U_{OUT}$  with  $a = b = \text{const}$

$l(\text{mm})$	$\delta(\text{mm})$			
	1	3	5	7
10	0.38	0.22	0.15	0.09
15	0.55	0.32	0.19	0.12
20	<b>0.75</b>	<b>0.45</b>	<b>0.28</b>	<b>0.17</b>

Using (8.1), (8.2) and (8.5), it is possible to obtain the dependence of sensor output voltage  $U_{OUT}$  on rectangular magnet geometry:

$$U_{OUT} = \frac{\mu_0 M^2 d_{ij} V S}{8\pi C} \left( \frac{l}{a^2 + u^2} + \frac{l}{b^2 + u^2} \right)^2. \tag{8.6}$$

Using the correlation (8.6), we can trace the dependence of the sensor output voltage on ЮНДК15 (Alnico15) rectangular magnets width  $a$ , length  $l$  and correlation change  $a/b$ .

The sensor output voltage dependence on gap  $\delta$  with various length  $l$  values is shown in Fig. 8.6.

The dependences represented by Fig. 8.6 are in the form of exponential function  $y = 1/n^\delta$ . Constant  $n$  value decreases with length  $l$  increase.

As is shown in Fig. 8.6, the sensor output voltage decreases with gap  $\delta$  increase. The smaller the magnet length  $l$  is, the smaller the output voltage value is (Table 8.5).

The sensor output voltage dependence on the gap  $\delta$  with various  $a/b$  correlations and length  $l = 10$  mm ( $V = 1 \text{ cm}^3$ ) is shown in Fig. 8.7.

The dependences obtained in Fig. 8.7 are of a linear character, and can be approximated by the dependence:  $y = -k\delta + b$ . Bigger  $k$  and  $b$  values correspond to bigger  $a/b$  correlation value.



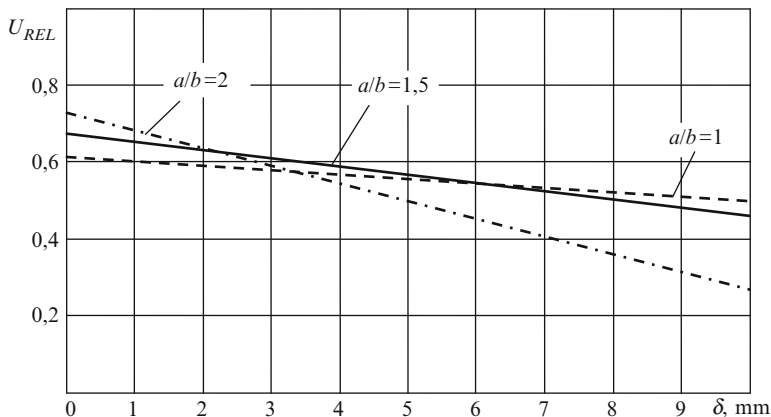


Fig. 8.7 Sensor voltage-gap  $\delta$  dependence with various  $a/b$  correlation

Table 8.6 Output voltage  $U_{REL}$  with  $l = \text{const}$  and  $V = \text{const}$

$a/b$	$\delta(\text{mm})$		
	1	5	9
1	0.6	0.56	<b>0.52</b>
1.5	0.66	<b>0.57</b>	0.49
2	<b>0.7</b>	0.5	0.3

As can be seen in Fig. 8.7, the sensor output voltage increases if gap  $\delta$  decreases. The bigger  $a/b$  value is, the faster the output voltage with gap  $\delta$  between magnets increase drops.

$a/b$  correlation with the maximum output voltage level corresponds to each gap  $\delta$  value. The bigger the gap  $\delta$  is, the stronger the  $a/b \rightarrow 1$  correlation (Table 8.6).

The sensor output voltage dependence on gap  $\delta$  with various magnet width  $a$  values and constant magnet length of  $l = 10$  mm is shown in Fig. 8.8.

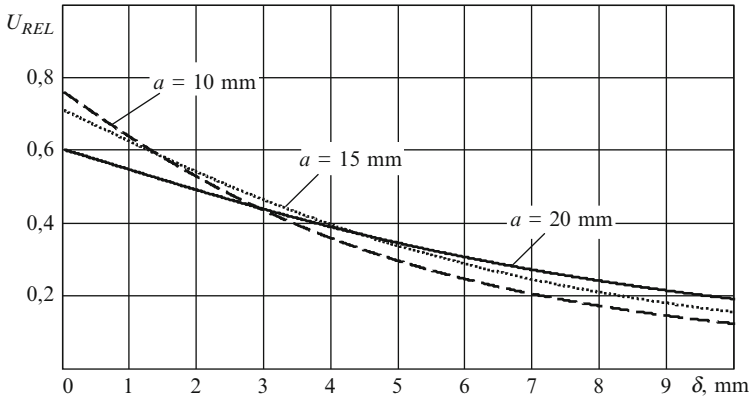
The dependences presented in Fig. 8.8 can be approximated by power function  $y = 1/(\delta^m + 1/m)$ . Constant  $m$  decreases with the increase in magnet width  $a$ .

As is shown in Fig. 8.8, the sensor output voltage increases with the gap  $\delta$  decrease. The smaller the magnet width  $a$ , the faster the increase in output voltage with gap  $\delta$  between magnets drops.

Magnet width  $a$  with the maximum output voltage level corresponds to each gap  $\delta$  value. The bigger the gap  $\delta$  is, the bigger the magnet width  $a$  (Table 8.7).

The diagrams of magnet width-gap  $\delta$  dependences and their approximating curves for certain length  $l$  values are represented in Fig. 8.9.

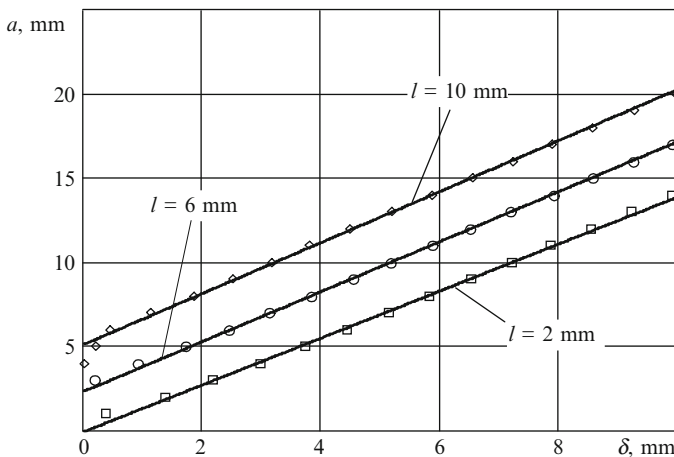
They are of a linear character, and can be shown by the equation:  $y = kx + b$ . This helps calculate the necessary width  $a$  value for any gap  $\delta$  value.



**Fig. 8.8** Sensor output voltage dependence on gap  $\delta$  if magnet width  $a$  and  $l = \text{const}$  are changed

**Table 8.7** Output voltage  $U_{OUT}/U_{MAX}$  with  $l = \text{const}$

$a(\text{mm})$	$\delta(\text{mm})$		
	0.5	2.5	7.0
10	<b>0.7</b>	0.47	0.2
15	0.6	<b>0.51</b>	0.23
20	0.58	0.45	<b>0.3</b>



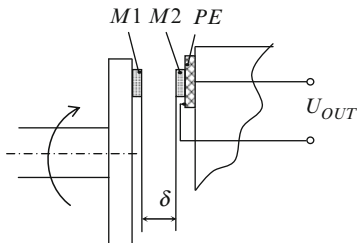
**Fig. 8.9** Diagrams of magnet width-gap  $\delta$  dependences and their approximating curves

$k$  and  $b$  values of approximating curves equations for magnets with various length  $l$  values are shown in Table 8.8.

Thus, the dependences discussed can help determine the design factors of cylindrical and rectangular magnets which are needed to have the required characteristics of piezomagnetic transducers [4-6].

**Table 8.8** Approximating curve values

$l$ (mm)	2	4	6	8	10
$k$	1.4	1.47	1.49	1.5	1.52
$b$	-0.1	0.9	2.3	3.7	5.1



**Fig. 8.10** Scheme of tachometer piezomagnetic sensor

## 8.2 Piezomagnetic Sensors of Tachometers

Piezomagnetic sensors of tachometers have a bigger sensitivity, small weight and dimensions. They do not need power supplies, and can work when environmental temperatures are comparatively high, etc. [4, 9, 11–14].

The scheme of a tachometer piezomagnetic sensor is shown in Fig. 8.10.

Constant magnet  $M1$  is attached to the shaft of the mechanism studied. Piezoelement  $PE$  with two electrodes is attached to the stator. The second constant magnet  $M2$  is attached to the piezoelement. Constant magnet  $M1$  passes close to the stable magnet  $M2$  on each shaft rotation. Interaction magnetic forces draw or repel the magnets (depending on their polarity). The influence of the forces causes deformation of the piezoelement  $PE$ . This results in the appearance of voltage  $U_{OUT}$  on the piezoelement electrodes [9].

Below, we will determine the force influencing the piezoelement. If the magnet is rigidly fastened to the piezoelement, the force will be equal to the magnetic attraction force.

To determine this force, we will consider the area of two environments – magnet and air. As the magnet with material permeability  $\mu_1$  is surrounded by air with permeability  $\mu_0$ , we assume that there is a super thin transitive layer on the magnet surface. In this layer, the permeability of both normal component of magnetic field  $H_n$  intensity and magnetization  $I_n$  intensity changes gradually: (Fig. 8.11) [15].

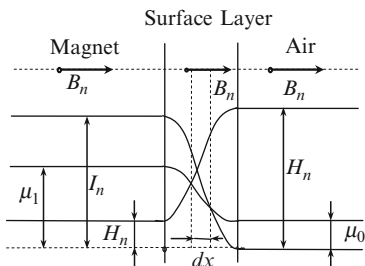
The normal component of magnetization  $I_n$  intensity equals [16]:

$$I_n = B_n - \mu_0 H_n = (\mu_1 - \mu_0) H_n, \tag{8.7}$$

where  $B_n$  is the normal component of magnetic induction.

As  $B_n = \text{const}$ , then

$$dI_n = -\mu_0 dH_n. \tag{8.8}$$



**Fig. 8.11** Values change of magnetic field in magnet surface layer

We will take a small area with  $dx$  thickness in the transitive layer. This area is the distance between “southern” and “northern” surfaces of an elementary magnetic sheet. Southern surfaces are in  $H_n$  intensity field, while northern are in  $H_n + dH_n$ . Thus, each magnetic sheet of  $dx$  thickness is subject to  $dH_n$  force. If  $I_n$  is considered as the surface density of magnetic masses, then the pressure strength in the  $dx$  layer will be [15]:

$$dp = I_n dH_n = -\frac{1}{\mu_0} I_n dI_n. \tag{8.9}$$

Integrating and substituting from (8.7), we will obtain:

$$P = \int_{I_n}^0 dp = \frac{I_n^2}{2\mu_0} = \frac{(B_n - \mu_0 H_n)^2}{2\mu_0}. \tag{8.10}$$

Then, the attraction force on the magnet surface equals [15]:

$$F = \frac{(B_n - \mu_0 H_n)^2 S}{2\mu_0}, \tag{8.11}$$

where  $S$  is the surface area of a magnet pole.

As  $B_n \gg \mu_0 H_n$ , the formula (8.11) will be:

$$F = \frac{B_n^2 S}{2\mu_0}. \tag{8.12}$$

The attraction force  $F$ , influencing the magnet rigidly fastened to the piezoelement, causes appearance of voltage  $U_{OUT}$  on the piezoelement electrodes.

As the normal component of magnetic induction is not always known, the formula (8.11) is not convenient for calculations.

On the other hand, constant magnet attraction force can be calculated by using the general energy formula as the magnetic system energy–air gap ratio [10]:

$$F = \frac{W}{\delta}, \quad (8.13)$$

where:  $W$  – magnetic system energy;  $\delta$  – air gap length.

Magnetic system energy on a loop segment of magnetization reversal cycle equals [15]:

$$W = \frac{1}{2} B_i H_p V_M, \quad (8.14)$$

where:  $B_i$  – internal magnet induction;  $H_p$  – demagnetizing field intensity;  $V_M$  – magnet volume.

Magnet internal induction and demagnetizing field intensity depend on magnet form permeability and its (magnet) magnetization [10]:

$$B_i = \mu_0 M \left( 1 - \frac{1}{m} \right), \quad (8.15)$$

where:  $M$  – magnet magnetization;  $m$  – magnet form permeability.

$$H_p = \frac{M}{m}. \quad (8.16)$$

Magnet permeability depends on its form.

Form permeability of a rotation ellipsoid with semi-axes  $a$ ,  $b$  and  $c$  is calculated by using the following [10]:

For an oblong ellipsoid ( $a > b$ ,  $c = b$ ):

$$m = \frac{\gamma^3}{(1 - \gamma^2) \left( 0.5 \ln \frac{1+\gamma}{1-\gamma} - \gamma \right)}, \quad (8.17)$$

where  $\gamma = \sqrt{1 - (b/a)^2}$ ;

for a sphere ( $a = b = c$ )

$$m = 3, \quad (8.18)$$

for an oblate (prolate) ellipsoid ( $a < b$ ,  $c = b$ )

$$m = \frac{\beta^3}{(1 + \beta^2)(\beta - \arctg\beta)}, \quad (8.19)$$

where  $\beta = \sqrt{(b/a)^2 - 1}$ .

To calculate form permeability  $m$  for non-ellipsoid-shaped magnets, empirical formulas or graphs are used. This causes problems when mathematical models of devices with constant magnets are produced.

Cylinder form permeability is calculated by using Thompson and Moss's experimental curves with Arkadiev correction. Using ballistic method curves, axial (bar) magnet form permeability  $m$ -relative length  $\lambda$  dependence can be determined by the formula [10]:

$$\lambda = \frac{l_M}{\sqrt{S_M}}, \quad (8.20)$$

where:  $\lambda$  – magnet relative length;  $l_M$  – magnet length.

Relative length  $\lambda$  of modern axial (bar) magnets is in the range  $\lambda = 1 - \lambda = 10$ . In this range, solid cylindrical magnet curves are easily approximated by the formulas [10]:

$$m = \frac{(1.06\lambda)^2 - 1}{\frac{1.06\lambda}{\sqrt{(1.06\lambda)^2 - 1}} \ln \left[ 1.06\lambda + \sqrt{(1.06\lambda)^2 - 1} \right] - 1} + 0.9\lambda e^{-0.2\lambda}, \quad (8.21)$$

for a hollow (quill) cylinder:

$$m_n = m \frac{d_{ex}^2}{d_{ex}^2 - d_{in}^2}, \quad (8.22)$$

where  $d_{ex}$  and  $d_{in}$  are the external and internal cylinder diameters.

Diametrically magnetized short cylinders are also referred to axial magnets. This cylinder form permeability is calculated by using the formula:

$$m = 2 + \frac{d_m}{l_m}, \quad (8.23)$$

where  $d_m$  is magnet diameter. For a cube  $m = 3$ .

A sensor design with cylindrical-shaped magnets is considered below. Substituting values (8.14), (8.15), (8.16), (8.21) in (8.13), the dependence of constant magnet attraction force on its geometry, magnetization and air gap is obtained:

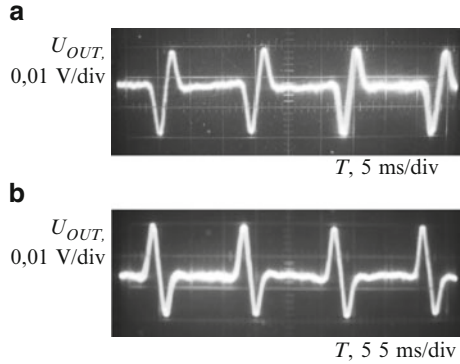
$$F = \frac{1}{2} \frac{\mu_0 M^2 V_m (m - 1)}{m^2 \delta}. \quad (8.24)$$

Piezoelement electrode voltage caused by constant magnet attraction force:

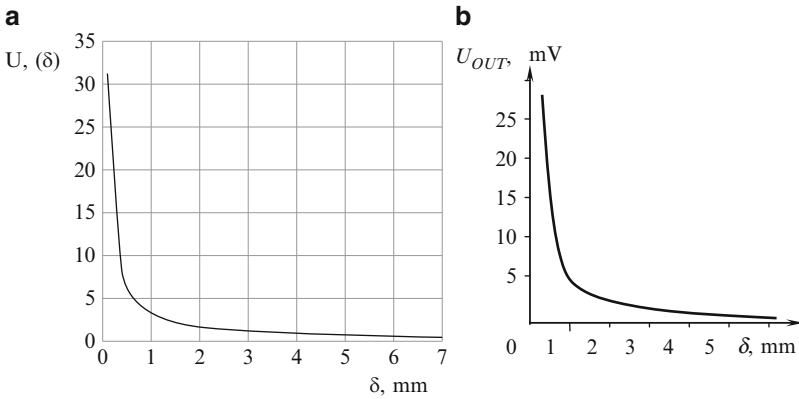
$$U_{OUT} = d_{ij} F / C = \frac{1}{2} \frac{d_{ij} \mu_0 M^2 V_m (m - 1)}{C m^2 \delta}, \quad (8.25)$$

where:  $d_{ij}$  – piezomodule,  $C$  – piezoelement capacity.

For experimental investigation, the following device was made: engine ДПМ-20-Н3-01, disk piezoelement  $\varnothing 15 \times 1$  mm made of ИТС-19, samarium-cobalt  $\varnothing 10 \times 2$  disk magnets. The engine was connected to a Б5-50 (B5-50) power supply.



**Fig. 8.12** Output signal of tachometer piezomagnetic sensor



**Fig. 8.13** Dependence of magnetic tachometers piezosensor output voltage on distance between magnets: (a) estimated dependence, (b) experimental dependence

Measurements were made by oscillograph C1–55 and by B7–68 (V7–68) voltmeter, and photographs by digital camera Canon Power Shot G2.

Piezomagnetic sensor output electric signals are shown in Fig. 8.12.

When magnets pass along each other, there arises attraction or repulsive (repelling) force, depending on the magnet’s polarity. When magnets approach each other, like-sign signals are generated on the piezoelement; when they move away, opposite-sign signals are indicated (Fig. 8.12a).

The change in a magnet’s polarity results in a polarity change to the output signal impulses (Fig. 8.12b).

The dependence of magnetic tachometers piezosensor output voltage on the distance between the magnets  $\delta$  is shown in Fig. 8.14 [17, 18].

Using Mathcad 7.0, the estimated dependence, obtained from the formula (8.25), is presented in Fig. 8.13. To obtain mathematical models of magnetic piezosensors with the other magnet shape, it is enough to insert in (8.24) the corresponding form

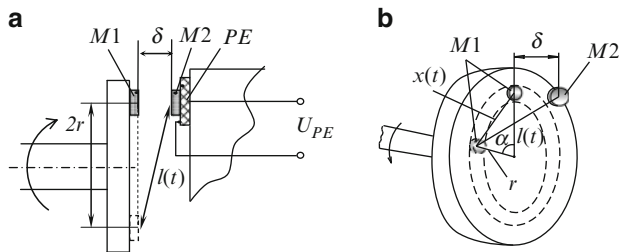


Fig. 8.14 Tachometer piezomagnetic sensor

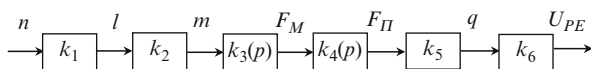


Fig. 8.15 Schematic diagram of tachometer piezomagnetic sensor

permeability value of the magnets used. The experimentally obtained dependence is given in Fig. 8.13.

As the Fig. 8.13 shows, experimental results are not much different from the theoretical.

### 8.2.1 Piezomagnetic Sensor Models

It is a well-known fact that a piezoceramic element has oscillatory link properties [19–21]. However, as it is seen in Fig. 8.15, there is no oscillating process in the output signal of the tachometer piezomagnetic sensor.

To explain this, we will design and study a transducer model, using the methods of automatic control theory [22].

The piezomagnetic sensor is shown in Fig. 8.14 [23].

The sensor schematic diagram is shown in Fig. 8.15.

Here, link  $k_1$  corresponds to shaft rotation frequency transformation  $n$  in distance change between magnets  $l(t)$ .

It can be seen in Fig. 8.14b that the unknown quantity  $l(t)$  equals:

$$l(t) = \sqrt{x^2(t) + \delta^2}, \quad (8.26)$$

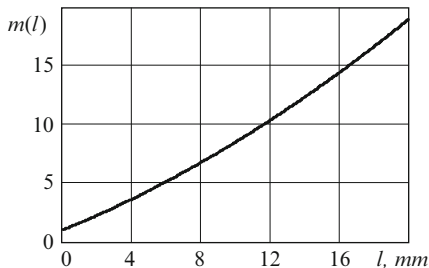
where  $x(t) = 2r \sin(\alpha/2)$ ,  $\alpha = kt$ ,  $k = 2\pi n$ .

Then

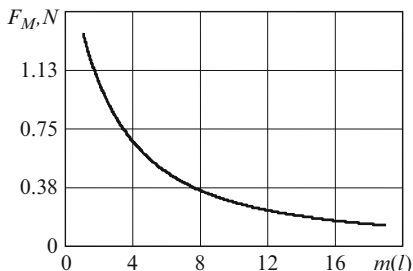
$$l(t) = \sqrt{4r^2 \sin^2(\pi nt) + \delta^2}. \quad (8.27)$$

Link  $k_2$  describes the change of permeability form of air gap  $m$  if the distance between magnets  $l$  changes.





**Fig. 8.16** Form permeability of axial (bar) air gap



**Fig. 8.17** Force  $F_M - m(l)$  dependence

$m$  value depends only on the air-gap form. It is convenient to calculate  $m$  for an ellipsoid-shaped gap. For non-ellipsoid-shaped gaps, empirical formulas or graphs which have been discussed above are used [4, 7, 9–11].

In Fig. 8.16,  $m$  calculation results for an axial (bar) air gap are shown.

As can be seen in Fig. 8.16,  $m-l$  dependence can be considered approximately linear; thus link  $k_2$  is inertialess.

Link  $k_3$  corresponds to  $m$  transformation into interaction force between magnets  $F_M$  which can be determined by the formula [24, 25]:

$$F_M(l) = \frac{1}{2} B^2 \frac{\mu_0 S l_M}{[\rho + m(l)\mu_0]^2} \frac{dm(l)}{dl}, \tag{8.28}$$

Where:  $\mu_0$  – magnetic constant ( $\mu_0 = 4\pi \times 10^{-7}$  H/mm),  $B$  – magnetic induction (T),  $\rho$  – reset coefficient (H/m),  $l_M$  – magnet thickness.

To determine  $k_3$  link transfer function, Laplace representation of composite function is needed:

$$L [F (l)] = L [f (l) \times m' (l)], \tag{8.29}$$

where  $f(l) = \mu_0 S l_M / [\rho + m(l)\mu_0]^2$ .

We will determine link type  $k_3$  below, using  $F_M$  design dependence on air-gap magnetic permeability  $m(l)$  which is shown in Fig. 8.17.

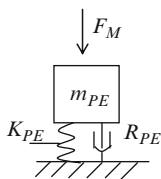


Fig. 8.18 Equivalent mechanical model of link  $k_4$

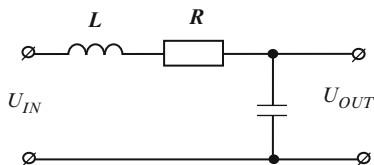


Fig. 8.19 Equivalent electric scheme of link  $k_4$

Calculations are made by the technique [10], used for disk magnets 5 mm in diameter and 3 mm thick,  $I_n = 0.1$  T,  $\rho = 5 \times 10^{-6}$  H/m.

As can be seen in Fig. 8.17, a  $k_3$  link is a differentiating inertial link [22, 26, 27].

Transfer function and transitive characteristic of this link are described by the following:

$$k_3(p) = \frac{kp}{Tp + 1}, \quad (8.30)$$

$$h_3(t) = \frac{k}{T} e^{-\frac{t}{T}}. \quad (8.31)$$

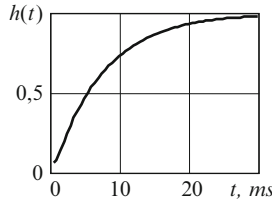
Link  $k_4$  corresponds to  $F_M$  interaction force between magnet transformation into the force creating pressure in the piezoelement. If the magnet is considered to be an incompressible solid which transfers  $F_M$  force without distortions, the  $k_4$  equivalent mechanical link model will look as shown in Fig. 8.18.

Using the electromechanical analogies method [27, 28], the equivalent mechanical model in Fig. 8.18 can be transformed into the equivalent electric scheme, represented in Fig. 8.19.

Here,  $m_{PE}$  – mass of piezoelement,  $K_{PE}$  – piezoelement material elasticity,  $R_{PE}$  – losses in piezoelement.

This system motion equation, connecting  $U_s$  voltage on the condenser (equivalent to  $F_p$  force) with input signal  $U_{in}$  (equivalent to force  $F_M$ ), will look like [27]:

$$CL \frac{dU_c^2(t)}{dt^2} + RC \frac{dU_c(t)}{dt} + U_c(t) = U_{in}. \quad (8.32)$$



**Fig. 8.20** Transitive characteristic of link  $k_4$

The following symbols are used:  $CL = T_2^2$ ,  $RC = T_1$ ,  $U_c(t) = y(t)$ ,  $U_{in}(t) = kx(t)$ . Transiting to Laplace space, the (8.32) is:

$$T_2^2 p^2 Y(p) + T_1 p Y(p) + Y(p) = kX(p). \tag{8.33}$$

Whence

$$k_4(p) = \frac{Y(p)}{X(p)} = \frac{1}{T_2^2 p^2 + T_1 p + 1}. \tag{8.34}$$

Equation (8.34) is the transfer function of inertial (aperiodic) second order link.

This link transitive characteristic is described by the following [26, 27]:

$$h_4 = k \left[ 1 - \frac{1}{T_3 - T_4} \left( T_3 e^{-\frac{t}{T_3}} - T_4 e^{-\frac{t}{T_4}} \right) \right], \tag{8.35}$$

where  $T_{3,4} = 1/2 \left( T_1 \pm \sqrt{T_1^2 - 4T_2^2} \right)$ : this is shown in Fig. 8.20.

The link with coefficient transfer  $k_5$  corresponds to force  $F_p$  transformation into charge  $q$  on the piezoelement electrodes. As  $q = d_{31} F_p$ ,

$$k_5 = \frac{q}{F_p} = d_{31}. \tag{8.36}$$

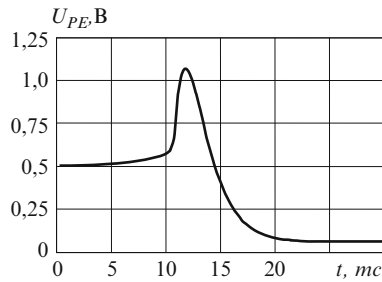
where  $d_{31}$  is the piezomodule.

Link  $k_6$  is charge  $q$  transformation into voltage  $U_{PE}$  on the piezoelement electrodes. In general, the transfer characteristic of the given link looks like:

$$k_6 = \frac{U_{PE}}{q} = \frac{1}{\left( 1 + \frac{1}{p R_{PE} C_{PE}} \right) C_{PE}}, \tag{8.37}$$

where:  $R_{PE}$  – resistance,  $C_{PE}$  – piezoelement capacity,  $p = j\omega$ . However, taking into account the high value of piezoelement resistance  $R_{PE}$ , it is possible to consider

$$k_6 = \frac{1}{C_{PE}}. \tag{8.38}$$



**Fig. 8.21** Output characteristic of piezomagnetic tachometer sensor

The general transfer function will look like this [5, 6, 8]:

$$K(p) = k_1 k_2 k_3(p) k_4(p) k_5 k_6. \quad (8.39)$$

To get the input characteristic, we use the formula of frequency-transfer interconnection characteristics [27]:

$$h(t) = \frac{2}{\pi} \int_0^{\infty} \frac{\text{Re}[K(p)] \sin \omega t}{\omega} d\omega, \quad (8.40)$$

where  $\text{Re}[K(p)]$  is the real component of the frequency characteristic.

In Fig. 8.21 (8.39), the output characteristic of the piezomagnetic tachometer sensor, calculated by using the formulas (8.39) and (8.40), is shown.

As is shown in Fig. 8.21, the signal form coincides with the positive half-wave of the experimentally received signal (Fig. 8.12). The negative half-wave corresponds to the piezoelement initial distortion process, which occurs when the distance between magnets increases. Theoretically, this signal form may be received when the limits of integration are changed in the formula (8.40).

Thus, the sensor transfer function has the following links: second order aperiodic (inertial), differentiating inertial, and instantaneous (proportional, linear). The experimental characteristics obtained coincide with the theoretical research results, proving the correctness of the piezomagnetic tachometer sensor model designed.

The transitive characteristic of piezomagnetic sensor rotary speed (number of revolutions/turns) is studied below [29].

As is known, a system dynamic properties or its separate link can visually be expressed by a transitive characteristic (transitive function). This shows the system reaction on the unit function influence (unit step signal) [22, 26, 27].

The use of coil  $K$  as a rotor magnet to obtain the unit influence was suggested. In this coil, magnetic field influence imitation of a moving magnet is achieved by the feed (supply) of the demanded voltage form on the coil block (Fig. 8.22) [29].

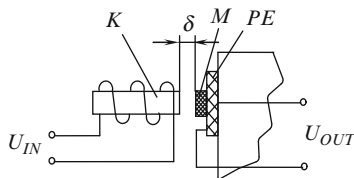


Fig. 8.22 Scheme of piezomagnetic sensor: *K* – coil, *M* – magnet, *PE* – piezoelement

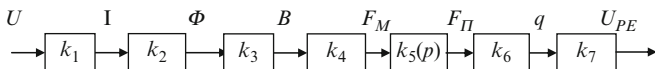


Fig. 8.23 Block scheme of tachometer piezomagnetic sensor

Using the methods of automatic control theory [22, 26, 27], the transitive characteristic can be received from the transfer function of the piezomagnetic sensor.

In this case, it is better to represent the transducer block scheme as it is shown in Fig. 8.23 [29].

In Fig. 8.26, link  $k_1$  shows the input voltage transformation into the coil current  $I$  :  $I = U/R$ , where  $U_{IN}$  is the voltage impressed on the coil, and  $R$  is coil resistance. Thus,  $k_1 = I/U = 1/R$ .

Link  $k_2$  describes the appearance of magnetic stream  $J$  under the  $I$  coil current action:  $J = LI$ , where  $L$  is coil inductance. From here,  $k_2 = F/I = L$ .

Link  $k_3$  describes transformation of coil  $J$  magnetic flow (flux) into magnetic induction  $B$  :  $F = BS$ , where  $S$  is magnet area. We obtain:  $k_3 = 1/S$ .

Link  $k_4$  corresponds to  $B$  transformation into  $F_M$  force, influencing the magnet [10, 25]:

$$F_M = \frac{1}{2} \frac{B^2 S}{\delta}, \tag{8.41}$$

where  $\delta$  is the gap between coil and magnet.

Link  $k_5(p)$  corresponds to  $F_M$  force transformation into the force, creating voltage in piezoelement  $F_p$ .

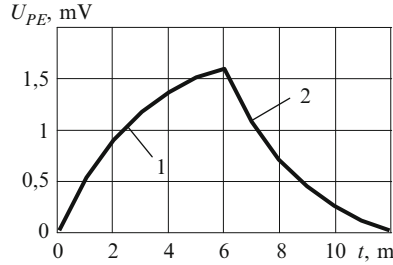
Transfer function expression for link  $k_5(p)$  is obtained by an electromechanical analogy theory method [27, 28]. This is a transfer function of inertial (aperiodic) second order link.

The link transitive characteristic is described by the expression (8.35), and is shown in Fig. 8.23.

The link with  $k_6$  transfer constant corresponds to force  $F_p$  transformation into charge  $q$  on the piezoelement electrodes. As  $q = d_{31} F_p$ ,

$$k_6 = \frac{q}{F_p} = d_{31}, \tag{8.42}$$

where  $d_{31}$  is the piezomodule.



**Fig. 8.24** Transitive characteristic of piezomagnetic sensors

Link  $k_7$  – charge  $q$  transformation into voltage  $U_{PE}$  on the piezoelement electrodes:

$$k_7 = \frac{1}{C_{PE}}, \tag{8.43}$$

Where:  $R_{PE}$  – resistance,  $C_{PE}$  – piezoelement capacity.

The general transfer function is represented as:

$$K(p) = k_1 k_2 k_3 k_4 k_5(p) k_6 k_7. \tag{8.44}$$

To obtain the transfer characteristic, the interrelation frequency-transfer characteristics formula is used [27]:

$$h(t) = \frac{2}{\pi} \int_0^{\infty} \frac{\text{Re}[K(\omega)] \sin \omega t}{\omega} d\omega + h(0), \tag{8.45}$$

where  $\text{Re}[K(\omega)]$  is the real component of frequency characteristic.

In Fig. 8.24, the transitive characteristic obtained by Mathcad 2001 programs is shown.

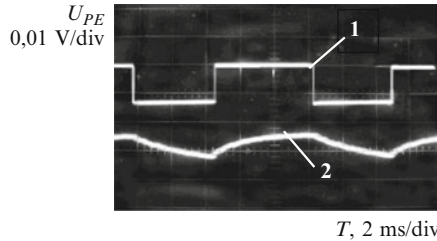
The following parameters were used in calculation: coil inductance  $L = 1$  H, resistance of winding  $R = 325$  Ohm, piezomodule  $d_{31} = 75 \times 10^{-12}$  k/N.

To obtain the system reaction on the rectangular impulse action, two signals were considered:

- System reaction within 6 ms to the positive voltage step (jump) signal (curve 1 in Fig. 8.24):

$$h_1(t) = \frac{2}{\pi} \int_0^{\infty} \frac{\text{Re}[K(\omega)] \sin \omega t}{\omega} d\omega, \tag{8.46}$$

where  $t = 1-6$  ms;



**Fig. 8.25** Output signals of tachometer piezomagnetic sensor: 1 – input voltage; 2 – output voltage

- System reaction to the negative voltage step (jump) signal (curve 2 in Fig. 8.24), subject to  $\tau = 6$  ms delay and nonzero entry conditions

$$h_2(t) = \frac{2}{\pi} \int_{\infty}^0 \frac{\text{Re}[K(\omega)] \sin \omega(t - \tau)}{\omega} d\omega + h_1(6 \times 10^{-3}). \tag{8.47}$$

A piezomagnetic sensor, consisting of  $\varnothing 15 \times 1$  ИТС-19 disk piezoelement,  $\varnothing 10 \times 2$  samarium–cobalt disk magnet,  $L = 1$  H coil with 325 ohm field resistance, was used for the experimental check.

The measurements were made by C1–55 oscillograph and B7–68 (V7–68) voltmeter. The voltage on the coil was transferred from Г5–67 (G5–67) generator. Photographs were taken using a Canon Power Shot G2 digital camera.

The output signals obtained are shown in Fig. 8.25.

As is shown in Figs. 8.24 and 8.25, the experimental data coincide with the theoretical research results [29].

Thus, the tachometer piezomagnetic sensor has inertial (aperiodic) link properties. This explains the absence of system oscillatory properties. However, there is a piezoelement with oscillatory properties in the system.

### 8.3 Improvement of Piezomagnetic Sensor Characteristics

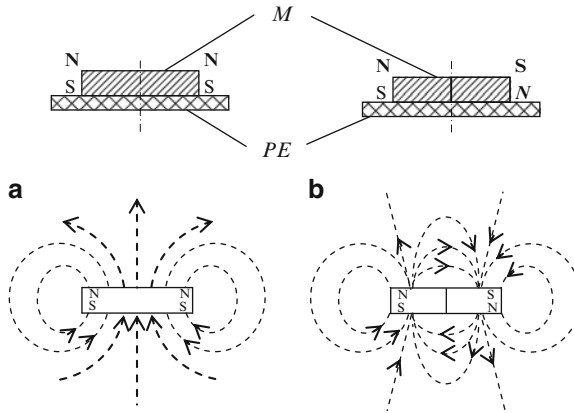
#### 8.3.1 Output Signal Enhancement

One of the drawbacks of piezomagnetic transducers is the comparatively low amplitude of output voltage.

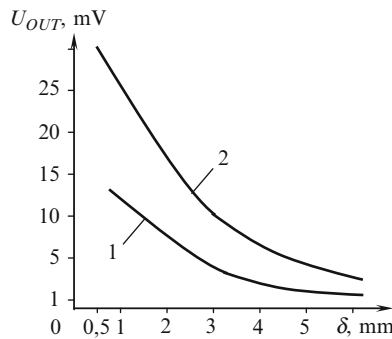
Several output signal enhancement methods have been developed [9, 30–35].

One of them is the pattern change of the magnet’s magnetic field constant. It is reached by a change in magnet design.

Examples of the transducers are given in Figs. 8.26 and 8.28 [36, 37].



**Fig. 8.26** Designs of piezomagnetic rotation frequency sensors: (a) solid magnet (as in Fig. 8.10), (b) two-piece magnet with opposite directions magnetizations; *M* – magnet, *PE* – piezoelement



**Fig. 8.27** Dependence of output signal amplitude on distance between magnets  $\delta$ . 1 – with magnet field shown in Fig. 8.26a, 2 – with magnet field shown in Fig. 8.26b

As can be seen in Fig. 8.26, the transducer magnet is split into two parts; the polarisation direction is changed in one of them (Fig. 8.26b) [36].

Force lines join if the design is changed. This results in a pattern change of the magnetic field. Piezomagnetic transducer properties are changed too.

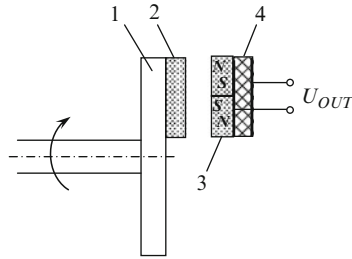
The dependence of output signal amplitude on the distance between magnets  $\delta$  is shown in Fig. 8.27 [9,35].

As can be seen in Fig. 8.27, the output signal amplitude was increased twice as a result of design changes.

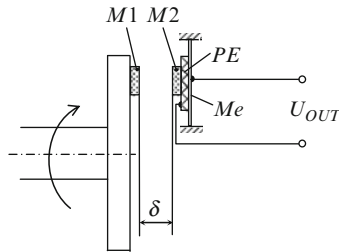
The other variant of the change in sensor magnet design is shown in Fig. 8.28 [37].

After the design change to the magnet constant, the signal amplitude was increased four times [37].

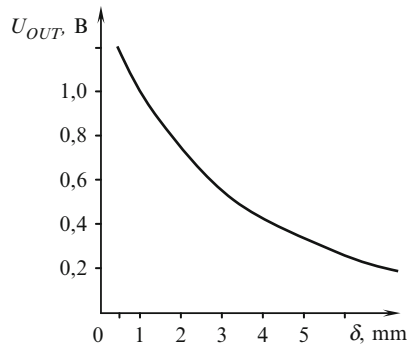




**Fig. 8.28** Design of tachometer piezomagnetic sensor: 1 – rotor; 2, 3 – magnets; 4 – piezoelement



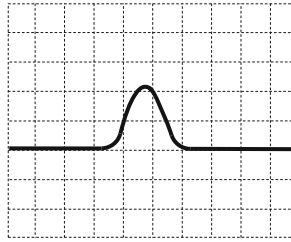
**Fig. 8.29** Piezomagnetic sensor of rotation frequency with bimorph piezoelement:  $M1$ ,  $M2$  – constant magnets;  $PE$  – piezoelement;  $Me$  – metal plate;  $\delta$  – distance between magnets



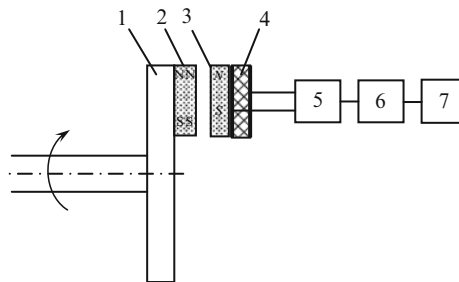
**Fig. 8.30** Dependence of piezomagnetic sensor (with bimorph piezoelement) output signal amplitude on distance between magnets  $\delta$

Output signal amplitude can be increased by means of a bimorph piezoelement [9, 35, 38]. A sensor design with a bimorph piezoelement is shown in Fig. 8.29.

The dependence of piezomagnetic sensor (with a bimorph piezoelement) output signal amplitude on the distance between magnets  $\delta$  is shown in Fig. 8.30. The bimorph piezoelement of a 3П-19 (in Russian) electro-acoustic (call) transducer was used in the experiment [9, 35].



**Fig. 8.31** Output signal of piezomagnetic sensor



**Fig. 8.32** Piezomagnetic tachometer: 1 – rotor; 2, 3 – constant magnets; 4 – piezoelement; 5 – amplifier; 6 – rectifier; 7 – impulse counter

As is shown in Fig. 8.30, the sensor signal amplitude was twice that of the signal amplitude of the monomorph piezoelement sensor (Fig. 8.10).

In this case, the considerable amplitude increase is connected with the use of piezoelement flexural vibrations (earlier, thickness vibrations were used) when the piezoelement is more deformed.

### 8.3.2 Accuracy Improvement Methods

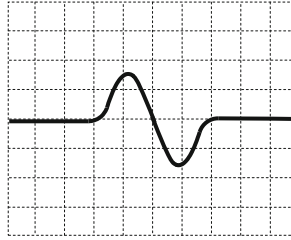
Use of thickness-polarized magnets results in interaction (attraction or repulsion) which causes an impulse appearance on the piezomagnetic sensor output (Fig. 8.31) [39].

This tachometer signal is amplified by an amplifier. It proceeds to the impulse counter input.

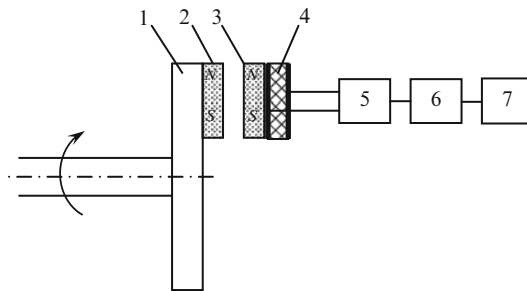
Several methods of accuracy improvement of tachometer piezomagnetic sensors [40, 41] have been developed.

One of the designs is shown in Fig. 8.32 [40].

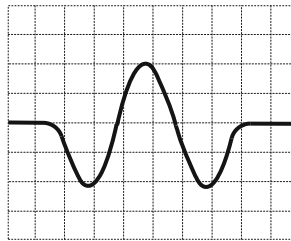
If the rotor rotates, a magnet magnetization direction change results in the following: (1) two interactions – attraction and repulsion (or vice versa, depending on the rotation direction), (2) the appearance of two impulses (Fig. 8.33) [40].



**Fig. 8.33** Form of piezomagnetic sensor output signal, shown in Fig. 8.32



**Fig. 8.34** Piezomagnetic tachometer: 1 – rotor; 2, 3 – constant magnets; 4 – piezoelement; 5 – amplifier; 6 – rectifier; 7 – impulse counter



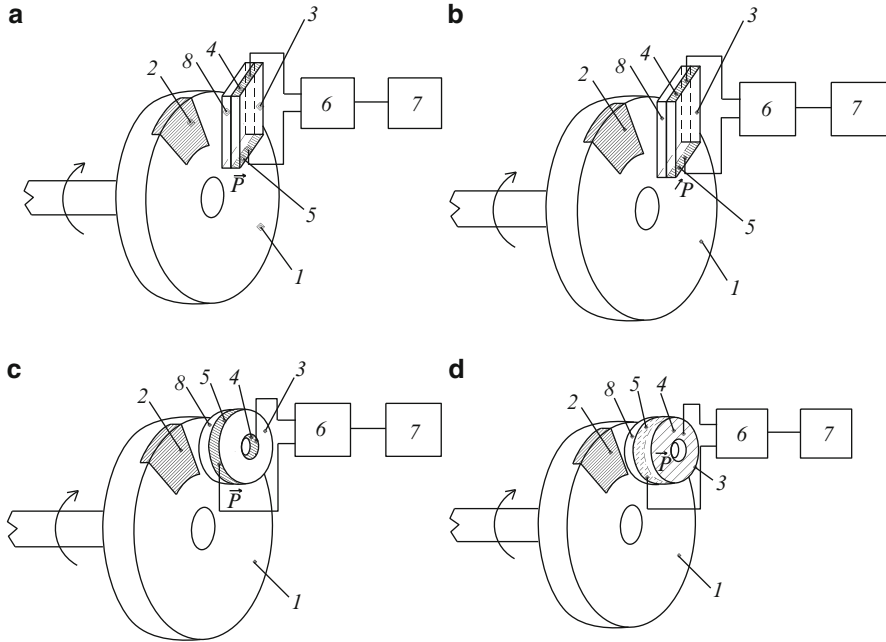
**Fig. 8.35** Output signal of piezomagnetic sensor shown in Fig. 8.34

Piezoelement (4) output impulses are amplified by electric oscillation amplifier (5), rectified by the detector (7) based on full-wave rectifier scheme, and are counted by the impulse counter (8).

The availability of two impulses in the tachometer piezomagnetic sensor output signal permits and increase in the measurement accuracy of working shaft revolutions [40].

To obtain more accurate results, the sensor design shown in Fig. 8.34 should be made [40].

This transducer output signal is shown in Fig. 8.35 [41].



**Fig. 8.36** Piezomagnetic tachometers with domain-dissipative piezoelements: 1 – rotor; 2 – rotor magnet; 3 – piezoelement; 4, 5 – electrodes; 6 – amplifier; 7 – impulse counter; 8 – sensor magnet

The use of two magnets, magnetized along the rotor rotation plane, causes three interactions. Thus, it results in the appearance of three impulses on the piezomagnetic sensor input [41].

To increase the accuracy of tachometer piezomagnetic sensor, domain-dissipative piezoceramic elements, described in detail in Chap. 3, are used.

These transducer designs are shown in Fig. 8.36 [42–45].

Piezoelement oscillatory properties can cause the appearance of additional, exponentially decaying pulses. This may result in impulse counter malfunction, and consequently in rotor rotation speed inaccuracy.

As was mentioned in Chap. 3, the piezoelement loses its oscillatory properties and acquires differentiating properties in domain-dissipative transducers.

Thus, use of domain-dissipative transducers in piezomagnetic tachometer sensor designs (Fig. 8.36) will make it possible to eliminate malfunction, and to improve the accuracy of shaft revolution speed calculation of operating mechanisms [42–45].

### 8.3.3 Sensor Design Simplification

Two methods of piezomagnetic tachometer sensors design simplification have been developed [38, 46].

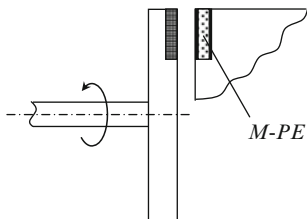


Fig. 8.37 Tachometer piezomagnetic sensor

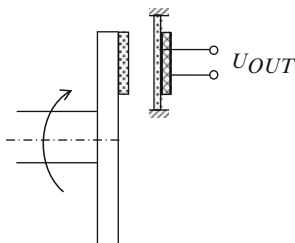


Fig. 8.38 Bimorph piezomagnetic sensor of tachometer

One of them is making a piezoelement from a mixture of piezoceramic and magnetic material powder. This transducer design is shown in Fig. 8.37 [46].

Here, a  $M-\Pi\Theta$  (M-PE) plate is simultaneously used as both a magnet and a piezoelement.

The piezoelement used in the experiment was plate-shaped,  $30 \times 30 \times 5$  mm. It was made of piezoceramic powder (zirconate–titanate–lead; 70%) and magnetic powder (barium ferrite; 30%. The electrodes were placed on the plate bases, and were connected to the electric oscillation amplifier, based on ОУ К140У Д8А (in Russian). The rotor magnet is made of samarium–cobalt.

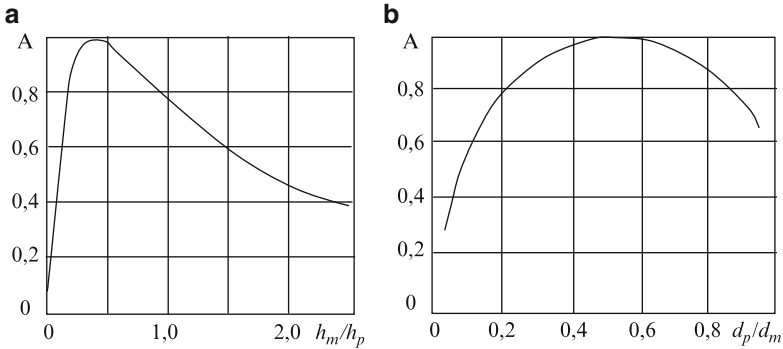
The experiments showed the count pulse availability, corresponding to the rotor revolutions. This proves the operability of the tachometer [46].

The combination of piezoelectric and magnetic properties in one sensor enables simplification of the transducer design.

The other simplification method is to use a metal plate of asymmetric bimorph piezoelement as the sensor magnet [38].

It has been shown that bimorph piezoelement use may raise the output signal level (approximately 100 times). Bimorph piezomagnetic sensor design (Fig. 8.29) can be simplified if the sensor magnet is removed and the attraction properties of the metal plate to the magnet are used. This sensor variant is shown in Fig. 8.38 [38].

ИТС-19 piezoceramics piezoelement (diameter 30 mm, thickness 0.3 mm), samarium–cobalt constant magnet (diameter 30 mm, thickness 3 mm), 50 НП low nickel soft magnetic alloy plate (diameter 36 mm, thickness 0.2 mm) and ДПМ-20Н3–01 (in Russian) engine were used in the experiment.



**Fig. 8.39** Dependence of piezomagnetic sensor output signal level on following ratios: (a) plate  $h_m$  – piezoelement  $h_p$  thickness, (b) piezoelement  $d_p$  – plate  $d_m$  diameters

The sensor registered the output signal with amplitude 225 mV when the distance between the rotor magnet and the stator plate was 2 mm. The engine rotation speed was 9,000 turns/min.

In Fig. 8.39, the normalized dependences of the transducer output signal on the metal plate and the piezoelement thicknesses (Fig. 8.39) and diameters (Fig. 8.39) ratio are shown [38].

As can be seen in Fig. 8.39, the maximum level of output signal is reached if plate–piezoelement thickness ratio ( $h_m/h_p$ ) equals

$$0.25 < h_m/h_p < 0.6, \quad (8.48)$$

and also if piezoelement–plate diameter ratio ( $d_p/d_m$ ) equals

$$0.4 < d_p/d_m < 0.7. \quad (8.49)$$

Thus, to simplify the tachometer piezomagnetic sensor design with an insignificant decrease in output signal level, the transducer shown in Fig. 8.38, subject to (8.48) and (8.49) correlations, should be made.

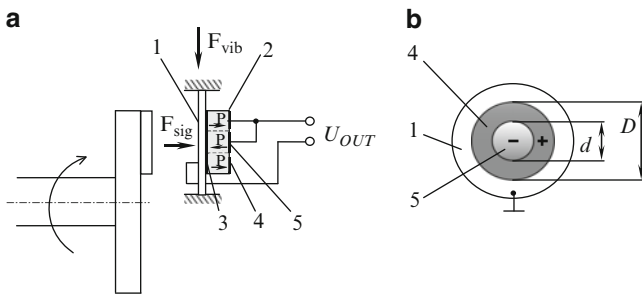
### 8.3.4 Suppression of Vibration Hindrances

The influence of vibration hindrances is one of the drawbacks of piezomagnetic sensors.

A piezomagnetic sensor also has accelerometer properties where the sensor magnet is used as inertia mass.

Several designs of tachometer piezomagnetic sensors with reduced vibration hindrances have been developed [47, 48].

A piezomagnetic sensor is shown in Fig. 8.40. The difference is that one of the electrodes is split into two parts: one is ring-shaped with external diameter  $D$ , and



**Fig. 8.40** Piezomagnetic tachometer: (a) piezomagnetic sensor, (b) piezoelement design; 1 – soft magnetic material plate; 2 – piezoelement; 3, 4, 5 – electrodes

the other is a disk with diameter  $d$ , while  $D = 1.4d$ . The electrodes are located on piezoelement areas with different polarization  $\mathbf{P}$  [48].

Under the influence of vibration hindrance  $\mathbf{F}_{vib}$ , the piezoelement experiences lateral (transverse) vibrations [21]. If electrode parts 4 and 5 of equal area, located on the piezoelement areas with different polarization  $\mathbf{P}$ , are connected, the resultant signal, caused by vibration, equals 0.

Under the useful signal  $\mathbf{F}_{sig}$  influence, the piezoelement experiences flexural vibrations. It is known [21] that the signal level on the piezoelement ring electrode  $U_R$  equals  $\sim 0.5$  of the signal level on the piezoelement disk electrode  $U_D$ , if its area equals the disk electrode area. Thus, when electrode parts 4 and 5 are connected and the different polarity of piezoelement  $\mathbf{P}$  under these parts is considered, the resultant signal equals:

$$U_{OUT} = U_D + U_R = U_D - 0.5U_D = 0.5U_D. \tag{8.50}$$

Thus, it is possible to considerably reduce the vibration hindrance (theoretically to zero) if the useful signal is insignificantly decreased [48].

The other design variant is shown in Fig. 8.44 [47].

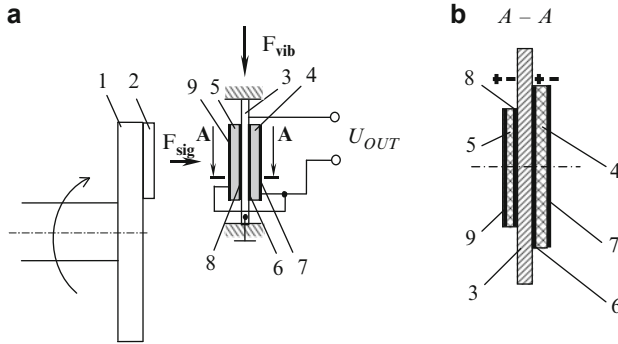
The transducer sensor is a trimorphous piezoelement.

Thickness-polarized piezoelements 4 and 5 with electrodes 6, 7 and 8, 9 accordingly are attached to the plate 3, made of 50HΠ magnet soft material, fastened along the generating line. Heteropolar electrodes 6 and 8 are attached to the plate 3 and the scheme common wire, while electrodes 7 and 9 are interconnected and are attached to the amplifier.

An aspect of the design is that piezoelements are of equal thickness and depth (height), but of different width (Fig. 8.41) [47].

Under the vibration hindrance influence  $\mathbf{F}_{vib}$ , the piezoelement experiences lateral (transverse) oscillations [21]. The sensitivity of transverse piezoelements is calculated by using the formula:

$$S = -d_{11} \frac{h}{a}, \tag{8.51}$$



**Fig. 8.41** Piezomagnetic tachometer: (a) sensor, (b) piezoelements design; 1 – rotor; 2 – constant magnet; 3 – soft magnet material plate; 4, 5 – piezoelements; 6–9 – electrodes

where:  $d_{11}$  – piezomodule,  $h$  – depth (height),  $a$  – piezoelement thickness.

As piezoelements 4 and 5 have identical depth (height) and thickness, there will be one level signals on electrodes 6, 7 and 8, 9, created as a result of vibration hindrance influence  $F_{\text{vib}}$ . If electrodes 6, 8 and 7, 9 are interconnected, the resultant signal will equal 0.

Under the influence of useful signal  $F_{\text{sig}}$ , the piezoelement experiences longitudinal vibrations. Their output voltage level depends on piezoelement capacity [21]:

$$U_{\text{OUT}} = \frac{Q}{C} = \frac{d_{31}F}{C}, \quad (8.52)$$

where:  $d_{31}$  – piezomodule,  $Q$  – charge,  $F$  – force,  $C$  – capacity.

As piezoelements 4 and 5 have different width and capacity, under the influence of useful signal  $F_{\text{sig}}$  there will be different level signals on electrodes 6, 7 and 8, 9. If electrodes 6, 8 and 7, 9 are interconnected the resultant signal will be nonzero.

Thus, if useful signal is insignificantly reduced, vibration hindrance is also decreased (theoretically to zero) [47].

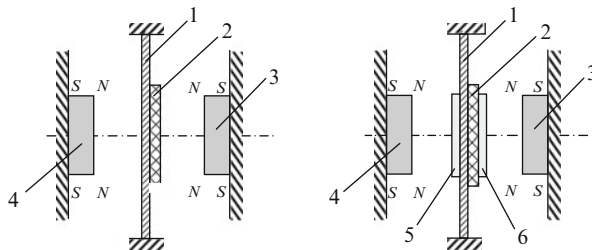
The experimental research showed that due to the designs application offered (Figs. 8.40 and 8.41), the useful–vibrating signal ratio increased from 7 to 24 dB.

## 8.4 Piezomagnetic Electro-acoustic Transducers

A design variant of electro-acoustic transducer is shown in Fig. 8.42 [49]. The bimorph piezoelement, consisting of magnet soft material membrane 1, piezoelement 2 and two magnets 3 and 4 are used here. The analogue poles of the magnets face the membrane (Fig. 8.42a).

The bimorph piezoelement is attracted to magnets 3 and 4 with identical force because of their location. The bimorph element vibrates if some voltage is supplied





**Fig. 8.42** Piezomagnetic electro-acoustic bimorph transducer

**Table 8.9** Sound pressure of transducers

Sound pressure (dB)	Transducer		
	Without magnets	According to Fig. 8.42a	According to Fig. 8.42b
	94	103	98

to the piezoelement. If the bimorph element is moved to a magnet, for instance magnet 3, attraction force to this magnet is increased, while the attraction force to the other magnet decreases. This results in bimorph element oscillation amplitude increase, i.e., its sensitivity increase. If voltage polarity changes, the membrane moves to magnet 4 and the described process repeats.

In the case of diamagnetic material membrane (e.g., brass B63 or phosphor bronze) use, magnet soft material plates 5 and 6 should be pasted on the bimorph element in (Fig. 8.42b).

Two piezoelectric transducers were made for the experimental research:

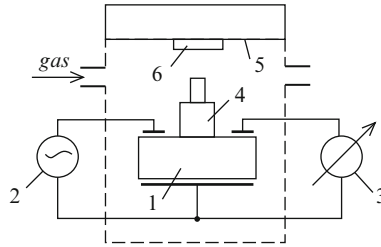
- In the first, the bimorph element consisted of 65Г spring steel membrane (0.12 mm thick and 32 mm in diameter) and IITC-19 piezoceramic piezoelement (22 mm in diameter and 0.18 mm thick). The bimorph element and the piezoelement were glued together with epoxy adhesive (as shown in Fig. 8.42a)
- In the second transducer, the bimorph element membrane was made of semi-solid brass B63 0.18 mm thick and 32 mm in diameter. IITC-19 piezoceramic piezoelement was 22 mm in diameter and 0.18 mm thick. The bimorph element and the piezoelement were glued together with epoxy adhesive. Two permalloy overlays 0.3 mm thick and 6 mm in diameter were axis-symmetrically pasted on the bimorph element.

Samarium–cobalt magnets 16 mm in diameter and 5 mm thick were used.

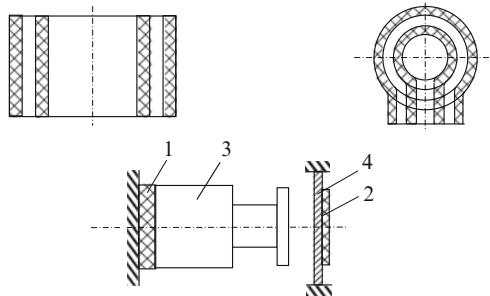
The transducers were connected to G3–106 generator, voltage 2 V. Sound pressure on resonance (resonant) frequency (2.35 kHz) for transducers with and without magnets was measured by ИШВ-1(acoustic level meter) from 15 cm distance.

The measurement data are given in Table 8.9.

The other application of electro-acoustic piezomagnetic transducers is connected with the study of gas properties.



**Fig. 8.43** Piezomagnetic resonant humidity sensor



**Fig. 8.44** Piezotransducers based on acoustically connected resonators: 1, 2 – piezoelements; 3 – step concentrator; 4 – metal plate

A piezomagnetic resonant humidity sensor [49], consisting of piezotransformer 1, connected to electric oscillations generator 2 and to measuring device 3 with ultrasonic step concentrator 4 on its surface, made of magnet soft material, is shown in Fig. 8.43. Magnet 6 is fastened to hydro-sensitive grid 5.

The magnet 6 is attracted to concentrator 4. Magnet attraction force, counterbalanced by grid 5 elastic properties, influences the ultrasonic concentrator oscillation amplitude and as a consequence the piezotransformer output voltage [49].

If gas humidity change,s the grid elastic properties change too: magnet-concentrator position is changed, which results in output voltage change.

Use of electro-acoustic piezomagnetic transducers in acoustically connected resonator designs is of scientific interest. Some scheme variants are shown in Fig. 8.44 [50–52].

Operating principles of these sensors are described in Chap. 14.

## References

1. G.V. Kats (ed.), *Magnetic and Dielectric Devices* (Energiya, Moscow, 1964), p. 416 (in Russian)
2. V.M. Pluzhnikov, V.S. Semenov, *Piezoceramic Solid Schemes (Circuits)* (Energiya, Moscow, 1971) (in Russian)

3. A.M. Balbashov et al., in *Elements and Devices Based on Cylindrical Magnetic Domains: Reference Book*, ed. by N.N. Evtikiev (Radio and Communication, Moscow, 1987) (in Russian)
4. V.M. Sharapov, M.P. Musiyenko, E.V. Sharapova, in *The Piezoelectric Sensors*, ed. by V.M. Sharapov (Technosfera, Moscow, 2006), p. 632 (in Russian)
5. V.M. Sharapov, M.P. Musiyenko, S.V. Marchenko, Influence of cylindrical magnet design data on tachometer piezomagnetic sensor output voltage. *Bull. Cherkasy State Technol. Univ.* **1** (2005) (in Russian)
6. V.M. Sharapov, M.P. Musiyenko, S.V. Marchenko, Influence of rectangular magnet design data on tachometer piezomagnetic sensor output voltage. *Bull. Cherkasy State Technol. Univ.* **1** (2005) (in Russian)
7. E.S. Levshina, P.V. Novitskiy, *Electric Measurements of Physical Values: (Measuring Transducers). The Textbook for Higher Educational Establishments* (Energoatomizdat, Leningrad, 1983), p. 320 (in Russian)
8. P.V. Novitskiy (ed.), *Electric Measurements of Non-Electric Values* (Energiya, Leningrad, 1975), p. 576 (in Russian)
9. V.M. Sharapov, M.P. Musiyenko, S.V. Marchenko, Study of tachometer piezomagnetic sensors. *Bull. Cherkasy State Technol. Univ.* **4**, 90–93 (2003) (in Russian)
10. A.B. Altman, A.N. Gerberg, P.A. Gladyshev et al., in *Constant Magnets: Reference Book*, ed. by Yu.M. Pyatin (Energiya, Moscow, 1980), p. 488 (in Russian)
11. V.G. Domrachev et al., *Digital Displacement Transducer Engineering: Handbook* (Energoatomizdat, Moscow, 1987), p. 392 (in Russian)
12. Yu.M. Kelim, *Electromechanical and Magnetic Elements of Automatic Systems* (Viysh.shk., Moscow, 1991), p. 304 (in Russian)
13. M.B. Paperno, Yu.N. Zhigulin, P.S. Gorbachev, Patent of USSR No 461370. Tachometer, bul. 7 (1975) (in Russian)
14. M.B. Paperno, P.S. Gorbachev, Patent of USSR No 650009. Tachometer, bul. 8 (1979) (in Russian)
15. V.A. Govorkov, *Electric and Magnetic Fields* (Svyazizdat, Moscow, 1951), p. 339 (in Russian)
16. I.V. Savelyev, *Course of General Physics. Manual. Electricity and Magnetism. Waves. Optics* (Science, Moscow, 1988), p. 496 (in Russian)
17. V.M. Sharapov, M.P. Musiyenko, S.V. Marchenko, Mathematical models of tachometer magnetic piezomagnetic sensors. *Math. Model.* **1**(11), 61–63 (2004) (in Russian)
18. V.M. Sharapov, M.P. Musiyenko, S.V. Marchenko, Mathematical model of tachometer piezomagnetic sensors. Works of the Interstate SIC “Problems of Mathematical Modeling”, Dniprodzerzhinsk, p. 151–152 (2004) (in Russian)
19. P.G. Dzhagupov, A.A. Erofeev, *Piezoelectronic Devices of Computer Facilities, Monitoring Systems and Control* (Politechnica, St. Petersburg, 1994), p. 608 (in Russian)
20. V. Domarkas, R.J. Kazhys, *Control Piezoelectric Transducers* (Mintis, Vilnius, 1974), p. 258 (in Russian)
21. V.M. Sharapov, M.P. Musiyenko et al., in *Piezoelectric Transducers (Reference Book)*, ed. by V.M. Sharapov (ChSTU, Cherkasy, 2004), p. 435 (in Russian)
22. V.M. Sharapov, I.G. Minaev, M.P. Musiyenko, *Automatic Control Theory* (ChSTU, Cherkasy, 2004), p. 200 (in Russian)
23. V.M. Sharapov, M.P. Musiyenko, S.V. Marchenko, Study of tachometer piezomagnetic sensors model. *Bull. Cherkasy State Technol. Univ.* **4** (2004) (in Russian)
24. R.R. Arnold, *Calculation and Designing of Constant Magnets* (Energiya, Moscow, 1969), p. 186 (in Russian)
25. A.G. Slivinskaya, A.V. Gordon, *Constant Magnets* (Energiya, Moscow, 1965), p. 130 (in Russian)
26. I.M. Makarov, B.M. Menskiy, *Linear Automatic Systems (Theoretical Issues, Calculation Methods and Reference Material). The Manual for Higher Educational Establishments* (Mashinostroenie, Moscow, 1977), p. 464 (in Russian)

27. L.A. Ostrovskiy, *Basics of Electric Device Theory* (Energiya, Leningrad, 1971), p. 544 (in Russian)
28. P.M. Talanchuk, V.T. Ruschenko, *Basics of Measuring Device Theory and Designing: Manual* (Vish. shk. Golovnoye Publishing House, Kiev, 1989), p. 454 (in Russian)
29. V.M. Sharapov, M.P. Musiyenko, S.V. Marchenko, Study of tachometer piezomagnetic sensor transitive characteristics. *Bull. Cherkasy State Technol. Univ.* **4** (2004) (in Russian)
30. M.P. Musiyenko, Shaft rotation speed magnetic piezosensors of operating devices. Works International STC “Progressive Directions of Machine, Instrument Making Branches and Transport Development”, Sevastopol, p. 165–167 (2004) (in Russian)
31. M.P. Musiyenko, Piezomagnetic sensors of tachometers. Works STC “Automatics and Electric Equipment Problems of Vehicles”, Nikolaev (2004) (in Russian)
32. V.M. Sharapov, M.P. Musiyenko, S.V. Marchenko, *Study of Shaft Rotation Speed of Piezomagnetic Sensors* (Lviv, 2005) (in Russian)
33. V.M. Sharapov, M.P. Musiyenko, S.V. Marchenko, *Study of Operating Shaft Rotation Speed of Piezomagnetic Sensors* (Odessa, 2005) (in Russian)
34. V.M. Sharapov, M.P. Musiyenko, S.V. Marchenko, V.V. Tuz, Magnetic piezosensors of tachometers. Collected Papers of International STC “Instrument Making–2004”, Vinnitsa-Yalta, p. 4–6 (2004) (in Russian)
35. V.M. Sharapov, M.P. Musiyenko, I.B. Chudaeva, S.V. Marchenko, Piezomagnetic sensor of device shaft rotation speed. Collected Papers of International STC “Sensor–2004”, Moscow, p. 35–36 (2004) (in Russian)
36. V.M. Sharapov, M.P. Musiyenko, S.V. Marchenko, Patent of Ukraine 7943. Piezomagnetic tachometer, bul. 7 (2005) (in Ukrainian)
37. V.M. Sharapov, M.P. Musiyenko, S.V. Marchenko, Patent of Ukraine 7944. Piezomagnetic tachometer, bul. 7 (2005) (in Ukrainian)
38. V.M. Sharapov, M.P. Musiyenko, S.V. Marchenko, Patent of Ukraine 8500. Piezomagnetic tachometer, bul. 8 (2005) (in Ukrainian)
39. V.M. Sharapov, M.P. Musiyenko, S.V. Marchenko, Patent of Ukraine, order number 20041210464. Piezomagnetic tachometer (in Ukrainian)
40. V.M. Sharapov, M.P. Musiyenko, S.V. Marchenko, Patent of Ukraine 8502. Piezomagnetic tachometer, bul. 8 (2005) (in Ukrainian)
41. V.M. Sharapov, M.P. Musiyenko, S.V. Marchenko, Patent of Ukraine 8504. Piezomagnetic tachometer, bul. 8 (2005) (in Ukrainian)
42. M.P. Musiyenko, Patent of Ukraine 69873. Piezomagnetic tachometer, bul. 9 (2004) (in Ukrainian)
43. V.M. Sharapov, M.P. Musiyenko, S.V. Marchenko, Patent of Ukraine 70590. Piezomagnetic tachometer, bul. 10 (2004) (in Ukrainian)
44. V.M. Sharapov, M.P. Musiyenko, S.V. Marchenko et al., Patent of Ukraine 70591. Piezomagnetic tachometer, bul. 10 (2004) (in Ukrainian)
45. V.M. Sharapov, M.P. Musiyenko, S.V. Marchenko, Patent of Ukraine 71257. Piezomagnetic tachometer, bul. 11 (2004) (in Ukrainian)
46. V.M. Sharapov, M.P. Musiyenko, Patent of Ukraine 69872. Piezomagnetic tachometer, bul. 9 (2004) (in Ukrainian)
47. V.M. Sharapov, M.P. Musiyenko, S.V. Marchenko, Patent of Ukraine 8505. Piezomagnetic tachometer, bul. 8 (2005) (in Ukrainian)
48. V.M. Sharapov, M.P. Musiyenko, S.V. Marchenko, Patent of Ukraine 8509. Piezomagnetic tachometer, bul. 8 (2005) (in Ukrainian)
49. V.M. Sharapov, M.P. Musiyenko, I.B. Chudaeva et al., Study of tachometer piezomagnetic sensors. “Scientific Notes of Simferopol State University” (Collected Papers of International STC “Instrument Making–98”), Vinnitsa, p. 302–304 (1998) (in Russian)
50. V.M. Sharapov, I.B. Chudaeva, M.P. Musiyenko et al., Patent of Ukraine 35761. Piezoelectric sensor of pressure, bul. 3 (2001) (in Ukrainian)

51. V.M. Sharapov, I.B. Chudaeva, M.P. Musiyenko et al., Patent of Ukraine 35762. Piezoelectric sensor of pressure, bul. 3 (2001) (in Ukrainian)
52. V.M. Sharapov, I.B. Chudaeva, M.P. Musiyenko et al., Patent of Ukraine 35763. Piezoelectric sensor of pressure, bul. 3 (2001) (in Ukrainian)
53. I.B. Chudaeva, Development of piezoelectric transducers of polymorphic type mechanical values. PhD thesis. Odessa, OSPU, p. 196 (1999) (in Russian)

# Chapter 9

## Hydroacoustic Transducers

### 9.1 Classification and Characteristics

A hydro-acoustic transducer (HAT) is a vibration system created for reception of radiation and acoustic signals in a water environment [1].

Depending on their functions, transducers are divided into radiators, receivers and reversible transducers. Depending on the energy transformation principle, transducers can be piezoelectric, magnetostrictive, electrodynamic, electromagnetic and electrostatic.

Transducers can be bar (rod), lamellar, cylindrical and spherical, depending on the oscillatory system structure.

Depending on constructive performance, there are power and compensated transducers.

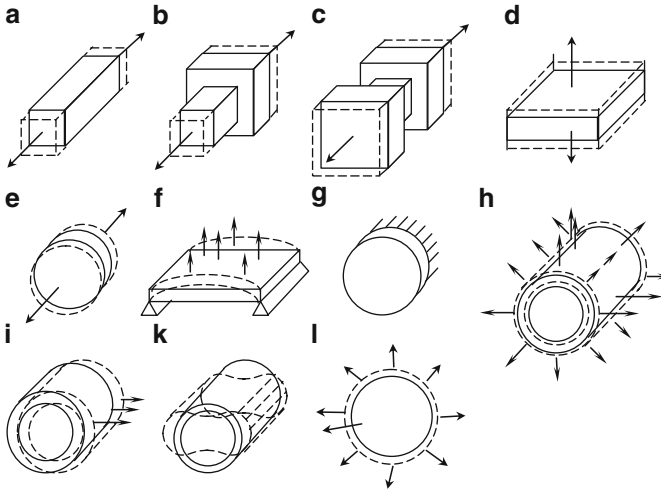
Monomorph (Chap. 2) and bimorph (Chap. 6) piezoelements are used for HAT manufacturing.

Bar (rod) systems have a free electromechanically active bar (Fig. 9.1a) or a bar from one side (Fig. 9.1b), with two overlays (Fig. 9.1c) or with a number of layers from a passive material. Longitudinal vibrations are created in such systems along the axis bar with certain distribution of amplitudes and elastic stress. These oscillations are considered piston.

Lamellar systems are made in the form of a rectangular (Fig. 9.1d) or a round (Fig. 9.1e) plate, vibrating along the thickness. They are also made in the form of plates, supported by two opposite sides (Fig. 9.1f) or by the circumference (Fig. 9.1g), performing lateral flexural vibrations.

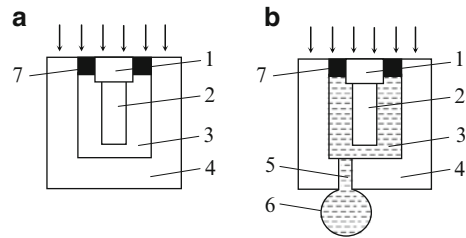
In cylindrical systems which form active material rings, radial pulsing vibrations (Fig. 9.1h), oscillating (Fig. 9.1i) and flexures with four knots along the circumference (Fig. 9.1k) can be created.

A spherical system is a thin homogeneous spherical cover (Fig. 9.1l), performing practically radial pulsing vibrations.



**Fig. 9.1** Typical oscillatory (vibrating) systems

**Fig. 9.2** Load-bearing (a) and compensated (b) units: 1 – work overlay, 2 – active element, 3 – internal cavity, 4 – case, 5 – pressure equalizing aperture, 6 – compensator, 7 – acoustic element



Because of mechanical transformation in load-bearing units (Fig. 9.2a) overboard hydrostatic pressure causes unilateral stress (compression) in active element 2 as the internal volume of case 4 is filled by air if atmospheric pressure is normal.

In the compensated units (Fig. 9.2b) the active element experiences even uniform compression, equal to overboard hydrostatic pressure, as internal volume 3 is filled by gas or liquid if pressure is the same.

*Transducers–radiators* are evaluated by the following work quality indicators.

*Acoustic power*  $P_A$  – a quantity of sound energy, radiated by the transducer in a certain amount of time. Value  $P_A$ , referring to the emitting area, is called specific acoustic power  $P_{A.SP}$ .

*Electro-acoustic efficiency coefficient*  $\eta_{EA}$  – the ratio of radiated acoustic power to active electric power  $P_E$  consumed by the transducer from the excitation generator.

*Input electric resistance*  $Z$  – the ratio of voltage applied  $U$  to current  $I$  in the radiator chain.

*Directional characteristic* estimates spatial field distribution. It is represented by the ratio of acoustic pressure, created by the radiator in the distant field, to the maximum value, depending on the angular coordinates of the observation point.

*Directivity factor*  $K_a$  is determined by the ratio of acoustic intensity, created by the radiator in the principal maximum direction in a distant field point, to the intensity of non-directional radiator with the same radiated power at the same distance.

*Transducers–receivers* are characterized by the following work indicators.

*Sensitivity*  $M$  determines the ratio of open-circuit (no-load, idle) voltage on the transducer output to acoustic pressure, influencing on it in the undistorted free field of the plane wave.

*Electric resistance*  $Z$  establishes the ratio of voltage, developed on the receiver output, to current in its chain.

*Directional characteristic* is normalized angular distribution of the receiver sensitivity in the relation to the maximum.

*Concentration factor*  $K_0$  is the ratio of sensitivity square in the maximum direction to sensitivity average square in all directions. For reversible transducers, the concentration coefficients in radiation and reception modes are numerically equal.

*Receiver efficiency* is also determined by specific sensitivity  $M_{SP} = M/\sqrt{|Z_i|}$ . Here  $M$  is open-circuit (idle) sensitivity and  $|Z_i|$  is the receiver internal (output) resistance module. The sensitivity characterizes its noise stability (immunity) to electric chains noises.

All these transducer parameters depend on frequency.

## 9.2 Ratios of Electromechanical Transformations

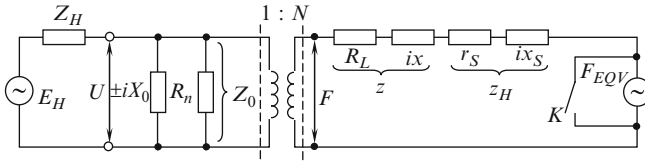
Linear reversible and passive hydro-acoustic transducers can possibly be represented in the form of a generalized quadripole with electric and mechanical sides [1, 2]. Force  $F$  and vibrational speed  $v$ , characterizing the mechanical side condition, voltage  $U$  and current  $I$ , characterizing the electrical side condition, satisfy electromechanical reciprocity relations. The greatest practical application belongs to the following relationships [3, 4]:

$$\left. \frac{I}{v} \right|_{U=0} = \left. \frac{F}{U} \right|_{v=0} = N_{U,v}; \quad \left. \frac{I}{v} \right|_{F=0} = \left. \frac{F}{U} \right|_{I=0} = N_{F,I}, \quad (9.1)$$

named electromechanical transformation coefficients. The indexes mean:  $U = 0$  – short circuit;  $I = 0$  – idling (open-circuit) of the electric side;  $v = 0$  and  $F = 0$  – hindered and free mechanical sides. Transducer intrinsic resistance: electric  $Z_0 = U/I$  if  $v = 0$ ; mechanical  $Z_I = F/v$  if  $I = 0$  and  $Z_U = F/v$  if  $U = 0$ .

An equivalent scheme of a transducer–radiator (Fig. 9.3) consists of excitation generator with electromotive force  $E_G$  and internal resistance  $Z_H$ , electric chain – resistance  $Z_0$  in the form of parallel connection  $R_L$  and  $\pm iX_0$ , the electromechanical





**Fig. 9.3** Equivalent electromechanical scheme of radiator and receiver

transformer and mechanical chain – constituents of intrinsic and load resistance (contact  $K$  is closed). Component  $x$  is inertial and elastic resistance of the transducer;  $x_S$  – inertial resistance of co-vibrating mass  $m_S$ . Values  $R_L$ ,  $r_S$  reflect energy losses in the electric chain, the mechanical part (mainly in the design elements) and for radiation.

Condition  $x + x_S = x_M = 0$  determines resonance of the mechanical vibrating system. Resonating, the radiator consumes active power  $P_E = U^2/R_L + U^2/R_M = P_L + P_M$ , where  $P_L$  – electric loss power;  $P_M$  – mechanical power,  $R_M = (r_\Pi + r_S)/N^2$ . Mechanical power

$$P_M = \frac{U^2}{R_M^2} R_S + \frac{U^2}{R_M^2} R_{M,L} = P_A + P_{M,L},$$

where  $P_A$  is radiated acoustic power, and  $P_{M,P}$  is mechanical loss power.

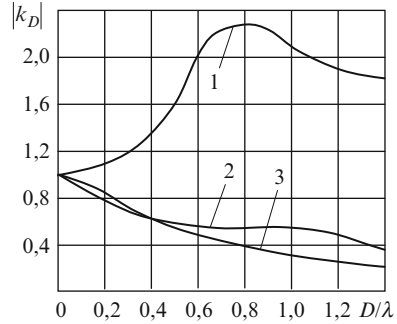
According to the stages of transformation of energy (transmitted to the radiator), the following efficiency coefficient is considered  $\eta_E = P_M/P_E$  – electromechanical;  $\eta_{AM} = P_A/P_M$  – acoustical–mechanical;  $\eta_{EA} = \eta_{EM}/\eta_{AM} = P_A/P_E$  – electroacoustic. The acoustical–mechanical efficiency coefficient of sound underwater radiators with resonance  $\eta_{AM} = 0.5\text{--}0.8$ .

In some cases, radiator efficiency is evaluated by sound pressure  $p$ , created by the radiator at a point on the acoustic axis if distance  $r$  and voltage  $U$  (or current  $I$ ) on the electric input is unit. Relation  $pr/U = S$  is called voltage radiator sensitivity. It is measured in  $\text{Pa} \cdot \text{m}/\text{V}$ . Relation  $pr/I = S$  is called current radiator sensitivity. It is measured in  $\text{Pa} \cdot \text{m}/\text{A}$ .

A transducer–receiver equivalent scheme (see Fig. 9.3) consists of a sound field energy source with emf  $F_{EQV}$  (contact  $K$  is open), mechanical resistance  $Z_H$  and  $Z$ , (electromechanical transformer and electric resistance  $Z_0$  and  $Z_H$  load is not shown). If pressure  $p$ , caused by sound field, is evenly distributed along the transducer reception surface (which occurs when the wave surface area is small), electromotive force equals  $F_{EQV} = pS$ . Generally,  $F_{EQV} = k_D pS$ , where  $k_D$  is the diffraction coefficient, depending on the receiver wave sizes, its form and incident wave direction.

In Fig. 9.4 the dependences of module  $|k_D|$  on diameter wave size  $D/\lambda$  [5] are shown. If distribution of vibration speed on reception surface  $S$  is described by surface coordinate function  $f(r)$ , average area  $S_{av} = \int_S f(\bar{r})dS$  should be substituted in formula  $F_{EQV}$ .

**Fig. 9.4** Dependence of diffraction factor on circular piston disk surface (1), pulsing infinitely long cylinder (2) and pulsing sphere (3) on the wave diameter size



When voltage on the receiver output refers to sound pressure in a free field (the receiver is absent) field  $M$  sensitivity is obtained.

Equality

$$x + x_s \pm X_0 N^2 = 0 \tag{9.2}$$

determines electromechanical resonance with the maximum receiver sensitivity. If resistance  $X_0$  is of inductive character electromechanical resonance frequency  $f_p'$  is lower than mechanical resonance  $f_p$ . If resistance  $X_0$  is of capacitive character, electromechanical resonance frequency  $f_p'$  is higher than mechanical resonance  $f_p$ .

Transducer  $Z$  electric impedance consists of parallel connection of electric side  $Z_0$  elements and reduced to it mechanical impedance  $Z_M$ , therefore

$$1/Z = 1/Z_0 + 1/Z_M,$$

where

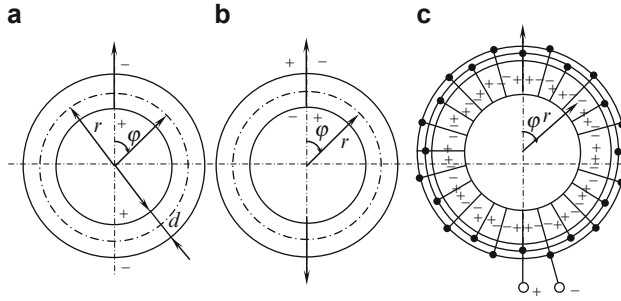
$$Z_0 = \pm i X_0 R_{\Pi} / (R_{\Pi} \pm i X_0); Z_M = (z + z_H) / N^2.$$

Module  $|Z|$  is minimal at resonance  $f_p$  frequency and is maximal at anti-resonance  $f_a$  frequency. Due to the transducer active resistance, frequencies  $f_p$  and  $f_a$  do not coincide with frequencies of mechanical and electromechanical resonances.

Energy transformation is also evaluated by the electromechanical coupling factor.

The energy electromechanical coupling factor (EMCF) is determined by the relation of mechanical (electric) energy, generated by an active element, to total electric (mechanical) energy, reserved in it. This serves as a measure of effectiveness of electromechanical transformation in the active material ( $k_M^2$ ) and in transducers ( $k_C^2$ ). In static mode, in practice, with frequencies considerably lower, the principal resonance EMCF depends only on the active material properties. In dynamic mode transducer  $k_C^2$  EMCF depends on the type of vibrations and the distribution of elastic stress along the active element volume. This is called effective EMCF, and  $k_C^2 \leq k_M^2$ . Value  $k_C^2$  is connected with resonance  $f_p$  and anti-resonance  $f_a$  frequencies by the reduced correlation

$$k_C^2 \approx 1 - (f_p / f_a). \tag{9.3}$$



**Fig. 9.5** Piezoceramic ring: (a) continuous pulsing, (b) continuous oscillating, (c) sectioned pulsing

### 9.3 Cylindrical Piezoceramic Transducers

Below we will consider formulas to calculate piezoceramic thin and short ring [thickness and depth (height) are considerably smaller than the mean radius], performing radial pulsing (zero mode) and oscillating (first mode) (Fig. 9.5) [1].

In general, distribution of vibrations in radial direction is described by the function  $v(\varphi) = v_0 \cos \varphi$ , in the tangential direction by  $v(\varphi) = v_0 \sin \varphi$ , where  $v_0$  is the amplitude of vibration radial speed with  $\varphi = 0$  [3, 4, 6, 7]. In practice, the transducer designs are represented as a set of glued rings.

Piezoceramic ring with the use of transverse piezoelectric effect (electrodes are on lateral surfaces)

Mechanical resonance frequency:

(a) Unloaded ring

$$\left. \begin{aligned} f_0 &= \sqrt{\frac{E_{Yul}^E / \rho}{2\pi K r}} && \text{(pulsation)} \\ f_0 &= \sqrt{2} f_p && \text{(oscillation)} \end{aligned} \right\}, \quad (9.4)$$

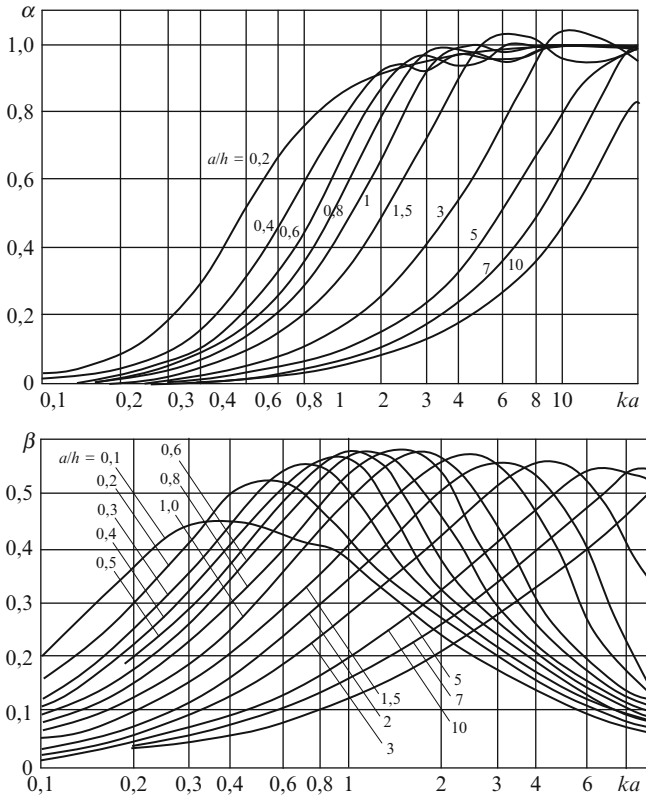
where:  $r$  – ring mean radius;  $E_{Yul}^E$  ( $Y_{ul} - Y$  from Young) – elasticity modulus and ring material density; index 01 refers to the first mode of vibrations.

(b) Loaded ring

$$f_p = f_0 / \sqrt{1 + \beta(\rho c)_B / (\omega_p \rho d)} \approx f_0 / \sqrt{1 + \beta(\rho c)_B r / (\rho c_1^E d)}, \quad (9.5)$$

where  $\beta$  is dimensionless coefficient of radiation reactance, preliminarily determined at frequency  $f_0$  (Fig. 9.6).

If the difference between frequencies  $f_p$  and  $f_0$  exceeds the permitted value, mean radius should be changed. Coefficient  $\beta$  at frequency  $f_p$  with previously found



**Fig. 9.6** Dimensionless coefficients of pulsing ring radiation active  $\alpha$  and reactive resistances  $\beta$  in rigid infinite screen with various mean radius–ring depth (height) ratio

$r$  value is determined; the new  $r^*$  value is calculated. It is recommended that this procedure be repeated.

Electromechanical transformation coefficient (factor):

- (a) If polarization is radial (electrodes are on lateral surfaces)

$$N = 2\pi d_{31} E_{Yu1}^E h; N = 8d_{31} E_{Yu1}^E h.$$

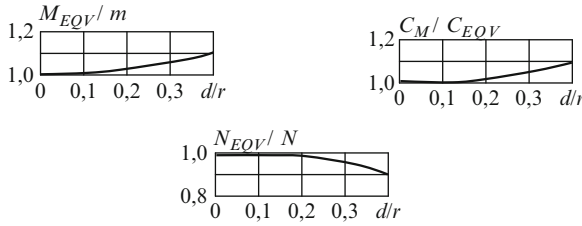
- (b) In 180° screen is available

$$N = 8d_{31} E_{Yu1}^E h,$$

where  $h$  is ring depth (height).

- (c) If polarization is axial (electrodes are on ends)

$$N = 2\pi d_{31} E_{Yu1}^E h.$$



**Fig. 9.7** Dependence of ring equivalent parameters on its thickness–mean radius ratio

Equivalent concentrated parameters

$$m_{EQV} = m_0 = m_1 = 2\pi r d h \rho; \quad (9.6)$$

$$C_{EQV}^E = C_{M0}^E = 2C_{MIEQV}^E = r / (2\pi E_{Yul}^E h d).$$

For a ring with  $d \geq 0.2r$  parameters  $m_{EQV}$ ,  $C_M$  and  $N_{EQV}$  are calculated by using the graphs (Fig. 9.7).

If reinforcing bandage and hermetic sealing cover, rigidly fastened to the piezoceramic ring, are available, equivalent parameters equal

$$m_{EQV} = m_{0C} + m_{0B} + m_{0C} + m_{1C} + m_{1B} + m_{1H};$$

$$1/C_{EQV}^E = 1/C_{M0C}^E + 1/C_{M0B}^E + 1/C_{M0H}^E + 1/C_{M1C}^E + 1/C_{M1B}^E + 1/C_{M1H}^E,$$

where indexes 0.1 are numbers of vibration modes; “C”, “B”, “H” – ceramics, bandage and hermetic sealing.

*Mechanical Q*

$$Q_M = \omega_p (m_{EQV} + m_S) / r = \rho c_1^E \eta_{AM} d f_p / (\alpha_\omega \alpha_p (\rho c)_B r f_0), \quad (9.7)$$

where  $\alpha$  and  $\alpha_p$  are dimensionless coefficients of radiation active resistance at the given frequency and at resonance frequency, and  $m_S = \beta (\rho c)_B S / \omega$  is the vibrating mass;

$$S = 2p rh; \alpha_\omega = 1 - (1 - \alpha / \alpha_p) \eta_p.$$

Excitation voltage, necessary for given specific power receipt when resonance,

$$U = [S / (N \eta_p)] \sqrt{\alpha_p (\rho c)_B P_{a.sp.p.}} \quad (9.8)$$

Frequency dependence of acoustic power

$$P_a / P_{a.p} = \alpha / (\alpha_p \alpha_\omega^2) [1 + Q_M^2 (f / f_p - f_p / f)^2], \quad (9.9)$$

where  $P_{ap}$  – acoustic power on mechanical resonance frequency equals

$$P_{a,p} = \frac{N^2 \eta_p^2 U^2}{\alpha_p (\rho c)_B S}. \quad (9.10)$$

*Electric resistance:*

(a) Capacitive resistance (capacitance)

$$X_C = 1/(i\omega C_0), \quad (9.11)$$

where  $C_0 = 2\pi \varepsilon_{33}^T$ .

(b) Active insertion resistance

$$R_M = \alpha_\omega \alpha_p (\rho c)_B S / (N^2 \eta_p) = \alpha_\omega r_p / N^2. \quad (9.12)$$

(c) Electric loss resistance

$$R_L = \frac{1}{\omega C_0 \operatorname{tg} \delta} = \frac{Q_E}{\omega C_0}. \quad (9.13)$$

(d) Impedance at resonance

$$Z_p = \left[ \frac{R_{M,R.} + R_{F,R.}}{R_{M,R.} R_{F,R.}} + i\omega_p C_0 \right]^{-1} = \left[ \frac{1}{R_R} + i\omega_p C_0 \right]^{-1}. \quad (9.14)$$

(e) Impedance near resonance

$$Z = \left[ \frac{1}{R_M + iX_M} + \frac{1}{R_\Pi} + i\omega C_0 \right]^{-1}, \quad (9.15)$$

where  $X_M = (rQ/N^2)(f/f_p - f_p/f)$ .

Consumed electric power

$$P_E = U^2/R = U^2(R_L + R_M)/(R_L R_M) = P_a/(\eta_{EM} \eta_{AM}), \quad (9.16)$$

where  $\eta_{EM} = [1 + \alpha_p (\rho c)_B S \omega_p C_0 / (N^2 \eta_p Q_E)]^{-1}$ .

Electromechanical resonance frequency

$$f'_p = f_p / \sqrt{1 - k_{31}^2}; \quad f'_{p1} = \sqrt{2} f'_p.$$

Reception mode sensitivity:

(a) At electromechanical resonance frequency

$$M_p = N \eta_p / \left[ \alpha_p (\rho c)_B \omega_p' C_0 \right].$$

(b) At frequencies near resonance

$$M = N\eta_p / \left[ \alpha_p \alpha_\omega (\rho c)_B \omega C_0 \sqrt{1 + \left[ Q_M^D \left( f/f'_p - f'_p/f \right) \right]^2} \right].$$

(c) At low frequencies

$$M_{L.F.} \approx NS C_{EQV}^E / C^T;$$

$$Q_M^D = Q_M / \sqrt{1 - k_{31}^2}; \quad C^T = \varepsilon_{33}^T S / d.$$

## 9.4 Lamellar and Spherical Piezoceramic Transducers

Transducers, mechanical systems which perform lateral flexural vibrations, are used if frequencies are in the lower than 5–10 kHz range. As a rule, these transducers are used in the field of frequencies, lower than the resonant frequency. Their mode shape, intrinsic frequencies and electro-acoustic parameters depend on the conditions of fastening active elements [8].

A vibrating system of lamellar transducers is made in the form of two-layer rectangular or round piezoceramic plates, supported by opposite edges (Fig. 9.8a) or by perimeter (Fig. 9.8b) (i.e., symmetric or asymmetric bimorph elements, see Chap. 6).

The form of thin plate vibrations

$$f(x) = \sin(\pi x/l); \quad f(r) = 1.04J_0(2.2r/a) - 0.04N_0(2.2r/a),$$

where  $J_0$  and  $N_0$  are Bessel functions of first and second kinds.

Equivalent concentrated parameters

$$m_{EQV} = \rho a h l; \quad m_{EQV} = 0.6\pi\rho a^2 h;$$

$$C_{EQV} = 3(1 - \mu^2)l^3 / (\pi^4 E_{Yu1}^E a h^3); \quad C_{EQV} = 3(1 - \mu^2)a^2 / (46 E_{Yu1}^E h^3),$$

where:  $\mu = -s_{12}^E / s_{11}^E$  – Poisson ratio;  $E_{Yu1}^E = 1 / s_{11}^E$  – Young's modulus of plate material.

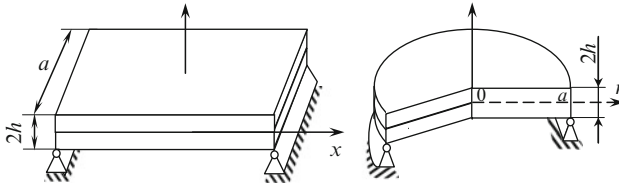


Fig. 9.8 Vibrating systems of rectangular (a) and round (b) lamellar transducers

Resonant frequencies of non-load transducer

$$f_0 \approx 0.9c_1^E h / (l^2 \sqrt{1 - \mu^2}); \quad f_0 \approx 0.45c_1^E h / (a^2 \sqrt{1 - \mu^2}),$$

where  $c_1^E = \sqrt{E_{Y_{u1}}^E \rho}$ .

Electromechanical transformation coefficient (factor)

$$N = \pi d_{31} E_{Y_{u1}}^E a h / [l(1 - \mu)]; \quad N = 4.5 d_{31} E_{Y_{u1}}^E h / (1 - \mu).$$

Transducers with an active element in the form of a hollow spherical cover are used as measuring radiators and receivers [4]. The spherical transducer calculation is the same as the cylindrical transducer calculation described in Sect. 9.3 [9].

Mechanical resonance frequency:

(a) Unloaded cover

$$f_0 = [1 / (2\pi r)] \sqrt{2E_{Y_u} / [\rho(1 - \mu)]},$$

where:  $r$  – mean radius ( $r \gg d$ );  $d$  – cover thickness;  $\mu$  and  $E_{Y_u}$  – Poisson ratio and cover material elasticity module.

(b) Loaded cover – formula (9.5), in which  $c_1^E$  should be substituted by value

$$\sqrt{2E_{Y_u} / [\rho(1 - \mu)]}, \quad \beta = kr / (1 + k^2 r^2).$$

Electromechanical transformation coefficient (factor)

$$N = 8\pi d_{31} r E_{Y_u} / (1 - \mu).$$

Equivalent concentrated parameters

$$m_{EQV} = 4\pi r^2 \rho d + 2\beta(\rho c)_B r^2 / f; \quad C_{EQV} = (1 - \mu) / (8\pi E_{Y_u}^d d).$$

Capacitance

$$C_0 = 4\pi \varepsilon_{33}^T (1 - k_p^2) r^2 / d,$$

$k_p^2 = 2d_{31}^2 E_{Y_u} / [\varepsilon_{33}^T (1 - \mu)]$  – energy EMCF for a sphere.

Electromechanical resonance frequency

$$f_p' = f_p / \sqrt{1 - k_p^2}.$$

Reception mode sensitivity

$$M = \frac{2d_{31} d \eta_p k_D E_{Y_u}}{\alpha_p \alpha_\omega (\rho c^2)_B (1 - \mu) \varepsilon_{33}^T (1 - k_p^2) k r} \left(1 + [Q^D (f/f_p' - f_p'/f)]^2\right)^{-0.5},$$



where  $\alpha_\omega = 1 - (1 - \alpha/\alpha_p)\eta_p$ ;  $\alpha = k^2 r^2 / (1 + k^2 r^2)$ ;  $Q^D = Q / \sqrt{1 - k_p^2}$ ;  
 $Q$  – formula (9.7) with the replacement mentioned above  $c_1^E$ .

## 9.5 Basic Requirements for Projected Transducers

As transducer radiation is most effective at the resonance frequency of their mechanical vibratory system, transducers in radiation mode are mainly used at resonant frequencies or those close to them. Modern hydro-acoustic stations work in a 1 to several megahertz frequency range. To block this range a number of hydro-acoustic transducers are used. The transducers vary in their methods of energy transformation, mode shapes and design types [1].

For minimization of transducer broadbandness dimension-type rich transducers are needed. Transducer broadbandness is assured by domain-dissipative piezoelements (Chap. 3) and application of negative feedback (Chap. 5).

To have the given antenna concentration factor and its radiated power, the transducers used in it should have corresponding wave sizes, permissible dispersion of amplitude and phase errors and also necessary values of specific radiated power and efficiency.

As hydro-acoustic antennas are set in overboard space of various carriers, their work depths (transducer hydrostatic pressure values are changed accordingly) can be in the range of several meters to several kilometers.

Immunity from antenna [10] noise depends on vulnerability of electric noises emitted by receivers, and attached radio-electronic elements. It also depends on sea and object noise hindrances – the antenna carrier. Generally, receiver electronic elements and noise immunity defines its threshold (minimal) pressure as  $p_{th}$ . Immunity from piezoelectric receiver primary noise (electric noise of preamplifiers) is assured by [6] the specific value selection of its idle sensitivity  $M$  and internal resistance  $Z$ , i.e., specific receiver sensitivity  $M = M/\sqrt{Z}$ .

To ensure the necessary broadbandness a uniform below-resonance part of amplitude-frequency receiver characteristic is usually used.

Thus, modern transducers should have work frequencies, wave sizes, specific power, efficiency, specific sensitivities, broadbandness and work depths, ensuring the necessary range of a hydro-acoustic station.

Transducers are used in sea water. They are influenced by various aggressive factors: corrosion, cavitation, fouling, wide temperature range and hydrostatic pressure. In addition, radiating, transducers are influenced by considerable electric and cyclic mechanical pressure, and also by heating of deformed elements caused by them. As a result of all these factors, mechanical and electric damages accumulation, water vapor diffusion inside the transducer, material ageing, etc., occur in the corresponding elements of the design. Designing a transducer considerable attention should be paid to its reliability and durability. Electrical, mechanical, thermal,

chemical and other influences, and also physical and chemical phenomena, caused by them, should be considered in their evaluation.

To provide the corresponding knot-tying, transforming energy (of a so-called active element), its electro-insulation and hermetic sealing, and also mechanical durability and acoustic shielding, special constructive elements made of corresponding materials should be introduced into the transducer design. All this makes hydro-acoustic transducers quite complex and expensive. The transducer design task is to select the following: a transducer type, materials used and detailed sizes to ensure intended efficiency, reliability and durability with the minimum cost.

## 9.6 Selection of Energy Transformation Method and Mode Shape

According to the energy transformation method (electric energy into mechanic energy and vice versa), modern hydro-acoustic transducers are divided into piezoelectric, magnetostrictive, electromagnetic, electro-dynamic, electrochemical, electric-spark, hydraulics–acoustics, steam-gas–acoustical, optical–acoustical, etc. [6, 8].

The analysis of possibilities of various energy transformation methods in the necessary wide frequency and depth ranges shows that only piezoelectric and magnetostrictive energy transformation methods meet modern requirements. To solve partial problems in the range not exceeding 1 kHz frequency and 200 m depth, transducers based on other energy transformation methods are used in some cases.

As is known, EMCF characterizes the ability of active materials to transform electrical energy into mechanical energy in static mode

$$k_C^2 = W_M / (W_M + W_E),$$

where  $W_E$  and  $W_M$  are the energy accumulated by the transducer's electrical and mechanical parts.

The main characteristics of the radiator, working at close to resonant frequencies, essentially depending on material parameters, are its overall resonant size  $d_G$ , mechanical–electrical efficiency  $\eta_{ME}$  and maximum radiated specific power  $P_{sp \max}$ . They are connected with active material parameters by the following correlations [6]:

$$d_G \equiv c; (\Gamma - G \text{ from generator}) \eta_{ME} = \frac{1}{1 + \frac{1 - k_C^2}{k_C^2 Q_E Q_M}};$$

$$P_{sp \max} = \frac{\sigma_{eM.ex}^2 B_1}{(\rho c)_M^2} = \frac{\sigma_{ex}^2 B_2}{(\rho c)_M^2},$$

where:  $\sigma_{eM.ex}$  and  $\sigma_{ex}$  – maximum permissible electromechanical driving voltage and mechanical stress;  $(\rho c)_M$  – specific acoustic material resistance;  $B_1$  and  $B_2$  – factors determined by mode shape and design parameters.

For piezoelectric and magnetostrictive materials voltage and stress are

$$\sigma_{eM.ex1} = d_{ik} E_{Yu} E; \sigma_{eM.ex2} = a_{ik} B,$$

Where:  $d_{ik}$  and  $a_{ik}$  – tensor components of piezomodules and magnetostrictive constants;  $E_{Yu}$  – Young's modulus;  $E$  and  $B$  – electric field intensity and magnetic induction.

The receiver's main characteristic – specific sensitivity – determines signal-to-noise ratio on the receiver output or depending on its threshold pressure. For piezoelectric and magnetostrictive receivers, functioning at below resonant frequencies, specific sensitivity is connected to active material parameters by this correlation

$$M_{SP} = k_C B_3 \sqrt{\rho_M},$$

where  $B_3$  is a factor determined by mode shape and design parameters.

Parameters of the main modern magnetostrictive and piezoelectric materials which determine the efficiency of a mechanical–electrical energy transducer are shown in Table 9.1. As can be seen from the table, piezoelectric materials have considerably better specifications than magnetostrictive. The advantage of metal magnetostrictive materials is their high mechanical durability, which facilitates the measurement of the level of permissible mechanical stress. However, modern armoring (reinforcement) methods increase the mechanical durability of piezoceramic active elements to the required level. Thus, they neutralize this disadvantage of piezoelectric materials.

The piezoelectric method of energy transformation is mainly used in modern home radiators and receivers. The most effective are radiators with piezoceramic ИТБС-3, and receivers – with ИТЧВ-1 [6].

## 9.7 Certain Transducer Designs

Designing a transducer, the necessary mode shape of the chosen active element is realized by using the corresponding active element fastening to the transducer or antenna housing (case) and by the necessary electric switching of the active element corresponding parts (see Fig. 9.9) [1].

As hydro-acoustic transducers are meant for continuous duty in sea water, electric insulation and hermetic sealing of those active elements parts under voltage is necessary to ensure the specified reliability and durability.

The required mechanical durability of transducer–radiator active elements is assured by armoring (reinforcement) with special strengthening details (bandages, buckles, etc.), made of metal or polymeric materials. For electrochemical corrosion

**Table 9.1** Specification values of magnetostrictive and piezoceramic materials

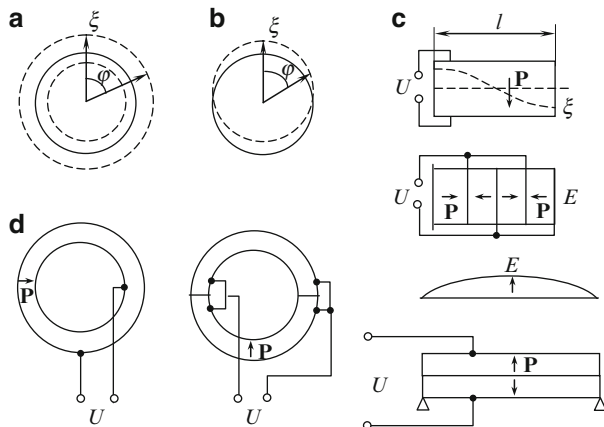
Specification	Nickel HΠ-2 (low-nickel alloy)	Permendur 50 K Φ	Piezoceramic ИТБС-3	ИТЧНВ-1
1	2	3	4	5
EMCF $k_C$ :				
In weak fields	0.3	0.4	0.65	0.72
In strong fields	0.2	0.1	0.65	0.7
$Q$ factor in strong fields:				
Electric $Q_E$	2.6	1.9	40	11
Mechanical $Q_M$	21	20	200	60
Sound speed $c \cdot 10^{-3}$ (m/s)	4.9	5.2	3.1	2.6
Mechanical durability (mPa):				
Tensile strength $\sigma$	100	100	19.6	16.7
Compression strength $\sigma_{COM}$	100	100	350	345
Density				
$\rho \cdot 10^{-3}$ (kg/m <sup>3</sup> )	8.8	8.2	7.25	7.3
Pressure				
$\sigma_{EM}$ (V/cm <sup>2</sup> )	0.71	1.55	2.6	-
Mechanic-electric				
efficiency $\eta_{ME}$	0.5	0.5	0.95	0.9
$k_C/\sqrt{\rho_M}$ ratio	2.07	2.68	7.8	10.5

prevention (protection), corrosion-proof material (titan) or special measures (coverings, protectors, etc.) are used. Electrical insulation elements, hermetic sealing and armoring (reinforcement) should form a unified vibratory system with an active element. Therefore their corresponding mechanical conjugation (interface) is needed. To remove unnecessary sound radiation (receipt), rear and anti-phase transducer surface patches, shielded by sound-soft or sound-rigid acoustic reflecting or absorbing (in the case with receivers) screens (barriers), are used.

Thus, the transducer design task is to choose key constructive elements and their conjugations (couplings), ensuring the necessary transducer efficiency, reliability and durability with its minimal sizes, weight and cost [8, 11–13].

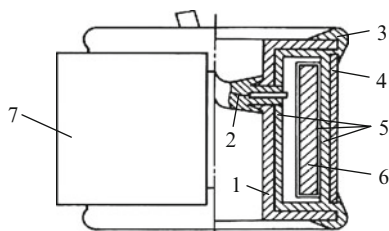
Piezoceramic transducers, ensuring the best operation efficiency and reliability in radiation and reception modes, are widely used in modern hydro-acoustics. At frequencies below 1 kHz they rival with compound magnetostrictive and electro-magnetic transducers.

One of the modern hydro-acoustic transducer widespread designs is shown in Fig. 9.10. This transducer active element 6 consists of elementary piezoelements (prisms) glued to each other. The electrical insulation of the active element is ensured by the layers of firm, liquid and gaseous electric insulating material 5, located between the active element 6 and the transducer housing (cover) 1 or sea water. The active element is sealed hermetically, combining the vulcanized or glued layers of sealing materials (parts 7, 3, 4). The corresponding choice of materials and part sizes ensures mechanical durability of all elements.



**Fig. 9.9** Piezoceramic transducers fundamental mode and electric activation of piezoelements, realizing them: (a, b) pulsing and oscillating cylinders, (c) round flexural plate, (d) half-wave bar

**Fig. 9.10** Cylindrical piezoceramic transducer of load-bearing unit: 1 – housing (case), 2 – current lead, 3 – fastening, 4 – bandage, 5 – electric insulation, 6 – active element, 7 – acoustic baffle (screen)



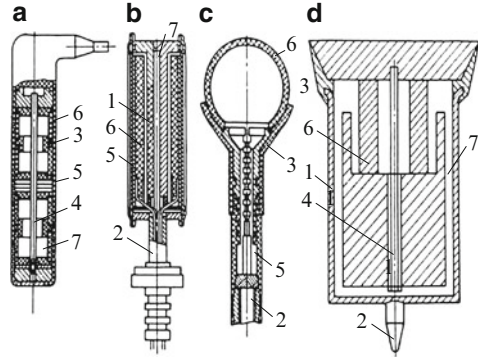
If necessary, the mechanical durability of the active element can be improved by application (overlay) of armoring (reinforcement) elements 4, creating special compression stress. By means of elastic fastening 3, made of polymeric or metal materials, the active element is attached to the housing (case) 1. Layers of materials with high acoustic reflection coefficients in water (air layers, and also air-filled polymers and metal designs) are used as acoustic baffle (screen) 7.

Depending on the influence of methods of neutralizing hydrostatic pressure on the efficiency of transducers, all possible designs with any mode shape can be divided into *load-bearing* and *compensated*.

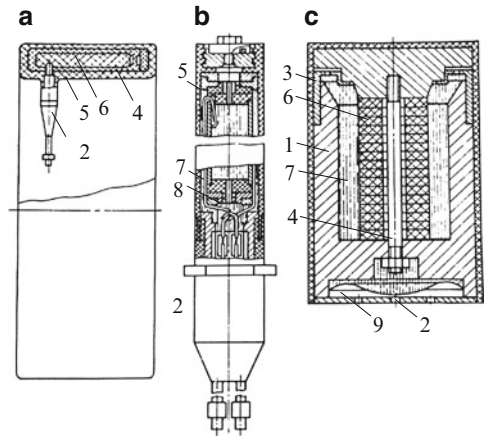
In load-bearing designs (Figs. 9.10 and 9.11) the active element and housing (case) internal volumes are filled with air or electric insulation gas. These active element designs and the strong housing (case) can resist hydrostatic pressure. Hydrostatic pressure is transformed in the design loaded elements into one-, two- or three-axis mechanical stress, which is considerably (up to 10–15 times) bigger than the hydrostatic pressure causing it.

Electrical insulation gas, filling internal volumes of load-bearing units' transducers, also functions as an internal acoustic baffle (screen). Hermetic sealing and electrical insulation of load-bearing units' active elements from basic (housing, case) parts are ensured by polymeric materials and metal layers.

**Fig. 9.11** Load-bearing units of hydro-acoustic piezoceramic transducers: (a) tubular, (b) round plate, (c) spherical, (d) rod (bar): 1 – housing (case), 2 – current lead, 3 – fastening, 4 – bandage, 5 – electric insulation, 6 – active element, 7 – acoustic baffle (screen)



**Fig. 9.12** Compensated piezotransducer designs: (a) cylindrical, hermetically sealed by layers metal–compound (a) and oil-flooded rubber (b) materials; rod (bar) oil-flooded low frequency: 1–6 – see Fig. 9.11, 7 – oil, 8 – capillary, 9 – pressure compensator (pressurizer)



In compensated designs (Fig. 9.12) active and all other design elements, operating under hydrostatic pressure, are uniformly compressed  $\sigma_{COM} = p_H$ .

Electrical insulation and hermetic sealing of compensated designs are created by polymeric material layers, and also by combinations of metal layers with insulating liquid and polymeric materials.

Acoustic shielding of transducer surfaces (internal inclusive) is performed by screens (baffles) designed for work under the corresponding hydrostatic pressure [14].

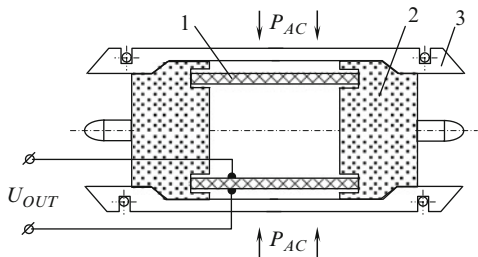
The other industrially produced receiving transducer is shown in Fig. 9.13 [15].

This is a cylinder-shaped piezoelement 1. The cylinder ends are sealed by covers 2 and clamped by metal brackets 3 for durability increase.

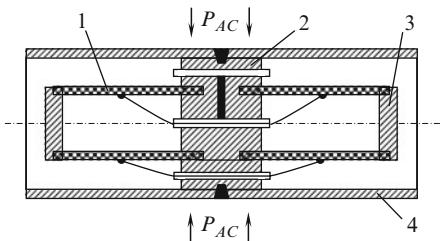
In Fig. 9.14, a vibration-resistant design variant of a receiving transducer ПСП-ТБ is represented.

The receiver consists of two piezoceramic cylinders 1, attached to the washer 2 from both sides, and by covers 3, closing the ends. The receiver is closed by protective cover 4. As the piezoelements in the receiver are attached to the central

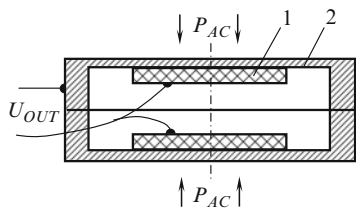
**Fig. 9.13** Piezotransducer  
ПКС-4



**Fig. 9.14** Piezotransducer  
ПСП-ТБ



**Fig. 9.15** Piezotransducer  
ПКС-6



washer, heteropolar electrical signals, arising with vibration in both cylinders, are compensated with their parallel connection.

However, the receiver mentioned is not widely used because of its non-manufacturability and heavy weight. Disk type transducer (ПКС-6) is shown in Fig. 9.15.

Flexural vibrations of flat disk piezoelements are used in it. Disk-shaped 1 ПТС-19 piezoelements are pasted on the metal membranes 2, making a single unit with the housing (case).

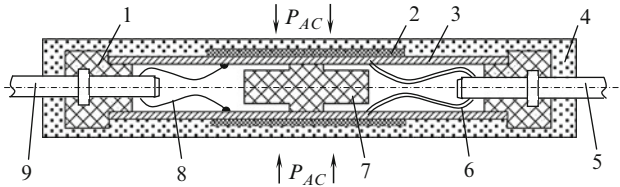
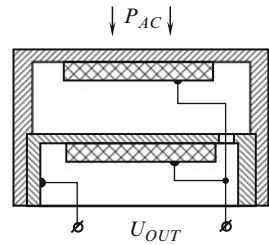
Transducer ПК-19, shown in Fig. 9.16, contains a piezoceramic transformation disk-shaped element, rigidly connected to the metal membrane, perceiving sound pressure, and a piezoceramic element for vibration hindrances compensation.

Heteropolar signals, arising with vibration in two parallel connected disks, are compensated.

One more transducer is shown in Fig. 9.17.

This transducer consists of plastic encapsulation (case) 1 of a monolithic design to which two rectangular metal membranes 3 with piezoelements 2 are glued. Piezoelements are of a rectangular-lamellar form. Piezoelements are attached to membranes with conductive adhesive. Silver conductors 8 are contact-welded

**Fig. 9.16** Piezotransducer ПК-19



**Fig. 9.17** Piezotransducer ПДС-13

on membranes. The other ends of conductors are soldered to the minus clamp (terminal) 9.

Conductors with insulation 6 are attached to the second piezoelement electrodes with conductive adhesive. The other ends of these conductors are soldered to clamp (terminal) 5. The transducer is completely hermetically sealed by sealant 4. Elastic padding 7 protects piezoelements from destruction if the receiver depth limit is exceeded.

A transducer with advanced noise immunity is shown in Fig. 9.18.

This contains a sensitive element, consisting of two cylindrical piezoelements 1, console-fixed in foundation 2 and muffled by plastic covers 5 from other ends. The transducer is set through vibration-isolating padding 6 into the split plastic housing (case) 7 with holes for free access to piezoelements liquid filler. Split housing (case) 7 is fastened by two ring springs 3 and has webbing along the outer contour for increased durability. The vibration-isolating padding ensures mechanical compensation for vibration hindrances. Depending on the vibration factor transmission of the material, the elastic padding thickness and rigidity (stiffness) is selected.

Specifications of the receiving transducers described are shown in Table 9.2 [15].

As a result of analysis of converter specifications, the following drawbacks should be noted:

- Quite complicated transducer designs
- Narrow frequency range
- Low measurement accuracy
- Low temperature stability



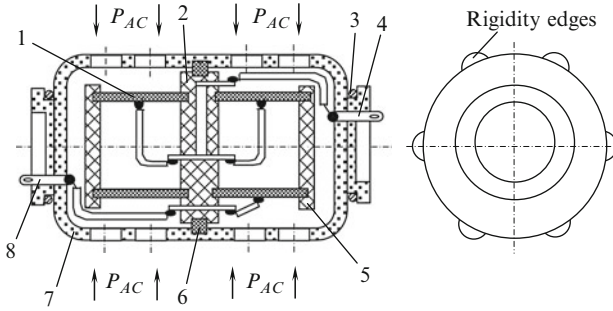


Fig. 9.18 Piezotransducer ПДС-21

Table 9.2 Receiving transducer specifications

No.	Type	Material	Form	Sensitivity, $B/(N/m^2) \times 10^{-5}$	Capacity (nF)	Resonant frequency (kHz)
1.	ПКС-4	(ПТС-19) Barium titanate	Cylinder Double cylinder	7.5	13	1
2.	ПСП-ТВ	titanate	cylinder	5	25	1.5
3.	ПКС-6	(ПТС-19)	Two disks	30	10	1
4.	ПК-19	(ПТС-25)	Two disks Two	9	10	1
5.	ПДС-13	(ПТС-19)	rectangle Two	15	3	4.5
6.	ПДС-21	(ПТС-19)	Two cylinders	10	14	16

Table 9.3 Influence of temperature on receiving transducer specifications

No.	Material	$\epsilon$ (%)		$d_{31}$ (%)	
		$(-40/20)^\circ C$	$(20/60)^\circ C$	$(-40/20)^\circ C$	$(20/60)^\circ C$
1.	ПТС-19	-16.2	+19.8	-14.6	+9.75
2.	ПТВС-1	-33.6	+35	-25	+18
3.	ПТЧНВ-1	-17.1	+19.5	-15.5	+10.3
4.	ПТСС-1	-6	+12.3	0	+7.7
5.	ПТС-23	-12	+13	-2	+7.0
6.	ПТВС-3	-16.7	+16.7	-10.6	+2.1

The low measurement accuracy and low temperature stability of transducers is caused by instability of the piezomodules or electromechanical coupling factor under the influence of destabilizing factors (temperature, etc.). Dependence of dielectric permeability and piezomodule  $d_{31}$  on temperature for different piezoceramic materials is shown in Table 9.3 [15].

Specifications of piezoelectric hydro-acoustic transducers can be considerably improved by using asymmetric bimorph elements (Chap. 6), domain-dissipative piezoelements (Chap. 3), and negative electromechanical feedback (Chap. 4).

## 9.8 On One Method of Low-Frequency Acoustic Vibration Creation

Hollow cylinder-shaped monomorph piezoelectric transducers and disk-shaped asymmetric bimorph piezoelements are most widely used as hydro-acoustic transducers [1, 6, 9, 13, 16, 17].

Resonant frequency of round bimorph element can be approximately determined by using the formula [1]:

$$f_0 \approx \frac{0,45ch}{r^2 \sqrt{1 - \mu^2}}, \quad (9.17)$$

where  $c = \sqrt{E\rho}$ ;  $h$  – piezoelement thickness;  $r$  – piezoelement radius;  $E$  – Young’s modulus;  $\rho$  – piezoelement material density;  $\mu$  – Poisson coefficient.

As follows from formula (1), a decrease in bimorph element resonant frequency is possible with reduced piezoelement thickness and also with increased radius, i.e., piezoelement dimension increase. These parameter alterations have technological and dimensional restrictions. In practice, resonant frequency of bimorph elements used is usually about some kilohertz [16].

In addition, it is known that low-frequency sound is propagated in water to a depth of several thousand kilometers practically without attenuation. This happens because of deep (undersea) sound channel formation in the ocean upper level – acoustic wave guide of the refraction type. Due to this, low-frequency acoustics has its obvious advantages in a wide range of problems. Among these problems one can mention the creation of sound channels of several thousand kilometers, such as Kamchatka–Hawaii (4,700 km) for instance, and also a system of ultrasonic illumination of underwater conditions, etc. [18–20] (<http://www.ipfran.ru>).

As a rule, piezoceramic radiators work at resonant frequency because of their low efficiency in a low-resonance area [1, 6, 13].

However, a decrease in resonant frequency results in a considerable increase in radiator dimensions. For example, the radiator with 20.5 Hz working frequency developed by the Institute of Applied Physics of Russian Academy of Sciences (Nizhniy Novgorod), weighs 4,500 kg and is more than 3 m in diameter (Fig. 9.19) [21] (<http://www.ipfran.ru>).

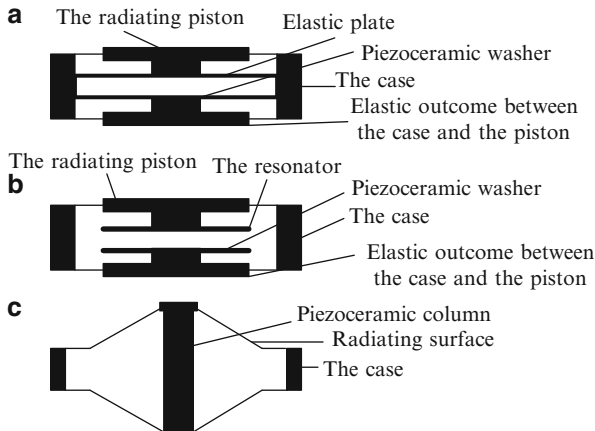
At present a significant number of engineering solutions for low-frequency piezoceramic radiators [5, 17, 22] are known. In Fig. 9.20 some of their schemes [20] (<http://www.ipfran.ru>) are shown.

To decrease the radiator dimensions a known radio-engineering solution is proposed. It is used in superheterodyne receivers for intermediate frequency receipt [23, 24].

The point of this idea, applied for example to hydroacoustic radiators, is that a piezoelement with two systems of electrodes (piezotransformer) is used as radiator. Voltage from a first generator is delivered to one system of electrodes. Voltage oscillation frequency of this generator is made equal to or close to a piezoelement resonant frequency. Voltage from a second generator is delivered to the other system



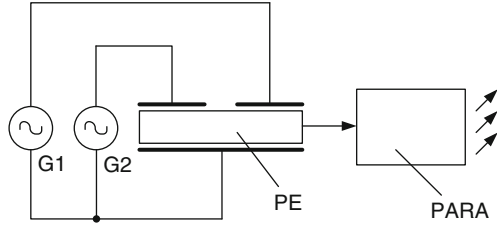
**Fig. 9.19** Independent radiating complex ( $f = 20.5$  Hz) Institute of Applied Physics of Russian Academy of Sciences (<http://www.ipfran.ru>)



**Fig. 9.20** Low-frequency piezoceramic radiators: type A –  $f_p = 650$  Hz,  $\varnothing 310$  mm, type B –  $f_p = 2,800$  Hz,  $\varnothing 220$  mm, type C –  $f_p = 700$  Hz,  $\varnothing 700 \times 700$  mm

of electrodes. Voltage oscillation frequency of this generator is also made close to the same resonant frequency to make the difference between the first and the second generators oscillation frequency equal to the radiator working frequency (Fig. 9.21) [25].

**Fig. 9.21** Low-frequency piezoceramic radiator: *G1*, *G2* – oscillation generators, *PE* – piezoelement, *PARA* – piezoelement acoustic radiation amplifier



If signals from two generators are delivered to a piezoelement with two systems of electrodes (piezotransformer) it performs amalgamator functions more precisely – adder, summer, summator [23, 24, 26–28].

As is known, if a sinusoidal electric field is applied to the piezoelectric, direct and return (back) progressive waves of displacement, deformation, and voltage arise in it because of the inverse piezoelectric effect. These waves make a standing wave in stationary mode. Of course, if several progressive waves are created in the piezoelectric volume, then using the superposition principle (if oscillations in the element work linear section are created), algebraic addition of the energy flux in each point of the volume driven is received [18, 19, 29].

Adding together two voltages of identical resonant frequency  $\omega$

$U_{in1} = U_{m1} \sin(\omega t + \varphi_1)$  and  $U_{in2} = U_{m2} \sin(\omega t + \varphi_2)$  we receive:

$$U_{out} = k_1 U_{in1} + k_2 U_{in2} = U_m \sin(\omega t + \varphi), \tag{9.18}$$

where  $U_m = \sqrt{k_1^2 U_{m1}^2 + k_2^2 U_{m2}^2 + 2U_{m1} U_{m2} k_1 k_2 \cos(\varphi_2 + \varphi_1)}$ ,

$$\text{tg} \varphi = \frac{k_1 U_1 \sin \varphi_1 + k_2 U_2 \sin \varphi_2}{k_1 U_1 \cos \varphi_1 + k_2 U_2 \cos \varphi_2}.$$

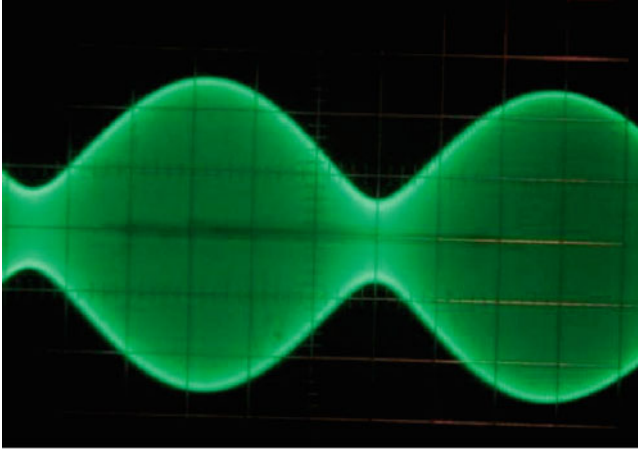
Here  $k_1$  and  $k_2$  are coefficients determining connection by voltage between output and each input.

Thus, in this case mechanical vibrations proportional to the sum of input voltage arise in the piezoelement (Fig. 9.22) [27, 28].

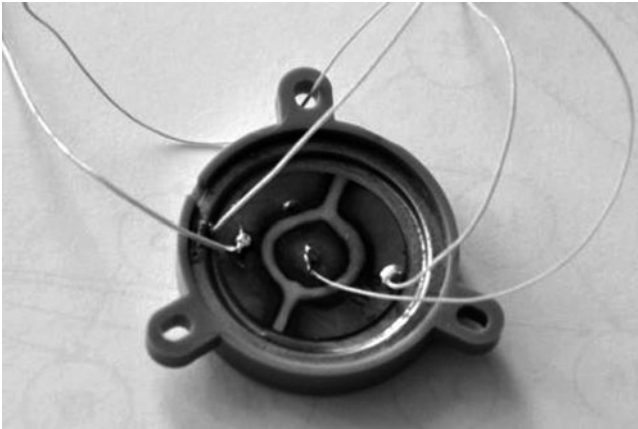
We should note that the difference signal amplitude can run to half of the total signal value, i.e., the difference (low-frequency) signal amplitude can be quite big.

The method proposed has been checked experimentally. The electro-acoustic transducer 3Π-19 manufactured by the public corporation Aurora (Volgograd, Russia) was used in the experiment. The transducer consists of 40× steel plate 32 mm in diameter and 0.15 mm thick. A piezoelement 23 mm in diameter and 0.2 mm thick is glued to the plate with epoxide compound. The bimorph element obtained is fastened in the case of high-impact polystyrene (Fig. 9.23).

One of the piezoelement electrodes was split into three parts. Generators Γ3-106 were attached to two of them. The third disk-shaped electrode was used to control the output electro-acoustic signal of the piezoelement. The first generator frequency



**Fig. 9.22** Oscillogram of piezoceramic summer input signal



**Fig. 9.23** Electro-acoustic transducer 3Π-19

equaled 98.2 kHz. It was resonant to piezoelement 3Π-19 radial oscillations. The frequency of the second generator was 100.7 kHz.

If two generators were simultaneously connected, 3Π-19 sounded at a frequency of 2.5 kHz – the resonant frequency of flexural vibration.

The result obtained is quite surprising: oscillations are created at unheard frequencies – 98.2 and 100.7 kHz while 2.5 kHz transducer sounds. If the vibration frequency of a generator is changed, oscillations are also created at other frequencies.

The piezoelement vibration level can be increased if flexural vibrations from the generator are created (harmonics for the main resonant frequency of flexural vibrations – 2.5 kHz).

It is also known that in amplitude modulators schemes the output signal can be proportional to the product of the input signals; therefore, such devices are sometimes called multipliers in technical literature [24].

Amplitude-modulated oscillation expression will generally look like this:

$$i = I_m [1 + mf(t)] \sin \omega_0 t, \quad (9.19)$$

where  $f(t)$  is any signal transferred (it is supposed that  $|f(t)| < 1$ ).

As we see, the modulation process consists of the multiplication of two time functions –  $1 + mf(t)$  и  $I_m \sin \omega_0 t$ . The modulator should be a multiplying device, i.e., the device with two inputs and one output: if two functions  $x(t)$  and  $X_0(t)$  are inputted

$$y(t) = y(t)X_0(t) \text{ is outputted.}$$

Multiplication by the given function  $X_0(t)$  is linear, as it is seen from the following ratio:

$$y(t) = [x_1(t) + x_2(t)] X_0(t) = x_1(t)X_0(t) + x_2(t)X_0(t) = y_1(t) + y_2(t).$$

Devices for multiplication of two time functions, used for modulation and frequency transformation, are usually called amalgamators (mixers). This term is inappropriate, as it is not descriptive enough. The device for multiplication of two functions will simply be called a multiplier [24].

The development of a piezoelectric multiplier scheme requires additional research, as in this case the acoustic signal proportional to the product of input electric signals should be obtained.

Acoustic resonators and also ultrasound concentrators – ultrasound intensity amplifiers (of vibration displacement amplitude) – can be used as acoustic signals amplifiers [8].

Two types of concentrators – focusing or high-frequency, and rod or low-frequency – are known. For the solution of the problem discussed, both of them are irrelevant. Additional research is needed for the solution of this problem.

In this case the application of meander-shaped electrical signals seems promising [30].

## References

1. A.P. Evtyutov, A.E. Kolesnikov, E.A. Korepin et al., *Reference Book on Hydroacoustics* (Sudostroenie, Leningrad, 1988), p. 552 (in Russian)
2. G.V. Cats (ed.), *Magnetic and Dielectric Devices, P. 1* (Energiya, Moscow, 1964), p. 416 (in Russian)
3. D.B. Dianov, V.M. Kuznetsov, Influence of transitive layers on rod piezotransducer frequency characteristics. News of Leningrad Electrotechnical Institute Release **63**, 60–78 (1968) (in Russian)

4. G.M. Sverdlin, *Applied Hydro-acoustics* (Sudostroenie, Leningrad, 1976) (in Russian)
5. V.N. Tyulin, *Introduction in Radiation and Sound-Scattering Theory* (Nauka, Moscow, 1976) (in Russian)
6. V.V. Bogorodskiy, Underwater electro-acoustic transducers: the Directory (Sudostroenie, Leningrad, 1983), p. 248 (in Russian)
7. G.M. Sverdlin, Yu.P. Ogurtsov, *Calculation of Transducers* (Publishing House LKI, Leningrad, 1976–1977) (in Russian)
8. I.P. Golyamina (ed.), *Ultrasound (Small Encyclopedia)* (Soviet Encyclopedia, Moscow, 1979), p. 400 (in Russian)
9. A.E. Kolesnikov, *Ultrasonic Measurements* (Standards Publishing House, Moscow, 1982), p. 248 (in Russian)
10. M.D. Smaryshev, Yu. Yu. Dobrovolskiy, *Hydroacoustic Antennas. Reference Book* (Sudostroenie, Leningrad, 1984), p. 300 (in Russian)
11. ITC, *Catalog of Underwater Transducers* (ITC, Golta, 1976)
12. I.M. Pawers, Piezoelectric polymeric emerging hydrophone technology. EASCON'79
13. G.M. Sverdlin, *Hydroacoustic Transducers and Antennas* (Sudostroenie, Leningrad, 1980), p. 232 (in Russian)
14. V.E. Glazanov, *Shielding of Hydro-acoustic Antennas* (Sudostroenie, Leningrad, 1985), p. 145 (in Russian)
15. Yu.N. Kuliev et al., *Piezoreceivers of Pressure* (Publishing House of Rostov University, Rostov, 1976), p. 152 (in Russian)
16. V.M. Sharapov, M.P. Musienko, E.V. Sharapova, *Piezoelectric Sensors*, ed. by V.M. Sharapov (Technosphaera, Moscow, 2006), p. 632 (in Russian)
17. S.I. Pugachev (ed.), *Piezoceramic Transducers: The Directory* (Sudostroenie, Leningrad, 1980), p. 232c (in Russian)
18. A.G. Sazontov, A.L. Matveyev, N.K. Vdovicheva, Rough surface scattering effect on acoustic coherence and shallow water: theory and observation. *JEEE. Oceanic End.* **27**(3), p. 653 (2002) (in Russian)
19. A.L. Virovlyansky, V.V. Artelny, A.A. Stromkov, Proc. U.S. – Russia Workshop on Experimental Underwater Acoustics. Nizhny Novgorod. Inst. Appl. Phys. RAS, 33 (2000) (in Russian)
20. Patent of Russian Federation No 2112326, H04R 17/00, 1998. Central research Institute “Morfizpribor” (Saint-Peterburg). Hydro-acoustic radiator (in Russian)
21. P.I. Korotin, B.M. Salin, Independent measuring sea complex. Systems of supervision, measurement and control in vibro- and hydro-acoustics. Collected Papers of Institute of Applied Physics of Russian Academy of Sciences – Nizhni Novgorod: IAPH RAS, p. 13 (2002) (in Russian)
22. V. Sharapov, A. Vladisauskas, K. Bazilo, L. Kunitskaya, Zh. Sotula, *Methods of Synthesis of Piezoceramic Transducers: Spatial Energy Force Structure of Piezoelement*, ISSN 1392–2114 (Technologia, Kaunas, 2009), *Ultragarsas (Ultrasound)* **4**(64), 44–50
23. V.A. Kotelnikov, *Bases of Radio-Engineering* (Gostehizdat, Moscow, 1950) (in Russian)
24. A.A. Harkevich, *Bases of Radio-Engineering* (Radio and Communication, Moscow, 1963) (in Russian)
25. V.M. Sharapov et al., Patent of Ukraine № U2010.00620 from 22.01.2010. Piezoelectric transducer of mechanical value (in Ukrainian)
26. V.M. Pluzhnikov, V.S. Semenov, *Piezoelectric Firm Schemes* (Energiya, Moscow, 1971), p. 168 (in Russian)
27. V.M. Sharapov, S.A. Filimonov, K.V. Bazilo, Zh.V. Sotula, L.G. Kunitskaya, Study of piezoceramic adder (summer, summator) based on bimorph piezoelement. *Bull. Cherkasy State Technol. Univ.* **4** (2009) (in Russian)
28. V.M. Sharapov, K.V. Bazilo, L.G. Kunitskaya, Zh.V. Sotula, S.A. Filimonov, Adders (summers, summators) based on disk monomorph piezotransformer. *Bull. Cherkasy State Technol. Univ.*, **4** (2009) (in Russian)

29. V. Sharapov, A. Vladisauskas, S. Filimonov, *Bimorph Cylindrical Piezoceramic Scanner for Scanning Probe Nanomicroscopes*, ISSN 1392–2114 (Technologia, Kaunas, 2009), *Ultragarsas (Ultrasound)* **4**(64)
30. V. Sharapov, M. Musienko, Zh. Sotula, L. Kunitskaya, *About the Effect of Expansion of Reproduced Frequency Band Be Elektroacoustic Transducer*, ISSN 1392–2114 (Technologia, Kaunas, 2009) **3**(64)
31. I.S. Gonorovskiy, *Radio-Engineering Networks and Signals* (Radio and Communication, Moscow, 1986), p. 512 (in Russian)



## Chapter 10

# Transducers with Non-destructive Control

Non-destructive quality control of materials and products is one of the most important directions of science and technology. Its goal is to improve reliability and durability of machines, mechanisms, designs and constructions.

Among numerous methods of non-destructive control, using various physical fields, interacting with the object of control, acoustic (ultrasonic) methods are widely spread. This is explained by many factors. For example, as is stated in [1], they do not have such drawbacks of magnetic and electromagnetic methods as ambiguity of device data, or strong dependence on minor changes in material chemistry even within one brand. Acoustic methods are often indispensable in non-metal material (ceramics, concrete) control.

Many types of ultrasonic waves without velocity dispersion are used in non-destructive control. Among them are body longitudinal and transverse (shear) waves, surface Rayleigh waves and surface (subsurface) longitudinal, or as they are also called, head “purely” longitudinal waves [1, 2].

Sensitivity, resonant frequency, frequency band, directionality, dead zone, acoustic hindrance level generated by the transducer, and double conversion ratio refer to specifications of transducers with non-destructive control.

Practically all piezotransducers of non-destructive control devices work in pulse mode. Therefore, bandwidth is one of the main transducer specifications. The wider the bandwidth, the higher the device resolution, the smaller the dead zone, the better the product thickness measurement, defect co-ordinates and ultrasound (US) speed accuracy.

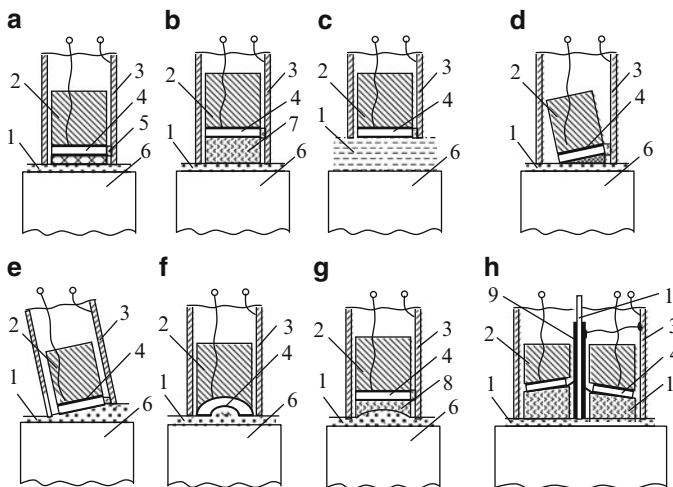
It is necessary to note that similar transducers are used in hydroacoustics (see Chap. 9), and also in medicine, in sonoradiography devices.

## 10.1 Designs and Specifications of Ultrasonic Monitor Piezotransducers

Fundamental work of the following scientists is devoted to the development of piezoelectric transducers with non-destructive control: I.N. Ermolov [1, 3–7], M.V. Korolev [2, 8–11], A.E. Karpelson [8, 10], and also V.M. Bobrenko and A.N. Kutsenko [12], A.H. Vopilkin [3, 5], U. Mason [13], I.A. Viktorov [14], B.I. Vybornov [15], A.K. Gurvich [4], V.V. Klyuev [16], P.I. Beda [17], B.A. Kasatkin [18, 19], N.A. Evdokimov [18, 19], A.F. Melkanovich [18, 20], V.I. Zaklyukovskiy and G.T. Kartsev [21], Yu.V. Lange [22], N.P. Aleshin [23], S.P. Perevalov and A.Z. Rajhman [24], V.E. Polyakov, A.I. Potapov and A.K. Sborovskiy [25], M.V. Rozina [26], S.A. Filimonov [7, 27], Yu.M. Shkarlet [28], D.S. Shrayber [29], V.M. Sharapov [30], etc.

Depending on US device type and purpose, various types of piezotransducers are used: (1) contact and immersion, (2) with and without ultrasonic delay line (UDL), (3) normal and angle, (4) causing longitudinal, shear, surface, normal and head waves, (5) separate, combined and separate–combined, (6) low- and high-frequency, (7) narrow- and broadband, (8) focusing and non-focusing, etc. [1, 6, 8].

Main types of piezotransducers for ultrasonic devices are represented in Fig. 10.1.



**Fig. 10.1** Basic types of ultrasonic equipment transducers: (a) normal contact, (b) normal contact with solid (-state) ultrasonic delay line, (c) normal immersion, (d) contact angle, immersion angle, (e) focusing, (g) focusing with a lens, (h) separate–combined: 1 – contact lubricant layer or immersion liquid, 2 – damper, 3 – housing (case), 4 – piezoelement, 5 – protector, 6 – object investigated, 7 – solid (-state) ultrasonic delay line, 8 – acoustic lens, 9 and 10 – electro-acoustic baffle (screen), 11 – prism

Normal piezotransducers (Fig. 10.1a–c) radiate and receive longitudinal US waves into the object investigated. They can be of contact (Fig. 10.1a) or immersion (Fig. 10.1c) variant, and also with solid (-state) UDL (Fig. 10.1b). Angle transducers (Fig. 10.1d,e) are used for radiation and reception of oblique longitudinal waves. In addition, as a transformation result, shear, superficial, normal and head waves appear on environment interface. Focusing piezotransducers focus ultrasonic US waves using the piezoelement form (Fig. 10.1f) or an acoustic lens (Fig. 10.1g). In Fig. 10.1h, a separate–combined transducer, having advantages over combined transducers, is shown. In particular, it has a smaller dead zone.

In contact transducers (Fig. 10.1a–c), the thickness of contact lubricant layer is much smaller than the wave length  $\lambda$  of US vibrations radiated. In immersion transducers (Fig. 10.1c,e), the thickness of immersion liquid layer ( $\lambda$ ) is much bigger. So-called slit transducers with a liquid thickness layer of several  $\lambda$  between the object investigated and the transducer are often used.

Contact transducers are used in the study of products with thoroughly machined surface if there are no high requirements for acoustic contact stability. A running immersion transducer and the object investigated (usually of a small size) are drowned in a tank with liquid. Thus, the acoustic contact stability with the product is considerably increased. There appears to be the possibility of a product automation control process.

Using a slit transducer, a gap appears between it and the product, into which contact liquid is continuously supplied. This allows automation of large-sized product control without placing them in a tank with immersion liquid.

Combined transducers with solid (-state) UDL (Fig. 10.1b) are used for the dead zone decrease (i.e., uncontrolled product area). This mainly arises because of the powerful electric excitation pulse influence on the input of a sensitive receiving amplifier. Separate–combined transducers are also used for this (Fig. 10.1h).

Focusing transducers (Fig. 10.1f,g), allowing an increase in frontal equipment resolution assuming other conditions are equal, are used for radiation directivity, received signal amplitude and signal-to-hindrance ratio improvement.

To study objects with the help of shear, head, surface or normal waves, angle transducers (Fig. 10.1d,e) with different angles of US vibration input are used. Depending on the product form and specifications character controlled, a certain type of wave is preferred or is even indispensable. For example, if thin-walled products are defectoscoped – normal waves are used if subsurface defects are detected – head waves are applied, etc. [8].

At present, piezoelements, radiating and receiving longitudinal body US waves, are mainly used for realization of all the transducer designs mentioned above. These designs differ in US waves radiated and received, focusing degree and type, types of contact with the device and acoustic vibrations input in it, and positional relationship of radiator and receiver, etc.

Different operating modes can be received if piezoelements of various shapes are used, if they are positioned differently relative to the object studied, and operate in radiator, receiver or radiator–receiver mode. Therefore, creation of a basic broadband longitudinal wave piezotransducer opens the possibility of designing and

manufacturing various types of broadband transducers. Transducer specifications can be determined by characteristics of a piezoelement, generating and receiving longitudinal US waves, in accordance with the acoustics principles known. For example, in angle transducers the amplitude of the US signal radiated and received, and also the acoustic field created in the product, can be determined by piezoelement characteristics, using the method of image US wave radiator.

We will consider specifications and defining properties of a longitudinal US wave piezotransducer below [8].

### 10.1.1 Coefficient of Electromechanical Transformation

Forward transformation coefficient  $L$  characterizes piezoelement efficiency in radiation mode:

$$L = P_{1CP}/U_0, \quad (10.1)$$

where:  $P_{1CP}$  – average value of the radiated wave acoustic pressure amplitude;  $U_0$  – amplitude of voltage, activating the transducer in radiation mode.

Inverse transformation coefficient  $M$  characterizes piezotransducer efficiency in reception mode:

$$M = U/P_{2CP} \quad (10.2)$$

or

$$M = I/P_{2CP}, \quad (10.3)$$

where  $P_{2CP}$  is the average value of US wave amplitude coming to the transducer, and  $U$  and  $I$  are voltage and current respectively, arising between piezotransducer electrodes in reception mode. In most cases, it is more reasonable to use formula (10.3) for  $M$  determination.

Double electromechanical transformation coefficient characterizes the combined piezotransducer efficiency in radiation–reception mode:

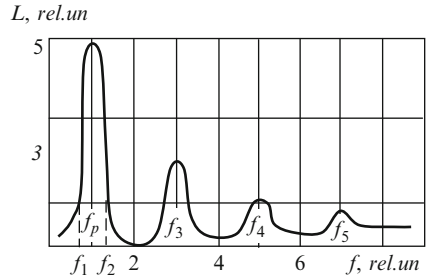
$$D = LM. \quad (10.4)$$

### 10.1.2 Piezotransducer Amplitude–Frequency Response (AFR)

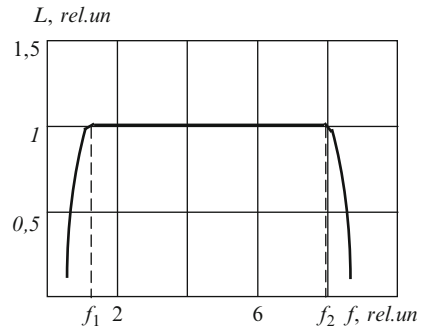
AFR shows change of transformation coefficient module, depending on frequency. In Fig. 10.2, typical AFR of a half-wave resonant piezoplates is represented.

The following sizes are considered to be AFR factors:  $f_0$  – frequency, corresponding to the first maximum AFR (first harmonic),  $f_1$  and  $f_2$  – frequencies, when AFR in the first harmonic region is 6 dB below the maximum in double transformation mode (or 3 dB below – in forward or inverse transformation mode),  $f_3, f_4$ , etc. – odd harmonics frequencies,  $\Delta f = f_1 - f_2$  – pass band. For broadband

**Fig. 10.2** AFR of half-wave resonant piezoelement:  
 $L$  – coefficient of forward electromechanical transformation,  
 $f$  – frequency



**Fig. 10.3** AFR of broadband piezotransducer



piezotransducers (we will discuss them below), AFR appears as is represented in Fig. 10.3. This AFR can be characterized by boundary frequencies  $f_1$  and  $f_2$  and strip  $\Delta f$  width, for example.

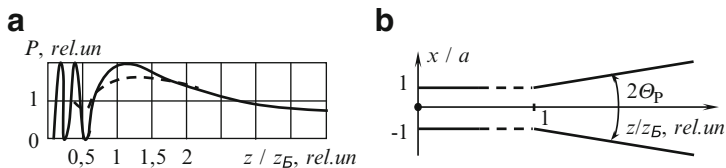
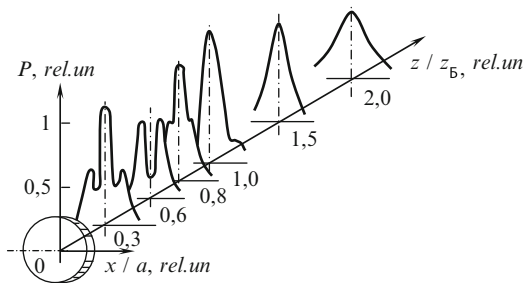
### 10.1.3 Form of Acoustic Field Created

Created acoustic field form is spatial distribution of acoustic pressure  $P$  amplitude, created by the piezotransducer in the object studied. The pressure field, created by a cylindrical piezoelement at various distances  $z$  (from the radiating plane) and  $x$  (from the symmetry axis), is represented in Fig. 10.4. The concepts of near- and far-field zones, divergence angle and directivity diagrams are used for the radiation field characteristic. Pressure distribution along radiation axis  $z$  (an acoustic axis) and general field pattern are represented in Fig. 10.5. As can be seen from Figs. 10.4 and 10.5, acoustic pressure amplitude changes non-steadily in the transducer near-field zone if distance  $z$  changes [8]:

$$P(z) = P(0) \left| 2 \sin \left[ \frac{2}{k} \left( \sqrt{z^2 + a^2} - z \right) \right] \right|, \tag{10.5}$$

where  $a$  is transducer radius and  $k$  is wave number.

**Fig. 10.4** Piezotransducer radiation field:  
 $Z_B$  – near-field zone border,  
 $a$  – piezotransducer radius



**Fig. 10.5** US field of piston piezotransducer: (a) pressure distribution along the transducer acoustic axis, (b) general field pattern; *continuous curve* – radiator nonstop run, *dashed curve* – pulsed mode

The near-field zone border is determined by expression:

$$Z_B = a^2/\lambda. \tag{10.6}$$

Divergence angle (Fig. 10.5b)

$$\Theta_P = \arcsin (0.61 \lambda/a) . \tag{10.7}$$

In the transducer distant-field zone, the acoustic pressure amplitude monotonously decreases with  $z$  increase (see Figs. 10.4 and 10.5a).

Field distribution in the distant-field zone is characterized by the directional diagram concept

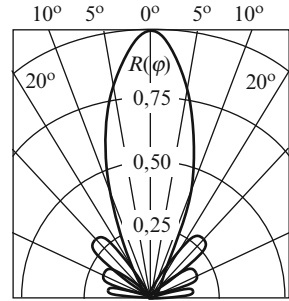
$$\Theta_P = \arcsin (0.61 \lambda/a) \quad D(\theta) = \left| \frac{P(\theta)}{P(0)} \right| = \left| \frac{2J_1(ak \sin \theta)}{ak \sin \theta} \right|, \tag{10.8}$$

where  $J_1$  is a Bessel function of the first kind.

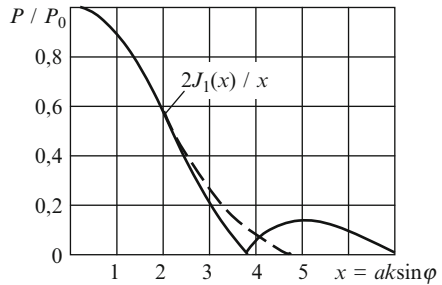
A directional diagram example in polar and Cartesian coordinates is represented in Figs. 10.6 and 10.7.

Various factors, listed above, influence piezotransducer specifications. Specifications of the piezomaterial used in piezoelement production are of the greatest importance. The specifications influence the electromechanical transformation coefficient and piezotransducer AFR (see Chap. 1).

**Fig. 10.6** Transducer directional diagram in polar coordinates with  $2a/\lambda = 5$



**Fig. 10.7** Transducer directional diagram in cartesian coordinates: *continuous curve* – radiator nonstop run, *dashed curve* – pulsed mode



## 10.2 Resonant Volume Piezotransducers

Piezotransducers with a wide continuous spectrum of work frequencies, allowing radiation and reception of short US impulses, have been considered till present.

In the majority of modern US devices, resonant (volume) piezotransducers (VP), effectively working only at intrinsic fundamental (basic) frequency, are used. These transducers have a high electromechanical transformation coefficient, and assure very high signal-to-hindrance ratio (approximately 100 dB). This ratio does not exceed 50 dB in the best types of broadband transducers. Frequently it is necessary to use VP at high frequencies, in the 20–50 MHz range. These VP are not serial in Ukrainian industry. Low-frequency VP (2–5 MHz) can also be used for this purpose if they run at higher harmonics. However, they will be extremely inefficient: signal amplitude at harmonics, compared to the signal at intrinsic fundamental (basic) frequency, decreases approximately in inverse proportion to the harmonic number and even faster. Therefore, this VP operation mode is not widely used in practice.

If VP is in US reception mode and it is current, but not voltage, of the transducer output signal that is measured, then the signal amplitude on harmonics (frequency dependent attenuation not inclusive) will equal the signal amplitude at intrinsic fundamental (basic) frequency. Therefore, this run mode considerably expands VP work frequency range and spectrum, and allows creation of high-frequency transducers without using very thin piezoplates.

Determination to expand VP work frequency range and spectrum, with all their preservation advantages, has resulted in creation of surface active volume piezotransducers (SAVP). These transducers can work effectively at intrinsic fundamental (basic) frequency and at even and odd harmonics. In comparison with VP, the number of their fixed work frequencies is two-fold higher.

In addition, at mechanical attenuation of these transducers, their AFR is much more uniform than VP AFR. Therefore, SAVP are more broadband transducers. These transducers are also of scientific interest. They, as well as surface active thick piezotransducers (SATP), transform a weakly diverging US beam into the drive force of inhomogeneous electric field.

SAVP have planar electrodes, located only on one transducer side (Fig. 10.8). SAVP are resonant transducers, which effectively radiate and receive US vibrations with an integer number of half-waves along the piezoplate thickness. Therefore, the piezoelement volume in SAVP participates in the creation of standing mechanical waves and in the formation of US radio pulses radiated and received. All piezotransducer volume is deformed in radiation and reception mode.

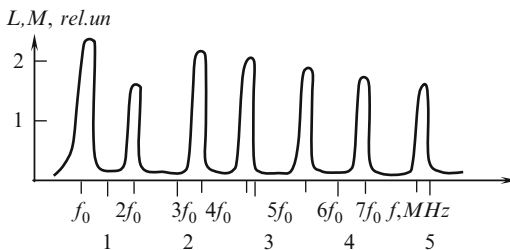
SAVP has a variety of interesting features due to its surface drive and resonant properties.

In Fig. 10.9, SAVP AFR is shown. It was experimentally obtained in radiation mode. An SAVP 3 mm thick, 30 mm in diameter, with 0.2 mm diametrical slit gap between electrodes was used as a US wave radiator. A US wave receiver, an SATP 23 mm thick and 30 mm in diameter with the same gap as in SAVP, was located in water at a distance of 30 mm from the radiator. The transducers were located with their gaps parallel to and in front of each other.

SAVP was activated by radio pulses with rectangular envelope (curve) and various filling frequency. SATP electrical signal was taken in a mode close to piezoelement short circuit. As can be seen from Fig. 10.9, SAVP radiates US waves at its fundamental (basic) frequency (0.7 MHz in this case) and at all even and odd harmonics (1.4, 2.1, 2.8, 3.5 MHz, etc.).



**Fig. 10.8** Surface active volume piezotransducer



**Fig. 10.9** SAVP AFR for radiation and reception modes:  $L$  and  $M$  – forward and inverse electromechanical transformation factors respectively





**Fig. 10.10** Transducer designs: (a) NPSAVP-1, (b) NPSAVP-2; polarization directions are shown by arrows, depolarization zone is marked by the cross

The result received in reception mode practically coincided with SAVP AFR in radiation mode.

In Fig. 10.10, designs of non-uniformly polarized surface active volume piezotransducers (NPSAVP) of two types – NPSAVP-1 and NPSAVP-2 – are shown. NPSAVP-1 is polarized only under one electrode (Fig. 10.10a), NPSAVP-2 is polarized under different electrodes in opposite directions (Fig. 10.10b). It is easier to make these piezotransducers by gluing together homogeneously polarized and depolarized piezoelements. The influence of the glue (epoxy resin) layer on acoustic and electric fields, arising in transducers, is practically absent. This fact was also established for non-uniformly polarized surface active thick piezotransducers (NPSATP), by comparing SAVP characteristics of two glued-together parts with SAVP, made on a monolithic piezoelement (See also Chap. 3).

VP AFR, having peaks at fundamental (basic) intrinsic transducer frequency ( $f_0 = 0.7$  MHz) and at odd harmonics [8] as expected, is represented in Fig. 10.11a.

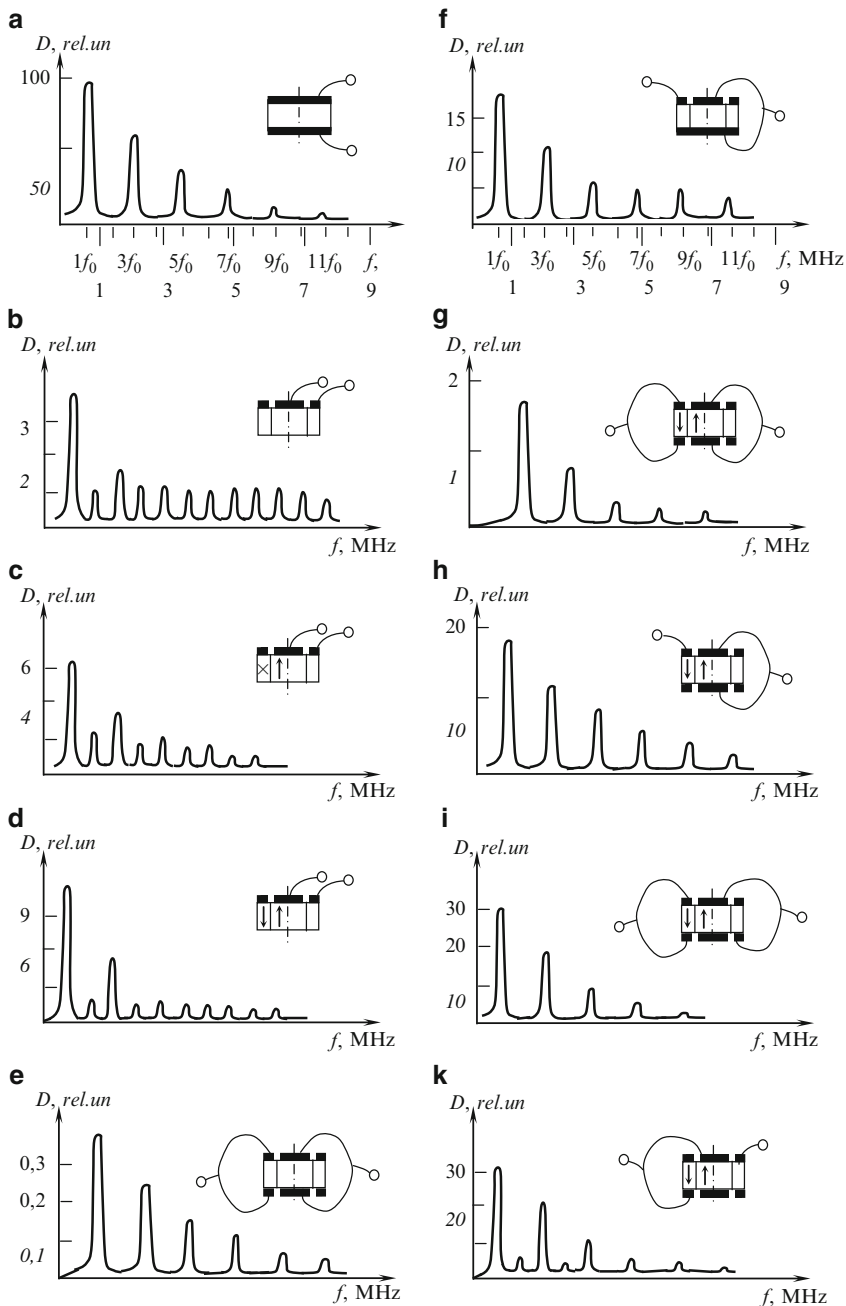
SAVP, NPSAVP-1 and NPSAVP-2 AFR are represented in Fig. 10.11b–d.

As can be seen from the figures, these transducers work not only at odd, but also at even harmonics, as the source, generating longitudinal US waves in the transducers, is located only on one surface. NPSAVP-2 assures the maximum amplitude of signals radiated and received (Fig. 10.11d), as US wave in-phase summation, arising under different electrodes, occurs in it.

SAVP and NPSAVP-2 AFR with an electrode connection in which transducers are symmetrically activated from both bases are represented in Fig. 10.11e,g. Thus, mechanical vibration sources generate in-phase US longitudinal waves on both bases. As a result of the composition of these waves, their cancellation occurs in the transducer volume if an odd number of half-waves can be located along the piezoplate thickness. Their reciprocal gain occurs if an even number of half-waves is located along the plate thickness. Therefore, transducers AFR, represented in Fig. 10.11e,g, have resonant peaks only at even harmonics. We should emphasize, that the situation with VP is different (Fig. 10.11a). As was expected, the signals amplitude in NPSAVP-2 (Fig. 10.11g) is considerably bigger than in SAVP (Fig. 10.11e).

SAVP AFR with complex electrode connection is shown in Fig. 10.11f. This transducer runs only at odd harmonics, and assures (Fig. 10.11b–e) a sufficiently high signal amplitude [8] in comparison with the others.

NPSAVP-2 AFR with various complex electrode connections are represented in Fig. 10.11h–k. As follows from their analysis, all these transducers work at odd harmonics and assure high signal amplitude.



**Fig. 10.11** Designs and AFR of various transducer types: (a) usual resonant piezotransducer, (b) SAVP, (c) NPSAVP-1, (d) NPSAVP-2, (e), (f) SAVP with complicated electrode connection, (g–k) NPSAVP-2 with complicated electrode connection

### 10.3 Non-resonant Excitation of Piezoelements

Two basic conditions under which creation of longitudinal US waves in a broadband aperiodic piezotransducer occurs are formulated in work [8]. First, there should be only one cut in the piezoelement volume (in that specific case, it can coincide with its surface). Driven electric field density or piezoactivity level ( $d_{33}$ ) or both simultaneously experience a sharp step in this cut. Secondly, the piezoelement should have only those forms or dimensions which eliminate the occurrence of standing waves generated in the cut or work surface (see Chaps. 3, 5 and also [30]).

These two principles assure transducer broadbandness and aperiodicity in radiation and reception modes.

In addition to these two principles, there exists one more principle (the third and the last) which should be considered in reception mode. Only output electric current (but not voltage) impulses, measured from the piezotransducer in reception mode, repeat the form and duration of acoustic pressure impulses, influencing the transducer. Therefore, a current amplifier with small (units in ohm) input resistance should be used in conjunction with a broadband piezoreceiver. This amplifier practically assures transducer short circuit mode at US impulse reception. As a result, current impulses of the transducer are measured. These impulses have the same form as the acoustic signals received, while the voltage pulses are calculated by the time integral from US pressure impulses [8].

When the piezoelement is in radiation and reception modes, electromechanical transformation occurs mainly in the thin piezostance layer. The piezoelement volume in this case is mainly passive, and is only a wave guide – the environment of US wave propagation.

Non-uniformly polarized thick piezotransducers (NTP) are referred to as the first type of broadband aperiodic US wave transducers [8]. They differ from usual thick piezotransducers (TP) by polarization degree which smoothly decreases in volume from the maximum value at the front surface (radiating into useful acoustic load) to zero at the opposite (back) surface.

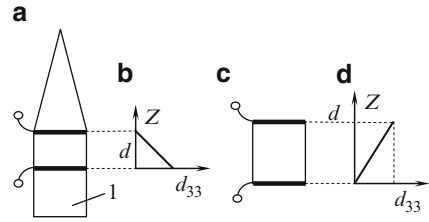
Electromechanical transformation occurs in them mainly on one piezoelement surface.

Non-uniform polarization in NTP is reached by partial depolarization of standard uniformly polarized piezoelements as a result of short-term heating of a part of their volume to a temperature exceeding the top piezoceramic Curie point (Patent of USSR 381021).

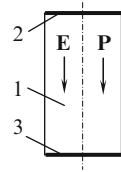
In US control practice, NTP with solid (-state) US delay line 1 (Fig. 10.12a) between the front piezoelement surface and the environment (the device controlled) in which it radiates US waves is of interest.

The NTP design shown in Fig. 10.12a is much more complex than the one represented in Fig. 10.12c. However, the second design, where the role of US delay line is performed by the polarized piezoelement body as shown in Fig. 10.12d, is practically suitable only when a small (1–2  $\mu$ s) delay time is required.

**Fig. 10.12** Various types of NTP: (a) with ultrasonic delay line, (b) graph of polarization degree change, (c) NTP, in which the piezoelement body serves as ultrasonic delay line, (d) graph of polarization degree change in the piezoelement



**Fig. 10.13** Thick piezotransducers



Piezoelectric transducers in which the piezoelement is activated by a non-uniform electric field (Patent No. 539265, 590662, 595880, 658408, 658469), created, for example, by coplanar electrodes located on one of its surfaces while its piezoelectric properties experience a break, represent the second type of broadband aperiodic US transducers.

This method of US wave activation was offered by S.Ya. Sokolov and G.E. Grachev for the first time in 1948. It was used for generation of hypersound in piezoelectric quartz samples and for creation of a monolithic solid (-state) US delay line. In this type of thick piezotransducer, the described US waves in radiation mode are mainly created on one surface. Electrical charges of maximal value are also measured from the same surface by means of the electrodes located on it. These charges are generated on this surface in US wave reception mode. This type of transducer is named [8] a surface active thick piezotransducer (SATP).

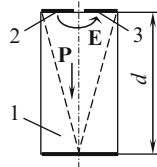
We will study SATP work in comparison with usual TP work of the same dimensions. If TP (Fig. 10.13) is activated by a short electric impulse on electrodes 2, 3, then short US pulses will arise at each of its surfaces. They will propagate in the volume between TP bases, alternately reflecting from them and gradually fading along the amplitude.

If the bottom electrode, for example, is removed from the transducer while the head electrode is split into two parts as is shown in Fig. 10.14, and an identical short electric impulse is supplied to the new pair of electrodes, located on a piezoelement surface, then, as expected, odd impulses will disappear and even pulses will remain, i.e., those pulses which appeared on the head piezotransducer base. This base is represented as an elementary SATP variant.

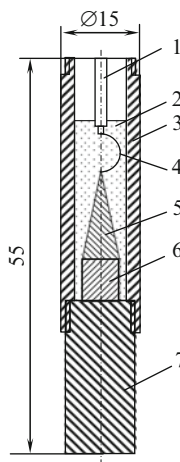
When the head (Fig. 10.14) SATP base borders with air, and the bottom with the device controlled, the piezoelement body 1 is nothing but a US delay line between “infinitely thin” piezotransducers and the device.

Several designs of the non-uniformly-polarized thick transducers are shown in Figs. 10.15–10.17.

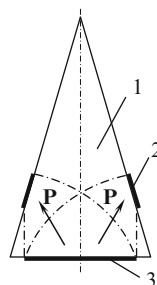
**Fig. 10.14** Surface active piezotransducer



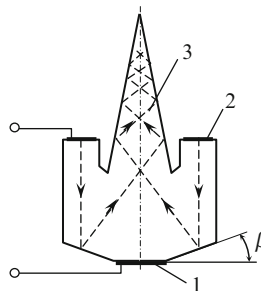
**Fig. 10.15** NTP contact variant: 1 – contact nest, 2 – resin  $\varnothing$ Л-5, 3 – housing (case), 4 – conductor; 5 – acoustic trap, 6 – piezoelement, 7 – US delay line



**Fig. 10.16** Design of monolithic NTP



**Fig. 10.17** Monolithic broadband piezotransducers without depolarization



A schematic image of a NTP variant, explaining its operating principle, is given in Fig. 10.16. NTP is a piezoceramic monolithic cone-shaped block (1). Bottom electrode 3 is located on its radiating surface. Ring electrode 2 is located on its lateral surface. The piezoelement is polarized as usual, by application of constant voltage on electrodes 2, 3. Then the part of the piezoelement, directly adjacent to electrode 2, is depolarized to make the polarization degree decrease evenly from the maximum at electrode 3 to zero at electrode 2.

US waves appear only at electrode 3 when a voltage impulse is supplied to the electrodes as the piezoelement areas adjacent to electrode 2 are depolarized. As a result, the transducer responds to each arising electric impulse by a single acoustic impulse. Some types of these transducers are described in USSR Patents No. 539265, 590662, and 595880.

One more variant of a monolithic piezotransducer, advantageously different from the previous by the absence of depolarization sites, is shown in Fig. 10.17. The design of this transducer is represented by a piezoceramic monolithic block. There is a cone-shaped acoustic trap in front of silver electrode 1, located on its front surface (radiating to useful load). The second electrode 2 is located on the back surface (not radiating to useful load).

Longitudinal US waves arise along electrodes 1 and 2 if the transducer is activated. A part of the US wave energy arising at electrode 1 goes to the transducer useful acoustic load (down in Fig. 10.17). The other part propagates into the piezoelement and enters the acoustic trap 3, where it fades. US waves arising at electrode 2 propagate into the transducer and, having reflected from the slant edge around electrode 1, also enter the acoustic trap, not reaching the front piezoelement surface.

Such types of thick piezotransducers as NTP have been analyzed above. They are non-uniformly polarized along the piezoelement volume. They are activated by a homogeneous electric field, concentrated only on one transducer surface. Non-uniformly polarized surface active thick piezotransducers (NPSATP) are further analyzed. They are non-uniformly polarized along the volume. These piezotransducers are activated by a non-uniform electric field, concentrated at a surface.

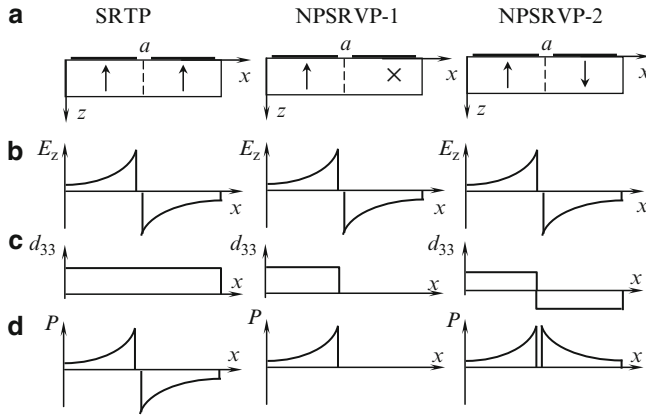
The designs of SATP and two types of NPSAVP are schematically shown in Fig. 10.18: NPSAVP-1 is polarized only under one electrode, NPSAVP-2 is polarized under different electrodes in opposite directions.

For better understanding of NPSAVP work, the following features are shown in Fig. 10.18b–d: distributions of driving electric field density constituent  $E_z$  along axis  $z$ , perpendicular to electrodes and piezomodule  $d_{33}$  of acoustic pressure  $P$ , generated by the transducer on the surface with electrodes ( $z = 0$ ).

The elementary designs of NPSAVP shown in Fig. 10.18 can be made either by non-uniform polarization of piezoelements, or by gluing homogeneously polarized (or depolarized) piezoelements together [8].

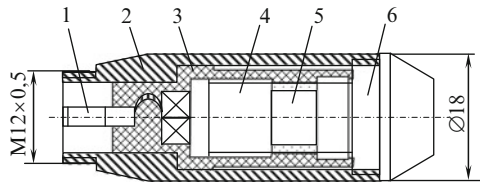
Two more transducer designs are shown in Figs. 10.19 and 10.20 [8].

Now Ukrainian industry commonly produces two variants of broadband thick piezotransducers. They are direct combined contact NTP (Fig. 10.19) and direct combined contact–immersion SATP (Fig. 10.20). Serial echo pulse US thickness gauges YT-30K, YT-30ΠII and YT-31MII [11] are batched with these piezotransducers.

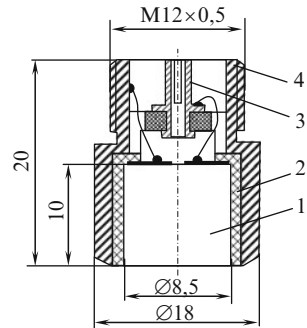


**Fig. 10.18** SATP and NPSAVP features: (a) schematic designs of SATP and NPSAVP, (b-d) distribution curves of  $E_z$ ,  $d_{33}$ , and  $P$  in each design

**Fig. 10.19** Design of direct combined contact NTP variant: 1 – connector, 2 – case, 3 – plug, 4 – bar, 5 – piezoelement, 6 – US delay line



**Fig. 10.20** Design of direct combined contact-immersion NTP variant NTP: 1 – piezoelement, 2 – textolite plug, 3 – connector, 4 – case



## References

1. I.N. Ermolov, *Theory and Practice of Ultrasonic Control* (Mashinostroenie, Moscow, 1981), p. 240 (in Russian)
2. M.V. Korolev et al., *Ultrasonic Pulse Devices of Materials for Durability Control* (Mashinostroenie, Moscow, 1987), p. 112 (in Russian)

3. A.H. Vopilkin, I.N. Ermolov, V.G. Staseev, *Spectral Ultrasonic Methods of Defect Type Detection* (Mashinostroenie, Moscow, 1979), p. 60 (in Russian)
4. A.K. Gurvich, I.N. Ermolov, *The Ultrasonic Control of Weld Seams* (Technics, Kiev, 1972), p. 460 (in Russian)
5. A.H. Vopilkin, I.N. Ermolov, V.I. Ivanov et al., Theoretical study of broadband transducers. *Defectoscopy* **2**, 7–13 (1977) (in Russian)
6. I.N. Ermolov (ed.), *Ultrasonic Piezotransducers of Non-destructive Control* (Mashinostroenie, Moscow, 1986), p. 280 (in Russian)
7. S.A. Filimonov, I.N. Ermolov, On the theory of a resonant control method. *Defectoscopy* **5**, 9–16 (1970); **1**, 19–28 (1971) (in Russian)
8. M.V. Korolev, A.E. Karpelson, *Broadband Ultrasonic Piezotransducers* (Mashinostroenie, Moscow, 1982), p. 160 (in Russian)
9. M.V. Korolev, Surface active piezoelectric transducers. *Defectoscopy* **9**, 13–19 (1978) (in Russian)
10. M.V. Korolev, V.G. Shevaldykin, A.E. Karpelson, Ultrasonic fields of surface active thick transducers. *Defectoscopy* **5**, 80–87 (1979) (in Russian)
11. M.V. Korolev, *Echo-Pulse Ultrasonic Thickness Gauges* (Mashinostroenie, Moscow, 1980), p. 112 (in Russian)
12. V.M. Bobrenko, A.N. Kutsenko, A.S. Sheremetikov, Acoustic tensometry. *Flaw Detection* **3**, 70–87 (1980) (in Russian)
13. U. Mason (ed.), *Physical Acoustics. Methods and Devices of Ultrasonic Research* (Mir, Moscow, 1966), p. 592 (in Russian)
14. I.A. Viktorov, *Ultrasonic Surface Waves in Solids* (Nauka, Moscow, 1981), p. 288 (in Russian)
15. B.I. Vybornov, *Ultrasonic Defectoscopy* (Metallurgy, Moscow, 1974), p. 240 (in Russian)
16. V.V. Klyuev (ed.), *Devices for Non-destructive Control of Materials and Devices. Directory* (Mashinostroenie, Moscow, 1986), p. 352 (in Russian)
17. P.I. Beda (ed.), *Detailed Defectoscopy in Aeronautical Engineering* (Voenizdat, Moscow, 1978), p. 231 (in Russian)
18. N.A. Evdokimov, B.A. Kasatkin, A.F. Melkanovich, Optimum modes in ultrasonic defec-toscopy. *Defectoscopy* **1**, 5–10 (1972) (in Russian)
19. B.A. Kasatkin, I.Ya. Pavin, On a method of piezotransducer work frequency reorganization. *Defectoscopy* **1**, 17–21 (1980) (in Russian)
20. N.A. Evdokimov, A.F. Melkanovich, A.A. Pranitskiy, Operation of piezovibrators with bilateral load in pulse mode. *Defectoscopy* **2**, 91–99 (1969) (in Russian)
21. V.I. Zaklyukovskiy, G.T. Kartsev, Piezoelectric transducer use for contactless ultrasonic control of devices. *Defectoscopy* **3**, 28–34 (1978) (in Russian)
22. Yu.V. Lange, *Acoustic Low-Frequency Methods of Non-destructive Multilayered Designs* (Mashinostroenie, Moscow, 1991) (in Russian)
23. N.P. Aleshin (ed.), *Methods of Metal Acoustic Control* (Mashinostroenie, Moscow, 1989), p. 456 (in Russian)
24. S.P. Perevalov, A.Z. Raihman, Ultrasound reflection from welded connection irregularity. *Defectoscopy* **4**, 7–15 (1978) (in Russian)
25. V.E. Polyakov, A.I. Potapov, A.K. Sborovskiy, *Ultrasonic Control of Design Quality* (Sudostroenie, Leningrad, 1978), p. 238 (in Russian)
26. M.V. Rozina, Some features of revolution body ultrasonic control. *Defectoscopy* **4**, 16–21 (1966) (in Russian)
27. S.A. Filimonov, B.A. Budenko, I.A. Gluhov, Ultrasonic resonant contactless control method. *Defectoscopy* **1**, 129–132 (1971) (in Russian)
28. Yu.M. Shkarlet, *Contactless Methods of Ultrasonic Control* (Mashinostroenie, Moscow, 1974), p. 56 (in Russian)
29. D.S. Shrayber, *Ultrasonic Defectoscopy* (Metallurgiya, Moscow, 1965), p. 392 (in Russian)
30. V.M. Sharapov, M.P. Musienko, E.V. Sharapova, *Piezoelectric Sensors*, ed. by V.M. Sharapov (Technosphaera, Moscow, 2006), p. 632 (in Russian)



# Chapter 11

## Sensors of Korotkoff Sounds

### 11.1 General Information

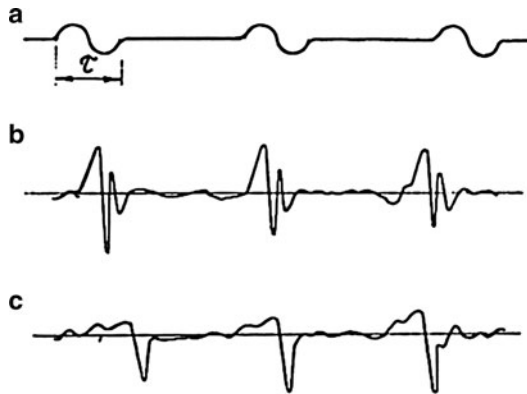
Korotkoff sound sensors (KSS) are used for arterial blood pressure (AP) measurement following Korotkoff's method [29].

The method consists of acoustic signal correlation: Korotkoff sounds, arising in a patient's tissues when the artery is squeezed by the cuff, with the corresponding value of pneumatic pressure in this cuff. The moments of Korotkoff sound occurrence and termination characterize upper (systolic) and lower (diastolic) arterial pressure (AP) respectively. The method has a number of methods of technical implementation. The elementary implementation consists of sound registration by a mechanical phonendoscope. Important drawbacks of this implementation are low phonendoscope sensitivity, and also the fact that the pulse signals spectrum lies in a low-frequency area in which the human ear has minimum sensitivity.

A typical signal oscillogram, received by a piezoelectric sensor when AP was measured, is shown in Fig. 11.1. As can be seen from Fig. 11.1, pulse signals and Korotkoff sounds (KS) differ in form, amplitude, spectral composition and dynamic characteristics. Pulse signals are almost sine pulses with approximately 0.1–0.15 s period and 1–2 Hz repetition frequency. The occurrence of the first Korotkoff sound in systolic AP area leads to an almost doubling of the pulse rate (Fig. 11.1b).

On the basis of the research conducted by a cardiological centre and a research and test institute of medical engineering and a considerable amount of statistical material, it is considered that values in 3–10 Hz range correspond to the pulse spectrum and the values in 20–500 Hz range to Korotkoff sounds. As a result of this, the frequency characteristic of a serially produced measuring AP device of type ИАД-1, for example, has 12 dB raise in 20–80 Hz range and 7 dB drop in 80–500 Hz range.

As also follows from Fig. 11.1, to improve the accuracy of AP measurement, Korotkoff sounds should be selected, according to amplitude, frequency and dynamic characteristics, based on signal rise speed or acceleration.



**Fig. 11.1** Oscillograms of sensor signal when AP is measured: (a) pulse signals, (b) systolic AP area, (c) diastolic AP area

As the research showed [29], when KS occur, the following factors can influence the sensor, located under the cuff on the patient's forearm (and also the pulse sensor, located in other places on the patient's body):

- Acoustic signal (Korotkoff sounds)
- Dynamic pressure caused by pressure oscillations in the cuff or caused by heart beat and muscle contraction
- Linear or vibration accelerations

Thus, pulse and KS sensors can be represented as acoustic transducers (contact microphones), dynamic pressure (force) transducers and accelerometers.

It is necessary to note that an acoustic signal, a dynamic force and acceleration usually influence any sensor simultaneously. As the experiments showed, the contribution of each to the general signal can be evaluated as 90.0; 9.0 and 1.0% respectively [29].

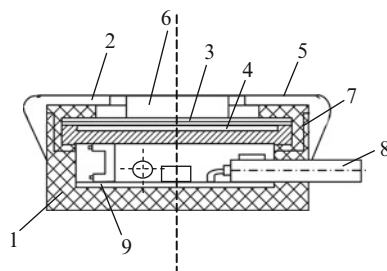
We should also mention that, according to the definition, only acoustic transducers can be called KSS. However, all the transducers used to measure AP by the Korotkoff method are called KSS. At the same time, transducers, receiving force action, when the pulse wave passes, are often called pulse waves sensors (PWS).

A number of KS and pulse wave sensors designs are considered below.

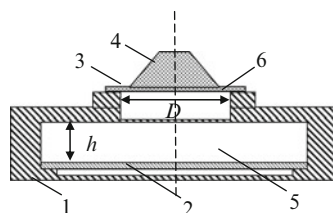
A KS sensor is described in American patent [19]. This consists of a housing (case), a cover with the central aperture, a piezoceramic element, located in the housing (case) parallel to the cover, and a pellet, fastened in the centre of the piezoceramic element.

The sensor described in [1], unlike the previous sensor, has a membrane 5 (Fig. 11.2). As the authors state, this membrane is used for suppression of acoustic hindrance coming from the cuff. However, as the research showed [29], this membrane is unnecessary. Moreover, this membrane decreases sensitivity by three to five times.

**Fig. 11.2** Design of KSS sensors: 1 – housing (case), 2 – cover with the central aperture, 3, 4–piezoceramic bimorph element, 5 – membrane, 6 – pelot, 7 – membrane, 8 – cable, 9 – preamp board



**Fig. 11.3** Pulse sensor: 1 – housing (case), 2 – piezoelement, 3 – membrane, 4 – pelot, 5, 6 – internal cavities



The sensor, using its resonant properties for KS selection, is described in [2]. The sensor consists of a housing (case) and three bimorph piezoplates, supported in the insulator as a cantilever. The piezoplates are of a different length. They are anti-parallel coupled. This sensor of complex design is not reliable [29].

Modification of the sensor, using resonant properties of bimorph piezoplates, is described in [3]. This KSS is also rather complex.

Piezoelectric pulse sensors are described in [4–7]. Their distinctive feature is the pelot, rigidly fastened on the membrane. The piezoelement is located in the housing (case) some distance from the membrane.

The sensor represented in Fig. 11.3 [4] consists of housing (case) 1, piezoelement 2, membrane 3 and pelot 4. For this increase in sensor sensitivity, height  $h$  of cavity 5 is selected from the correlation:

$$0.03D < h < 0.42D,$$

where  $D$  is the diameter of cavity 6.

A KS piezotransducer (sensor), based on modified USA Patent No. 3573394 (USSR Patent No. 651786) was produced industrially (Fig. 11.2) [8, 20].

As the serial production experience showed, the sensor had a number of drawbacks. AP meter reclamations reached 10.7%. Approximately 300,000 of device meters were produced annually at three enterprises.

They had the following drawbacks:

1. Comparatively low sensitivity (approximately 2.92 mV/Pa)
2. Temporary sensitivity instability (up to 50% for 6 months of storing)

3. Varying sensitivity level of each serially produced item
4. Dependence of sensor sensitivity on location on a patient's forearm
5. Low sensor reliability as a result of low mechanical durability of symmetric bimorph piezoelement and low electrical durability under the static electricity influence
6. Sensitivity to in-phase and vibration hindrances

An acoustic camera was used in the experiments. This acoustic camera created sound pressure up to 120 dB in 20–200 Hz frequency range (this is KSS work range). This range was expanded later.

A test bed scheme is shown in Fig. 11.4. Sensor characteristics were measured under pressure of 10 Pa in the 20–200 Hz frequency range.

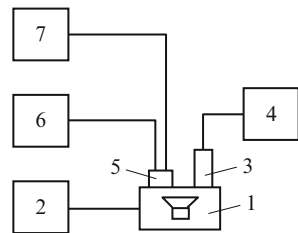
The sensor electric scheme is represented in Fig. 11.5. This consists of an amplifier based on chip field-effect transistor KP201E-1. The measurements of 10,000 sensors showed that, as a result of spread of transistor parameters, distribution of the coefficient of amplifier gain is close to normal law. Average value 5.3 is minimal and maximal for the given sample 2.7 and 7.6 respectively.

The following transformation coefficient was measured for 1,000 randomly sampled sensors, produced according to USSR sensor patent No. 651786 [8]:

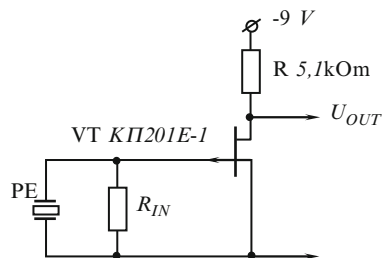
$$K_{TR} = U_{OUT} / P_{SOUND}$$

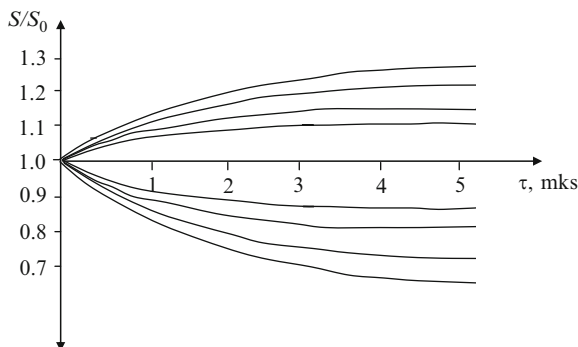
the level of sound pressure was 10 Pa and the frequency was 40 Hz. Average value of  $K_{TR} = 3.7$ , mV/Pa (specifications of 3–15 mV/Pa were required), average-quadratic value  $\sigma = 1.1$  mV/Pa. Minimum and maximum  $K_{TR}$  values for the given sample are 2.2 and 5.4 respectively. The number of sensors from the sample  $K_{TR}$  which did

**Fig. 11.4** Test set of KSS:  
 1 – acoustic chamber,  
 2 – generator G3-109,  
 3 – microphone, 4 – noise meter ИИИВ-1, 5 – KS sensor, 6 – power supply, 7 – millivoltmeter B3-38



**Fig. 11.5** Electric scheme of KSS-1 sensor





**Fig. 11.6** Dependence of transformation coefficient relative sensitivity on storage time of ten sensors KSS-1M (random sample)

not meet the specifications requirements (less than 3.0 mV/Pa) was 172 items; this is 17.2% of the sample volume.

Ten sensors were randomly selected from the batch and were aged naturally (within 6 months).

The dependence of relative transformation coefficient  $K/K_0$  (where  $K_0$  is the transformation coefficient before the ageing began) on ageing time is shown in Fig. 11.6. As can be seen from Fig. 11.6, the transformation coefficient change for some sensors reaches 50%.

## 11.2 Enhancement of KSS Sensitivity

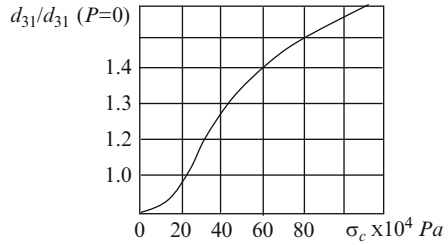
It has been experimentally established that piezomodule  $d_{31}$  increases under the influence of stress  $\sigma_c$ , perpendicular to the polar axis. The piezomodule change is connected to reorientation of domains in piezoceramics under the influence of mechanical stress [18].

Let one-dimensional compression stress  $\sigma_3$  influence the ceramics, directed across axis  $OZ$ . This coincides with the direction of remanent polarization.

The components of tensor stress will look like this:

$$\begin{aligned}
 \sigma_{31} &= \sigma_{31} \cos^2 v; \\
 \sigma_{11} &= \sigma_{31} \sin^2 v \sin^2 \varphi; \\
 \sigma_{22} &= \sigma_{31} \sin^2 v \cos^2 \varphi; \\
 \sigma_{12} &= \sigma_{31} \sin^2 v \sin \varphi \cos \varphi; \\
 \sigma_{13} &= \sigma_{31} \cos v \sin v \sin \varphi; \\
 \sigma_{23} &= \sigma_{31} \sin v \cos v \cos \varphi;
 \end{aligned} \tag{11.1}$$

**Fig. 11.7** Piezomodule  $d_{31}$  change dependence under the influence of mechanical stress  $\sigma_c$



where  $\nu$ ,  $\varphi$  are the angles formed by the corresponding axes of coordinates after the domain rotation to the initial condition.

If polarized ceramics is compressed across axis  $Z$  its polarization increases in  $\Delta P_r$  at the expense of reorientation of domain polar axes. The value of polarization change  $\Delta P$  can be calculated, integrating the expression:

$$\Delta P = \frac{P}{4\pi' \rho_0} \iint \cos \nu \sin \nu \rho(\nu, \varphi) d\nu d\varphi. \quad (11.2)$$

After the elementary transformations we obtain:

$$\Delta P = \frac{4P}{\pi} \left[ \frac{\pi}{12} \left( 1 - \frac{\sigma_c}{\sigma'_c} \right) + \frac{1}{2} \left( 1 - \frac{\sigma_c}{\sigma'_c} \right) \left( \frac{\arcsin Z}{1 + Z^2} - \frac{1}{\sqrt{2}} \arctg \sqrt{2} \frac{Z}{\sqrt{1 - Z^2}} \right) \right], \quad (11.3)$$

where

$$Z^2 = \frac{\cos^2 \nu - \frac{\sigma_c}{\sigma'_c}}{\sin^2 \nu};$$

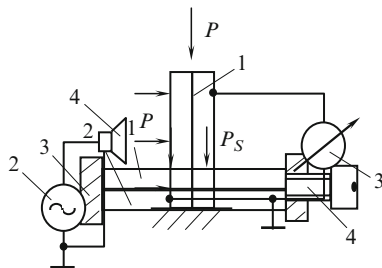
$\sigma_c$  – value of external one-dimensional mechanical stress;  $\sigma'_c$  – critical mechanical stress when  $90^\circ$  rotation of domain polar axis.

The experimental dependence of piezomodule  $d_{31}$  on stress  $\sigma_c$  is shown in Fig. 11.7. It follows from the figure that the bimorph piezoelement sensitivity can be controlled.

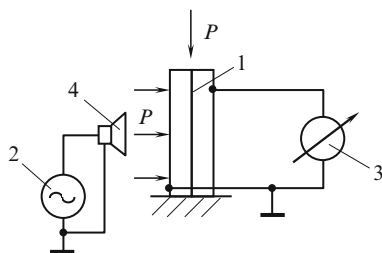
A variant of the sensor design, implementing this idea in real life, is shown in Fig. 11.8 [29]. Using screw 4, it is possible to control the piezosensor sensitivity in a wide range (two to five times). It is necessary to note, that the KS sensor being considered (Fig. 11.8) (a sound pressure sensor) can easily be transformed into a static pressure sensor (Fig. 11.9) [29]. The sensor is activated by harmonious sound pressure  $P_S$  from loudspeaker 4. Output voltage is measured by millivoltmeter 3.

It is also necessary to note that unlike resonant transducers of piezotransformers type (see Chap. 14) these sensors can be activated at any frequency, not only resonant. In addition, the possibility of acoustic activation of a bimorph element can be used when access to the sensor is hindered.

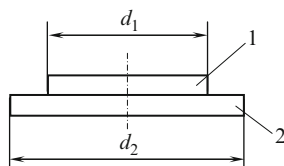
**Fig. 11.8** KS sensor:  
 1, 2 – piezoelements, 3 – ring,  
 4 – screw



**Fig. 11.9** Sensor of static force:  
 1 – bimorph element,  
 2 – generator, 3 – measuring device,  
 4 – loudspeaker



**Fig. 11.10** Design of asymmetric bimorph element:  
 1, 2 – piezoelements



Asymmetric bimorph elements are studied in the work by Rudnitskiy et al. [25] (see Chap. 6). It has been shown that if piezoelement and metal plate dimensions are optimally chosen, maximum sensitivity can be reached.

Similar results can be reached for a bimorph element consisting of two piezoelements. Their diameters, unlike the diameters in traditional design, are not equal to each other (Fig. 11.10). We should comment on the terms “symmetric” and “asymmetric” bimorph elements here.

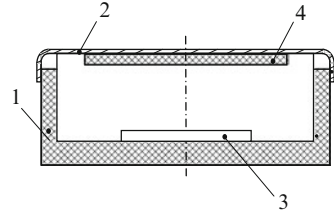
Known “symmetric” bimorph elements consist of two piezoelements of identical dimensions and form. They are also made of the same material. Thus, these bimorph elements have a full geometrical and material symmetry.

The bimorph element shown in Fig. 11.10 has axial symmetry, but is asymmetrical relative to the neutral plane. In addition, if piezoelements are made of the same piezomaterial, we can talk about “symmetry” of piezoelement material piezocharacteristics.

As the experiments showed, if piezoelements are of the same thickness (0.3 mm) the sensitivity for the transducer represented in Fig. 11.10 increases. The minimal sensitivity is reached if piezoelement diameters are correlated  $d_1/d_2 = 1.0$ .

It has already been mentioned that asymmetric bimorph elements are more mechanically durable than bimorph elements consisting of two piezoelements. It is

**Fig. 11.11** KS sensor with asymmetric bimorph piezoelement: 1 – housing (case), 2 – cover, 3 – coupling amplifier plate, 4 – piezoelement



natural that, as a result of this advantage, the transducer sensitivity decreases almost twice in comparison with the symmetric bimorph element.

Optimal sensitivity can be reached by reasonable suitable choice of metal plate, piezoelement materials and their dimensions [25].

Considering the above-mentioned ideas, the use of asymmetric bimorph elements in KSS designs seems natural [21].

The elimination of a so-called pelot from the sensor design seems logical (see Fig. 11.2). This term is introduced in the description of Patent No. 651786 [8] and in the US Patent No. 3573394 [20]. Its meaning is not explained [8,20]. In addition, an asymmetric bimorph element should contact a patient's forearm directly.

The design of this sensor is shown in Fig. 11.11 [21].

For calculation of this sensor transfer function it is necessary to realize that incident and reflected pressure waves  $P_{\text{INC}}$  and  $P_{\text{REF}}$  influence the transitive layer surface (metal membrane), contacting with the work environment (a patient's body). Full pressure  $P_{\text{P}}$  on the layer surface is:

$$P_{\text{F}} = P_{\text{FAL}} + P_{\text{REF}}. \quad (11.4)$$

On the other hand:

$$\frac{P_{\text{REF}}}{P_{\text{FAL}}} = \frac{Z_{\text{IN}} - Z_2}{Z_{\text{IN}} + Z_2}, \quad (11.5)$$

where  $Z_{\text{IN}}$  is input specific acoustic impedance.

The following is obtained from (11.4) and (11.5):

$$P_{\text{F}} = P_{\text{FAL}} \frac{2Z_{\text{IN}}}{Z_{\text{IN}} + Z_2}.$$

As the force operating on the metal membrane surface, is determined by expression:

$$F_{\text{F}} = A_0 P_{\text{F}} = A_0 P_{\text{FAL}} \frac{2Z_{\text{IN}}}{Z_{\text{IN}} + Z_2} = A_{22} U, \quad (11.6)$$

where:  $A_{22}$  – coefficient of a system matrix sensor – electric circuit;  $U$  – voltage on the electric circuit output.

$$P_{\text{FAL}} = \frac{2Z_{\text{IN}} + Z_2}{2Z_{\text{IN}} A_0} A_{22} U. \quad (11.7)$$



From quadrupole equations:

$$Z_{\text{IN}} = \frac{1}{A_0} \frac{A_{22}}{A_{21}}. \quad (11.8)$$

Substituting (11.7) in (11.8), we obtain an expression for the sensor transfer function:

$$K_{\text{TR}} = \frac{U}{P_{\text{FAL}}} = \frac{2}{(A_{22}/A_0) + Z_2 A_{21}}. \quad (11.9)$$

To determine  $A_{21}$  and  $A_{22}$  a matrix of coefficients of sensor with electric circuit should be equated; the matrixes should be multiplied. After the transformations and substitution of the coefficients obtained for (11.9) we have the following [17]:

$$K_{\text{TR}}(x) = K_{\text{TR0}} \Phi_{\text{II}}(x) e^{j\varphi_{\text{TR}}(x)}, \quad (11.10)$$

where

$$K_{\text{TR}} = \frac{4e}{\omega_0^\varepsilon Z_2} e^{-j\frac{\pi}{2}}.$$

Value  $K_{\text{TR}}$  is the maximum transfer coefficient of mechanically undamped sensor with electrical idle at resonant frequency  $f_0$ . Transfer function normalization occurs relative to this coefficient.

The reduced transfer function of the sensor does not consider absorption in transitive layers (membrane, glue layer). For absorption, normalized transfer function of the sensor with one transitive layer (metal membrane) will look like [17]:

$$\Phi_{\text{TR}}(X) = \frac{1}{2\sqrt{a_1 sh 2\alpha_3 l_3 + b_1 ch 2\alpha_3 l_3 + c_1 \cos 2m_3 l_3 + d_1 \sin 2m_3 l_3}}; \quad (11.11)$$

$$\varphi_{\text{TR}}(X) = -\text{arctg} \frac{Y_1 + M_1 \text{tg} m_3 l_3 + (N_1 + X_1 \text{tg} m_3 l_3) t h \alpha_3 l_3}{X_1 - N_1 \text{tg} m_3 l_3 + (M_1 - Y_1 \text{tg} m_3 l_3) t h \alpha_3 l_3} + \frac{\pi}{2}; \quad (11.12)$$

where

$$a_1 = Y_1 N_1 + X_1 M_1,$$

$$b_1 = \frac{1}{2} (X_1^2 + Y_1^2 + N_1^2 + M_1^2),$$

$$c_1 = \frac{1}{2} (X_1^2 + Y_1^2 - N_1^2 - M_1^2),$$

$$d_1 = Y_1 M_1 - X_1 N_1,$$

$$X_1 = \frac{k_t^2}{\pi x} \left[ \left( a_{11} + \frac{a_{12}}{k_2} \right) u X_{\text{C0}} - \left( b_{11} + \frac{b_{12}}{k_2} \right) v X_{\text{C0}} \right] \\ + \left( b_{21} + \frac{b_{22}}{k_2} \right) (u X_{\text{C0}} - qx) + \left( a_{21} + \frac{a_{22}}{k_2} \right) \times (v X_{\text{C0}} + px);$$

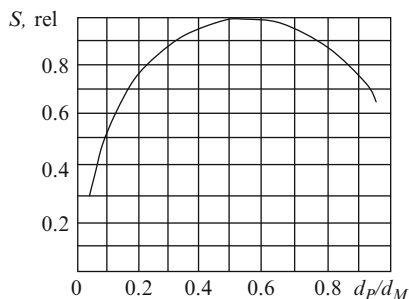
$$\begin{aligned}
 Y_1 &= \frac{k_t^2}{\pi x} \left[ \left( a_{11} + \frac{a_{12}}{k_2} \right) v X_{C0} + \left( b_{11} + \frac{b_{12}}{k_2} \right) u X_{C0} \right] \\
 &\quad + \left( b_{21} + \frac{b_{22}}{k_2} \right) (n X_{C0} + p x) - \left( a_{21} + \frac{a_{22}}{k_2} \right) \times (u X_{C0} - q x); \\
 M_1 &= \frac{k_t^2}{\pi x} \left[ \left( \frac{a_{11}}{k_4} + \frac{a_{12}}{k_3} \right) u X_{C0} - \left( \frac{b_{11}}{k_4} + \frac{b_{12}}{k_3} \right) v X_{C0} \right] \\
 &\quad + \left( \frac{b_{21}}{k_4} + \frac{b_{22}}{k_3} \right) (u X_{C0} - q x) + \left( \frac{a_{21}}{k_4} + \frac{a_{22}}{k_3} \right) (v X_{C0} + p x); \\
 N_1 &= \frac{k_t^2}{\pi x} \left[ \left( \frac{a_{11}}{k_4} + \frac{a_{12}}{k_3} \right) v X_{C0} + \left( \frac{b_{11}}{k_4} + \frac{b_{12}}{k_3} \right) u X_{C0} \right] \\
 &\quad + \left( \frac{b_{21}}{k_4} + \frac{b_{22}}{k_3} \right) (v X_{C0} + p x) - \left( \frac{a_{21}}{k_4} + \frac{a_{22}}{k_3} \right) (u X_{C0} - q x).
 \end{aligned}$$

Dependence of sensitivity on the piezoelement diameter–membrane diameter ratio  $d_p/d_M$  is shown in Fig. 11.12. As can be seen from Fig. 11.12 at  $d_p/d_M = 0.5$  sensitivity reaches the maximum.

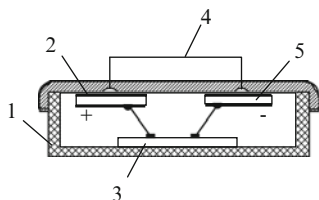
In the research discussed the membrane was made of semi-firm brass Л163.

The sensor sensitivity can be increased if piezoelement electrodes or the piezoelement itself are segmented, and the piezoelement parts are connected. The charge sign and phase arising in them should also be considered. In the simplest case the piezoelement can be divided into two parts and is glued to the cover by heteropolar electrodes (Fig. 11.13).

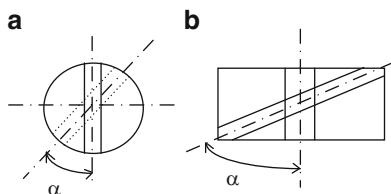
The same effect is reached if one piezoelement with separate electrodes is used (Fig. 11.14). The variants of these piezoelements connections are shown in



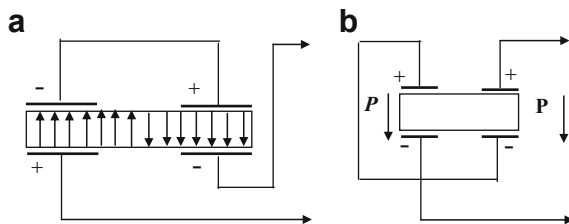
**Fig. 11.12** Dependence of relative sensitivity on  $d_p/d_M$  ratio



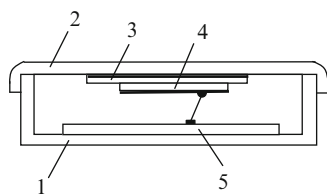
**Fig. 11.13** KSS with two piezoelements: 1 – housing (case), 2, 5 – piezoelements, 3 – amplifier plate, 4 – cover



**Fig. 11.14** Piezoelement electrode division: (a) disk piezoelement, (b) rectangular piezoelement



**Fig. 11.15** Connection schemes of piezoelement electrodes: (a) for piezoelement with two systems of electrodes and counter polarization, (b) for piezoelement with identical polarization direction



**Fig. 11.16** KSS with asymmetric coplanar threemorph piezoelement: 1 – housing (case), 2 – cover, 3 – basic piezoelement, 4 – additional piezoelement, 5 – amplifier plate

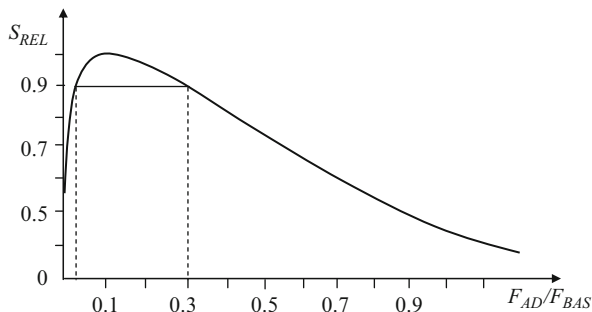
Fig. 11.15. A piezoelement oppositely polarized within each system of electrodes is shown in Fig. 11.15a. As is shown in Fig. 11.15b, piezoelement sections are connected between themselves by an additional conductor.

However, the following should be considered: if piezoelement parts are consecutively connected, their capacity decreases, while their internal (capacitive) resistance increases.

If piezoelement electrodes are divided so that when the division line on one piezoelement side makes angle  $\alpha$ , relative to the line on the other side (Fig. 11.14), then, depending on  $\alpha$  angle, the sensitivity can be in the  $0-2S_0$  range, where  $S_0$  is sensitivity of a sensor with one piezoelement [9].

KS sensor sensitivity can be further increased if additional piezoelements are used [26, 27].

A variant of this sensor design is shown in Fig. 11.16, and an electric scheme in Fig. 11.17.



**Fig. 11.17** Sensitivity dependence of sensor with additional coplanar piezoelement on  $F_{AD}/F_{BAS}$  correlation

In this case sensitivity increase is obvious; in the extreme case, the sensitivity is doubled. However, this sensitivity increase is possible only under certain conditions.

Maximum sensitivity can be reached if the neutral plane is located between the metal plate and the piezoelement. We should remember a well-known fact, that a neutral plane is a plane on one side of which the piezoelement is compressed in bending and is stretched from the other. In this case, piezoelements experience like-sign deformation and should be connected with unlike electrodes. Maximum sensitivity may be reached if the neutral plane is located between two piezoelements. In this case piezoelements should be connected by unipolar electrodes.

In all other cases sensitivity will be below maximum, as fastening one more piezoelement on the asymmetric bimorph element results in system hardening, sensitivity reduction and, consequently, resonant frequency increase.

Two competing processes – sensitivity increase if the second piezoelement is used and sensitivity reduction at hardening if the second piezoelement is fastened – should lead to the maximum sensitivity with precise correlation of piezoelement dimensions.

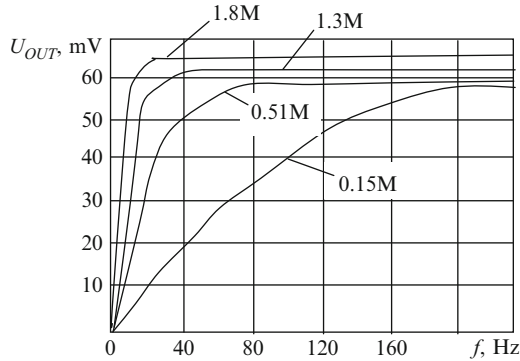
The maximum sensitivity  $S_{REL} = S/S_{MAX}$  is also reached (see Fig. 11.17) when additional piezoelement  $F_{AD}$  area and basic piezoelement area  $F_{BAS}$  are correlated in the following limits:

$$0.03 < \frac{F_{AD}}{F_{BAS}} < 0.3.$$

It is necessary to note that the neutral plane location depends not only on piezoelement and membrane dimensions, but also on the mechanical characteristics of the materials, they are made of (Young's modulus, Poisson coefficient).

### 11.3 On Optimum Load Resistance of KSS Piezoelements

Piezoelements of KS sensors are usually loaded on the amplifier with a very big input resistance. The bigger this resistance is, the lower the sensor lower work frequency. The last peculiarity is not technically necessary. It is more stereotypical



**Fig. 11.18** Amplitude–frequency characteristics of sensors for various values of amplifier input resistance

and traditional. In fact, the current produced by the piezoelement [28] is the signal proportional to the sound pressure (and consequently, to Korotkoff sounds). The charge and the voltage are integral to this current. Therefore, piezoelectric sensors of Korotkoff sounds should be loaded on the current amplifier. This allows defining the occurrence of Korotkoff sounds more accurately, i.e., raising the accuracy of AD measurement.

Even loading KS piezosensor on voltage amplifiers, it is unnecessary to get very high input resistance. The point of this comment is that the pulse signals spectrum differs essentially from Korotkoff sounds. Therefore, changing  $R_{IN}$  it is possible to improve the correlation of the KS signal/pulse signal, i.e., to measure the occurrence and the termination of KS more accurately. As a result, AD measurement accuracy is increased [28].

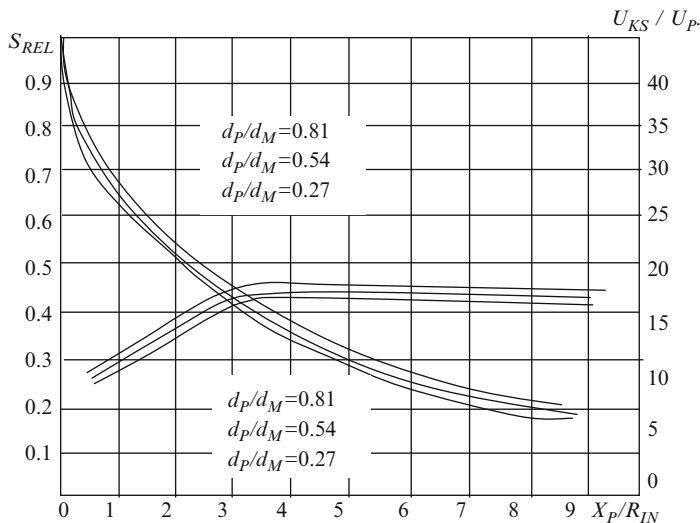
Amplitude–frequency characteristics of KS sensors for various values of amplifier input resistance are shown in Fig. 11.18. As can be seen from the figure, the correlation of KS signal–pulse signal can be improved if  $R_{IN}$  is changed.

Dependences of relative sensitivity  $S_{REL}$  at the frequency of 40 Hz on piezoelement reactive resistance  $X_P = 1/\omega C_P$  also at the frequency of 40 Hz on amplifier input resistance  $R_{IN}$  ratio for piezoelement with various diameters  $d_P$  (the metal membrane diameter  $d_M = 37$  mm) are shown in Fig. 11.19.

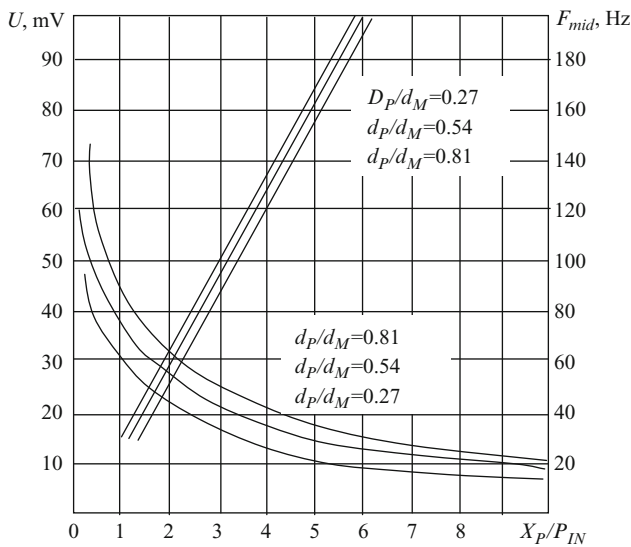
As can be seen from Fig. 11.19, sensitivity decreases if the amplifier input resistance is reduced (i.e.,  $X_P/R_{IN}$  increase). The measurements were made when the sound pressure was 10 Pa.

The dependence of the ratio between KS signals  $U_{KS}$  and pulse signals  $U_P$  on the amplifier input resistance  $X_P/R_{IN}$  for piezoelements with various diameters is also shown in this figure. As can be seen from the graph, at first when  $X_P/R_{IN}$  increases  $U_{TK}/U_P$  the ratio is also increased, and then when  $X_P/R_{IN} > 3.5$  it starts to decrease.

The dependence of the sensor output voltage  $U$  on  $X_P/R_{IN}$  ratio is shown in Fig. 11.20.



**Fig. 11.19** Dependence of relative sensitivity  $S_{REL}$  at 40 Hz frequency and  $U_{KS}/U_P$  correlation on  $X_P/R_{IN}$  correlation for piezoelements with various diameters



**Fig. 11.20** Dependence of sensor output voltage  $U$  and cutoff frequency  $f_{cut}$  on  $X_P/R_{IN}$  ratio

The  $f_{cut} = 1/2\pi R_{IN}C_P - X_P/R_{IN}$  diagram is given in the same figure.

Analysis of the diagrams shown in Figs. 11.19 and 11.20 demonstrates that  $1 < X_P/R_{IN} < 3.5$  can be considered optimal. Cutoff frequency of 40–140 Hz

corresponds to these  $X_P/R_{IN}$  values. Using expressions  $f_{cut} = 1/2\pi R_{IN}C_P$  and  $Z = 1/2\pi fC_P$ , we can easily obtain the correlation for the required determination of input resistance for  $f_{cutoff} = 40\text{--}140$  Hz, depending on piezoelement capacity  $C_P$ :

$$\frac{1}{830C_P} < R_{IN} < \frac{1}{250C_P}.$$

The measurements were made by the piezoelements 10, 20 and 30 mm in diameter ( $d_P/d_M = 0.27, 0.54$  and  $0.81$ , respectively). The piezoelement capacity was:  $\varnothing 10$  mm – 2,730 pF ( $X_n = 1.45$  Mohm on  $f = 40$  Hz),  $\varnothing 20$  mm – 12,000 pF ( $X_n = 332$  kohm),  $\varnothing 30$  mm – 3,000 pF ( $X_n = 133$  kohm). The sensors were tested in the following way. They were set in an acoustic chamber, creating sound pressure of 10 Pa. The voltage on the sensor output at 40 Hz frequency, depending on  $X_P/R_{IN}$  resistance, was measured. The dependence of cut-off frequency  $f_{cut} = 1/2\pi R_{IN}C_P$  on  $X_P/R_{IN}$  for each piezoelement was made.

When AD was measured, the pulse–KS oscillogram of these sensors was recorded with oscillograph K12-22. The ratio of sound signal amplitude  $U_{KS}$  to pulse signal amplitude  $U_P$  was determined. The  $U_{KS}/U_P$  dependence on  $X_P/R_{IN}$  was made.

### 11.4 Feedback in Korotkoff Sound Sensors

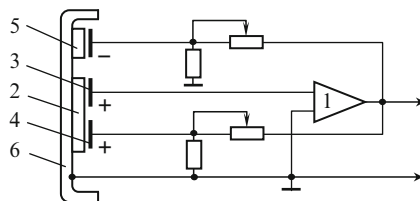
Use of feedback in KSS seems quite promising [10–12].

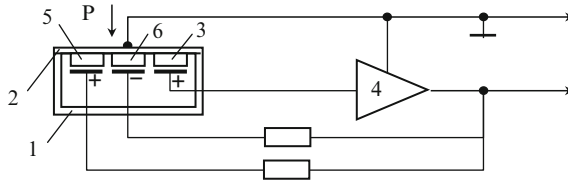
For feedback introduction a signal from the output of coupling amplifier 1 is transmitted to additional electrode 3 of the basic piezoelement or to additional piezoelement 5 (Fig. 11.21).

Two variants of sensor design are shown in Figs. 11.22 and 11.23 [11, 12]. In the sensor, represented in Fig. 11.22 [11] one basic piezoelement 3, and two additional piezoelements 5 and 6, located on metal plate 2 with heteropolar electrodes, are used. A signal to piezoelements is transmitted from the inverting or non-inverting amplifier output.

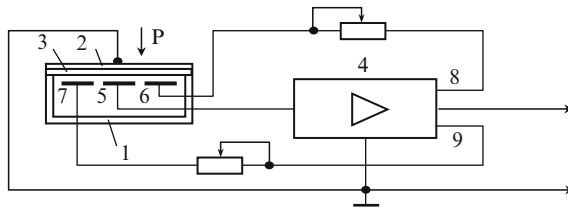
A piezoelement with base 5 and two additional electrodes 6 and 7, connected to inverting and non-inverting inputs 8, 9 of amplifiers 4 [12] is used in the sensor represented in Fig. 11.23. Basic diagrams of these sensors are represented in Figs. 11.24 and 11.25.

**Fig. 11.21** KS sensor with electromechanical feedback: 1 – amplifier, 2 – basic piezoelement, 3 – basic electrode, 4 – additional electrode, 5 – additional piezoelement, 6 – cover

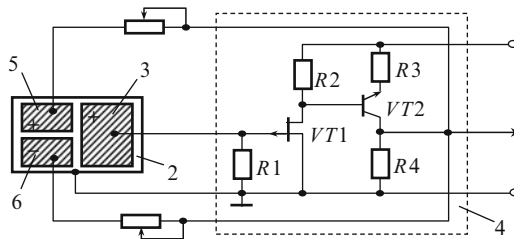




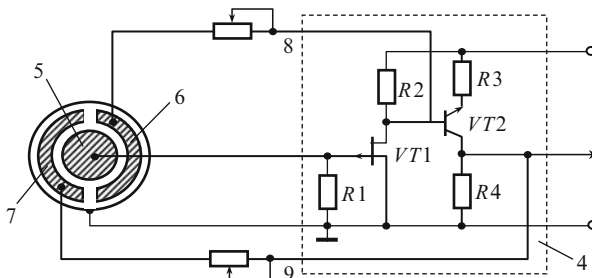
**Fig. 11.22** KS sensor with electromechanical feedback: 1 – housing (case), 2 – cover (membrane), 3 – basic piezoelement, 4 – amplifier, 5, 6 – additional piezoelements



**Fig. 11.23** Sensor with electromechanical feedback: 1 – housing (case), 2 – plate, 3 – piezoelement, 4 – amplifier, 5 – basic electrode, 6, 7 – additional electrode, 8, 9 – inverting and non-inverting outputs of amplifier

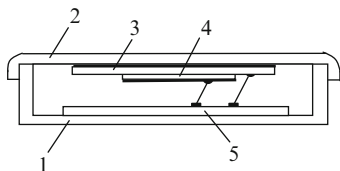


**Fig. 11.24** Diagram of sensor with feedback and rectangular bimorph element

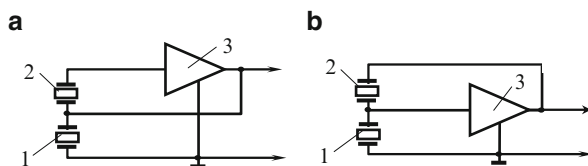


**Fig. 11.25** Diagram of sensor with feedback and round bimorph element

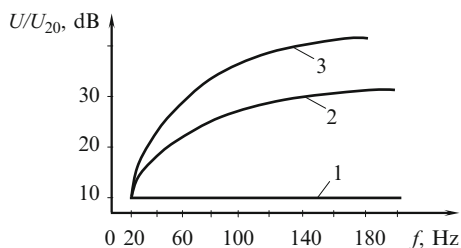




**Fig. 11.26** KSS with coplanar location of additional piezoelement: 1 – housing (case), 2 – cover, 3 – basic piezoelement, 4 – additional piezoelement, 5 – amplifier plate



**Fig. 11.27** KSS schemes with coplanar location of additional piezoelement: 1, 2 – basic and additional piezoelement, 3 – amplifier

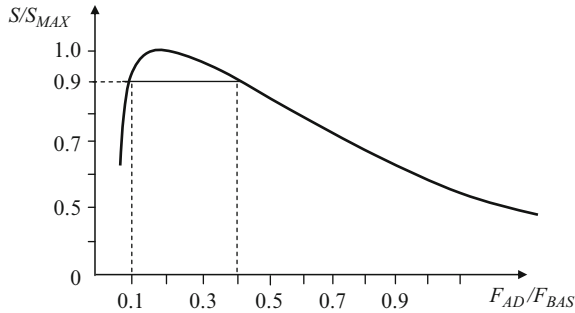


**Fig. 11.28** KSS amplitude–frequency characteristics with coplanar location of additional piezoelement: 1 – sensor in Fig. 11.5, 2 – sensor in Fig. 11.27a, piezoelements are connected with heteropolar electrodes, 3 – the same, with unipolar electrodes

A variant of sensor with coplanar position of additional piezoelement [22] has also been developed. The sensor design is represented in Fig. 11.26, and the connection schemes in Fig. 11.27.

Inclusion of the additional piezoelement in the positive feedback circuit (Fig. 11.27) leads to sensitivity increase and deformation of frequency characteristics (Fig. 11.28). As it is seen from the figure, the ratio between output voltage at frequencies of 20–200 Hz and output voltage at 20 Hz frequency is shown along the ordinate axis. As Fig. 11.28 shows, if the amplifier (3 Mohm)  $R_{IN}$  is big enough, frequency characteristic in 20–200 Hz range for the sensor without feedback is practically linear. For sensors with positive feedback, depending on the piezoelements polarity, the raise of AFC (20–30 dB) in 20–200 Hz range is observed.

It is easy to see that the scheme of the sensor with additional coplanar piezoelement and positive feedback (Fig. 11.27) is an active filter of Chebyshev



**Fig. 11.29** Dependence of relative sensitivity  $S/S_{MAX}$  on  $F_{AD}/F_{BAS}$  ratio for the sensor in Fig. 11.27

upper frequencies of the second order [16]. In this case piezoelements are used as filter condensers.

There exists an optimal correlation of additional and basic piezoelements areas for a scheme with positive feedback at which maximum sensitivity is reached (Fig. 11.29).

## 11.5 Hindrances at Arterial Pressure Measurement

The following “interfering” factors influence the sensor at AP measurement, characterizing all Korotkoff sounds:

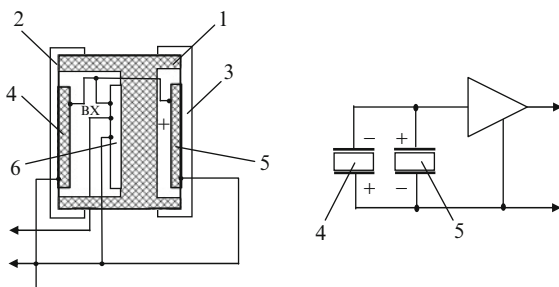
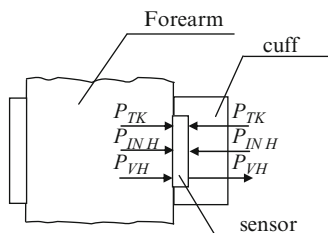
1. In-phase hindrances: These hindrances arise at pressure fluctuations in the cuff because of the arm movement. The signal of these hindrances coincides in direction and phase with the Korotkoff sounds signal.
2. Vibrating hindrances: These hindrances usually arise while walking. Their peculiarity is that they come to any sensor point in one direction.

As research has shown [29], an acoustic signal of Korotkoff sounds comes to the sensor located under the cuff, from both the forearm tissue and from the cuff side (Fig. 11.30).

It has been experimentally established that the level of KS influence on the sensor back side (i.e., from the cuff side) equals approximately 0.4 of the influence on the front cover (i.e., from the arm side). The character of the influence of in-phase hindrances on the front and back sensor sides is the same as Korotkoff sounds; the signal level is approximately identical.

Vibration hindrances, influencing the sensor front and back parts, are from the same direction; their level is also approximately identical.

**Fig. 11.30** Scheme of influence on sensor:  
 $P_{KS}$  – Korotkoff sound,  
 $P_{INH}$  – in-phase hindrances,  
 $P_{VH}$  – vibrating hindrances



**Fig. 11.31** Suppression of in-phase hindrances: 1 – housing (case), 2, 3 – covers, 4, 5 – piezoelements, 6 – amplifier plate; **a** sensor design, **b** scheme of piezoelement connection

The level of vibration and in-phase hindrances can be more or less than Korotkoff sound influences. For convenience we will assume that all of them are approximately identical and equal an arbitrary unit.

Several sensor designs for hindrance level reduction have been developed [13–15].

Two identical bimorph elements with piezoelements 4, 5, fastened on covers 2, 3 by heteropolar electrodes (Fig. 11.31) are proposed for use in the sensor referred to in [13] for suppression of in-phase hindrances.

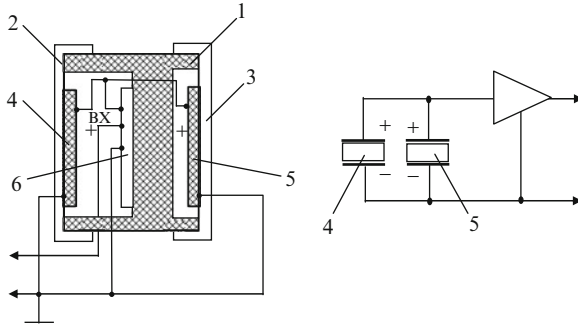
In-phase hindrances create charges  $Q_{P1}$  and  $Q_{P2}$  in piezoelements. The total charge and voltage equal 0 if piezoelements capacities are equal.

Korotkoff sounds create charges  $+Q_{KS}$  and  $-0.4Q_{KS}$  in piezoelements. Total voltage equals:

$$U = \frac{+Q_{TK} - 0.4Q_{TK}}{2C} = 0.3 \frac{Q_{TK}}{C}.$$

Thus, the total hindrance signal, independent from its level, should always equal 0, i.e., in-phase hindrance suppression occurs. Then the level of KS signal decreases by approximately three times.

However, signal hindrance will never equal 0 in practice. This happens because of piezoelements’ parameters spread, technological factors, and also inequalities in the influence of in-phase hindrances. They influence the sensor from the sides of forearm and cuff.



**Fig. 11.32** Suppression of vibration hindrances: 1 – housing (case), 2, 3 – covers, 4, 5 – piezoelements, 6 – amplifier plate

Two identical bimorph elements, piezoelements of which are fastened on the covers by unipolar electrodes (Fig. 11.32) are proposed for use for suppression of signal vibro-hindrances in the sensor [14].

Vibro-hindrance appears in one point at a definite moment. Therefore, it comes to the sensor and the piezoelements from one direction.

Approximately similar voltage, but of the opposite polarity, appears on the piezoelements, independent on the direction of vibration. As a result, the signal received equals 0.

The fact that the total signal does not equal 0 in practice is explained by variation of piezoelectric characteristics technology and piezoelements capacity (see State Standard 13927-80), and also by the different position of bimorph elements, processing factors, etc.

Korotkoff sounds create charge  $+Q_{TK1}$  on the first piezoelement (pos. 2, Fig. 11.32), and charge  $-0.4Q_{TK1}$  on the second (pos. 3).

Net voltage of sounds on two piezoelements when  $C_1 = C_2 = C$  equals:

$$U = \frac{Q_{TK} + 0.4Q_{TK}}{2C} = 0.7U_{TK}.$$

The sensor described in [15] allows the suppression of both in-phase and vibration hindrances.

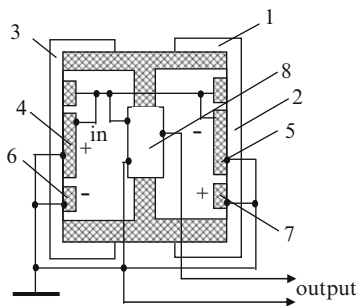
The sensor is represented in Fig. 11.33.

The sensor has two disk and two ring piezoelements of identical thickness. The area of disk piezoelements equals the areas of the ring piezoelements.

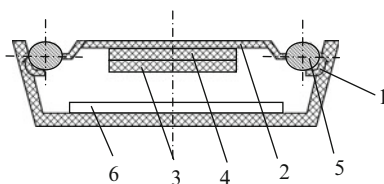
Below we will consider the signals, arising in piezoelements under the influences mentioned. Assuming that piezoelements areas and thickness are equal (they are made of the same material), we consider that the piezoelements capacities are equal:

$$C_1 = C_2 = C_3 = C_4 = C.$$

**Fig. 11.33** Suppression of in-phase and vibration hindrances: 1 – housing (case), 2, 3 – covers, 4, 5 – disk piezoelements, 6, 7 – ring piezoelements, 8 – amplifier plate



**Fig. 11.34** Sensor of Korotkoff sounds: 1 – housing (case); 2 – membrane; 3 – piezoelement; 4 – rigid centre; 5 – rubber ring; 6 – amplifier plate



We will mark the charge arising on disk piezoelement 4 on the front cover (i.e., the cover adjacent to the forearm), with  $Q$  (considering  $- +Q$  sign). The voltage on this piezoelement is:

$$U = \frac{Q}{C}.$$

It has been experimentally established that the signal level on the ring piezoelement (if its area equals the area of the disk piezoelement) equals  $\sim 0.5$  of the signal level on the disk piezoelement.

Then, on the ring piezoelement on the same side the charge is  $-0.5Q$ .

The signal, approximately equal to 0.4 of the signal on piezoelement 4, is created in piezoelement 5 on the cuff side. Then, considering the piezoelement polarity, the charge on it equals  $(-0.4Q)$ . On piezoelement 7,  $0.5 \times 0.4Q = +0.2Q$ .

Total charge on piezoelements:

$$+0.1q - 0.5q - 0.4q + 0.2q = +0.3q,$$

and total voltage

$$U = \frac{0.3q}{4C} = 0.075U_1.$$

Thus, the useful signal decreases in the given sensor by approximately ten times. Considering that it is practically impossible to make the in-phase and vibro-hindrances signals equal 0, the correlation of useful signal/hindrance for the given sensor improves by approximately two to three times.

Pinning of bimorph element membrane 2 (Fig. 11.34) is used for sensitivity increase in the sensor, made on the basis of patent number 1826862 [23]. Rigid centre 4, decreasing the piezoelement bend under the influence of hindrance, is used to reduce the level of in-phase hindrances.

### 11.6 Sensors of Pulse Waves

Meanwhile, there exists one more sensor implementation, for electronic tonometers. This makes it possible to obtain information on the occurrence and termination of Korotkoff sounds, and consequently on systolic and diastolic pressure. This implementation is based on the pulse wave passage along the artery. Then the information on Korotkoff sounds is disseminated in time and in space.

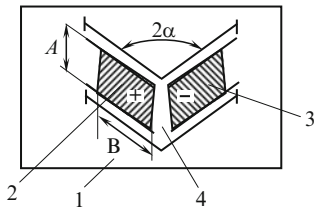
The sensor [24] has a high sensitivity because the piezoelements are supported as a cantilever. Two piezoelements, fastened on the metal cover by parallel-connected heteropolar electrodes, are used in the sensor. This allows almost complete suppression of both in-phase and vibration hindrances. The sensor reacts to the pulse wave movement. The sensor is practically insensitive to the acoustic component of the signal (Fig. 11.35).

Consoles (cantilevers) are made in the form of parallelograms, the long sides of which are angularly ( $2\alpha$ ) located to each other.

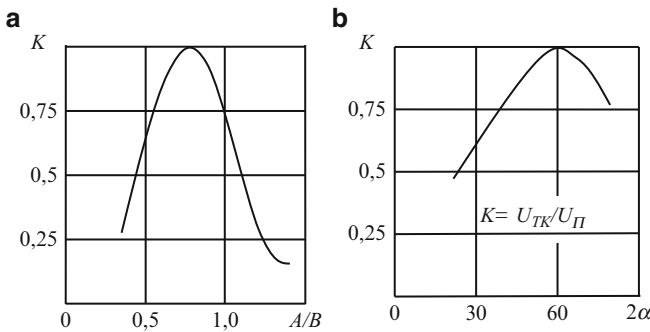
It has been experimentally established that the signal/hindrance ratio reaches maximum (Fig. 11.36), if  $A/B$  console (cantilever) values and corner  $2\alpha$  are correlated in a certain way.

It has also been experimentally established that at optimum  $A/B$  and  $2\alpha$  angle values the signal/hindrance reaches 15–20 dB in the design given.

The information given in this chapter may also be useful for the design of contact piezoelectric microphones.



**Fig. 11.35** Pulsation wave sensor: 1 – membrane; 2, 3 – piezoelement; 4 – membrane aperture



**Fig. 11.36** (a)  $K$  dependence on  $A/B$  ratio, (b)  $K$  dependence on  $2\alpha$  angle;  $U_{KS}$  – voltage of Korotkoff sounds;  $U_P$  – pulse voltage

## References

1. V.B. Bolshov et al., Patent of USSR 651786. Sensors of Korotkoff sounds, No 10 (1979) (in Russian)
2. V.V. Vladimirov et al., Patent of USSR 1026763. Sensors of Korotkoff sounds, No 25 (1983) (in Russian)
3. V.V. Vladimirov et al., Patent of USSR 1189427. Sensors of Korotkoff sounds, No 41 (1985) (in Russian)
4. D.S. Volpyanskiy, A.A. Smerdov, E.V. Storchun, Patent of USSR 927228. Piezoelectric sensor of pulse, No 18 (1982) (in Russian)
5. E.V. Storchun et al., Patent of USSR 993915. Piezoelectric sensor of pulse, No 12 (1983) (in Russian)
6. E.V. Storchun et al., Patent of USSR 1007653. Piezoelectric sensor of pulse, No 13 (1983) (in Russian)
7. P.G. Dzagupov et al., Patent of USSR 1181626. Piezoelectric sensor of pulse, No 36 (1985) (in Russian)
8. V.M. Bolshov et al., Patent of USSR 651786 A61B 5/02. Sensors of Korotkoff sounds (in Russian)
9. V.M. Sharapov et al., Patent of USSR 1431732. Sensors of Korotkoff sounds, No 39 (1988) (in Russian)
10. V.M. Sharapov et al., Patent of USSR 1463225. Sensors of Korotkoff sounds, No 9 (1989) (in Russian)
11. V.M. Sharapov, A.A. Zlatkin et al., Patent of USSR 1534759. Piezoelectric receiver of sound pressure, No 1 (1990) (in Russian)
12. V.M. Sharapov, I.M. Allaverdiev, A.A. Zlatkin, O.M. Boev, Patent of USSR 1534760. Piezoelectric receiver of sound pressure, No 1 (1990) (in Russian)
13. V.M. Sharapov et al., Patent of USSR N1463225. Sensors of Korotkoff sounds, No 9 (1989) (in Russian)
14. V.M. Sharapov et al., Patent of USSR 1482656. Sensors of Korotkoff sounds, No 20 (1989) (in Russian)
15. V.M. Sharapov, V.F. Konopkin et al., Patent of USSR 1646542. Sensors of Korotkoff sounds, No 17 (1991) (in Russian)
16. D. Jonson, Mur.G. Jonson Jr., *Directory of Active Filters* (Energoatom, Moscow, 1983), p. 128 (in Russian)
17. V. Domarkas, R.J. Kazys, *Piezoelectric Transducers for Measuring Devices* (Mintis, Vilnius, 1974), p. 258 (in Russian)
18. A.I. Lurie, *Spatial Problems of Elasticity Theory* (State Publishing House of Technical Literature (ГИИТЛ), Moscow, 1965) (in Russian)
19. Patent of USA No 3573394. A6 5/02 (1971) (in Russian)
20. Patent of USA No 3573394. A.61B 5/02 (1971) (in Russian)
21. V.M. Sharapov et al., Patent of USSR 1776189. Piezoelectric sensor of Korotkoff sounds (1993) (in Russian)
22. V.M. Sharapov et al., Patent No 4373584/14 from 8.02.88. Piezoelectric sensor of Korotkoff sounds (in Ukrainian)
23. V.M. Sharapov, N.A. Shulga et al., Patent of USSR 1826862. Sensors of Korotkoff sounds, No 25 (1993) (in Russian)
24. V.M. Sharapov, S.P. Varavka, Patent No 5061882/28–14/04200 from 14.09.92 (RF). Sensor of pulse wave (in Russian)
25. S.I. Rudnitskiy, V.M. Sharapov, N.A. Shulga, Vibrations of disk bimorph transducer of metal–piezoceramics type. *Appl. Mech.* **26**(10) (1990) (in Russian)
26. I.B. Chudaeva, Resistance load optimization of Korotkoff sounds piezosensors. Collected Papers of International Conference Instrument Making–97, Vinnitsa-Simeiz (1997) (in Russian)

27. I.B. Chudaeva et al., Coplanar threemorph piezoelements with feedback. Collected Papers of the Fourth Ukrainian Conference Automatics-97. Cherkassy (1997) (in Russian)
28. I.B. Chudaeva et al., Coplanar threemorph piezoelements in electronic tonometer sensors. Collected Papers of the Fourth Ukrainian Conference "Automatics-97" Cherkassy (1997) (in Russian)
29. V.M. Sharapov, M.P. Musienko, E.V. Sharapova, *Piezoelectric Sensors*, ed. by V.M. Sharapov (Technosphaera, Moscow, 2006), p. 632 (in Russian)



# Chapter 12

## Electro-acoustic Transducers

### 12.1 General Information

Electro-acoustic transducers (EAT) are intended for transformation of electric voltage into acoustic signal and vice versa. EAT work in gaseous medium, and are widely used in measuring, computing, consumer equipment, etc. [1].

EAT elaboration is based on various physical principles.

There are mechanical, electrodynamic, magnetostrictive, electrostatic, and piezoelectric EAT [2]. At present, piezoelectric transducers are most commonly used. For example, in Table 12.1 characteristics of distometers with various EAT types of ultrasonic range [2–4] are shown.

The distances, indicated in brackets, are measured under the ideal work conditions of the meters, smooth reflecting surface for instance.

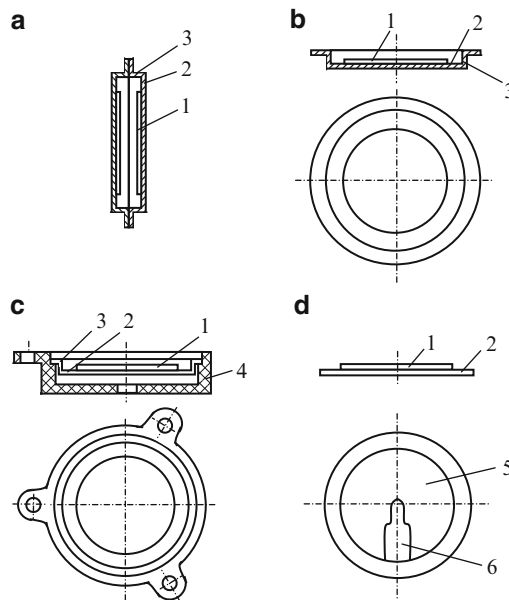
As can be seen from Table 12.1, piezoceramic transducers, working on flexural vibrations, have the widest range of the distances measured.

Piezoceramic, as well as magnetostrictive, transducers, working on longitudinal vibrations, have rather small displacement amplitudes on the work surface. Displacement amplitude increase can be reached by introduction of additional matching liquid [5,6] or air layer [7,8] between the transducer surface and air. This additional layer should be separated from the work medium by a thin acoustically transparent membrane. These transducers are narrowband because of the resonant properties of matching layers. However, transfer coefficient of these transducers can be increased up to nine times in comparison with the transducers, working on longitudinal vibrations without the matching layers [8]. Displacement amplitude increase can be reached by using ultrasonic concentrators [9].

Use of flexural vibrations in EAT is the most effective: acoustic impedance of the transducers in this case is considerably smaller than when other kinds of vibrations are used. These transducers have a rather high coefficient of electro-acoustic transformation. They make it possible to receive higher displacement amplitudes.

**Table 12.1** Technical characteristics of distometers

Type of electro-acoustic transducer (gaseous medium)	Work frequency range (kHz)	Range of distances measured (m)
Electrodynamic	5–15	To 30 (50)
Magnetostrictive – with transformation of vibration	16–30	To 70
Magnetostrictive – longitudinal vibrations	16–30	To 30
Electrostatic	16–30	To 10
Piezoceramic – with transformation of vibration	16–60	To 30
Piezoceramic – longitudinal vibrations	20–60	To 30
Piezoceramic – flexural vibration	40–60	To 70 (100)



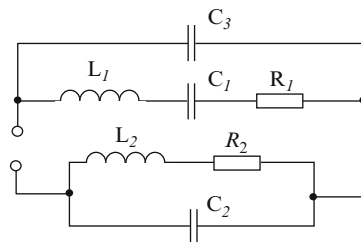
**Fig. 12.1** Design of electro-acoustic transducers. (buzzers, piezoringers): (a) 3Π-1, (b) 3Π-2, (c) 3Π-19, (d) CB 35BBK (by Taiyo Yuden Co., Ltd.): 1 – piezoelement, 2 – membrane, 3 – ledge, 4 – housing (case), 5, 6 – electrodes

Flexural vibrations can easily be created in asymmetric bimorph piezoceramic transducers (see Chap. 6).

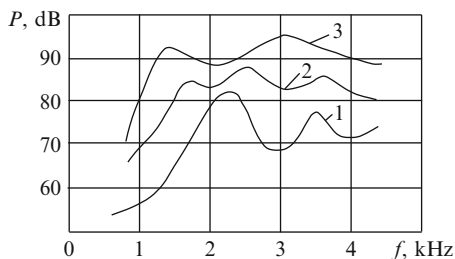
Some EAT (buzzers, piezoringers) are shown in Fig. 12.1.

EAT are connected to the oscillation generator or included in the active oscillator scheme. They can be used as phones, buzzers, sirens, etc.

**Fig. 12.2** Equivalent electric scheme of transducer ЗП-19



**Fig. 12.3**  
Amplitude–frequency characteristic: 1 – ЗП-1;  
2 – ЗП-19; 3 – ЭП-3



Transducer ЗП-1 has two bimorph elements, soldered to each other. The transducer is intended for sound pressure level increase. It is also used in active oscillator schemes.

This design has a low sound pressure level for two bimorph elements.

In transducer ЗП-19, the bimorph element is rigidly fastened in the plastic housing (case). There is an aperture in the housing (case), improving the frequency characteristic and raising the sound pressure.

As the experiments showed, the given transducer creates sound pressure approximately 4.6 dB higher than ЗП-1. The equivalent electric scheme of the transducer received as a result of the electromechanical analogy method, is shown in Fig. 12.2.

In this scheme the following elements correspond to each other: consecutive (oscillatory circuit, vibration contour)  $L_1$ ,  $C_1$ ,  $R_1$  to bimorph piezoelement, inductance  $L_2$  to air mass between the housing (case) and the bimorph element,  $C_2$  to air elasticity in this volume and finally,  $R_2$  resistance to losses when air passes through the aperture.  $C_3$  is the static capacitance between the piezoelement electrodes.

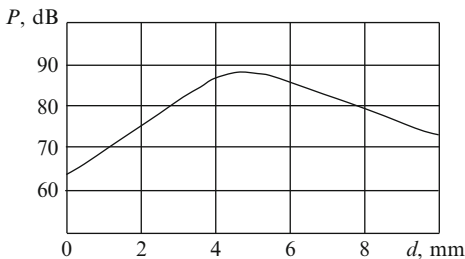
As can be seen from Fig. 12.3, transducer ЗП-19 creates higher sound pressure and has a wider frequency band than transducer ЗП-1.

It is necessary to note that the size of the aperture in the transducer housing (case) considerably influences the level of the sound pressure  $P$  created (Fig. 12.4).

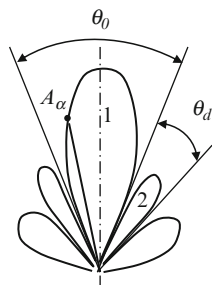
There is an additional electrode 6 on the piezoelement in the CB35BBK transducer produced by Taiyo Yuden Co, LTD. This allows switching of this transducer in the active oscillator scheme.

Common drawbacks of electro-acoustic transducers are a comparatively low level of sound pressure created (i.e., their sensitivity), and also a narrow range of frequencies reproduced.

**Fig. 12.4** Dependence of sound pressure  $P$  for 3Π-19 on aperture diameter in the housing (case)



**Fig. 12.5** Directional diagram and its parameters: 1 – basic and 2 – additional lobes (of maxima),  $\theta_0$  and  $\theta_d$  – angles characterizing directional operation sharpness and width of the first additional maximum respectively,  $A_\alpha$  – current DD value in  $\alpha$  direction



In addition, the transmission coefficient of a bimorph piezoelectric transformer and the resistance value of the piezoelectric transformer output section are important for transducers with an additional electrode.

The directional diagram (DD), determining the spatial efficiency of electro-acoustic transformation, is the major EAT characteristic.

An electro-acoustic radiator DD is usually characterized by many features. The most important among them are: (1) sharpness of directional operation, (2) maximum sharpness, (3) amount, directions and values of additional maxima, and (4) amount and directions of complementary maxima. The following parameters are also important: concentration, amplification, interference immunity factors, the effective area of the radiator aperture, and the utilization coefficient of the aperture area [10]. DD in polar system of coordinates and some of its important parameters are shown in Fig. 12.5.

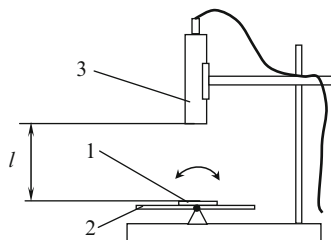
It is known that acoustic radiation DD depends on the radiative signal frequency [11, 12]. The transducer is deformed differently under various conditions. As a result, a sound front determining the directional characteristic is formed. Analytical dependences, describing acoustic directivity, are proposed in [10].

The acoustic pressure, created by the transducer [13]:

$$p = \int_{-l}^l A \cos \left[ (N - 1) \frac{\pi x}{2l} \right] e^{jkx \sin \theta} dx, \tag{12.1}$$

where  $N$  – amount of nodal lines,  $l$  – the transducer width,  $k$  – propagation constant of a flexural wave  $k = 2\pi/\lambda$ ,  $\lambda$  – wavelength in the medium,  $\theta$  – opening angle

**Fig. 12.6** Scheme of unit for transducer directional diagram measurement: 1 – transducer, 2 – rotary device, 3 – microphone,  $l$  – distance between transducer and microphone



of DD basic lobe, and  $A$  – a constant, depending on voltage on the transducer clips (clamps, binders) and on transducer parameters.

After integration and normalization (12.1) relative to  $p_{\max} = 1$ , we obtain the following expression for the transducer directional diagram:

$$R = \frac{(N - 1)\pi \cos \eta}{\frac{\pi^2(N-1)^2}{4} - \eta^2}, \quad (12.2)$$

where  $\eta = kl \sin \theta$ .

Directional diagrams are measured by the unit represented in Fig. 12.6.

To measure the radiator sound pressure level, the measuring device microphone should be positioned in the spherical radiation area (Fraunhofer diffraction region) [10, 14], i.e.:

$$l \geq 2d^2\lambda^{-1},$$

where  $d$  is the biggest linear dimension of the transducer.

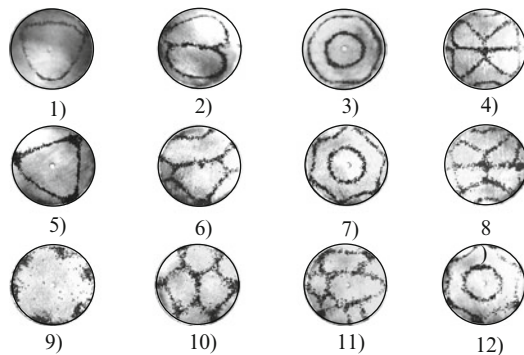
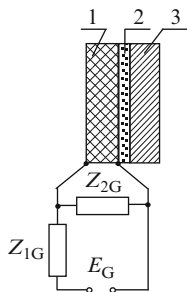
The pattern of antinode nodal distributions in the transducer plane is determined by the Chladni figures method [9].

## 12.2 Transfer Function Calculation of Electro-acoustic Transducers

EAT are based on asymmetric bimorph piezoceramic transducers. Such transducers can be described by electro-elasticity theory methods [17, 33]. In the general case, a piezoelectric element is described by a system of 22 differential equations. It is a well-known fact that the exact solution of this task is practically impossible [33]. It is possible only for special cases.

Transfer functions of electro-acoustic transducers can be simply described if each transducer layer is considered as a quadripole. A transfer function calculation of mechanically damped piezoelectric radiator with an arbitrary number of transitive layers (m-layer piezoelectric system) can be found in the literature [15]. Electric circuit of the generator should be considered also.

**Fig. 12.7** Asymmetric bimorph piezoradiator with electric circuit switching: 1 – piezoplate, 2 – glue layer, 3 – metal plate;  $Z_{1G}$ ,  $Z_{2G}$  – electric resistance of piezoradiator connections to generator,  $E_G$  – generator emf



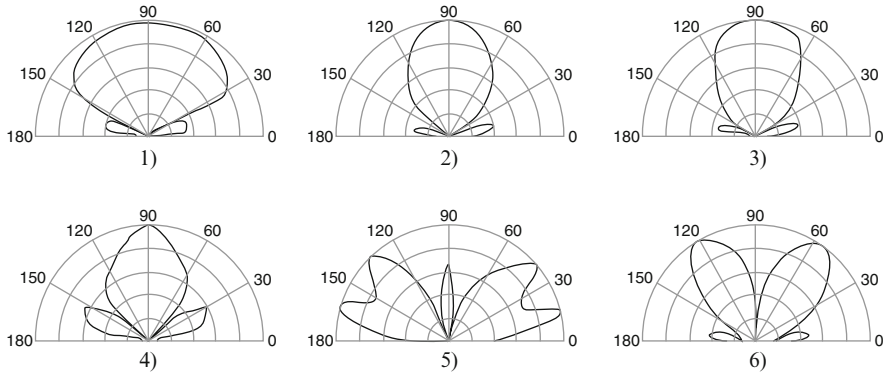
**Fig. 12.8** Chladni figures for round transducer: 1–4 (2.25; 4; 6.85; 8.6 kHz) – when the transducer is loose; 5–8 (2.3; 3.84; 7.1; 8.9 kHz) – fastened at three points; 9–12 (1.19; 4.7; 6.3; 7.5 kHz) – fastened at six points

The scheme of the transducer discussed is shown in Fig. 12.7 [16]. It consists of piezoelement 1, glue layer 2 and a metal plate which can be regarded as a transitive layer. The radiator layers accordingly have thickness  $l_1$ ,  $l_2$  and  $l_3$ , while  $l_2 \ll l_1$  and  $l_2 \ll l_3$ . Air is the work environment.

$E_G$  – generator emf;  $I$  – current, passing through the generator;  $p$ ,  $v$ ,  $F$  – pressure, speed and force respectively upon the border of the third transitive layer (metal plate) work environment;  $z_1$ ,  $z_B$  – wave acoustic resistance of the piezoelement and the work medium respectively;  $z_2$ ,  $z_3$  – wave acoustic resistance of the glue layer and the metal plate respectively;  $e$  – piezoelectric constant of the piezoelement.

Propagation constant in each transitive layer is  $\gamma_n$ , active radiating surface of the piezoelectric transducer is  $A_1$ . The first transitive layer (glue) has index  $n = 2$ . Regarding each piezotransducer element as a quadripole, the matrix system equation can look like this [15]:

$$\begin{pmatrix} E_G \\ I \end{pmatrix} = \begin{pmatrix} 1 & E_{1G} \\ 0 & 1 \end{pmatrix} \times \begin{pmatrix} 1 & 0 \\ \frac{1}{E_{2G}} & 1 \end{pmatrix} \times \begin{pmatrix} A_{11} & A_{12} \\ A_{21} & A_{22} \end{pmatrix} \times \begin{pmatrix} S_{11}^{(m)} & S_{12}^{(m)} \\ S_{21}^{(m)} & S_{22}^{(m)} \end{pmatrix} \times \begin{pmatrix} F \\ v \end{pmatrix}, \tag{12.3}$$



**Fig. 12.9** Directional diagrams of round transducer: 1, 2 (3.9; 6.8 kHz) – when the transducer is loose; 3, 4 (2.32; 7.27 kHz) – fastened at three points; 5, 6 (1.78; 9.55 kHz) – fastened at six points

where  $\|S_{ij}^{(m)}\|$  ( $i, j = 1, 2$ ) is the structure matrix with several transitive layers. It is determined by the expression [15]:

$$\|S_{ij}^{(m)}\| = \|P_{ij}^{(2)}\| \times \|P_{ij}^{(3)}\| \times \dots \times \|P_{ij}^{(m)}\|, \tag{12.4}$$

where  $m$  is the total number of layers, in this case  $m = 3$ ;

$$\|P_{ij}^{(n)}\| = \left\| \begin{array}{cc} \text{ch}\gamma_n l_n & A_1 z_n \text{sh}\gamma_n l_n \\ \frac{\text{sh}\gamma_n l_n}{A_1 z_n} & \text{ch}\gamma_n l_n \end{array} \right\| - \text{matrix of each transitive layer;}$$

$\gamma_n = \alpha_n + j(2\pi/\lambda_n)$ , with  $\alpha_n$  and  $\lambda_n$  – absorption coefficient of and wavelength factor in each transitive layer respectively;  $l_n$  – the thickness of each transitive layer, fulfilling the condition  $\lambda_n \ll l_n$ .

Matrix coefficients of  $\|S_{ij}^{(m)}\|$  are found from expression (12.4).

Expressions of coefficients  $S_{ij}^{(3)}$  for a three-layered piezoelectric system with absorption coefficients  $\alpha_n = 0$  are shown in Table 12.2 [15].

**Table 12.2** Coefficients  $S_{ij}^{(3)}$  for three-layered piezoelectric system

Number of layers	Coefficient name	Expressions for coefficients
3	$S_{11}^{(3)}$	$\cos 2\pi k_2 x \cos 2\pi k_3 x - \frac{z_2}{z_3} \sin 2\pi k_2 x \sin 2\pi k_3 x$
	$S_{12}^{(3)}$	$jA_1 z_3 \left( \sin 2\pi k_3 x \cos 2\pi k_2 x - \frac{z_2}{z_3} \sin 2\pi k_2 x \cos 2\pi k_3 x \right)$
	$S_{21}^{(3)}$	$\frac{j}{A_1 z_3} \left( \frac{z_3}{z_2} \sin 2\pi k_2 x \cos 2\pi k_3 x + \sin 2\pi k_3 x \cos 2\pi k_2 x \right)$
	$S_{22}^{(3)}$	$\cos 2\pi k_2 x \cos 2\pi k_3 x - \frac{z_3}{z_2} \sin 2\pi k_2 x \sin 2\pi k_3 x$

In this table:  $k_n = \lambda_n/\lambda_{n0}$ , where  $\lambda_{n0}$  is the wave length in each transitive layer at piezoelement  $f_0$  anti-resonant frequency.

After matrix transformation into equation (12.3), we receive the following expression:

$$\begin{Bmatrix} E_\Gamma \\ I \end{Bmatrix} = \begin{Bmatrix} A_{11}^* & A_{12}^* \\ A_{21}^* & A_{22}^* \end{Bmatrix} \times \begin{Bmatrix} F \\ v \end{Bmatrix}, \quad (12.5)$$

where

$$A_{11}^* = \left(1 + \frac{Z_{1\Gamma}}{Z_{2\Gamma}}\right) (A_{11}S_{11}^{(3)} + A_{12}S_{21}^{(3)}) + Z_{1\Gamma} (A_{21}S_{11}^{(3)} + A_{22}S_{21}^{(3)});$$

$$A_{12}^* = \left(1 + \frac{Z_{1\Gamma}}{Z_{2\Gamma}}\right) (A_{11}S_{12}^{(3)} + A_{12}S_{22}^{(3)}) + Z_{1\Gamma} (A_{21}S_{12}^{(3)} + A_{22}S_{22}^{(3)});$$

$$A_{21}^* = \frac{1}{Z_{1\Gamma}} (A_{11}S_{11}^{(3)} + A_{12}S_{21}^{(3)}) + (A_{21}S_{11}^{(3)} + A_{22}S_{21}^{(3)});$$

$$A_{22}^* = \frac{1}{Z_{2\Gamma}} (A_{11}S_{12}^{(3)} + A_{12}S_{22}^{(3)}) + (A_{21}S_{12}^{(3)} + A_{22}S_{22}^{(3)}).$$

Transfer function of the piezoradiator is calculated from the expression (12.5). It looks like this after identical transformation:

$$K_R = \frac{P}{E_G} = K_{R1} \Phi_R(x) e^{j\varphi_R(x)}, \quad (12.6)$$

where  $K_{R1} = 2e/l_1$ ;  $x$  – relative frequency;  $\Phi_R(x)$  – amplitude–frequency characteristic;  $\varphi_R(x)$  – phase–frequency characteristic;

$$\begin{aligned} \Phi_R(x) = \frac{1}{2} \left[ \left( S_{11}^{(3)} X - \frac{z_3}{z_B} S_{12}^{*(3)} M - \frac{z_1}{z_3} S_{21}^{*(3)} Y + \frac{z_1}{z_B} S_{22}^{(3)} N \right)^2 \right. \\ \left. + \left( S_{11}^{(3)} M + \frac{z_3}{z_B} S_{12}^{*(3)} X + \frac{z_1}{z_3} S_{21}^{*(3)} N + \frac{z_1}{z_B} S_{22}^{(3)} Y \right)^2 \right]^{-1/2}; \end{aligned} \quad (12.7)$$

$$\varphi_R = -\arctg \frac{S_{11}^{(3)} M + \frac{z_3}{z_B} S_{12}^{*(3)} X + \frac{z_1}{z_3} S_{21}^{*(3)} N + \frac{z_1}{z_B} S_{22}^{(3)} Y}{S_{11}^{(3)} X - \frac{z_3}{z_B} S_{12}^{*(3)} M - \frac{z_1}{z_3} S_{21}^{*(3)} Y + \frac{z_1}{z_B} S_{22}^{(3)} N}; \quad (12.8)$$



$$\begin{aligned}
S_{12}^{*(3)} &= \frac{S_{12}^{(3)}}{jA_1z_3}, \quad S_{21}^{*(3)} = -jA_1z_3S_{21}^{(3)}; \\
X &= (1 + \alpha) \left( \frac{k_t^2}{\pi x} a_{11} + b_{21} \right) - \beta \left( \frac{k_t^2}{\pi x} b_{11} - a_{21} \right) + x (\xi a_{11} - \psi b_{21}); \\
Y &= (1 + \alpha) \left( \frac{k_t^2}{\pi x} b_{12} - a_{22} \right) + \beta \left( \frac{k_t^2}{\pi x} a_{12} + b_{22} \right) + x (\xi b_{22} - \psi a_{22}); \\
M &= (1 + \alpha) \left( \frac{k_t^2}{\pi x} b_{11} - a_{21} \right) + \beta \left( \frac{k_t^2}{\pi x} a_{11} + b_{21} \right) + x (\xi b_{21} + \psi a_{21}); \\
N &= (1 + \alpha) \left( \frac{k_t^2}{\pi x} a_{12} + b_{22} \right) - \beta \left( \frac{k_t^2}{\pi x} b_{12} - a_{22} \right) + x (\xi a_{22} - \psi b_{22}); \\
\frac{Z_{1\Gamma}}{Z_{2\Gamma}} &= \alpha + j\beta\alpha; \quad \frac{Z_{1\Gamma}}{X_{C_0}} = \xi + j\psi,
\end{aligned}$$

where  $K_t$  – electromechanical coupling coefficient of the piezoelectric plate;  $X_{C_0}$  – electric resistance of capacity  $C_0$  at anti-resonant frequency  $f_0$ .

As air with resistance  $z_B \cong 0$  is the work medium, expressions (12.7), (12.8) will look like:

$$\Phi_R(x) = \frac{1}{2} \left[ \left( S_{11}^{(3)} X - \frac{z_1}{z_3} S_{21}^{*(3)} Y \right)^2 + \left( S_{11}^{(3)} M + \frac{z_1}{z_3} S_{21}^{*(3)} N \right)^2 \right]^{-1/2}; \quad (12.9)$$

$$\varphi_R = -\arctg \frac{S_{11}^{(3)} M + \frac{z_1}{z_3} S_{21}^{*(3)} N}{S_{11}^{(3)} X - \frac{z_1}{z_3} S_{21}^{*(3)} Y}. \quad (12.10)$$

Depending on the degree of EAT fastening, coefficients  $a_{ij}$  and  $b_{ij}$  are determined.  $a_{12} = b_{11} = a_{21} = b_{22} = 0$  if the transducer is mechanically undamped. Therefore, expressions for constants  $X, Y, M, N$  become simpler:

$$\begin{aligned}
X &= (1 + \alpha) \left( \frac{k_t^2}{\pi x} a_{11} + b_{21} \right) + x (\xi a_{11} - \psi b_{21}); \\
Y &= (1 + \alpha) \left( \frac{k_t^2}{\pi x} b_{12} - a_{22} \right) + x \psi a_{22}; \\
M &= \beta \left( \frac{k_t^2}{\pi x} a_{11} + b_{21} \right) + x \xi b_{21}; \\
N &= x \xi a_{22} - \beta \left( \frac{k_t^2}{\pi x} b_{12} - a_{22} \right).
\end{aligned}$$

Calculating these constants and knowing the parameters of each layer, transfer function of the whole asymmetric bimorph transducer can be determined:

$$K_R = \frac{e}{l_1} \left[ \left( S_{11}^{(3)} X - \frac{z_1}{z_3} S_{21}^{*(3)} Y \right)^2 + \left( S_{11}^{(3)} M + \frac{z_1}{z_3} S_{21}^{*(3)} N \right)^2 \right]^{-1/2} \quad (12.11)$$

$$\times \exp \left( -j \arctg \frac{S_{11}^{(3)} M + \frac{z_1}{z_3} S_{21}^{*(3)} N}{S_{11}^{(3)} X - \frac{z_1}{z_3} S_{21}^{*(3)} Y} \right).$$

### 12.3 Chladni Figures and Transducer Directional Diagrams

EAT with round bimorph elements are most widely used [11, 17]. However, in some cases transducers of rectangular and triangular form [12, 18] are applied.

Chladni figures for a round bimorph transducer with a metal plate (made of semi-firm brass Л163 40 mm in diameter, 0.3 mm thick) and a ПТС-19 (PZT-19) piezoceramic disk piezoelement (27 mm in diameter and 0.3 mm thick), rigidly connected to each other by epoxy adhesive ЭД-20, are shown in Fig. 12.8.

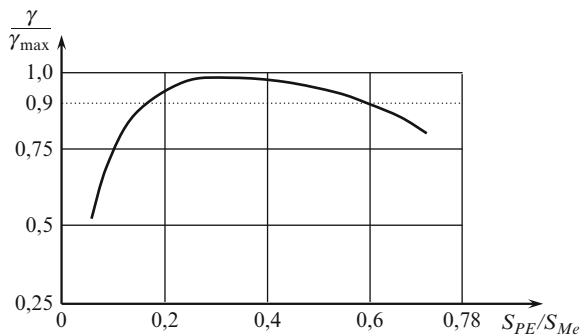
As can be seen from Fig. 12.8, nodal distribution on the transducer surface considerably changes, depending on the way of fastening.

Directional diagrams of this transducer are shown in Fig. 12.9. As it is seen from the figure, various DD forms can be received, depending on the method of fastening and driving frequency.

The number of lateral lobes in the diagram increases with the increase in transducer fastening rigidity.

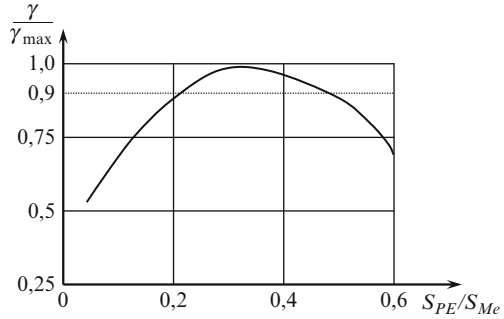
Two and more bimorph transducers should be connected together in a row of technical uses. It is necessary for formation of the required DD in distance and level meters, etc. [19].

Rectangular and triangular transducers are most suitable for this. A. Petrauskas, V. Domarkas, R. Kazhis, A. Vladishauskas, etc., studied rectangular transducers with rectangular piezoelements [13, 20–23]. V.M. Sharapov and S.V. Rotte studied



**Fig. 12.10** Relative sensitivity  $\gamma/\gamma_{max} - S_{PE}/S_{Me}$  ratio curve for rectangular transducer

**Fig. 12.11** Relative sensitivity  $\gamma/\gamma_{\max} - S_{PE}/S_{Me}$  ratio diagram for triangular transducer



rectangular and triangular transducers with round piezoelements [12, 18, 24–26]. If piezoelement PE and metal plate Me thicknesses of these transducers are equal, their sensitivity will depend on  $S_{PE}/S_{Me}$  areas correlation (Figs. 12.10 and 12.11).

Chladni figures for rectangular and triangular transducers are shown in Figs. 12.12 and 12.13, and directional diagrams for rectangular and triangular transducers in Figs. 12.14 and 12.15 respectively.

DD equation of planar rectangular antenna looks like:

$$R_p(\alpha, \vartheta) = \frac{\sin\left(\frac{\pi b}{\lambda} \sin \alpha \sin \vartheta\right) \sin\left(\frac{\pi a}{\lambda} \sin \alpha \sin \vartheta\right)}{\frac{\pi b}{\lambda} \sin \alpha \sin \vartheta \frac{\pi a}{\lambda} \sin \alpha \sin \vartheta},$$

where  $\alpha$  – angle between the radiation direction and the perpendicular to the radiator plane,  $\vartheta$  – angle between the secant plane and the radiation direction, and  $a, b$  – radiator dimensions.

A triangular antenna can be considered rectangular with a side degenerated into a point (Fig. 12.16).

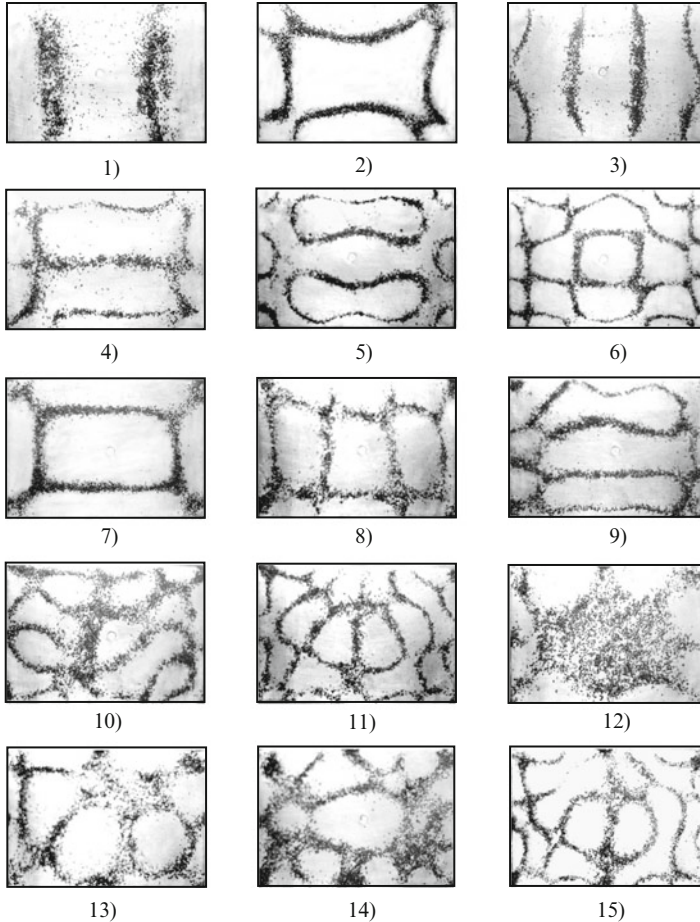
We should also mention that when triangular radiators had the central maximum, lateral lobes in DD in comparison with the rectangular samples were considerably smaller. As a result, triangular radiators should be used in narrow-band radiation equipment.

As can be seen from Fig. 12.7, comparatively narrow central DD lobes can be obtained for triangular transducers.

Volume transducers, made on the basis of rectangular and triangular transducers, are shown in Fig. 12.16, and their directional diagrams in Fig. 12.17. As can be seen from Fig. 12.17, the central lobe of volume transducer DD is even narrower.

## 12.4 Methods of Electro-acoustic Transducer Uprating

Certain methods of electro-acoustic transducers frequency band and sensitivity enhancement are considered below.

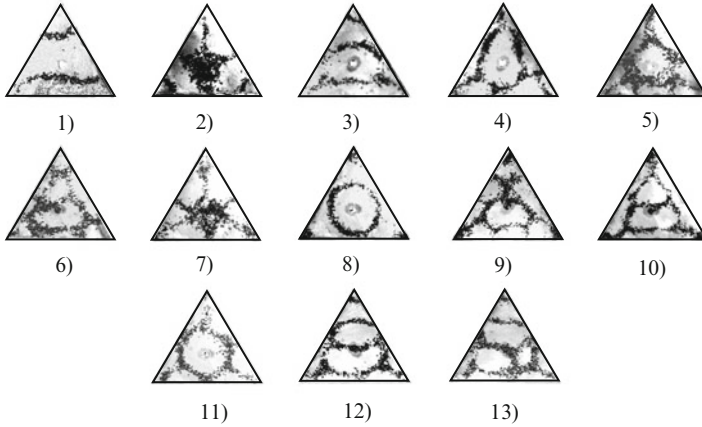


**Fig. 12.12** Nodal distribution when rectangular transducer vibrates: 1–6 (0.42; 1.64; 1.96; 3; 5.2; 6.9 kHz) – transducer is loose; 7–11 (1.64; 3.2; 5.15; 7.35; 8.4 kHz) – fastened at four points, 12–15 (2.1; 3; 4.8; 8.7 kHz) – fastened at eight points

Series connection with resonant electro-mechanical oscillation system (i.e., resistive impedance) is an apparently known method of frequency band enhancement. However, it is connected with the reduction of the pressure level created. Therefore, this method is not considered in this chapter.

Series or parallel connection of LCR chains relative to the transducer is more promising.

As the work [27] by Thurston shows, a piezotransducer with consecutive or parallel inductance can be considered as an electric filter. Its equivalent scheme is represented in Fig. 12.18. The pass-band of the filter, with zero inherent vibration damping, is calculated by using the formula



**Fig. 12.13** Chladni figures for triangular sample with 40 mm side: 1–6 – transducer is loose (1.72; 3.1; 4.1; 5.2; 5.85; 9.2 kHz), 7–10 – fastened at threepoints (2.95; 4.35; 6.3; 9 kHz), 11–13 – fastened at six points (4.9; 6.7; 7.5 kHz)

$$\frac{2\Delta f}{f} \approx \frac{K_t}{\sqrt{1 - K_t^2}}, \quad (12.12)$$

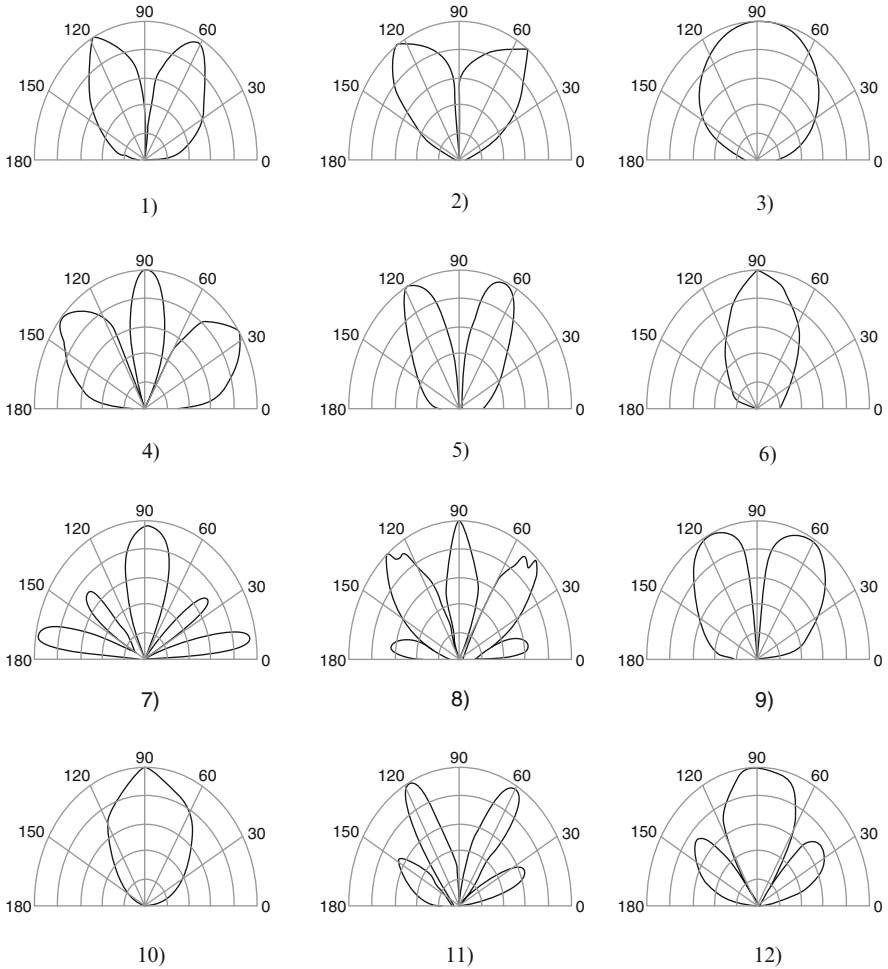
where  $K_t$  is the coefficient of piezoceramic electromechanical communication.

In this case, band enhancement occurs simultaneously with the transfer coefficient increase. As a result,  $R_2$  resistance series connection and further frequency band enhancement are also possible.

It is a well-known fact that the band frequency of two-circuit electro-mechanical oscillation systems is wider than the band of a single-circuit system. Therefore, the frequency band enhancement is possible with series or parallel connection of oscillatory circuit with the transducer. However, as in the previous case, it is connected not only with the energy consumption increase, but also with the considerable dimension increase. To obtain resonant frequencies in the 1–2 kHz range, inductance and capacitance of high values are needed.

For this purpose, application of electromechanical oscillatory systems seems more promising. For example, an air resonator is used for this in transducer  $3\Pi-19$  (see Figs. 12.1c and 12.2).

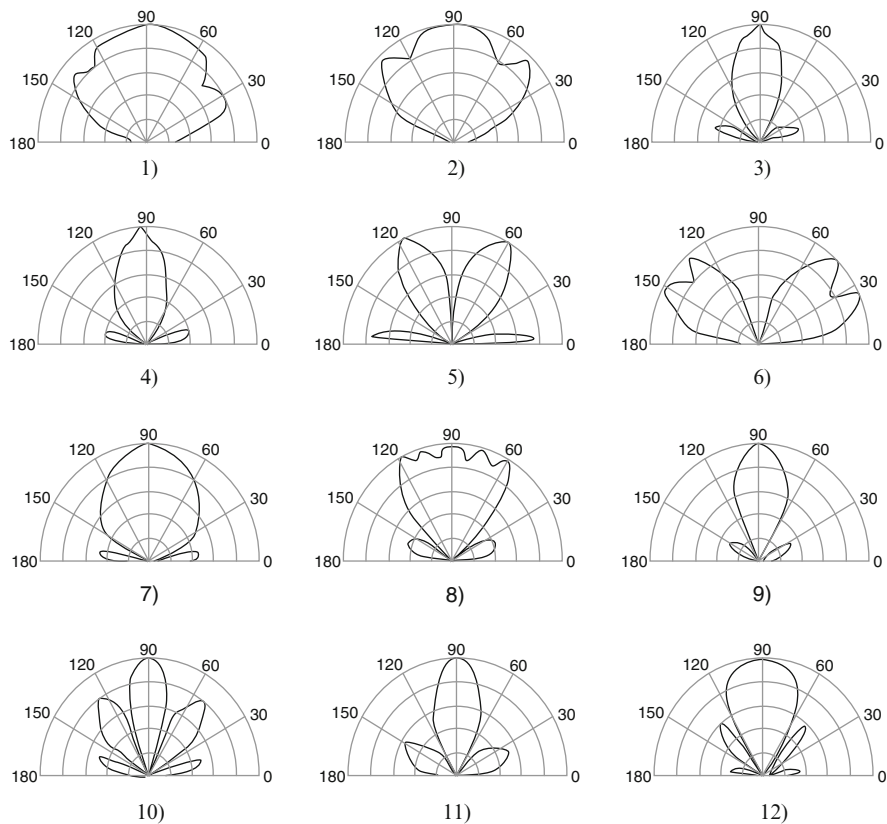
Pinning of the bimorph element in the housing (case) should considerably increase the level of the sound pressure [28]. A design of this transducer is shown in Fig. 12.19. Resonant frequency decrease and sound pressure increase in comparison with  $3\Pi-19$  is explained by the elimination of technological ledge 3 from the bimorph element design (Fig. 12.1c) and consequently the effective radius increase. The bimorph element is fastened in the housing (case) through rubber ring (gasket) 4. As can be seen from Fig. 12.3, this transducer has higher characteristics than  $3\Pi-19$ .



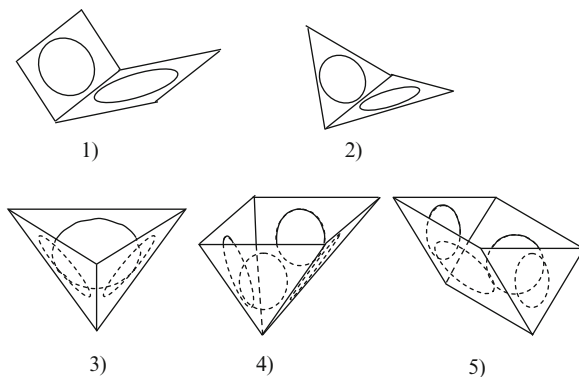
**Fig. 12.14** Directional diagrams of rectangular transducer: 1–4 (1.95; 3.7; 5.03; 6.62 kHz) – transducer is loose; 5–11 (2.42; 3.3; 5.55; 7.8; 8.6 kHz) – fastened at four points; 12–14 (2.2; 3.18; 7.55 kHz) – fastened at eight points

Low frequencies of the frequency band are enhanced if the additional contour resonant frequency is lower than the bimorph element resonant frequency. It is hard to implement this practically because of the rigid dimensional requirements. The transducer resonant frequency cannot be lower than a certain value, determined by the bimorph element diameter under other conditions.

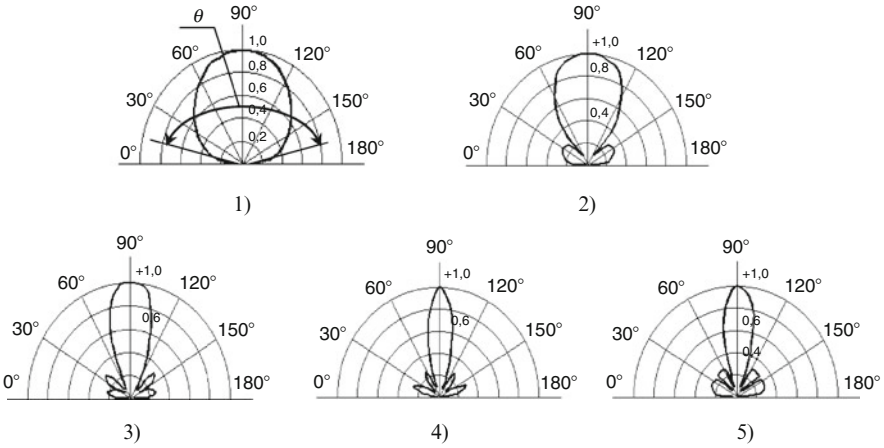
Meanwhile, lower frequency bands are required in a number of technical applications. For example, the frequency band in diaphragm cases and ear caps is normalized. It is 300–3,000 Hz.



**Fig. 12.15** Directional diagrams of triangular transducer: 1–6 (2.96; 4.05; 6.21; 6.6; 7.2; 8.62 kHz) – transducer is loose; 7–9 (2.95; 4.35; 5.6 kHz) – fastened at three points; (completion): 10–12 (2.34; 2.65; 3.46 kHz) – fastened at six points

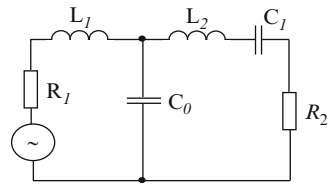


**Fig. 12.16** Volume transducers, made on the basis of bimorph piezoceramic transducers, connected among themselves as: two rectangular (1) and triangular (2) transducers; trihedral (3) and tetrahedral (4) pyramids; prisms (5)

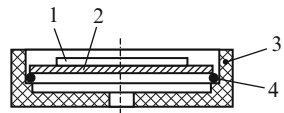


**Fig. 12.17** Directional diagrams of volume transducers, shaped as: two rectangular (1) (11.65 kHz) and triangular (2) (11.03 kHz) transducers; trihedral (3) (11 kHz) and tetrahedral (4) (11.5 kHz) pyramids; prisms (5) (11.6 kHz);  $\theta$  – opening angle of the basic lobe

**Fig. 12.18** Equivalent scheme of electro-acoustic transducer with consecutive close-in  $R_2L_2$



**Fig. 12.19**  $\ominus\Pi$ -3 transducer design: 1 – piezoelement, 2 – metal plate, 3 – housing (case), 4 – rubber ring (gasket)



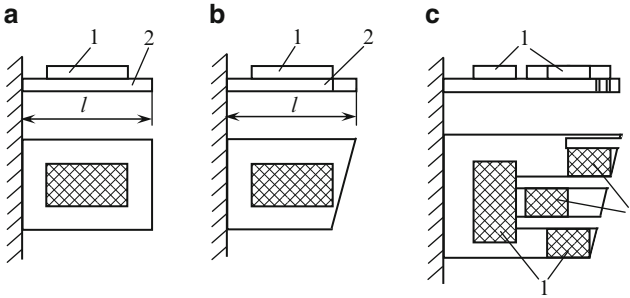
Fastening additional inertia masses on the bimorph element reduces resonant frequency. However, the sensitivity decreases also.

Bimorph piezoelements with console fastening should be used for transducer resonant frequency decrease. As is known [29], bending of these transducers is considerably greater, and resonant frequency is much lower, than of the disk transducers. Combining flexural elements of various types in one construction, the required resonant characteristic can be created.

Some console bimorph elements designs are represented in Fig. 12.20. Their amplitude–frequency characteristics are shown in Fig. 12.21.

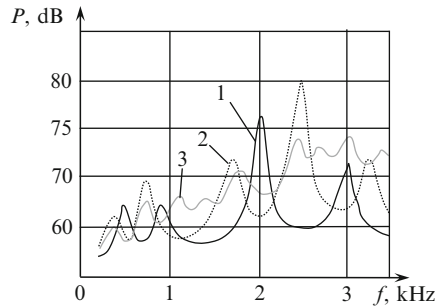
As can be seen from Fig. 12.21, electro-mechanical oscillations at 300–400 Hz frequencies can be started if console elements are used. Use of a variable length console (Fig. 12.20b) enhances the frequency band. Transducer broadbandness grows if three consoles of variable length are positioned on its basic console. Four parallel connected piezoelements are used here (Fig. 12.20c).





**Fig. 12.20** Console bimorph elements: 1 – piezoelement, 2 – metal plate

**Fig. 12.21**  
Amplitude–frequency characteristics of console bimorph piezoelements: 1 – Fig. 12.20a, 2 – Fig. 12.20b, 3 – Fig. 12.20c



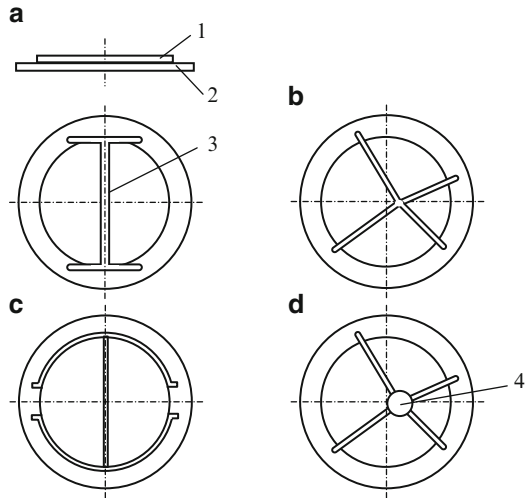
Some more console bimorph elements are shown in Fig. 12.22. An asymmetric disk bimorph piezoelement used in transducer  $\Theta\Pi-2$  is taken here as a base. The transducer is sectioned on a laser cutting device as shown in Fig. 12.22a,b. In this transducer the internal part of the bimorph element, shown in Fig. 12.22c, is cut out in the form of semi-disks. They are fastened into the bimorph by two necks [21]. The following flexural electro-mechanical oscillations can arise in this transducer: of the whole bimorph element, of the disk cutout, and also of the semi-disk-shaped consoles. This amplitude–frequency characteristic of the transducer is shown in Fig. 12.23. As this figure shows, console elements use makes it possible to enhance lower frequencies of the band.

A transducer with sectored bimorph element has an even wider low frequency band. However, then the pressure level at resonant frequency of disk flexural vibrations becomes lower (Fig. 12.23b).

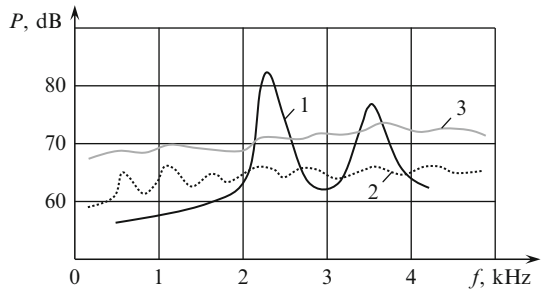
For AFC increase at this frequency and corrective equalization (Fig. 12.23, a curve 3) the sector tops are spring-linked, for example, with a rubber disk, shown in Fig. 12.22d.

The design of a transducer consisting of two bimorph elements of membrane and console types (Fig. 12.24), is developed. Both bimorph elements are pinned into the housing (case) by rubber rings (gaskets) 3.

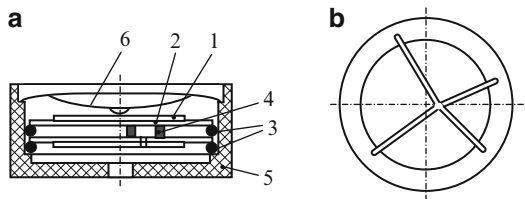
**Fig. 12.22** Variants of console bimorph piezoelements: 1 – piezoelement, 2 – metal plate, 3 – cut, 4 – rubber disk



**Fig. 12.23** Transducer amplitude–frequency characteristic: 1 – 3Π-19, 2 – transducer in Fig. 12.22b, 3 – same with 5 mm rubber disk in diameter (Fig. 12.22d)



**Fig. 12.24** Designs of 3Π-4 transducer (a) and bimorph element (b): 1 – piezoelement, 2 – metal plate, 3 – rubber rings (gaskets), 4 – rubber bosses, 5 – housing (case), 6 – diffuser

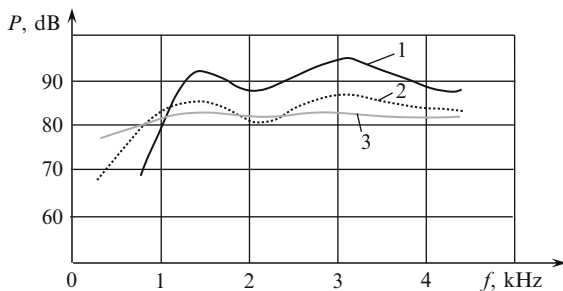


One of the bimorph elements is continuous disk-shaped 1, and the other (2) is sliced as shown in Fig. 12.24b. As a result, four console elements with resonant frequencies in 600–1,500Hz appeared.

The console bimorph elements are interconnected by rubber bosses 4Ø1.5 × 2 mm. The bosses represent frequency-dependent loose inter-linking between the bimorph elements. This allows enhancement of the general transducer low frequency characteristic (Fig. 12.25).

AFC was measured on an acoustic stand by ИШВ – 1 noise meter. The cut at low frequencies can be raised by an amplifier. It is impossible to do this with

**Fig. 12.25**  
Amplitude–frequency  
characteristic: 1 –  $\Theta\Pi$ -3, 2 –  
 $\Theta\Pi$ -4 without the diffuser,  
3 –  $\Theta\Pi$ -4 with the diffuser



the majority of the phones used, as there are no amplifiers in many of them. This correction is not supported by the design of phones with amplifiers either.

Diffuser 6, made of acetyl cellulose 0.2 mm thick, is introduced into the transducer design (Fig. 12.24a) for low frequency characteristic enhancement (Fig. 12.25, curve 3).

As was mentioned earlier, flexural vibrations arise in the designs of the bimorph transducers considered because of the following: anisotropy of the design element properties and electrodes and glue layers, connecting the piezoelement with the metal membrane [Chap. 9, p. 78, Fig. 2.12].

However, there are other methods of flexural vibration creation [29, 30]. In particular, the following methods can be used in the given bimorph element design for flexural vibration creation: creation of shear stress, creation of compression and stretching areas within a piezoelement plane, use of domain-dissipative piezoelements (see Chap. 3). Linear AFC can be received in the latter case. However, the sound pressure level will then decrease.

## 12.5 Electro-acoustic Transducers in Active Oscillator Schemes

In this case narrow-band EAT, activated at resonant frequency, can be used.

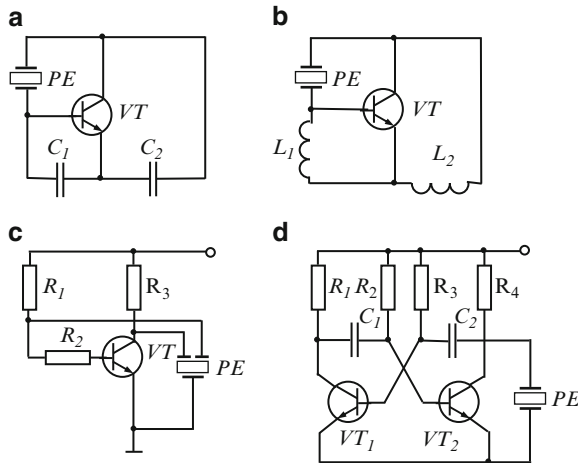
Some schemes of transducer activation are shown in Fig. 12.26. Among these schemes, Colpitts schemes, known for their simplicity and efficiency, are of the greatest interest (Fig. 12.26a, c).

The choice of bimorph piezotransformer dimensions and form is important for a Colpitts transformer scheme.

As is known, for active oscillator activation the following condition should be observed

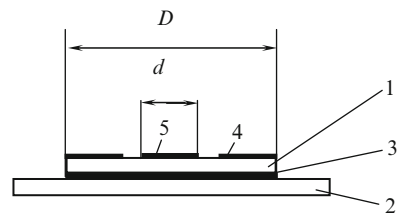
$$K_{AM}K_{FB} \geq 1,$$

where  $K_{AM}$ ,  $K_{FB}$  are complex coefficients of amplifier transfer and feedback circuit,  $K_{REV}$ , i.e., of the bimorph piezotransformer.



**Fig. 12.26** Schemes of electro-acoustic transducers activation: (a) Colpitts scheme, (b) Hartley scheme, (c) Colpitts transformer scheme, (d) multi-vibrator scheme

**Fig. 12.27** Bimorph piezotransformer: 1 – disk piezotransformer, 2 – metal plate, 3 – disk-shaped bottom electrode, 4 – ring electrode, 5 – disk electrode



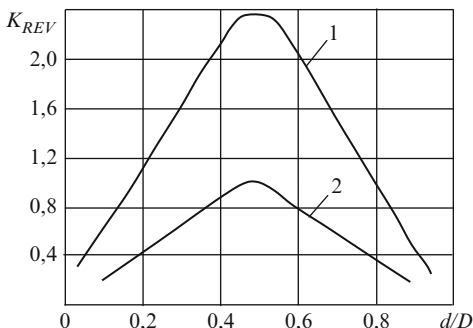
$K_{REV}$  transfer coefficient increase is desirable. This enhances the transitional process, permits amplifier scheme simplification and decreases power inputs.

Bimorph piezotransformers consist of a piezotransformer and a metal plate. Disk piezoelements with two systems of electrodes are used in most cases. A disk electrode is positioned from one piezoelement side, while a ring and a disk is positioned from the other (Fig. 12.27). Flexural vibrations are created in bimorph piezotransformers.

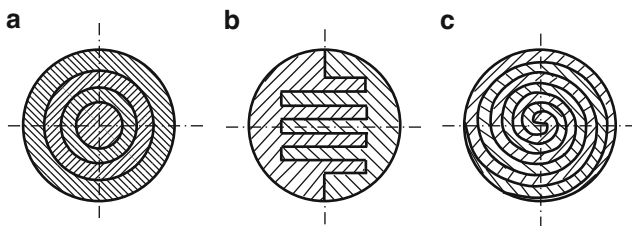
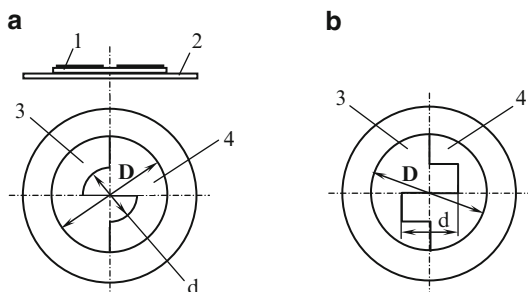
$K_{REV}$  dependence on  $d/D$  relation of the bimorph piezotransformer (Fig. 12.27) is shown in Fig. 12.28. As is seen from this figure, the greatest transfer coefficient is obtained when the piezotransformer is activated from the ring electrode (curve 1) and the disk electrode  $d$  diameter – the outside diameter  $D$  ratio equals  $d/D = 0.5$ . If the bimorph piezotransformer is activated from the disk electrode,  $K_{REV}$  is almost twice lower than in the previous case.

Piezotransformer idling is obviously desirable for an active oscillator with a piezotransformer in a feedback circuit (FC). This assures minimal power inputs in FC, i.e., minimum expenditures of energy in FC (i.e., minimum energy consumption, not connected with the transducer acoustic radiation).

**Fig. 12.28** Dependence of bimorph piezotransformer  $K_{REV}$  transfer coefficient on  $d/D$  ratio: 1 – generator connected to the ring electrode, 2 – generator connected to the disk electrode



**Fig. 12.29** Electro-acoustic transducer with piezoelement with separate electrodes: 1 – piezoelement, 2 – membrane, 3, 4 – electrodes



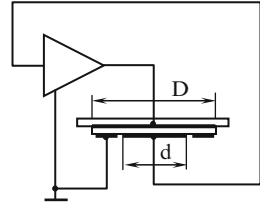
**Fig. 12.30** Topology of piezotransformer electrodes when flexural vibrations are created: (a) concentric circle- and disk-shaped, (b) comb-shaped, (c) spiral-shaped

This can be achieved by increase of the amplifier input resistance or by decrease of the piezotransformer output resistance.

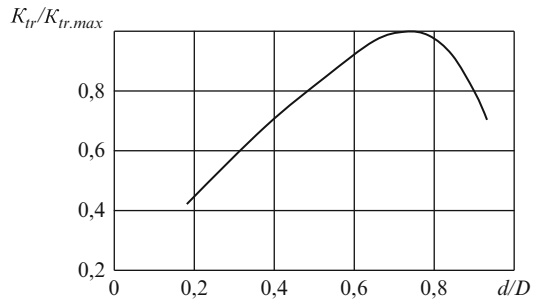
However, we should mention here that to reach maximum sound pressure the following known condition should be observed: the amplifier output resistance should equal the transducer input resistance.

As has been established experimentally [31], these contradictory requirements can be satisfied if electrodes from a piezoelement side are symmetric. There should be ledges on the central part of each electrode. These ledges should enter the hollows of the second electrode (Fig. 12.29). A disk-shaped electrode should be attached to the other piezoelement side. These electrode position allows the reception of the maximum transfer coefficient if the capacitances of input and output electrodes are equal. For example, the transfer coefficient of this transducer in a transformer

**Fig. 12.31** Switching of bimorph transducer in active oscillator scheme



**Fig. 12.32** Dependence of relative transfer coefficient on  $d/D$  for transducer in Fig. 12.31



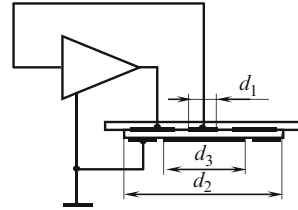
mode is approximately (sample of 30 transducers) three times higher than the of a transducer with semi-disk-shaped electrodes. It approximately equals the transfer coefficient of CB 35BBK transducer made by Taiyo Yuden Co, Ltd (Fig. 12.1d); it should be activated from the bigger electrode. However, the output resistance of the transducer developed is approximately ten times less than the similar characteristic of CB 35BBK transducer.

This transducer design allows effective activation of practically 100% of transducers, despite their parameters being spread in serial production.

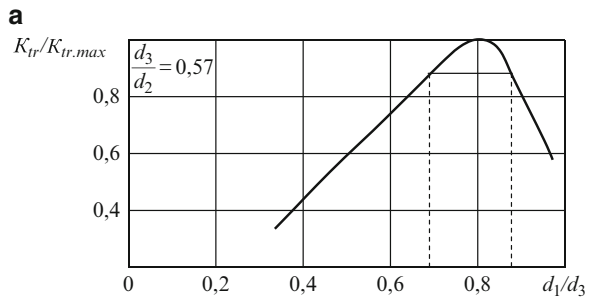
We should also notice that because of the importance of the piezoelement diameter–thickness ratio for effective introduction of positive feedback along the whole piezoelement, electrode topology on the piezoelement should be made in the form of concentric circles, combs and spirals (Fig. 12.30). To conclude this section, we will consider certain designs of bimorph piezotransformers which ensure a high transformation coefficient, and also their schemes for switching an active oscillator. The first design (Fig. 12.31) consists of a membrane and a disk piezotransformer with disk- and ring-shaped electrodes from one side, and a disk electrode from the other. However, the amplifier output of the active oscillator is connected to the big disk electrode, the amplifier input to the small diameter disk electrode, and the amplifier common wire to the disk electrode. Thus, the transfer coefficient of the piezotransformer is increased approximately 1.3 times. As the experiments showed, there is also an optimum  $d/D$  value ratio for this case (Fig. 12.32).

An even greater transfer coefficient is received for the transducer represented in Fig. 12.33. There are electrode size correlations when the transfer coefficient reaches its maximum (Figs. 12.34 and 12.35).

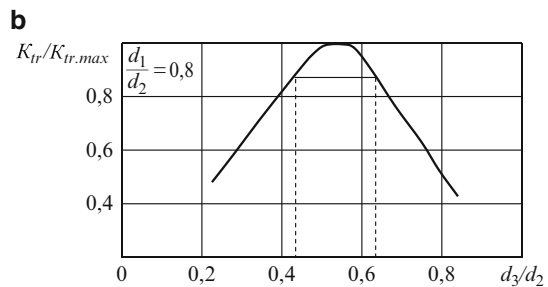
**Fig. 12.33** Switching of bimorph transducer in active oscillator scheme



**Fig. 12.34** Dependence of relative transfer coefficient for transducers: in Fig. 12.33 on  $d_1/d_2$  ratio with  $d_3/d_2 = 0.57$



**Fig. 12.35** Dependence of relative transfer coefficient for transducers: in Fig. 12.33 on  $d_3/d_2$  ratio with  $d_1/d_2 = 0.8$



## References

1. A.A. Gorbatov, G.E. Rudashevskiy, *Acoustic Methods of Distance Measurement and Control* (Energoizdat, Moscow, 1981), p. 208 (in Russian)
2. J. Coulthard, Ultrasonic sensing of objects in gaseous media. *Ultrasonics* **6**(3), 167–174 (1968)
3. D.A. Gershgal, V.M. Fridman, *Ultrasonic Equipment* (Gosenergoizdat, Moscow, 1961) (in Russian)
4. N.A. Kallistratova, Research method of sound scattering in atmosphere. *Acoustic Mag.* **4**, 496–498 (1959) (in Russian)
5. L.C. Lynnworth, Ultrasonic impedance matching from solids to gases. *IEEE Trans. Sonics Ultrasonics* **SU-12**, 2 (1965)
6. V.B. Aranovich, I.A. Prudov, Patent of USSR 251970. Ultrasonic radiator (in Russian)
7. V.B. Aranovich, I.A. Prudov, On resonant matching in thin transitive layers. *Acoustic Mag.*, **17**, 4 (1971) (in Russian)
8. I.A. Prudov, G.A. Shehovtsov, Acoustic radar profilograph 3ПП-2Н for shooting of inaccessible steeply falling rooms. *Nonferrous Met.* **8**(301) (1966) (in Russian)
9. I.P. Golyamina (ed.), *Ultrasound (Small Encyclopedia)* (Soviet Encyclopedia, Moscow, 1979), p. 400 (in Russian)

10. A.P. Evtyutov, V.B. Mitko, *Engineering Calculations in Hydroacoustics* (Sudostroenie, Leningrad, 1988), p. 234 (in Russian)
11. V.M. Sharapov et al., Study of round and oval asymmetric bimorph piezoelectric transducers. *Visnyk ChITI* **1**, 45–49 (2001) (in Russian)
12. V.M. Sharapov et al., Study of rectangular asymmetric bimorph piezoelectric transducers. *Visnyk ChITI* **2**, 18–22 (2001) (in Russian)
13. V. Domarkas, A. Majonas, A. Petrauskas, Study of directional characteristics of piezotransducer flexural vibrations. Proceedings of the Lithuanian Soviet Socialist Republic Educational Institutions. *Ultrasound* **15**, 48–51 (1983) (in Russian)
14. A.E. Kolesnikov, *Acoustic Measurements* (Standards Publishing House, Moscow, 1983), p. 292 (in Russian)
15. V. Domarkas, R.J. Kazys, *Piezoelectric Transducers for Measuring Devices* (Mintis, Vilnius, 1974), p. 258 (in Russian)
16. N.A. Shulga, A.M. Bolkisev, *Vibrations of Piezoelectric Solids* (Naukova Dumka, Kiev, 1990) (in Russian)
17. S.I. Rudnitskiy, V.M. Sharapov, N.A. Shulga, Vibrations of disk bimorph transducer of metal–piezoceramic type. *Appl. Mech.* **T26**(10), 64–72 (1990) (in Russian)
18. V.M. Sharapov et al., Study of triangular asymmetric bimorph piezoelectric transducers. *Visnyk ChITI* **4**, 39–43 (2000) (in Russian)
19. A.P. Evtyutov, A.E. Kolesnikov, E.A. Korepin et al., *Hydroacoustics Handbook* (Sudostroenie, Leningrad, 1988), p. 552 (in Russian)
20. A. Vladisauskas, Study of flexural vibrations of piezotransducers with variable cross-section. Proceedings of the Lithuanian Soviet Socialist Republic Educational Institutions. *Ultrasound* **12**, 89–96 (1980)
21. V. Domarkas, A. Petrauskas, Bimorph piezoceramic transducers for measurements in gas environments. Proceedings of the Lithuanian Soviet Socialist Republic Educational Institutions. *Ultrasound* **10**, 55–64 (1978) (in Russian)
22. A. Petrauskas, V. Domarkas, Designs of Ultrasonic Bimorph Transducers. Abstracts of XX II Scientific–Technical and Scientifically–Methodological Conference of Taganrog Radio Engineering Institute, Taganrog (1972) (in Russian)
23. A. Petrauskas, V. Domarkas, Work features of rectangular bimorph electro-acoustic transducers with free edges. Proceedings of Higher Educational Institutions of the Lithuanian Soviet Socialist Republic. *Ultrasound* **6**, 103–107 (1974) (in Russian)
24. V.M. Sharapov, S.V. Rotte, Patent of Ukraine No 53211. Piezoelectric sensor (2003) (in Ukrainian)
25. V.M. Sharapov, S.V. Rotte, Patent of Ukraine No 53953. Piezoelectric sensor (2003) (in Ukrainian)
26. V.M. Sharapov, M.P. Musienko, E.V. Sharapova, in *Piezoelectric Sensors*, ed. by V.M. Sharapov (Technosphaera, Moscow, 2006), p. 632 (in Russian)
27. R. Thurston, Effect of electrical and mechanical terminating resistance on loss and bandwidth according to the conditional equivalent circuit of a piezoelectric transducer. *IRE Transact. Ultrasonics. Eng.* **1** (1960)
28. V.M. Sharapov (ed.), *Piezoelectric Transducers (Handbook)* (Cherkasy State Technological University, Cherkassy, 2004), p. 435 (in Russian)
29. R.G. Dzagupov, A.A. Erofeev, *Piezoelectronic Devices in Computing Machinery, Monitoring Systems and Control* (Politehnika, St. Petersburg, 1994), p. 608 (in Russian)
30. P.E. Kandyba, P.G. Pozdnyakov (ed.), *Quartz Resonators. Directory*, (Energoizdat, Moscow, 1989), p.374 (in Russian)
31. V.M. Sharapov et al., Patent of RF No 2003238. Electro-acoustic transducer, N41–42 (1993) (in Russian)



# Chapter 13

## Piezoceramic Accelerometers

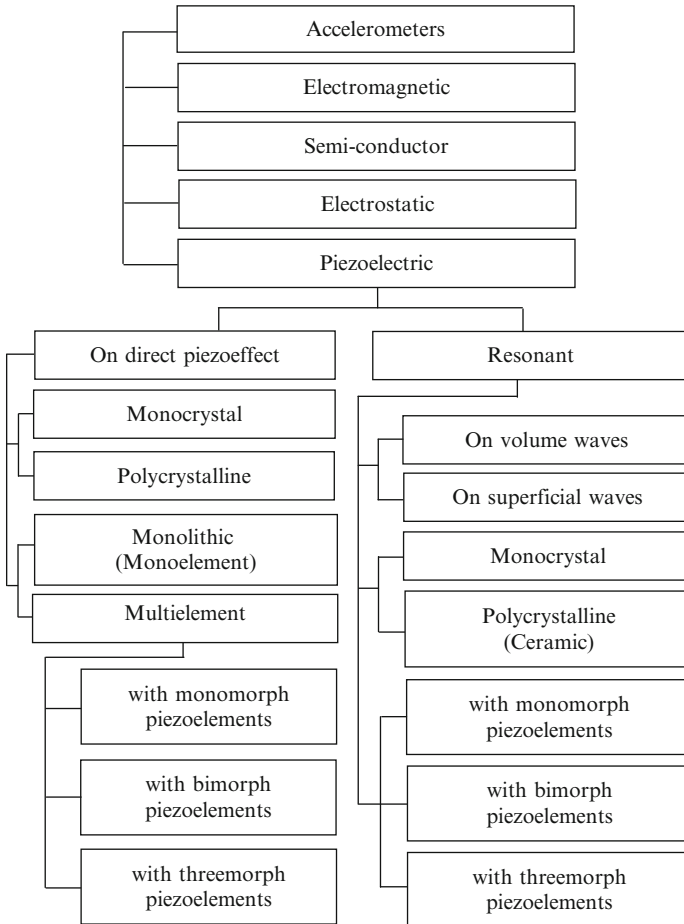
Piezoceramic accelerometers are sensors for measurement of vibration parameters and impacts. These accelerometers together with semiconductor sensors dominate other transducers based on different physical principles [1]. Piezoelectric accelerometers have:

- A rather wide work frequency range
- Linear characteristic in a wide dynamic range
- Output electric signal, proportional to vibration acceleration. This signal can be electrically transformed into a signal proportional to vibration velocity or vibration displacement
- High resistance to environmental influences and high precision even in difficult environments
- Active transducer character which does not require a power supply
- No moving details, guaranteeing exclusive durability
- A possibility of designing compact transducers and a high value of sensitivity–dead load ratio

A sensitive element (sensor) of any accelerometer usually consists of a piezoelement, inertia mass and a resilient member. The sensitive element is usually positioned in the housing (case) which may consist of a base and a cover, a built-in amplifier and a socket for cable connection. The sensitive element discussed will be called multi-element (or polymorphic) [1–3].

However, there are accelerometers in which the piezoelement, inertia mass, resilient member and base consist of a monolithic piezoelectric block [4, 5]. This accelerometer is called monolithic or monomorph.

Considering the things discussed, the following accelerometer classification (Fig. 13.1) is proposed: (1) monolithic and multi-element (depending on the number of elements used), (2) direct piezoeffect and resonance (depending on the type of the piezoeffect used), (3) volume waves and surface acoustic waves (SAW) (wave modes), and (4) monocrystal and piezoceramic (the type of piezoelectric material used). Multi-element accelerometers can consist of monoelement piezoelements (one or several), bimorph and trimorphic piezoelements.



**Fig. 13.1** Classification of accelerometers

Accelerometers based on other physical effects are shown in the classification in Fig. 13.1.

### 13.1 Monolithic Accelerometers

As has been discussed, piezoelectric accelerometers are usually produced in the form of fabricated designs. They consist of different interconnected separate elements.

Use of various constructional materials, and also mechanical connections which are insufficiently stable and difficult to control, negatively affect the stability and

repeatability of accelerometer data. High-quality processing of contact surfaces, surface finish in assembly and adjustment makes them more expensive.

Piezoelectric accelerometers designs without the drawbacks mentioned were created because of a piezoceramics attribute to become only partly piezoelectric when biased by electric field in the polarization process, and because of the suitability of piezoceramics for creating irregular-shaped products. In some cases multi-element designs were replaced by a monolithic piezoceramic block. Its various areas perform functions of basic accelerometer work elements – base, piezoelectric element and inertia mass [4, 5].

Two designs of monolithic accelerometers – of rectangular and cylindrical form (Fig. 13.2) – are described in [4, 5].

These accelerometers consist of polarized areas between the electrodes, positioned on the internal surface apertures of the monoceramic block. The non-polarized part of the block, located over the polarized part, is the inertia mass.

The advantages of these accelerometers are their design simplicity and high resonant frequency. The disadvantage is their considerable lateral sensitivity.

The transducer described in [4], also has a rather complicated design and a quite high transverse sensitivity, changing along the azimuth. It is caused by the accelerometer design asymmetry.

A cylinder-shaped monolithic accelerometer [5] with a simpler design than the rectangular-shaped monolithic accelerometer design is still considered quite complicated because of the conic apertures on the cylindrical surface.

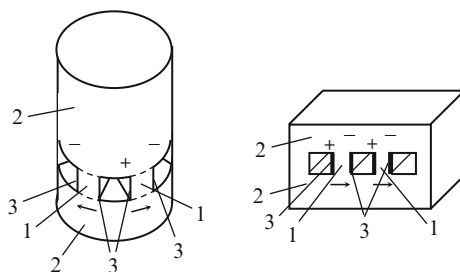
We should also note that it is necessary to attach electrodes in the conic apertures mentioned and polarize the piezoceramics between the electrodes.

A design of a monolithic cylinder-shaped accelerometer without conic apertures is proposed. Its electrodes are located on the cylindrical surface (Fig. 13.3).

This simpler design also allows change to the sensitivity of accelerometer charge at the cost of electrode width.

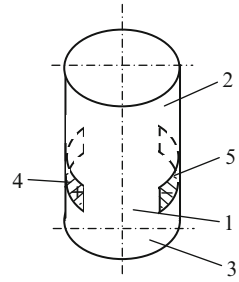
The monolithic accelerometers represented in Figs. 13.2 and 13.3 have essential transverse sensitivity because of their design asymmetry. In the latter case, it is the asymmetry of electrode arrangement and therefore, of the accelerometer polarized zones.

A monolithic accelerometer has better specifications. It is cylinder-shaped with disk electrodes at the ends (Fig. 13.4) [6].

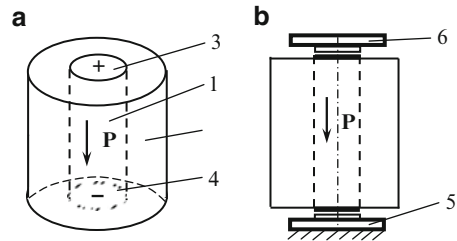


**Fig. 13.2** Monolithic accelerometers: 1 – polarized part, 2 – non-polarized part, 3 – electrodes

**Fig. 13.3** Monolithic accelerometer: 1 – polarized zone, 2 – non-polarized zone (inertia mass), 3 – non-polarized zone (base), 4, 5 – electrodes



**Fig. 13.4** Monolithic accelerometer: (a) sensitive element design, (b) sensitive element fastening: 1 – polarized zone, 2 – non-polarized zone, 3, 4 – electrodes, 5 – base, 6 – fastening



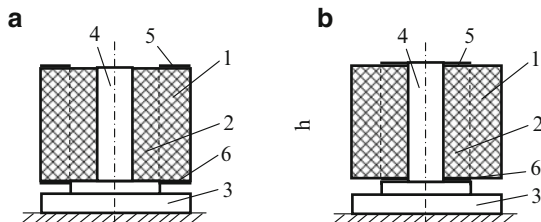
This accelerometer is attached to the base, as shown in Fig. 13.4b. The non-polarized cylinder part tends to displacement relative to the polarized part under the influence of acceleration along the accelerometer axis. It creates voltage and deformations, respectively, on the border with the polarized zone. As a result, an electric charge, proportional to acceleration, is created in the polarized zone. Heteropolar charges at the piezoelectric cylinder ends are created under the acceleration action, perpendicular to the accelerometer axis. As a result, the accelerometer has zero transverse sensitivity. The design becomes more complex as the accelerometer should be fastened in the piezoelement electrode field. This demands isolation of an attachment element from the housing (case). It also reduces the dynamic range of measurement.

The majority of these drawbacks can be overcome if the piezoelement has a hollow cylinder form. Two variants of a monolithic accelerometer design with a hollow ceramic cylinder are shown in Fig. 13.5 [7, 8].

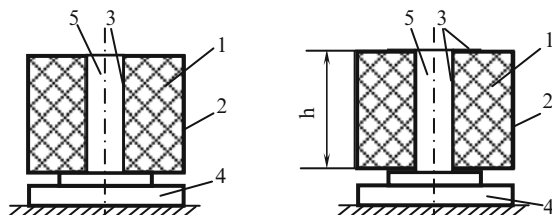
The external cylinder part is polarized in the first case (Fig. 13.5a), while non-polarized zone 2 is supported by base 3. In this case, the external part is simultaneously both piezoelement and inertia mass. This reduces requirements to cylinder fastening to the base.

In the second case (Fig. 13.5b) the internal part is polarized, and the external non-polarized part is inertia mass.

Use of transverse piezoelements in monolithic accelerometers design is more scientifically interesting (see Chap. 3). The polarization and acceleration vectors are perpendicular in them.



**Fig. 13.5** Monolithic accelerometer with hollow ceramic cylinder: (a) polarization of cylinder external part, (b) internal part polarization: 1, 2 – polarized and non-polarized zones respectively; 3 – base, with cylindrical ledge 4; 5, 6 – electrodes



**Fig. 13.6** Monolithic accelerometer with hollow piezoceramic cylinder: 1, 2 – cylindrical piezoelement, 2, 3 – electrodes, 4 – base, with cylindrical ledge 5

An example of monolithic accelerometer with transverse piezoelement is shown in Fig. 13.6.

A design of a monolithic accelerometer with a transverse hollow cylinder-shaped piezoelement, polarized along the radius, is shown in Fig. 13.6a [9].

In this case the whole cylinder is a piezoelement. The cylinder external part is simultaneously its inertia mass. In addition, a part of the cylinder end surface, supported by the base, compresses. This results in the generation of an additional signal, influencing the accelerometer output signal.

To reduce this influence on the accelerometer shown in Fig. 13.6b, electrodes are attached to the cylinder parts used for fastening. These electrodes are connected between themselves and with the housing (case).

The cylindrical accelerometer sensitivity [10]

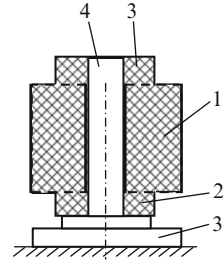
$$S = \frac{Q_x}{F_y} = \frac{2}{\pi} d_{11} \frac{h}{a},$$

where:  $Q_x$  – charge;  $F_y$  – force, influencing piezoelement;  $d_{33}$  – piezomodule;  $h$ ,  $a$  – height and thickness of cylinder wall.

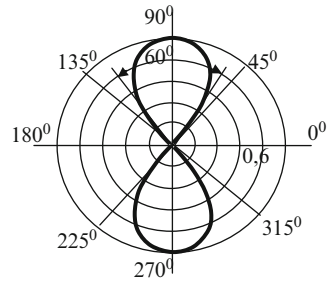
The same problem can be solved in an accelerometer with a more complex-shaped sensitive element (Fig. 13.7) [11, 12].

A monolithic ceramic cylinder-shaped block is the sensitive element of the accelerometer. It has a radius polarized zone, shaped like a big diameter cylinder, and non-polarized zones, shaped like smaller diameter cylinders.

**Fig. 13.7** Monolithic accelerometer with compound ceramic cylinder: 1, 2 – polarized and non-polarized zones respectively, 3 – base, with cylindrical ledge 4



**Fig. 13.8** Directional diagram of accelerometer in Fig. 13.7



Axial sensitivity of this accelerometer is proportional to the height of the polarized cylinder part. It has a quite high resonant frequency, determined by the diameter of the polarized part.

The directional diagram of this accelerometer is shown in Fig. 13.8. As can be seen from the figure, its transverse sensitivity equals zero. The directional diagram (on acceleration) was made by 4805 vibro stand and 2650 preamplifier by Brüel and Kjer. In Fig. 13.8 and in all subsequent figures, the directional diagram is made under the normalized acceleration  $1 g$  ( $9.81 \text{ m/s}^2$ ) influence at 100 Hz frequency.

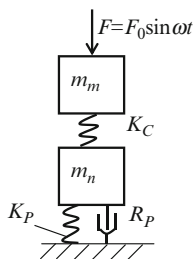
## 13.2 Multi-element Accelerometers

As mentioned above, accelerometers with one or several piezoelements, inertia masses, resilient elements, base [housing (case)], etc., can be called multi-element. In some cases the piezoelement is rigidly glued, soldered or screwed to its inertia mass and base.

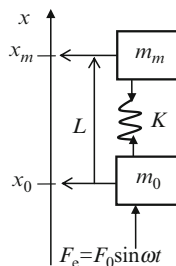
A mechanical model of a multi-element piezoelectric accelerometer is shown in Fig. 13.9.

A piezoelectric accelerometer usually [2] consists of two-circuit vibration systems. One of them replaces the piezoelement where  $m_p$  is piezoelement mass,  $K_p$  is piezoelement material elasticity and  $R_p$  is piezoelement losses. The second consists of inertia mass  $m_m$ , a piezoelement and inertia mass connection elasticity  $K_c$ . The vibration action is represented as harmonic force, applied to inertia mass (Fig. 13.9).

**Fig. 13.9** Traditional mechanical model of piezoelectric accelerometer



**Fig. 13.10** Specified mechanical model of piezoelectric accelerometer



In this model the piezoelement base mass and object fastening elasticity are not considered. And finally, not only inertia mass but also the base are influenced by shaking force.

The specified accelerometer mechanical model, consisting of a piezoelement and inertia mass, attached to the piezoelement, is shown in Fig. 13.10.

This is a degree of freedom (DOF) model. It contains two masses, interconnected by an ideal resilient element.  $m_m$  and  $m_0$  are dead loads of inertia and base masses, while  $K$  is piezoelement (piezoelements) equivalent rigidity. This approach to a piezoelectric accelerometer working in the pre-resonance area is reasonable [12]. In addition, as the piezoelement rigidity is considerably higher than contact rigidity or glue connection rigidity, the latter two will not be considered. The other parameters denoted in Fig. 13.10 are:  $x_m$  and  $x_0$  – movements of inertia mass and base respectively;  $L$  – distance between the centre of gravity and the base;  $F_e$  – harmonious driving force;  $F_0$  – amplitude of harmonious driving force;  $\omega$  – angular frequency of this driving force;  $\omega = 2\pi f$ .

Considering the forces influencing the accelerometer elements, the following equations can be written:

Force influencing the resilient element

$$F = k(x_m - x_0 - L); \tag{13.1}$$

Force influencing the accelerometer base

$$m_0 \ddot{x}_0 = F + F_e; \tag{13.2}$$

Force influencing inertia mass

$$m_m \ddot{x}_m = -F, \quad (13.3)$$

where  $\ddot{x}_m = d^2x_m/dt^2$ .

The movement of the model elements shown in Fig. 13.10 is determined by the equation:

$$\ddot{x}_m - \ddot{x}_0 = -\frac{F}{m_m} - \frac{F + F_e}{m_0} = -\frac{k}{\mu}(x_m - x_0 - L) - \frac{F_e}{m_0} \quad (13.4)$$

or

$$\mu \ddot{r} = -kr - \frac{\mu}{m_0} F_0 \sin \omega t,$$

where  $1/\mu = 1/m_m + 1/m_0$ , whence  $\mu = m_m m_0 / m_m + m_0$  – reduced mass of the accelerometer;  $r = x_m - x_0 - L$  – inertia mass movement relative to the accelerometer base.

Coordinate  $r$  selection allowed the smaller number of motion equations for two-mass vibration system.

In cases where the accelerometer is not fastened to the object and is not subject to external force actions ( $F_e = 0$ ) the equation of natural vibrations will look like:

$$\mu \frac{d^2 r}{dt^2} = -kr. \quad (13.5)$$

Equation  $\ddot{r} + (k/\mu)r = 0$  is a harmonic vibration equation. Its solution is  $r = R \sin(\omega_a t + \phi)$ .

Whence the frequency of the accelerometer's own vibrations, i.e., its resonant frequency is:

$$\omega_a = \sqrt{\frac{k}{\mu}}$$

or

$$\omega_a^2 = k \left( \frac{1}{m_m} + \frac{1}{m_0} \right). \quad (13.6)$$

If the accelerometer is ideally rigidly fastened to the object one can assume that the base mass increases. This leads to an important practical conclusion: resonant frequency of the accelerometer fastened to the object decreases.

If the object mass is rather large, one can consider that  $m_0 \gg m_m$ . Then:

$$\omega_a^2 \approx \frac{k}{m_m}.$$

One can conclude that it is in practice necessary to tend to make the accelerometer mass  $m_m$  considerably smaller than the object mass  $m_0$  to which the accelerometer is fastened.



The resonant frequency of the fastened accelerometer decreases with the decrease in object rigidity and the increase in compliance of the fastening device, ensuring mechanical connection between the accelerometer base and the object studied. The type of fastening used can cause a new resonant peak at a frequency lower than the resonance frequency of the fastened accelerometer. When accelerometer vibrations are analyzed, the accelerometer is influenced by driving force. The previously discussed resonant frequency  $\omega_a$  and harmonic force with amplitude  $F_0$  and frequency  $\omega$  are considered. Considering the model, shown in Fig. 13.10 and the equation (13.3), the differential equation describing the forced vibration movement of the accelerometer without attenuation looks like:

$$\ddot{r} + 2\beta\dot{r} = \frac{F_0}{m_0} \sin \omega t. \quad (13.7)$$

Its solution is either

$$\ddot{r}, \text{ or } d^2r/dt^2, \dot{r} \text{ or } dr/dt. \quad (13.8)$$

or

$$R = \frac{F_0}{m_0(\omega_a^2 - \omega^2)}. \quad (13.9)$$

At frequencies considerably lower than the frequency of the accelerometer's own resonance, i.e., ( $\omega \ll \omega_a$ ), the motion amplitude  $R_0$  can be described by the expression:

$$R_a = \frac{F_0}{m_0\omega_a^2}. \quad (13.10)$$

The ratio of the correlation of motion amplitude in a high frequency area to that in a low frequency area, i.e.,  $R/R_0$  looks like:

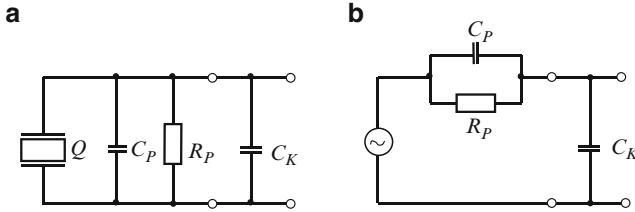
$$\frac{R}{R_0} = \frac{1}{1 - \left(\frac{\omega}{\omega_a}\right)^2} = A. \quad (13.11)$$

This known expression points to the increase in basic motion, relative to inertia mass in the area in which the driving force frequency is commensurable with the frequency of the accelerometer's own resonance. Therefore, in this area there are the increase in the force influencing the piezoelements, and the increase in amplitude of the electric signal released by the accelerometer. This corresponds to the accelerometer's own resonance.

The frequency value of the unfastened accelerometer own resonance depends on the ratio of general inertia mass to the whole accelerometer mass value, and to the base mass value in particular.

A practical rule emerges: accelerometer inertia mass is almost identical to its base mass.

Analysis of the equivalent mechanical scheme permits the following conclusions:



**Fig. 13.11** Equivalent electric scheme of piezoelectric accelerometer: (a) with charge source, (b) with voltage source

1. The inertia mass size should be increased for an increase in accelerometer sensitivity.
2. It is necessary to reduce the size of this mass for frequency range expansion (i.e., upper frequency limit expansion of this range).

We should also remark that the piezoelement mass was not considered in the scheme discussed, as it was assumed that this is essentially lighter than the inertia mass.

Using an electromechanical analogy method, it is easy to transform the mechanical scheme into an electrical one. However, this scheme does not allow evaluation of the physical processes in the accelerometer. Therefore, two equivalent electric schemes for the pre-resonance area, in which the piezoelement is presented as a charge or voltage source, are proposed below (Fig. 13.11) (see also Chap. 4).

An accelerometer piezoelement for the pre-resonance area can be represented as a parallel connection of capacity  $C_P$  and resistance  $R_P$ .  $C_K$  cable capacitance is the piezoelement load.

It follows from the simplified equivalent electrical schemes shown that the accelerometer output voltage  $V_A = Q_P / (C_P + C_K)$  depends on the connecting cable capacitance, while charge  $Q_P$  does not depend on this capacitance.

Therefore, use of various connecting cables or cables of various lengths affects the accelerometer voltage sensitivity, determining whether repeated calibration is necessary.

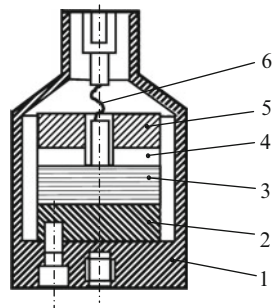
As has been mentioned already, this is the main drawback of the use of voltage amplifiers for piezoelectric accelerometers, and at the same time the reason why charge amplifiers are so widely used.

### 13.3 Accelerometer Designs

The piezoelectric accelerometers made by Kistler Instrumente AG (Switzerland), are widely known (Fig. 13.12) [13]. Depending on the measurement scheme, two sensor systems by this firm – piezoelectric (Fig. 13.13) and piezotron (Fig. 13.14) – are known.

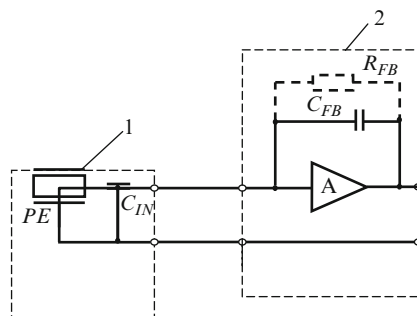
**Fig. 13.12** Accelerometer by Kistler Instrumente AG:

1 – case, 2 – base, 3 – quartz piezoelements, 4 – inertia mass, 5 – elastic element, 6 – electric contact



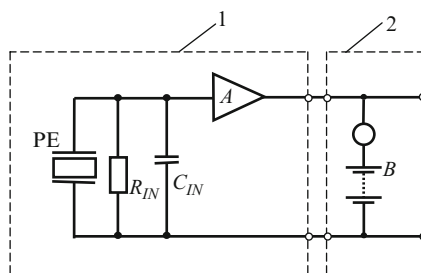
**Fig. 13.13** Piezoelectric system of sensors by Kistler [13]:

1 – sensor, 2 – charge amplifier



**Fig. 13.14** “Piezotron” system of sensors by Kistler [13]:

1 – “piezotron” acceleration sensor with built-in piezotransducer, 2 – “piezotron” communication element



The piezoelectric system (Fig. 13.13) consists of piezoelements  $PE$  and inertia mass  $IN$ , positioned in housing (case) 1. The sensor with high output resistance is connected with the charge amplifier by a low-noise cable.

The full resistance miniaturized transducer is built in the sensor in the piezotron system. A piezotron communication element is required for power supply and signal formation between the sensor indicator or measurement processing device.

The sensor has a low-resistance electric output (no special cables needed).

Specifications of Kistler sensors of piezoelectric and piezotron systems are given in Table 13.1.

Brüel and Kjer is a leader in production of devices for vibrations, impacts and noise measurement. Specifications of accelerometers made by this firm are represented in Table 13.2.

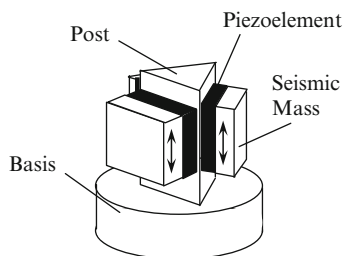
**Table 13.1** Specifications of accelerometers by Kistler

Specifications	Modification				
	8042	8044	8002	8005	8007
Range (g)	-50,000 to 11,000	-20,000 to 30,000	±10,000	±5,000	±100
Threshold reactions (g)	0.6	0.1	0.03	0.006	0.0003
Overload (g)	-6,000 to 11,000	-30,000 to 100,000	±20,000	±7,000	±200
Reduced sensitivity (pKl/g)	-0.05	-0.3	-1	-5 ± 2%	-100 ± 2%
Resonant frequency (of accelerometer, attached on the object) (kHz)	70	60	40	20	1.8
Frequency range (Hz)	0-8,000	0-8,000	0-7,000	0-4,400	0-400
Transverse direction sensitivity (%)	< 5	< 5	< 5	< 5	< 3
Work temperature range (°C)	-150 to 240	-150 to 240	-150 to 240	-150 to 240	-150 to 240
Temperature coefficient of sensitivity (%/°C)	-0.04	-0.02	-0.02	-0.02	-0.01
Capacitance (pF)	25	50	90	175	22
Mass (g)	8	7	20	65	490

**Table 13.2** Specifications of accelerometers by Brüel and Kjer

Specifications	Modification				
	861285	8614 A500 A1000	8616 A500 A1000	8618 A500 A2000	8620
1	2	3	4	5	6
Range (g)	±5	±500 to ±1,000	±500 to ±1,000	±500 to ±2,000	±500
Noise background (g)	0.0003	0.1 to 0.04	0.1 to 0.04	0.01 to 0.1	0.01
Overload (g)	±50	±200 to ±2,000	±200 to ±2,000	±1,000 to ±5,000	±2,000
Sensitivity (Kl/g)	-10,000	42.5	42.5	10.1	10
Resonant frequency (of the sensor attached) (kHz)	23	125	125	30	50
Frequency range ±5% (Hz)	0.5-5,000	1-25,000	1-25,000	2-4,000; 0.8-4,000	1-80,000
Transverse direction sensitivity (%)	5:5	< 5	< 5	< 5	< 5
Work temperature range (°C)	-65 to 100	-50 to 120	-50 to 120	-50 to 120	-50 to 120
Temperature coefficient of sensitivity (%/°C)	-0.06	-0.06	-0.06	-0.07	-0.061
Feeding voltage	20-30	12, 30, 20, 30	12-30, 20-30	20-30	20-30
Mass (g)	70	0.7	0.5	20	45

**Fig. 13.15** Simplified model of piezoelectric accelerometer “Delta Shear” by Brüel and Kjer



A simplified design of a piezoelectric accelerometer, produced by this firm with the label Delta Shear, is shown in Fig. 13.15 [14, 15]. Active elements of this accelerometer are made of a piezoelectric material (quartz or ceramics) and connected to the base with a triangular-section-shaped post and with three seismic (inertia) masses. The influence of vibration on the accelerometer base leads to dynamic force effect on each piezoelement. This force is the product of acceleration and the corresponding mass.

Piezoelements generate an electrical charge proportional to the dynamic force influencing them. As the amplitude and the acceleration phase of seismic masses is identical to the amplitude and the acceleration phase of the accelerometer base in a wide frequency range, the electrical charge is proportional to the acceleration of the surface vibrations of the object. The accelerometer is fastened on the object.

Specifications of some accelerometer types produced by Brüel and Kjer are shown in Table 13.2.

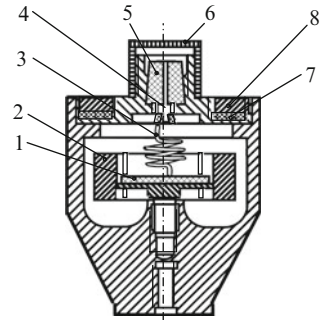
Despite their good characteristics, the accelerometers of these firms have a series of drawbacks. Among them are considerable transverse sensitivity, changing along the azimuth, and also the comparatively complex design, demanding final individual adjustment [14]. In addition, these accelerometers are very expensive. For example, the 6213 sensor by Kistler costs US \$2,300 [13].

The inertia mass, piezoelements and the housing (case) are soldered in the accelerometer, described in [16]. Therefore, the sensor can work at temperatures up to 200 °C. Its resonant frequency can also be raised.

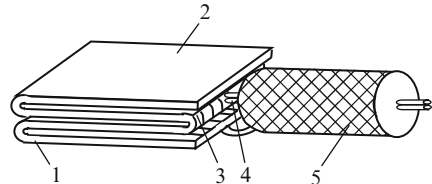
The cable connecting the accelerometer sensor with the amplifier has the following requirements: high insulation resistance, small capacitance between cord and the screen, flexibility and anti-vibration. The latter means, that emf should not be induced to the amplifier input by the cable with vibration. Emf appears as a result of insulation and the screen friction under the influence of vibration.

The design of  $\Delta 19$  sensor type with a bimorph piezoelement is shown in Fig. 13.16. Piezoceramic IITC-19 piezoelement 1 is glued to resilient element 2. The latter is a round flat spring with a ring-shaped channeled inertia mass. The resilient element is centrally fastened. It experiences flexural deformation under the acceleration influence. The dimensions of piezoelement and resilient element are chosen so that the piezoelement only experiences like-sign deformation. The piezoelement charge is taken off by flexible conductor 3, soldered to the upper elec-

**Fig. 13.16** Accelerometer Д-19 made by Vibropribor (Taganrog, Russia):  
 1 – piezoelement, 2 – resilient element with inertia mass,  
 3 – conductor, 4 – contact, 5 – fluoroplastic padding,  
 6 – protecting cap, 7 – rubber padding, 8 – nut



**Fig. 13.17** Accelerometer with sensitive element made of piezopolymer film:  
 1 – piezopolymer film,  
 2, 3 – electrodes, 4 – current outputs, 5 – insulator



trode and contact 4. The latter is isolated from the housing (case) by fluoroplastic padding 5; it is closed by protecting cap 6.

The sensor is encapsulated with rubber padding 7, clamped by nut 8. The sensor weighs 100 g. The sensor sensitivity is  $S = 20 \text{ mV/m/c}^2$ , the frequency range is 20–500 Hz, the self capacitance is 3,400 pF, and the input resistance of the voltage amplifier is 2 Mohm.

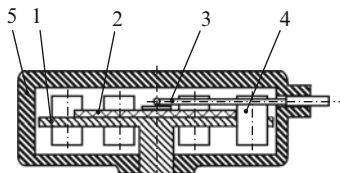
An accelerometer with the sensitive element, made of piezopolymer film 1, folded an even number of times, with electrodes 2 and 3, connected to signal core 4 and to the coaxial cable screen, shown in (Fig. 13.17), is described in [17].

The sensor is glued to the object under study. The sensitive element is synchronously deformed with the surface under study. The sensitive element generates voltage proportional to its deformation. The sensor signal is supplied to the measuring equipment (not shown) via a connecting cable. The immunity to sensor noise increases because of the signal electrode screening. Its lower dynamic range limit decreases in this case.

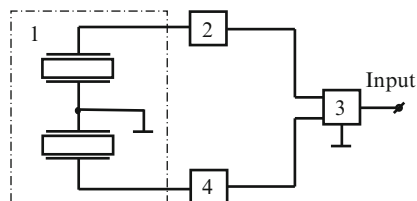
In addition, the dynamic range can be expanded if the matching between the piezoelement and the connecting cable is improved and if the capacitance of the folded sensitive element is increased while its lateral dimension remains the same. If  $C_0$  is a layer capacitance,  $C_C$  is cable capacitance, and  $n$  is the number of layers, then sensor sensitivity and its dynamic range consequently increases by  $x$  times

$$x = n \frac{C_0 + C_K}{nC_0 + C_K}.$$

**Fig. 13.18** Accelerometer with bimorph element:  
 1 – disk, 2 – piezoelement,  
 3 – cable, 4 – loads (weights),  
 5 – housing (case)



**Fig. 13.19** Accelerometer with sensitive differential element:  
 1 – differential piezosensor,  
 2 – voltage amplifier, 3 – adder (summer, summator), 4 – inverting amplifier



A series of piezoelectric vibro-transducers, developed in the Central Research Institute of Mechanical Engineering (Moscow), is of scientific interest.

In the transducer [18], piezoelement 2 is attached to disk-shaped sensitive element 1 (Fig. 13.18). Disk 1 is made of a diamagnetic material, for example, titan. Identical loads (weights) 4 are spread on the inertia element periphery of disk 1. These loads (weights) 4 are a cylinder insertion of diamagnetic material with density 2.5–10 times bigger than the disk material.

The material can also be tungsten. Output cable 3 goes from piezoelement 2.

When the working transducer is attached to a vibrating machine or its node, disk 1 of the sensitive element, the inertia element loads (weights) 4 fastened to it and piezoelement 2 start to vibrate. The electrical signal induced on the piezoelement goes along output cable 3 to the measuring and recording block (unit).

The transducer can be used for vibration measurement if considerable magnetic fields are available, for example, for bar and iron vibration measurement of powerful generators stator.

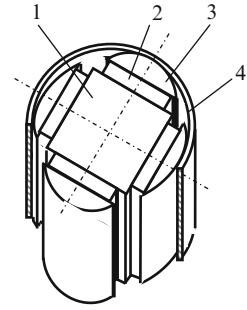
The piezoelectric accelerometer, described in [19] (Fig. 13.19) consists of serially connected differential piezosensor 1, voltage amplifier 2 and adder (summer, summator) 3, inverting adjustable charge amplifier 4.

Sensitive differential element 1, consisting of two heteropolarized piezoplates, transforms vibrations  $S(t)$  into an electrical signal coming to amplifier inputs. Sign-like signals are produced on the outputs of voltage amplifier 2 and adjustable inverting charge amplifier 4. The voltages on the voltage amplifier output 2 and on the charge amplifier output 4 are totalled by the adder (summer, summator).

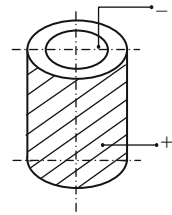
The analysis of information shows that:

1. Transverse piezoelements should be used for increase in axial (work) sensitivity.
2. Axially symmetric designs of sensitive elements should be used for reduction in lateral sensitivity.

**Fig. 13.20** Transverse accelerometer with tetrahedral prism: 1 – prism, 2 – piezoelement (four pieces), 3 – inertia mass (four pieces), 4 – resilient element



**Fig. 13.21** Cylindrical piezoelement



3. Piezoelement and inertia mass dimensions should be reduced for frequency range expansion; the dimensions of these elements should be increased for axial sensitivity.

Piezoceramic cylindrical piezoelements are less rigid. However, a ceramic piezomodule is approximately ten times higher than a quartz piezomodule.

Cylindrical transverse piezoelement has one more advantage – axial symmetry. This makes it suitable for use in accelerometers.

We should also note that other geometrical figures can also have axial symmetry, for example, a prism with an even number of faces. An example of an accelerometer designed by analogy to Delta Shear by Brüel and Kjer is shown in Fig. 13.20.

This accelerometer has a small lateral sensitivity.

The design can become essentially simpler, but still will give high characteristics if the number of prism faces is increased up to  $n \rightarrow \infty$ , which corresponds to the transition to a cylinder (Fig. 13.21).

Two variants of this design are shown in Fig. 13.22.

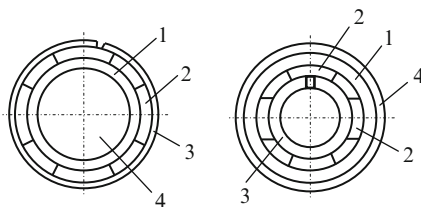
In the first case [20], resilient element 3 presses inertia masses 2 against cylindrical transverse piezoelement 1. There is a cylindrical metal housing (case) 4 inside this. In the second case, piezoelement 1, inertia masses 2, and resilient element 3 are in housing (case) 4.

The directional diagram of the accelerometer represented in Fig. 13.22a is shown in Fig. 13.23.

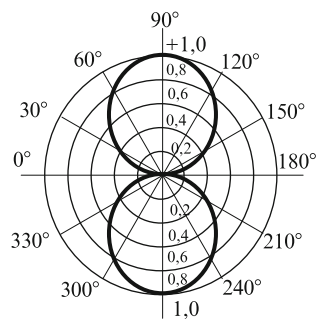
The accelerometer design can be simplified if the resilient element is excluded (Fig. 13.24) [21].



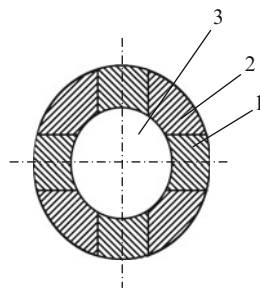
**Fig. 13.22** Transverse cylindrical accelerometer:  
 1 – cylindrical transverse piezoelement, 2 – inertia masses, 3 – resilient element, 4 – housing (case)



**Fig. 13.23** Directional diagram of cylindrical transverse accelerometer (Fig. 13.22a)



**Fig. 13.24** Accelerometer:  
 1 – piezoelements, 2 – inertia masses, 3 – housing (case)



Piezoelements 1 look like sectors of a hollow piezoceramic cylinder with electrodes on the internal and external cylindrical surfaces.

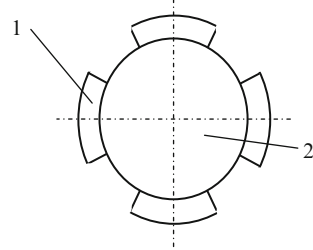
The piezoelements are symmetrically positioned along the circumference and are pressed against metal cylinder 3, also used as the base. Intervals 2 between piezoelements are filled with epoxy compound, based on resin  $C\text{ЭДМ-2}$  with a filler resembling metal powder, and are used as inertia masses. Accelerometer sensitivity can be changed by changing the metal powder concentration.

The assembly of epoxy compound filling is made of fluoroplastic.

Metal sectors, shaped as piezoelements, can also be used as inertia masses. As in the previous case, the accelerometer is assembled in fluoroplastic demountable form by epoxy compound.

The sensitive element of the developed accelerometer is circularly symmetrical. As a result, lateral sensitivity was essentially reduced, even in comparison with monolithic piezotransducers.

**Fig. 13.25** Accelerometer:  
1 – piezoelement, 2 – base



The design of the accelerometer, shown in Fig. 13.25 [22], is even simpler.

The sectors 1 of cylindrical transverse piezoelement are soldered to housing (case) 2 in this accelerometer. They are also inertia masses.

### 13.4 Three-Dimensional Accelerometers

In a series of technical uses there is a necessity to measure linear or vibration accelerations with simultaneous information on the acceleration vector position along the coordinate axes, for example, when testing items, in seismometry, various moving objects, etc. The so-called vector receivers are a special case in hydro-acoustics [1].

Accelerometers of this type can be based on at least two schemes.

In the first case, single-axis accelerometers with a satisfactory directional diagram (this quality standard will be specified later) are positioned on the common base on co-ordinate axes.

In the second case, for example, in seismometry, an accelerometer design usually includes common inertia mass, elastically attached to the three sensitive elements, located on coordinate axes.

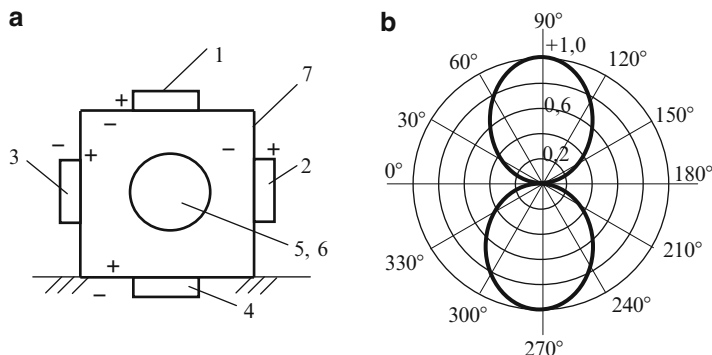
The complexity of these designs is obvious.

Certain design requirements are formulated. They are based on the analysis of the known three-dimensional accelerometer designs. One should take into account that to receive unequivocal information on the acceleration vector position in space, the signal received from each sensitive element should also be interpreted unequivocally.

An electric signal polarity should change to the opposite if the vector direction is changed through  $180^\circ$ . If the acceleration vector orthogonally influences the given axis, there should be no signal on the sensitive element, i.e., the transverse sensitivity should equal zero.

If the acceleration affects at  $45^\circ$  angle to axis, the signal level must be at several times smaller than at acceleration action is axially.

A piezoelectric accelerometer design with rectangular parallelepiped base 2 with selected disk piezoceramic elements pairwise on the opposite faces 1 [23] is proposed. The piezoelements are soldered and glued with epoxy compound to the base faces by heteropolar electrodes (Fig. 13.26).



**Fig. 13.26** Three-dimensional piezoelectric accelerometer: (a) design: 1–6 – piezoelements, 7 – base; (b) directional diagram for accelerometer piezoelement pair

The piezoelements fastened to the opposite faces are parallel inter-connected. Inertia masses are either soldered or glued with epoxy compound to the piezoelements (not shown in Fig. 13.26).

Under the influence of acceleration on the piezoelements, fastened to the faces normally located on the acceleration vector, one piezoelement is compressed, while the second is stretched. This leads to the occurrence of like-sign signals. Therefore, charge sensitivity is increased twice.

If the direction of acceleration vector changes to the opposite, the charge sign changes to the opposite too.

Opposite signs, but of the same level of charges, are created in piezoelements under the influence of transverse acceleration. This leads to their full compensation.

Charges appear on the piezoelements pairs located on other faces normally to the acceleration vector.

Thus, the developed accelerometer provides unequivocal information on the acceleration vector value and direction.

The accelerometer described above is rather complex, as it contains 6 piezoelements.

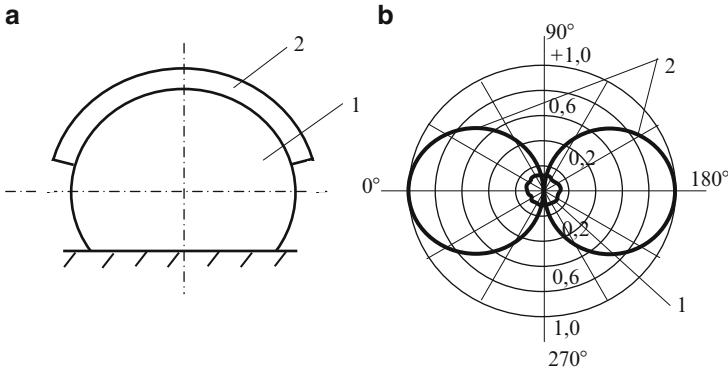
The authors also developed an accelerometer consisting of three sensitive elements, positioned to coordinate axes.

An element of this accelerometer is shown in Fig. 13.27a [24], and its directional diagram in Fig. 13.27b [24].

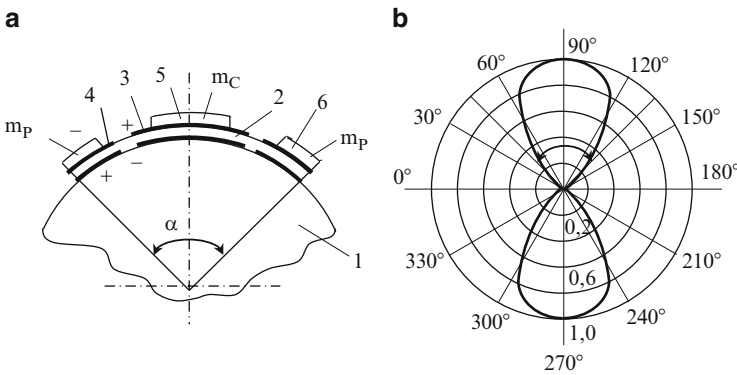
The accelerometer shown in Fig. 13.28a [25] has a sharper directional diagram lobe (Fig. 13.28b).

Here spherical piezoelement segment 2 with solid angle is fastened to base 1. Piezoelement has three electrode systems where inertia masses 5, 6 ( $m_P$  and  $m_C$ ) is fastened. This permit to receive sharper directional diagram lobe.

We should admit that both inertia mass and resilient element are optional in accelerometer designs. The piezoelement can perform their functions. The piezoelement upper part can influence its lower part as inertia mass under the



**Fig. 13.27** Accelerometer with spherical segment-shaped piezoelement: (a) design: 1 – sphere-shaped base, 2 – piezoelement; (b) directional diagram of transverse sensitivity: 1 – accelerometer developed, 2 – Delta Shear accelerometer by Brüel and Kjer



**Fig. 13.28** Sensitive element of three-dimensional accelerometer: (a) design, (b) directional diagram; 1 – base, 2 – piezoelement, 3, 4 – opposite polarized piezoelement parts, 5, 6 – inertia masses

influence of acceleration if any width of piezoelement is available. Piezoelement material is used as a resilient element.

However, the sensitivity decreases while the accelerometer frequency range extends simultaneously.

### 13.5 Accelerometers Based on Bimorph and Piezoelectric Elements

Bimorph and trimorphic sensitive piezoelectric elements (bimorph piezoelements) are widely used in accelerometer design [3, 26–31]. They have a number of advantages; high sensitivity is among them. At the same time, they have a rather

narrow frequency and dynamic range, considerably high lateral sensitivity and low stability of sensitivity because of the glued connections used.

The fact that some accelerometer characteristics are interconnected should be considered. For example, in most cases, the higher the axial sensitivity, the narrower the transducer dynamic range. Therefore, there is no universal way to improve all accelerometer specifications simultaneously. In the majority of cases, each new specification improvement causes a reduction in another specification or specifications. A developer should evaluate the choices rationally and compromise reasonably.

The remarks discussed concern not only accelerometers, but also any other device.

We should also add that as inertia masses are not centered and balanced, bimorph transducers have essential, transverse sensitivity, changing along the azimuth.

The authors have developed a series of designs in which the mentioned drawbacks are partially eliminated. An accelerometer sensitive element design with two bimorph piezoelements is shown in Fig. 13.29 [32].

Here bimorph elements 1, 3 and 2, 4 are fastened in case 8 and are tied 7. Inertia masses 5, 6 are soldered to piezoelements 3, 4. Piezoelements are also soldered to membranes from the heteropolar electrode side.

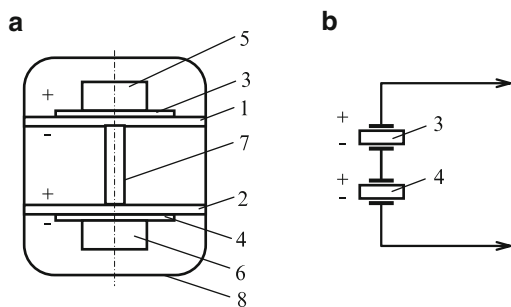
Like-sign charges appear on the piezoelements under the axial influence of acceleration. Heteropolar charges on the piezoelements are compensated under the influence of transverse acceleration.

Sensitivity diagrams of the accelerometer consisting of a bimorph sensitive element represented in Fig. 13.29 are shown in Fig. 13.30.

As can be seen from the figure, the accelerometer developed has a rather low transverse sensitivity. Then axial voltage sensitivity and frequencies work range are approximately 1.5 times increased in comparison with an accelerometer with one bimorph element [32].

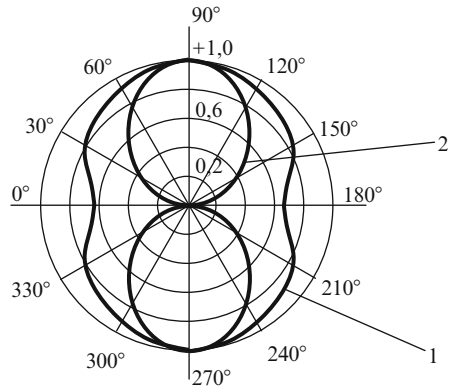
The accelerometer represented in Fig. 13.31 has better specifications. In this case, the inertia mass is between bimorph elements. The piezoelements are parallel-connected [33].

The bimorph transducer sensitivity can be increased with simultaneous expansion of the frequency range. Then one more piezoelement should be added to the

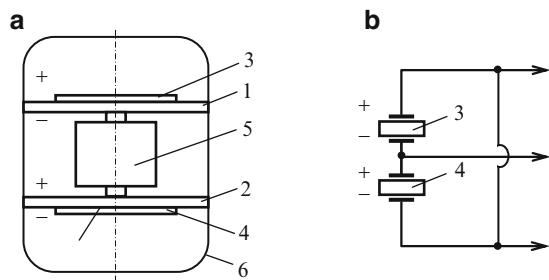


**Fig. 13.29** Accelerometer with two bimorph elements: (a) design, (b) piezoelements connection scheme; 1, 2 – membranes, 3, 4 – piezoelements, 5, 6 – inertia masses, 7 – tie, 8 – housing (case)

**Fig. 13.30** Accelerometer directional diagram: 1 – with one bimorph element, 2 – with two bimorph elements



**Fig. 13.31** Accelerometer with two bimorph elements: (a) design, (b) piezoelement connection scheme; 1, 2 – membranes, 3, 4 – piezoelements, 5 – inertia mass, 6 – housing (case)



bimorph sensitive element, coplanar-positioned to the main piezoelement. In fact, this transforms a bimorph element into trimorphic (see Chap. 6).

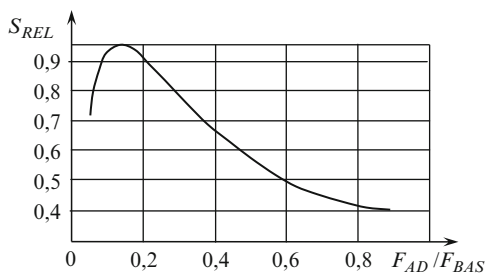
Piezoelements and metal membrane can be glued, soldered or diffusively welded. Depending on the electrical scheme, the piezoelements are series- or parallel-connected by unipolar or heteropolar polar electrodes.

It is necessary to note that one more piezoelement attachment to the bimorph element results in vibration system rigidity and an increase in resonant frequency, while its sensitivity decreases. Simultaneous switching of the second piezoelement leads to charge sensitivity increase with parallel connection, voltage increase with series connection. These two processes should result in the occurrence of a maximum sensitivity dependence on additional  $F_{AD}$  and basic  $F_{BAS}$  piezoelement area ratio (Fig. 13.32).

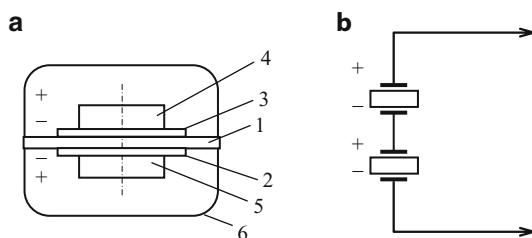
A symmetric trimorphic piezoelement can be used as an accelerometer [34]. Voltage sensitivity of this transducer is approximately 1.4 times higher than that of an asymmetric transducer.

The introduction of the second piezoelement opens additional possibilities for the design of piezoelectric transducers. For example, electromechanical feedback can be introduced to the transducer because of this piezoelement. The feedback allows control of its characteristics [15, 35].

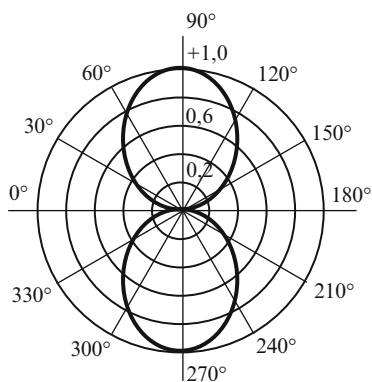
**Fig. 13.32** Dependence of asymmetric trimorphic element relative sensitivity  $S_{REL}$  on piezoelements area ratio



**Fig. 13.33** Accelerometer with trimorphic element: (a) design: 1 – membrane, 2, 3 – piezoelements, 4, 5 – inertia masses, 6 – case; (b) piezoelements connection scheme



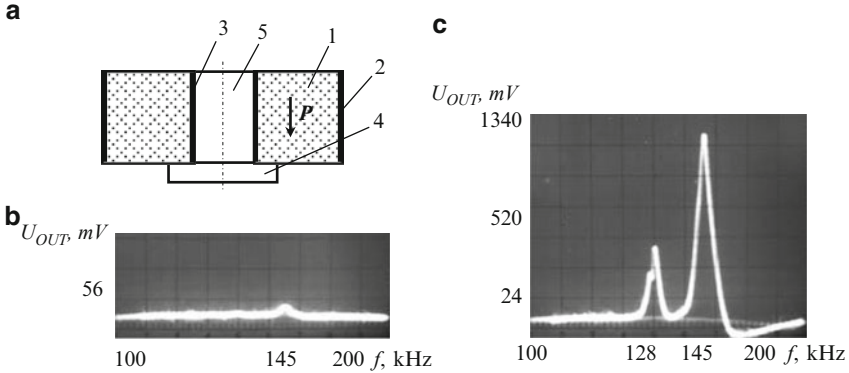
**Fig. 13.34** Directional diagram of accelerometer with trimorphic element



An accelerometer design with a trimorphic sensitive element [36] is shown in Fig. 13.33. Its directional diagram is given in Fig. 13.34.

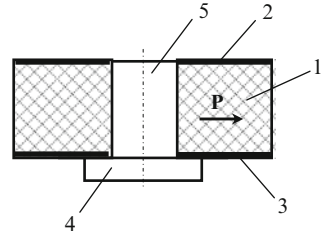
The accelerometer in Fig. 13.33 consists of metal membrane 1, two disk piezoelements 2 and 3, two inertia masses 4 and 5, and housing (case) 6.

An accelerometer with trimorphic element has zero transverse sensitivity if the axial sensitivity increases by approximately 1.5 times in comparison with the bimorph element.



**Fig. 13.35** Domain-dissipative accelerometer: (a) scheme, (b) AFC of domain-dissipative accelerometer, (c) AFC of traditional accelerometer: 1 – piezoelement, 2, 3 – electrodes, 4 – base, 5 – post

**Fig. 13.36**  
Domain-dissipative accelerometer:  
1 – piezoelement, 2, 3 – electrodes, 4 – base, 5 – post



### 13.6 Domain-Dissipative Accelerometer and Accelerometers with Feedback

Extremely low work frequency range, low measurement and parameter stability accuracy under the influence of destabilizing factors can be referred to as drawbacks of the accelerometers considered.

The work range of piezoaccelerometers can be expanded if they are made according to the domain-dissipative transducer scheme described in Chap. 3. An example is shown in Fig. 13.35a [37].

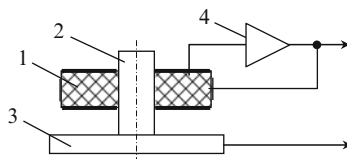
For this purpose, the electrodes on the piezoelement are positioned in the following way: the electric-field vector of the output signal creates angle  $\alpha$  with the polarization vector  $P$ , with  $0 << \alpha \leq 90^\circ$ . As a result, AFC is leveled (resonances disappear). Therefore, the frequency work range extends (Fig. 13.35b). The AFC of a traditional accelerometer has two resonances in the range studied (Fig. 13.35c).

The other variant of a domain-dissipative accelerometer is shown in Fig. 13.36 [38].

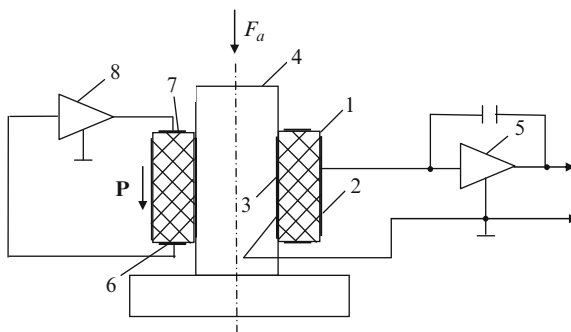
In this case, the piezoelement is radially polarized. The electrodes are attached to the end surfaces of the hollow piezoelectric cylinder. Under this condition, the angle



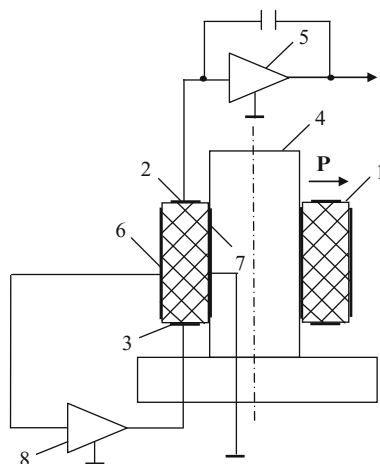
**Fig. 13.37** Scheme of accelerometer with feedback:  
 1 – piezoelement, 2 – post,  
 3 – base, 4 – amplifier



**Fig. 13.38** Piezoceramic accelerometer with two-circuit feedback:  
 1 – piezoelement, 2, 3, 6, 7 – electrodes, 4 – post, 5, 8 – amplifiers



**Fig. 13.39** Piezoceramic accelerometer with two-circuit feedback:  
 1 – piezoelement, 2, 3, 6, 7 – electrodes, 4 – post, 5, 8 – amplifiers



between the polarization vector  $\mathbf{P}$  and the electric-field vector of the output signal is right. This corresponds to the domain-dissipative transducer scheme. Therefore, this accelerometer will have a several times wider work frequency range.

The Accuracy of accelerometer measurement can be increased with the introduction of spatial electromechanical negative feedback. In addition, as was shown in Chap. 5, time and temperature stability of piezoceramic sensors was also raised.

Three variants of feedback schemes are shown in Figs. 13.37–13.39.

The accelerometer in Fig. 13.38 consists of a hollow cylinder-shaped monolithic sensitive element 1, polarized along the height and established on cylindrical ledge

**Table 13.3** Comparative characteristic of accelerometers

Parameter	Accelerometers	
	Model 4393 Delta Shear by Brüel and Kjer	Accelerometer developed
Complexity (number of details)	11	5
Frequency range, limit (+10%), kHz	16.5	200
Sensitivity (mV/g)	4.8	15
Lateral sensitivity	Yes	Tends to zero
Necessity and control and adjustment levels	Yes/difficult	No

4. Output matching charge amplifier 5, connected to electrodes on cylindrical surfaces 2 and 3, is positioned to the basic channel. There is a voltage amplifier, connected to the electrodes on end surfaces 6 and 7 [39] in the second channel.

Another accelerometer variant is shown in Fig. 13.39 [40].

A hollow piezoceramic cylindrical radially polarized element is used in the transducer shown in Fig. 13.39.

In Table 13.3, comparative specifications of both the known piezoceramic accelerometer Delta Shear model 4393 by Brüel and Kjer (Denmark) – the acknowledged world leader in the vibromasuring equipment market – and the domain-dissipative feedback piezoceramic accelerometer developed are given.

As can be seen from Table 13.3, the accelerometer developed is simpler, cheaper and has higher specifications.

Accuracy can be increased by the two-circuit feedback described in Chap. 5, using the devices described in [39, 40].

An accelerometer with a hollow, polarized along the height, cylindrical piezoelement with external diameter 15 mm, internal 5 mm, and height 5 mm, made of piezoceramic ИТС-19, with electrodes on cylindrical and end surfaces, was used in the experimental research. A charge amplifier assembled according to К140УД8А microcircuit was connected to the electrodes on the cylinder surfaces. A voltage amplifier based on transistor КТ315В with input resistance 2.2 mohm was connected to the electrodes on the end surfaces. Amplification coefficient values were selected to have a minimum error (see Chap. 6).

## References

1. V.M. Sharapov, M.P. Musienko, E.V. Sharapova, *Piezoelectric Sensors*, ed. by V.M. Sharapov (Technosphaera, Moscow, 2006), p. 632 (in Russian)
2. Yu.I. Iorish, *Vibrometers* (Mashizdat, Moscow, 1961) (in Russian)
3. Piezoelectric accelerometers and preamplifiers/Directory of theoretical and practical use – Denmark, 1987 (in Russian)
4. O.P. Kramarov et al., Patent of USSR 361723. Piezoelectric accelerometer (1975) (in Russian)
5. V.V. Yanchich, O.P. Kramarov, Patent of USSR No 472587. Piezoelectric accelerometer (1976) (in Russian)

6. V.M. Sharapov, Yu.G. Lega, M.P. Musienko, S.V. Rotte, N.V. Saenko, Patent of Ukraine No 45703. Piezoelectric accelerometer (2002) (in Ukrainian)
7. V.M. Sharapov, Yu.G. Lega, M.P. Musienko, N.V. Saenko, Yu.V. Andriyako, M.O. Shulga, Patent of Ukraine No 45702. Piezoelectric accelerometer (2002) (in Ukrainian)
8. V.M. Sharapov, Yu.G. Lega, M.P. Musienko, N.V. Saenko, I.M. Zlatyeva, N.A. Shulga, Patent of Ukraine No 46274. Piezoelectric accelerometer (2002) (in Ukrainian)
9. V.M. Sharapov, Yu.G. Lega, M.P. Musienko, N.V. Saenko, N.A. Shulga, I.M. Zlatyeva, Patent of Ukraine No 46299. Piezoelectric accelerometer (2002) (in Ukrainian)
10. E.A. Kudryashov, V.E. Mager, S.H.M. Rafikov, Piezoelements for force and voltage sensors. Devices and control systems **9** (1989) (in Russian)
11. V.M. Sharapov, Yu.G. Lega, M.P. Musienko, S.V. Rotte, N.V. Saenko, Patent of Ukraine No 45705. Piezoelectric accelerometer (2002) (in Ukrainian)
12. V.M. Sharapov, Yu.G. Lega, M.P. Musienko, S.V. Rotte, N.V. Saenko, Patent of Ukraine No 46298. Piezoelectric accelerometer (2002) (in Ukrainian)
13. Kistler Instrumente AG, *Accelerations, Blows, Vibration. Reliable and Exact Measurement by Means of Quartz Gauges of Acceleration* (Kistler Instruments AG, Switzerland, 1986)
14. Brüel and Kjer. *Short Catalogue* (Nerum, Denmark, 1989/1990)
15. V. Sharapov, I. Sarwar, *Electromechanical Feedback in Piezoceramic Sensors and Transducers* (IEEE International Ultrasonics Symposium, Sendai, 1998)
16. P.V. Novitskiy (ed.), *Electric Measurements of Non-electric Values* (Energiya, Leningrad, 1975), p. 576 (in Russian)
17. D.L. Rastorguev et al., Patent of USSR No 1357723. Vibration sensor. Discoveries. Inventions (1986) (in Ukrainian)
18. D.L. Rastorguev et al., Patent of USSR No 487312. Vibration sensor. Discoveries. Inventions (1986) (in Ukrainian)
19. K.R. Tsehanskiy, B.M. Makeev, Patent of USSR No 634493. Piezoelectric vibromeasuring transducer. Discovery. Inventions (1978) (in Russian)
20. G.P. Nubert, *Measuring Transducers of Non-electric Sizes (Translation from English)* (Energiya, Leningrad, 1970), p. 360 (in Russian)
21. V.M. Sharapov, I. Sarvar et al., *Partitioned Piezoelectric Accelerometer/Collected Papers of International Conference "Sensor-98"* (Gurzuf, Moscow, 1998) (in Russian)
22. V.M. Sharapov, Yu.G. Lega, M.P. Musienko, S.V. Rotte, Yu.V. Andriyako, N.V. Saenko, Patent of Ukraine No 45704, G01P15/09. Piezoelectric accelerometer (2002) (in Ukrainian)
23. V.M. Sharapov, I. Sarvar, Yu.G. Lega, M.P. Musienko, Patent of Ukraine No 47575. Piezoelectric accelerometer (2002) (in Ukrainian)
24. S.V.M. Sharapov, I. Sarvar, Yu.G. Lega, M.P. Musienko, Patent of Ukraine No 33858. Piezoelectric accelerometer (2001) (in Ukrainian)
25. V.M. Sharapov, I. Sarvar, M.P. Musienko, Patent of Ukraine No 47576. Three-axis piezoelectric accelerometer (2002) (in Ukrainian)
26. A.M. Allaverdiev, N.B. Akhmedov, *Physics of Microelectronic Devices* (MIET, Moscow, 1984), p. 29 (in Russian)
27. R.G. Dzagupov, A.A. Erofeev, *Piezoelectronic Devices in Computing Machinery, Monitoring Systems and Control* (Politechnika, St. Petersburg, 1994), p. 608 (in Russian)
28. R.J. Kazys, *Ultrasonic Information-Measuring Systems* (Mokslas, Vilnius, 1986) (in Russian)
29. V.M. Sharapov, Yu.G. Lega, M.P. Musienko, S.V. Rotte, N.V. Saenko, Patent of Ukraine No 45706. Piezoelectric accelerometer (2002) (in Ukrainian)
30. S.I. Rudnitskiy, V.M. Sharapov, N.A. Shulga, Vibrations of a bimorph disk transducer of the metal-piezoceramic type. Appl. Mech. **T. 26**(10), 64–72 (1990) (in Russian)
31. A.P. Evtyutov, A.E. Kolesnikov, E.A. Korepin et al., *Directory on Hydro-acoustics* (Sudostroenie, Leningrad, 1988), p. 552 (in Russian)
32. V.M. Sharapov, Yu.G. Lega, M.P. Musienko, S.V. Rotte, N.V. Saenko, I.M. Zlatyeva, Patent of Ukraine No 46267. Piezoelectric accelerometer (2002) (in Ukrainian)
33. V.M. Sharapov, Yu.G. Lega, M.P. Musienko, S.V. Rotte, N.V. Saenko, Patent of Ukraine No 46268. Piezoelectric accelerometer (2002) (in Ukrainian)

34. V.M. Sharapov, I.B. Chudaeva, M.P. Musienko, E.V. Bykova, I. Sarvar, Coplanar trimorphic piezoelements with feedback. Collected papers of the Fourth Ukrainian Conference "Automatics-97". T.4. - Cherkassy (1997) (in Russian)
35. V.M. Sharapov, I. Sarvar et al., Feedback in mechanical value piezoelectric transducers. "Measuring and computer facilities in technological processes", Release No 2, Khmelnytskyi, p. 64–67 (1998) (in Russian)
36. V.M. Sharapov, Yu.G. Lega, M.P. Musienko, S.V. Rotte, N.V. Saenko, N.A. Shulga, Patent of Ukraine No 46269. Piezoelectric accelerometer (2002) (in Ukrainian)
37. V.M. Sharapov, M.P. Musienko, Patent of Ukraine No 69871. Piezoelectric accelerometer (2004) (in Ukrainian)
38. V.M. Sharapov, M.P. Musienko, Patent of Ukraine No 69870. Piezoelectric accelerometer (2004) (in Ukrainian)
39. V.M. Sharapov, V.M. Nikolaenko, N.Yu. Ploskonos, O.V. Sharapova, Patent of Ukraine No 17436. Piezoelectric accelerometer (2006) (in Ukrainian)
40. V.M. Sharapov, M.Yu. Ploskonos, Patent of Ukraine No 18015. Piezoelectric accelerometer (2006) (in Ukrainian)

## Chapter 14

# Resonant Piezoceramic Sensors

Resonant piezoceramic sensors are prospective devices with rather high technical and metrological characteristics and numerous applications. These sensors are used for various measurements: of mechanical (forces and pressure; static, including linear and vibrating accelerations), electric and magnetic values, temperature, viscosity, humidity, movement, etc. In addition, these transducers are used in piezoelectric engines, gyroscopes, automatic devices, communication, computer facilities, etc. [3, 23, 29, 30, 33, 50, 57, 58].

The following effects are at the background of these sensors:  $Q$  factor changes under the mechanical influence or transfer coefficient change of radiating–receiving resonator system under the influence of gas pressure in the interval between the resonators.

The following scientists worked on their creation and perfection: R.G. Dzhagupov, E.A. Kudryashov, V.V. Malov, M.G. Minaev, I.E. Syrmolotnov, V.J. Snitko, A.I. Trofimov, V.M. Sharapov, etc.

Resonant piezoelectric transducers are made of monocrystal (quartz, lithium niobate, etc.) or piezoceramic materials. Monocrystal transducers are known for their high accuracy and stability. At the same time, their field of use is limited by their high price. V.V. Malov's monograph [33] is devoted to these sensors.

Piezoceramic sensors are not quite as accurate and stable. They have a simpler design and are less expensive. This is the crucial factor in some cases.

Piezoresonant sensors (PRS) can be classified according to the nature of influence, measured by a sensor (mechanical, thermal, electromagnetic, etc.). One more classification, according to the main effect (mechanism) type, is crucial in transformation.

According to the classification by the effect or mechanism type (crucial for transducer parameters modulation), almost all PRS can be allocated to one of the following groups. These PRS groups are the most widespread [33]:

- PRS on the basis of piezoelement tensosensitivity. The action measured creates mechanical deformations in the piezoelement directly or indirectly. Transformation into a parameter is achieved by the piezoelement tensosensitivity.

- PRS on the basis of piezoelement thermosensitivity. In these PRS, the parameter measured influences the piezoelement average temperature (or its volume distribution) directly or indirectly.
- PRS on the basis of the sensitivity of the piezoelements to acoustic load and complex resistance  $Z_m$ . In these devices, the parameter measured modulates the ultrasound radiation conditions from the vibrating piezoelement surfaces. The mechanism on which these PRS, named acoustic in [33], are based is called acoustic sensitivity.
- PRS on the basis of mass-sensitive piezoelements, using the dependence of the piezoelement parameters on the substance mass of the surface attached (sorbate) piezoelement. The parameter transformation in them is made via the mass sensitivity of the piezoelement.
- PRS on the basis of sensitivity to device geometry variations, in which piezoelement equivalent parameters vary with mutual displacement of piezoelement design members, for example, with the gap change between the electrode and vibrator.
- PRS on the basis of piezotransducer gyrosensitivity. In these devices, the piezovibrator rotation frequency around the axis, perpendicular to the resonant vibrations plane, is the action measured. Work of this PRS is based on the appearance of the sign-changing Coriolis forces in the vibrator, rotating and oscillating with resonant frequency. These forces are proportional to the rotation frequency. They change their direction with the vibration frequency. This transformation mechanism is called gyrosensitivity.

A wide range of resonant sensors based on bimorph elements should be included in the given classification. The work and use of these sensors are described in R.G. Dzhagupov's and A.A. Yerofeev's monographs [23].

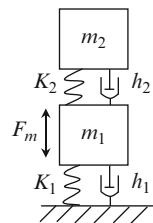
The given classification [33] is not exhaustive. In addition, the PRS group named "acoustic" in this classification is a special PRS case. An intermediate solid influences the vibrating piezoelement.

The output signal of these PRS depends on the contact phenomena between the piezoelement and the details transferring mechanical influence to it. Therefore, the name "contact PRS" is more accurate for them. Several books of A.I. Trofimov (for example, [49, 50]), and a considerable number of papers by I.G. Minaev and V.M. Sharapov [56–58] are devoted to these sensors.

## 14.1 Resonant Contact Sensors

Output characteristics of contact piezoceramic sensors are substantially determined by the force applied to the vibrating piezoelement. The piezoelement can be practically of any configuration. However, disk-shaped piezoelements are mainly used in sensors [7, 8, 50, 56]. In this case, the piezoelement is activated whether

**Fig. 14.1** Mechanical model of resonant contact transducer



along radial vibration mode, or along its thickness. Both piezoresonators and piezotransformers are used in sensor design [41, 50, 56–58].

The force measured is applied to both flat piezoelement faces and the cylindrical surface. Sensors with the force measured, applied to the piezoelement cylindrical surface, vibrating at resonant frequency of a radial oscillation mode [8], have maximum sensitivity.

Certain parts of the piezoelement surface forming the actual contact area sense the force applied [22, 45]

Control of contact characteristics (contact rigidity and the contact actual area) enables the control of transducer characteristics [8, 34, 59].

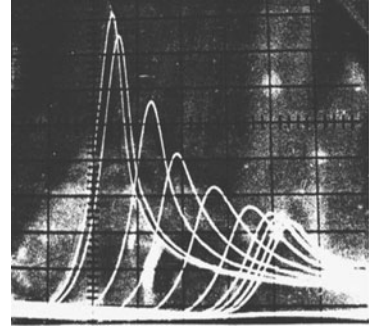
A piezosensor is an electromechanical oscillatory system, having a rather high  $Q$  factor. Therefore, it can be considered an oscillatory system with concentrated parameters [47, 48]. This method is widespread when the influence of external factors on the oscillatory system parameters is determined. Internal connections are not considered then.

A piezosensor mechanical model with the concentrated constants is represented in Fig. 14.1. The choice of this model is caused by the following reasons. Noded mass  $m_1$ , elasticity  $k_1$  and friction element  $h_1$  correspond to the piezoelement in this case. This connection of mechanical elements corresponds to a consecutive electric contour [28, 38–40]. This fully refers to a piezoelectric resonator, and only approximately to a piezotransformer [28, 38], because transformation factor is not considered in the final case.

The piezoelement vibrates under the influence of driving harmonious force  $F_m \sin \omega t$ , proportional to voltage excitation. The force measured is represented by mass  $m_2$  force action of the solid, interacting with the piezoelement via imponderable spring linkage with  $k_2$  rigidity coefficient. It reflects the contact elastic properties between the solid specified and the piezoelement. Contact losses are represented by viscous friction coefficient  $h_2$ . Dependence of contact rigidity on force is nonlinear [45]. However, if the load changes in a small neighborhood of its specified value, the contact rigidity coefficient can be considered constant.

This assumption is proved by the AFC form of piezosensor, characteristic of systems with linear restoring force (Fig. 14.2). It is assumed that there is no connection via friction forces.

**Fig. 14.2** AFC of resonant sensor  $\varnothing 30 \times 10$  mm with force change from 0 to 50 N



The vibration system represented in Fig. 14.1 has two degrees of freedom, and under the conditions specified above can be described by the system of linear differential equations:

$$\begin{cases} m_1 \ddot{x}_1 + (k_1 + k_2)x_1 - h_2 x_2 + h_1 \dot{x}_1 = F_m \sin \omega t, \\ m_2 \ddot{x}_1 - k_2 x_1 + k_2 x_2 - h_2 \dot{x}_2 = 0, \end{cases} \quad (14.1)$$

where  $x_1$  and  $x_2$  are displacement of masses  $m_1$  and  $m_2$  respectively relative to the static balance position. The system solution (14.1) for the piezoelement vibration amplitude looks like [56]:

$$x_1 = \frac{F_m(k_2 - m_2 \omega^2 + i h_1 \omega)}{(k_1 + k_2 - m_2 \omega^2 + i h_1 \omega)(k_2 - m_2 \omega^2 + i h_2 \omega) - k_2^2}. \quad (14.2)$$

As the piezoelement works at resonant frequency, then

$$m_1 \omega^2 = k_1. \quad (14.3)$$

From the other side, the piezoelement resonant frequency is so high that the following inequality is always fulfilled in practice:

$$m_2 \omega^2 \gg k_2. \quad (14.4)$$

If the internal friction in piezoceramics and contact losses are ignored, and the following conditions (14.3) and (14.4) are considered, the expression (14.2) becomes simpler and will look like this:

$$X_1 \approx \frac{F_m}{k_2}. \quad (14.5)$$

Thus, the amplitude of piezoelement resonant vibrations, and consequently, connected with it, piezoelement output voltage, are proportional to contact rigidity if the assumptions discussed above are true.

The expression (14.5) is correct only under the condition that the details contact area, transferring the force to the piezoelement, is insignificant in comparison with the piezoelement total surface area. This is true for the devices described in [7, 8].



As it is known [22, 45], the real bodies surfaces have a microrelief – roughness. The smoothest metal surfaces have asperities of the order of  $0.1 \mu\text{m}$ , and roughly machined surfaces have ledges  $100\text{--}200 \mu\text{m}$  high.

Two kinds of micro-deviations, from an ideal surface profile to roughness and waviness, are distinguished.

If the surfaces contact, their roughness and waves are simultaneously deformed. There are also three contact areas: (1) nominal, determined by the contacting bodies' geometry, (2) contour, equal to crumpling of elastically deformed bodies, and (3) actual, created as a result of roughness deformation. Thus, the real contact area is the sum of bonding discrete pads. This area determines the contacting bodies area in which their power interaction occurs.

There are four types of ledge deformation when physical mechanical properties of contacting bodies are considered [22]: elastic and elastic–plastic, plastic, and plastic with hardening. As the pressure on the actual contact areas is high and close to the plasticity limit, the roughness (ledges) deformation and surface approach value can be comparatively high. This approach value is not different for the first and the second loads. This divergence is caused by the fact that plastic deformation occurs only with the first load, and can be absent with the subsequent one. It has been experimentally proved [22, 45] that the loading process does not influence the restoration of elastic roughness. Piezosensor surfaces never lose their contact in the permanently working piezosensor. Therefore, the contact zone deformation can be considered elastic.

The real area contact is calculated by reading profilograms of the contacting surfaces and by plotting the bearing surface. The relative real area of the contact between the flat surfaces and the elastic contact is determined by the expression [22]:

$$\eta = \left(\frac{b}{2}\right) \frac{1}{2\nu + 1} \left(\frac{1}{h_{\max}}\right)^{\frac{\nu}{2\nu+1}} \times \left(\frac{1.5\pi I}{k_1 A_c}\right)^{\frac{2\nu}{2\nu+1}} \times F^{\frac{2\nu}{2\nu+1}}, \quad (14.6)$$

where:  $b$  and  $\nu$  – contacting surfaces parameters;  $h_{\max}$  – maximum height of surface micro-roughness;  $k_1$  – coefficient depending on  $n$ ;  $I = (1 - \mu)/E$  – generalized elastic Kirchhoff constant;  $E$  и  $\mu$  – Young's modulus and Poisson coefficient;  $r$  – ledge radius.

These characteristics are determined for a conjugate surface with a bigger surface roughness. In case of the contact of two surfaces with one order of roughness, parameters  $I$ ,  $n$ ,  $b$ ,  $r$  and  $h$  are calculated by using the formulas:

$$I = \frac{1 - \mu_1^2}{E_1} + \frac{1 - \mu_2^2}{E_2}; \quad r = \frac{r_1 r_2}{r_1 + r_2};$$

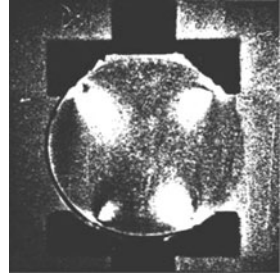
$$\gamma = 0.9(\nu_1 + \nu_2);$$

$$b = \frac{k_2 b_1 b_2 (h_{1\max} + h_{2\max})(\nu_1 + \nu_2)}{h_{1\max}^{\nu_1} h_{2\max}^{\nu_2}}; \quad k_1 = \frac{\Gamma(\nu_1 + 1) \times \Gamma(\nu_2 + 1)}{\Gamma(\nu_1 + \nu_2 + 1)};$$

$$h_{\max} = h_{1\max} + h_{2\max},$$

where  $\gamma$  – gamma function; 1, 2 – indexes of contacting surfaces.

**Fig. 14.3** Local stresses in disk piezoelement under the force supplied to it from prisms



Contact elastic properties are characterized by contact rigidity, determined by the ratio of force  $F_1$ , applied to contacting surfaces, and surfaces approach under the influence of this force.

The contact rigidity value depends on the same surface characteristics as the real contact area. It is determined by the expression [45]:

$$K = \frac{2\nu + 1}{2} \left[ \frac{bk_1 EA_c h m^{0.5}}{1.5\pi(1 - \mu)r^{0.5}} \right]^{\frac{2\nu}{2\nu+1}} \times F^{\frac{2\nu}{2\nu+1}}. \quad (14.7)$$

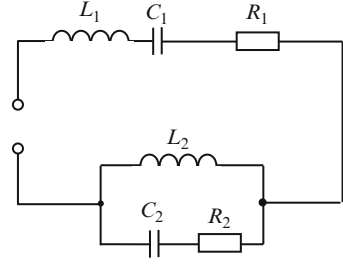
Thus, the real area of the contact surfaces of the vibrating piezoelement and details transferring the force to it, and the contact rigidity, are changed under the influence of the force measured.

Finishing consideration of a resonant piezosensor mechanical model, we should make some remarks concerning the internal friction in piezoceramics. V.S. Postnikov's monograph [42] is devoted to internal friction in the study of metals and piezoceramics. As follows from [42], mechanical stress relaxation, arising with piezoceramics polarization, is the basic process forming internal friction. V.M. Sharapov tested internal friction in piezoceramics under the influence of pressure. As follows from the results obtained, the internal friction of piezoceramics in the piezosensor measurement range does not practically depend on pressure [35]. We should also admit that the force influence on the vibrating piezoelement is of a more complicated character: local stresses which can hardly be considered in calculations appear in the contact places (see Fig. 14.3). Therefore, the problem can be solved only approximately.

Using an electromechanical analogy method [39, 40], the mechanical equivalent scheme is transformed into electric (Fig. 14.1). This scheme is represented in Fig. 14.4 [64]. Here, consecutive contour  $L_1 C_1 R_1$  corresponds to the piezoelement. This is a variant of a piezoresonator and piezotransformer equivalent scheme [1, 31, 41, 58].  $L_2$ ,  $C_2$  and  $R_2$ , connected into a parallel oscillatory contour, correspond to mass  $m_2$ , elasticity  $k_2$ , and quality losses  $h_2$ .

We should note the points from the electromechanical analogy method. Large capacity  $C_2$  and small capacitance  $1/\omega C_2$  correspond to small contact rigidity  $k_2$ . And vice versa, small capacity  $C_2$  and large capacitance  $1/\omega C_2$  corresponds to large contact rigidity  $k_2$ .

**Fig. 14.4** Electric equivalent scheme of resonant contact transducer



Small resistance  $R_2$  corresponds to small losses in contact  $h_2$ . And vice versa, large resistance  $R_2$  corresponds to large losses  $h_2$ .

The oscillatory contour processes have been thoroughly studied [27]. Consecutive contour  $L_1C_1R_1$  can only be studied if there is no influence on the piezoelement. Condenser  $S_1$  voltage is considered to be an output signal. This corresponds to the physical nature of the piezotransducer.

The voltage equation for this contour is:

$$U_{L_1} + U_{R_1} + U_{C_1} = L_1 \frac{di}{dt} + R_1 i + \frac{1}{C} \int i di = e, \tag{14.8}$$

where  $e$  is external emf.

If

$$U = U_{C_1} = \frac{1}{C} \int i di.$$

The following is obtained

$$L_1 C_1 \frac{d^2 U}{dt^2} + R_1 C_1 \frac{dU}{dt} + U = e. \tag{14.9}$$

Contracted notation:

$$\omega_0^2 = \frac{1}{L_1 C_1}, 2\alpha = \frac{R_1}{L_1}.$$

The equation (14.8) is rewritten like this:

$$\frac{d^2 U}{dt^2} + 2\alpha \frac{dU}{dt} + \omega_0^2 U = \omega_0^2 e. \tag{14.10}$$

For sinusoidal electromotive force

$$e = E \exp(j\omega t).$$

The equation (14.10) can be written in the complex form

$$(\omega_0^2 - \omega^2 + i2\alpha\omega)U = \omega_0^2 E. \tag{14.11}$$

Here, complex amplitudes are denoted by points.

The transfer coefficient is found from (14.11)

$$K = -\frac{1}{1 - \frac{\omega^2}{\omega_0^2} + id \frac{\omega}{\omega_0}},$$

where  $d = 2\alpha/\omega_0 R_1/\sqrt{L_1/C_1}$  is contour attenuation,  $\sqrt{L/C} = \rho$  is characteristic resistance, and  $1/d = Q = \rho/R$  is contour  $Q$  factor.

Coefficient transfer module

$$A = |k| = \frac{1}{\sqrt{\left(1 - \frac{\omega^2}{\omega_0^2}\right)^2 + \frac{\omega^2}{\omega_0^2} d^2}} \quad (14.12)$$

expresses the relation of output voltage  $U$  amplitude to emf  $E$  amplitude.

The expression (14.12) is the contour AFC. At resonance  $A = 1/d = 0$ .

The transfer coefficient module is maximal at frequency

$$\omega_1 = \omega_0 \sqrt{1 - \frac{1}{2}d^2} = \omega_0 \sqrt{1 - \frac{1}{2Q^2}}. \quad (14.13)$$

Introducing the denotation

$$\varepsilon = 1 - \frac{\omega^2}{\omega_0^2}.$$

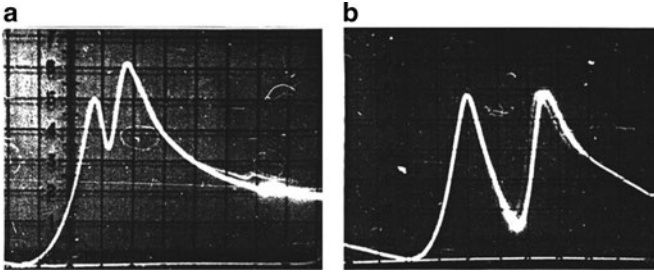
Equation (14.12) can be rewritten as

$$A = \frac{1}{\sqrt{\varepsilon^2 + \frac{\omega^2}{\omega_0^2} d^2}}. \quad (14.14)$$

Working at piezotransducer (contour  $L_1 C_1 R_1$ ) resonant frequency, the condition  $\omega L_2 \gg \frac{1}{\omega C_2}$  is satisfied.

In addition,  $R_2 > 0$  if contact areas are small. In this case, the current in the contour is shunted by capacitance  $1/\omega_0 C_2$ . This leads to a change in the contour  $Q$  factor. Thus, as follows from (14.12) and (14.13), not only module reduction of the transfer factor and piezotransducer output voltage, but also AFC shift to the higher frequency area, occur. This is clearly seen from experimental data obtained (Fig. 14.2).

If the force is increased further, contact rigidity  $k_2$  increases and capacity  $C_2$  decrease accordingly. Thus, parallel contour  $L_2 C_2$  resonant frequency becomes close to the piezotransducer (contour  $L_1 C_1 R_1$ ). As a result, the second ‘‘hump’’ appears at the transducer AFC. Under the influence of some force, the transducer AFC will look like a typical two-contour system (Fig. 14.5a, b).



**Fig. 14.5** AFC of resonant piezosensor under large force influence: (a)  $F = 700$  N, (b)  $F = 950$  N

We will study a piezosensor pulse excitation below.

This problem can be solved by the operational method with Duhamel and Fourier integrals, or by the classical method with voltage differential equation.

A transfer characteristic – unit function action response – should be found first.

The voltage equation in this case looks like

$$LC \frac{d^2U}{dt^2} + RC \frac{dU}{dt} + U = e.$$

Dividing the result on  $LC$  and using the usual symbols we will obtain

$$\frac{d^2U}{dt^2} + 2a \frac{dU}{dt} + \omega_0^2 U = \omega_0^2 e. \quad (14.15)$$

Equation (14.15) is rewritten in the operational form

$$(p^2 + 2\alpha p + \omega_0^2)U = \omega_0^2 e. \quad (14.16)$$

Hence

$$K(p) = \frac{\bar{U}}{\bar{e}} = \frac{\omega_0^2}{p^2 + 2\alpha p + \omega_0^2}.$$

The transitive function will be found as the original for this image, considering that  $e(t) = \sigma(t)$ , and  $U(t) = h(t)$ .

The characteristic equation is worked out first

$$H_2(p) = p^2 + 2\alpha p + \omega_0^2 = 0.$$

Roots of this equation are

$$p_1 = -\alpha + i\omega_1, p_2 = -\alpha - i\omega_1,$$

where

$$\omega = \sqrt{\omega_0^2 - \alpha^2} = \omega_0 \sqrt{1 - \frac{1}{4}d^2}$$

As is clearly seen, the so-called own frequency is always smaller than the resonant frequency.

So,

$$\begin{aligned} H_1(p) &= \omega_0^2, H_2'(p) = 2(p + \alpha), \\ H_2'(p_1) &= 2i\omega_1, H_2'(p_2) = -2i\omega_2, \\ H_2(0) &= \omega_0^2. \end{aligned}$$

Substituting this all in the Heaviside formula [27], we obtain

$$L(t) = 1 + \frac{\omega_0^2 e^{(-\alpha+i\omega_1)t}}{2(-\alpha+i\omega_1)i\omega_1} - \frac{\omega_0^2 e^{(-\alpha-i\omega_1)t}}{2(-\alpha-i\omega_1)i\omega_1}.$$

Removing the common factors, reducing to a common denominator and using Euler formulas, we finally have

$$h(t) = 1 - e^{-\alpha t} \left[ \frac{\alpha}{\omega_1} \sin \omega_1 t + \cos \omega_1 t \right] \quad (t > 0). \quad (14.17)$$

With small attenuation  $\alpha/\omega \ll 1$ , the first member in parentheses can be neglected and then

$$h(t) = 1 - e^{-\alpha t} \cos \omega_1 t \quad (t > 0).$$

The pulse characteristic can be found, having differentiated (14.17)

$$g(t) = \frac{\omega_0^2}{\omega_1} e^{-\alpha t} \sin \omega_1 t \quad (14.18)$$

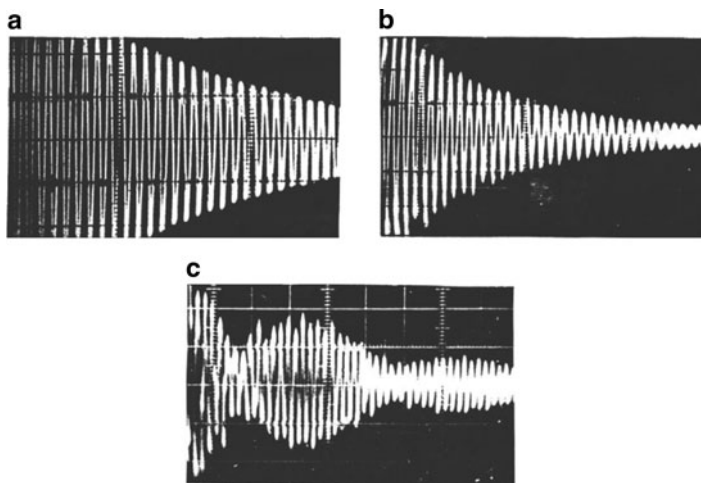
or approximately with small attenuation

$$g(t) = \omega_0 e^{-\alpha t} \sin \omega_0 t. \quad (14.19)$$

So, we obtained the known result which can be formulated in the following way with the regard to the piezosensor. Oscillation with own frequency, fading along the exponential sign, with  $\alpha = R_1/2L_1$  attenuation index, depending on the internal friction in piezoceramics  $R_1$ , is received with piezosensor pulse excitation.

As the experiments showed, free oscillations are raised in the piezosensor if the pulse duration equals half of the own oscillation period (Fig. 14.6) with the greatest amplitude and the least distortions.

Under the forces influencing the transducer and the small contact area, the free oscillation mode does not change (Fig. 14.6a). If the force is subsequently increased and the piezosensor is transformed into a two-circuit system, free oscillations will be of the typical two-circuit system mode (Fig. 14.6c).



**Fig. 14.6** Free oscillation oscillograms of resonant transducer: (a)  $F = 0$  N, (b)  $F = 300$  N, (c)  $F = 950$  N

The actual area increases if the contact area is bigger and the action influence is increased. This leads to an increase in losses. As a result, free oscillation attenuation occurs with  $\alpha = (R_1 + R_2)/2L_1$  index, depending on the contact actual area (Fig. 14.6b).

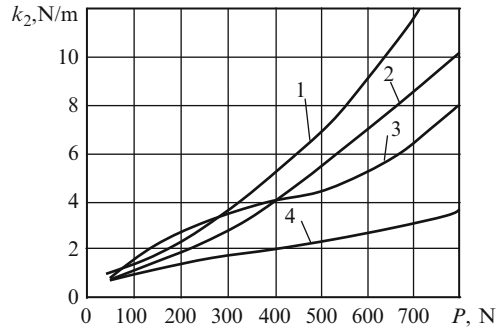
Two practically important conclusions can be drawn from the results of the mechanical and electrical models of a resonant piezotransducer. Contact rigidity and actual contact area – two main characteristics of mechanical contact – can be measured by piezosensors [8, 32, 34, 56–59].

## 14.2 Measurement of Contact Rigidity and Real Contact Area

A practically important conclusion follows from the study of physical and mathematical models of resonant piezotransducers: piezoelectric transducers can be used for contact rigidity and contact actual area measurement. The possibility of measuring these parameters with piezosensors is mentioned in V.M. Sharapov's work [8, 12, 34, 58, 59] for the first time.

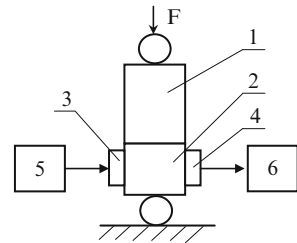
Contact rigidity and real contact area are important parameters, characterizing the mechanical contact condition, friction processes and durability [22, 45].

Indirect method is used for contact rigidity measurement. The two-sample approach is measured under static force  $F$  influence. Contact rigidity is calculated by an empirical formula. This is an essential drawback of this method [45]. If a piezoelement vibrating at resonant frequency is introduced into contact with the sample, then, as follows from (14.5), the amplitude of this piezoelement vibration is



**Fig. 14.7** Contact rigidity dependence on pressure force for piezoelement  $10 \times 15 \times 28$  mm contact with steel 45 (1), aluminium (2), glass-cloth laminate (3), unplasticized polyvinylchloride (PVC) samples (4)

**Fig. 14.8** Scheme of contact rigidity measurement with resonant vibrations in a sample: 1, 2 – samples, 3, 4 – piezoelements, 5 – oscillations generator, 6 – measuring device



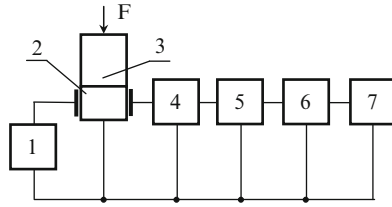
a function of contact rigidity. The contact rigidity results, measured by a  $10 \times 15 \times 28$  mm ИТС-19 piezoceramic piezoelement, are shown in Fig. 14.7 [35].

Contact rigidity is a relative characteristic of contacting details. In this case, coefficient  $k_2$  characterizes contact elastic properties between the sample studied and the piezoelement. Piezoelements with high surface hardness and contact surface finish can be used to reduce the influence of piezoelement surface characteristics on measurement results. In addition, in order that losses in contact do not alter the measurement results considerably, the piezoelement contact and sample areas should be insignificant in comparison with the total surface of the piezoelement. These conclusions are true in the case when the piezoelement is positioned between the samples studied: then the piezotransducer sensitivity obviously increases twice. It is also evident that the sensitivity will be maximal if the clamp direction coincides with the direction of piezoelement resonant vibrations. The piezotransducer is graduated if its data are compared to the contact rigidity value calculated by approach values with 3–4 force pressure values, and the average value of factor  $k_2$  in the formula (14.5) is determined.

More accurate results, independent from elastic piezoelement properties, can be obtained if resonant vibrations are activated in a contacting sample [8], as is shown in Fig. 14.8. This sample vibration amplitude is in inverse proportion to the contact force. As in the previous case, the piezoelement area should be small.

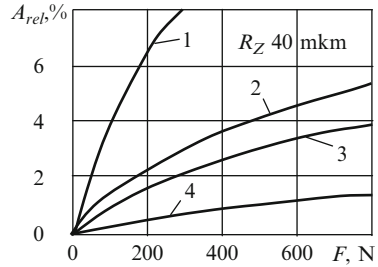
Piezotransducer pulse excitation is used for real contact area measurement [32, 59]. It is a well-known fact that the current in the oscillatory contour looks like





**Fig. 14.9** Block scheme for contact actual area measurement: 1 – pulse generator, 2 – piezotransformer, 3 – sample, 4 – matching device, 5 – discriminator, 6 – amplifier–terminator, 7 – counter

**Fig. 14.10** Dependence of real contact area  $A_C$  on force  $F$ : 1 – for Teflon-4, 2 – textolite, 3 – brass, and 4 – steels CT3



damped vibrations under pulse influence. The initial amplitude of these vibrations is determined by the spectral function emf module at resonant frequency. The phase displacement also equals this function argument at resonant frequency. If internal friction  $R_1$  [35] value is constant, vibration attenuation in the sample depends only on losses  $R_2$  in environment. The latter for specific contacting samples unequivocally depend on the contact real area and acoustic resistance of sample materials ratio.

It is easy to show [35] that the vibration number, exceeding the fixed level  $a$  (where  $a$  is given partly from vibration initial amplitude), will be determined by the expression

$$N = f_{pr} f_r \frac{2L_1}{R_2 + R_1} \ln \frac{1}{a}, \tag{14.20}$$

where:  $f_{pr}$  – pulse repetition frequency;  $f_r$  – piezoelement resonant frequency;  $L_1$  – equivalent inductance of the piezoelement.

Therefore, the contact actual area can be determined by vibration number  $N$ .

A unit with a piezotransformer (Fig. 14.9) for the contact actual area measurement consists of pulse generator 1 and piezotransformer 2, contacting with sample 3. The piezotransformer output signal goes through matching device 4, discriminator 5, and amplifier–terminator 6 to counter 7.

Free oscillations (vibrations) are activated by the piezoelement in a contacting sample to eliminate the influence of piezotransformer elastic properties, just as when contact rigidity was measured.

Actual area measurement data for various materials are shown in Fig. 14.10. Modifications of the methods described can be found in papers by A.I. Trofimov and his co-workers [11, 12].

### 14.3 Frequency-Modulated Oscillation Use for Resonant Piezosensor Excitation

Piezoelectric sensors are fed from high-frequency alternating current (ac) generators. Transducers will work stably if the sensor frequency corresponds to the oscillating system resonant frequency [50, 58]. This condition is violated if the generator frequency is unstable, and if the oscillating system resonant frequency is changed. Stabilization of generator frequency only will not bring the results needed. In addition, to fulfill this condition, generator frequency for each sensor should be individually adjusted. Therefore, a common generator cannot be used for homogeneous sensor feed in protecting control systems.

A measurement method not demanding the non-repudiation of frequency correspondence is proposed in those cases when transformation is based on a change in  $Q$  factor of the measuring transducer oscillatory system [6]. The gist of the method is excitation of the sensor oscillatory system by frequency-modulated (FM) signal. The output voltage and measurement of the maximal AFC value are detected further. The maximal AFC value is the oscillatory system  $Q$  factor function. Carrier frequency is selected to be approximately equal to the resonant frequency. The frequency deviation exceeds the possible range of resonant frequency change caused by the action of destabilizing factors [36].

The question of the influence of frequency-modulated oscillations on oscillatory systems has been thoroughly studied [18, 19, 21, 51, 52]. Studies of emf influence with various velocities and any law of frequency change lead to very complicated expressions [19]. Therefore, the influence of the influence of oscillation FM parameters and the sensor oscillatory system on measurement error will be considered using the example of linear frequency change.

It is known that dynamic AFC can differ from static, received point by point. This difference lies in dynamic characteristic expansion, in dynamic AFC maximum displacement, relative to the static AFC maximum, and in this maximum value change [51, 52]. In the method proposed, the maximum dynamic AFC is measured. Therefore, the first two factors can be practically neglected.

The amount of dynamic AFC deflection from the static is caused by the transient process occurring as a result of frequency change with some velocity. The deflection amount can be calculated by the known formula [52]:

$$\Delta\lambda S(\omega) = \frac{i\omega d^2 S(\omega)}{2d\omega^2}, \quad (14.21)$$

where:  $\lambda$  – frequency change velocity  $\omega$ ;  $S(\omega)$ – static AFC equation.

The formula of error estimation arising because of the maximum deflection of dynamic AFC from the static maximum, looks like this [18] for oscillatory contours:

$$d(\lambda) = 0.4\mu^2, \quad (14.22)$$

where:  $\mu = \lambda/(2\Delta f_0)^2$  – parameter depending on frequency change velocity  $\lambda$ ;  $2\Delta f_0$  – contour pass-band.

Minimum condition of this error:

$$m \ll 1. \quad (14.23)$$

Expression (14.23) is a condition of the “instant” frequency method. It is based on the change slowness of this frequency. The other form of this condition was noted by Gonorovskiy [21]:

$$\frac{\Delta t}{\tau} \gg 1, \quad (14.24)$$

where:  $\Delta t$  – instant frequency residence time in the contour pass-band;  $\tau = 2L/r$  – contour time constant.

Assuming that  $\Delta t$  is approximately equal to the modulating voltage period  $T_\Omega$ , we obtain:

$$\frac{T_\Omega}{2L} \gg 1 \quad (14.25)$$

or

$$\frac{p f_0}{Q \Omega} \gg 1, \quad (14.26)$$

where  $f_0$  is contour resonant frequency, and  $Q$  is  $Q$  factor.

The final expression is the condition for modulating voltage frequency choice.

If the frequency  $\Omega$  is constant, the change in instant frequency velocity emf depends on frequency deviation amplitude (deviation)  $\omega_d$ . Therefore, this inequality will be an additional condition:

$$\frac{\omega_d}{\Delta \omega_0} \ll 1. \quad (14.27)$$

where  $\Delta \omega_0 = 2\pi \Delta f_0$ .

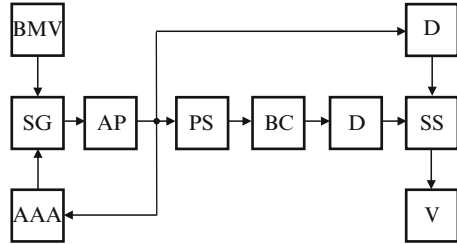
If these conditions (14.23–14.27) are fulfilled, the voltage on the oscillatory circuit output reproduces the circuit resonant curve form. The resonant characteristic maximum is determined by its  $Q$  factor [21]:

$$U(t) = \frac{1}{\sqrt{1 + [(\omega - \omega_0)\tau]^2}} Q \cos \left[ \frac{\lambda t^2}{2} - \varphi \right], \quad (14.28)$$

where  $\varphi$  is phase displacement.

To illustrate the method discussed, the piezotransducer AFC oscillogram is offered in Fig. 14.2. This piezotransducer is  $\varnothing 30 \times 10$  mm. It is made of piezo-ceramic IITC-23. Its  $Q$  factor depends on the force applied, made with the camera shutter open by a device of XI-27 type for AFC study. The force was continuously changed from 0 to 5 kg. As can be seen from Fig. 14.2, the AFC maximum gives an idea of the force applied.

**Fig. 14.11** Measuring device block scheme



Obviously, the carrier frequency choice, relative to the oscillatory system resonant frequency, deviation value, and also frequency change deviation from the linear law, will affect the output voltage form. This form can vary. However, if these conditions (14.23–14.27) are fulfilled, the value measured will be definitely determined by the AFC maximum.

Output voltage envelope frequency is two-fold higher than modulation frequency with harmonious modulation and equality of carrier frequency and resonant frequency of a single oscillatory contour. The complex transfer coefficient will look like this [21]:

$$k(i\omega) = \frac{1}{\sqrt{1 + [\omega_d \tau \cos(\Omega t)]^2}} e^{i\varphi}. \quad (14.29)$$

A measuring device block scheme, accomplishing the offered work method with a piezoelectric sensor, is represented in Fig. 14.11. Here, the voltage on the piezoelectric transducer arrives from the frequency-modulated oscillation generator. The generator consists of a driving oscillator (DO), a modulating voltage block of (MVB), a power amplifier (PA) and an automatic amplitude adjustment scheme (AAAS). As the experiments showed, AAAS use allows reduction of the nonlinear distortion factor. It also assures output voltage amplitude non-uniformity of the generator in the frequency range change from 52 to 54 kHz (less than 2%). However, working with high  $Q$  factor transducers, it is insufficient for high accuracy.

The measuring transducer output voltage arrives at detector (D) through the buffer stage (BS). An additional detector and a subtractor (S) are introduced into the scheme for reception of direct calibration characteristics. The voltage to this detector arrives from the generator. Difference voltage, proportional to the force measured, is measured by the direct current voltmeter (V).

Depending on the measurement accuracy demanded, a passive or active peak value transducer can be used as a detector. The passive transducer transformation error in large signals field is 1.5–4%. This limits its application. Peak value active transducers are characterized by a wide range of the voltages transformed and an error about 0.1% [20]. The negative feedback method is used for linearization of the transfer characteristics of these transducers.

As the tests showed, the maximum permissible basic error of the measuring device with active transducers and a direct current digital voltmeter (not including the measuring transducer error) does not exceed 0.2% of the measurement range.

## 14.4 Negative Feedback in Resonant Piezosensors

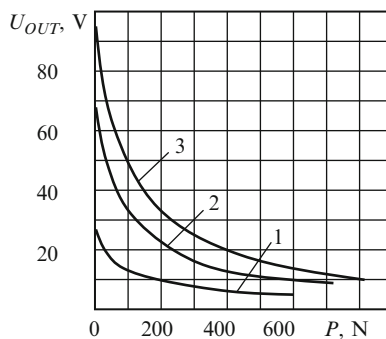
Mechanical values – force, pressure, acceleration, etc. – are input influences for piezoelectric sensors. Therefore, as it was mentioned earlier, feedback introduction according to the traditional scheme (see Chap. 4) considerably complicates sensor design, demanding creation of power compensators, etc. Moreover, as a feedback circuit determines the piezosensor parameters and accuracy in this case, the requirements to this circuit will be as high with regard to the sensor [43].

Meanwhile, as was mentioned before, this problem was solved and simplified by I.G. Minaev and V.M. Sharapov [33]. They considered that piezoelectric sensors are reversible. Input mechanical parameter change can be compensated on the piezosensor second input, i.e., along the electric channel. This method is applicable not only for piezosensors, but also for any other sensors if their output characteristics are functions of two or more parameters. In this case, feedback covering the auxiliary channel can be introduced [26].

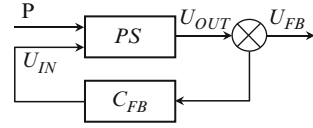
This problem is considered in more detail below in the example of a contact resonant piezosensor, output characteristics of which are of a strongly expressed nonlinear character [23].

The family of characteristics of these piezosensors is shown in Fig. 14.12. The transducer is disk-shaped ( $\varnothing 30 \times 5$  mm). It is made of IITC (PZT) piezoceramics. Curves 1, 2 and 3 are received at excitation voltage 5, 10 and 15 V respectively at the resonant frequency of radial oscillations of the given piezoelement (70 kHz). The linear part of the given characteristics, depending on the approach accuracy, is no more than 10–15% of the total measurement range.

**Fig. 14.12** Output characteristics of resonant piezosensor with  $U_{\text{GEN}}$ :  
1–5 V, 2–10 V, 3–15 V  
( $f_p = 70$  kHz)



**Fig. 14.13** Block scheme of resonant transducer with feedback



There are various methods of linearization of sensor output characteristics. The method of negative feedback is popular among them. The feedback covers the sensor basic measuring channel. However, as it was mentioned before, this method use for force measuring sensors is connected with the design of power compensators. This limits their use of large forces measurement.

Therefore, feedback covering the auxiliary channel can be introduced for a sensor with output characteristics which are functions of two or more parameters.

As can be seen from Fig. 14.12, the sensor output characteristic can be presented like this:

$$U_{OUT} = f(P, U_{IN}).$$

Differential of this function:

$$dU_{OUT} = \frac{\partial U_{OUT}}{\partial P} dP + \frac{\partial U_{OUT}}{\partial U_{IN}} dU_{IN}.$$

As follows from this expression, the measured parameter  $P$  change can be compensated by the corresponding change of the auxiliary parameter  $U_{IN}$  change, as is shown in Fig. 14.13. Here,  $C_{FB}$  is a static coefficient of the feedback transfer link:

$$C = -\frac{\partial U_{OUT}}{\partial U_{IN}};$$

PS – piezosensor.

Then the new output characteristic of this transducer will look like:

$$U_{IN} = \varphi(P).$$

It is shown that sensitivity  $S$  of the device with feedback is determined by the expression:

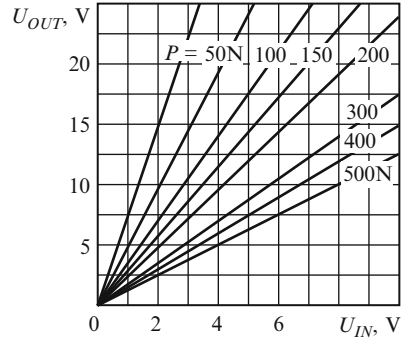
$$S = \frac{dU_{IN}}{dP} = -\frac{\frac{dU_{OUT}}{dP}}{\frac{1}{C_{FB}} + \frac{dU_{OUT}}{dU_{IN}}}. \quad (14.30)$$

For astatic feedback, and also for static with  $C \rightarrow \infty$ , this expression will look simpler:

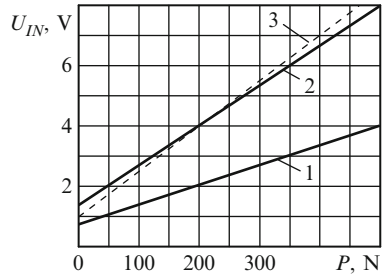
$$S = -\frac{\frac{dU_{OUT}}{dP}}{\frac{dU_{OUT}}{dU_{IN}}}. \quad (14.31)$$

This equality is the obvious condition of complete linearization of the new output characteristic, i.e., the sensitivity stabilization condition of a measuring device with feedback:

**Fig. 14.14** Amplitude characteristics of IITC-19 piezosensor ( $\varnothing 30 \times 5$  mm)



**Fig. 14.15** Linearized transducer characteristics:  
 1 – with  $U_{OUT} = 5$  V and  
 2 – with  $U_{OUT} = 10$  V,  
 3 – experimental characteristic



$$\frac{dS}{dP} = 0. \tag{14.32}$$

Its fulfillment can be checked by substitution of the right parts of equations (14.30) or (14.31) in (14.32). The analytical solution of this problem without the exact expression of  $U_{OUT} = f(P, U_{IN})$  causes the difficulties known. The experimental families of curves  $U_{OUT} = f_1(P)$  with variable parameters of  $U_{IN}$  or  $U_{OUT} = f_1(U_{IN})$  and  $P$  (Figs. 14.12 and 14.14 respectively) can be used for solution of the problem. The line of constant value  $U$  (for astatic feedback) should be drawn parallel to  $X$ -axis in these cases. A new output characteristic should be created according to its intersection points with curves of the family discussed.  $U_{IN} = f(P)$  with  $U_{OUT} = \text{const}$ .

The results of this plotting with  $U_{OUT} = 5$  and 10 V are shown in Fig. 14.15. An experimental output characteristic is constructed for comparison (astatic negative feedback). As can be seen from Fig. 14.15, a considerable output characteristic linearization for resonant piezoelectric sensors of static pressure can be reached by negative feedback introduction along the auxiliary channel.

Feedback can be practically introduced if an additional electrode system is attached to the piezoelement. The feedback circuit is connected to it.

## 14.5 Piezosensors with Ultrasonic Concentrators

Ultrasonic concentrators are devices for ultrasound (US) intensity increase, i.e., the amplitude of particle vibration displacement [3, 53].

An ultrasonic concentrator is a mechanical transformer of vibrations. This means that displacement amplitude on the output concentrator side is  $K$  times higher than on the input, where  $K$  is the concentrator transfer coefficient.

Two types of concentrators, based on different action principles, are distinguished: focusing or high-frequency, and rod or low-frequency. In this section, the influence of US rod concentrators on piezoelectric sensor parameters is studied.

Thus, a rod US concentrator (RUSC) is a device for increase of particle vibration displacement amplitude (or particle oscillatory velocity) in a low-frequency range. RUSC is a hard rod of variable section or variable density, attached to the radiator by its wider end, or by the part of greater material density.

RUSC action principle is based on an increase in particle vibration displacement amplitude as a result of its cross-section reduction or density, according to the momentum conservation law. Then, displacement amplitude increases with the difference in the diameters or densities of opposite ends of the rod.

RUSCs are widely used in ultrasonic technology. RUSCs are components of ultrasonic vibration systems. An RUSC can be considered as an acoustic waveguide in which a zero vibration mode is propagated. It is characterized by a constant section amplitude. The maximum linear size of the concentrator  $D$  wide should be less than  $\lambda/2$ , where  $\lambda$  is wave length in the concentrator material.

RUSCs usually work at resonant frequency; therefore, length  $L$  of the concentrator should be a multiple of the half-waves integer:  $L = n\lambda/2$ , where  $n = 1, 2, 3$ . If the frequency is intended,  $\lambda$  depends on RUSC form as a result of US propagation velocity in wave guides with variable cross-section.

An RUSC with variable density is usually made of two interconnected rods of various materials  $\lambda/4$  long with identical variable cross-section.

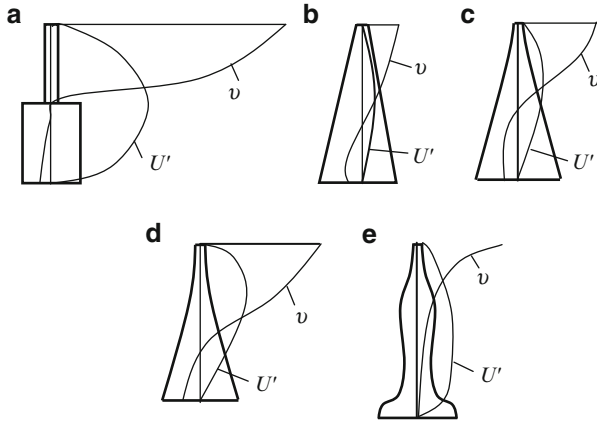
RUSCs are usually classified according to the following features [53]:

- (a) Longitudinal section form (Fig. 14.16)
- (b) Cross-section form (round, sphenoid, etc.)
- (c) Number of elements with various longitudinal section profiles (simple, compound – Fig. 14.17)
- (d) Number of tandem resonant concentrators of half-wave length (one, two, etc., stage – Figs. 14.18 and 14.19)
- (e) Mean line form (rectilinear, bent)
- (f) Concentrator vibration type (longitudinal, shear, torsion)

RUSC cross-section change can occur as a result of rod external and internal profile change (Figs. 14.16 and 14.19) respectively.

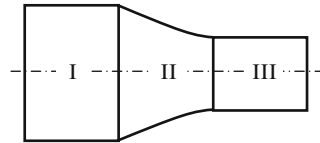
The RUSC force coefficient is  $C = \xi/\xi_0$ , where  $\xi$  and  $\xi_0$  are displacement amplitudes on its narrow and wide ends respectively, under the influence of harmonic vibration with circular frequency  $\omega$ , the vibrational speed amplitude  $V = \omega\xi$ ,



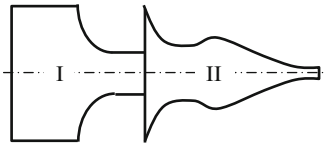


**Fig. 14.16** Sections of round simple one-step concentrators of longitudinal vibrations: (a) step-wise, (b) conic, (c) exponential, (d) catenoidal, (e) gausses (ampoule); curves show the distribution of amplitude oscillatory velocity  $v$  and deformations  $U'$  along the concentrator length

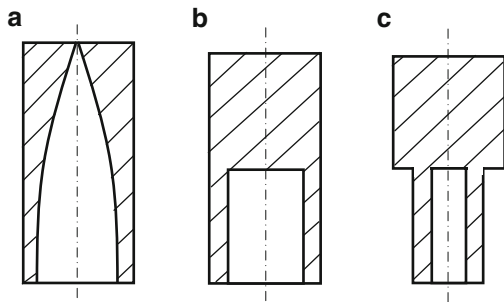
**Fig. 14.17** Compound concentrator: *I* – big diameter cylinder, *II* – conic or exponential-shaped rod part, *III* – small diameter cylinder



**Fig. 14.18** Two-step concentrator: *I* – step concentrator, *II* – ampoule concentrator



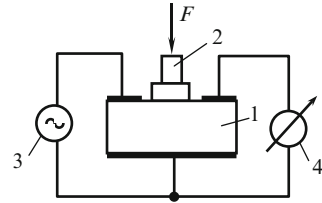
**Fig. 14.19** Concentrators with variable internal profile: (a) exponential, (b) and (c) stepwise



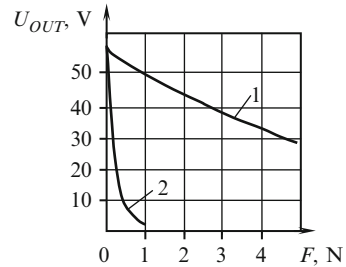
and consequently  $C = V_i/V_0$ . For step RUSC,  $C = N^2$ , where  $N = R_0/R_e$ , and  $R_e$  and  $R_0$  are radiuses of narrow (output) and wide (input) ends respectively. For exponential  $C = N$ , catenoid  $C = N/\cos(2\pi l/\lambda)$ , and for conic  $C < N$  and always  $C < 4.6$  [59].

**Fig. 14.20** Resonant piezosensor with ultrasonic concentrator:

1 – piezotransformer,  
2 – concentrator,  
3 – generator, 4 – measuring device



**Fig. 14.21** Piezosensor static characteristics: 1 – without concentrator, 2 – with concentrator



The maximum amplitude of vibrational speed  $V_m$ , received on the narrow RUSC end, depends on the properties of the concentrator material, destroying the fatigue stress  $F$ , and wave resistance  $\rho c$  (where  $\rho$  – density,  $c$  – US wave propagation velocity), and on dimensionless function  $T$ , depending only on the concentrator form:

$$V_m = \frac{F}{\rho c} T. \quad (14.33)$$

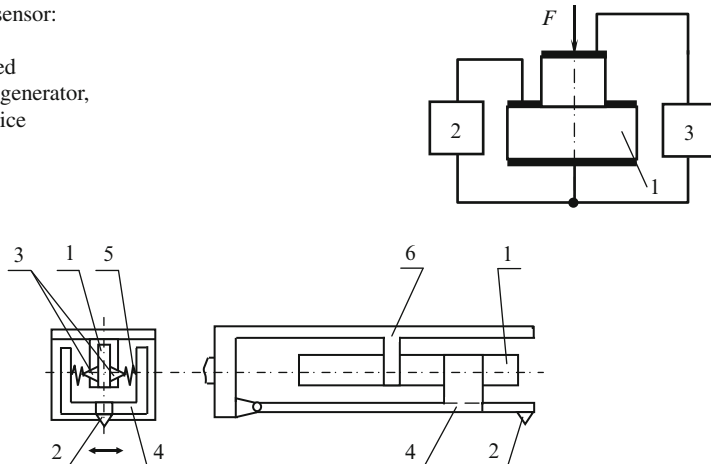
RUSCs are widely used in US technology as various US tools, with US machine working, soldering, crushing, dispersion, clearing, in medicine, etc. [24].

The sensitivity increase effect of mechanical value resonant piezoceramic transducers with RUSC use was discovered and partially studied by I.G. Minaev and V.M. Sharapov in 1976 [56–58]. Some RUSC uses in piezosensors are described in papers by A.I. Trofimov [50] and V.M. Sharapov [56–58].

A simple sensor with RUSC is shown in Fig. 14.20 [3]. Here, stepwise concentrator 2 is attached to the surface of piezotransformer 1. The piezotransformer is connected to oscillation generator 3 and measuring device 4. The dependence of piezotransformer output voltage on the force is shown in Fig. 14.21 for a sensor without concentrator (curve 1) and for the sensor in Fig. 14.20 (curve 2). As can be seen from Fig. 14.21, the transducer sensitivity was increased ten-fold because of the use of the concentrator.

One more variant of the sensor design is shown in Fig. 14.22 [14]. Here, the piezoelement is built as a stepwise concentrator. It can be practically achieved if two piezoelements of different diameters and lengths, satisfying the creation condition of resonant vibrations in piezoelements, are interconnected. The connections can be glued with epoxy compound or soldered (Rose's and Wood's alloys, etc.). Sensitivity increases for the given design can reach  $D^2/d^2$ , where  $D$  and  $d$  are piezoelement diameters.

**Fig. 14.22** Piezosensor:  
 1 – stepwise  
 concentrator-shaped  
 piezoelement, 2 – generator,  
 3 – measuring device



**Fig. 14.23** Monophonic resonant piezoelectric pickup: 1 – piezoelement, 2 – needle, 3 – concentrators, 4 – needle carrier, 5 – wrap compression springs, 6 – housing (case), 7 – flat springs

Not only a considerable sensitivity increase, but also accuracy improvement can be seen as advantages of concentrator use. This can be achieved if the concentrator is made of a material with better elastic characteristics than piezoceramics (steel, quartz and bronze). In addition, the force can be applied to the point through spherical elements, as, for example, in force measuring equipment. Fastening the transducer to the concentrator vibration node, losses in the environment can be avoided completely. Finally, the force can be transferred through a resilient precision element, rigidly welded or soldered to the concentrator. This makes it possible to avoid the influence of contact rigidity and the linearization of static characteristics.

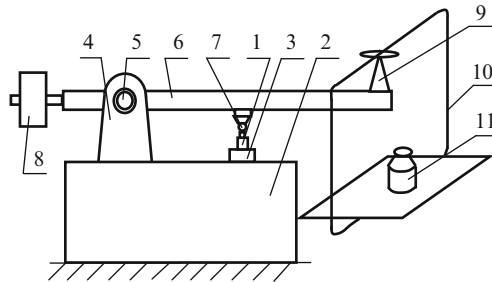
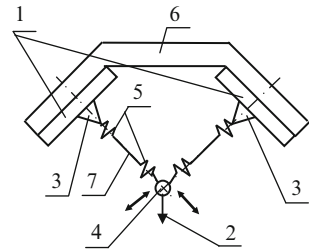
For example, in a piezoelectric resonant transducer pickup head [10], represented in Fig. 14.23, concentrators 3, fastened on the surface of piezoelement 1, are connected with helical springs 5 by needle carrier 4. When the needle moves along the gramophone record groove, the gramophone signal is transformed into a dynamic force by needle carrier 4. Then, the frequency and amplitude change law of this force corresponds to the gramophone signal. This force is transferred to concentrator 3. The needle carrier force limits the vibration amplitude of the smaller concentrator section base. This leads to a change in piezoelement output voltage.

As a result, piezoelement output voltage appears to be amplitude-modulated. As the output voltage is of a high value, the detecting is of a high quality. It is done by the known schemes. We should note that the frequency range reproduced by the given transducer practically begins at zero. It is limited by resonant frequency of the piezoelement (70–100 kHz).

A transducer variant for a stereophonic pickup is shown in Fig. 14.24 [53].

The influence of design, material and concentrator dimensions on force transducer sensitivity are considered below.

**Fig. 14.24** Stereophonic resonant piezoelectric pickup:  
 1 – piezoelement, 2 – needle, 3 – concentrators, 4 – needle carrier, 5 – wrap compression springs, 6 – housing (case), 7 – flat springs



**Fig. 14.25** Load unit: 1 – concentrator, 2 – base, 3 – piezoelement, 4 – support, 5 – bearing, 6 – lever, 7 – ball, 8 – counterbalance, 9 – prisms, 10 – supporting bracket (suspension), 11 – weights

The load unit represented in Fig. 14.25 was used in the research. The unit can create 1,000 N forces with less than 0.1% error.

The following series of concentrators were made for study:

1. Conic, exponential, catenoid, gaussians and stepwise titan concentrators. The diameter of the wide base is 18 mm. The top end diameter is 3 mm.
2. Titan stepwise concentrators with a wide base diameter of 15 mm and upper end diameter of 3 mm, and heights of 12, 14, 16, 18, 20, 22, 24, 26, and 28 mm.
3. Titan stepwise concentrators with a wide base diameter of 15 mm, height of 18 mm and upper end diameter of 3 mm, made of titan, У8А and CM3 steels, brass Л163, bronze БрОФ 6.5–1.5 and polystyrene.

The ends of all concentrators were burnished and polished.

A 38 mm-diameter and 15 mm-thick piezotransformer made of piezoceramic ПТС-19 was used in the research. A piezoelement electrode was divided into two disk-shaped parts: 22 mm in diameter and a ring with 22.5 mm internal and 38 mm external diameter. The concentrator was fastened to the centre of the ring electrode. The force was applied to the concentrator top through the ball 12 mm in diameter (from the ball-bearing).

The sensitivity of output voltage on force dependence was determined on the initial site.

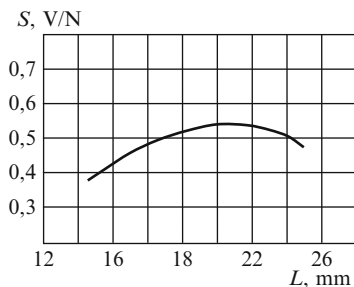
**Table 14.1** Sensitivity of piezosensor ( $\varnothing 38 \times 16$  mm) with rod ultrasonic concentrator

No.	Concentrator type	Amplification coefficient, $K$	Sensitivity (V/N)
1.	Conic, truncated	3.6	2.3
2.	Exponential	4.7	3.2
3.	Catenoid	4.2	2.7
4.	Gausses (ampoule)	3.4	2.3
5.	Stepwise	22	5.2

**Table 14.2** Sensitivity of piezosensor ( $\varnothing 38 \times 16$  mm) with stepwise concentrator ( $\varnothing 15 \times \varnothing 3 \times 18$  mm)

No.	Concentrator material	Young's modulus $E \times 10^{-12}$ (dyne/cm <sup>2</sup> )	Longitudinal			Sensitivity $S$ (V/N)
			waves velocity, $c \times 10^{-5}$ (cm/c)	Rupture stress $F \times 10^{-9}$ , dyne/cm <sup>2</sup>	$F/\rho c \times 10^{-3}$ (cm/c)	
1	2	3	4	5	6	8
1.	Titan	1.16	4.9	7.2	3.35	5.2
2.	Steel У8А	2.18	5.24	5.5	1.28	4.9
3.	Steel CT3	2.09	5.14	2.2	0.57	2.2
4.	Bronze	0.99	3.36	3.2	1.08	2.1
5.	Brass	0.89	3.24	1.5	0.56	1.6

**Fig. 14.26** Dependence of transducer sensitivity  $S$  on stepwise concentrator height



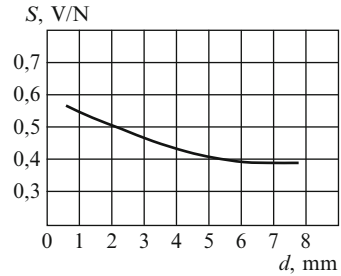
As follows from Table 14.1 data, a transducer with a stepwise concentrator has maximum sensitivity. It also has the highest coefficient of vibration amplitude amplification.

As can be seen from Fig. 14.26, the dependence of concentrator sensitivity  $S$  on length  $L$  has a maximum evidently corresponding to the concentrator resonance.

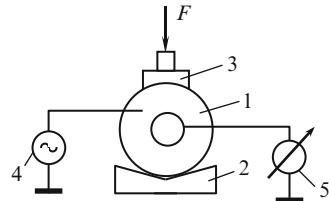
If the concentrator amplification factor increases, the transducer sensitivity also increases (Fig. 14.27). For a compound concentrator, this corresponds to the upper end diameter decrease in particular.

However, the amplification coefficient and vibration amplitude on the concentrator output are the only determining parameters influencing the piezotransducer sensitivity. As the resonant transducer sensitivity depends also on the contact rigidity between the piezoelement and the details transferring force [34] to it, the

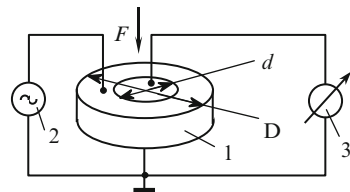
**Fig. 14.27** Dependence of transducer sensitivity  $S$  on stepwise concentrator upper end



**Fig. 14.28** Sensor with stepwise concentrator:  
1 – piezoelement, 2 – prism,  
3 – concentrator,  
4 – generator, 5 – voltmeter



**Fig. 14.29** Sensor:  
1 – piezoelement,  
2 – generator, 3 – voltmeter,  
 $F$  – force influencing the transducer,  $d$  – disk electrode diameter,  $D$  – piezoelement external diameter



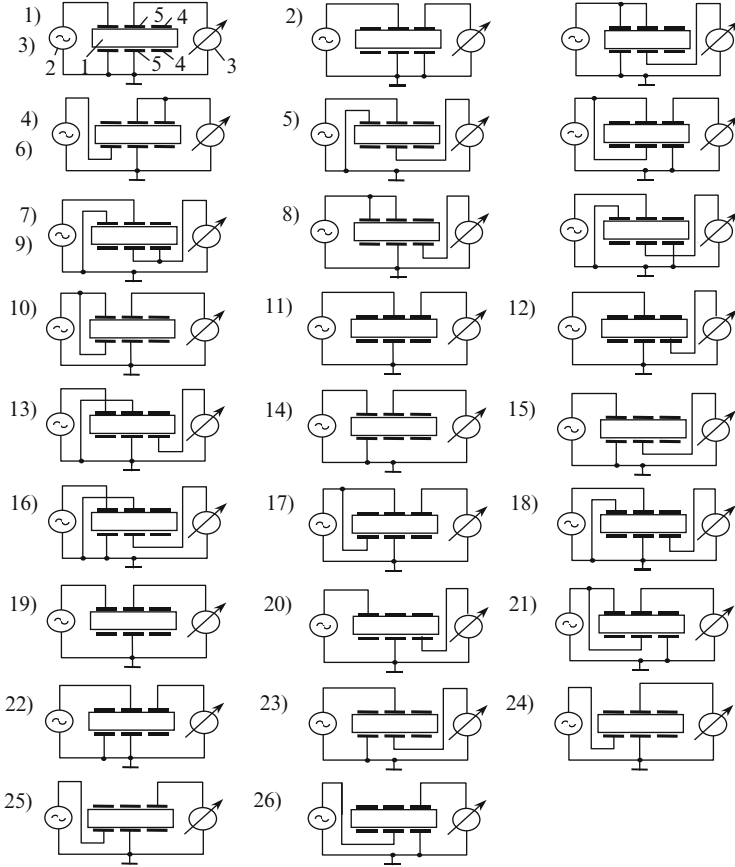
elastic properties of the concentrator material influence resonant piezotransducer sensitivity (Table 14.2).

Force application towards the resonant vibrations of the piezoelement leads to an increase in sensor sensitivity. A sensor with a concentrator is shown in Fig. 14.28. Piezoelement 1 ( $\varnothing 38 \times 16$  mm), fastened to prism 2 is used here. The force to the piezoelement is sent through titan stepwise concentrator 3 ( $\varnothing 15 \times 3 \times 18$  mm). As in the previous cases, the piezoelement is activated at resonant frequency ( $\sim 53$  kHz) by generator 4. The output voltage is measured by voltmeter 5.

As the measurements showed, in this case the transducer sensitivity is 3.3 times higher than when the force was supplied to the piezoelement end.

A disk with disk- and ring-shaped electrodes on its ends is the most widespread piezoelement form for resonant piezoelectric sensors. Traditionally, the generator is connected to the ring electrode, and the measuring device to the disk (Fig. 14.29) [8]. It is shown in the work by Sharapov [15] that the sensitivity maximum for this scheme is reached when disk electrode diameter  $d$  is correlated to the piezoelement external diameter  $D$ , equal to 0.578.

However, as the experiments showed, this piezoelement connection scheme is not optimal from the point of maximal amplitude achievement and, consequently, sensor sensitivity.



**Fig. 14.30** Sensors excitation scheme: 1 – piezotransformer, 2 – generator, 3 – measuring device, 4 – ring electrode, 5 – disk electrode

The sensors of which schemes are shown in Fig. 14.30 were studied. Resonant frequency of radial vibrations and transfer coefficient at this frequency were measured. The generator voltage equals 1. Measurement results are given in Table 14.3.

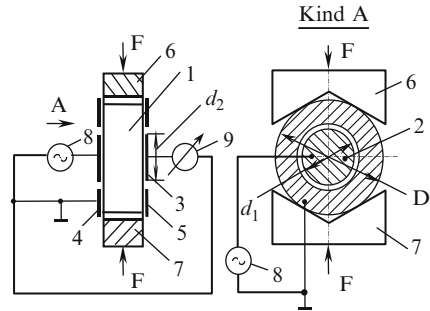
As can be seen from Table 14.3 and Fig. 14.30, the greatest transfer coefficient is received for schemes with the generator connected to the electrodes, located on one piezoelement end (variants 4, 5, 7, 24, 26). The best results (almost twice higher than in the known scheme) are obtained for the case when signal wires are connected to disk electrodes (variant 5).

A sensor design of static forces based on the given scheme is shown in Fig. 14.31. The sensor consists of cylindrical piezotransformer 1 with disk-shaped 2 and 3 and ring-shaped 4 and 5 electrodes on its ends. The piezotransformer is located between prisms 6 and 7, through which force  $F$  is supplied. The piezotransformer is connected to generator 8 and measuring device 9. The generator signal wire is

**Table 14.3** Transfer coefficient and resonant frequency of sensor ( $\varnothing 38 \times 16$  mm)

Scheme variant, Fig. 14.30	Transfer coefficient	Resonant frequency (kHz)	Scheme variant, Fig. 14.30	Transfer coefficient	Resonant frequency (kHz)
1.	2.9	72.2	14	2.2	74.5
2.	1.8	71.2	15	1.75	74
3.	2.6	72.3	16	3.15	72
4.	4.6	77.8	17	2.25	71.5
5.	5.7	79.1	18	2	71
6.	1.5	71.3	19	3.3	74.5
7.	5.2	78	20	1.8	74
8.	1.8	71	21	3.4	72
9.	3.2	72	22	1.8	74.5
10.	3.3	72	23	3.1	74
11.	1.1	72.5	24	4.5	77.5
12.	0.9	71.5	25	3.35	79
13.	1.65	71	26	3.8	79

**Fig. 14.31** Static force sensor: 1 – piezoelement; 2, 3 – disk electrodes; 4, 5 – ring electrodes; 6, 7 – prisms; 8 – generator; 9 – voltmeter



connected to the larger diameter disk electrode 2. The measuring device signal wire is connected to the smaller diameter disk electrode 3. Common wires of the devices are connected to the smaller area ring electrode 4.

It appeared that electrode sizes influence sensor sensitivity.

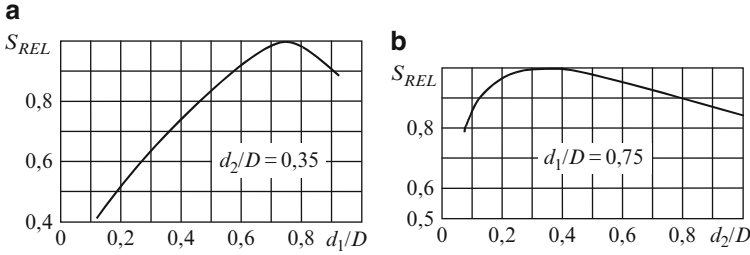
The dependence of relative sensitivity  $S_{REL} = S/S_{max}$  on disk electrode diameters to the ring electrode external diameter ratio is shown in Fig. 14.32. The sensitivity maximum for this sensor is reached with  $d_1/D = 0.75$  and  $D_2/D = 0.35$ .

As was mentioned above, a piezotransformer made as a stepwise concentrator (see Fig. 14.22) is rather prospective for use as a static forces resonant sensor [14].

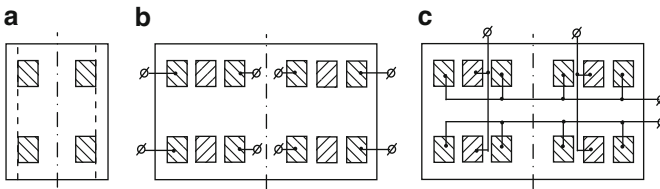
As is known [30], the highest transfer coefficient, and hence sensitivity, can be reached in a piezotransformer if transverse–longitudinal vibrations are used (Rosen design). A combination of Rosen and a stepwise concentrator design allows essential sensitivity improvement [56–58].

A transducer designed for measurement of moments, friction forces, liquid properties, etc. is considered.





**Fig. 14.32** Dependence of relative sensitivity  $S_{REL}$  (a) on  $d_1/D$  at  $d_2/D = 0.35$  ratio and (b) on  $d_2/D$  at  $d_1/D = 0.75$  ratio



**Fig. 14.33** Piezoelectric transducer of torsion vibrations: (a) appearance, (b) polarization scheme, (c) activation scheme

This transducer is the combination of a piezoceramic torsion transducer and a rod torsion concentrator. The transducer looks like a hollow IITC-23 piezoceramic cylinder with two groups of electrodes on its external surface Fig. 14.33a. Electrodes are simultaneously used for polarization, and then for vibration activation. Electrode connection schemes under polarization and activation are shown on the transducer external surface scan (Fig. 14.33b,c).

Activation of voltage connection causes piezoelement twist. A condenser with activated torsion vibrations is fastened to the piezoelement end surface. The equation for the concentrator torsion vibrations looks like this [2]:

$$\frac{\partial^2 \varphi}{\partial x^2} + \frac{1}{I_p(x)} \frac{\partial J_p(x)}{\partial x} \frac{\partial \varphi}{\partial x} - \frac{\rho}{\mu} \frac{\partial^2 \varphi_1}{\partial t^2} = 0, \tag{14.34}$$

where:  $\varphi_1$  – measurement, section angular deflection;  $\rho$  and  $\mu$  – measurement, density and rod material shear (rigidity) modulus;  $I_p(x)$  – measurement, inertia polar moment of rod cross-section.

One should note that the equation is true under the condition that the concentrator sections rotate as a whole, without distortion when vibrating. This condition can be violated in some cases. Nevertheless, the equation (14.34) can be used in practical calculations.

For harmonious vibrations, the equation (14.34) can be rewritten like this [54]:

$$\varphi'' + \frac{1}{I_p(x)} \frac{\partial I_p(x)}{\partial x} \varphi' + k^2 \varphi = 0, \quad (14.35)$$

where

$$k^2 = \frac{\omega^2 \rho}{\mu} = \frac{\omega^2}{c_{hp}^2}; \omega = 2\pi f$$

The solution of this and equation analysis in the work by Haritonov [54] show the following.

There is a certain critical frequency  $\omega_{cr}$  under which vibrations cannot propagate in the concentrator, therefore

$$\omega_{work} \approx (1.5 - 3)\omega_{cr},$$

where  $\omega_{cr} = \gamma c_{cr}$ ;  $\gamma = (1/l)A_{rch}N^2$ ;  $N = r_0/l$ ;  $r_0$ ,  $r_l$  – radiuses of input and output concentrator sections accordingly;  $l$  – concentrator length.

Twist angle amplification coefficient:

$$K_T = \frac{N^2}{\cos kl}. \quad (14.36)$$

Linear displacement amplification coefficient on the surface concentrator:

$$K_{LIN} = \frac{N}{\cos kl}. \quad (14.37)$$

Concentrator resonant length:

$$l = \frac{\lambda}{2} \sqrt{\frac{(kl)^2 + (A_{rch}N^2)^2}{\pi^2}}. \quad (14.38)$$

Completing consideration of torsion vibration transducers, we should note that the technique for fastening them to the housing (case) by so-called torsion insulators is important at the design stage [44].

## 14.6 Constructive Control Methods of Force and Pressure Piezosensor Characteristics

The first designs of resonant piezosensors [4, 5] had low sensitivity, accuracy, and linearity.

Some circuit methods of sensitivity, linear static characteristic increase and sensor error reduction were described earlier.

Certain sensor designs allowing resonant piezotransducer sensitivity, accuracy, and linearity improvement are considered in this section.

Static characteristic non-linearity is an essential drawback of resonant piezosensors. There are various methods of static characteristic linearization. Negative feedback introduction methods have a special place among them (see Chap. 5).

The method of static characteristic linearization by means of resilient elements is of a certain scientific interest [37].

As is proved in [9, 34], contact rigidity between the piezoelement and the details transferring force to it is the factor which influences the piezoresonant sensor output signal at resonant vibrations. Contact rigidity increases non-linearly [51] with the force increase. This determines nonlinearity of the static characteristic.

If force to the piezoelement is applied through the resilient element, causing total rigidity and contact rigidity for this element to increase linearly with the force increase, the piezoelement input stress will also decrease linearly.

A formed wrap compression spring is the resilient element with nonlinearly changing rigidity.

The resilient element (wrap spring) and contact rigidity total rigidity can be calculated by the formula

$$C_{\text{sum}} = \frac{C_{\text{cont}}C_{\text{el}}}{C_{\text{cont}} + C_{\text{el}}}, \tag{14.39}$$

where  $C_{\text{cont}}$  is contact rigidity, and  $C_{\text{el}}$  is resilient element rigidity.

The linearization condition of calibration characteristics is expressed by the equation:

$$C_{\text{sum}} = \frac{C_{\text{cont}}C_{\text{el}}}{C_{\text{cont}} + C_{\text{el}}} = aF, \tag{14.40}$$

where  $F$  is force measured, and  $a$  is constant.

From the equality (4.11)

$$C_{\text{sum}} = \frac{aFC_{\text{cont}}}{C_{\text{cont}} - aF}. \tag{14.41}$$

Introducing proportionality coefficient, we obtain the law of spring winding diameter change:

$$D = b \frac{aFC_{\text{cont}}}{C - aF}. \tag{14.42}$$

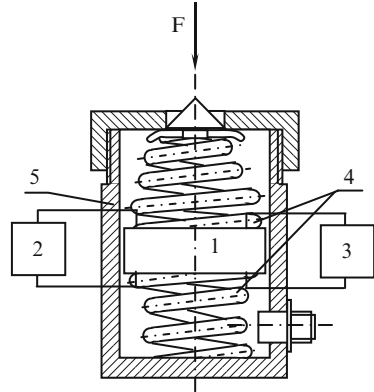
The law of spring winding diameter change can be calculated by the formula (14.42). It assures the device linear graduation characteristic.

If  $C_{\text{sum}} \ll C_{\text{el}}$ , the formula (14.39) is simpler and becomes

$$C_{\text{sum}} \approx C_{\text{el}}, \tag{14.43}$$

i.e., in this case the total rigidity is determined only by the resilient element rigidity. Therefore, this element rigidity and its change law in the force function

**Fig. 14.34** Force transducer with correcting resilient elements: 1 – piezoelement, 2 – generator, 3 – voltmeter, 4 – formed compression springs, 5 – housing (case)



will determine the transducer output stress change. However, we should remark that use of other elements, calculated by the formula (14.43), is connected with reduction in device essential sensitivity.

A transducer design achieving this method is shown in Fig. 14.34. Here, the force to the piezoelement is supplied through formed compression springs 4. The piezoelement is activated by generator 2 at resonant frequency. The output voltage is measured by voltmeter 3.

The resilient element calculation method is reduced to the following:

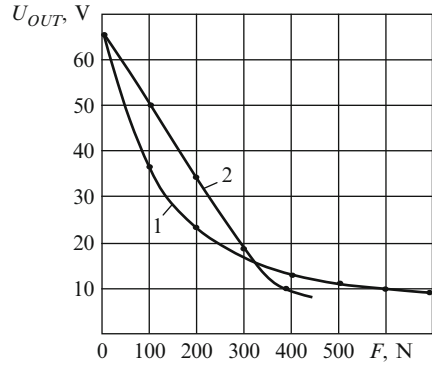
1. First, a contact rigidity experimental characteristic in the load range, exceeding the measurement range by three to four times, is measured by the technique described by Ryzhov [45].
2. The demanded (linear) total rigidity change law is determined by the contact rigidity dependence diagram.
3.  $C_{el}$  and coefficient  $a$  values are calculated by using the formula (14.40) for a transient value of the total rigidity.
4. The required law for the change in resilient element rigidity is determined by the formula (14.41). The spring winding change law is calculated by the formula (14.42).

Static characteristics of a piezoresonant transducer are shown in Fig. 14.35, whence the efficiency of the method offered is seen.

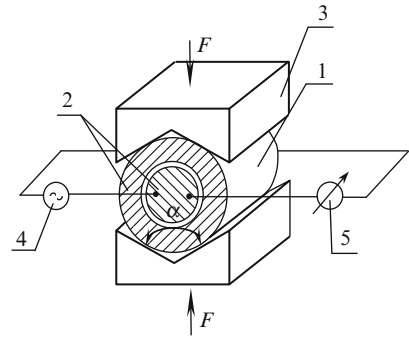
Resonant piezosensor sensitivity can be increased by various methods. The simplest of them consists in affecting a vibrating piezoelement with a force in the direction of piezoelement vibrations [8, 15].

The transducer achieving this method consists of cylindrical piezotransformer 1 with electrodes 2 to which generator 4 and measuring device 5 are connected. Force  $F$  is supplied to the piezoelement by prisms 3, contacting those surfaces of these which are located at the angle of  $90^\circ < \alpha < 180^\circ$  (Fig. 14.36).

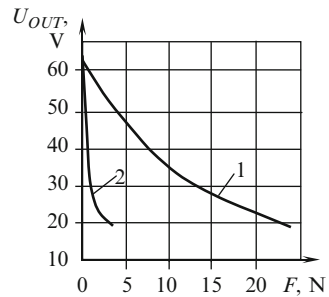
**Fig. 14.35** Output voltage–force diagram:  
 1 – non-linearization,  
 2 – linearization



**Fig. 14.36** Resonant sensor with prisms:  
 1 – piezotransformer,  
 2 – electrodes, 3 – prisms,  
 4 – generator, 5 – measuring device

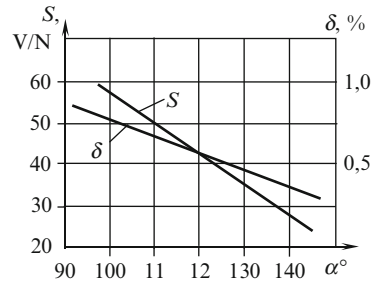


**Fig. 14.37** Dependence of output voltage on forces for transducer:  
 1 – without prisms,  
 2 – with prisms

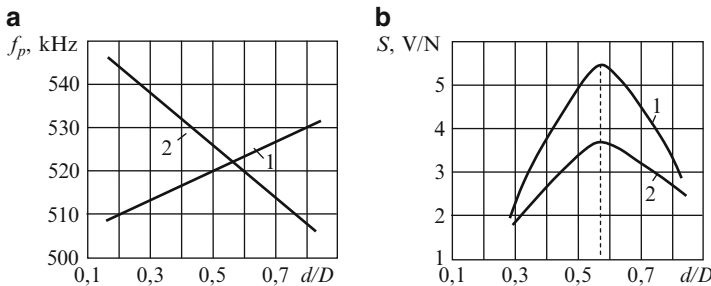
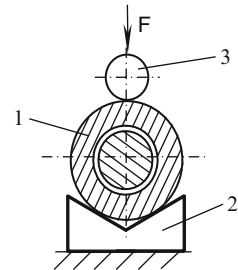


Prisms are made of tool steel 45 or Y8A. Then they are quenched. Work surfaces are burnished and polished. This transducer sensitivity is 10 times higher than this (Fig. 14.37) [5]. In addition, as the piezotransformer touches prisms only along four contact lines, but not along the whole cylinder surface, and also because of plastic deformations in contact reduction, the measurement accuracy increases 3 to 4 times in comparison with this [5]. Dependences of measurement error  $\delta$  (%) and sensitivity  $S$  (V/N) on angle  $\alpha$  are shown in Fig. 14.38. As can be seen from Fig. 14.38, measurement error and sensitivity increase with  $\alpha$  reduction. This is caused by a tangential force component increase in the contact place. Angle increase

**Fig. 14.38** Dependence of measurement error and sensitivity on angle  $\alpha$



**Fig. 14.39** One prism sensor design: 1 – piezoelement, 2 – prism, 3 – ball



**Fig. 14.40** Dependence of piezotransformer ( $\varnothing 38 \times 16 \text{ mm}$ ) resonant frequency (a) and transformation factor (b) on  $d/D$  ratio when ring (1) and central (2) electrodes are activated

to  $180^\circ$  is connected not only with sensitivity reduction, but also with the cylindrical piezoelement stability loss.

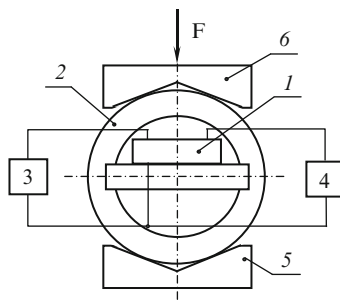
In the trade-off decision (Fig. 14.39) the piezoelement is positioned on the prism with  $\alpha = 120^\circ\text{--}150^\circ$  angle. The force is supplied either through the ball or through the flat clamp. It allows almost double error reduction with a 20–30% sensitivity decrease.

The transducer sensitivity depends also on the piezotransformer electrode dimensions (Fig. 14.40). As follows from Fig. 14.40,  $d/D = 0.58$  ratio is considered to be optimal [15].

In a piezoelement–prism contacting pair, the piezoelement is a “weak” link. The inferior elastic properties of the piezoelement do not permit an increase in measurement accuracy. This problem can be solved in the following way [13].

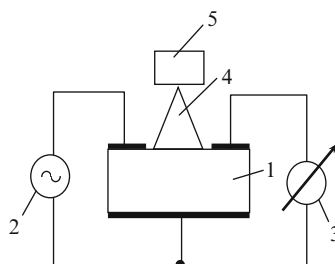
**Fig. 14.41** Sensor with additional metal resonator:

1 – piezoelement,  
2 – resonator, 3 – generator,  
4 – voltmeter, 5 – axial bearing, 6 – prism



**Fig. 14.42** Resonant accelerometer:

1 – piezotransformer,  
2 – oscillation generator,  
3 – measuring device,  
4 – ultrasonic concentrator,  
5 – inertia mass



Piezoelement 1 is positioned inside hollow resonator 2, made of heat-treated steel (Fig. 14.41). Resonant vibrations are activated in the resonator. The resonator is attached to axial bearing 5. The force is supplied through prism 6.

The resonator can be spherical or cylindrical-shaped.

## 14.7 Piezorezonant Accelerometer

Quartz resonant accelerometers are known for their high accuracy. However, they are rather complex. Their elements should be individually selected. Therefore, they are expensive [33].

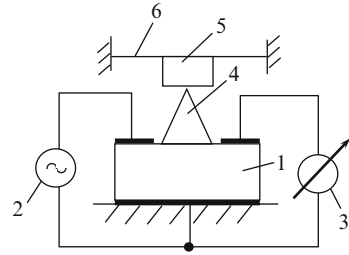
Resonant piezoceramic accelerometers are less accurate, but are of a simpler design [50]. Both accelerometers have essential transverse (lateral) sensitivity, varying along the azimuth.

Ultrasonic concentrators are used in the designs developed. In the simple design represented in Fig. 14.42 [56], conic ultrasonic concentrator 4 with inertia mass 5 on top is attached to the piezoelectric transformer. Oscillation generator 2 activates resonant oscillations in the piezotransformer. The piezotransformer output voltage is controlled by measuring device 3 [62].

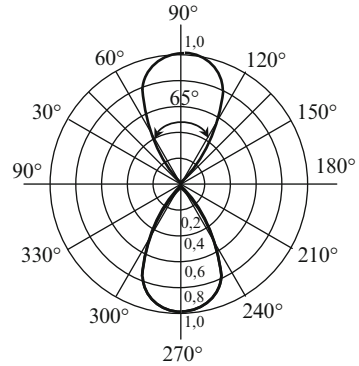
The acceleration influencing the inertia mass modulates the output voltage. The influencing acceleration can be determined by this voltage. The accelerometer described has simultaneously high axial and lateral (transverse) sensitivity.

**Fig. 14.43** Resonant accelerometer:

1 – piezotransformer,  
2 – oscillation generator,  
3 – measuring device,  
4 – ultrasonic concentrator,  
5 – inertia mass,  
6 – membrane

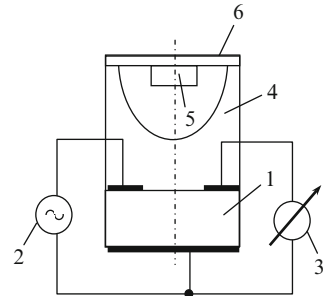


**Fig. 14.44** Directional diagram of resonant accelerometer (Fig. 14.43)



**Fig. 14.45** Resonant accelerometer:

1 – piezotransformer,  
2 – generator, 3 – measuring device,  
4 – US concentrator,  
5 – inertia mass,  
6 – membrane



The accelerometer [63] with inertial mass 5 on membrane 6 has small lateral sensitivity (Fig. 14.43). The lower frequency limit in resonant accelerometers equals 0, and the upper is limited by the piezotransformer resonant frequency. For the case shown in Fig. 14.43, it is limited by the resonant frequency of membrane–inertia mass system.

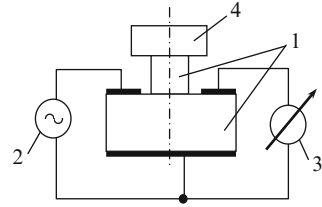
The directional diagram of the accelerometer shown in Fig. 14.43 is represented in Fig. 14.44.

Two more designs of resonant accelerometers are shown in Figs. 14.45 and 14.46 [60, 61].

Ultrasonic concentrator 4 with the change according to the parabolic law internal diameter, and inertia mass 5, attached to membrane 6, are used in the accelerometer design represented in Fig. 14.45 [61].



**Fig. 14.46** Resonant accelerometer:  
 1 – concentrator-shaped piezotransformer,  
 2 – generator, 3 – measuring device, 4 – inertia mass



In the design shown in Fig. 14.46 [60], accelerometer piezotransformer 1 is built as a stepwise ultrasonic concentrator with inertia mass 4 on top. This allows considerable design simplification.

Accelerometers based on surface acoustic waves (SAW) are mainly based on a frequency input scheme. An active oscillator is the basis of frequency sensors. Delay line and SAW resonator are used as a frequency mastering element. As a rule, a differential scheme with two active oscillators and the difference frequency signal shaper [33] are used.

SAW sensor schemes are SAW generator schemes. SAW delay lines or SAW resonators are used as frequency mastering elements. In addition, matching quadripoles and frequency-selective elements, assuring mode selection, can be included in the generator scheme. A higher level of constructive integration is a potential advantage of SAW accelerometers.

## 14.8 Sensor on Acoustically Connected Resonators

Oscillatory systems of two resonators or piezotransformers, acoustically coupled via gas gap, are used in sensors in acoustically connected resonators [55]. This sensor can be considered as a transformer in which the transformation coefficient depends on acoustic coupling value. The coupling is determined by the distance between them and gas  $Z_r$  acoustic resistance if the radiator and receiver geometries are present as their oscillations. This resistance consists of active component  $R_a$ , characterizing the resonator acoustic energy losses on radiation into the environment, and jet  $X_a$ , determined by energy dissipation in the environment at the expense of viscous friction.

The work of these sensors is based on energy transfer from the radiating to the receiving resonator. The quantity of the energy transferred depends on the gas acoustic resistance:

$$R_a = \rho c S,$$

where:  $\rho$  – gas density,  $c$  – wave propagation speed,  $S$  – radiating and receiving surface area.

The gas density, as it is known, is determined by pressure  $P$ , molar mass  $\mu$  and absolute temperature  $T$ :

$$\rho = \frac{P\mu}{RT}.$$

Wave propagation speed:

$$c = \sqrt{\frac{\gamma P}{\rho}},$$

where:  $R$  – universal gas constant,  $\gamma$  – gas specific heat ratio with constant pressure and volume.

### 14.8.1 For Gases

$$R = \sqrt{\frac{\gamma P}{\rho} SP}$$

If gas gap  $l$  is much smaller than the wave length, then transfer coefficient  $k$  for ideal gas in adiabatic approach is determined as output voltage  $U_2$  – input  $U_1$  voltage ratio [33]:

$$k = U_2/U_1 = A\rho_0 C_0^2 \frac{P}{760} \frac{S}{l},$$

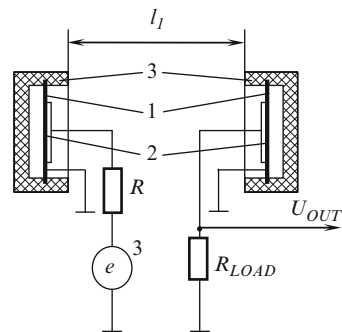
where:  $S$  – radiator and receiver areas,  $\rho_0$ ,  $C_0$  – density and sound velocity accordingly for gas with  $t = 0^\circ C$ ,  $A$  – constant.

For binary gas mixes with  $P = \text{const}$ , gas analyzers can be designed according to this principle.

The radiator and the receiver can be either monolithic (crystals, piezoceramic), or compound. A sensor variant and output voltage dependence on pressure are shown in Figs. 14.47 and 14.48 [25, 33, 46]. Each bimorph resonator consists of metal plate  $1$  and niobium lithium piezoelement  $2$ . The dependence of this transducer output voltage on pressure is linear in the high range, beginning with vacuum (10 Pa) to dozens of kPa (Fig. 14.48).

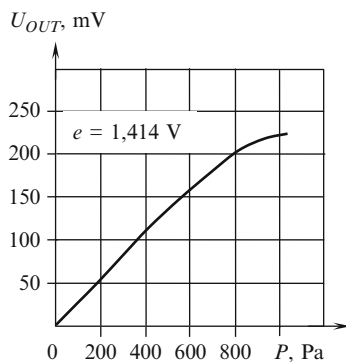
The disadvantage of this transformation is its ability to work only in a pure, content-stable atmosphere.

In the sensor described in [16], a radiating resonator  $2$  and two tandem receiving resonators  $1, 3$  (Fig. 14.49) are used for sensitivity increase. The voltage of generator

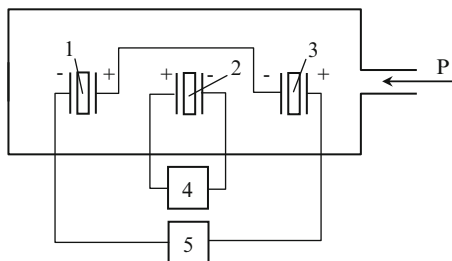


**Fig. 14.47** Scheme of gas pressure sensor on acoustically coupled resonators:  $1$  – metal plate,  $2$  – piezoelement,  $3$  – housing (case),  $4$  – generator

**Fig. 14.48** Work characteristic of gas pressure sensor on acoustically coupled resonators



**Fig. 14.49** Pressure sensor: 1, 2, 3 – piezoelements, 4 – generator, 5 – measuring device



4 activates oscillations in resonator 2. They are supplied through gas to resonators 1 and 3, and cause oscillations in them at driving frequency. As a result of their oscillations, electric signals appear, connected with gas pressure value. These signals arrive at the pressure indicator in one phase and frequency.

The sensor sensitivity is almost twice higher than that for sensors with two resonators, because the acoustic signal is perceived by two piezoresonators simultaneously and allows a reduction in energy losses.

Resonators reciprocal phasing, shown in Fig. 14.49, is essential for maximal sensitivity reception.

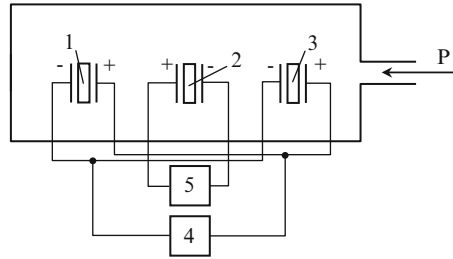
In the sensor variant described in [17], external piezoresonators 1, 3 are connected to generator 5, and resonator 2 to the measuring device (Fig. 14.50). Resonator reciprocal phasing is also important in this case. This sensor has sensitivity 4 times higher than the sensor (Fig. 14.49). The transducer static characteristic is shown in Fig. 14.51.

Sensors based on longitudinal oscillation resonators have some disadvantages: (1) considerable dimensions, and (2) of the requirement for accurate fastening in the oscillation node.

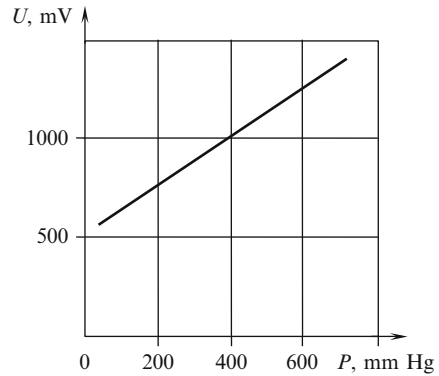
Flexural oscillation resonators, based on bimorph piezoelements, are more convenient in this case.

The sensitivity can be increased if the radiating resonator oscillations are intensified. In this case, ultrasonic concentrators are used. A sensor variant design with a concentrator is shown in Fig. 14.52.

**Fig. 14.50** Pressure sensor:  
 1, 2, 3 – piezoelements,  
 4 – generator, 5 – measuring  
 device



**Fig. 14.51** Sensor static  
 characteristic



**Fig. 14.52** Sensor with  
 ultrasonic concentrator:  
 1, 2 – piezoelements,  
 3 – concentrator,  
 4 – fastening, 5 – base,  
 6 – plate

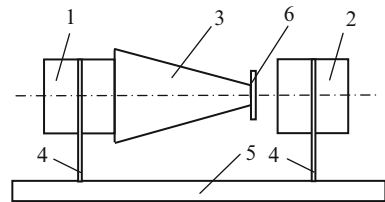


Plate 6 is attached to the concentrator external side to improve the coordination between the concentrator and environment and with reception. An ultrasonic acoustic lens [64] can be used instead of plate 6 in work at high frequencies.

Application of transverse–longitudinal piezotransformers, and also piezoelements with concentrator functions, are of scientific interest in the transducers considered.

The sensitivity of transducers on acoustically coupled resonators depends also on the receiving resonator sensitivity.

## References

1. E.C. Munk, The equivalent electrical circuit for radial modes of a piezoelectric ceramic disk with concentric electrodes. Philips Res. Rep. **20**, 170–189 (1965)

2. H. Kolsky, *Stress Waves in Solids* (Dover, Oxford, 1953)
3. V.M. Sharapov, I.B. Chudaeva, A.N. Podlipenets, On application on ultrasonic concentrators in piezoelectric transducers. Proceeding of International Conference "Actuator-96", Bremen (1996)
4. A.M. Chikonai, F.F. Gaman, Patent of USSR No 143585. Pressure measurement device, No 24 (1961) (in Russian)
5. I.G. Minaev, A.I. Trofimov, Patent of USSR No 315963. Sensor of static pressure, No 24 (1969) (in Russian)
6. I.G. Minaev, V.M. Sharapov, A.I. Trofimov, Patent of USSR No 453598. Static pressure measurement methods, No 46 (1974) (in Russian)
7. A.I. Trofimov, B.M. Kerbel, Patent of USSR No 501305. Device for force application No 4 (1976) (in Russian)
8. I.G. Minaev, V.M. Sharapov, Patent of USSR No 501306. Piezoelectric sensor of static forces, No 4 (1976) (in Russian)
9. V.M. Sharapov, V.I. Maksak, Patent of USSR No 532786. Method of material module elasticity measurement, No 39 (1976) (in Russian)
10. I.G. Minaev, V.M. Sharapov, Patent of USSR No 590868. Sound pickup head, No 4 (1978) (in Russian)
11. A.I. Trofimov, B.M. Kerbel, A.I. Nazarov, Patent of USSR No 796651. Method of relay contact actual field measurement, No 2 (1981) (in Russian)
12. A.I. Trofimov, B.M. Kerbel, Yu.A. Mitrofanov, Patent of USSR No 879299. Method of contact rigidity calculation in the details joint lap, No 41 (1981) (in Russian)
13. V.M. Sharapov, I.G. Minaev, B.S. Yakunin, Patent of USSR No 884172. Ultrasonic piezoelectric sensor, No 43 (1981) (in Russian)
14. V.M. Sharapov et al., Patent of USSR No 951754. Ultrasonic piezoelectric force sensor (1982) (in Russian)
15. V.M. Sharapov et al., Patent of USSR 1332166. Piezoelectric sensor of static forces, No 31 (1987) (in Russian)
16. V.M. Sharapov et al., Patent of USSR No 1339422. Pressure sensor (1987) (in Russian)
17. V.M. Sharapov et al., Patent of USSR No 1384977. Pressure sensor (1988) (in Russian)
18. P. Adomenas et al., *Meters of Amplitude-Frequency Characteristics and Their Application* (Cvyaz, Moscow, 1968) (in Russian)
19. D. Vakman, *Asymptotic Methods in Linear Radio Engineering* (The Soviet Radio, Moscow, 1962) (in Russian)
20. L.I. Volgin, *Linear Electric Transducers for Measuring Devices and Systems* (The Soviet Radio, Moscow, 1971) (in Russian)
21. I.S. Gonorovskiy, *Radio Engineering Circuits and Signals* (The Soviet Radio, Moscow, 1964) (in Russian)
22. N.B. Demkin, *Rough Surface Contact* (Nauka, Moscow, 1970), p. 227 (in Russian)
23. P.G. Dzagupov, A.A. Erofeev, *Piezoelectronic Devices in Computer Facilities, Monitoring and Control Systems. Directory* (Polytechnics, St. Petersburg, 1994) (in Russian)
24. Sources of powerful ultrasound (Powerful ultrasound physics and equipment), ed. by L.D. Rozenberg (Publishing House of USSR AS, Moscow, 1967) (in Russian)
25. I.N. Kanevskiy, *Focusing of Sound And Ultrasonic Waves* (Publishing House of USSR AS, Moscow, 1977) (in Russian)
26. G.F. Konovalov, *Radio Automatics (Automatic Devices): Textbook for High Schools, Speciality "Radio Automatics"* (High School, Moscow, 1990), p. 335 (in Russian)
27. V.A. Kotelnikov, *Basics of Radio Engineering* (State Publishing House of Technical Literature, Moscow, 1950) (in Russian)
28. W. Cady, *Piezoelectricity and Its Practical Application* (Publishing House of Foreign Literature, Moscow, 1949), p. 718 (in Russian)
29. V.V. Lavrinenko, I.A. Kartashev, V.S. Vishnevskiy, *Piezoelectric Engines* (Energiya, Moscow, 1980), p. 110 (in Russian)
30. V.V. Lavrinenko, *Piezoelectric Transformers* (Energiya, Moscow, 1975), p. 111 (in Russian)

31. G. Katz (ed.), *Magnetic and Dielectric Devices* (Energiya, Moscow, 1964) (in Russian)
32. V.I. Maksak, I.G. Minaev, V.M. Sharapov, Use of piezoelectric transducers for mechanical contact strength and dissipative characteristics. Materials of all-USSR Conference "Automation of aircraft bearing ability and long durability", Kharkov (1975) (in Russian)
33. V.V. Malov, *Piezoresonant Sensors* (Energoatizdat, Moscow, 1989), p. 272 (in Russian)
34. I.G. Minaev, V.M. Sharapov, On a contact rigidity measurement method. News of USSR High Schools – "Mashinostroenie", No 7 (1976) (in Russian)
35. I.G. Minaev, V.M. Sharapov, On pressure influence on piezoceramics IITC internal friction. News of USSR High Schools – "Physics", No 9 (1976) (in Russian)
36. I.G. Minaev, V.M. Sharapov, Application of frequency-modulated oscillations in measuring transducers. News of USSR High Schools – "Priborostroenie", No 8 (1976) (in Russian)
37. I.G. Minaev, V.M. Sharapov, B.G. Shelestovskiy, Linearity increase of static characteristics of piezoresonant measuring transducers. News of USSR High Schools – "Priborostroenie", No 5 (1982) (in Russian)
38. Y. Mezon, *Piezoelectric Crystals and Their Application in Ultra-acoustics* (Publishing House of Foreign Literature, Moscow, 1952), p. 448 (in Russian)
39. G. Olson, *Dynamic Analogies* (Publishing House of Foreign Literature, Moscow, 1947) (in Russian)
40. L.A. Ostrovskiy, *Basics of Electric Devices* (Energiya, Moscow, 1965), p. 532 (in Russian)
41. V.M. Pluzhnikov, V.S. Semenov, *Piezoceramic Firm Schemes* (Energiya, Moscow, 1971), p. 168 (in Russian)
42. V.S. Postnikov, *Internal Friction in Metals* (Mashinostroenie, Moscow, 1975) (in Russian)
43. Firm prospectuses Kistler Instrumente AG, Winterthur, Switzerland (1996) (in Russian)
44. L.D. Rosenberg et al., *Ultrasonic Cutting* (Publishing House of USSR AS, Moscow, 1962) (in Russian)
45. E.V. Ryzhov, *Contact Rigidity of Machine Details* (Mashinostroenie, Moscow, 1966) (in Russian)
46. A.P. Evtyutov, A.E. Kolesnikov, E.A. Korepin et al., *Directory on Hydro-acoustics* (Sudostroenie, Leningrad, 1982), p. 344 (in Russian)
47. S.P. Strelkov, *Introduction to Vibration Theory* (Nauka, Moscow, 1964), p. 436 (in Russian)
48. I.I. Teumin, *Ultrasonic Oscillatory Systems* (Mashgiz, Moscow, 1959), p. 331 (in Russian)
49. A.I. Trofimov, *Piezoelectric Measuring Transducers in Nuclear Engineering* (Energoatizdat, Moscow, 1983) (in Russian)
50. A.I. Trofimov, *Piezoelectric Transducers of Static Load* (Mashinostroenie, Moscow, 1981), p. 126 (in Russian)
51. I.T. Turbovich, *Close Systems Method and Their Use for Engineering Calculation Methods of Linear and Nonlinear Radio Engineering Systems Creation* (Publishing House of USSR AS, Moscow, 1961) (in Russian)
52. I.T. Turbovich, On frequency characteristics measurement error when frequency modulation method is used. Radiotekhnika (Radio Engineering) **T.9**(2) (1954) (in Russian)
53. I.P. Golyamina, *Ultrasound (Small Encyclopedia)* (Soviet Encyclopedia, Moscow, 1979), p. 400 (in Russian)
54. A.V. Haritonov, Torsion ultrasonic concentrators. Acoustic Mag. **3** (1961) (in Russian)
55. I.B. Chudaeva et al., The piezoelectric sensor on acoustically coupled resonators. Proceedings of International Conference "Sensor-98", Moscow-Gurzuf (1998) (in Russian)
56. V.M. Sharapov, M.P. Musienko, E.V. Sharapova, in *Piezoelectric Sensors*, ed. by V.M. Sharapov (Technosfera, Moscow, 2006), p. 632 (in Russian)
57. V.M. Sharapov, M.P. Musienko, *Piezoelectric Transducers (Manual)* (ChSTU, Cherkasy, 2004), p. 435 (in Russian)
58. V.M. Sharapov, Development and study of piezoelectric measuring transducers. Candidate's Thesis, Tomsk (1977) (in Russian)
59. V.M. Sharapov, A.K. Polischuk, V.M. Gluschenko, Determination of mechanical contact strength and dissipative characteristics by using ultrasonic method. Factory Laboratory, 1985, No 5, p. 15–17 (in Russian) Определение прочностных и диссипативных

- характеристик механического контакта ультразвуковым методом
60. V.M. Sharapov, I.B. Chudaeva, I. Sarvar, Sensitivity increase of resonant type piezoelectric converters. Papers of the Branch of Moscow State Technological University named after N. E. Bauman (special release), p. 258–261 (1999) (in Russian)
  61. V.M. Sharapov, I.B. Chudaeva, I. Sarvar, Use of ultrasonic concentrators in piezoelectric transducers. Proceedings of International Conference “Instrument Making–99” (special release), p. 285–288 (1999) (in Russian)
  62. V.M. Sharapov, I. Sarvar et al., Piezoelectric transducers on acoustically coupled resonators. Visnyk ChITI, No 4, p. 89–93 (1999) (in Russian)
  63. V.M. Sharapov, I. Sarvar et al., Resonant transducers with ultrasonic concentrators. Visnyk ChITI, No 3, p. 30–34 (1999)
  64. V.M. Sharapov, I.B. Chudaeva, E.V. Bykova, Ultrasonic information mosaic transducer with binary spherical-gauss concentrator. Proceedings of international Conference “The Theory and Methods of Information Transfer, Reception and Processing,” Kharkov, Tuapse (1996) (in Russian)

# Chapter 15

## Sensors with Piezoelements in Scheme Electric Filters

These sensors are based on the following idea: if sensor piezoelement (-s) are switched onto the electric filter scheme, the sensor amplitude–frequency characteristics (AFC) will correspond to the filter AFC.

### 15.1 Schemes of Electric Filters

Electric filters are sufficiently studied and described in literature [1, 2].

An electric filter is a device to single out (or suppress) voltage or currents of the intended frequency.

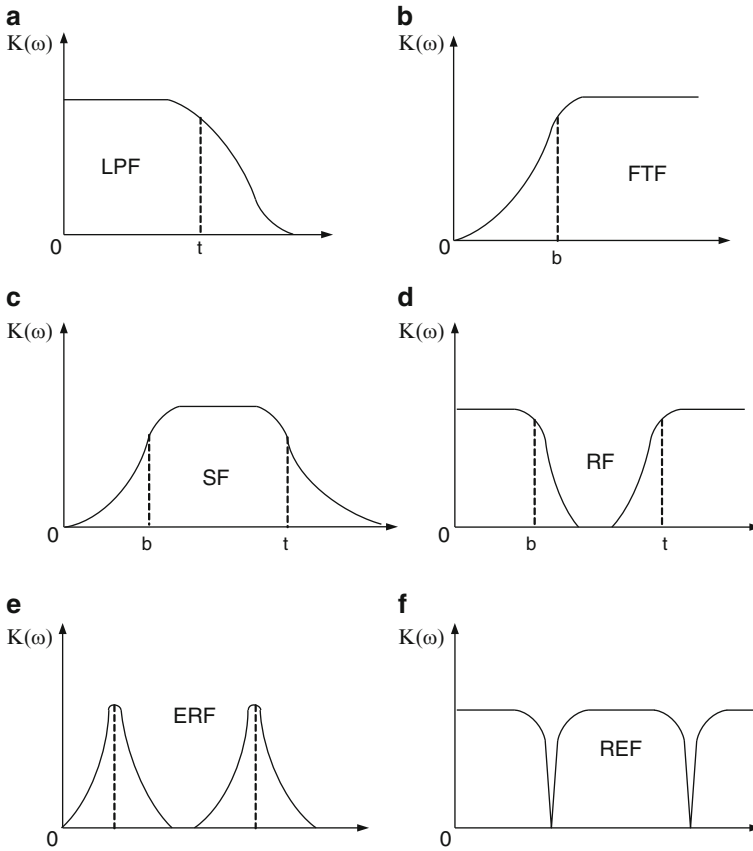
Depending on the frequency range and specifications required, the following filters [1] are known:

- Passive LC filters and RC filters made of resistors, inductance coils and condensers
- Piezoelectric, electromechanical, magnetostrictive filters, analogues to LC filters with small losses. Electromechanical filters can work at frequencies from several dozen hertz to several megahertz, magnetostrictive at frequencies from several kilohertz to several hundred kilohertz, and piezoelectric at frequencies from several hertz to dozen megahertz
- Active LC–RC filters, which are usually used at ultrasonic, sound and infrasonic frequencies

The basic filter characteristics are pass-band width and selectivity. There are six types of filters, depending on the frequency band:

- Low-pass filter (LPF), passing all frequency oscillations, beginning with direct current and finishing with a specific upper boundary frequency  $\omega_u$  (Fig. 15.1a)
- High-pass filter (HPF), passing oscillations, starting with a specific lower frequency limit  $\omega_l$  and finishing with infinitely high (Fig. 15.1b)





**Fig. 15.1** Amplitude–frequency characteristics of filters: (a) low-pass filter (LPF), (b) high-pass filter (HPF), (c) band-pass filters (BPF), (d) rejection filters (RF), (e) comb filters (CF), (f) rejection comb filters (RCF)

- Band-pass filters (BPF), passing frequency oscillations higher than a specific low frequency  $\omega_l$  and lower than the upper frequency  $\omega_u$  (Fig. 15.1c)
- Rejection (band-elimination) filters (RF), blocking oscillations of a specific frequency or frequency band from  $\omega_l$  to  $\omega_u$  (Fig. 15.1d)
- Comb filters (CF), having several pass-bands (Fig. 15.1e)
- Rejection comb filters (RCF) (Fig. 15.1f)

AFC filters shown in Fig. 15.1 are idealized, and true to some extent only for first-order filters.

In higher-order filters, AFC in pass-band can have essential non-uniformity (usually in oscillations form). In addition to that, phase-frequency characteristics of filters should be considered, as their nonlinearity leads to various delay times of frequencies components in a signal and, as a result to signal form distortion [1, 2].

There is a particular filter for each case. This filter makes it possible to get rid of hindrances with minimal form and helpful signal spectrum distortions most effectively. It should cover not only low or upper frequencies, band or rejection filter, it should also have an intended AFC. However, for the majority of cases AFC filters can be chosen from an almost standard set, consisting of Butterworth, Chebyshev, Bessel and elliptic filters [1, 2].

*Butterworth Filter.* LPF filters with zero attenuation at zero frequency are called Butterworth filters. Their attenuation increases monotonously in the pass-band. It reaches 3 dB at threshold frequency, then steadily increases in the suppression band. The more sections the filter has (i.e., the higher its order is) the steeper its characteristics in the suppression band and the lower the attenuation is in the pass-band.

*Chebyshev Filter.* Filters with attenuation characteristics in a pass-band of a vibrational character with an amplitude not exceeding 3 dB are called Chebyshev filters. In addition, their attenuation characteristic increases monotonously in the suppression band. The curve slope is bigger than the Butterworth filter curve slope of the same order.

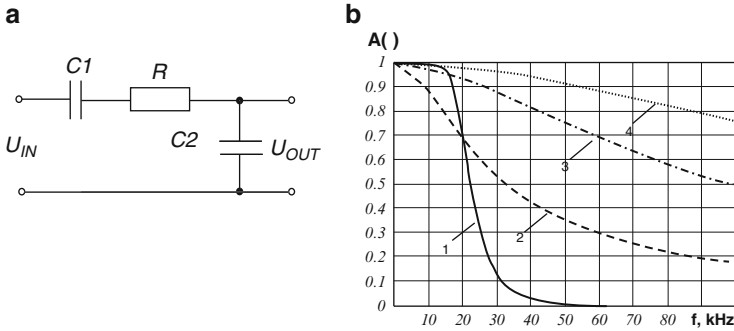
*Bessel Filter.* It is a well-known fact about Butterworth and Chebyshev filters that spectral components of an input signal passing through them experience time delay. Time delay change in the filter pass-band is called distortion. It is caused by the signal delay. This distortion increases with the filter order and pulsation levels increase. However, there are filters which ensure constant delay for all signal spectral components in the pass-band.

The primary function of *low-pass filters (LPF)* is to pass oscillations to the output with the minimum attenuation. The frequencies of these oscillations do not exceed the intended threshold frequency (cutoff frequency)  $\omega_c$  for the filter. At the same time, oscillations with higher frequencies should be essentially weakened. An ideal frequency dependence of power transfer coefficient for LPF with cutoff frequency  $\omega_c$  looks like this [1]:

$$K_p(\omega) = \begin{cases} 1, & 0 \leq \omega \leq \omega_c \\ 0, & \omega > \omega_c \end{cases}, \quad (15.1)$$

This frequency characteristic is obviously impossible. Reduction to zero of the  $K_p(\omega)$  function, and consequently of the  $K(p)$  function, contradicts the well-known Paley–Wiener criterion. The frequency transfer coefficient of the physically realized system should not contradict this integral:  $\int_{-\infty}^{+\infty} (|\ln |K(j\omega)||/1 + \omega^2) d\omega < \infty$ . Thus, a permissible approximating function should be selected [1].

Low- and high-pass filters are the most interesting in the case discussed.



**Fig. 15.2** Low-pass RC-filter: (a) L-connection scheme, (b) filter AFC: curve 1 – Butterworth approximating characteristic, curve 2 – with  $R = 600$  ohm, curve 3 – with  $R = 200$  ohm, curve 4 – with  $R = 100$  ohm

### 15.1.1 Low-Pass Filters

The L-scheme of an RC filter is often used as an LP filter (Fig. 15.2a) [1, 2]. The filter consists of a longitudinal shoulder in which condenser  $C_1$  and resistor  $R$  are serially connected. Condenser  $C_2$  is connected to the transverse shoulder.

The frequency transfer coefficient can be determined directly from the circuit [3]:

$$K_U(j\omega) = \frac{Z_l}{(A_{11}Z_l + A_{12})} = \frac{Z_2Z_l}{Z_1Z_2 + (Z_1 + Z_2)Z_l}, \tag{15.2}$$

where:  $A_{11}$  – quadripole voltage transformation coefficient in idle mode  $A_{11}=1+(Z_1/Z_2)$ ;  $Z_1$  – complex resistance of quadripole longitudinal shoulder  $Z_1 = R + (1/j\omega C_1)$ ;  $Z_2$  – complex resistance of quadripole transverse shoulder  $Z_2 = 1/j\omega C_2$ ;  $A_{12}$  – quadripole coefficient  $A_{12} = Z_1$ ;  $Z_l$  – load resistance (of matching voltage amplifier).

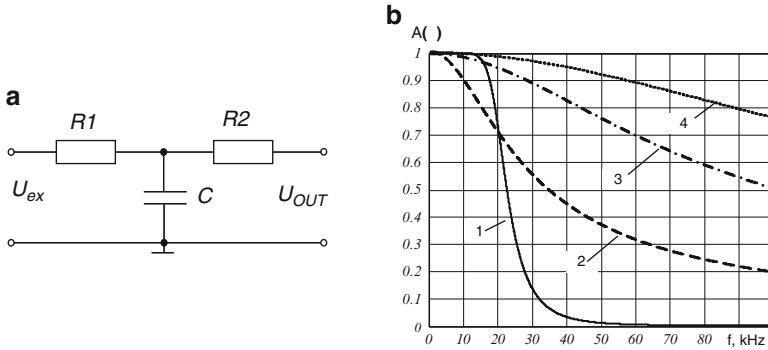
Then normalized transfer function of the filter will look like:

$$K(P) = \frac{Z_H C_1 P \omega_c}{Z_H C_1 P \omega_c + Z_H P^2 \omega_c^2 C_2 C_1 R + Z_H C_2 P \omega_c + Z_H C_1 P \omega_c R + 1}, \tag{15.3}$$

where:  $P$  – normalized complex variable:  $P = p/\omega_c = j\omega/\omega_c$ ;  $\omega_c$  – circular frequency of quasi-resonance;  $p = j\omega + \sigma$  – complex frequency.

The transfer function (operational transfer coefficient) is:

$$K(p) = \frac{a_0 + a_1 \frac{p}{\omega_c}}{b_0 + b_1 \frac{p}{\omega_c} + b_2 \frac{p^2}{\omega_c^2}}, \tag{15.4}$$



**Fig. 15.3** Low-pass RC-filter: (a) T-connection scheme, (b) filter AFC: curve 1 – approximating Butterworth characteristic, curve 2 – with  $R = 600$  ohm, curve 3 – with  $R = 200$  ohm; curve 4 – with  $R = 100$  ohm

where  $a_0, b_0, b_1, b_2$  are polynomial coefficients of transfer function;  $a_0 = 0; a_1 = Z_l \omega_c C_1; b_0 = 1; b_1 = Z_l \omega_c (C_1 + C_2) + R \omega_c C_{10}; b_2 = Z_l \omega_c^2 C_2 C_1 R$ .

The module of frequency transfer function determines the AFC of the filter  $A(\omega) = |K(j\omega)|$ .

The results of a computer-simulated AFC filter with L-connection scheme, made in MathCAD 2001 software, are presented in Fig. 15.12b [4–6].

As can be seen from Fig. 15.2b, the LPF amplitude–frequency characteristic depends on the longitudinal shoulder of the L-scheme. AFC filter nonlinearity decreases and the work band increases if the resistance is changed. For a filter with  $R = 600$  ohm resistance, the pass-band is 20 kHz, and for a filter with  $R = 100$  ohm the pass-band is 120 kHz (level 0.7).

The elementary scheme of a T-shaped RC filter (Fig. 15.3a) [1, 2] is also used in filtration schemes.

The scheme consists of longitudinal and transverse shoulders. Serially connected resistors  $R_1$  and  $R_2$  are switched to the longitudinal shoulder, while condenser  $C$  is switched to the transverse shoulder. Frequency coefficient of voltage transfer for the filter looks like this [1, 2]:

$$K_U(j\omega) = \frac{Z_H}{(A_{11}Z_H + A_{12})} = \frac{Z_H}{Z_H(1 + jR_1\omega C) + R_1 + R_2 + jR_1R_2\omega C}. \tag{15.5}$$

Normalized transfer function of the filter looks like:

$$K_U(P) = \frac{Z_H}{Z_H(1 + R_1\omega_c P C) + R_1 + R_2 + R_1R_2\omega_c P C} = \frac{a_0}{b_0 + b_1 P}, \tag{15.6}$$

where  $a_0, b_0, b_1$  are polynomial coefficients of quadripole,  $a_0 = Z_l; b_0 = Z_l + R_1 + R_2; b_1 = Z_l R_1 \omega_c C + R_1 \omega_c C R_2$ .

The results of a computer-simulated AFC filter with T-connection scheme, made in MathCAD 2001 software, are presented in Fig. 15.3b.

As can be seen from Fig. 15.3b, the LPF amplitude–frequency characteristic depends on longitudinal shoulder resistance of the T-shaped scheme. The AFC nonlinearity of the filter is decreased and the work band is increased if the resistance is changed. As for a filter with  $R_1 = R_2 = 300$  ohm resistances, the pass-band is 20 kHz, and if  $R_1 = R_2 = 50$  ohm the pass-band is 120 kHz.

### 15.1.2 High-Pass Filters

A high-pass filter is intended to handle oscillations passing with small attenuation. The frequencies of these oscillations do not exceed the cutoff frequency  $\omega_c$  [1, 2].

As is known [1, 2] the elementary passive high-pass filter is a differentiating RC section (Fig. 15.4).

Selectivity of single pole RC filter is low, and is 6 dB per octave. Use of multi-section (divided by the followers) filters, as in the case with low-pass filters, permits selectivity increase.

T-shaped (a) and U-type (b) HPF sections are shown in Fig. 15.5a.

A circuit consisting of two parallel connected T-shaped sections [2] (Fig. 15.6a) is considered below.

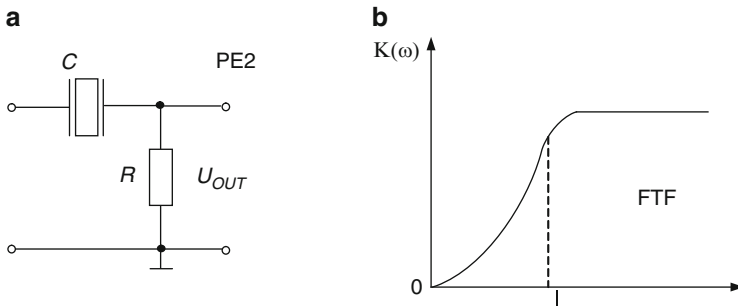


Fig. 15.4 High-pass RC filters: (a) electric scheme, (b) filter AFC

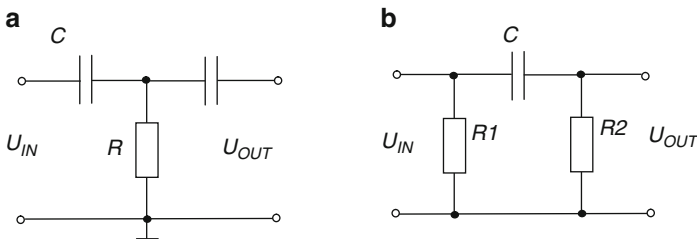


Fig. 15.5 Passive RC-filters: (a) T-shaped connection scheme, (b) U-type connection scheme

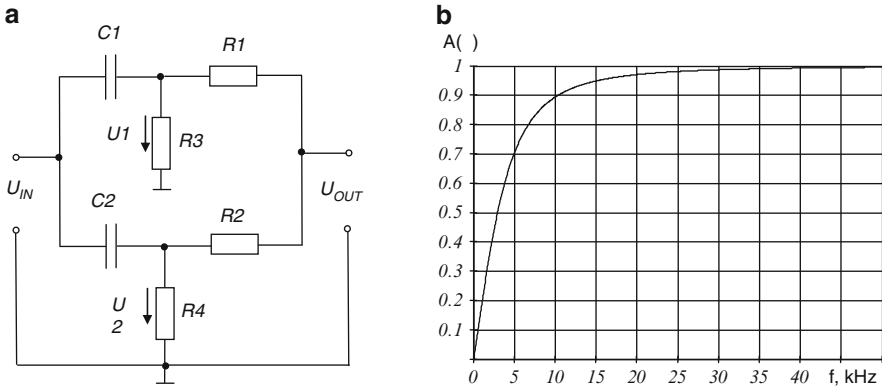


Fig. 15.6 High-pass filter: (a) double T-shaped scheme, (b) filter AFC

There are a capacitance element and a resistor in longitudinal shoulders of the section. The connection point of these elements through resistor  $R_3$  is attached to the scheme common wire.

The transfer function or operational transfer coefficient for this scheme [1, 2] is:

$$K(p) = \frac{U_{OUT}(p)}{U_{IN}(p)} = \frac{a_2 \frac{p^2}{\omega_c^2} + a_1 p + a_0}{b_2 \frac{p^2}{\omega_c^2} + b_1 p + b_0}, \quad (15.7)$$

where  $a_0, a_1, a_2, b_0, b_1, b_2$  are polynomial coefficients of quadripole,  $a_0=0$ ;  $a_1 = \omega_c [R_4 C_2 (R_3 + R_1) + R_3 C_1 (R_2 + R_4)]$ ;  $a_2 = \omega_c^2 [C_2 R_4 C_1 R_3 (R_1 + R_2)]$ ;  $b_0 = R_1 + R_3 + R_4 + R_2$ ;  $b_1 = \omega_c [C_2 R_4 (R_3 + R_1 + R_2) + C_1 R_3 (R_1 + R_4 + R_2)]$ ;  $b_2 = a_2$ .

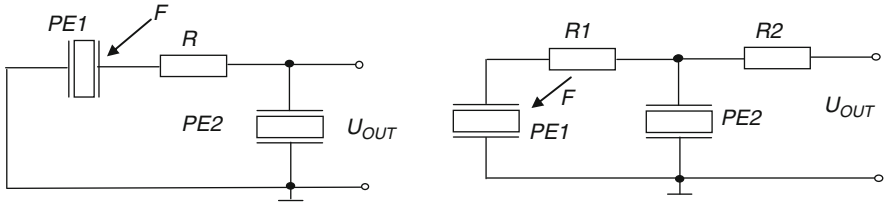
The results of a computer-simulated AFC high-pass filter, made in MicroCap 9.6.1 software, are presented in Fig. 15.6b [3, 7, 8].

## 15.2 Sensors with Piezoelements in Low-Pass Filter Schemes

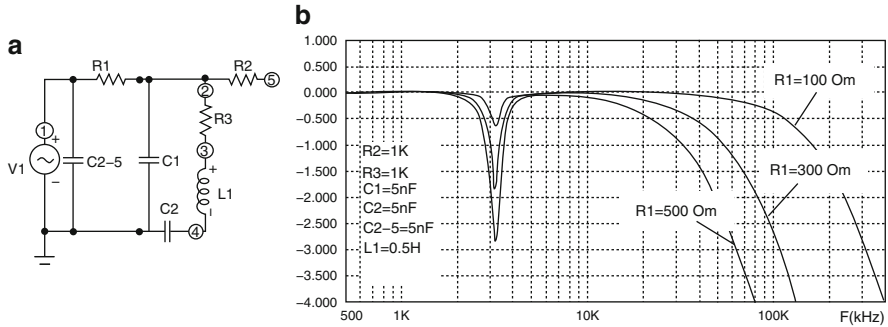
Two variants of sensor with piezoelements in an LPF scheme are shown in Fig. 15.7 [4–6].

In this case, force  $F$  influences a piezoelement (PE1). The second piezoelement is used as a condenser.

A sensor based on a bimorph element was used in the research. The sensor consists of a semi-solid brass Ø36 metal plate 0.3 mm thick and a piezoceramic IITC-19 piezoelement 30 mm in diameter and 0.8 mm thick. The basic resonant frequency of the transducer flexural vibrations is 3.5 kHz.



**Fig. 15.7** Sensors of mechanical values with piezoelements in LPF scheme



**Fig. 15.8** Equivalent scheme and sensor AFC (Fig. 15.1a): (a) equivalent scheme, (b) AFC with resistance change  $R_1$  with  $R_3 = 1 \text{ kohm}$ ,  $C_1 = 5 \text{ nF}$ ,  $C_2 = 5 \text{ nF}$ ,  $C_{2-5} = 5 \text{ nF}$ ,  $L_1 = 0.5 \text{ H}$

The results of a computer-simulated sensor shown in Fig. 15.7, made in MicroCap 9.6.1, are represented in Fig. 15.8.

As can be seen from Fig. 15.8, the sensor AFC depends on the resistance value of resistor  $R$ . There is a “dip” of AFC at the frequency of 3.5 kHz. This frequency corresponds to the resonant frequency of the bimorph element.

Similar results are obtained for this sensor (Fig. 15.7b).

### 15.3 Sensors with Piezoelements in High-Pass Filter Schemes

Two schemes of sensors with piezoelements in HPF scheme are shown in Fig. 15.3 [3, 7, 8].

Force  $F$  influences only one piezoelement (PE1) in the sensor (Fig. 15.9a). In the second case (Fig. 15.9b), the force influences both piezoelements.

The computer simulation results of the sensor shown in Fig. 15.9a are represented in Fig. 15.10.

As can be seen from the simulation results, the sensor AFC depends on the resistance  $R_3$  value.

Similar results are received for the sensor in Fig. 15.9b.

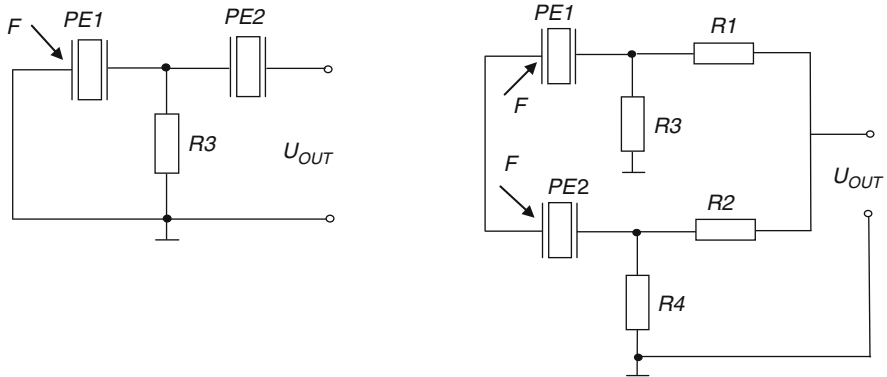


Fig. 15.9 Sensors of mechanical values with piezoelements in HPF scheme

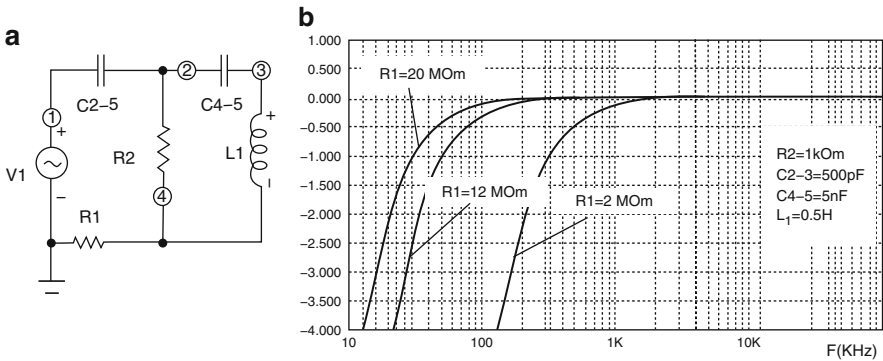


Fig. 15.10 Equivalent scheme and sensor AFC (Fig. 15.9a): (a) equivalent scheme, (b) amplitude-frequency responses with resistance  $R_1$  change with  $R_2 = 1 \text{ kohm}$ ,  $C_{2-5} = 500 \text{ pF}$ ,  $C_{4-5} = 5 \text{ nF}$ ,  $L_1 = 0.5 \text{ H}$

### 15.4 Sensors with Piezotransformers in Electric Filter Schemes

The disadvantage of the sensors discussed in Sects. 15.2 and 15.3 is the necessity to use two piezoelements or a piezoelement and a condenser in certain schemes.

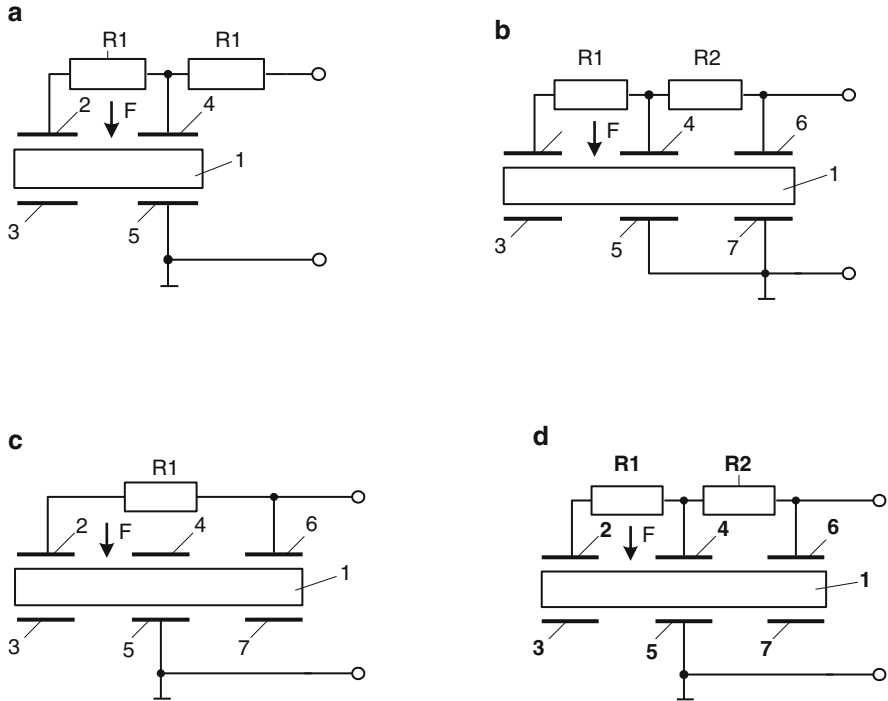
To eliminate this disadvantage, it is proposed that piezotransformers should be used, i.e., piezoelements with two systems of electrodes in the sensor schemes.

In addition, it is proposed that position electrodes for the electric field vector between them should be at the angle  $\alpha$  to the polarization vector ( $0 < \alpha \leq 90^\circ$ ) for one or two systems of electrodes. As a result, voltage on these electrodes is obtained. It exceeds the traditional case voltage when  $\alpha = 0$  [9–11] (see also Chap. 3).

The relevant sensor schemes are shown in Fig. 15.11 [12–15].

The mechanical value sensor (Fig. 15.11a) consists of piezoelement 1 with two systems of electrodes 2, 3 and 4, 5 and resistors  $R_1$  and  $R_2$ . The resistors





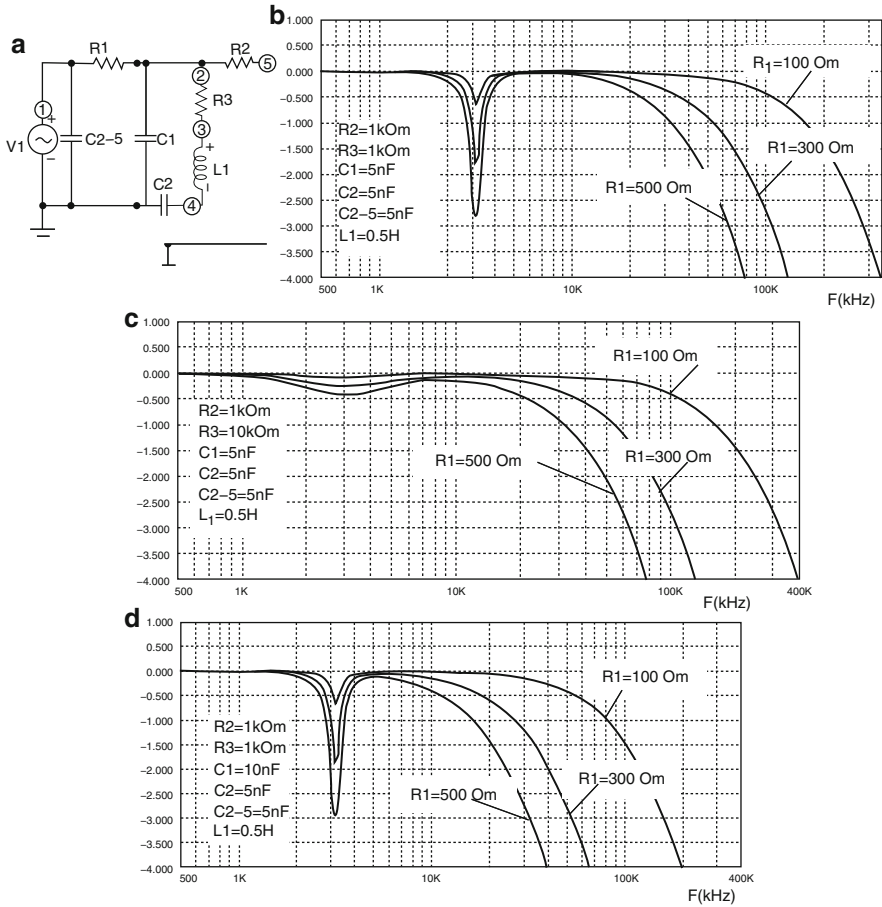
**Fig. 15.11** Sensors with piezotransformers in LPF schemes

are connected to piezoelement electrodes and the sensor output. Electrode 5 is connected to the general wire of the scheme. Electrodes 2, 3, 4 and 5 are of the identical area. An identical electric charge appears on them under identical mechanical action. Meanwhile, capacitance  $C_{2-5}$  between electrodes 2 and 5 is considerably smaller than capacities  $C_{4-5}$  between electrodes 4 and 5. This is evidently connected with the increase resulting from the distance between electrodes and, probably, with the change of dielectric permeability in piezoelectric material. Capacitance is measured at the angle  $\alpha (0 < \alpha \leq 90^\circ)$  to the polarization vector  $\mathbf{P}$  [9–11]. Therefore, voltage on electrode 2 is higher than on electrode 4. This creates favorable conditions for the sensor and filter work.

ИТС-19 piezoceramic piezoelement (30 mm in diameter and 0.8 mm thick) and brass Л63 metal plate (36 mm in diameter and 0.3 mm thick) were used in the experiment.

Computer simulation of piezoceramic sensors was carried out with MicroCAP. The sensor AFC can be forecast in this program.

The equivalent scheme and AFC of the sensor, based on the scheme in Fig. 15.11, are shown in Fig. 15.12.

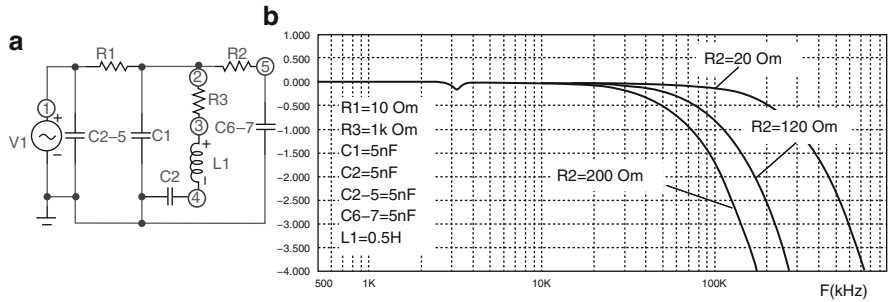


**Fig. 15.12** Equivalent scheme and sensor AFC (Fig. 15.11a): (a) equivalent scheme, (b) AFC with resistance  $R_1$  change with  $R_3 = 1 \text{ kohm}$ ,  $C_1 = 5 \text{ nF}$ ,  $C_2 = 5 \text{ nF}$ ,  $C_{2-5} = 5 \text{ nF}$ ,  $L_1 = 0.5 \text{ H}$ , (c) AFC with resistance  $R_1$  change with  $R_2 = 10 \text{ kohm}$ ,  $C_1 = 5 \text{ nF}$ ,  $C_2 = 5 \text{ nF}$ ,  $C_{2-5} = 5 \text{ nF}$ ,  $L_1 = 0.5 \text{ H}$ , (d) AFC with resistance  $R_1$  change with  $R_3 = 1 \text{ kohm}$ ,  $C_1 = 10 \text{ nF}$ ,  $C_2 = 5 \text{ nF}$ ,  $C_{2-5} = 5 \text{ nF}$ ,  $L_1 = 0.5 \text{ H}$

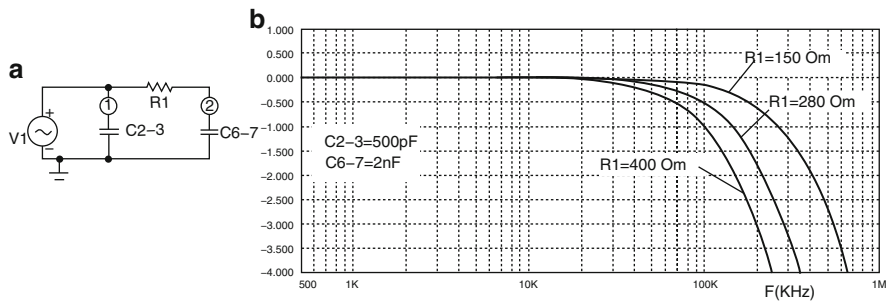
In the equivalent scheme (Fig. 15.12a) the parameters of the consecutive contour  $L_1$ ,  $C_2$ ,  $R_3$  correspond to the bimorph piezoelement parameters: capacitance  $C_1$ , inter-electrode capacitance  $C_{4-5}$ . Electrode 2 voltage is represented by generator  $V_1$ .

As can be seen from Fig. 15.2, there is a “dip” in AFC at a frequency of  $\sim 3.5 \text{ kHz}$ . It corresponds to the resonant frequency of the bimorph piezoelement. The depth of this “dip” depends on the bimorph element Q factor, i.e., resistance value  $R_3$ .

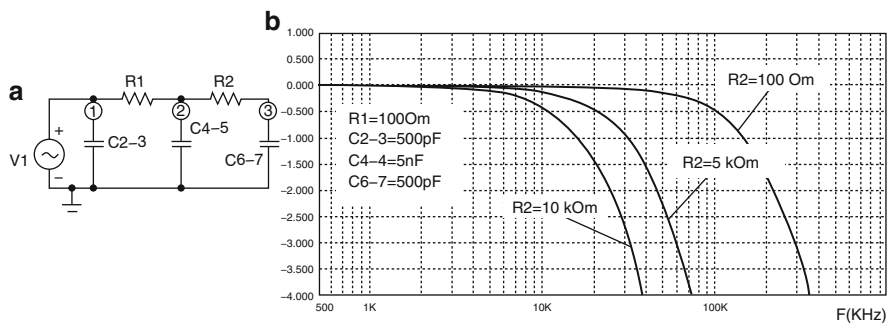
Additionally, AFC linearity and the work band width depend on resistance  $R_1$ .



**Fig. 15.13** Equivalent scheme and sensor AFC (Fig. 15.11b): (a) equivalent scheme, (b) AFC with resistance  $R_2$  change with  $R_1 = 100$  ohm,  $C_1 = 5$  nF,  $C_2 = 5$  nF,  $C_{2-5} = 5$  nF,  $C_{6-7} = 5$  nF,  $L_1 = 0.5$  H



**Fig. 15.14** Equivalent scheme and sensor AFC (Fig. 15.11c): (a) equivalent scheme, (b) AFC with resistance  $R_1$  change with  $C_{2-3} = 500$  pF,  $C_{6-7} = 2$  nF



**Fig. 15.15** Equivalent scheme and sensor AFC (Fig. 15.11d): (a) equivalent scheme, (b) AFC with resistance  $R_2$  change with  $R_1 = 100$  ohm,  $C_{2-3} = 500$  pF,  $C_{4-5} = 5$  nF,  $C_{6-7} = 500$  pF

The sensor in Fig. 15.11b differs from the sensor in Fig. 15.5a: an additional  $R_2$  ( $C_{6-7}$ ) circuit is introduced. As a result, an additional integration of the input signal, created on electrode 2, becomes possible.

The equivalent scheme and the sensor AFCs designed by the scheme in Fig. 15.11b are shown in Fig. 15.13.

As can be seen from Fig. 15.13, the sensor has more linear frequency characteristic in this case.

The sensor scheme in Fig. 15.11c differs from the scheme in Fig. 15.5a: electrodes 2, 5, 6 from electrode systems 2–3, 4–5, 6–7 are used in this case. Electrode 5 is connected to the common wire of the scheme. Electrode 2 area  $S_2$  is smaller than electrode 5 area  $S_5$ . Electrode 6 area  $S_6$  equals area  $S_5$ , i.e.,  $S_2 < S_5$  and  $S_5 = S_6$ . This leads to the increase of interelectrode capacities  $C_{2-5} < C_{5-6}$ , and consequently, voltage on electrode 2 appears to be bigger than on electrode 6. It is experimentally proved that resonant frequency of the bimorph sensor increases too.

The equivalent scheme and AFC of the sensor created by the scheme shown in Fig. 15.11c are represented in Fig. 15.14.

The equivalent scheme and AFR of the sensor produced by the scheme in Fig. 15.11d are shown in Fig. 15.15.

Some sensors with piezotransformers in high frequency filters schemes are shown in Fig. 15.16 [16–19].

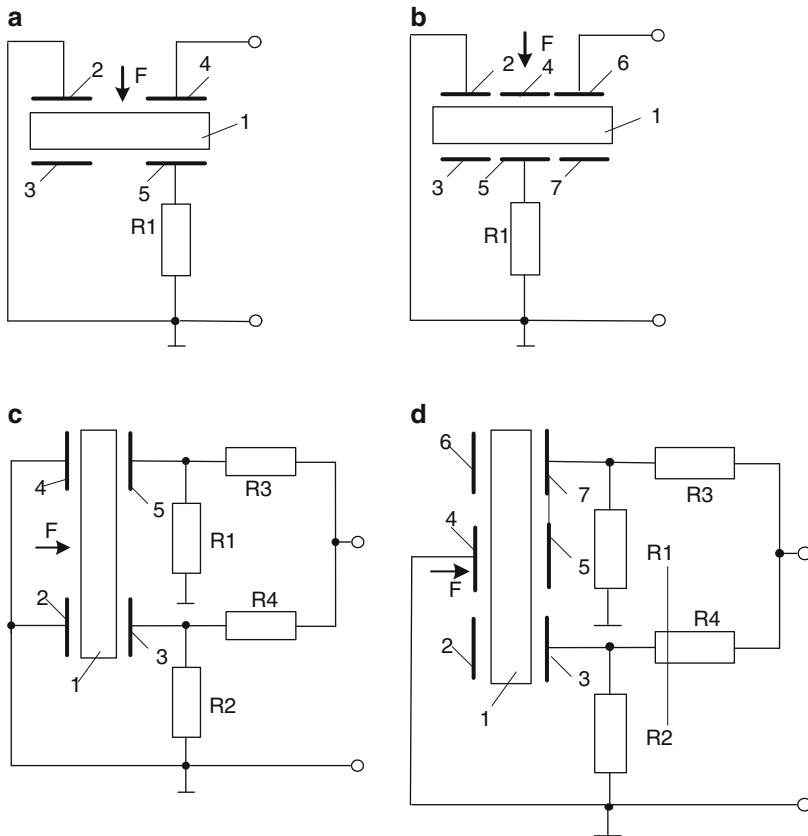
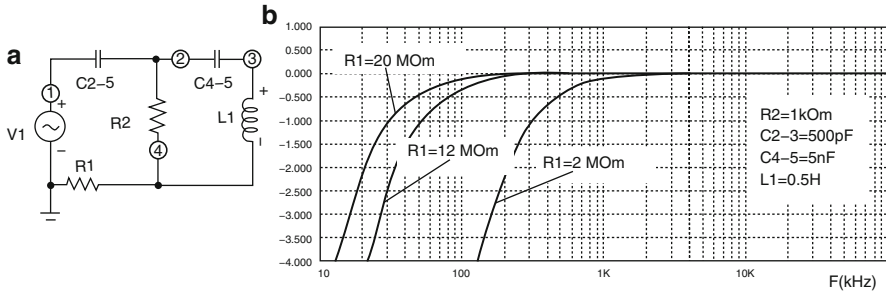


Fig. 15.16 Sensors with piezotransformers in HPF schemes



**Fig. 15.17** Equivalent scheme and sensor AFC (Fig. 15.16a): (a) equivalent scheme, (b) AFC of resistance  $R_1$  change with  $R_2 = 1 \text{ kohm}$ ,  $C_{2-5} = 500 \text{ pF}$ ,  $C_{4-5} = 5 \text{ nF}$ ,  $L_1 = 0.5 \text{ H}$

The sensor in Fig. 15.16a consists of piezoelement 1 with two systems of electrodes 2, 3 and 4, 5 and resistor  $R_1$ . Electrode 4 is connected to the sensor output. Electrode 5 is connected through resistor  $R_1$  to electrode 2 and to the scheme common wire. Electrodes 2, 3 and 5 are of identical area. Therefore, an identical electric charge is formed on them under identical mechanical influence. Meanwhile, capacitance  $C_{2-5}$  between electrodes 2 and 5 is much smaller than capacitances  $C_{4-5}$  between electrodes 4 and 5. It is obviously connected with the distance increase between the electrodes and, probably, the dielectric permeability change in piezoelectric material. The capacitance is measured at the angle of  $\alpha (0 < \alpha \leq 90^\circ)$  to the polarization vector  $\mathbf{P}$  [9–11]. Piezoceramic IITC-19 piezoelement (30 mm in diameter and 0.8 mm thick) and brass JI63 metal plate (36 mm in diameter and 0.3 mm thick) were used in the experiment.

The sensor computer simulation was carried out in MicroCAP.

The equivalent scheme and AFC of the sensor made by the scheme shown in Fig. 15.16a are represented in Fig. 15.17.

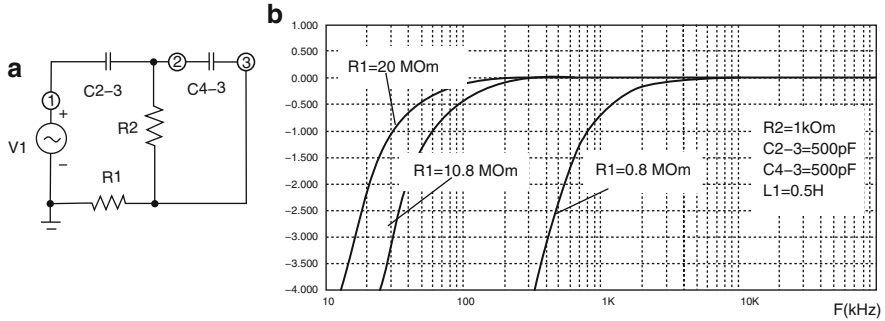
As can be seen from Fig. 15.17, the sensor has linear AFC, and the working bank width depends on resistance  $R_1$ .

The sensor in Fig. 15.16b differs from the sensor in Fig. 15.16a: the sensor has three systems of electrodes 2–3, 4–5, 6–7. Electrode 5 is connected to resistor  $R_1$ , electrode 2 to the common wire, and electrode 6 to the sensor output.

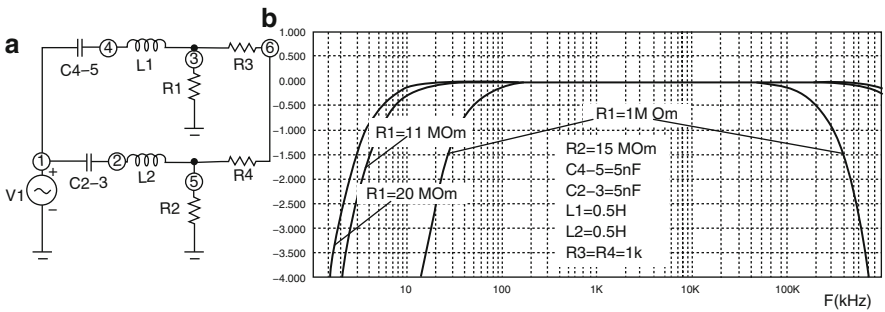
The equivalent scheme and AFC of the sensor constructed by the scheme shown in Fig. 15.16b are represented in Fig. 15.18.

As can be seen from Fig. 15.18, the sensor has more linear frequency characteristics with smaller  $R_1$  values in this case.

The sensor scheme in Fig. 15.16c differs from the scheme in Fig. 15.16a: two pairs of electrode systems 2–3, 4–5 and four resistors in this case are used. Electrodes 2 and 4 are connected to the common wire. Electrode 3 is connected to resistors  $R_2$  and  $R_4$ .  $R_2$  is connected to the common wire. The second resistor  $R_4$  output is connected to the sensor output. Electrode 5 is connected to resistors  $R_1$  and  $R_3$ . The second resistor output  $R_1$  is connected to the common wire, and the second resistor  $R_3$  output to the sensor output. The equivalent scheme and



**Fig. 15.18** Equivalent scheme and sensor AFC (Fig. 15.16b): (a) equivalent scheme, (b) AFC with resistance  $R_1$  change with  $R_1 = 1 \text{ kohm}$ ,  $C_{2-3} = 500 \text{ pF}$ ,  $C_{4-3} = 500 \text{ pF}$ ,  $L_1 = 0.5 \text{ H}$



**Fig. 15.19** Equivalent scheme and sensor AFC (Fig. 15.16c): (a) equivalent scheme, (b) AFC with resistance  $R_1$  change with  $C_{2-3} = 5 \text{ nF}$ ,  $C_{4-5} = 5 \text{ nF}$ ,  $R_2 = 15 \text{ mohm}$ ,  $R_3 = R_4 = 1 \text{ kohm}$ ,  $L_1 = L_2 = 0.5 \text{ H}$

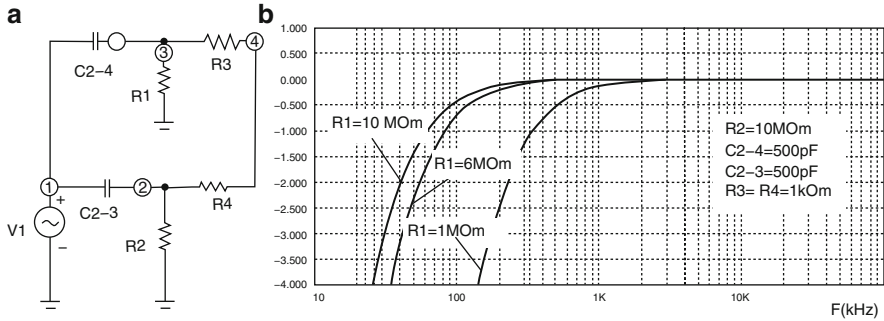
amplitude–frequency responses of the sensor constructed by the scheme shown in Fig. 15.16c are shown in Fig. 15.19.

As can be seen from Fig. 15.19, the operating band of this sensor extends essentially.

The equivalent scheme and AFC of the sensor based on the scheme shown in Fig. 15.16d are represented in Fig. 15.20.

As can be seen from Figs. 15.17–15.20, working bank is expanded 10- to 15-fold, and even more if the corresponding resistance and piezoelement capacitances are selected.

Sensors with piezotransformers in the electric filter schemes are developed and studied. Creation of integrating and differentiating circuits in the piezotransformer scheme allowed the expansion of the sensor operating band. Then AFC remains linear in the wide range of frequencies. Computer models to predict AFC of sensors with piezotransformers in electric high-pass filter schemes are created.



**Fig. 15.20** Equivalent scheme and sensor AFC (Fig. 15.16d): (a) equivalent scheme, (b) AFC with resistance  $R_1$  change with  $R_2 = 10$  Mohm,  $C_{2-3} = 500$  pF,  $C_{2-4} = 500$  pF,  $R_3 = R_4 = 1$  kohm

## References

1. U. Titse, K. Shenk, *Semi-conductor Circuitry* (Mir, Moscow, 1983) (in Russian)
2. M. Kaufman, A.G. Sidman, *Handbook on Scheme Calculations in Electronics. Directory*, ed. by F.N. Pokrovskiy (in Russian)
3. V.M. Sharapov, R.V. Trembovetskaya, Piezoelectric transducers of mechanical values with a piezoelement in the scheme of the high-pass filter. *Bull. Cherkasy State Technol. Univ.* **2**, 32–35 (2005) (in Russian)
4. V.M. Sharapov, R.V. Trembovetskaya et al., Piezoelectric transducers of mechanical values with a piezoelement in the scheme of a low-pass filter. *Bull. Cherkasy State Technol. Univ.*, 86–89 (2005) (in Russian)
5. V.M. Sharapov, M.P. Musienko, R.V. Trembovetskaya, Patent of Ukraine No 8606. Piezoelectric transducers of mechanical values (2005) (in Ukrainian)
6. V.M. Sharapov, R.V. Trembovetskaya, Patent of Ukraine No 8609. Piezoelectric transducers of mechanical values (2005) (in Ukrainian)
7. V.M. Sharapov, R.V. Trembovetskaya, Patent of Ukraine No 8613. Piezoelectric transducers of mechanical values (2005) (in Ukrainian)
8. V.M. Sharapov, R.V. Trembovetskaya, M.P. Musienko, Patent of Ukraine No 8604. Piezoelectric transducers of mechanical values (2005) (in Ukrainian)
9. V.M. Sharapov, M.P. Musienko, E.V. Sharapova, *Piezoelectric Sensors*, ed. by V.M. Sharapov (Technosphera, Moscow, 2006), p. 632 (in Russian)
10. V. Sharapov, B. Vladisaukas, L. Kunitskaya, Z. Sotula, Methods of synthesis of piezoceramic transducers: spatial energy force structure of piezoelement. *Ultragarsas (Ultrasound)* **4**(64), 44–50 (Technologia, Kaunas, 2009), ISSN 1392–2114
11. V. Sharapov, R. Kazys, A. Vladisaukas, L. Kunitskaya, Z. Sotula, V. Tuz, K. Bazilo, Transducers with piezoelements in schemes of electric filters. *Ultragarsas (Ultrasound)* **1**(65) (Technologia, Kaunas, 2010), ISSN 1392–2114
12. V.M. Sharapov et al., Patent of Ukraine No U2010.00638 from 22.01.2010. Piezoelectric transducers of mechanical values (in Ukrainian)
13. V.M. Sharapov et al., Patent of Ukraine No U2010.00623 from 22.01.2010. Piezoelectric transducers of mechanical values (in Ukrainian)
14. V.M. Sharapov et al., Patent of Ukraine No U2010.00620 from 22.01.2010. Piezoelectric transducers of mechanical values (in Ukrainian)
15. V.M. Sharapov et al., Patent of Ukraine No U2010.00616 from 22.01.2010. Piezoelectric transducers of mechanical values (in Ukrainian)

16. V.M. Sharapov et al., Patent of Ukraine No U2010.00617 from 22.01.2010. Piezoelectric transducers of mechanical values (in Ukrainian)
17. V.M. Sharapov et al., Patent of Ukraine No U2010.00618 from 22.01.2010. Piezoelectric transducers of mechanical values (in Ukrainian)
18. V.M. Sharapov et al., Patent of Ukraine No U2010.00619 from 22.01.2010. Piezoelectric transducers of mechanical values (in Ukrainian)
19. V.M. Sharapov et al., Patent of Ukraine No U2010.00621 from 22.01.2010. Piezoelectric transducers of mechanical values (in Ukrainian)



# Chapter 16

## Piezoceramic Scanners for Probe Nanomicroscopes

### 16.1 Nanotechnologies and Nanomicroscopes

*Nanotechnologies* are a set of methods which make it possible to create and modify objects with components sized 100 nm and smaller. These components have principally new qualities. They assure integration into fully functioning systems of a larger scale [1, 2].

Materials which contain structural elements, the geometry of which does not exceed 100 nm in at least one measurement, are called *nanomaterials*. They also have qualitatively new properties, functional and operational characteristics.

*Nanosystem equipment* describes functionally complete systems and devices which are fully or partially based on nanomaterials and nanotechnologies.

Use of nanotechnologies for creation of nanomaterials with unique properties is rather experimental in electronics, biology, medicine, etc. [1].

Progress in nanotechnologies has been stimulated by development of experimental research methods. Methods of scanning probe microscopy are the most informative among them. They were invented and disseminated by two Nobel laureates of 1986, Prof. Heinrich Rohrer and Dr. Gerd Binnig.

The application of probe microscopy has made possible the achievement of unique scientific results in various fields of physics, chemistry and biology in recent years.

Whereas the first scanning probe microscopes were indicators of qualitative research, modern scanning probe microscopes are devices integrating up to 50 various research techniques. They can move on demand between probe-sample systems, accurate within 0.1%, count probe form-factors, and precisely measure in large scales (up to 200  $\mu\text{m}$  in the scanning plane and 15–20  $\mu\text{m}$  high), ensuring sub-molecular resolution [3, 4].

Scanning probe microscopes have become one of the types of research devices most demanded in the world market. New devices for various purposes are constantly designed.

The modern probe microscope as a research device can be presented as the sum of four components [5].

The *mechanical part* includes:

- Probe sensor
- Probe movement scanner
- Coordinate table to place and maintain the sample studied
- System of rough advance of the probe to the sample
- Irrelevant side influences protector; it also creates certain conditions in the probe–sample zone

*Electronic system:*

- Control unit of mechanical part nodes
- Electronic board (plate) for influencing pulse formation
- Electronic controlling electrical circuit

*Measurement and action methods,* including:

- Justification of the measurement method used
- Adequate interpretation of the results received
- Time coordination of tunnel current tracking and local substrate action processes

*Software,* including:

- Microscope work control
- Technological operations fulfillment
- Accumulation and processing of the data received

### ***16.1.1 Functional Mechanical Nodes***

The useful development of a microscope depends on its *probe*. The most important probe characteristic is tip/edge rounding radius. This influences the area transverse dimensions of maximum attainable resolution. Probes with smaller tip/edge radius values are usually preferred. However, occasionally lateral dimensions of the structures studied do not require that. The smaller the tip/edge radius is, the more complicated probe manufacturing becomes.

The tip/edge radius is the basic, but not the only one, probe characteristic. Probe resistance to physical and chemical influences depends on its material. If the probe is used as a nanotechnology tool, it should have special chemical stability, hardness, frequency flexural vibrations (especially for cantilevers), mechanical durability, geometry repeatability, etc. In a probe with appropriate tip/edge radius, required physical and chemical characteristics and geometry are used in each particular case.

*Scanner of probe micro-movements.* To study the sample surface in a certain area, the measurement of its properties using a certain set of points, evenly spread in the area, is used in the microscope. The probe is moved from point to point by a scanner with the following specifications:

- No drifts; accuracy and probe positioning repeatability
- Long-term stability parameters
- Thermal stability of positioning
- Required range of movements along each coordinate
- Sufficient response speed

There are many physical effects which can be used for probe moving. However, the reversible piezoeffect in polarized piezoceramics, based on lead zirconate titanate, is mainly used for this purpose at present.

The *coordinate table* is intended for movement of the sample studied. Additionally, the sample surface location in space is very important. Its horizontal position when the normal to the surface is directed upwards, allows a quite simple realization of some technological methods, for example work in a fluid medium. This orientation has been used in microscopes [5].

*System of rough advance along Z coordinate.* While working, the microscope probe tip/edge moves with some delay along the surface of the sample studied, touching it. This delay is approximately 1 nm (in *Z* direction), depending on the scanning mode. As the probe movement range (assured by the scanner) toward the normal to the sample surface usually does not exceed 1–2  $\mu\text{m}$ , it is necessary to have a system for advancing along the *Z* coordinate in the microscope design.

## 16.2 Methods of Scanning Probe Microscopy

Creation of precision gauges to control functional elements and medium properties and to form active structures is needed for sub-micrometer and nanotechnology development. As a result, scanning probe microscopes with built-in lithographer functions are needed. Micromechanical probe tools should also be studied. Development of algorithm and nanostructure research methods using the methods discussed above are required.

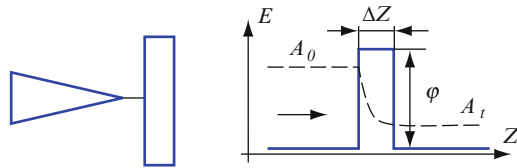
There are many advantages and disadvantages in the variety of microscopic systems. On the one hand, they are prospective in the field of research, and on the other they require the development of theoretical methods to study electro-physical properties of the concrete materials used. This considerably decreases expenses and research time for the synthesis of compounds synthesis. A comparative characteristic of various microscopic research methods of solid surfaces is presented in Table 16.1.

### 16.2.1 Scanning Tunneling Microscopy

The history of the scanning tunneling microscope (STM) began in the late 1960s when R. Young with employees created a device called a “topographiner” [3],

**Table 16.1** Comparative characteristics of various microscopic research methods of solid surfaces

Method	Increase	Work medium	Image dimension	Action on sample
Optical microscope	$10^3$	Air, liquid	2D	Non-destructive
Scanning laser microscope	$10^4$	Air	2D	Non-destructive
Scanning ionic microscope	$10^5$	Vacuum	2D	Non-destructive
Scanning electronic microscope	$10^6$	Vacuum	2D	Non-destructive
Scanning probe microscope	$10^9$	Vacuum, air, liquid	3D	Non-destructive

**Fig. 16.1** Scheme of electrons tunneling through potential barrier in tunnel microscope

used for investigation of surface geometrical structure. All elements relevant to modern microscopes were used in it: electrochemically etched tungsten tip (probe), micro-movement devices, negative feedback circuit for tunnel current measurement and maintenance, and a vibro-protection system. However, no atomic dimension images were received at that time because of various reasons. Among them are the following: (1) no aim to obtain atomic dimension, and (2) use of a large tunnel interval of 10–100 nm.

A possibility to observe separate atoms on the solid's surface appeared in 1982, when Gerd Karl Binnig and Heinrich Rohrer, employees of IBM's Swiss organization, received the utility patent for STM [4, 6].

The working principle of STM is based on electrons tunneling through the narrow potential barrier between the metal probe and the conducting sample in the external electric field.

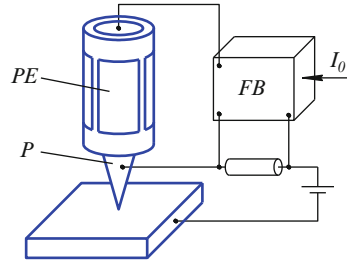
In STM, the probe is supplied to the sample surface at a distance of some angstroms. Then a tunnel-transparent potential barrier is created. Its value is determined by the electron work function values from the probe material  $\varphi_p$  and the sample  $\varphi_s$ . Considered qualitatively, the barrier can be considered rectangular, with an effective height equal to the average material work function (Fig. 16.1):

$$\varphi^* = \frac{1}{2}(\varphi_p + \varphi_s). \quad (16.1)$$

As is known from quantum mechanics [7, 8], the probability of electron tunneling (transmission coefficient) through the rectangular one-dimensional barrier equals

$$W = \frac{|A_t|^2}{|A_0|^2} \cong e^{-k\Delta Z}, \quad (16.2)$$

**Fig. 16.2** Simplified scheme of tunnel current feedback organization: *FB* feedback, *P* probe, *PE* piezoelement



where:  $A_0$  – wave function amplitude of the electron, moving to the barrier;  $A_t$  – wave function amplitude of the electron, passed through the barrier;  $k$  – attenuation constant of wave function in the area, corresponding to the potential barrier;  $\Delta Z$  – the barrier width.

The attenuation constant for tunnel contact of two metals can be presented like this:

$$k = \frac{4\pi \sqrt{2m\varphi^*}}{h}, \quad (16.3)$$

Where:  $m$  – electron mass;  $\varphi^*$  – average electron work function;  $h$  – Planck constant.

Tunnel current appears between the probe and the sample if potential difference  $V$  is applied to the tunnel contact.

The dependence of tunnel current on the distance is nonlinear. As a result, the distance between the probe and the sample can be accurately regulated.

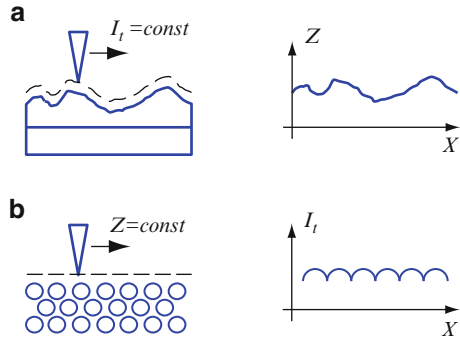
STM is an electromechanical system with negative feedback. The feedback system maintains the tunnel current value between the probe and the sample at the prescribed level ( $I_0$ ), selected by the operator. The tunnel current value and, consequently, probe–surface distance is controlled by the probe movement along  $Z$ -axis by means of the piezoelectric element (Fig. 16.2) [9].

Scanning the surface, the piezoelement is simultaneously moving the probe along  $X$  and  $Y$  coordinates.

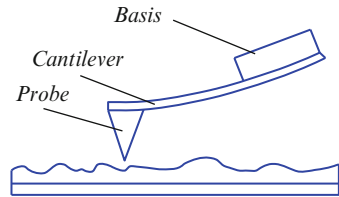
The surface relief image is formed in two ways in STM. In constant tunnel current mode (Fig. 16.3a), the probe moves along the surface, scanning. The voltage change on the piezoelement  $Z$ -electrode in feedback circuit, accurately repeating the sample surface, is recorded in computer memory as function  $Z = f(x, y)$ . It is reproduced in computer graphics.

Studying atom smooth surfaces, the STM surface image is often more accurately obtained in constant height mode ( $Z = \text{const.}$ ). In this case, the probe moves above the surface at a distance of several angstroms. Then the tunnel current changes are registered as STM surface images (Fig. 16.3b). The surface is scanned without the FB, or with the velocities exceeding the FB reaction speed. Thus, the FB fulfills only smooth changes of the surface relief. Very high scanning velocities and a high frequency of STM image reception are achieved in this case. As a result, the changes occurring on the surface can be observed almost in real time [9].

**Fig. 16.3** Formation of STM surface images in constant tunnel current mode (a) and constant average distance (b)



**Fig. 16.4** Diagram of AFM probe sensor



## 16.2.2 Atomic-Force Microscopy

The atomic-force microscope (AFM) was invented in 1986 by Gerd Karl Binnig, Calvin F. Quate and Christopher Herber [10]. AFM is based on power interaction between the probe and the surface. This interaction is registered by special probe sensors. The sensors consist of an elastic (cantilever) console with a sharp probe on the end (Fig. 16.4). The force influencing the probe from the surface side causes the (cantilever) console to bend. Registering the bend value, the interaction force between the probe and the surface can be controlled.

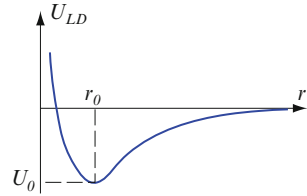
AFM work can be qualitatively explained through the example of Van der Waals forces [11]. Van der Waals energy from the interaction of two atoms located at  $r$  distance from each other is approximated by the power function known as Lennard–Jones potential (Fig. 16.5) [9]:

$$U_{LD}(r) = U_0 \left[ -2 \left( \frac{r_0}{r} \right)^6 + \left( \frac{r_0}{r} \right)^{12} \right]. \quad (16.4)$$

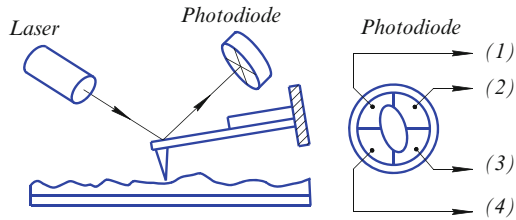
The augend in this expression describes the long-range attraction caused, mainly, by dipole–dipole interaction of atoms, dipole. The addend considers atom repulsion at small distances. Parameter  $r_0$  is equilibrium distance between atoms,  $U_0$  is energy value at minimum.

The interaction between the probe and the sample is determined by Lennard–Jones potential [9]. The system total energy can be received by summing elementary interactions for each of the probe and the sample atoms.

**Fig. 16.5** Qualitative view of Lennard–Johns potential



**Fig. 16.6** Optical registration scheme of AFM probe sensor console curvature



Then for interaction energy we obtain:

$$W_{PS} = \int_{V_P} \int_{V_S} U_{LD}(r - r') n_P(r') n_S(r) dV dV', \quad (16.5)$$

where  $n_S(r)$  and  $n_P(r')$  are atoms density in the sample and probe materials. Therefore, the force influencing the probe from the surface side can be calculated like this:

$$\vec{F}_{PS} = -\text{grad}(W_{PS}). \quad (16.6)$$

In the common case, the given force has both normal to the surface and lateral (lying in the sample surface plane) components. The real interaction between the probe and the sample is more complex. However, the main features of this interaction remain that probe AFM is attracted to the sample at large distances and is repulsed at small distances.

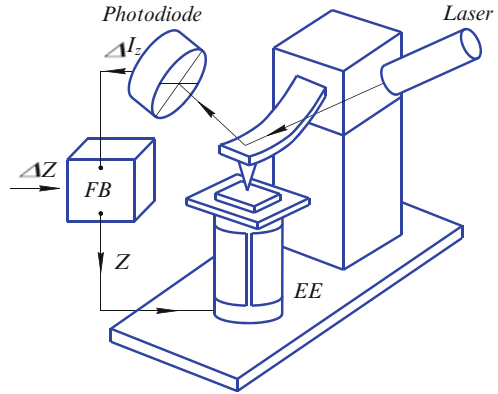
AFM relief surface imaging is connected with the small curvature registration of the elastic console of the probe sensor. Therefore, optical methods are widely used in atomic-force microscopy (Fig. 16.6).

The AFM optical system is adjusted for semi-conductor laser radiation to focus on the probe sensor console. Then the reflected beam goes to the center of the photosensitive area of the photodetector. Four-section semi-conductor photo diodes are used as position-sensitive photodetectors (Fig. 16.7).

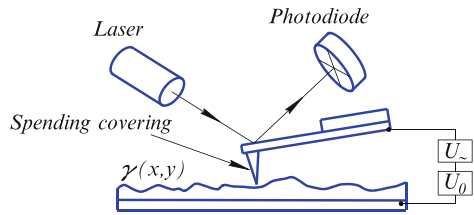
Scanning the sample in  $AZ = \text{const.}$  mode, the probe moves along the surface. Then the voltage on the scanner Z-electrode is recorded in computer memory as the surface  $Z = f(x, y)$  relief. AFM spatial resolution is determined by the probe curvature radius and system sensitivity, registering console deflection. Now AFM aims at obtaining the atomic resolution when the sample surfaces are studied.

Special probe sensors probe the surface in an AFM. These sensors consist of an elastic console (cantilever) with a sharp probe at the end. The sensors are made by

**Fig. 16.7** Simplified scheme of feedback organization in AFM (*FB* feedback, *EE* executive element)



**Fig. 16.8** Measurement scheme of probe and sample electric interaction



photolithography and etching of silicon plates. The elastic consoles (cantilevers) are usually made of alloyed silicon thin layers, SiO<sub>2</sub> or Si<sub>3</sub>N<sub>4</sub>.

### 16.2.3 Electric Force Microscopy

Electric interaction between the probe and the sample is used in electric power microscopy to obtain information about the surface properties. The system contains a probe sensor with conductive coating on the probe, and a sample consisting of the material thin layer on the conducting substrate (Fig. 16.8) [9].

Let constant voltage  $U_0$  and alternating voltage  $U = U_1 \sin(\omega t)$  be supplied between the probe and the sample. If the thin layer on the substrate is a semiconductor or a dielectric, it may have a surface charge. Therefore, there is potential distribution  $\varphi(x, y)$  on the sample surface. The voltage between the probe and the sample surface can be represented like this:

$$U = U_0 + U_1 \sin(\omega t) - \varphi(x, y). \tag{16.7}$$

The probe–sample system has an electric capacitance  $C$ . Therefore, the energy of this system can be represented like this:



$$E = \frac{CU^2}{2}. \quad (16.8)$$

The interaction force between the probe and the surface, based on a simple flat condenser model, can be represented like this [9]:

$$F_{PS} = -\frac{1}{2}U^2 \frac{\partial C}{\partial z} \cong -\frac{1}{2}\alpha U^2 \frac{\pi R^2}{h^2}, \quad (16.9)$$

where:  $a$  – constant;  $R$  – characteristic rounding radius of the probe end;  $h$  – probe–surface distance (or the dielectric film thickness on the conducting substrate).

On the other hand, the force influencing the cantilever from the sample side may be expressed as follows:

$$F_{CS} = -\frac{1}{2}U^2 \frac{\partial C}{\partial z} \cong -\frac{1}{2}\alpha U^2 \frac{LW}{H^2}, \quad (16.10)$$

where:  $a$  – constant;  $L$  – cantilever length;  $W$  – cantilever width;  $H$  –  $d$  distance to the surface (determined by the probe dimension).

As follows from  $F_{PS} > F_{CS}$ :

$$h < \sqrt{\frac{\pi R^2 H^2}{LW}}. \quad (16.11)$$

Hence,  $h < 10$  nm value can be obtained for typical values of probe sensor parameters ( $L \sim 100 \mu\text{m}$ ,  $W \sim 30 \mu\text{m}$ ,  $H \sim 30 \mu\text{m}$ ,  $R \sim 10$  nm).

### 16.2.4 Magnetic Force Microscopy

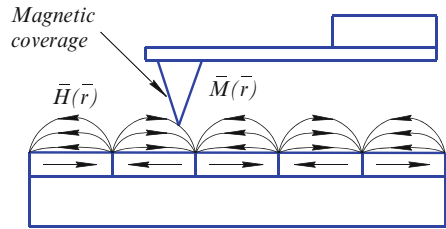
A magnetic force microscope (MFM) [12, 13] was invented by Y. Martin and H. K. Wickramasinghe in 1987 for study of the local magnetic properties of samples. This device is an AFM with the probe covered by a ferromagnetic material layer with specific magnetization  $\overline{M}(\overline{r})$ .

In the common case, the description of MFM probe interaction with the sample field  $\overline{H}(\overline{r})$  is a complex task. In the elementary MFM model, the probe can be represented as a single magnetic dipole, characterized by magnetic moment  $\overline{m}$  [14]. Potential energy of this system equals (Figs. 16.9 and 16.10) [9]

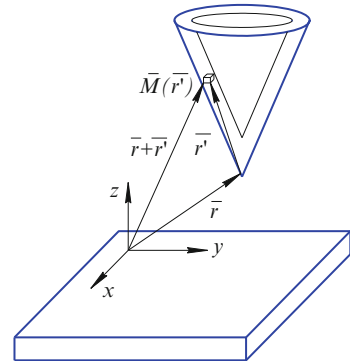
$$w = -(\overline{m}\overline{H}). \quad (16.12)$$

Force  $\overline{f} = -\text{grad}(w) = \overline{\nabla}(\overline{m}\overline{H})$  and a force moment equal to  $\overline{N}(\overline{m}\overline{H})$  influence the magnetic dipole in the field  $H$ .

**Fig. 16.9** MFM probe in sample magnetic field



**Fig. 16.10** Interaction of MFM probe and sample magnetic field



Force  $\vec{f} = 0$  in a homogeneous magnetic field. The dipole is influenced by the force moment, turning magnetic moment  $\vec{m}$  along the field. In the non-uniform field, the dipole is drawn into the area with bigger intensity  $H$ .

In the common case, the MFM probe magnetic moment can be represented as dipole superposition, thus

$$\vec{M}(r)dV, \tag{16.13}$$

where  $\vec{M}$  is coating specific magnetization, and  $dV$  is elementary volume.

Probe-sample field interaction force equals [9]

$$\vec{F} = -\text{grad}(W_{\text{mag}}) = \int_{V_p} \vec{\nabla}(\vec{M} \vec{H})dV'. \tag{16.14}$$

Accordingly, force  $Z$ -component equals

$$F = -\frac{\partial W}{\partial Z} = \int_{V_p} \left( M_x \frac{\partial H_x}{\partial z} + M_y \frac{\partial H_y}{\partial z} + M_z \frac{\partial H}{\partial z} \right) dV. \tag{16.15}$$

Quasi-static and vibration techniques are used to obtain MFM images [9].

## 16.3 Scanners on Hollow Piezoceramic Cylinders

A tripod – a combination of three piezoceramic bars in a node [9] – was used as a scanner in the first nanomicroscope.

In 1986 piezoceramic hollow cylinders (tubes) with a special electrode configuration were offered for use in scanner manufacturing [15, 16]. As a result of essential simplification of tubular scanner design, they have been used in various commercial devices. They allow creation of center-symmetric designs. They also considerably decrease the temperature drift value.

Tubular piezoelements are widespread in scanning probes (Fig. 16.11). Rather large movements of objects with extremely small control voltage can be received by them. Electrodes in thin metal layers are usually positioned on the tube external and internal surfaces while the tube ends remain uncovered. The tube changes its longitudinal dimensions under the influence of the potential difference between the internal and external electrodes. In this case, the longitudinal deformation under the influence of the radial electric field can be written as:

$$u_{xx} = \frac{\Delta x}{l_0} = d_{\perp} E_r, \quad (16.16)$$

where  $l_0$  is the tube length in undeformed condition.

Absolute elongation of the piezotube equals

$$\Delta x = d_{\perp} \frac{l_0}{h} V, \quad (16.17)$$

where  $h$  is piezotube wall thickness, and  $V$  is the potential difference between internal and external electrodes.

Thus, the longer the tube and the thinner the wall is, the bigger its elongation with the constant voltage  $V$ .

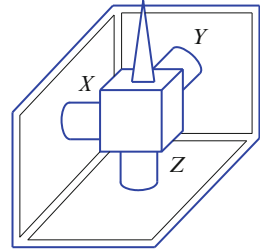
The probe can move in three reciprocally perpendicular directions if three tubes are connected in a node (Fig. 16.12). This scanning element is called a tripod [9].

Difficulty of manufacture and strong design asymmetry are disadvantages of this scanner. Scanners based on a tubular element are most widely used in scanning probe microscopy. The general view of a tubular scanner and the electrode positioning scheme are shown in Fig. 16.13. The tube material has radial direction of the polarization vector.

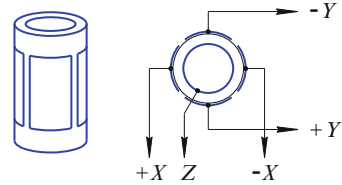


**Fig. 16.11** Tubular piezoelement

**Fig. 16.12** Tripod scanner on tubular piezoelements



**Fig. 16.13** Scanner based on a tubular piezoelement



The internal electrode is usually solid. The scanner external electrode is quartered in sections along the cylinder elements. If anti-phase voltage is supplied to the opposite sections of the external electrode (relatively to the internal electrode), the tube is reduced where the field direction coincides with the polarization direction; it is elongated when these directions are opposite. As a result, the tube is bent in the corresponding direction. Thus,  $X$ ,  $Y$  planes are scanned.

The potential change of the internal electrode relative to all external sections leads to elongation or reduction of the tube along the  $Z$ -axis [9]. Real scanning elements are often of a more complicated design. However, their work principles remain the same.

Oscillations of a radial polarized piezoceramic cylinder, activated by external harmonious voltage [according to the load character, and, consequently, min and max boundary (edge) conditions], are described by the following system of equations (these variables  $u_z$ ,  $\sigma_{rr}$ ,  $\sigma_{rz}$ ,  $u_r$ ,  $\varphi$ ,  $D_r$  are used as independent functions) [17]:

$$\begin{aligned} \frac{\partial u_z}{\partial r} &= -\frac{\partial u_r}{\partial z} + \frac{1}{c_{55}^E} \left( \sigma_{rz} - e_{15} \frac{\partial \varphi}{\partial z} \right), \\ \frac{\partial \sigma_{rr}}{\partial r} &= \frac{1}{r} \left( c_{12}^E + \frac{\Delta_2}{\Delta_1} \right) \frac{\partial u_z}{\partial z} - \frac{1}{r} \left( 1 - \frac{\Delta_4}{\Delta_1} \right) \sigma_{rr} - \frac{\partial \sigma_{rz}}{\partial z} \\ &\quad - \left[ \rho \omega^2 - \frac{1}{r^2} \left( c_{11}^E + \frac{\Delta_2}{\Delta_1} \right) \right] u_r + \frac{1}{r} \frac{\Delta_3}{\Delta_1} D_r, \\ \frac{\partial u_r}{\partial r} &= \frac{1}{\Delta_1} \left( \Delta_4 \frac{\partial u_z}{\partial z} + \varepsilon_{33}^S \sigma_{rr} - \frac{1}{r} \Delta_4 u_r + e_{33} D_r \right), \end{aligned}$$

$$\begin{aligned}
\frac{\partial \sigma_{rz}}{\partial r} &= -\rho w^2 u_z - \left( c_{11}^E + \frac{\Delta_2}{\Delta_1} \right) \frac{\partial^2 u_z}{\partial z^2} - \frac{\Delta_4}{\Delta_1} \frac{\partial \sigma_{rr}}{\partial z} - \frac{1}{r} \sigma_{rz} \\
&\quad - \frac{1}{r} \left( c_{12}^E + \frac{\Delta_2}{\Delta_1} \right) \frac{\partial u_r}{\partial z} - \frac{\Delta_3}{\Delta_1} \frac{\partial D_r}{\partial z}, \\
\frac{\partial \varphi}{\partial r} &= \frac{1}{\Delta_1} \left( -\Delta_3 \frac{\partial u_z}{\partial z} + \varepsilon_{33} \sigma_{rr} - \frac{1}{r} \Delta_3 u_r + c_{33}^E D_r \right), \\
\frac{\partial D_r}{\partial r} &= \frac{1}{c_{55}^E} \left( -e_{31} \frac{\partial \sigma_{rz}}{\partial z} + \Delta_5 \frac{\partial^2 \varphi}{\partial z^2} \right) - \frac{1}{r} D_r,
\end{aligned} \tag{16.18}$$

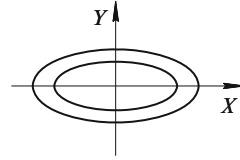
where:  $\Delta_1 = e_{33}^2 + c_{33}^E \varepsilon_{33}^S$ ;  $\Delta_2 = c_{33}^E e_{31}^2 - 2c_{13}^E e_{31} e_{33} - c_{31}^2 \varepsilon_{33}^S$ ;  $\Delta_3 = c_{13}^E e_{33} - c_{33}^E e_{31}$ ;  $\Delta_4 = c_{13}^E \varepsilon_{33}^S + e_{31} c_{33}$ ;  $\Delta_5 = e_{15}^2 + c_{15}^E \varepsilon_{11}^S$ ;  $\varepsilon_{31}^S$  – deformation tensor;  $\rho$  – density;  $r$  – cylinder mean radius;  $c_{33}^E$  – elasticity module tensor;  $e_{31}$  – piezoelectric constant.

One can prove that the solution of the forced oscillations problem of the radial polarized cylinder under the electric load is reduced to the solution of an infinite sequence of ordinary differential equation systems [17]:

$$\begin{aligned}
\frac{du_z^{(n)}}{dr} &= -\eta_n u_r^{(n)} + \frac{1}{c_{55}^E} \left( \sigma_{rz}^{(n)} - \eta_n e_{15} \varphi^{(n)} \right), \\
\frac{d\sigma_{rr}^{(n)}}{dr} &= \frac{1}{r} \eta_n \left( c_{12}^E + \frac{\Delta_2}{\Delta_1} \right) u_z^{(n)} - \frac{1}{r} \left( 1 + \frac{\Delta_4}{\Delta_1} \right) \sigma_{rr}^{(n)} + \eta_n \sigma_{rz}^{(n)} \\
&\quad - \left[ \rho w^2 - \frac{1}{r} \left( c_{11}^E + \frac{\Delta_2}{\Delta_1} \right) \right] u_r^{(n)} + \frac{1}{r} \frac{\Delta_3}{\Delta_1} D_r^{(n)}, \\
\frac{d\sigma_{rz}^{(n)}}{dr} &= \left[ -\rho w^2 - \eta_n^2 \left( c_{11}^E + \frac{\Delta_2}{\Delta_1} \right) \right] u_z^{(n)} - \eta_n \frac{\Delta_4}{\Delta_1} \sigma_{rr}^{(n)} \\
&\quad - \frac{1}{r} \sigma_{rz}^{(n)} - \frac{\eta_r}{r} \left( c_{11}^E + \frac{\Delta_2}{\Delta_1} \right) u_r^{(n)} + \eta_n \frac{\Delta_3}{\Delta_1} D_r^{(n)}, \\
\frac{du_r^{(n)}}{dr} &= \frac{1}{\Delta_1} \left( \eta_n \Delta_4 u_z^{(n)} + \varepsilon_{33}^S \sigma_{rr}^{(n)} - \frac{\Delta_4}{r} u_r^{(n)} + e_{33} D_r^{(n)} \right), \\
\frac{d\varphi^{(n)}}{dr} &= \frac{1}{\Delta_1} \left( \eta_n \Delta_3 u_z^{(n)} + \varepsilon_{33}^S \sigma_{rr}^{(n)} - \frac{\Delta_3}{r} u_r^{(n)} + c_{33}^E D_r^{(n)} \right), \\
\frac{dD_r^{(n)}}{dr} &= \frac{\eta_r}{c_{55}^E} \left( e_{15} \sigma_{rz}^{(n)} - \eta_n^2 \Delta_5 \varphi^{(n)} \right) - \frac{1}{r} D_r^{(n)}.
\end{aligned} \tag{16.19}$$

With regional conditions

**Fig. 16.14** Interference of actuators along coordinates



$$\varphi^{(n)} \Big|_{r_0 \pm h} = \pm \frac{2V_0}{n\pi} \cdot [\sigma_{rr}^{(n)}(r) = \sigma_{rz}^{(n)}(r)] \Big|_{r_0 \pm h} = 0, \quad (16.20)$$

where:  $\eta = n\pi/l$ ;  $n$  – harmonic number;  $l$  – piezoceramic cylinder length;  $V_0$  – amplitude of activated oscillations.

The solution of these equations is hard. Therefore, the basic characteristics of a bimorph piezoceramic cylinder are determined experimentally.

One of the main drawbacks of these scanners is the deformation of the piezotube simultaneously in both the scanning direction and that perpendicular to it. There is a rigid interconnection between the actuators, ensuring the movement along XYZ coordinates, worsening positioning accuracy (Fig. 16.14). In addition to that, the probe (object) holder plane changes the slope at scanning. This narrows the scanning range. As the tubular scanner actuators are rigidly interconnected, the passive actuators also reduce the scanning range. High control voltage is also a negative factor (up to 300 V).

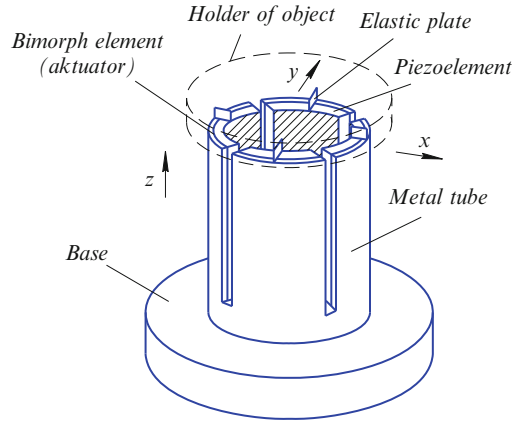
To eliminate the disadvantages specified, it was proposed that the interference between the actuators and XYZ coordinates should be reduced [18]. Communication reduction became possible because the scanner actuators are split along the XY coordinates. There are some cuts along the piezotube. Four independent actuators appear. They ensure movements along XY coordinates two by two. As a result, the scanner is positioned more accurately. In addition to that, the actuators are split along XY coordinates from the actuator on the Z coordinate. This is possible after the introduction of flat elastic elements (plates) of different rigidity along the XY coordinates. As a result, the object holder can be moved in one plane. In addition, actuators look like bimorph piezoelements. This leads to an essential change in piezoceramic scanner characteristics. The scanning range and mechanical durability considerably increase (Fig. 16.15) [18, 19]. A bimorph piezoelement is used as the probe (sample) holder.

Cylindrical bimorph piezoceramic elements have not been studied yet. Flat bimorph piezoelements are approximately close to cylindrical bimorph piezoelements. Their radiuses tend to infinity.

Free end movements of the cantilever-fastened bimorph piezoelement, and consequently, the scanning range, can be calculated approximately by using the formula [20]:

$$\xi \approx \frac{3}{2} \frac{d_{31} \left[ \left( h_P + \frac{h_M^2}{2} \right) - \frac{h_M^2}{4} \right] \left( 1 + 2 \frac{L-l}{l_P} \right) l}{\left[ E_M S_{11}^E \frac{h_M^3}{8} + \left( h_P + \frac{h_M}{2} \right)^3 - \frac{h_M^3}{8} \right] h_P} U, \quad (16.21)$$

**Fig. 16.15** Bimorph tubular piezoceramic scanner



where:  $E_M$  – Young’s modulus of metal platinum;  $d_{31}$  – piezomodule;  $S_{11}^E$  – elastic constant;  $h_M$  – metal plate thickness;  $h_P$  – piezoelement thickness;  $l$  – piezoelement length;  $L$  – metal plate length;  $U$  – control voltage.

## 16.4 Scanners Based on Flat Bimorph Piezoelements

Bimorph piezoelements are described in Chap. 6.

Joining three bimorph elements in one design, a tripod on bimorph elements can be obtained (Fig. 16.16) [9].

If bimorph element electrodes are quartered, the probe can move along axis  $Z$  and in the  $X, Y$  plane on a bimorph element (Fig. 16.17) [9].

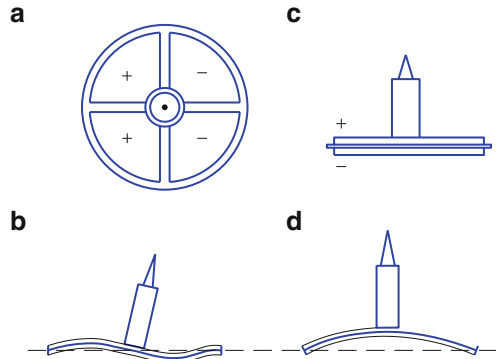
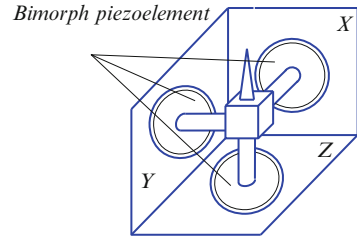
In fact, if anti-phase voltage is supplied to the opposite pairs of the external electrode sections, the bimorph can be bent for the probe to move in the  $X, Y$  planes (Fig. 16.17a, b). Changing the internal electrode potential relative to all external electrode sections, the bimorph can be bent, moving the probe in the  $Z$  direction (Fig. 16.17c). Trimorph piezoelements can be also used for this purpose (see Chap. 6).

The scanner shown in Fig. 16.16 is very asymmetrical. In addition, vibrations of this scanner along one coordinate cause vibrations along the other.

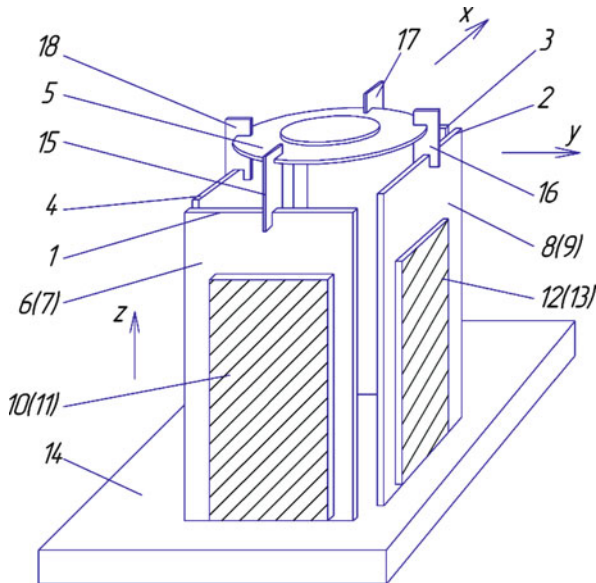
Non-central rectangular bimorph elements (1, 3 and 2, 4), fastened from the one basis side, are offered to eliminate the drawbacks specified (Fig. 16.18) [19, 21–23, 25]. These bimorph piezoelements (actuators) ensure probe movement along coordinates  $X$  and  $Y$ . Bimorph elements consist of metal (6, 7 and 8, 9) and piezoceramic (10, 11 and 12, 13) plates, glued with epoxy adhesive.

Bimorph piezoelement 5, assuring movement along coordinate  $Z$ , is disk-shaped. It is attached to bimorph piezoelements 1–4 by elastic elements 15–18. Elastic elements are rectangular-shaped plates, fastened to bimorph piezoelements 1–4

**Fig. 16.16** Three-coordinate scanner with three bimorph elements



**Fig. 16.17** Scanner with a bimorph element



**Fig. 16.18** Piezoceramic scanner based on flat bimorph piezoelements: 1–5 – bimorph elements, 6–9 – metal plates, 10–13 – piezoelements, 14 – basis, 15–18 – elastic plates



in the following way: when bimorph piezoelements 1, 3 move along coordinate  $X$ , elastic elements 15, 17 have great rigidity, while elastic elements 16, 18 have small rigidity. As a result, bimorph piezoelement 5 moves along coordinate  $X$ , not influencing bimorph elements 2, 4.

Bimorph piezoelements 1–4 are cantilever-fastened. This lowers their resonant frequency to several hundred hertz.

The section rigidity of the bimorph piezoelement, consisting of a metal plate and a piezoelement, is determined by the formula [20]:

$$\lambda_B = E_M J_M + E_P J_P^* = \frac{12}{b \left\{ E_M h_M^3 + E_P h_P^3 \left[ 1 + 3 \left( 1 + \frac{h_M}{h_P} \right)^2 \right] \right\}}, \quad (16.22)$$

where  $E_M$  is the metal plate elasticity module, and  $E_P$  is the piezoelement elasticity module. It can be found by the polarized piezoceramic compliance, given in handbooks,  $E_P = (s_{11}^E)^{-1}$ ;  $J_M = bh_M^3/12$ ;  $J_P^* = J_P + [(h_M + h_P)^2 / 4] \Omega_P$ ;  $J_P = bh_P^3/12$ ;  $\Omega_P = bh_P$ ;  $b$  – bimorph piezoelement width;  $h_M$  – metal plate thickness;  $h_P$  – piezoelement thickness.

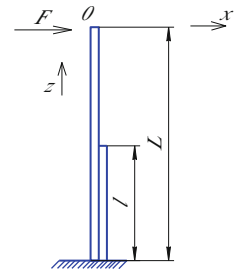
A design diagram to determine the bimorph element rigidity is shown in Fig. 16.19.

The scanner equivalent electric scheme (equivalent circuit), designed by an electromechanical analogy method, is shown in Fig. 16.20 [21, 24].

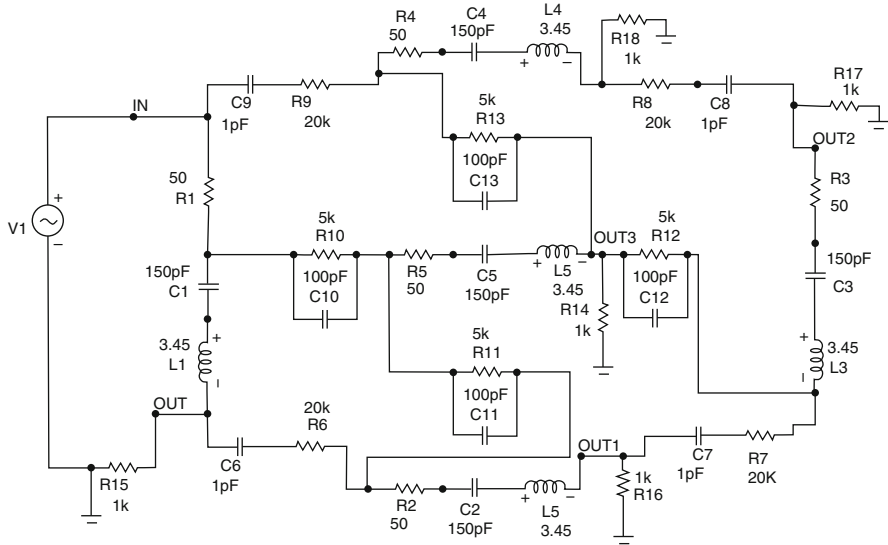
Oscillatory contours R1-C1-L1, R2-C2-L2, R3-C3-L3, R4-C4-L4, R5-C5-L5 correspond of bimorph piezoelements 1–5 (Fig. 16.18). Inter-electrode piezoelements capacitance was not considered in this case. Bimorph piezoelements 1–5 are elastically interconnected with losses (R6-C6, R7-C7, R8-C8, R9-C9). These losses correspond to elastic elements 15–18. The masses of these elastic elements were not considered.

The scanner (Fig. 16.18) with these specifications is being studied experimentally.

Bimorph piezoelements (BPE) 1–4 are semi-firm J163 brass metal plates (dimensions: 40 × 20 × 0.3 mm) and piezoceramic IITC-19 piezoelements (dimensions: 27 × 20 × 0.3 mm). Bimorph element 5 is a metal plate (steel 40×) 20 mm in



**Fig. 16.19** Design diagram to determine bimorph element rigidity:  $F$  – force,  $l$  – piezoelement length,  $L$  – metal plate length



**Fig. 16.20** Scanner equivalent electric scheme

diameter and 0.15 mm thick. The piezoelement is 16 mm in diameter and 0.2 mm thick. Elastic plates 15–18 are  $10 \times 3 \times 0.1$  mm.

The voltage from generator G3-109 was supplied to this bimorph piezoelement to determine the influence of a bimorph element's oscillations on other bimorph elements. The amplitude of all oscillations of bimorph elements was measured by a capacitive sensor. As the measurements showed, BPE-1 oscillations practically do not influence BPE-2, -4 and -5.

## References

1. P.P. Maltsev (ed.), *Nanomaterials. Nanotechnologies. Nanosystem Equipment* (Tekhnosfera, Moscow, 2006) (in Russian)
2. U.A. Chaplgin (ed.), *Nanotechnologies in Electronics* (Tekhnosfera, Moscow, 2005), p. 448 (in Russian)
3. R. Young, I. Ward, F. Scire, The topographiner: an instrument for measuring surface microtopography. *Rev. Sci. Instrum.* **43**, 999 (1972)
4. G. Binning, H. Rohrer, Scanning tunneling microscope. U.S. Patent 4343993, 10 Aug 1982 (Filed: 12 Sept 1980)
5. V.K. Nevolin, *Probe Nanotechnologies in Electronics* (Tekhnosfera, Moscow, 2005), p. 152 (in Russian)
6. G. Binnig, H. Rohrer, Scanning tunneling microscopy. *Helv. Phys. Acta* **55**(6), 726–735 (1982)
7. D.I. Blohintsev, *Basics of Quantum Mechanics* (Nauka, Moscow, 1983) (in Russian)
8. L.D. Landau, E.M. Lifshits, *Theoretical Physics, Quantum Mechanics*, vol. 3 (Phizmatlit, Moscow, 2001), p. 804 (in Russian)

9. V.L. Mironov, *Basics of Scanning Probe Microscopy* (Technosfera, Moscow, 2004), p. 144 (in Russian)
10. G. Binnig, C.F. Quate, Ch. Gerber, Atomic force microscope. *Phys. Rev. Lett.* **56**(9), 93–933 (1986)
11. Yu.S. Barash, *Van der Waals Forces* (Nauka, Moscow, 1988), p. 344c
12. Y. Martin, Wickramasinghe. Magnetic imaging by force microscopy with 1000 Å resolution. *Appl. Phys. Lett.* **50**(20), 1455–1457 (1987)
13. D. Rugar, H. Mamin, P. Guethner et al., Magnetic force microscopy: general principles and application to longitudinal recording media. *J. Appl. Phys.* **68**(3), 1169–1182 (1990)
14. I.E. Tamm, *Basics of Electricity Theory* (Nauka, Moscow, 1976), p. 616 (in Russian)
15. G.M. Binnig, D. Smith, Tubular three-coordinate transducer for scanning electron microscope, *Devices for scientific researches* (1986), p. 152
16. G.M. Binnig, D. Smith, Single-tube three-dimensional scanner for scanning tunneling microscopy. *Rev. Sci. Instrum.* **58**(8), 1688 (1986)
17. N.A. Shulga, A.M. Bolkisev, *Vibrations of Piezoelectric Bodies* (Naukova Dumka, Kiev, 1990), p. 228 (in Russian)
18. V. Sharapov, A. Vladisauskas, S. Filimonov, Bimorph cylindrical piezoceramic scanner for scanning probe nano-microscopes, *Ultragarsas (Ultrasound)* **4**(64), ISSN 1392–2114 (Technologia, Kaunas, 2009)
19. V.M. Sharapov, A.N. Ghyrzhly, S.O. Filimonov, Piezoelectric scanner, Patent of Ukraine No 22601 (2007) (in Ukrainian)
20. A.B. Smirnov, *Mechatronics and Robotics. Micro-movement Systems with Piezoelectric Actuators: Teaching Aid* (SPbSPU Publishing, St. Petersburg, 2003) (in Russian)
21. V. Sharapov, A. Vladisauskas, S. Filimonov, Piezoceramic scanners on the basis of planar bimorph piezoelements for scanning probe nanomicroscopes. *Ultragarsas (Ultrasound)* **1**(65) (Technologia, Kaunas, 2010), ISSN 1392–2114
22. V.M. Sharapov, M.P. Musienko, E.V. Sharapova, in *Piezoelectric Sensors*, ed. by V.M. Sharapov (Technosfera, Moscow, 2006), p. 632 (in Russian)
23. V.M. Sharapov et al., in *Sensors*, ed. by V.M. Sharapov, E.S. Polischuk (Brama, Cherkasy, 2008), p. 1072 (in Russian)
24. L.A. Ostrovskiy, *General Theory Basics of Electric Devices* (Energia, Leningrad, 1971), p. 544 (in Russian)
25. V.M. Sharapov, A.N. Ghyrzhly, A.P. Alpatov, S.A. Filimonov, Piezoscanner, Patent of Ukraine No 22600, Cl. G12B 21/20 H01L 41/00, Bull. No 5 (2007) (in Ukrainian)

# Index

- 22 differential equations, 8
- 27 components, 6
  
- Accelerometers, 388, 393–395, 397, 398, 401–403
  - by Kistler instrumente AG, 391
  - with sensitive element, 394
  - with spherical segment-shaped piezoelement, 400
- Acoustic power, 296
- Acoustic resonators, 313
- Acoustic signal (Korotkoff sounds), 334
- Acoustically coupled resonators, 446
- Active oscillator circuit, 247
- Additional metal resonator, 443
- Additional piezoelement, 224
- Advantages, 7
- AFC., *see* Amplitude–frequency characteristics
- All types of fluctuations, 46
- Amplifier, 126, 127, 135, 160
- Amplifier input resistance, 345
- Amplitude and phase characteristics of
  - accelerometer, 105
- Amplitude–frequency, 88–90
- Amplitude–frequency characteristics (AFC), 76, 232
  - asymmetric trimorph planar transducer (variant 1), 198
  - of filters, 454
  - of sensors, 345
  - of symmetric bimorph, 234
  - of traditional piezotransformers, 88
  - of transducers, 77
- Analysis, 86, 389
- Anisotropy of piezoceramic materials
  - characteristics, 79
  
- Antiresonant frequencies, 10, 60
- Aperiodic networks, 245
- Application of electro-acoustic piezomagnetic transducers, 283
- Arterial blood pressure, 333
- Astatic feedback, 426
- Asymmetric bimorph, 188
  - piezoelements, 184, 340
  - piezosensors, 145, 185
  - sensor, 151
- Asymmetric coplanar
  - threemorph piezoelement, 343
  - trimorph piezotransducers, 201
- Asymmetric planar trimorph piezoelements, 196
- Asymmetric trimorph
  - coplanar transducer, 206, 207, 209, 211
  - piezoelements, 205
  - planar transducer, 200, 201, 203
- Atomic-force microscopy, 476
- Autotransformer coupling, 243
  
- Basic designs, 51
- Basic feedback circuits, 117
- Basic requirements for transducers, 300
- Basic types of ultrasonic equipment transducers, 318
- Bessel filter, 455
- Bessel functions, 55, 61, 220, 298
- Bimorph, 189, 400
  - element, 348, 395, 486
  - piezoceramic cylinder, 484
  - piezoelements, 179, 194, 232, 237, 275
  - piezomagnetic sensor of tachometer, 279
  - sensor, 195
  - transducers, 180

- tubular piezoceramic scanner, 485
- Block, 421
- Block diagram, 142, 145, 169, 173
  - of bimorph piezotransducers with FB, 183
  - of piezoceramic sensor with
    - electromechanical FB, 121
  - of piezoelectric sensor with electric FB, 139
  - of piezosensor, 164
  - of piezosensor with double-loop FB, 158
  - of sensors with double-loop FB, 158
- Block scheme, 426
- Block scheme of tachometer piezomagnetic sensor, 271
- Brüel and Kjer, 393
- Butterworth filter, 455
  
- Calculation, 18, 35, 340
- Calibration, 439
- Capacitance, 297
- Capacitance–resistance, 108
- Certain transducer designs, 302
- Characteristic equation, 417
- Characteristics, 200, 202, 203, 207, 210–213, 215, 216, 289, 325, 484
  - of a piezoelement, 135
  - of soft solders, 225
- Charge, 60, 160, 161, 164, 175
  - amplifier intrinsic noise, 109
  - amplifiers, 99, 106, 165, 166, 169, 173, 174
- Chebyshev filter, 455
- Circuit
  - and characteristics of piezoelement with amplifier, 136
- Circuits, 94, 126, 200
  - of piezoelectric accelerometer, 104
  - of piezotransformers, 86, 88, 91
  - of traditional piezotransformers, 87
- Class of piezoceramic sensors, 3
- Classification, 289, 410
  - of accelerometers, 382
  - of piezoceramic transducers, 74
- Coefficients, 62, 416
  - inductance, 67
  - of electromechanical communication, 31
  - of electromechanical transformation, 320
  - of transformation, 52
  - transfer, 269
  - transfer module, 416
- Combined transducers, 319
- Combined FB, 145
- Communication circuit of transducer, 205
  
- Comparative characteristic of accelerometers, 406
- Compensated piezotransducer designs, 305
- Complex sensitivity, 148
- Component of magnetic induction, 261
- Compound, 429
- Compound ceramic cylinder, 386
- Concentration, 227
- Concentrators, 428, 429, 432
- Condenser, 103
- Condition, 439
- Conductive, 227
- Conductive adhesives, 226
- Connection schemes, 343, 457
- Constructive control methods, 438
- Contact actual area measurement, 421
- Contact rigidity, 419
  - dependence, 420
  - measurement, 420
- Contour equivalent, 248
- Control, 245, 246
- Coplanar location of additional piezoelement, 349
- Correcting resilient elements, 440
- Crystal structure, 5
- Cylinder, 254, 293
- Cylinder form permeability, 264
- Cylindrical piezoceramic transducers, 294, 304
- Cylindrical piezoelements, 307, 396
  
- $d_{\Gamma} \equiv c$ ; ( $\Gamma - G$  from generator), 301
- Decision, 30
- Defect diagnostics, 232
- Defects of bimorph piezoelements, 231
- Deformations, 29, 60, 413
- Delta shear, 393
- Dependence, 67, 194, 256
  - of magnetic tachometers piezosensor
    - output voltage on distance between magnets, 265
  - of transformation coefficient relative sensitivity, 337
- Descriptions, 21
- Design(s), 335
  - and AFR of various transducer types, 326
  - of asymmetric bimorph element, 339
  - of direct combined contact-immersion, 331
  - of piezomagnetic rotation frequency sensors, 274
  - of tachometer piezomagnetic sensor, 275
- Determination and classification of piezoelectric sensors, 2

- Determining piezoceramic element parameters, 9
- Development of the theory and practice of piezoelectric devices, 2
- Devices, 236, 245
  - to control and diagnose bimorph, 231
  - to diagnose defects of bimorph piezoelement based, 240
- Diagnostics of defects by pulse characteristic, 237
- Diagnostics of defects by transitive characteristic, 241
- Diagrams, 256
  - of AFM probe sensor, 476
  - of magnet, 260
  - of trimorph symmetric transducer, 214
- Differential equation, 102, 134, 147
- Differential equation with constant coefficients, 75
- Differentiating circuit, 94, 245
- Diffraction factor, 293
- Dimensionless sensitivity, 194
- Directional diagram, 397, 402
- Direct transform, 125
- Direct transform circuit, 224
- Disks, 58, 293
  - piezoelement, 414
  - piezotransformers, 93
  - radius, 61
- Distribution, 60
- Divided electrodes, 58
- Domain structure of piezoceramic, 81
- Domain-dissipative, 73
  - accelerometer, 404
  - circuit, 86
  - piezoceramic sensors, 126
  - piezoelements, 278
- Dynamic, 13
- Dynamic pressure, 334
- $E_{Yul}^E$  ( $Y_{ul} - Y$  from Young), 294
- Electric, 461
  - charges, 103
  - contact, 226
  - damping of piezoceramic sensors with feedback, 147
  - equivalent scheme of resonant contact transducer, 415
  - feedback in piezoceramic sensors, 139
  - field, 220
  - filter scheme, 453
  - force microscopy, 478
  - parameters, 34
  - potential, 221
  - properties, 226
  - scheme, 268, 336, 458
- Electro-acoustic sensitivity, 219
- Electrodes, 309
- Electroelastic plates, 189
- Electromechanical, 127
  - feedback, 347
  - transformation, 327
  - transformation coefficient, 299
- Electro-optical materials, 17
- Electrostatics equations, 190
- Enhancement, 337
- Epoxy glues, 226
- Equations, 28, 30, 58, 438
- Equivalent circuit, 236
  - of charge amplifier, 134
  - of device, 236
  - of element  $W_3$  transformation, 121
  - of piezoelectric sensor with feedback, 114
- Equivalent diagrams, 236
- Equivalent electric circuit, 104, 107, 110
  - of charge amplifier, 100, 102
  - of piezoelectric accelerometer and charge amplifier, 108
- Equivalent electric scheme, 27, 52
- Equivalent electric scheme of piezoelectric accelerometer, 390
- Equivalent electromechanical scheme of radiator and receiver, 292
- Equivalent mechanical model of link, 268
- Equivalent mechanical scheme, 389
- Equivalent noise charge, 108
- Equivalent piezoelement scheme, 32
- Equivalent scheme, 34, 52, 460
  - and sensor, 463, 464, 466
  - disk piezoelectric transformer, 54
- Errors, 22, 423
- Excitation scheme, 435
- FB, *see* Feedback, *see* Feedback, *see* Feedback, *see* Feedback, *see* Feedback
- FB channel, 174
- FB circuit, 141
- FB., *see* Feedback
- Feedback (FB), 126, 348, 404, 405, 426
  - Feedback in piezoceramic sensors, 113
  - in Korotkoff sound sensors, 347
  - influence on nonlinear and frequency distortions, 117
  - influence on static systems errors, 119
  - influence on time constant of sensors, 118
- Ferro-soft, 16

- Ferro-stiffness, 17
- Filter, 456
- Filter schemes, 460, 461
- First harmonic, 248
- First overtone, 11, 61
- Flat bimorph piezoelements, 486
- Flexural, 180
- Flexural equations of bimorph vibrations, 192
- Flow frequency, 111
- Fluctuation, 58
- Fluctuations of piezoceramic rods, 47
- Fluctuations piezoceramic disk, 50
- Flux characteristics, 225
- Force transducer, 440
- Form of acoustic field created, 321
- Formulas, 18, 25
- Free oscillation oscillograms of resonant transducer, 419
- Freedom, 412
- Frequencies, 294
- Frequency, 62, 296, 416, 424
- Frequency characteristic, 149
- Frequency range, 123
- Frequency the formula, 57
- Frequency transfer coefficient, 456
- Frequency-independent FB, 116
- Frequency-modulated oscillation, 422
- Frequency-selective, 17
- Fulfills, 475
- Full electric conductivity, 46
- Full system, 28
- Fundamental constant, 29
  
- Gain coefficient, 106
- General transfer function, 124
- Glued, 226
- Good mechanical quality  $Q_m$ , 15
  
- Hamilton principle, 186
- Harmonic vibration equation, 388
- Harmonious fluctuations, 30
- Harmonious modulation, 424
- Harmonious vibrations, 438
- Heaviside formula, 239, 418
- High-pass, 460
- High-pass filters, 458, 459
- High-temperature, 17
- Hindrances, 351
- Hindrances at arterial pressure measurement, 350
- Hollow ceramic cylinder, 385
- Hollow cylinder-shaped monomorph, 309
- Hollow piezoceramic cylinder, 385
- Hydro-acoustic antennas, 300
- Hydro-acoustic piezoceramic transducers, 305
- Hydro-acoustic transducer, 289
- Hydroacoustic, 309
  
- Impedances, 108
- Independent frequency equations of piezoceramic disk, 193
- Influence of frequency-dependent feedback, 114
- Influence of input capacitive load on charge amplifier, 107
- Input, 118
- Integral condition, 190
- Integrating circuit, 245
- Integrating properties, 94
  
- Jahn–Teller effect, 80
- Jahn–Teller pseudo-effect, 80
  
- Kinematic hypotheses, 185
- Kirchhoff's condition, 222
- Kistler, 391
- Korotkoff sound sensors, 333
  
- Label, 393
- Lamellar, 298
- Lennard–Jones potential, 476
- Linear, 184
- Linear or vibration accelerations, 334
- Linear theory of piezoelectricity, 59
- Linearization, 439
- Local, 414
- Longitudinal fluctuations of a rod in a longitudinal field, 49
- Longitudinal fluctuations of a rod in a transverse field, 48
- Longitudinal polarization, 32, 34
- Low-frequency, 76
- Low-frequency acoustic vibration creation, 309
- Low-frequency piezoceramic radiator, 311
- Low-pass, 456, 457
- Low-pass filter schemes, 459
  
- Magnet, 253
- Magnet diameter–gap, 256
- Magnetic system energy, 263

- Magnetostrictive constants, 302
- Magnets, 254
- Main types of piezotransducers, 318
- Material correlations, 190
- Maximal voltage ratio, 151
- Maximum transfer coefficient, 341
- Meander-shaped oscillation, 244
- Measurement, 11
- Measurement circuits, 202, 203
- Measurement circuits of asymmetric trimorph coplanar transducer, 208
- Measurement diagrams, 207, 210–213, 215–217
- Measurement of resonant frequency  $f_r$ , 9
- Measurement scheme, 478
- Measuring circuit, 235
- Measuring circuits of piezoelectric sensors, 99
- Measuring device block scheme, 424
- Mechanical, 226
- Mechanical model of piezoelectric accelerometer, 387
- Mechanical model of resonant contact transducer, 411
- Mechanical resonance frequency, 294
- Mechanical scheme, 54
- Mechanical stress, 338
- Mechanical vibrations, 311
- Metal membranes, 306
- Metal plate, 179
- Methods of scanning probe microscopy, 473
- Minimum, 423
- Minimum relative error, 205
- Model elements, 388
- Model of piezoelectric accelerometer, 393
- Modified differentiating circuit, 122, 124
- Module, 148
- Monitoring circuit of asymmetric bimorph piezoelements, 233
- Monitoring circuit of symmetric bimorph piezoelements, 233
- Monocrystal, 409
- Monolithic, 330
- Monolithic accelerometers, 383–386
- Monolithic broadband piezotransducers, 329
- Monolithic piezoelement, 325
- Monomorph Piezoceramic Elements, 25
- Movements, 191, 388
- Multi-element accelerometers, 386
  
- Nanomaterials, 471
- Nanomicroscopes, 471
- Nanosystem, 471
- Nanotechnologies, 471
  
- Negative, 127
- Negative feedback, 116
- Negative feedback in resonant piezosensors, 425
- Noise, 111
- Non-destructive quality control of materials and products, 317
- Non-resonant excitation of piezoelements, 327
  
- One prism sensor design, 442
- Operating principle, 330
- Operational form, 417
- Optical registration scheme, 477
- Optimum load resistance, 344
- Oscillations, 482
- Oscillatory, 94
- Oscillatory contour, 241–243
- Oscillogram of piezoceramic summer input signal, 312
- Oscillograms of piezotransformer signals, 96
- Output resistances, 118
- Output signal, 277
- Output signals of piezomagnetic sensor, 276
- Output signals of tachometer piezomagnetic sensor, 265, 273
- Overtone, 62
  
- Parameters, 8
- Parameters of disk transformers, 65
- Phase characteristics, 150
- Phase–frequency, 148
- Phase–frequency characteristic, 76
- Piezo-modules, 13
- Piezoceramic, 432
- Piezoceramic accelerometer, 405
- Piezoceramic accelerometers are sensors, 381
- Piezoceramic bar, 19
- Piezoceramic cylinders, 305
- Piezoceramic disk, 18, 186
- Piezoceramic element, 135
- Piezoceramic materials, 8, 16, 409
- Piezoceramic radiators, 309
- Piezoceramic rectangular plate, 19
- Piezoceramic scanners, 471, 486
- Piezoceramic sensor, 120, 124, 128, 130–132, 149
- Piezoceramic sensors, 130
- Piezoceramic transducer, 218
- Piezoceramic transducers fundamental mode and electric activation, 304
- Piezoceramic transformers, 51
- Piezoceramics, 383



- Piezoeffect, 236
- Piezoelectric, 382, 383, 398
- Piezoelectric asymmetric, 196
- Piezoelectric body, 8
- Piezoelectric Elements, 400
- Piezoelectric pulse sensors, 335
- Piezoelectric sensor, 195
- Piezoelectric system of sensors, 391
- Piezoelectric transducers, 147
- Piezoelectric transformers, 51, 54
- Piezoelement, 29, 34, 72, 135, 153, 269, 309, 311, 327, 331, 412, 436
- Piezoelement diameter, 195
- Piezoelement electrode division, 343
- Piezoelement electrodes, 342
- Piezoelement in FB circuit, 134
- Piezoelement in FB circuit of charge amplifier, 130
- Piezoelement movement equation, 33
- Piezoelement vibration, 312
- Piezoelements, 180, 220, 222, 306, 319, 344, 352, 447, 459, 460
- Piezoelements design, 282
- Piezoelements in a non-rigid fluctuation mode, 35
- Piezoelements in a rigid fluctuation mode, 36
- Piezomagnetic electro-acoustic transducers, 282
- Piezomagnetic resonant humidity sensor, 284
- Piezomagnetic sensor models, 266
- Piezomagnetic sensors, 253, 275, 281
- Piezomagnetic sensors of tachometers, 261
- Piezomagnetic tachometer sensor, 270
- Piezomagnetic tachometer sensors design simplification, 278
- Piezomagnetic tachometers, 277, 278, 282
- Piezomagnetic transducers, 273
- Piezomodules, 302, 338
- Piezopolymer film, 394
- Piezoresonator, 28, 34
- Piezorezonant accelerometer, 443
- Piezorezonator calculations, 35
- Piezosensor characteristics, 438
- Piezosensor circuit and characteristics, 137, 138
- Piezosensors, 125, 145, 161, 166, 169, 170, 173–175, 428, 431, 433
- Piezotransducer, 306–308, 335
- Piezotransducer amplitude–frequency response (AFR), 320
- Piezotransducer radiation field, 322
- Piezotransducer with feedback, 114
- Piezotransformer, 141, 244, 432, 435, 443, 444
- Piezotransformer circuits, 86, 95
- Piezotransformer in FB circuit, 142
- Piezotransformers, 85, 90, 461, 462, 465
- Piezotron system, 391
- Planar, 192
- Poisson coefficients, 189
- Poisson's coefficient, 12
- Polarization is radial, 295
- Potential distribution, 195
- Powder, 227
- Preamplifier, 102, 106
- Pressure force, 420
- Pressure sensor, 447
- Prisms, 441
- Probe, 480
- Probe sensor console curvature, 477
- Properties, 75
- Properties and descriptions of piezomaterials, 5
- Pulsation wave sensor, 354
- Pulse, 200, 202, 203, 210, 212, 213, 215, 216
- Pulse characteristics, 238, 242–244
- Pulse characteristics for device, 241
- Pulse sensor, 335
- Pulse waves, 354
- $Q$  factor, 150
- Quartz, 5
- Quartz transverse cylinder-shaped piezoelement, 84
- Radial polarized piezoceramic cylinder, 482
- Radiators, 309
- Range, 108
- Range of measurements, 21
- Ratios of electromechanical transformations, 291
- Real area contact, 413
- Real contact area, 419
- Receiving transducer specifications, 308
- Reception, 327
- Rectangular magnets, 257
- Rectangular parallelepiped base, 398
- Rectangular parallelepiped-shaped, 72
- Rectangular pulse, 245
- References, 97, 111, 176, 228, 249, 284, 313, 331, 355, 406, 448, 468, 488
- Relative dielectric permeability, 12
- Relative error, 142, 165
- Relative resonant interval, 67
- Relative sensitivity, 437
- Resistance, 297
- Resonance area, 309

- Resonance frequencies, 25
- Resonant, 60, 424
- Resonant accelerometer, 444
- Resonant contact sensors, 410
- Resonant frequency, 34, 309, 388
- Resonant frequency conductivity, 57
- Resonant interval overtone, 64
- Resonant piezoceramic sensors, 409
- Resonant piezosensor, 417, 422, 430
- Resonant sensor, 441
- Resonant transducer, 426
- Resonant volume piezotransducers, 323
- Resonators, 55, 235, 443
- Rings, 55
- Roots of the frequency, 67
- Round bimorph plate, 180
  
- $\sigma_{ex}$ , 302
- $\sigma_{eM.ex}$ , 302
- Sample magnetic field, 480
- Scanner, 486
- Scanner equivalent electric scheme, 488
- Scanner of probe micro-movements, 472
- Scanners based, 485
- Scanners on hollow piezoceramic cylinders, 481
- Scanning tunneling microscopy, 473
- Schematic diagram, 266
- Schematic image, 330
- Scheme, 405, 420, 421, 459
- Scheme of gas pressure sensor, 446
- Scheme of influence on sensor, 351
- Scheme of piezomagnetic cylindrical transducer, 254
- Scheme of tachometer piezomagnetic sensor, 261
- Schemes, 349, 462, 465
- Sections of round simple, 429
- Seismometry, 398
- Selection of energy transformation method, 301
- Sensitive differential element, 395
- Sensitive element of three-dimensional accelerometer, 400
- Sensitivity, 21, 150, 224, 337, 345, 426, 433
- Sensitivity of trimorph, 222
- Sensor, 21, 32, 102, 141, 282, 336, 338, 340, 341, 347, 348, 443, 448, 460
- Sensor characteristics, 336
- Sensor design, 96, 264
- Sensor of Korotkoff sounds, 353
- Sensor of static force, 339
- Sensor on acoustically connected resonators, 445
- Sensor output voltage, 254–256, 259, 345
- Sensor output voltage dependence, 260
- Sensor output voltage–gap, 258
- Sensor piezoelement, 453
- Sensor sensitivity, 165, 342
- Sensor transfer function, 270, 340
- Sensor voltage–gap, 259
- Sensors, 160, 165, 335, 435, 459–462, 465
- Sensors of Korotkoff sounds, 333
- Sensors with combined feedback, 143
- Sensors with two feedback channels, 151
- Short historical essay, 1
- Signal spectrum, 244
- Simplified equivalent electric circuit of charge amplifier, 100
- Simplified scheme of tunnel current feedback organization, 475
- Spatial electromechanical NFB, 120
- Spatial energy–force structure, 71
- Speed of sound, 15
- Sphere, 293
- Spherical piezoceramic transducers, 298
- Stabilization condition, 426
- Static correlation conditions, 221
- Static electromechanical coupling coefficients, 180
- Static force sensor, 436
- Static mode, 14
- Stepwise concentrator, 433
- Stepwise concentrator-shaped piezoelement, 431
- Stereophonic resonant piezoelectric pickup, 432
- Stress, 440
- Stresses, 414
- Suppression of in-phase and vibration hindrances, 353
- Suppression of vibration hindrances, 280, 352
- Surface active piezotransducer, 329
- Surface active volume piezotransducer, 324
- Symmetric, 180
- Symmetric bimorph sensor, 183, 185
- Symmetric bimorph transducers, 182
- Symmetric coplanar trimorph transducer, 209
- Symmetric trimorph transducer, 215
- System reaction, 238
  
- Tachometer piezomagnetic sensor, 266
- Taylor series, 149
- Technology of bimorph piezoelement production, 224

- Tensor, 6
- Tensor components, 302
- Test set, 336
- Tetrahedral prism, 396
- Theory, 189
- Thick piezotransducers, 328, 330
- Thin disks, 54
- Three bimorph elements, 486
- Three-coordinate scanner, 486
- Three-dimensional piezoelectric accelerometer, 399
- Traditional, 88
- Transducer, 142, 145, 222
- Transducer block diagram, 206
- Transducer characteristics, 427
- Transducer output, 135
- Transducer research methods, 7
- Transducer sensitivity, 143, 433
- Transducer without, 219
- Transducer works, 123
- Transducers, 317, 338
- Transfer coefficient, 436
- Transfer coefficient (sensitivity), 76
- Transfer function, 125, 153, 164
- Transfer function Laplace, 267
- Transformer, 240, 242
- Transformer Problem, 222
- Transformers internal, 75
- Transient characteristics, 88–90
- Transient characteristics of piezotransformers, 91, 92
- Transient characteristics of traditional piezotransformers, 89
- Transient characteristics of transducers, 78
- Transitive, 200, 202, 203, 207, 210–213, 215, 216
- Transitive characteristic, 246, 247, 269
- Transitive characteristic of piezomagnetic sensors, 272
- Transitive function, 239
- Transverse accelerometer, 396
- Transverse ceramic piezoelement, 85
- Transverse cylinder-shaped element, 85
- Transverse piezoelectric transducers, 82
- Transverse piezoelements, 73
- Transverse polarization, 28
- Transverse–longitudinal transformer, 52
- Trimorph, 179
- Trimorph piezoelements, 196
- Trimorph transducer, 200, 202, 204, 206, 208–210, 212, 213
- Trimorphic element, 403
- Tripod scanner on tubular piezoelements, 482
- Two bimorph elements, 401, 402
- Two charge amplifiers, 170
- Two degrees, 412
- Two systems, 309
- Two types of concentrators, 313
- Two-circuit feedback, 405
- Typical oscillatory (vibrating) systems, 290
  
- Ultrasonic concentrators, 428, 430, 448
- Ultrasonic devices, 318
- Ultrasonic technology, 428
- Unit pulse function, 238
  
- Various magnet, 255
- Vibration, 190, 381, 431
- Vibration equations, 191
- Vibration system, 412
- Vibrations, 388, 412, 435
- Vibrations of asymmetric coplanar trimorph piezotransducer, 216
- Vibronic theories of ferroelectricity, 80
- Voltage, 135, 160, 165, 166, 169, 174, 412, 431
- Voltage amplifiers, 110, 111, 161, 164, 175
- Voltage and resistance diagrams in piezosensor, 115
- Voltage equation, 417
  
- Young's modulus, 14, 298